BEILSTEIN JOURNAL OF ORGANIC CHEMISTRY

Superstructures with cyclodextrins: Chemistry and applications III

Edited by Gerhard Wenz and Eric Monflier

Imprint

Beilstein Journal of Organic Chemistry
www.bjoc.org
ISSN 1860-5397
Email: journals-support@beilstein-institut.de

The *Beilstein Journal of Organic Chemistry* is published by the Beilstein-Institut zur Förderung der Chemischen Wissenschaften.

Beilstein-Institut zur Förderung der
Chemischen Wissenschaften
Trakehner Straße 7–9
60487 Frankfurt am Main
Germany
www.beilstein-institut.de

BEILSTEIN JOURNAL OF ORGANIC CHEMISTRY

Superstructures with cyclodextrins: chemistry and applications III

Gerhard Wenz*[1] and Eric Monflier*[2]

Editorial

Open Access

Address:
[1]Saarland University, Organic Macromolecular Chemistry, Campus C4 2, 66123 Saarbrücken, Germany and [2]Université d'Artois, Unité de Catalyse et de Chimie du Solide (UCCS), CNRS, UMR 8181, Rue Jean Souvraz, SP 18, 62307 Lens, France

Email:
Gerhard Wenz* - g.wenz@mx.uni-saarland.de; Eric Monflier* - eric.monflier@univ-artois.fr

* Corresponding author

Keywords:
cyclodextrins

Beilstein J. Org. Chem. **2016,** *12,* 937–938.
doi:10.3762/bjoc.12.91

Received: 21 April 2016
Accepted: 26 April 2016
Published: 10 May 2016

This article is part of the Thematic Series "Superstructures with cyclodextrins: Chemistry and applications III".

Guest Editors: G. Wenz and E. Monflier

Cyclodextrins (CDs) are of increasing scientific and commercial interest because they are readily available, harmless and well-defined, forming sophisticated supramolecular structures in aqueous media. More than 2,300 publications and more than 1,200 patents appeared in 2015 in which CDs played a significant role. As exemplified in the following, CD chemistry has developed into a very attractive field of research.

The cell-penetrating peptide octa-arginine was conjugated to methylated β-CD. The resulting biofunctionalized host was able to transport a porphyrin sulfonate into HeLa cells used in photodynamic therapy [1]. Furthermore, it was found that lactose-appended β-CD lowers the cholesterol level in HepG2 cells – a result that is relevant for the treatment of Niemann–Pick-type C disease [2]. Metal-organic frameworks (MOFs) created from native CDs can be applied for the separation of isomeric xylenes or styrene from ethylbenzene [3,4]. Highly porous networks were synthesized by crosslinking β-CD with tetrafluoroterephthalonitrile. These networks were able to almost completely remove pollutants (e.g., bisphenol A) within a short time from wastewater [5]. Stimuli-responsive nanoparticles were assembled by the group of B. J. Ravoo using host–guest interactions between polyethyleneimine grafted with β-CD and a polyamidoamine dendrimer decorated with ferrocene. The formation of the superstructures was reversible by electrochemical oxidation of the ferrocene moieties [6].

Furthermore, significant progress has been achieved in the synthesis of CD polyrotaxanes. The one-pot and one-step polyrotaxane synthesis of β-CDs was performed in aqueous solution by employing a click reaction [7] as well as by radical copolymerization [8]. Slide-ring gels, synthesized by the group of K. Ito through the crosslinking of the hydroxy groups of CD polyrotaxanes, showed peculiar material properties [9] such as extreme stretchability [10]. These mobile networks are potentially useful as self-healing coatings [11].

Finally, recent results have shown that CDs are precious molecular tools that can be used for the design of highly active heterogeneous catalysts. Accordingly, the catalytic transformation of bio-oil has been achieved over Cu/MCM-41 and Cu/Kit-6 catalysts obtained by a CD assisted co-impregnation method [12].

Furthermore, the combination of template-directed colloidal self-assembly with a CD-assisted impregnation enabled to prepare highly active and selective Ru/TiO_2 catalysts for the hydrogenation of oleic acid methyl ester [13].

The latest results of CD chemistry have been exchanged at two international conferences in 2015. The *Joint Conference of 8th Asian Cyclodextrin Conference and 32nd Cyclodextrin Symposium* with 200 participants, 34 oral presentations and over 100 poster contributions took place in Kumamoto, Japan on May 14–16, 2015. The *4th European Conference on Cyclodextrins* was held in Lille, France on October 6–9, 2015 and brought together 170 researchers from 29 countries across the world. This congress with 130 presentations covered all fields of cyclodextrin research such as pharmacy, materials, catalysis, remediation, formulation and chemical analysis.

Some remarkable original papers and reviews are published in this Thematic Series of the *Beilstein Journal of Organic Chemistry*. In particular, the group of F. Estour has published an update on the current application of CDs for the detoxification of organophosphorus compounds [14]. In fact, the bowl-shaped structure of cyclodextrins is ideally suited for the design of new chemical scavengers for organophosphorus compounds, allowing these highly dangerous substances to be trapped and hydrolyzed before they reach their biological target. G. Cravotto et al. have reported on the recent advances in enabling technologies and green processes in CD chemistry [15]. By increasing heat and mass transfer, the protocols (assisted by microwaves, ultrasound or ball mills) appeared to be energetically more efficient as compared to classical synthetic tools.

Gerhard Wenz and Eric Monflier

Saarbrücken, Lens, April 2016

References

1. Kitagishi, H.; Chai, F.; Negi, S.; Sugiura, Y.; Kano, K. *Chem. Commun.* **2015,** *51,* 2421–2424. doi:10.1039/C4CC09042J
2. Motoyama, K.; Hirai, Y.; Nishiyama, R.; Maeda, Y.; Higashi, T.; Ishitsuka, Y.; Kondo, Y.; Irie, T.; Era, T.; Arima, H. *Beilstein J. Org. Chem.* **2015,** *11,* 2079–2086. doi:10.3762/bjoc.11.224
3. Holcroft, J. M.; Hartlieb, K. J.; Moghadam, P. Z.; Bell, J. G.; Barin, G.; Ferris, D. P.; Bloch, E. D.; Algaradah, M. M.; Nassar, M. S.; Botros, Y. Y.; Thomas, K. M.; Long, J. R.; Snurr, R. Q.; Stoddart, J. F. *J. Am. Chem. Soc.* **2015,** *137,* 5706–5719. doi:10.1021/ja511878b
4. Hartlieb, K. J.; Holcroft, J. M.; Moghadam, P. Z.; Vermeulen, N. A.; Algaradah, M. M.; Nassar, M. S.; Botros, Y. Y.; Snurr, R. Q.; Stoddart, J. F. *J. Am. Chem. Soc.* **2016,** *138,* 2292–2301. doi:10.1021/jacs.5b12860
5. Alsbaiee, A.; Smith, B. J.; Xiao, L.; Ling, Y.; Helbling, D. E.; Dichtel, W. R. *Nature* **2016,** *529,* 190–194. doi:10.1038/nature16185
6. Mejia-Ariza, R.; Kronig, G. A.; Huskens, J. *Beilstein J. Org. Chem.* **2015,** *11,* 2388–2399. doi:10.3762/bjoc.11.260
7. Yu, S.; Yuan, J.; Shi, J.; Ruan, X.; Wang, Y.; Gao, S.; Du, Y. *J. Mater. Chem. B* **2015,** *3,* 5277–5283. doi:10.1039/C5TB00627A
8. Kali, G.; Eisenbarth, H.; Wenz, G. *Macromol. Rapid Commun.* **2016,** *37,* 67–72. doi:10.1002/marc.201500548
9. Kato, K.; Mizusawa, T.; Yokoyama, H.; Ito, K. *J. Phys. Chem. Lett.* **2015,** *6,* 4043–4048. doi:10.1021/acs.jpclett.5b01782
10. Bin Imran, A.; Esaki, K.; Gotoh, H.; Seki, T.; Ito, K.; Sakai, Y.; Takeoka, Y. *Nat. Commun.* **2014,** *5,* No. 5124. doi:10.1038/ncomms6124
11. Noda, Y.; Hayashi, Y.; Ito, K. *J. Appl. Polym. Sci.* **2014,** *131,* No. 40509. doi:10.1002/app.40509
12. Karnjanakom, S.; Guan, G.; Asep, B.; Hao, X.; Kongparakul, S.; Samart, C.; Abudula, A. *J. Phys. Chem. C* **2016,** *120,* 3396–3407. doi:10.1021/acs.jpcc.5b11840
13. Bleta, R.; Noël, S.; Addad, A.; Ponchel, A.; Monflier, E. *RSC Adv.* **2016,** *6,* 14570–14579. doi:10.1039/C5RA27161D
14. Letort, S.; Balieu, S.; Erb, W.; Gouhier, G.; Estour, F. *Beilstein J. Org. Chem.* **2016,** *12,* 204–228. doi:10.3762/bjoc.12.23
15. Cravotto, G.; Caporaso, M.; Jicsinszky, L.; Martina, K. *Beilstein J. Org. Chem.* **2016,** *12,* 278–294. doi:10.3762/bjoc.12.30

License and Terms

BEILSTEIN JOURNAL OF ORGANIC CHEMISTRY

Qualitative evaluation of regioselectivity in the formation of di- and tri-6-*O*-tritylates of α-cyclodextrin

Keisuke Yoshikiyo*, Yoshihisa Matsui and Tatsuyuki Yamamoto

Full Research Paper

Address:
Faculty of Life and Environmental Science, Shimane University, 1060 Nishikawatsu, Matsue, Shimane, 690-8504, Japan

Email:
Keisuke Yoshikiyo* - yoshikiyo@life.shimane-u.ac.jp

* Corresponding author

Keywords:
^{1}H and ^{13}C NMR spectroscopy; quantitative analysis; regioselectivity; tritylation; ultra-fast liquid chromatography (UFLC)

Beilstein J. Org. Chem. **2015,** *11,* 1530–1540.
doi:10.3762/bjoc.11.168

Received: 20 May 2015
Accepted: 11 August 2015
Published: 02 September 2015

This article is part of the Thematic Series "Superstructures with cyclodextrins: Chemistry and applications III".

Guest Editor: G. Wenz

Abstract

The quantitative analysis of reaction products showed that the reaction of $6^A,6^D$-di-*O*-trityl-α-cyclodextrin (CD), AD-isomer, with trityl chloride in pyridine at 55 °C gave $6^A,6^B,6^E$-tri-*O*-trityl-α-CD, the amount of which was only 25% of that of simultaneously formed $6^A,6^B,6^D$-tri-*O*-trityl-α-CD. This indicates that the bulky trityl groups of glucopyranose-A and -D (Glu-A and -D, respectively) in the AD-isomer mainly retard the additional tritylation of the C(6)-OH of the adjacent glucopyranoses in a counter-clockwise direction (Glu-F and -C, respectively). ^{1}H NMR spectra of the AD-isomer showed that the O(6)-H and C(6)-H signals of Glu-C and -F are shifted upfield due to the ring current of the trityl groups. Thus, it is concluded that the bulky trityl groups on Glu-A and Glu-D are oriented to Glu-F and Glu-C, respectively, and sterically retard additional tritylation on Glu-F and Glu-C. Similar steric hindrance was also observed in the additional tritylations of mono-6-*O*-trityl-α-CD, $6^A,6^B$-di- and $6^A,6^C$-di-*O*-trityl-α-CD's.

Introduction

Regioselective modification and deprotection on the primary hydroxy side of cyclodextrins (CDs) are of great importance in supramolecular chemistry, as they allow the preparation of sophisticated concave molecules such as multi- or hetero-functionalized CD derivatives that are important intermediates for the preparation of enzyme mimics [1-5]. The tritylation of cyclodextrin (CD) has attracted much attention, since the tritylates are useful intermediates for the preparation of a variety of functionalized CD derevatives [6-19]. CDs have hydroxy groups at the 2-, 3- and 6-positions of their glucopyranose (Glu) residues. However, the reaction of CD with trityl chloride in pyridine gives exclusively 6-*O*-substituted CD. CD is composed of six (α-CD), seven (β-CD), eight (γ-CD), or more Glu residues. Thus, a reaction of α-CD, for example, with trityl chloride (TrCl) gives mono- [7], di- [13,15,16], tri- [9,11], tetra- [18], and per-6-*O*-trityl derivatives [19]. The di-6-*O*-tritylate of α-CD involves three regioisomers, that are, 6^A,6^B-, 6^A,6^C-, and 6^A,6^D-di-*O*-tritylates (AB-, AC-, and AD-isomers, respectively), as shown in Scheme 1. These regioisomers were well separated and characterized [13]. The tri-6-*O*-tritylate of α-CD involves four regioisomers, that are 6^A,6^B,6^C-, 6^A,6^B,6^D-, 6^A,6^B,6^E-, and 6^A,6^C,6^E-tri-*O*-tritylates (ABC-, ABD-, ABE-, and ACE-isomers, respectively, Scheme 1). Among them, only a symmetrical molecule of the ACE-isomer was separated and characterized [9]. The tetratritylate of α-CD involves three regioisomers, among which 6^A,6^B,6^D,6^E-tetra-*O*-tritylate was separated and characterized [18]. The trityl group is so bulky that the additional tritylation of C(6)-OH on Glu adjacent to a previously tritylated Glu is considered to be sterically hindered. Thus, a reaction of α-CD with 3.3 equivalents TrCl in pyridine at 55 °C gave selectively the ACE-isomer in good yield (23%) [9]. However, the regioselectivity in the formation of di- or tri-6-*O*-trityl-α-CD has not always been quantitatively evaluated. The present work deals with the analysis of products in the reaction of α-CD, as well as mono- and di-6-*O*-trityl-α-CD's, with TrCl in pyridine to evaluate quantitiatively the steric effect of the bulky trityl group on the regioselectivity of the reaction. For the sake of clarity, it must be noted here that letters from A to F that identify individual glucopyranose units are numbered along with the α1→4 linkage direction, and that the term "clockwise direction" refers to the direction when viewed from the secondary hydroxy side, as shown in Scheme 1.

Results and Discussion

Identification of di- and tri-6-*O*-tritylates of α-CD

Mono-, di-, and tri-6-*O*-tritylates of α-CD were prepared by a reaction of α-CD with TrCl in pyridine at 55 °C according to the direction of literature [9], and separated by means of reversed-phase column chromatography. Three regioisomers of di-6-*O*-trityl-α-CD obtained gave well-separated peaks in UFLC (ultra-fast liquid chromatography) experiment (Figure 1), details of which will be described in the Experimental part. Four regioisomers of tri-6-*O*-trityl-α-CD also gave well-separated peaks in the UFLC chromatography (Figure 2), when acetonitrile/methanol/water (40/45/15, v/v/v) was used as an eluent. The di-6-*O*-trityl-α-CD regioisomers which gave the first, second, and third peaks in the UFLC chromatogram afforded well-defined ^{13}C NMR spectra (Figure 3a, b, and c, respectively) in dimethyl sulfoxide-d_6 (DMSO-d_6) at 50 °C. Tanimoto, et al. [13], have already reported the ^{13}C NMR spectra of the isomers measured in C_5D_5N. On the basis of a comparison of their spectra with ours, we assigned that the isomers which gave the first, second, and third peaks in the UFLC chromatogram are the AD-, AC-, and AB-isomers, respectively. This assignment was confirmed by UFLC analysis on the products of reactions of these three regioisomers with TrCl

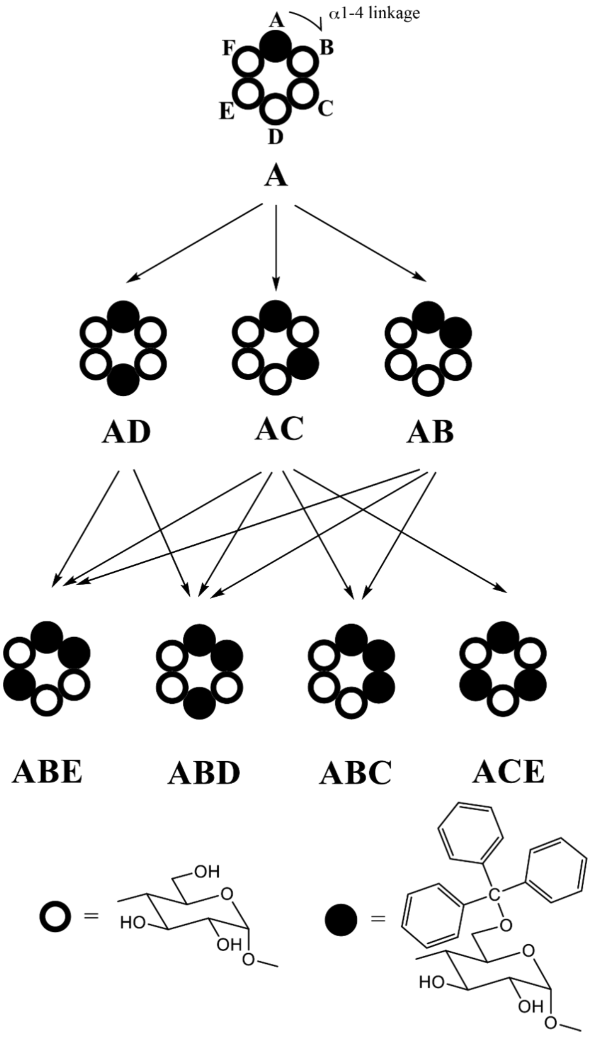

Scheme 1: Tritylates of α-CD examined in the present study and the reaction pathway. Letters A to F represent the glucopyranose units along with α1-4 linkage direction, numbered when viewed from the secondary hydroxy group side.

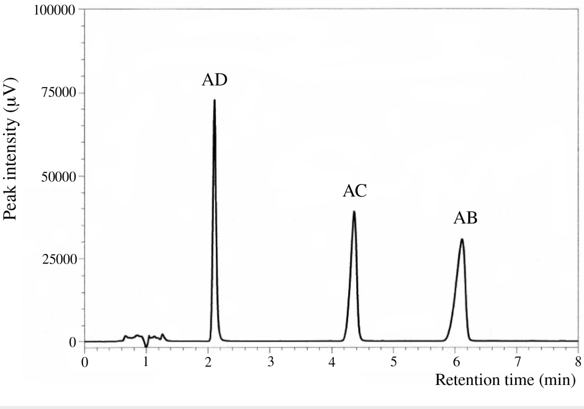

Figure 1: UFLC chromatogram of three regioismers of di-6-O-trityl-α-CD with 50% aqueous acetonitrile as an eluent.

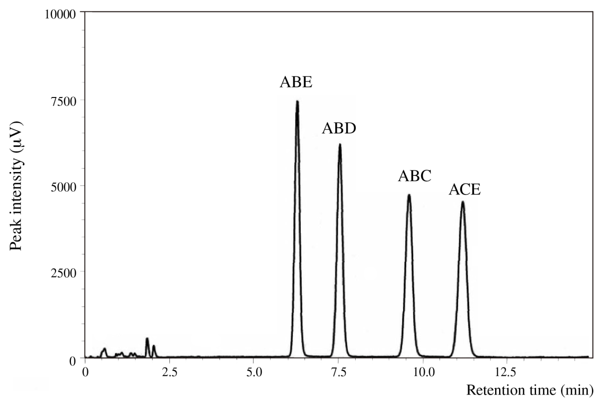

Figure 2: UFLC chromatogram of four regioisomers of tri-6-*O*-trityl-α-CD with an eluent of acetonitrile/methanol/water (40:45:15, v/v/v).

to give tri-6-*O*-trityl-α-CD. As Scheme 1 shows, the reaction of AD-isomer with TrCl gives only two tri-tritylates of ABD- and ABE-isomers. On the other hand, the additional tritylation of AB- and AC-isomers gives three (ABC-, ABD-, and ABE-) and four (ABC-, ABD-, ABE-, and ACE-) isomers, respectively. In practice, the additional tritylation of a ditritylate assigned to be AD-isomer by ^{13}C NMR spectroscopy gave only two (the first and second) peaks in UFLC analysis, whereas those assigned to be AB- and AC-isomers by ^{13}C NMR gave three (the first, second, and third) and four (the first, second, third, and fourth) peaks, respectively, in UFLC analysis. These results are in accord with the reaction pathway shown in Scheme 1. A similar method had been used for the identification of di- and tri-6-*O*-mesitylenesulfonyl-α-CD [20]. Scheme 1 also shows that the ACE-isomer is formed only by the reaction of the AC-isomer with TrCl, and we assigned that the fourth peak in UFLC chromatogram is due to the ACE-isomer. On the other hand, the ABC-isomer is not formed by the reaction of the AD-isomer with TrCl and is formed by the reactions of AC- and AB-isomers with TrCl. Thus, we assigned that the third peak is due to the ABC-isomer [20]. It is difficult to determine by UFLC analysis which of the ABD- or ABE-isomer gives the first or the second peak in UFLC. Here, we noted that $6^A,6^B,6^D$- and $6^A,6^B,6^E$-tri-6-*O*-mesitylenesulfonyl-α-CD's have already been identified by ^{1}H NMR spectroscopy [21,22]. Then, we tried to convert a regioisomer of tri-6-*O*-tritylates, which gave the first peak in UFLC, to tri-6-*O*-mesitylenesulfonyl-α-CD. The conversion pathway is shown in Scheme 2, where all the

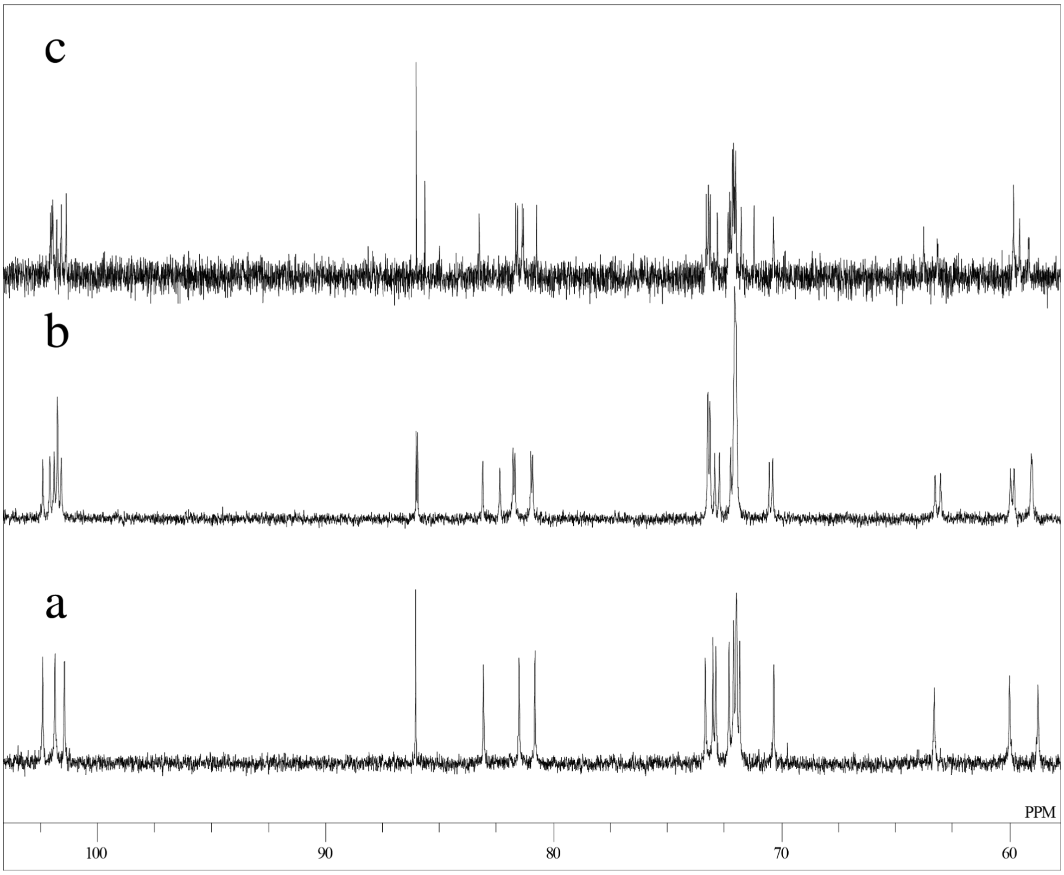

Figure 3: A part of ^{13}C NMR spectra of di-6-*O*-trityl-α-CD in DMSO-d_6 at 50 °C a) AD-isomer, b) AC-isomer, and c) AB-isomer.

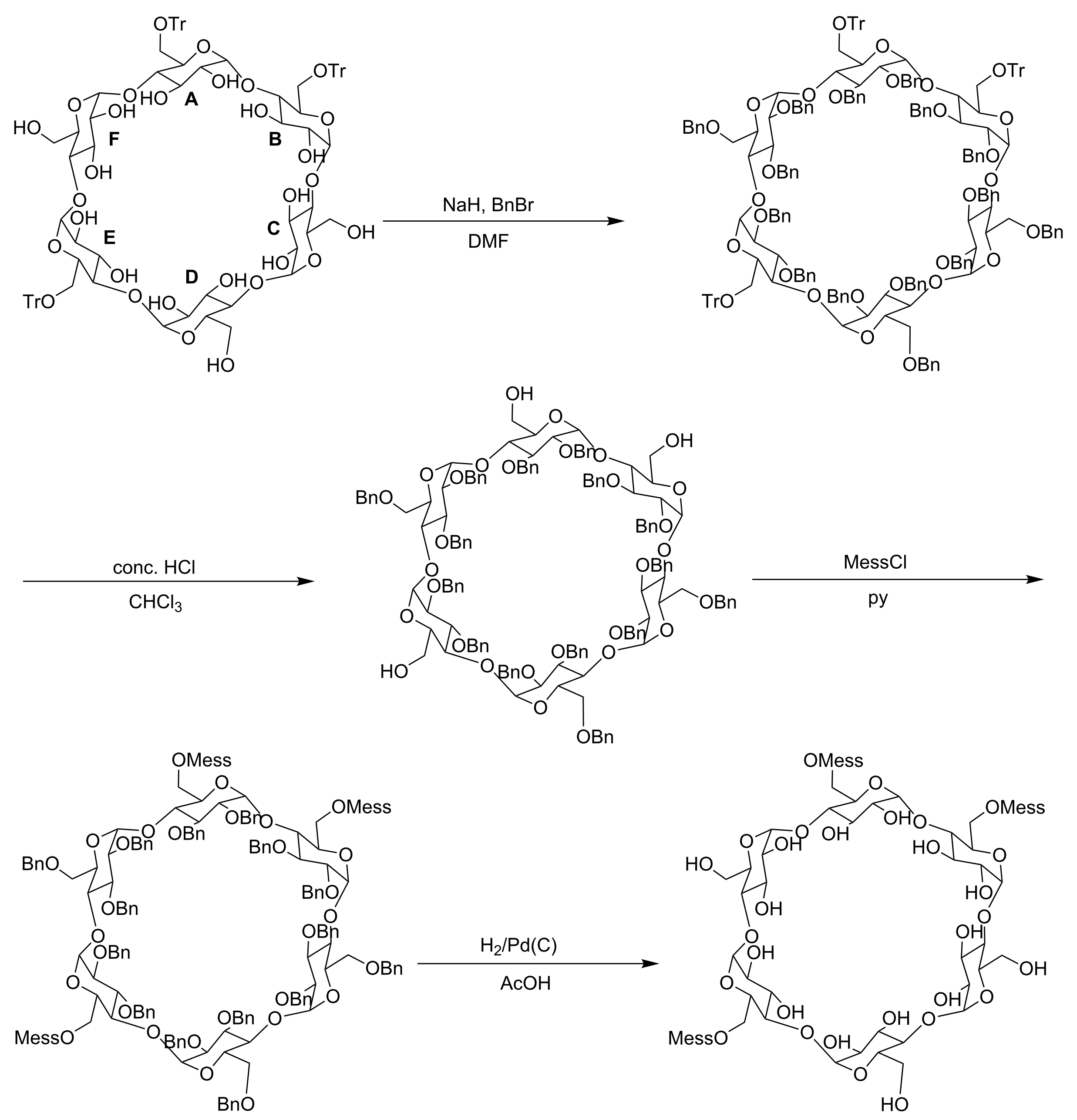

Scheme 2: A pathway of the conversion of a regioisomer of tri-6-*O*-trityl-α-CD (ABE isomer) to the corresponding tri-6-*O*-mesitylenesulfonyl-α-CD. Letters A to F represent the glucopyranose units, numbered in a clockwise direction when viewed from the secondary hydroxy group side. Abbreviations: Tr: trityl, Bn: benzyl, and Mess: mesitylenesulfonyl.

hydroxy groups of the regioisomer were substituted by benzyloxy groups, and the resulting per-benzylated compound was treated with conc. HCl to remove the trityl groups. The three hydroxy groups formed were mesitylenesulfonylated, and finally, the benzyl groups were removed by hydrogenation with Pd/C to form tri-6-*O*-mesitylenesulfonyl-α-CD. The retention time in UFLC and the ^{1}H NMR spectrum of the obtained mesitylenesulfonylate coincided with those of authentic $6^A,6^B,6^E$-tri-6-*O*-mesitylenesulfonyl-α-CD, respectively. Similar conversion of tri-6-*O*-trityl-α-CD to tri-6-*O*-mesitylenesulfonyl-α-CD was carried out for a regioisomer which gave the second peak in UFLC, and the ^{1}H NMR spectrum of the obtained mesitylenesulfonylate coincided with that of authentic $6^A,6^B,6^D$-tri-6-*O*-mesitylenesulfonyl-α-CD. Thus, we concluded that the regioisomers which gave the first and second peaks in UFLC are the ABE- and ABD-isomers, respectively. The ^{13}C NMR spectra for the four regioisomers of tri-6-*O*-trityl-α-CD in DMSO-d_6 at 50 °C are illustrated in Figure 4.

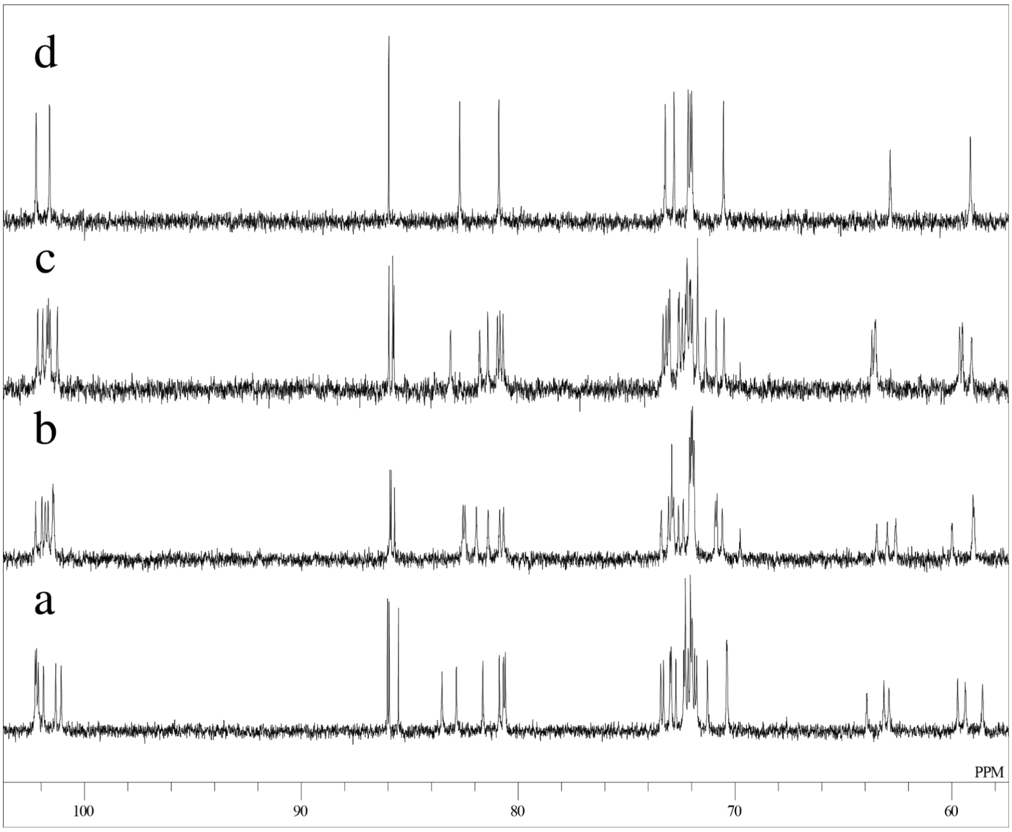

Figure 4: A part of ^{13}C NMR spectra of tri-6-*O*-trityl-α-CD in DMSO-d_6 at 50 °C. a) ABE-isomer, b) ABD-isomer, c) ABC-isomer, and d) ACE-isomer.

Regioselectivity in the formation of di- and tri-6-*O*-trityl-α-CD

Dried α-CD was allowed to react with TrCl in pyridine at 55 °C, and aliquots were withdrawn at hourly intervals to determine the concentrations of products by means of the UFLC analysis. The concentrations of mono-6-*O*-trityl-α-CD, α-CD(Tr)$_1$, and three regioisomers of ditritylates formed are plotted against reaction time in Figure 5. The concentration of α-CD(Tr)$_1$ smoothly increased with time. On the other hand, the concentrations of di-6-*O*-tritylates of α-CD were low at the beginning of the reaction and gradually increased with time, suggesting that the ditritylates are formed by additional tritylation of the previously formed α-CD(Tr)$_1$. If the reactivities of the C(6)-OH groups on the Glu residues of α-CD(Tr)$_1$ are equal to each other, AB- and AC-isomers would be produced in equal amount and in twice that of AD-isomer. In practice, the molar ratio of the products was about 0.40 ± 0.01:1.00:0.52 ± 0.01 (AB:AC:AD) in every aliquot. The AB-isomer was produced considerably less than the AC-isomer.

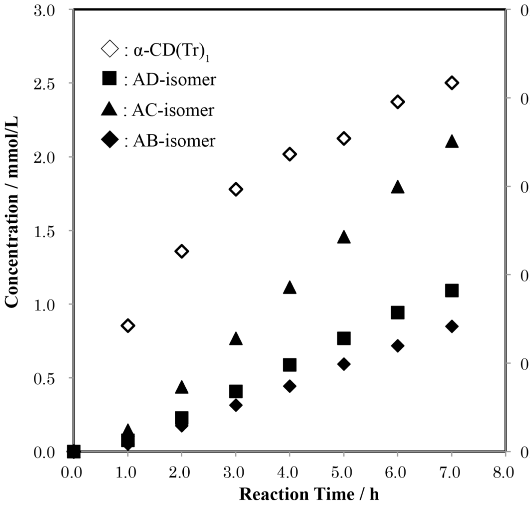

Figure 5: Time-course of the formation of mono- (left ordinate) and di-6-*O*-tritylates (right ordinate) of α-CD in a reaction of α-CD with TrCl in pyridine at 55 °C. Average mole ratio of AB:AC:AD = 0.40 ± 0.01:1.00:0.52 ± 0.02.

In order to investigate the formation of the ditritylates in detail, α-CD(Tr)$_1$ was directly tritylated in pyridine at 55 °C. Changes in concentration of three regioisomers of the ditritylates with time are illustrated in Figure 6. The average mole ratio of AB:AC:AD was 0.43 ± 0.01:1.00:0.50 ± 0.01, virtually the same as in the case when α-CD was used as reactant. We also tried to determine the concentrations of tri-6-*O*-tritylates of α-CD. However, the concentrations were so low that further

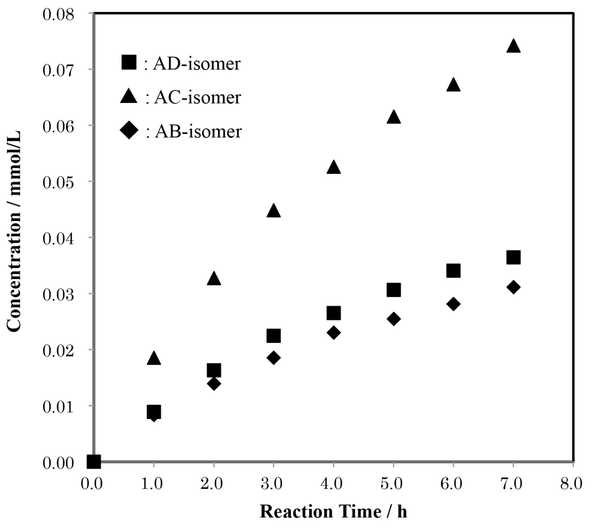

Figure 6: Time-course of the formation of the regioisomers of di-6-*O*-trityl-α-CD in a reaction of α-CD(Tr)$_1$ with TrCl in pyridine at 55 °C. Average mole ratios of AB:AC:AD = 0.43 ± 0.01:1.00:0.50 ± 0.01.

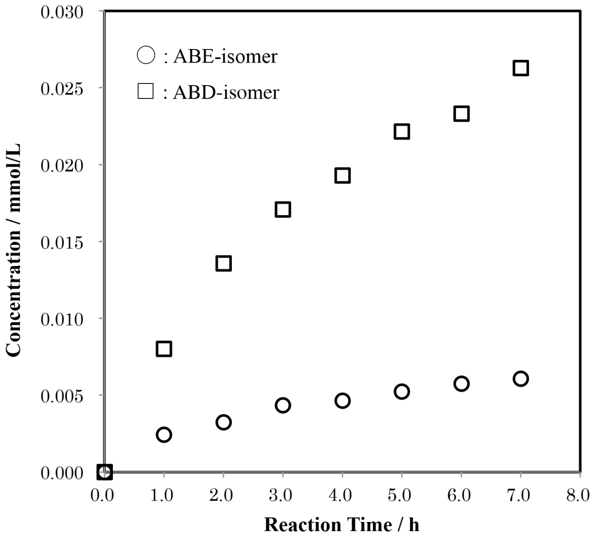

Figure 7: Time-course of the formation of the regioisomers of tri-6-*O*-trityl-α-CD in a reaction of AD-isomer with TrCl in pyridine at 55 °C. Average mole ratio of ABD:ABE = 1.00:0.25 ± 0.02.

tritylation of the ditritylates to tritritylates did not affect the mole ratio of the ditritylates. The small mole ratio of AB-isomer to AC-isomer suggests that the bulky trityl group on α-CD(Tr)$_1$ retards the additional tritylation of the C(6)-OH on the adjacent Glu-B and/or Glu-F. Glu-B is adjacent to Glu-A in a clockwise direction, and Glu-F, in a counter-clockwise direction.

Then, we carried out experiments using the AD-isomer as the reactant to elucidate which of the C(6)-OH of Glu-B or Glu-F is more restricted in the additional tritylation of α-CD(Tr)$_1$. If the trityl groups of Glu-A and -D of the AD-isomer retard the additional tritylation of the adjacent C(6)-OH in a clockwise direction (Glu-B and -E, respectively), the ABD-isomer will be the minor product and the ABE-isomer the major one. To the contrary, if they retard the additional tritylation of the adjacent C(6)-OH in a counter-clockwise direction (Glu-F and -C, respectively), the ABE-isomer will be the minor product and the ABD-isomer the major one. The quantitative analysis of the product in this reaction revealed that the ABE-isomer is formed in a smaller amount than the ABD-isomer, with a mole ratio of 0.25 ± 0.02:1.00 (Figure 7). This result indicates that the trityl groups of Glu-A and Glu-D in the AD-isomer mainly retard the additional tritylation of the C(6)-OH of the adjacent Glu in a counter-clockwise direction (Glu-F and Glu-C, respectively). Thus, the trityl group of Glu-A in α-CD(Tr)$_1$ will also mainly retard the additional tritylation of the C(6)-OH of the adjacent Glu in a counter-clockwise direction (Glu-F).

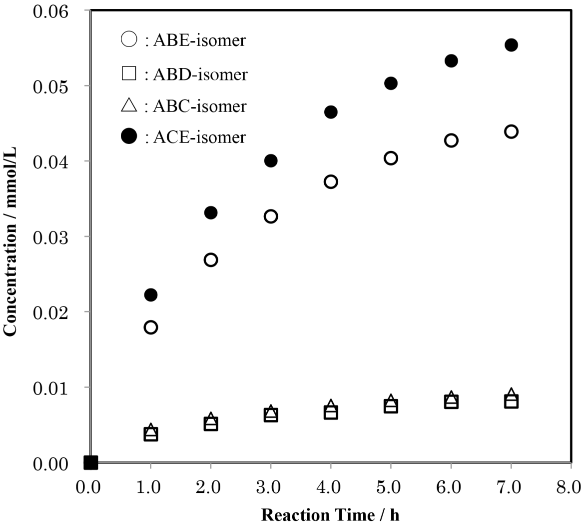

Figure 8: Time-course of the formation of the regioisomers of tri-6-*O*-trityl-α-CD in a reaction of AC-isomer with TrCl in pyridine at 55 °C. Average mole ratio of ABC:ABD:ABE:ACE = 0.17 ± 0.01:0.15 ± 0.01:0.80 ± 0.01:1.00.

Figure 8 shows the time-course of the formation of tri-6-*O*-tritylates of α-CD in the reaction of AC-isomer with TrCl in pyridine. In AC-isomer, Glu-B, -D, -E, and -F are chemically unequivalent to one another, and additional tritylation gives the four regioisomers of ABC-, ACD-, ACE-, and ACF. In this context, ACD- and ACF-isomers are identical to ABE- and ABD-isomers, respectively. If the additional tritylation occurs without regioselectivity, these regioisomers should be produced in an equal yield. In practice, the mole ratios of ABC-, ABD-, ABF-, and ACE-isomers in the reaction mixtures were virtually constant during the reaction time and equal to 0.17 ± 0.01:0.15 ± 0.01:0.80 ± 0.01:1.00. The additional tritylations of the C(6)-OHs on Glu-B and Glu-F, which are adjacent to Glu-C and Glu-A in a counter-clockwise direction, respectively, were again strongly retarded. Interestingly, the symmetrically substituted ACE-isomer was the major product, in clear contrast to the case of mesitylenesulfonylation of $6^A,6^C$-di-*O*-mesitylenesulfonyl-α-CD, where the ACE-isomer is the minor product [23].

Figure 9 shows the time-course of the formation of tri-6-*O*-tritylates of α-CD in the reaction of the AB-isomer with TrCl in pyridine. In the AB-isomer, the additional tritylation of Glu-C and -F gives the same product, the ABC-isomer. Thus, if the tritylation occurs without regioselectivity, the mole ratio of ABC-, ABD-, and ABE-isomers would be 2:1:1. In practice, the mole ratio was 0.71 ± 0.01:1.00:0.98 ± 0.01. Again, the tritylation of Glu-C and/or Glu-F, which are adjacent to Glu-B and Glu-A, respectively, was strongly retarded.

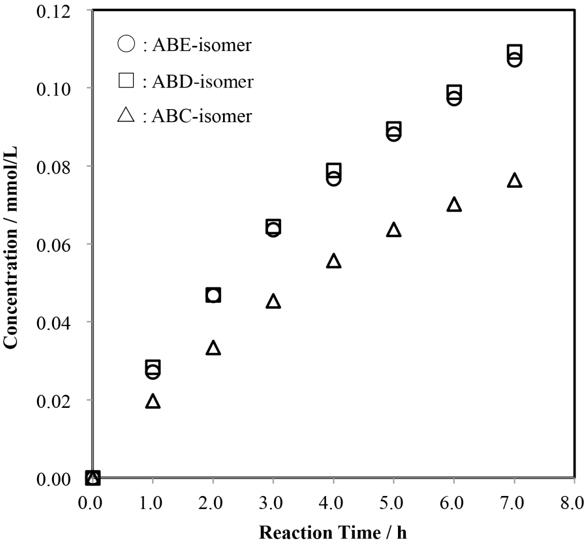

Figure 9: Time-course of the formation of the regioisomers of tri-6-*O*-trityl-α-CD in a reaction of the AB-isomer with TrCl in pyridine at 55 °C. Average mole ratios of ABC:ABD:ABE = 0.71 ± 0.01:1.00:0.98 ± 0.01.

^{1}H NMR spectroscopy of the AD-isomer

All the above results shows that the trityl group introduced to the C(6)-O of α-CD retards additional tritylation of the C(6)-OH of Glu adjacent to the previously tritylated Glu in a counter-clockwise direction. In order to confirm this suggestion, we estimated the orientation of the trityl groups in the AD-isomer by means of ^{1}H NMR spectroscopy in DMSO-d_6 (Figure 10). The AD-isomer is symmetrical and it is relatively easy to assign the ^{1}H NMR signals. The spectrum of the AD-isomer was fully assigned by means of 2D COSY, 2D ROESY, and 2D TOCSY spectra (Table 1). A 2D ROESY measurement gave a key spectrum (Figure 11) used for the assignment. The signal of the C(1)-H for Glu-A and -D in the F2 axis gave cross-peaks not only with the C(2)-H (δ 3.36) of the same Glu, but also with the C(4)-H (δ 3.56) of the adjacent Glu-B and -E. In the same manner, the signal of C(1)-H for Glu-B and -E gave a cross-peak with the C(4)-H (δ 3.47) of the adjacent Glu-C and -F, and that for Glu-C and -F gave a cross-peak with the C(4)-H (δ 3.37) of the adjacent Glu-D and -A. It is worth noting that the signal (δ 3.72) of the O(6)-H for Glu-C and -F was fairly up-field shifted (Δδ = −0.62 ppm) compared with that (δ 4.34) of α-CD. On the other hand, the signal of the O(6)-H for Glu-B and -E (δ 4.45) was slightly down-field shifted

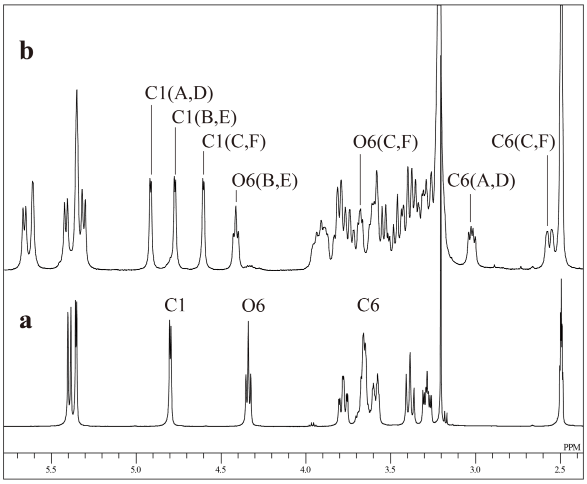

Figure 10: ^{1}H NMR spectra of α-CD (a) and the A,D-isomer (b) in DMSO-d_6 at 50 °C.

Table 1: Chemical shift of A,D-α-CD(tr)$_2$ in DMSO-d_6 at 50 °C.

	Chemical shift / ppm		
	Glu(A,D)	Glu(B,E)	Glu(C,F)
C(1)-H	4.92	4.78	4.61
C(2)-H	3.36	3.31	3.23
C(3)-H	3.80	3.82	3.72
C(4)-H	3.37	3.56	3.47
C(5)-H	3.89	3.75	3.68
C(6)-H(a)	3.40	3.96	3.30
C(6)-H(b)	3.02	3.62	2.55
O(2)-H	5.33	5.44	5.68
O(3)-H	5.63	5.37	5.37
O(6)-H	–	4.45	3.72
Tr(*o*)-H	7.32	–	–
Tr(*m*)-H	7.21	–	–
Tr(*p*)-H	7.13	–	–

(Δδ = 0.11 ppm). The signal (δ 2.55) of one of the C(6)-H's of Glu-C and -F was also significantly shifted up-field (Δδ = −1.11 ppm) compared with that (δ 3.66) of α-CD. These significant up-field shifts of the signals of the O(6)-H and C(6)-H for Glu-C and -F are attributable to the ring current of the phenyl moieties of the trityl groups on Glu-A and -D. Glu-C and -F are located at counter-clockwise directions from Glu-D and -A, respectively. Thus, it is reasonable to conclude that the trityl groups on Glu-A and -D are oriented to Glu-F and -C, respectively, and sterically retard additional tritylation of the C(6)-OHs on Glu-F and -C. Similar steric hindrance will occur in the tritylation of α-CD(Tr)$_1$ as well as in the tritylations of AB- and AC-regioisomers.

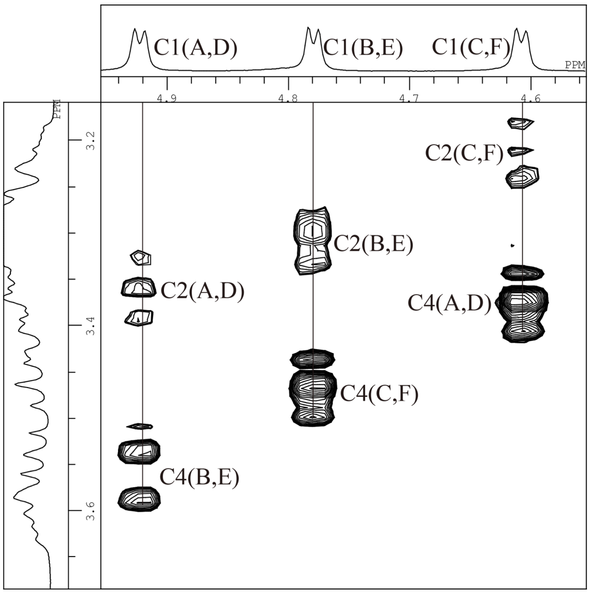

Figure 11: A part of 2D ROESY spectrum of the A,D-isomer in DMSO-d_6 at 50 °C.

In conclusion, the bulky trityl group on a tritylate of α-CD is oriented to the C(6)-OH on the adjacent glucopyranose in a counter-clockwise direction and sterically retards the additional tritylation of the C(6)-OH.

Experimental

Materials

The α-CD was supplied by Ensuiko Sugar Refining Co., Ltd., and dried overnight in vacuo at 110 °C before use. TrCl (Tokyo Chemical Industry Co., Ltd.), benzyl bromide and mesitylenesulfonyl chloride (Wako Pure Chemical Industries Ltd.) were used without further purification. Commercially available NaH in oil (50–77%) and Pd/C (Pd 10%) were used for the conversion of tri-6-*O*-trityl-α-CD to tri-6-*O*-mesitylenesulfonyl-α-CD. Reagent-grade pyridine was dried over CaH_2 and distilled in the presence of CaH_2 before use. *N*,*N*-Dimethylformamide (DMF) was also dried over CaH_2 and distilled before use. Acetonitrile for high performance liquid chromatography was purchased from Wako Pure Chemical Industries Ltd. DMSO-d_6 containing 0.05% v/v tetramethylsilane (Cambridge Isotope Laboratiories, Inc., 99.9 atom % D) was used for ^{1}H NMR measurements.

Apparatus

The tritylates of α-CD in a reaction mixture were quantitatively determined by means of a Shimadzu prominence UFLC system, which was composed of a pair of pumps (LC-20 AD), an autosampler (SIL-20 AC$_{HT}$), a column oven (CTO-20AC), a photodiode array detector (SPD-M20A), and a system controller (CBM-20A). Shim-pack XR-ODS (100 mm × 3.0 mm i.d. was used as a column, through which acetonitrile/water or acetonitrile/methanol/water was passed as an eluent. The flow rate of eluent was 0.5 mL/min, and the eluate was detected at 260 nm. The column temperature was maintained at 40 °C. Linear standard curves were prepared between the peak area of the tritylates and their concentrations. The ^{1}H and ^{13}C NMR spectra of the tritylates in DMSO-d_6 were recorded on a JEOL Model JNM-A400 FT NMR spectrometer (400 MHz for ^{1}H and 100 MHz for ^{13}C) with a sample tube of 5.0 mm diameter at 55 °C. Tetramethylsilane was used as an internal reference. High resolution ESIMS data were obtained using a Waters Synapt G2 mass spectrometer.

Synthesis of 6-*O*-tritylates of α-CD

6-*O*-Tritylates of α-CD were prepared by a reaction of α-CD with TrCl in pyridine at 55 °C according to a literature procedure [9], and separated by means of column chromatography with a Lober column LiChroprep RP-18 (Merck, 25 × 310 mm). Mono-, di-, and tri-6-*O*-tritylates were separated by the use of 30%, 40–50%, and 60% aqueous acetonitrile solutions, respectively, as eluents. Thin-layer chromagography (TLC) was carried out with Merck silica gel 60 F$_{254}$.

Mono-6-*O*-trityl-α-CD: ^{13}C NMR (100 MHz, DMSO-d_6) δ 144.03, 128.30, 127.57, 126.72, 102.28, 101.89, 101.85, 101.75, 85.97, 82.70, 82.03, 81.89, 81.84, 80.94, 73.21–73.12, 72.80, 72.21, 72.09–72.05, 71.89, 70.41, 63.08, 60.13, 59.96, 59.84, 58.96 ppm; HRMS–ESI *m/z*: [M + Na]$^+$ calcd for $C_{55}H_{74}O_{30}Na^+$, 1237.4163; found, 1237.4150.

Conversion of tri-6-O-trityl-α-CD to tri-6-O-mesitylenesuflonyl-α-CD

A regioisomer of tri-6-*O*-trityl-α-CD (605 mg, 0.356 mmol) which gave the first peak in UFLC was dissolved in DMF (30 mL). NaH in oil (1.00 g) and benzyl bromide (3.10 g, 18.1 mmol) were added to the solution in an ice bath, and the solution was stirred overnight. TLC on silica gel (hexane/ethyl acetate, 2:1) showed a product, having an R_f value of 0.60. The reaction mixture was diluted with $CHCl_3$ (100 mL) and washed with water (100 mL, 4 times). The $CHCl_3$ layer was dried over $CaSO_4$ and evaporated to dryness. The residue was chromatographed over Merck silica gel 60, using hexane/ethyl acetate (2:1) as an eluent. The crude tri-6-*O*-trityl-per-*O*-benzyl-α-CD (1.32 g) obtained was dissolved in $CHCl_3$ (100 mL), and the solution was vigorously shaken with concentrated HCl (30 mL) for 10 min to remove the trityl groups. TLC on silica gel (hexane/ethyl acetate, 1:1) showed a product, having an R_f value of 0.55. The $CHCl_3$ layer was washed with water (50 mL, 3 times), dried over $CaSO_4$, and evaporated to dryness. The residue was chromatographed over silica gel, using hexane/ethyl acetate (1:1) as an eluent to give a fairly pure product of trihydroxy-per-*O*-benzyl-α-CD (0.48 g, 0.21 mmol). The product was reacted with mesitylenesulfonyl chloride (0.62 g, 2.84 mmol) in pyridine (20 mL). TLC on silica gel (hexane/ethyl acetate 1:1) showed a product, having an R_f value of 0.91. The reaction mixture was evaporated to dryness, and the residue was dissolved in 50 mL of hexane/ethyl acetate (2:1). The solution was washed with water (50 mL, 3 times). The organic layer was dried over $CaSO_4$ and evaporated to dryness. The residue was chromatographed over silica gel, using hexane/ethyl acetate (2:1) as an eluent to give a fairly pure tri-6-*O*-mesitylenesulfonyl-per-*O*-benzyl-α-CD (0.51 g). The product was dissolved in 5 mL of acetic acid and hydrogenated in the presence of Pd/C (0.21 g) to remove the benzyl groups of the product. TLC on silica gel (butanone/ethanol/H_2O, 7:1:1) showed a product, having an R_f value of 0.47, which was equal to that of authentic tri-6-*O*-mesitylenesulfonyl-α-CD. The reaction mixture was filtered, and the filtrate was evaporated to dryness to give a fairly pure tri-6-*O*-mesitylenesulfonyl-α-CD (0.26 g, 0.17 mmol). The retention time of the product in UFLC with 43% aqueous acetonitrile as an eluent coincided with that of authentic A,B,E-tri-6-*O*-mesitylenesulfonyl-α-CD [23]. The ^{1}H NMR spectrum of the product in DMSO-d_6 at 50 °C also coincided with that of authentic A,B,E-tri-6-*O*-mesitylenesulfonyl-α-CD [23]. Thus, it was concluded that a regioisomer of tri-6-*O*-trityl-α-CD which gave the first peak in UFLC is A,B,E-tri-6-*O*-trityl-α-CD. Similar conversion of a regioisomer of tri-6-*O*-trityl-α-CD, which gave the second peak in UFLC, to tri-6-*O*-mesitylenesulfonyl-α-CD was carried out, and the resulting product was confirmed to be A,B,D-tri-6-*O*-mesitylenesulfonyl-α-CD by ^{1}H NMR spectroscopy.

Reaction of α-CD or α-CD(Tr)$_1$ with TrCl and product analysis

α-CD (202 mg, 0.208 mmol) or α-CD(Tr)$_1$ (102 mg, 0.084 mmol) was dissolved in pyridine (60 mL). The solution was boiled to remove trace amounts of water as an azeotropic mixture, and the resulting solution (50 mL) was stirred in an oil bath (55 °C). TrCl (111 mg, 0.399 mmol for α-CD or 41.5 mg, 0.149 mmol for α-CD(Tr)$_1$) was added to the stirred solution. At hourly intervals, 2.0 mL aliquots were withdrawn and added to 0.5 mL water to stop the reaction. The resulting solution was evaporated to dryness, and the residue was dissolved in 2.0 mL methanol. Concentrations of products in the methanol solutions were determined by UFLC with acetonitrile/water (30:70 and 45:55, v/v, for the separation of mono- and ditritylates, respectively) as mobile phase. Retention times of α-CD(Tr)$_1$ and the AD-, AC-, and AB-isomers were ca. 3.8, 2.7, 6.6, and 9.9 min, respectively.

6^A,6^B-Di-*O*-trityl-α- CD (AB-isomer): ^{13}C NMR (DMSO-d_6) δ 144.26, 143.80, 128.19, 128.07, 127.66, 127.41, 126.71, 126.58, 102.07, 102.00, 101.97, 101.79, 101.59, 101.37, 86.03, 85.65, 83.27, 81.67, 81.59, 81.38, 81.34, 80.76, 73.32, 73.22, 73.14, 72.83, 72.36, 72.30, 72.24, 72.17, 72.11, 72.02, 71.78, 71.22, 70.37, 63.78, 63.19, 59.84, 59.58, 59.17 ppm; HRMS–ESI (*m*/*z*): $[M + Na]^+$ calcd for $C_{74}H_{88}O_{30}Na^+$, 1479.5258; found, 1479.5217.

6^A,6^C-Di-*O*-trityl-α- CD (AC-isomer): ^{13}C NMR (DMSO-d_6) δ 144.06, 143.99, 128.34, 128.27, 127.63, 127.53, 126.76, 126.67, 102.40, 102.10, 101.90, 101.76, 101.59, 86.03, 85.97, 83.12, 82.36, 81.79, 81.70, 81.00, 80.92, 73.25, 73.16, 72.94, 72.74, 72.23, 72.07, 70.56, 70.40, 63.28, 63.04, 59.98, 59.83, 59.06, 59.02 ppm;. HRMS–ESI (*m*/*z*): $[M + Na]^+$ calcd for $C_{74}H_{88}O_{30}Na^+$, 1479.5258; found, 1479.5217.

6^A,6^D-Di-*O*-trityl-α- CD (AD-isomer): ^{13}C NMR (DMSO-d_6) δ 143.89, 128.29, 127.51, 126.69, 102.41, 101.87, 101.45, 86.06, 83.09, 81.52, 80.82, 73.35, 73.02, 72.89, 72.32, 72.12, 72.00, 71.85, 70.36, 63.32, 60.02, 58.77 ppm; HRMS–ESI (*m*/*z*): $[M + Na]^+$ calcd for $C_{74}H_{88}O_{30}Na^+$, 1479.5258; found, 1479.5217.

Reaction of AD-, AC-, or AB-isomers with TrCl and product analysis

The AD-isomer (78 mg, 0.053 mmol), AC-isomer (150 mg, 0.103 mmol), or AB-isomer (151 mg, 0.104 mmol) was dissolved in pyridine (35 mL). The solution was boiled to remove a trace amount of water as an azeotropic mixture, and the resulting solution (25 mL) was stirred in an oil bath (55 °C). TrCl (23 mg, 0.083 mmol for AD-isomer, 53 mg, 0.189 mmol for AC-isomer, or 58 mg, 0.207 mmol for AB-isomer) was added to the stirred solution. At hourly intervals, 2.0 mL aliquots were withdrawn, added to 0.5 mL water to stop the reaction. The resulting solution was evaporated to dryness, and the residue was dissolved in 2.0 mL methanol. Concentrations of products in the methanol solutions were determined by UFLC with acetonitrile/methanol/water (40:45:15, v/v/v) as mobile phase for the separation of tri-tritylates formed. Retention times of ABE-, ABD-, ABC-, and ACE-isomers were ca. 6.2, 7.5, 9.4 and 11.3 min, respectively.

6^A,6^B,6^C-Tri-*O*-trityl-α-CD (ABC-isomer): ^{13}C NMR (DMSO-d_6) δ 144.32, 144.20, 143.66, 128.24, 128.13, 127.93, 127.71, 127.39, 126.80, 126.61, 126.40, 102.16, 101.93, 101.73, 101.66, 101.59, 101.25, 85.97, 85.78, 85.73, 83.12, 81.78, 81.40, 80.95, 80.83, 80.69, 73.32, 73.18, 73.07, 73.00, 72.62, 72.57, 72.42, 72.28, 72.20, 72.09, 72.05, 71.96, 71.72, 71.35, 70.87, 70.51, 63.69, 63.52, 59.65, 59.51, 59.08 ppm; HRMS–ESI (*m*/*z*): $[M + Na]^+$ calcd for $C_{93}H_{102}O_{30}Na^+$, 1721.6345; found, 1721.6067.

6^A,6^B,6^D-Tri-*O*-trityl-α-CD (ABD-isomer): ^{13}C NMR (DMSO-d_6) δ 144.11, 143.79, 128.29, 128.15, 128.09, 127.54, 127.45, 127.38, 126.62, 102.25, 101.97, 101.82, 101.68, 101.46, 101.42, 85.92, 85.86, 85.69, 82.53, 82.44, 81.93, 81.38, 80.85, 80.67, 73.39, 73.07, 72.92, 72.83, 72.60, 72.38, 72.09, 72.01, 71.96, 71.89, 70.91, 70.83, 70.58, 69.76, 63.45, 62.97, 62.58, 59.99, 59.02, 58.97 ppm; HRMS–ESI) (*m*/*z*): $[M + Na]^+$ calcd for $C_{93}H_{102}O_{30}Na^+$, 1721.6345; found, 1721.6067.

6^A,6^B,6^E-Tri-*O*-trityl-α-CD (ABE-isomer): ^{13}C NMR (DMSO-d_6) δ 144.25, 143.69, 143.56, 128.28, 128.15, 127.96, 127.63, 127.42, 127.31, 126.68, 126.62, 126.53, 102.27, 102.22, 102.13, 101.89, 101.33, 101.08, 86.02, 85.95, 85.52, 83.51, 82.85, 81.63, 80.86, 80.68, 80.59, 73.42, 73.30, 72.99, 72.94, 72.73, 72.36, 72.29, 72.16, 72.05, 71.97, 71.86, 71.77, 71.27, 70.38, 70.35, 63.91, 63.13, 62.90, 59.73, 59.38, 58.58 ppm; HRMS–ESI (*m*/*z*): $[M + Na]^+$ calcd for $C_{93}H_{102}O_{30}Na^+$, 1721.6345; found, 1721.6067.

6^A,6^C,6^E-Tri-*O*-trityl-α-CD (ACE-isomer): ^{13}C NMR (DMSO-d_6) δ 143.98, 128.29, 127.54, 126.68, 102.23, 101.61, 85.97, 82.69, 80.89, 73.21, 72.81, 72.16, 72.06, 71.99, 70.53, 62.85, 59.14 ppm; HRMS–ESI (*m*/*z*): $[M + Na]^+$ calcd for $C_{93}H_{102}O_{30}Na^+$, 1721.6345; found, 1721.6067.

Supporting Information

Supporting Information File 1

^{1}H NMR spectra of mono-, di-, and tri-*O*-trityl-α-CD, together 2D COSY and TOCSY spectra of the AD-isomer.
[http://www.beilstein-journals.org/bjoc/content/supplementary/1860-5397-11-168-S1.pdf]

Acknowledgements

The authors thank the faculty of Life and Environmental Science in Shimane University for help in financial supports for publishing this report.

References

1. Tabushi, I.; Kuroda, Y.; Yokota, K.; Yuan, L. C. *J. Am. Chem. Soc.* **1981,** *10,* 711–712. doi:10.1021/ja00393a056
2. Bistri, O.; Sinaÿ, P.; Barbero, J. J.; Sollogoub, M. *Chem. – Eur. J.* **2007,** *13,* 9757–9774. doi:10.1002/chem.200700971
3. Guieu, S.; Sollogoub, M. *J. Org. Chem.* **2008,** *73,* 2819–2828. doi:10.1021/jo7027085
4. Gramage-Doria, R.; Rodriguez-Lucena, D.; Armspach, D.; Egloff, C.; Jouffroy, M.; Matt, D.; Toupet, L. *Chem. – Eur. J.* **2011,** *17,* 3911–3921. doi:10.1002/chem.201002541
5. Wang, B.; Zaborova, E.; Guieu, S.; Petrillo, M.; Guitet, M.; Blériot, Y.; Ménand, M.; Zhang, Y.; Sollogoub, M. *Nat. Commun.* **2015,** *5,* No. 5354. doi:10.1038/ncomms6354
6. Cramer, F.; Mackensen, G.; Sensse, K. *Chem. Ber.* **1969,** *102,* 494–508. doi:10.1002/cber.19691020217
7. Melton, L. D.; Slessor, K. N. *Carbohydr. Res.* **1971,** *18,* 29–37. doi:10.1016/S0008-6215(00)80256-6
8. Bergeron, R.; Machida, Y.; Bloch, K. *J. Biol. Chem.* **1975,** *250,* 1223–1230.
9. Boger, J.; Brenner, D. G.; Knowles, J. R. *J. Am. Chem. Soc.* **1979,** *101,* 7630–7631. doi:10.1021/ja00519a035
10. Eshima, K.; Mantsushita, Y.-i.; Hasegawa, E.; Nishida, H.; Tsuchida, E. *Chem. Lett.* **1989,** *18,* 381–384. doi:10.1246/cl.1989.381
11. Coleman, A. W.; Ling, C.-C.; Miocque, M. *Angew. Chem., Int. Ed. Engl.* **1992,** *31,* 1381–1383. doi:10.1002/anie.199213811
12. Ling, C.-C.; Coleman, A. W.; Miocque, M. *Carbohydr. Res.* **1992,** *223,* 287–291. doi:10.1016/0008-6215(92)80026-W
13. Tanimoto, T.; Tanaka, M.; Yuno, T.; Koizumi, K. *Carbohydr. Res.* **1992,** *223,* 1–10. doi:10.1016/0008-6215(92)80001-H
14. Tanimoto, T.; Sakaki, T.; Koizumi, K. *Chem. Pharm. Bull.* **1993,** *41,* 866–869. doi:10.1248/cpb.41.866
15. Tanimoto, T.; Ikuta, A.; Koizumi, K.; Kimata, K. *J. Chromatogr. A* **1998,** *825,* 195–199. doi:10.1016/S0021-9673(98)00712-2
16. Armspach, D.; Matt, D. *Carbohydr. Res.* **1998,** *310,* 129–133. doi:10.1016/S0008-6215(98)00139-6
17. Khan, A. R.; Forgo, P.; Stine, K. J.; D'Souza, V. T. *Chem. Rev.* **1998,** *98,* 1977–1996. doi:10.1021/cr970012b
18. Ward, S.; Zhang, P.; Ling, C.-C. *Carbohydr. Res.* **2009,** *344,* 808–814. doi:10.1016/j.carres.2009.02.005
19. Zhang, P.; Wang, A.; Cui, L.; Ling, C.-C. *Org. Lett.* **2012,** *14,* 1612–1615. doi:10.1021/ol300358u
20. Fujita, K.; Yamamura, H.; Matsunaga, A.; Imoto, T.; Mihashi, K.; Fujioka, T. *J. Am. Chem. Soc.* **1986,** *108,* 4509–4513. doi:10.1021/ja00275a042
21. Matsui, Y.; Fujie, M.; Sakate, H. *Bull. Chem. Soc. Jpn.* **1988,** *61,* 3409–3415. doi:10.1246/bcsj.61.3409
22. Yamamura, H.; Nagaoka, H.; Saito, K.; Kawai, M.; Butsugan, Y.; Nakajima, T.; Fujita, K. *J. Org. Chem.* **1993,** *58,* 2936–2937. doi:10.1021/jo00063a005
23. Yoshikiyo, K.; Shinjo, M.; Matsui, Y.; Yamamoto, T. *Carbohydr. Res.* **2015,** *401,* 58–63. doi:10.1016/j.carres.2014.10.027

License and Terms

BEILSTEIN JOURNAL OF ORGANIC CHEMISTRY

Cholesterol lowering effects of mono-lactose-appended β-cyclodextrin in Niemann–Pick type C disease-like HepG2 cells

Keiichi Motoyama[1], Yumi Hirai[1], Rena Nishiyama[1], Yuki Maeda[1,2], Taishi Higashi[1], Yoichi Ishitsuka[1], Yuki Kondo[1], Tetsumi Irie[1,2], Takumi Era[3] and Hidetoshi Arima*[1,2,§]

Full Research Paper

Open Access

Address:
[1]Graduate School of Pharmaceutical Sciences, Kumamoto University, 5-1 Oe-honmachi, Chuo-ku, Kumamoto 862-0973, Japan, [2]Program for Leading Graduate Schools "HIGO (Health life science: Interdisciplinary and Glocal Oriented) Program", Kumamoto University, 5-1 Oe-honmachi, Chuo-ku, Kumamoto 862-0973, Japan and [3]Department of Cell Modulation, Institute of Molecular Embryology and Genetics, Kumamoto University, 2-2-1 Honjo, Chuo-ku, Kumamoto 860-0811, Japan

Email:
Hidetoshi Arima* - arimah@gpo.kumamoto-u.ac.jp

* Corresponding author
§ Tel: +81 96 371 4160, Fax: +81 96 371 4160

Keywords:
asialoglycoprotein receptor; cholesterol; cyclodextrin; lactose; Niemann–Pick disease type C

Beilstein J. Org. Chem. **2015,** *11,* 2079–2086.
doi:10.3762/bjoc.11.224

Received: 30 July 2015
Accepted: 14 October 2015
Published: 03 November 2015

This article is part of the Thematic Series "Superstructures with cyclodextrins: Chemistry and applications III".

Guest Editor: G. Wenz

Abstract

The Niemann–Pick type C disease (NPC) is one of inherited lysosomal storage disorders, emerges the accumulation of unesterified cholesterol in endolysosomes. Currently, 2-hydroxypropyl-β-cyclodextrin (HP-β-CyD) has been applied for the treatment of NPC. HP-β-CyD improved hepatosplenomegaly in NPC patients, however, a high dose of HP-β-CyD was necessary. Therefore, the decrease in dose by actively targeted-β-CyD to hepatocytes is expected. In the present study, to deliver β-CyD selectively to hepatocytes, we newly fabricated mono-lactose-appended β-CyD (Lac-β-CyD) and evaluated its cholesterol lowering effects in NPC-like HepG2 cells, cholesterol accumulated HepG2 cells induced by treatment with U18666A. Lac-β-CyD (degree of substitution of lactose (DSL) 1) significantly decreased the intracellular cholesterol content in a concentration-dependent manner. TRITC-Lac-β-CyD was associated with NPC-like HepG2 cells higher than TRITC-β-CyD. In addition, TRITC-Lac-β-CyD was partially localized with endolysosomes after endocytosis. Thus, Lac-β-CyD entered NPC-like HepG2 cells via asialoglycoprotein receptor (ASGPR)-mediated endocytosis and decreased the accumulation of intracellular cholesterol in NPC-like HepG2 cells. These results suggest that Lac-β-CyD may have the potential as a drug for the treatment of hepatosplenomegaly in NPC disease.

Introduction

The Niemann–Pick type C disease (NPC) is one of inherited lysosomal storage disorders, emerges the accumulation of unesterified cholesterol in endolysosomes. NPC was caused by mutations in either the NPC1 or the NPC2 gene, and usually develops severe neurodegeneration, hepatosplenomegaly and failure to thrive childhood [1-3]. The NPC1 protein is localized in endolysosomes and plays an important role in cholesterol trafficking in cells [3,4]. An excessive amount of unesterified cholesterol accumulation in endolysosomes and a shortage of esterified cholesterol in other cellular compartments are observed. Therefore, the cholesterol sequestration is found to be a crucial factor in developing NPC disease.

Cyclodextrins (CyDs) are non-reducing cyclic glucose oligosaccharides obtained by enzymatic means from starch-containing raw materials and have been used for the enhancement of drugs solubility, stability and bioavailability, etc., through complex formation [5,6]. Recently, 2-hydroxypropyl-β-cyclodextrin (HP-β-CyD) has attracted considerable attention for the treatment of NPC disease [4,7-9]. The administration of HP-β-CyD to *NPC1*-knock out ($Npc1^{-/-}$) mice has been reported to remarkably prolong the life span of the mice through a reduction in cholesterol levels [7-9]. Most recently, it was reported that HP-γ-CyD, which has great advantages in biocompatibility compared to HP-β-CyD, can also reduce the cholesterol accumulation in NPC-like cells [10]. However, a high dose of HP-β-CyD or HP-γ-CyD was necessary to exert the pharmacological effects in vivo, since neither HP-β-CyD nor HP-γ-CyD enters cells effectively due to their hydrophilicity and high molecular weight.

Receptor-mediated endocytosis is an attractive approach to enhance the cellular uptake of drugs in target cells. It enables not only high drug concentrations within the cells but also minimum concentration at non-target cells, thereby amalgamating high treatment efficacy with low side effects. Of various receptors, asialoglycoprotein receptors (ASGPR) expressing in abundance on hepatocytes could provide advantages for hepatocyte-selective delivery [11]. Actually, the galactosylation of polymers or lipids has been utilized to develop drug carriers with hepatocyte specificity through ASGPR [11]. Therefore, ASGPR-mediated endocytosis seems to be a promising approach to deliver CyDs to hepatocytes for the treatment of hepatosplenomegaly in NPC disease. Therefore, in the present study, we newly fabricated mono-lactose-appended β-CyD (Lac-β-CyD) and evaluated its cholesterol lowering effect in NPC-like HepG2 cells, cholesterol accumulated HepG2 cells induced by U18666A, as a model of NPC hepatocytes.

Results and Discussion

Preparation of Lac-β-CyD

In the present study, we attempted to prepare Lac-β-CyD as a hepatocyte-selective cholesterol decreasing agent. Figure 1 shows the preparation pathway of Lac-β-CyD. Firstly, we

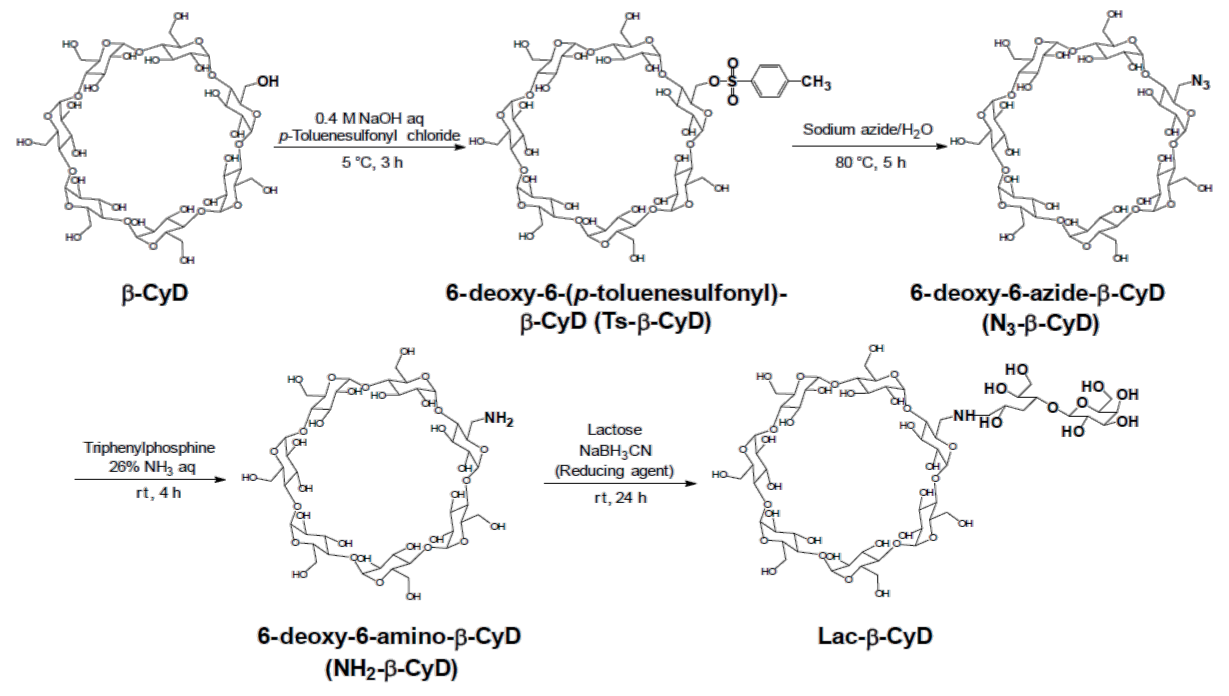

Figure 1: Preparation scheme of Lac-β-CyD.

synthesized NH_2-β-CyD through tosylation, and azidation of primary hydroxy groups of β-CyD, as reported previously [12,13]. Secondly, lactose was modified to NH_2-β-CyD using the reducing agent cyanotrihydroborate in dimethyl sulfoxide (DMSO) at room temperature for 24 h. No unreacted free lactose was confirmed by thin-layer chromatography (TLC). The MALDI–TOF MS spectrum of Lac-β-CyD showed a peak at *m*/*z* 1483 derived from lactose mono-substituted β-CyD (Figure 2A). There are undesired signals with high molecular weight. Therefore, further elaborate studies are necessary. From the integral values of the anomeric protons of lactose and anomeric protons of glucose in β-CyD obtained by ^{1}H NMR analysis (Figure 2B), the degree of substitution of lactose (DSL) was calculated as 1. These results suggest that Lac-β-CyD (DSL1) was almost successfully fabricated.

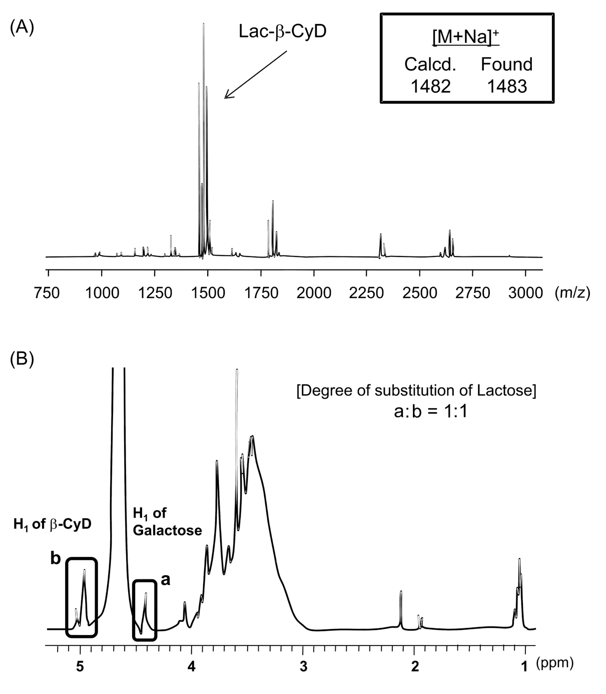

Figure 2: MALDI–TOF MS (A) and ^{1}H NMR (B) spectra of Lac-β-CyD.

It is well known that β-CyDs destroy caveolae structures and concomitantly affected various cellular functions through cholesterol depletion [14,15]. In NPC treatment, the interaction of Lac-β-CyD with cholesterol is thought to play a critical role. However, chemical modification of CyDs may often change the inclusion ability to guest molecules. Therefore, to examine whether Lac-β-CyD has inclusion ability or not, we preliminary determined the dissociation constant of Lac-β-CyD with adamantane, which is often used as a guest molecule for β-CyD, using the quartz crystal microbalance method (QCM) in phosphate-buffered saline (PBS, pH 7.4) at 37 °C. As a result, the dissociation constant of Lac-β-CyD with adamantane was 9.8×10^{-7} M due to the potent complex formation. Therefore, this preliminary result suggests that the inclusion ability of Lac-β-CyD is still maintained.

Cytotoxicity of Lac-β-CyD

To reveal the cytotoxicity of Lac-β-CyD, we examined the WST-1 method (Figure 3). Here, we used U18666A-treated HepG2 cells as NPC-like cells, because U18666A inhibits an intracellular cholesterol trafficking and has the potential to induce NPC disease phenotype [16]. No significant cytotoxicity of Lac-β-CyD was observed in U18666A-treated HepG2 cells at 1 mM for 24 h. The following studies were performed under the experimental conditions.

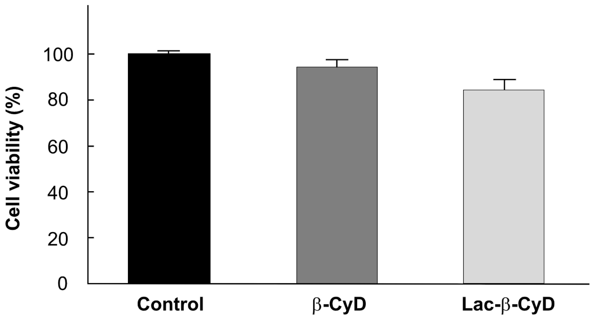

Figure 3: Cytotoxic activity of β-CyDs in U18666A-treated HepG2 cells after treatment for 24 h. U18666A-treated HepG2 cells were incubated with 100 μL of medium containing 1 mM β-CyDs for 24 h at 37 °C. After washing once with PBS, 100 μL of fresh HBSS and 10 μL of WST-1 reagent were added to plates, and incubated for 30 min at 37 °C. Each value represents the mean ± S.E.M. of 6–8 experiments.

Cellular uptake of TRITC-Lac-β-CyD

To reveal whether Lac-β-CyD can associate with ASGPR-expressing cells, we examined the cellular uptake of tetramethylrhodamine isothiocyanate (TRITC)-labeled Lac-β-CyD after treatment for 24 h in U18666A-treated HepG2 and NPC-like ASGPR-expressing cells, by a flow cytometric analysis (Figure 4). As a result, TRITC-Lac-β-CyD was found to be associated with U18666A-treated HepG2 cells, higher than TRITC-β-CyD, which is lacking the lactose moiety (Figure 4A,B).

Next, we examined the intracellular distribution of TRITC-Lac-β-CyD by confocal laser scanning microscopy (Figure 5). It should be noted that cellular uptake of TRITC-Lac-β-CyD in U18666A-treated HepG2 cells was observed at 24 h after incubation. In addition, TRITC-Lac-β-CyD was co-localized with endolysosomes stained by LysoTracker®. Taken together, these results suggest that Lac-β-CyD localized in endolysosomes of U18666A-treated HepG2 cells.

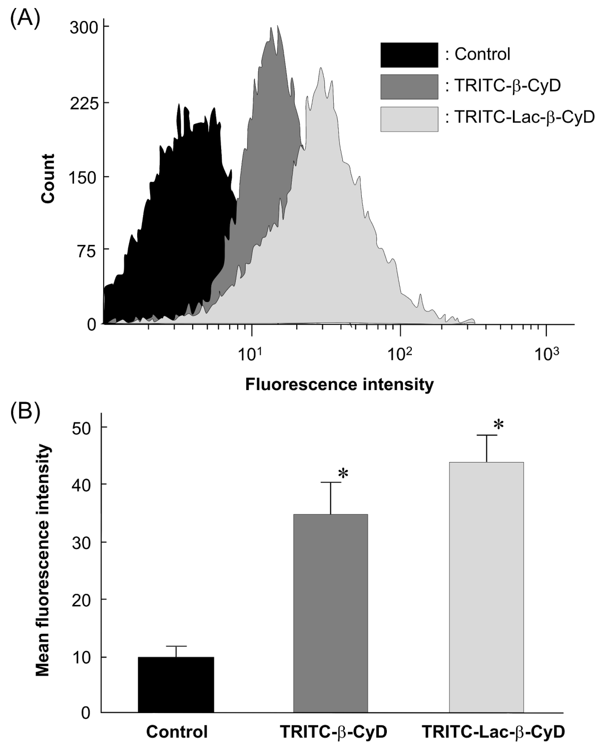

Figure 4: Cellular association of TRITC-Lac-β-CyD in U18666A-treated HepG2 cells after treatment for 24 h. The fluorescence intensity of TRITC in cells was determined 24 h after incubation at 37 °C by a flow cytometer. (A) The experiments were performed independently three times, and representative data are shown. (B) The fluorescent intensity was quantified by CellQuest software. Each value represents the mean ± S.E.M. of 6 experiments. $^{*}p < 0.05$, compared with control.

Effects of Lac-β-CyD on intracellular cholesterol levels

We examined the effects of Lac-β-CyD on cholesterol levels in U18666A-treated HepG2 cells using Filipin III, which can bind to unesterified cholesterol specifically. After treatment with 0.01 mM, 0.1 mM and 1 mM Lac-β-CyD for 24 h, the fluorescence intensity of Filipin III was detected by a fluorescence microscope (Figure 6). Herein, the experimental conditions of the treatment with 1 mM β-CyDs for 24 h are reported to decrease cholesterol in endolysosomes in NPC model cells [17,18]. As shown in Figure 6, the treatment with Lac-β-CyD for 24 h decreased the fluorescence intensity derived from Filipin III in a concentration-dependent manner. Taken together, these results suggest that Lac-β-CyD reduced the cholesterol levels in U18666A-treated HepG2 cells through ASGPR-mediated endocytosis.

The proposed mechanism for the cholesterol lowering effects of CyDs in NPC cells are as follows; 1) CyDs may extract the free form of cholesterol from plasma membranes of lipid rafts, and then cholesterol in endolysosomes are transported to plasma membrane to supply, 2) the endocytosed CyDs may transport cholesterol from endolysosomes, and 3) the endocytosed CyDs may elicit a perturbation in endolysosomes membranes through the interaction with membrane components, which would result in the efflux of cholesterol from endolysosomes. In our preliminary study, 1 mM Lac-β-CyD could not extract cholesterol from the plasma membrane of U18666A-treated HepG2 cells within 24 h (data not shown). Therefore, the lowering effects of Lac-β-

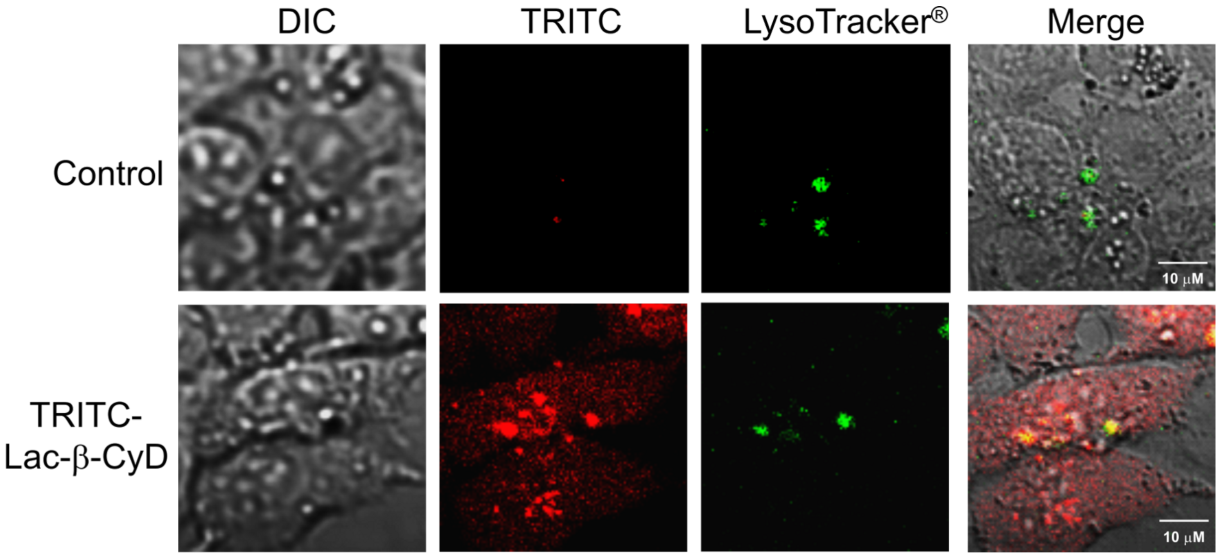

Figure 5: Intracellular distribution of TRITC-Lac-β-CyD in U18666A-treated HepG2 cells. U18666A-treated HepG2 cells were incubated in medium (FBS (−)) with or without 100 μM TRITC-Lac-β-CyD for 24 h. The experiments were performed independently three times, and representative images are shown.

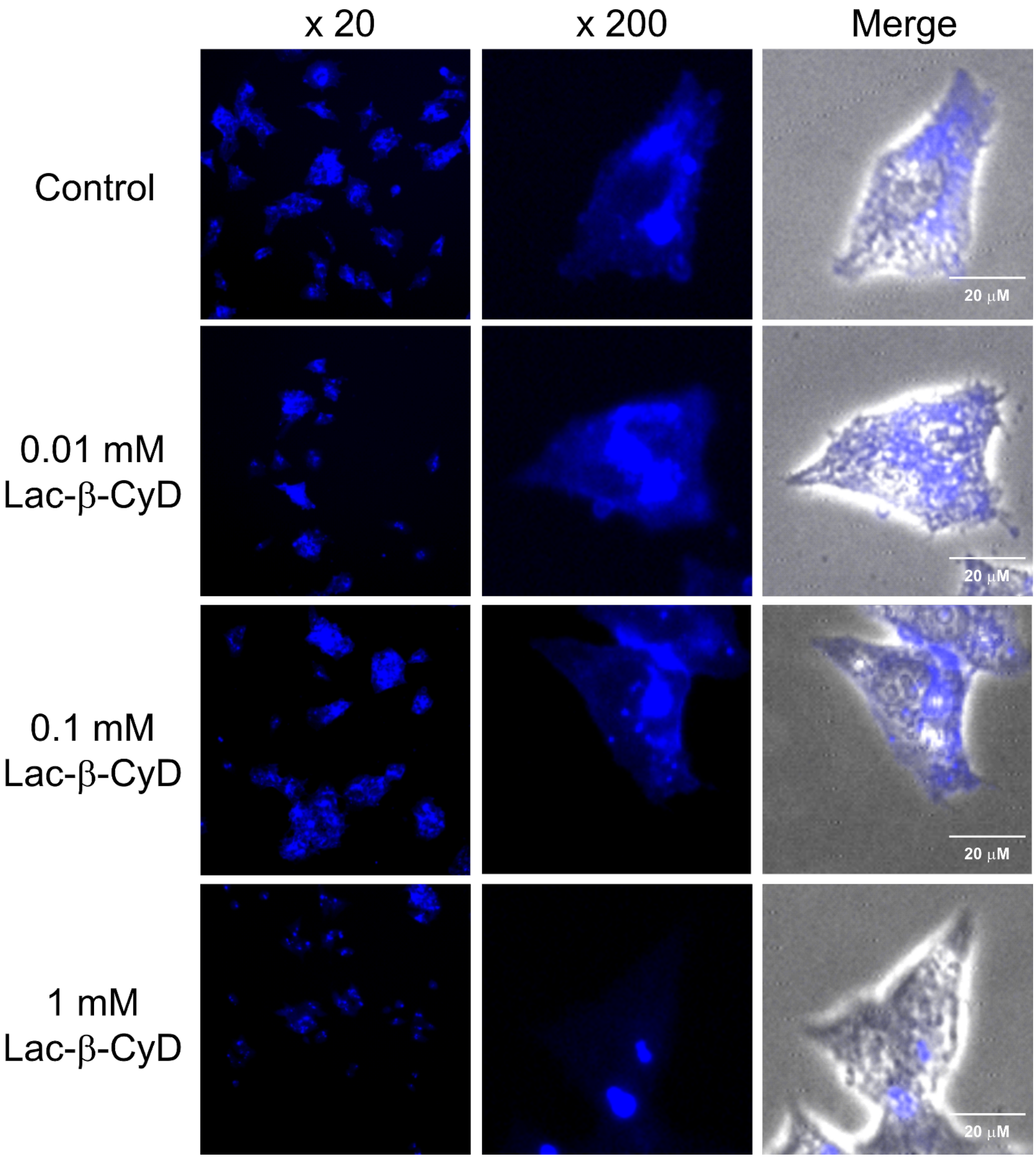

Figure 6: Effect of concentration of Lac-β-CyD on intracellular level of free form of cholesterol in U18666A-treated HepG2 cells. U18666A-treated HepG2 cells were incubated in medium (FBS (−)) with or without Lac-β-CyD for 24 h. The experiments were performed independently three times, and representative images are shown.

CyD can be hardly explained by the cholesterol extraction ability from plasma membranes. Recently, Rosenbaum et al. revealed that CyD accelerated the cholesterol trafficking through modulation of the endocytic system, leading to amelioration of cholesterol accumulation in NPC-like cells [19,20]. Although HP-β-CyD and HP-γ-CyD are known to insufficiently enter the cells, Lac-β-CyD endocytosed through ASGPR may have the lowering effects on cholesterol accumulation in U18666A-treated HepG2 cells. However, the role of endocytosed Lac-β-CyD for the cholesterol-lowering effect still remains unclear. To reveal the detailed mechanism of cholesterol lowering effects of Lac-β-CyD, further elaborate studies on not only cholesterol trafficking but also interaction with endolysosomes membranes are necessary.

Autophagy, a bulk digestion system of cytoplasmic aggregated proteins and organelles, plays an important role in regulating NPC disease [21-24]. In NPC disease, accumulation of autophagosomes has elicited even in the basal conditions [25,26]. Therefore, amelioration of impaired autophagy is necessary for the treatment of the NPC disease. Actually, Song et al. demonstrated that HP-β-CyD activated the transcription factor EB, a master regulator of lysosomal function and autophagy, and ameliorated the autophagic function in cells [27]. In addition, Tamura et al. reported that HP-β-CyD elevated LC3-II and p62 levels in NPC1 fibroblasts, indicating the improvement of impaired autophagy by HP-β-CyD [28]. Therefore, it is necessary to investigate whether Lac-β-CyD can improve an autophagy function in NPC-like cells.

Galactose density is one of the critical parameters of affinity to ASGPR. The binding affinity of galactose with ASGPR enhanced 100–1000 fold from mono- to triantennary galactose structure due to cluster effects [29]. Stokmaier et al. reported that the dissociation constant of monosaccharide with ASGPR was 10^{-4} M, while those of triantennary and tetraantennary with ASGPR were 5×10^{-9} M and 9×10^{-9} M, respectively [29]. Therefore, to provide the more potent recognition ability of Lac-β-CyD to ASGPR, we are preparing the multi-lactose-appended β-CyDs.

Conclusion

In the present study, we newly fabricated Lac-β-CyD and evaluated its cholesterol lowering effects in NPC-like HepG2 cells. As a result, Lac-β-CyD was endocytosed via ASGPR and decreased the accumulation of intracellular cholesterol in NPC-like HepG2 cells. This result suggests that Lac-β-CyD may have the potential as drug for the treatment of hepatosplenomegaly in NPC disease.

Experimental

Materials

β-CyD was kindly gifted by Nihon Shokuhin Kako (Tokyo, Japan). Lactose monohydrate was purchased from Wako Pure Chemical Industries (Osaka, Japan). LysoTracker® Yellow (LysoTracker®) was obtained from Life Technologies Japan (Tokyo, Japan). Dulbecco's modified Eagle's medium (DMEM) and fetal bovine serum (FBS) were purchased from Nissui Pharmaceuticals (Tokyo, Japan) and Nichirei (Tokyo, Japan), respectively. Tetramethylrhodamine isothiocyanate (TRITC) was obtained from Funakoshi (Tokyo, Japan). The cell counting kit was purchased from Wako Pure Chemical Industries (Osaka, Japan). The cholesterol cell-based detection assay kit was purchased from Cayman Chemical Company (Ann Arbor MI). All other chemicals and solvents were of analytical reagent grade, and deionized double-distilled water was used throughout the study.

Apparatus

Nuclear magnetic resonance (NMR) spectra were taken on a JEOL JNM-R 500 instrument (Tokyo, Japan), operating at 500 MHz for protons at 25 °C. The concentration of the sample was 1.5 mg/750 μL in deuterated oxide (D_2O), and the chemical shifts were given as parts per million (ppm) downfield from that of tetramethylsilane (TMS). MALDI-TOF mass spectra (MALDI–TOF MS) were measured in a positive mode at 25 °C by a JEOL JMS-DX 303 mass spectrometer (Tokyo, Japan).

Synthesis of Lac-β-CyD

We prepared mono-NH_2-β-CyD as reported previously [12,13]. Lactose residues were attached to the primary amino group of mono-NH_2-β-CyD, i.e., mono-NH_2-β-CyD (1 g) and lactose monohydrate (15.1 g) and sodium cyanotrihydroborate (27.7 g) were dissolved in 3.4 L of 0.2 M borate buffer (pH 7.5) and mixed at room temperature for 24 h. After dialysis using a dialysis membrane, Spectra/pore (MWCO = 1,000), in water at room temperature for 72 h, the sample was concentrated with a rotary evaporator (EYELA N-1000S, Tokyo Rikakikai, Tokyo, Japan), and lyophilized to obtain Lac-β-CyD. The reaction was monitored by TLC (silica gel F_{254}, Merck, Whitehouse Station, NJ). Eluent: methanol/water 9:1 (v/v), indicator: *p*-anisaldehyde for sugar and ninhydrin for amino groups. The Lac-β-CyD gave ^{1}H NMR spectra consisting of protons of both β-CyD and lactose. The ratios of peak areas of the anomeric proton of β-CyD and protons of the lactose were approximately 1.0, indicating that β-CyD covalently bound to the lactose in a molar ratio of 1:1, as shown in Figure 2B. ^{1}H NMR (500 MHz, D_2O) δ (from TMS), 5.00 (H1, β-CyD), 4.56−4.41 (anomeric proton of lactose), 3.84−3.62 (H3, H5, H6, β-CyD), 3.54−3.43 (H2, H4, β-CyD). The yield of Lac-β-CyD was 2.1%.

Synthesis of TRITC-Lac-β-CyD

TRITC was attached to the primary hydroxy group of Lac-β-CyD, i.e., Lac-β-CyD (10 mg) and TRITC (1 mg) were dissolved in 400 μL of DMSO and mixed at room temperature for 24 h under the protection from light. Then, the sample was gradually dropped into 50 mL of acetone. After centrifugation (10,000 rpm, 10 min), the precipitant was collected and dissolved with water. The sample was lyophilized to obtain TRITC-Lac-β-CyD.

Cell culture

HepG2 cells, a human hepatocellular carcinoma cell line, were obtained from Riken Bioresource Center (Tsukuba, Japan). HepG2 cells were grown in DMEM, containing 1×10^5 mU/mL of penicillin, 0.1 mg/mL of streptomycin supplemented with 7.5%, 10% and 10% FBS, respectively, at 37 °C in a humidified 5% CO_2 and 95% air atmosphere. NPC-like HepG2 cells, which accumulate the cholesterol and sphingolipids in cells, were prepared by the treatment with DMEM containing 1.25 μM U18666A for 48 h.

Cytotoxicity

In a similar manner as described in [30], cytotoxicity was assayed by the WST-1 method. Briefly, U18666A-treated HepG2 cells were seeded at 3 × 10^4 cells onto 96-well microplate (Iwaki, Tokyo, Japan), and incubated for 6 h in a humidified atmosphere of 5% CO_2 and 95% air at 37 °C. Cells were washed once with phosphate-buffered saline (PBS, pH 7.4), and then incubated for 24 h with 150 μL of DMEM containing Lac-β-CyD (0.01, 0.1 or 1 mM) or Tween 20 in a humidified atmosphere of 5% CO_2 and 95% air at 37 °C. After washing twice with PBS to remove Lac-β-CyD, 100 μL of fresh Hanks' balanced salt solution (HBSS, pH 7.4) and 10 μL of WST-1 reagent were added to the plates and incubated for 30 min at 37 °C. The absorbance at 450 nm against a reference wavelength of 630 nm was measured with a microplate reader (Bio-Rad Model 550, Tokyo, Japan).

Cellular association of Lac-β-CyD

Cellular association of Lac-β-CyD was determined by a flow cytometry. After incubation with TRITC-Lac-β-CyD for 1 h in U18666A-treated HepG2 cells, the cells were washed with PBS (pH 7.4) twice and immediately scraped with 1 mL of PBS (pH 7.4). The cells were collected and filtered through nylon mesh. Data were collected for 1 × 10^4 cells on a FACSCalibur flow cytometer using CellQuest software (Becton-Dickinson, Mountain View, CA).

Intracellular distribution of Lac-β-CyD

U18666A-treated HepG2 cells (5 × 10^4 cells/35 mm glass bottom dish) were incubated with 150 μL of DMEM containing 100 μM TRITC-β-CyDs for 24 h. After washing with PBS, 150 μL of LysoTracker® (final concentration: 100 nM) was added and further incubated for 1 h. After the cells were washed, the fluorescence derived from TRITC and LysoTracker® in U18666A-treated HepG2 cells was detected by confocal laser scanning microscopy. The fluorescence intensities were determined by a BZ-II analyzer (Keyence, Osaka, Japan).

Intracellular distribution of cholesterol

U18666A-treated HepG2 cells (5 × 10^4 cells/35 mm glass bottom dish) were incubated with 150 μL of DMEM containing Lac-β-CyD (0.01, 0.1, or 1 mM) for 24 h. After washing with PBS, intracellular cholesterol was detected by a cholesterol cell-based detection assay kit (Cayman Chemical Company, Ann Arbor, MI). Briefly, after fixation of the cell by treatment with 150 μL of cell-based assay fixative solution (4% formaldehyde), 150 μL of cholesterol detection assay buffer containing 50 μg/mL of Filipin III was added and further incubated at 37 °C for 1 h. After the cells were washed, the fluorescence derived from Filipin III in U18666A-treated HepG2 cells was detected by a KEYENCE Biozero BZ-8000, a fluorescence microscope. The fluorescence intensities were determined by a BZ-II analyzer (Keyence, Osaka, Japan).

Data analysis

The experimental results are shown as means ± S.E.M. Significance levels for comparisons between samples were determined with Scheffe's test. The level of statistical significance was set at $p < 0.05$.

Acknowledgements

This work was funded by the Ministry of Health Labor and Welfare of Japan.

References

1. Carstea, E. D.; Morris, J. A.; Coleman, K. G.; Loftus, S. K.; Zhang, D.; Cummings, C.; Gu, J.; Rosenfeld, M. A.; Pavan, W. J.; Krizman, D. B.; Nagle, J.; Polymeropoulos, M. H.; Sturley, S. L.; Ioannou, Y. A.; Higgins, M. E.; Comly, M.; Cooney, A.; Brown, A.; Kaneski, C. R.; Blanchette-Mackie, E. J.; Dwyer, N. K.; Neufeld, E. B.; Chang, T.-Y.; Liscum, L.; Strauss, J. F., III; Ohno, K.; Zeigler, M.; Carmi, R.; Sokol, J.; Markie, D.; O'Neill, R. R.; van Diggelen, O. P.; Elleder, M.; Patterson, M. C.; Brady, R. O.; Vanier, M. T.; Pentchev, P. G.; Tagle, D. A. *Science* **1997,** *277,* 228–231. doi:10.1126/science.277.5323.228
2. Naureckiene, S.; Sleat, D. E.; Lackland, H.; Fensom, A.; Vanier, M. T.; Wattiaux, R.; Jadot, M.; Lobel, P. *Science* **2000,** *290,* 2298–2301. doi:10.1126/science.290.5500.2298
3. Vanier, M. T. *Orphanet J. Rare Dis.* **2010,** *5,* No. 16. doi:10.1186/1750-1172-5-16
4. Matsuo, M.; Togawa, M.; Hirabaru, K.; Mochinaga, S.; Narita, A.; Adachi, M.; Egashira, M.; Irie, T.; Ohno, K. *Mol. Genet. Metab.* **2013,** *108,* 76–81.
5. Szente, L.; Szejtli, J. *Adv. Drug Delivery Rev.* **1999,** *36,* 17–28. doi:10.1016/S0169-409X(98)00092-1
6. Uekama, K.; Otagiri, M. *Crit. Rev. Ther. Drug Carrier Syst.* **1987,** *3,* 1–40.
7. Davidson, C. D.; Ali, N. F.; Micsenyi, M. C.; Stephney, G.; Renault, S.; Dobrenis, K.; Ory, D. S.; Vanier, M. T.; Walkley, S. U. *PLoS One* **2009,** *4,* e6951. doi:10.1371/journal.pone.0006951
8. Liu, B.; Turley, S. D.; Burns, D. K.; Miller, A. M.; Repa, J. J.; Dietschy, J. M. *Proc. Natl. Acad. Sci. U. S. A.* **2009,** *106,* 2377–2382. doi:10.1073/pnas.0810895106
9. Porter, F. D.; Scherrer, D. E.; Lanier, M. H.; Langmade, S. J.; Molugu, V.; Gale, S. E.; Olzeski, D.; Sidhu, R.; Dietzen, D. J.; Fu, R.; Wassif, C. A.; Yanjanin, N. M.; Marso, S. P.; House, J.; Vite, C.; Schaffer, J. E.; Ory, D. S. *Sci. Transl. Med.* **2010,** *2,* 56–81. doi:10.1126/scitranslmed.3001417
10. Soga, M.; Ishitsuka, Y.; Hamasaki, M.; Yoneda, K.; Furuya, H.; Matsuo, M.; Ihn, H.; Fusaki, N.; Nakamura, K.; Nakagata, N.; Endo, F.; Irie, T.; Era, T. *Stem Cells* **2015,** *33,* 1075–1088. doi:10.1002/stem.1917
11. D'Souza, A. A.; Devarajan, P. V. *J. Controlled Release* **2015,** *203,* 126–139. doi:10.1016/j.jconrel.2015.02.022
12. Okamatsu, A.; Motoyama, K.; Onodera, R.; Higashi, T.; Koshigoe, T.; Shimada, Y.; Hattori, K.; Takeuchi, T.; Arima, H. *Bioconjugate Chem.* **2013,** *24,* 724–733. doi:10.1021/bc400015r

13. Okamatsu, A.; Motoyama, K.; Onodera, R.; Higashi, T.; Koshigoe, T.; Shimada, Y.; Hattori, K.; Takeuchi, T.; Arima, H. *Biomacromolecules* **2013,** *14,* 4420–4428. doi:10.1021/bm401340g
14. Darblade, B.; Caillaud, D.; Poirot, M.; Fouque, M.-J.; Thiers, J.-C.; Rami, J.; Bayard, F.; Arnal, J.-F. *Cardiovasc. Res.* **2001,** *50,* 566–576. doi:10.1016/S0008-6363(01)00251-6
15. Parpal, S.; Karlsson, M.; Thorn, H.; Strålfors, P. *J. Biol. Chem.* **2001,** *276,* 9670–9678. doi:10.1074/jbc.M007454200
16. Sugimoto, Y.; Ninomiya, H.; Ohsaki, Y.; Higaki, K.; Davies, J. P.; Ioannou, Y. A.; Ohno, K. *Proc. Natl. Acad. Sci. U. S. A.* **2001,** *98,* 12391–12396. doi:10.1073/pnas.221181998
17. van Gelder, C. M.; Vollebregt, A. A. M.; Plug, I.; van der Ploeg, A. T.; Reuser, A. J. J. *Expert Opin. Pharmacother.* **2012,** *13,* 2281–2299. doi:10.1517/14656566.2012.729039
18. Vance, J. E.; Karten, B. *J. Lipid Res.* **2014,** *55,* 1609–1621. doi:10.1194/jlr.R047837
19. Rosenbaum, A. I.; Maxfield, F. R. *J. Neurochem.* **2011,** *116,* 789–795. doi:10.1111/j.1471-4159.2010.06976.x
20. Rosenbaum, A. I.; Zhang, G.; Warren, J. D.; Maxfield, F. R. *Proc. Natl. Acad. Sci. U. S. A.* **2010,** *107,* 5477–5482. doi:10.1073/pnas.0914309107
21. Elrick, M. J.; Yu, T.; Chung, C.; Lieberman, A. P. *Hum. Mol. Genet.* **2012,** *21,* 4876–4887. doi:10.1093/hmg/dds324
22. Ishibashi, S.; Yamazaki, T.; Okamoto, K. *J. Clin. Neurosci.* **2009,** *16,* 954–959. doi:10.1016/j.jocn.2008.09.020
23. Ordonez, M. P.; Roberts, E. A.; Kidwell, C. U.; Yuan, S. H.; Plaisted, W. C.; Goldstein, L. S. B. *Hum. Mol. Genet.* **2012,** *21,* 2651–2662. doi:10.1093/hmg/dds090
24. Sarkar, S.; Carroll, B.; Buganim, Y.; Maetzel, D.; Ng, A. H. M.; Cassady, J. P.; Cohen, M. A.; Chakraborty, S.; Wang, H.; Spooner, E.; Ploegh, H.; Gsponer, J.; Korolchuk, V. I.; Jaenisch, R. *Cell Rep.* **2013,** *5,* 1302–1315. doi:10.1016/j.celrep.2013.10.042
25. Lieberman, A. P.; Puertollano, R.; Raben, N.; Slaugenhaupt, S.; Walkley, S. U.; Ballabio, A. *Autophagy* **2012,** *8,* 719–730. doi:10.4161/auto.19469
26. Nixon, R. A. *Nat. Med.* **2013,** *19,* 983–997. doi:10.1038/nm.3232
27. Song, W.; Wang, F.; Lotfi, P.; Sardiello, M.; Segatori, L. *J. Biol. Chem.* **2014,** *289,* 10211–10222. doi:10.1074/jbc.M113.506246
28. Tamura, A.; Yui, N. *J. Biol. Chem.* **2015,** *290,* 9442–9454. doi:10.1074/jbc.M115.636803
29. Stokmaier, D.; Khorev, O.; Cutting, B.; Born, R.; Ricklin, D.; Ernst, T. O. G.; Böni, F.; Schwingruber, K.; Gentner, M.; Wittwer, M.; Spreafico, M.; Vedani, A.; Rabbani, S.; Schwardt, O.; Ernst, B. *Bioorg. Med. Chem.* **2009,** *17,* 7254–7264. doi:10.1016/j.bmc.2009.08.049
30. Onodera, R.; Motoyama, K.; Arima, H. *J. Inclusion Phenom. Macrocyclic Chem.* **2011,** *70,* 321–326. doi:10.1007/s10847-010-9843-z

License and Terms

The definitive version of this article is the electronic one which can be found at:
doi:10.3762/bjoc.11.224

BEILSTEIN JOURNAL OF ORGANIC CHEMISTRY

Synthesis, structure, and mechanical properties of silica nanocomposite polyrotaxane gels

Kazuaki Kato*, Daisuke Matsui, Koichi Mayumi and Kohzo Ito*

Full Research Paper

Open Access

Address:
Department of Advanced Materials Science, Graduate School of Frontier Sciences, The University of Tokyo, 5-1-5 Kashiwanoha, Kashiwa, Chiba 277-8561, Japan

Email:
Kazuaki Kato* - kato@molle.k.u-tokyo.ac.jp; Kohzo Ito* - kohzo@molle.k.u-tokyo.ac.jp.

* Corresponding author

Keywords:
cyclodextrin; gel; mechanical property; nanocomposite; polyrotaxane

Beilstein J. Org. Chem. **2015,** *11,* 2194–2201.
doi:10.3762/bjoc.11.238

Received: 31 July 2015
Accepted: 28 October 2015
Published: 16 November 2015

This article is part of the Thematic Series "Superstructures with cyclodextrins: Chemistry and applications III".

Guest Editor: G. Wenz

Abstract

A significantly soft and tough nanocomposite gel was realized by a novel network formed using cyclodextrin-based polyrotaxanes. Covalent bond formation between the cyclic components of polyrotaxanes and the surface of silica nanoparticles (15 nm diameter) resulted in an infinite network structure without direct bonds between the main chain polymer and the silica. Small-angle X-ray scattering revealed that the homogeneous distribution of silica nanoparticles in solution was maintained in the gel state. Such homogeneous nanocomposite gels were obtained with at least 30 wt % silica content, and the Young's modulus increased with silica content. Gelation did not occur without silica. This suggests that the silica nanoparticles behave as cross-linkers. Viscoelastic measurements of the nanocomposite gels showed no stress relaxation regardless of the silica content for <20% compression strain, indicating an infinite stable network without physical cross-links that have finite lifetime. On the other hand, the infinite network exhibited an abnormally low Young's modulus, ~1 kPa, which is not explainable by traditional rubber theory. In addition, the composite gels were tough enough to completely maintain the network structure under 80% compression strain. These toughness and softness properties are attributable to both the characteristic sliding of polymer chains through the immobilized cyclodextrins on the silica nanoparticle and the entropic contribution of the cyclic components to the elasticity of the gels.

Introduction

Nanocomposite materials, in which nanoparticles are distributed via a matrix such as resin or rubber, exhibit various functions that the matrix material cannot achieve by itself. For instance, polyurethane/magnetic nanoparticle nanocomposite elastomers permitted a wide range of elasticity modulation by controlling the magnetic field [1], owing to the alignment of nanoparticles within the polymer network. In addition to such functionalization, nanocomposition can effectively reinforce materials; a typical example is natural rubbers reinforced by nanoparticles such as carbon black and silica for practical use as tire materials. Because of adhesion of polymer chains to the nanoparticle surfaces, the chain mobility at the interface is considerably suppressed, thereby increasing the elastic modulus of the nanocomposite [2-6]. Although the nanocomposite strategy is promising for the design of relatively hard functional materials, it is not easy to realize soft nanocomposite materials because of the strong interactions at the interface that reduce the polymer chain mobility. For dielectric elastomers expected to be used as actuators and electric generating systems, nanocomposites should satisfy both a high dielectric constant that is assured by the nanoparticles and a low elastic modulus [7].

Mechanically interlocked supramolecular polymers, such as polyrotaxane [8,9], can control the interface between the matrix polymer and the nanoparticles. Polyrotaxane comprising an end-capped backbone polymer and threaded cyclic molecules such as cyclodextrins (CDs) can form a network structure by intermolecular binding of the cyclic components [10]. Since the polymer chains are topologically connected to each other without chemical bonds, the chains can slide through the cross-links and lead to several unique properties [11-16]. Polyrotaxanes were also applied for surface modification of substrates by attaching the cyclic components to the surface [17]. These results were based on the indirect connection among different polymers or between polymers and surfaces, so that the mobility of the polymers can be maintained at the cross-linking points or the interface.

We demonstrate here that the indirect connection between the backbone polymers and nanoparticles can be applied also for soft nanocomposite materials. As illustrated in Figure 1, formation of chemical bonds between the cyclic components of polyrotaxanes to the surface of a nanoparticle may result in a network structure where the nanoparticle acts as a cross-linker. As the first model system, we employed a silica nanoparticle and a CD-based polyrotaxane whose rings were chemically modified to react with the surface of silica. The inner structure and the mechanical properties of the silica nanocomposite polyrotaxane gels were studied by small-angle X-ray scattering and viscoelastic measurements, respectively.

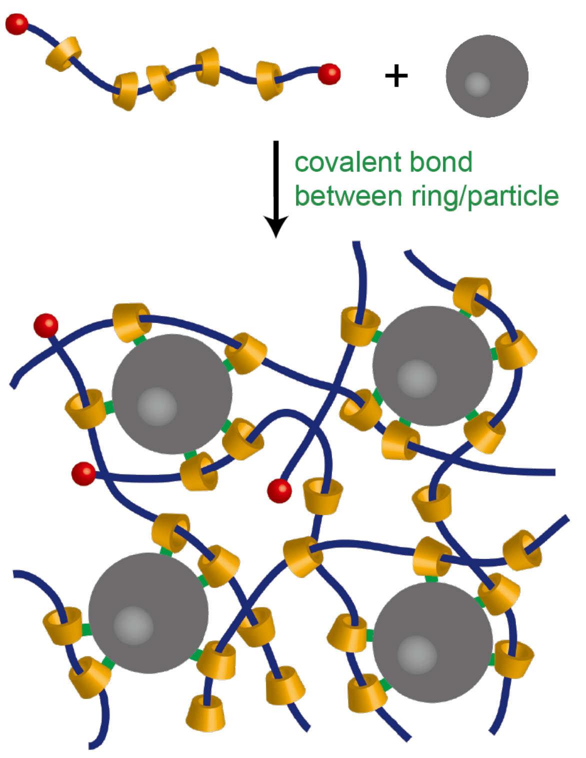

Figure 1: Nanocomposite polyrotaxane network formed by covalent bonds between cyclic components of polyrotaxane and the nanoparticle surfaces.

Results and Discussion

To achieve a covalent bond between the cyclic components (CDs, in this study) and the nanoparticle surfaces (SiO_2), hydroxy groups of the cyclic components of a polyrotaxane comprised of α-CD and PEG (PR) was modified as shown in Scheme 1. The polyrotaxane with triethoxysilylated CD (TES-PR) is suitable for the reaction with SiO_2 in the presence of base. Although TES-PR can be isolated just by vacuum drying to evaporate the reactant and solvent, the solid isolated in this way becomes insoluble in any solvent. This is due to the crosslinking induced by reactions between CDs. Thus, DMSO was added to the reaction solution first, followed by drying the solution under vacuum to eliminate acetone and reactant; as a result, a pure DMSO solution of TES-PR was obtained. The solution was used for the following characterization. Figure 2 shows the ^{1}H NMR spectra of TES-PR, PR, and an intermediate polyrotaxane with acryloyl groups at the CDs (Acryl-PR). All peaks were assigned as shown. From these integral values, the modification degree of Acryl-PR was calculated to almost 100% (corresponding to 18 acryloyl groups in each CD), with only 23% of the acryloyl groups reacted with triethoxysilane to generate TES-PR. GPC traces shown in Figure 3 indicate that the interlocked structure was retained throughout the modification and that the molecular weight of PR was increased with each modification step. The GPC trace of TES-PR also indicated the existence of high-molecular weight TES-PR. This probably multimeric TES-PR is the result of intermolecular reactions between triethoxysilyl groups during hydrosilylation. Since the pure TES-PR DMSO solution was stable at room temperature, the solution was used for the following reaction with silica nanoparticles.

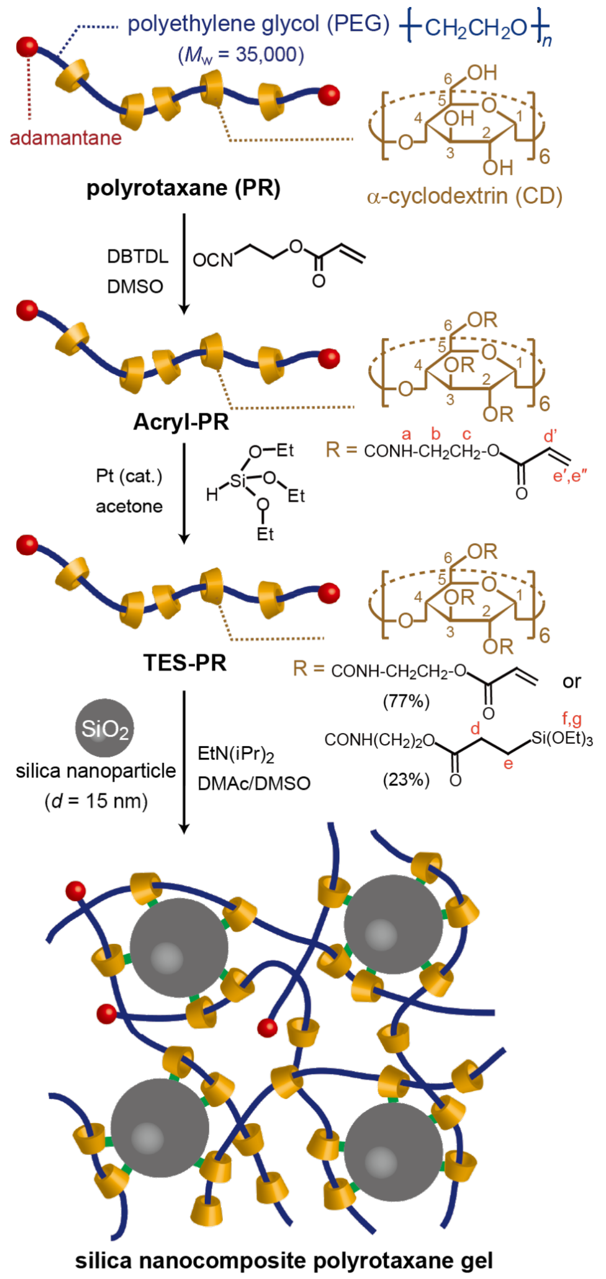

Scheme 1: Synthesis of polyrotaxane with partially triethoxysilylated α-CDs (TES-PR) and crosslinking of the polyrotaxane solution via the reaction between the CDs and the surface of silica nanoparticles.

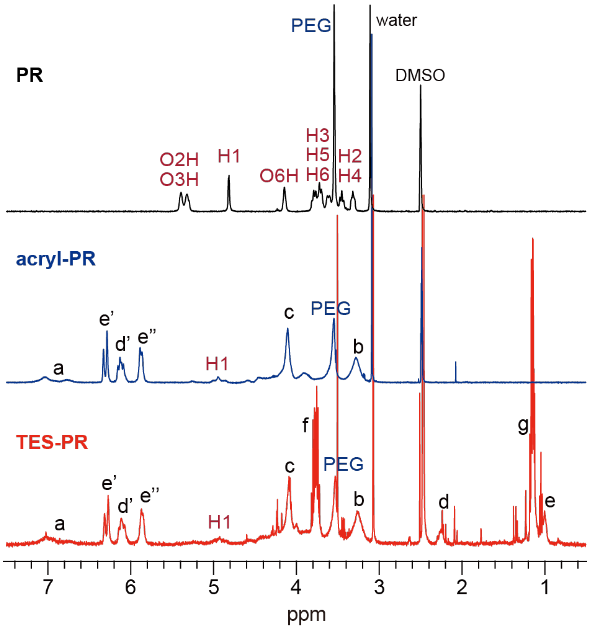

Figure 2: ^{1}H NMR spectra (400 MHz, DMSO-d_6, 343 K) of polyrotaxane and its derivatives with modified cyclic components.

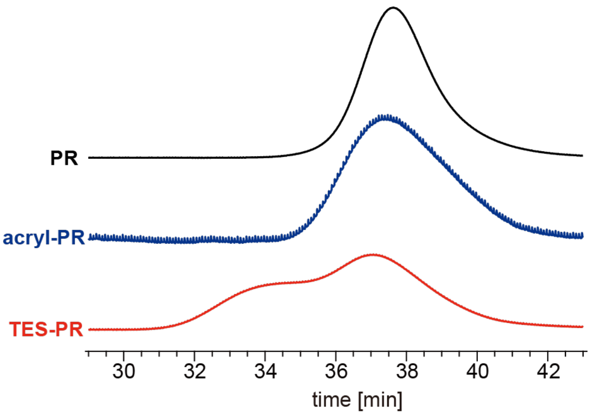

Figure 3: GPR traces of polyrotaxane and its derivatives; eluent: DMSO/LiBr (10 mM LiBr), detection: RI.

A TES-PR solution in DMSO was mixed with a dispersed solution of silica nanoparticles with 15 nm diameter in *N*,*N*-dimethylacetamide (DMAc) (20 wt %), followed by the addition of diisopropylethylamine to initiate the reaction between TES-PR and silica. The pre-gel solution was transferred to a glass mold with 3 mm thickness and cured for 16 h at 373 K. As shown in Figure 4, the obtained gel was transparent, indicating no significant aggregation. Five gels were synthesized in the same way with different initial concentrations of silica nanoparticles. Notably, in the absence of silica nanoparticles, gelation did not occur; only a slight increase of viscosity was observed. This result clearly shows that the gelation was achieved mainly by the reaction between silica and TES-PR, with a parallel minor reaction occurring between the triethoxysilyl groups of different TES-PRs.

To elucidate the dispersity of silica nanoparticles in the gels, small-angle X-ray scattering (SAXS) was carried out. Figure 5a

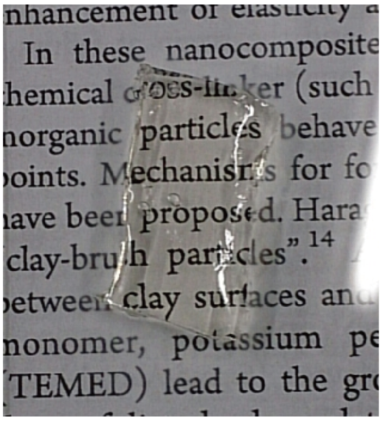

Figure 4: Photograph of silica nanocomposite polyrotaxane gel.

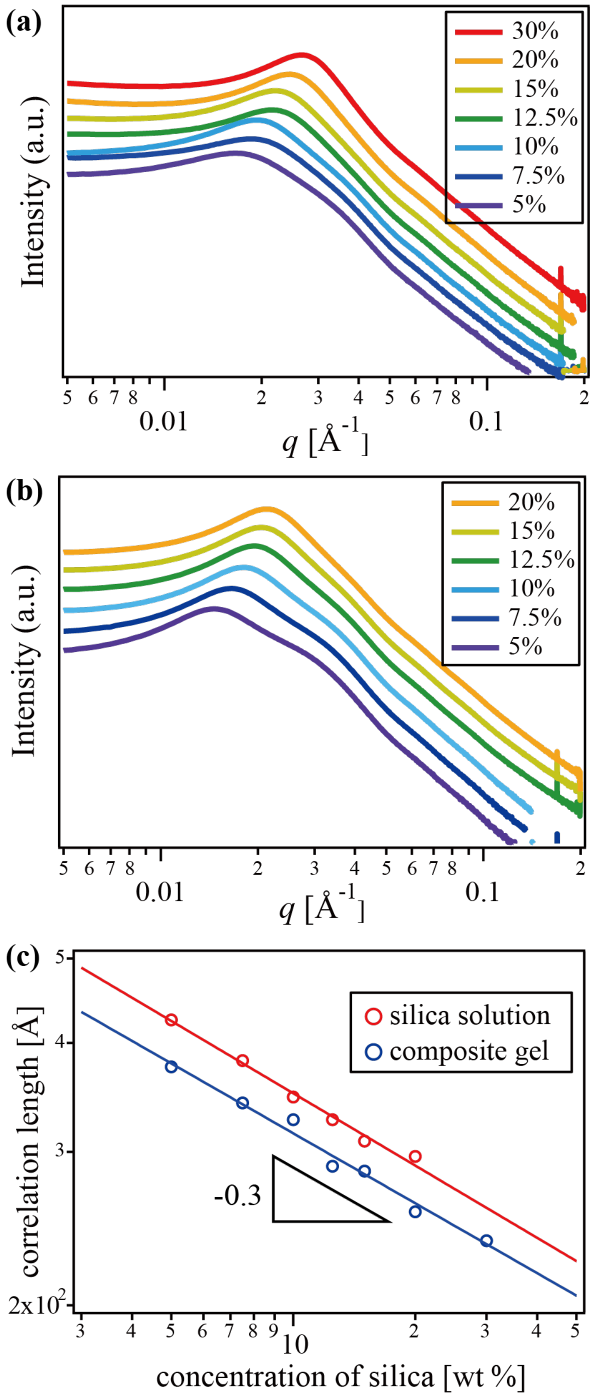

Figure 5: SAXS profiles of (a) silica nanocomposite polyrotaxane gels and (b) silica solutions with different concentration of silica; (c) double logarithmic plots of the correlation length against silica concentrations.

shows the SAXS profiles of silica nanocomposite gels with different silica concentrations. A Bragg's peak around $q = 0.01–0.05$ Å^{-1} was observed, with the peak shifting toward higher q with increasing silica concentration. It is noteworthy that no increase of scattering intensity toward the low q limit, indicating that no aggregation is seen even in that q range. Similar SAXS profiles were observed in silica solutions (Figure 5b). Since the correlation distance becomes shorter with the increase of concentration, the distance is thought to be the separation between silica nanoparticles. When we assume homogeneous distribution of particles, the following relation exists in the distance between particles d and the concentration c:

$$cd^3 = const. \qquad (1)$$

Figure 5c shows the double log arithmic plots of correlation length, which is obtained from the q of the peak top ($d = 2\pi/q$), against silica concentration for the nanocomposite gels and silica solutions. In both cases, a similar power dependence, $d \propto c^{-0.3}$, as in Equation 1, was obtained. Therefore, similarly to the silica solution, the homogeneous dispersion of silica nanoparticles was retained in the nanocomposite gels until at least 30 wt % silica content.

Viscoelastic measurements were carried out for the obtained gels. Figure 6a shows the results of stress relaxation tests. At high silica concentration (more than 15%), the Young's modulus is about 1 kPa, whereas a lower silica concentration yielded a lower modulus of about 0.5 kPa. In addition, as mentioned above, no gelation occurred without silica. Thus, the modulus tends to increase with the concentration of silica, though the incremental increase of modulus is not proportional to silica concentration but stepwise. This suggests that the cross-linking density becomes higher with increasing silica concentration because the silica acts as the polyrotaxanes cross-linker. The results of dynamic viscoelastic measurements shown in Figure 6b also suggest the network formation via silica nanoparticles. Dynamic storage Young's modulus E' was increased with silica content and the modulus was consistent with $E(t)$. On the other hand, the loss modulus E'' hardly changed with increasing of silica concentration. Thus, the ratio of the loss modulus to storage modulus, the so-called loss tangent, decreased with silica concentration. This typical tendency generally observed in chemical gels that is attributed to the decrease of dangling chains, resulting in the formation of a denser network. In addition, there was no stress relaxation with finite equilibrium modulus regardless of the silica content. Figure 6c shows the strain-dependence of the relaxation Young's modulus for the gel with 15% silica. The modulus was almost independent of the strain. These results clearly indicate that the silica nanocomposite polyrotaxane gels form an infinite network structure with negligible physical cross-links that have finite lifetime to exhibit stress relaxation, similar to ideal chemical gels. At the same time, the negligible relaxation indicates that almost all silica nanoparticles were bound to the polymer network.

However, the Young's modulus of the nanocomposite gels is abnormally low. From the Young's modulus, E, with an assumption of ideal polymer network, the averaged molecular weight between cross-links, M_x, can be estimated by the following equation:

$$M_\mathrm{x} = \frac{3\rho RT}{E} \qquad (2)$$

where ρ is the density of polymer, R the gas constant, and T the absolute temperature. M_x of the representative nanocomposite polyrotaxane gels with E = 1 kPa was calculated to be 7×10^5 g/mol. This M_x is considerably larger than the molecular weight of the precursor polyrotaxane, TES-PR (~2×10^5 g/mol). Thus, this result gives us an unlikely picture for the network where several polyrotaxanes are bound to form a single partial chain. This discrepancy probably arises from the assumption of the validity of rubber elastic theory for these gels. Surely, for most of composite gels or rubbers, the theory is already invalid due to the presence of strong interactions between polymers and embedded particles in addition to the covalent crosslinking points. However, such interactions increase not, decrease, modulus. Thus, the interactions between the polyrotaxane and silica cannot explain the significantly low modulus.

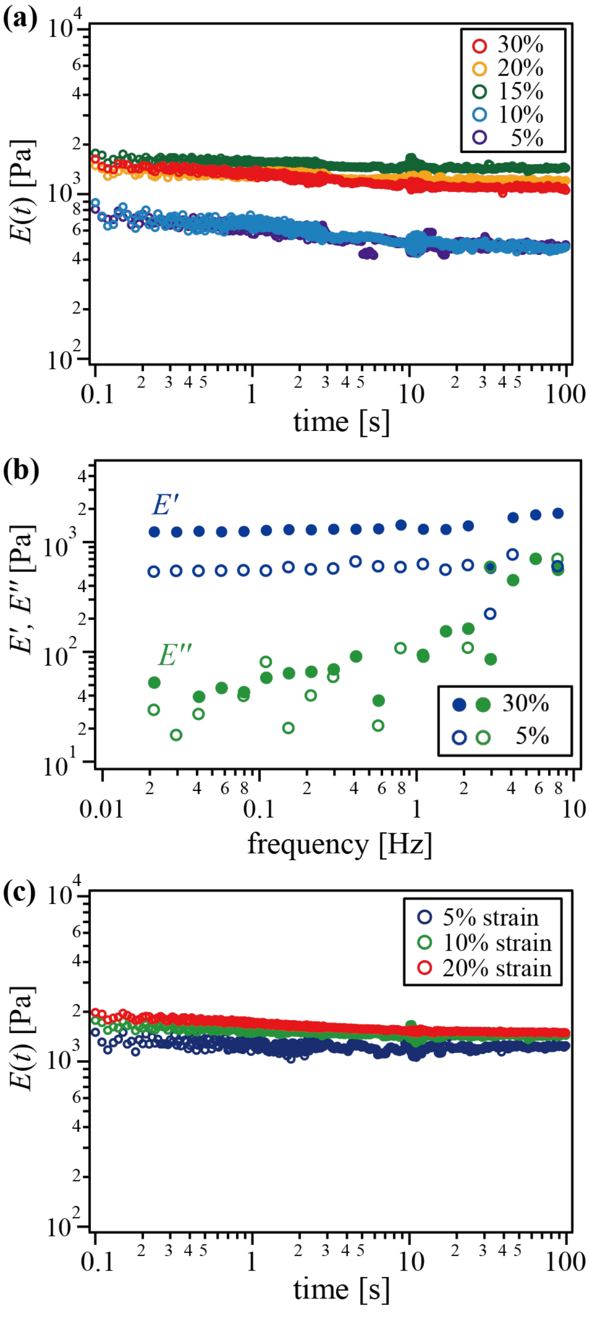

Figure 6: (a) Relaxation Young's modulus with 5% strain and (b) frequency-dependence of dynamic storage and loss moduli for silica nanocomposite polyrotaxane gels with different silica concentrations; (c) strain-dependence of relaxation Young's modulus for the gel with 15% silica.

Recent research in polyrotaxane gels, which were obtained by the simple cross-linking of polyrotaxanes via intermolecular covalent bonds between CDs, indicated a new origin of the elasticity experimentally and theoretically [12,14,16,18]. Since the polymer chains can slide through the cross-links, the anisotropic orientation of chain segments, which causes the entropic elasticity of rubbers and gels, can be relaxed. Simultaneously, the relaxation of chains results in inhomogeneous distribution of the threaded CDs. As the CDs continuously slide along the backbone polymer, their inhomogeneous distribution can generate entropic stress. Thus, the origin of elasticity is not the entropy of polymer chains but that of the CDs, and the abnormally small modulus of polyrotaxane gels can be explained by the characteristic elasticity. Similarly, the extremely low modulus of the nanocomposite polyrotaxane gels is attributable to the characteristic elasticity originated from the entropy of CDs. Since the infinite network was formed mainly by the covalent bonds between CDs and silica surface, the polymer chains are bound to neither CDs nor silica. If the polymer chains are directly attached to the silica surface, the chain mobility were drastically decreased, yielding an increased modulus as observed in conventional composite gels and rubbers. Therefore, the polymer chains slide through the immobilized CDs on the surface of silica, and thus the unique properties observed in polyrotaxane gels may also appear in these nanocomposite polyrotaxane gels.

In addition to the characteristic softness, the nanocomposite gels exhibited significant toughness. Figure 7 shows the stress–strain curves of one of the nanocomposite gels under compression. Since the fracture point is not always clear in the stress–compression behavior, the same measurement was repeated using the same gel. The two curves are in complete agreement, indicating that no fracture occurred during the first compression. This data proved that the gel is compressive to at least one-fifth of the original thickness without fracture or network structure recombination. The toughening mechanism may be essentially the same as that in polyrotaxane gels: the stress applied to chains can be distributed by chain sliding through the immobilized CDs on the silica surface, the so-called pulley effect [11]. In this way, the silica nanocomposite polyrotaxane gels exhibited two unique properties: soft and tough, through the novel method for nanocomposites without chemical bonds or significant interactions between polymers and nanoparticles.

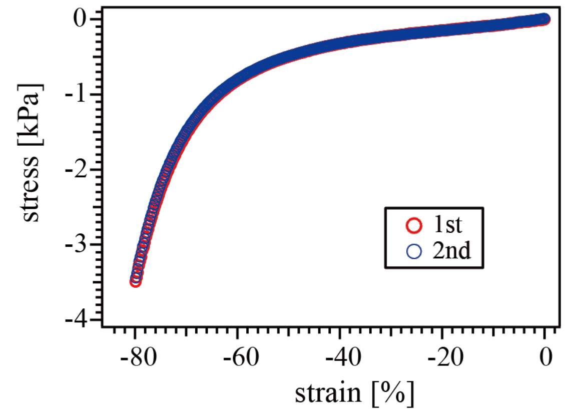

Figure 7: Repeated stress-strain curves for a silica nanocomposite polyrotaxane gel with 20% silica content.

Conclusion

Here we demonstrate the synthesis of a novel nanocomposite gel where the polymer chains were not directly bonded but rather mechanically interlocked to the silica surfaces. The silica nanoparticles were homogeneously distributed in the gel and worked as cross-linkers to immobilize the cyclic components of the polyrotaxanes on the silica surfaces. As the backbone polymer chains were not only free from adhesion to the silica surface but can also slide through the immobilized cyclic components, the nanocomposite gel achieved low Young's modulus and high toughness without any detectable fracture or recombination of network structure under 80% compression. These results suggest that the concept of topological cross-linking previously studied with polyrotaxane gels is applicable to other nanocomposite materials, though our model system utilized silica nanocomposites. Functionalization and applications of the nanocomposite polyrotaxane gels with other nanoparticles are now in progress.

Experimental

Materials

Crude polyrotaxane consisting of polyethylene glycol (PEG, M_n = 32,000) and α-cyclodextrin (CD) were purchased from Advanced Softmaterials, Inc. The crude polyrotaxane was purified by repeated reprecipitation from its DMSO solution into deionized water. The obtained precipitate was freeze-dried and the refined polyrotaxane (PR) obtained as a white powder. The coverage, which is a measure how densely the backbone PEG is covered with CDs, was calculated to be 25% based on the ^{1}H NMR spectrum. Standard polymers for the calibration of the molecular weights by size-exclusion chromatography (SEC) were purchased from Polymer Source, Inc. Solutions of silica nanoparticle with 15 nm of diameter in *N*,*N*-dimethylacetamide was kindly supplied by Nissan Chemical Industries, Ltd. 2-Isocyanatoethyl acrylate was purchased from Showa Denko K.K. Xylene solutions of platinum(0)-1,3-divinyl-1,1,3,3-tetramethyldisiloxane (~2%) was purchased from Sigma-Aldrich Corporation. All other chemicals were purchased from Tokyo Chemical Industry Co., Ltd., or Wako Pure Chemical Industries, Ltd., and all reagents were used as received without further purification except for PR.

Characterization measurements

^{1}H NMR spectra (400 MHz) were recorded on a JEOL JNM-AL400 spectrometer at 343 K. The chemical shift was calibrated using DMSO (2.50 ppm) as an internal standard. SEC was performed on TOSOH HLC-8220 with two Shodex OH Pack SB-806MHQ columns, with DMSO at 50 °C in the presence of 0.01 M lithium bromide as the eluent using RI detection and PEG standards. The flow rate was 0.4 mL/min.

Synthesis of acryloyl modified polyrotaxane (Acryl-PR)

Three grams of PR previously dried under vacuum was dissolved in anhydrous DMSO (60 mL). 2-Isocyanatoethyl acrylate (9 mL) and dibutyltin dilaurate (90 μL) were added and stirred at room temperature for 5 days. The product was precipitated by pouring the reaction solution into methanol. The precipitate was repeatedly washed with methanol and then dried. The dried product was again dissolved in acetone and then a large amount of methanol was added to precipitate the product. This process was repeated again followed by drying to yield acryloyl modified polyrotaxane (Acryl-PR, 5.41 g) as a white solid: ^{1}H NMR (400 MHz, DMSO-d_6, 343 K): 7.0 (NH of urethane), 6.3, 5.9 (CH_2 of vinyl), 6.1 (CH of vinyl), 4.9 ($C_{(1)}H$ of CD), 4.1 (C(=O)O-CH_2), 3.5 (PEG), 3.2 (-CH_2-NH).

Synthesis of triethoxysilyl modified polyrotaxane (TES-PR)

Two grams of Acryl-PR previously dried under vacuum was dissolved in anhydrous acetone (40 mL). Triethoxysilane (600 μL) and a xylene solution of platinum(0)-1,3-divinyl-1,1,3,3-tetramethyldisiloxane dibutyltin dilaurate (200 μL) were added followed by refluxing at 65 °C overnight. The reaction solution was then centrifuged to precipitate a minor insoluble component, and the supernatant collected. Because the product became insoluble in any solvent once it was completely dried, the crude acetone solution was stored at room temperature until just before use. For further characterization, DMSO or DMSO-d_6 was added to the acetone solution, and then the solution was dried under vacuum to evaporate unreacted reactants and non-DMSO solvent. As a result, pure solutions in DMSO or DMSO-d_6 were obtained because DMSO has a sufficiently high boiling point to resist evaporation. ^{1}H NMR (400 MHz, DMSO-d_6, 343 K): 7.0 (NH of urethane), 6.3, 5.9 (CH_2 of vinyl), 6.1 (CH of vinyl), 4.9 ($C_{(1)}H$ of CD), 4.1 (C(=O)O-CH_2), 3.8 (SiO-CH_2), 3.5 (PEG), 3.2 (-CH_2-NH), 2.3 (OC(=O)-CH_2), 1.1 (SiOCH_2-CH_3), 1.0 (Si-CH_2).

Synthesis of silica nanocomposite polyrotaxane gels

1.5 mL of DMSO was added to 3 mL of the crude acetone solution of TES-PR, whose silica content was known to be 5 wt %/vol. The solution was dried under vacuum to eliminate impurities, yielding 1.5 mL of 0.1 g/mL TES-PR solution in DMSO. A DMAc solution of silica nanoparticles was added to the TES-PR solution, and then the mixed solution was dried under vacuum to evaporate DMAc, resulting in 1.5 mL of TES-PR and silica pre-gel solution in DMSO. By changing the added volume of silica solution, five pre-gel solutions with different silica contents were obtained. Diisopropylethylamine (15 μL) was added to the pre-gel solution, and then the solution was transferred into a Teflon/glass mold with a 25 mm × 25 mm × 3 mm void. The reaction was carried out at 100 °C for 16 h to yield a transparent nanocomposite gel. In the same way, thinner gels were also prepared in a mold with a 20 mm × 20 mm × 1 mm void for the following structural analysis.

Small-angle X-ray scattering measurement

Synchrotron small-angle X-ray scattering (SAXS) experiments were carried out at the beamline 6A of Photon Factory, HighEnergy Accelerator Research Organization, KEK (Tsukuba, Japan). The wavelength λ of the incident X-ray beam was 1.50 Å and the beam size was 0.5 mm (vertical) × 0.5 mm (horizontal). PILATUS 300k (Dectris) was used to record SAXS patterns. The sample-to-detector distance was 2.6 m and the sample thickness was 1 mm. The exposure time for each sample was kept constant at 5 s. The scattering angle θ was calibrated by the diffraction pattern of chicken tendon collagen. The obtained SAXS patterns were converted into 1D profiles, scattering intensity I vs scattering vector q, by circular averaging. The scattering vector is defined as:

$$q = \frac{4\pi}{\lambda}\sin\left(\frac{\theta}{2}\right) \tag{3}$$

Mechanical measurements

Obtained silica nanocomposite polyrotaxane gels were cut into cylindrical shapes of 10 mm diameter and 3 mm thickness. All measurements were conducted with a strain-controlled oscillatory rheometer (RSAIII, TA Instruments) using a parallel plate geometry at room temperature. Frequency sweeps were conducted from 0.01 to 80 Hz, applying 1% of the oscillatory compressive strain amplitude, which was still within the range of linear viscoelasticity. Stress relaxation tests were also performed by the compression mode. Stress–compression curves were obtained at a sufficiently slow and constant rate of strain: 0.2%/s.

Acknowledgements

This work was partially funded by JSPS KAKENHI Grant Number 25220603 and ImPACT Program of Council for Science, Technology and Innovation (Cabinet Office, Government of Japan). The small-angle X-ray scattering experiments were performed at beamlines BL-6A at the Photon Factory, High Energy Accelerator Research Organization, KEK, with the approval of the Photon Factory Program Advisory Committee (Proposal No. 2013G662).

References

1. Mitsumata, T.; Ohori, S. *Polym. Chem.* **2011,** *2,* 1063–1067. doi:10.1039/c1py00033k
2. Fujiwara, S.; Fujimoto, K. *Rubber Chem. Technol.* **1971,** *44,* 1273–1277. doi:10.5254/1.3544806

3. Kaufman, S.; Slichter, W. P.; Davis, D. O. *J. Polym. Sci., Part A-2: Polym. Phys.* **1971,** *9,* 829–839. doi:10.1002/pol.1971.160090505
4. Nishi, T. *J. Polym. Sci., Polym. Phys. Ed.* **1974,** *12,* 685–693. doi:10.1002/pol.1974.180120405
5. O'Brien, J.; Cashell, E.; Wardell, G. E.; McBrierty, V. *Macromolecules* **1976,** *9,* 653–660. doi:10.1021/ma60052a025
6. Nishi, T.; Nukaga, H.; Fujinami, S.; Nakajima, K. *Chin. J. Polym. Sci.* **2007,** *25,* 35–41. doi:10.1142/S0256767907001820
7. Brochu, P.; Pei, Q. *Macromol. Rapid Commun.* **2010,** *31,* 10–36. doi:10.1002/marc.200900425
8. Wenz, G.; Han, B.-H.; Müller, A. *Chem. Rev.* **2006,** *106,* 782–817. doi:10.1021/cr970027+
9. Harada, A.; Hashidzume, A.; Yamaguchi, H.; Takashima, Y. *Chem. Rev.* **2009,** *109,* 5974–6023. doi:10.1021/cr9000622
10. Okumura, Y.; Ito, K. *Adv. Mater.* **2001,** *13,* 485–487. doi:10.1002/1521-4095(200104)13:7<485::AID-ADMA485>3.0.CO;2-T
11. Murata, N.; Konda, A.; Urayama, K.; Takigawa, T.; Kidowaki, M.; Ito, K. *Macromolecules* **2009,** *42,* 8485–8491. doi:10.1021/ma901661d
12. Kato, K.; Ito, K. *Soft Matter* **2011,** *7,* 8737–8740. doi:10.1039/c1sm06212c
13. Bitoh, Y.; Akuzawa, N.; Urayama, K.; Takigawa, T.; Kidowaki, M.; Ito, K. *Macromolecules* **2011,** *44,* 8661–8667. doi:10.1021/ma201530z
14. Mayumi, K.; Tezuka, M.; Bando, A.; Ito, K. *Soft Matter* **2012,** *8,* 8179–8183. doi:10.1039/c2sm25508a
15. Katsuno, C.; Konda, A.; Urayama, K.; Takigawa, T.; Kidowaki, M.; Ito, K. *Adv. Mater.* **2013,** *25,* 4636–4640. doi:10.1002/adma.201301252
16. Kato, K.; Yasuda, T.; Ito, K. *Polymer* **2014,** *55,* 2614–2619. doi:10.1016/j.polymer.2014.03.022
17. Seo, J.-H.; Kakinoki, S.; Inoue, Y.; Yamaoka, T.; Ishihara, K.; Yui, N. *J. Am. Chem. Soc.* **2013,** *135,* 5513–5516. doi:10.1021/ja400817q
18. Ito, K. *Polym. J.* **2012,** *44,* 38–41. doi:10.1038/pj.2011.85

License and Terms

The definitive version of this article is the electronic one which can be found at:
doi:10.3762/bjoc.11.238

BEILSTEIN JOURNAL OF ORGANIC CHEMISTRY

Self-assemblies of γ-CDs with pentablock copolymers PMA-PPO-PEO-PPO-PMA and endcapping via atom transfer radical polymerization of 2-methacryloyloxyethyl phosphorylcholine

Jing Lin, Tao Kong, Lin Ye, Ai-ying Zhang and Zeng-guo Feng*

Full Research Paper

Open Access

Address:
School of Materials Science and Engineering, Beijing Institute of Technology, Beijing 100081, China

Email:
Zeng-guo Feng* - sainfeng@bit.edu.cn

* Corresponding author

Keywords:
ATRP; γ-CD; double-chain-stranded; pentablock copolymer; poly(pseudorotaxane); polyrotaxane; single-chain-stranded

Beilstein J. Org. Chem. **2015,** *11,* 2267–2277.
doi:10.3762/bjoc.11.247

Received: 28 July 2015
Accepted: 04 November 2015
Published: 23 November 2015

This article is part of the Thematic Series "Superstructures with cyclodextrins: Chemistry and applications III".

Guest Editor: G. Wenz

Abstract

Pentablock copolymers PMA-PPO-PEO-PPO-PMA synthesized via atom transfer radical polymerization (ATRP) were self-assembled with varying amounts of γ-CDs to prepare poly(pseudorotaxanes) (PPRs). When the concentration of γ-CDs was lower, the central PEO segment served as a shell of the micelles and was preferentially bent to pass through the γ-CD cavity to construct double-chain-stranded tight-fit PPRs characterized by a channel-like crystal structure. With an increase in the amount of γ-CDs added, they began to accommodate the poly(methyl acrylate) (PMA) segments dissociated from the core of the micelles. When more γ-CDs were threaded and slipped over the segments, the γ-CDs were randomly distributed along the pentablock copolymer chain to generate single-chain-stranded loose-fit PPRs and showed no characteristic channel-like crystal structure. All the self-assembly processes of the pentablock copolymers resulted in the formation of hydrogels. After endcapping via in situ ATRP of 2-methacryloyloxyethyl phosphorylcholine (MPC), these single-chain-stranded loose-fit PPRs were transformed into conformational identical polyrotaxanes (PRs). The structures of the PPRs and PRs were characterized by means of ^{1}H NMR, GPC, ^{13}C CP/MAS NMR, 2D ^{1}H NOESY NMR, FTIR, WXRD, TGA and DSC analyses.

Introduction

Cyclodextrins (CDs) are a series of macrocyclic molecules composed of 6, 7, or 8 (α-, β-, and γ-CD, respectively) glucopyranose units. Their hydrophilic surface and hydrophobic inner cavity character and deformable cavity size allow for the self-assembly or inclusion of various polymer chains to generate poly(pseudorotaxanes) (PPRs) or polyrotaxanes (PRs) after endcapping with bulky stoppers. Since Harada et al. first reported the α-CD-based single-chain-stranded PPRs constructed from the inclusion complexation of α-CDs with poly(ethylene glycol) (PEG) [1], a great variety of polymers with different cross-sectional areas have been shown to thread CDs to create PPRs. For example, β-CDs are single-chain-stranded with poly(propylene glycol) (PPG) but not with PEG [2,3], and γ-CDs are not only single-chain-stranded with poly(methyl vinyl ether) (PMVE) [4] or poly(dimethylsiloxane) (PDMS) [5], but also double-chain-stranded with PEG and poly(ε-caprolactone) (PCL) [6]. Recently, Akashi et al. reported the single-chain-stranded inclusion complexation of γ-CDs with poly(methyl methacrylate) (PMMA) [7] and poly(methacrylic acid) (PMAA) [8]. It is worth noting that there is a significant correlation between the size of the CD cavity and the cross-sectional area of the fitting polymers. Accordingly, all the aforementioned PPRs and PRs were created from a matched recognition between the CD cavities and incoming polymer chains, showing the typical channel-like tight-fit crystal structure [1-8]. Due to the fantastic, mechanically interlocked architecture, these PPRs and PRs can be employed as candidates or precursors for complex supramolecular assemblies to realize novel functions [9].

In comparison to α- and β-CDs, γ-CDs possess a larger inner cavity diameter and a higher structurally deformable and adaptable capacity [10]. Recently, studies towards the synthesis and characterization of novel γ-CD-based unmatched PPRs and PRs have attracted attention for their unusual loose-fit and/or over-fit inclusion complexation structure other than the channel-like tight-fit structure [10-12]. It was shown that when self-assembling with PHEMA-PPO-PEO-PPO-PHEMA, γ-CDs could be threaded onto and moved over the 2-hydroxyethyl methacrylate (PHEMA) segments to form a mixed single-chain-stranded loose-fit (PEO) and over-fit (PHEMA) architecture [13]. Using in situ ATRP, those PPRs were successfully transformed into the same conformational PRs [14]. Owing to a more flexible or retardant movement of the entrapped γ-CDs along the thinner PEO and thicker PHEMA segments (as compared with PPO or PMAA), respectively, these unmatched PRs possess the potential to be applied as dynamic-responsive materials, carriers for controlled drug release, biosensors and catalysts.

Poly(methyl acrylate) (PMA) prepared via ATRP of methyl acrylate (MA) is a typical hydrophobic polymer with a more flexible main chain and smaller cross-sectional area as compared with PHEMA. Attaching PMA to two ends of PPO-PEO-PPO imparts the resulting amphiphilic copolymers with a unique core–shell micellar structure, showing different self-assembly behavior as compared with that of PHEMA-PPO-PEO-PPO-PHEMA. Therefore, a series of PMA-PPO-PEO-PPO-PMA pentablock copolymers were first prepared in this study via ATRP of MA using 2-bromoisobutyryl endcapped PPO-PEO-PPO as a macroinitiator, and then allowed to self-assemble with a varying amount of γ-CDs in aqueous solution. To further highlight the supramolecular architecture of the resulting PPRs, the second in situ ATRP of 2-methacryloyloxyethyl phosphorylcholine (MPC) was conducted to endcap them into the same conformational PR-based multiblock copolymers. A schematic description on the self-assembly evolution of varying amounts of γ-CDs with PMA-PPO-PEO-PPO-PMA and the one-pot endcapping via in situ ATRP of MPC is shown in Scheme 1.

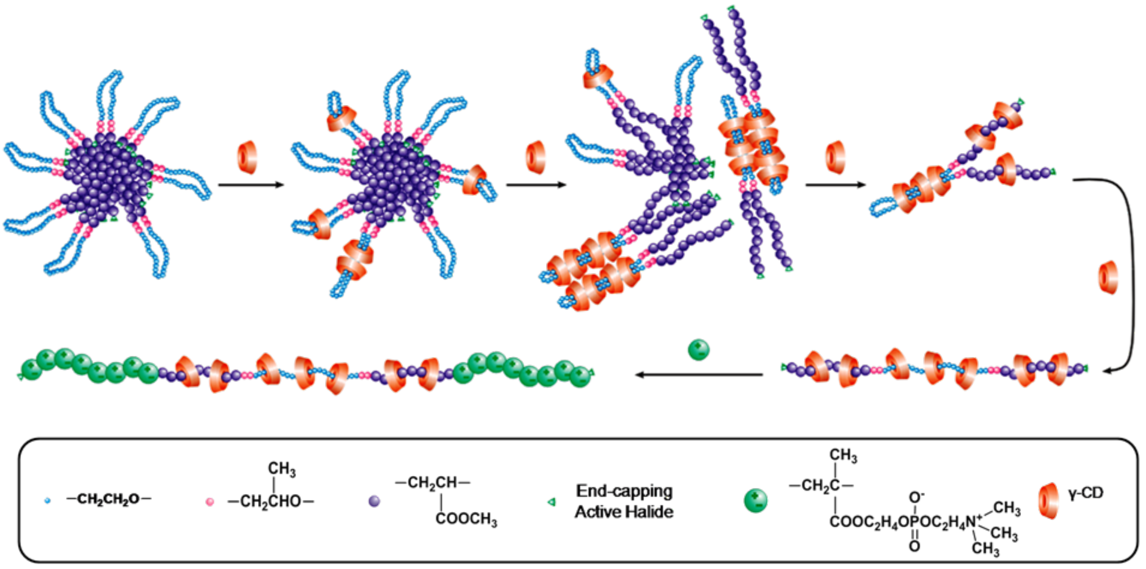

Scheme 1: Schematic description of self-assembly of γ-CDs with PMA-PPO-PEO-PPO-PMA and one-pot endcapping via in situ ATRP of MPC.

Results and Discussion

Preparation of PPRs and PRs

The synthesis of PMA-PPO-PEO-PPO-PMA via ATRP of MA is described in Scheme 2. With the goal of achieving a desired M_w, a narrow PDI and a high preservation of the active Br-terminals for the second in situ ATRP of MPC, the first ATRP of MA was carried out at room temperature using DMF as a solvent and Cu(I)Cl/N,N,N',N",N"-pentamethyldiethylenetriamine (PMDETA) as the catalyst.

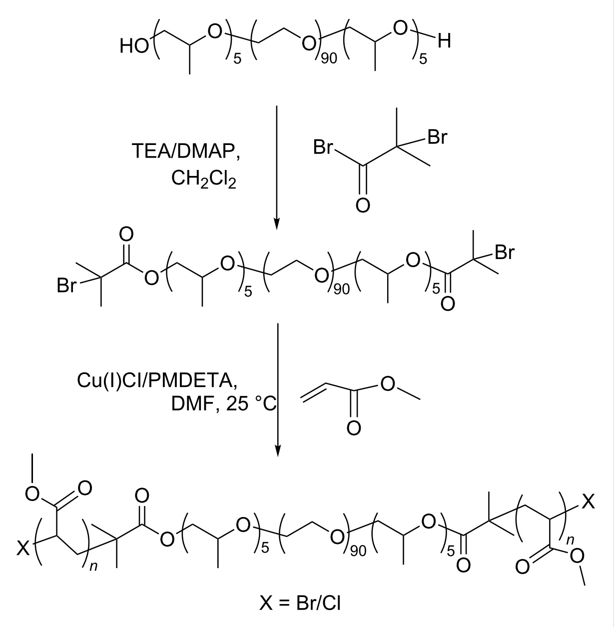

Scheme 2: Synthetic pathway of PMA-PPO-PEO-PPO-PMA.

The macroinitiator and resulting pentablock copolymers are designated as BrPEPBr and PEPxM, respectively, where x is the feed molar ratio of MA to PPO-PEO-PPO. The products were characterized by means of ^{1}H NMR and GPC analyses (Figure S1 and Figure S2, Supporting Information File 1). The degree of esterification of BrPEPBr determined by ^{1}H NMR was >99%. Additionally, the GPC curves of PEPxM presented a nearly symmetrical monomodal distribution with a narrow polydispersity index (PDI). These results suggested that the target PMA-PPO-PEO-PPO-PMA pentablock copolymers were obtained. The compositions, GPC data and yields are summarized in Table 1.

Pentablock copolymers were selected to self-assemble with γ-CDs to prepare PPRs in aqueous solution. The resulting PPRs are designated as PEPxMyCD, where x again is the feed molar ratio of MA to PPO-PEO-PPO and y is the feed molar ratio of γ-CD to PMA-PPO-PEO-PPO-PMA. The macroinitiator was also employed to fabricate the PPR with γ-CDs. Its self-assembled product is designated as PEP15CD, meaning the feed molar ratio is 1:15 for BrPEPBr:γ-CD. The compositions and yields are summarized in Table 2. As can be seen, in addition to good yields in the range of 62.5–73.2%, the resulting molar ratios of PEPxM to γ-CD in the PPRs (including PEP15CD) perfectly matched the feed values, demonstrating the good inclusion complexation ability between γ-CD and pentablock polymers.

As a typical example, the self-assembly evolution of PEP100M15CD is shown in Figure 1. When an aqueous solution of saturated γ-CD was mixed with a preset amount of PMA-PPO-PEO-PPO-PMA, the mixture immediately turned turbid, suggesting that the self-assembly of γ-CDs with the incoming polymer chain proceeded similar to the case of inclusion complexation of γ-CDs with the macroinitiator BrPEPBr [13]. Thereafter, the turbidity of the solution quickly increased as more γ-CDs were entrapped on different polymer segments. Surprisingly, a white gel was formed after the turbid mixture was stored at 6–8 °C for at least 24 h. The turbidity evolution and hydrogel formation were observed in other PPR samples, except that PEP15CD was rapidly precipitated from the mixture.

To endcap PPRs into PRs, the PEP40M30CD constructed from the self-assembly of PEP40M with γ-CD at a feed molar ratio of 1:30 was used as a supramolecular initiator. The one-pot ATRP of MPC was conducted in water at room temperature for 60 h

Table 1: Compositions, GPC data and yields of PMA-PPO-PEO-PPO-PMA.

Entry	Molar ratio of BrPEPBr:MA		M_n[a]	M_n[b]	M_w/M_n[b]	Yield/%[c]
	Feed ratio	Found ratio[a]				
BrPEPBr	1:0	1:0	4880	4750	1.15	81.5
PEP40M	1:40	1:22	6770	6880	1.27	65.9
PEP60M	1:60	1:35	7888	8085	1.47	67.5
PEP100M	1:100	1:54	9522	10453	1.31	62.3

[a]Determined by ^{1}H NMR analysis in $CDCl_3$/DMSO-d_6 (1:1, v/v). [b]Determined by GPC in DMF using PS standards. [c]Calculated based on the product weight divided by the raw material weight.

Table 2: Compositions and yields of PPRs.

Entry	Guest molecule	Molar ratio of guest molecule:γ-CD		Yield/%^{b}
		Feed ratio	Found ratio^a	
PEP40M10CD	PEP40M	1:10	1:11	68.5
PEP40M15CD		1:15	1:15	65.7
PEP40M30CD		1:30	1:23	66.4
PEP60M10CD	PEP60M	1:10	1:11	68.5
PEP60M15CD		1:15	1:16	69.5
PEP60M30CD		1:30	1:23	70.0
PEP100M10CD	PEP100M	1:10	1:12	62.5
PEP100M15CD		1:15	1:15	68.4
PEP100M30CD		1:30	1:24	66.7
PEP15CD	BrPEPBr	1:15	1:17	73.2

^{a}Determined by ^{1}H NMR analysis in $CDCl_3$/DMSO-d_6 (1:1, v/v). ^{b}Calculated based on the product weight divided by the raw material weight.

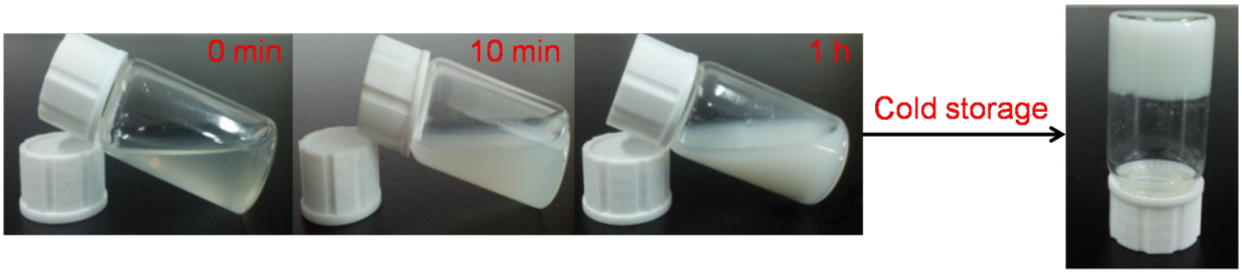

Figure 1: Photographs of the formation of a PEP100M15CD hydrogel.

using Cu(I)Br/tris(2-(dimethylamino)ethyl)amine (Me_6TREN) as a catalyst. The resulting PR-based multiblock copolymers are ascribed as PRmCDnP, where m and n stand for the feed molar ratio of γ-CD and MPC to PEP40M, respectively. The compositions, GPC data and yields are summarized in Table 3. As can be seen, the experimental molar ratio of γ-CD to PEP40M varied in the range of 5–8 and a feed molar ratio of 30 was maintained after the second in situ ATRP. However, the degree of polymerization (DP) of PMPC for all the copolymers was increased with the feed molar ratio of MPC to PEP40M, clearly suggesting that PEP40M30CD as an initiator in the form of PPR indeed held a very high degree of chain-end functionality and initiating efficiency for the second ATRP. Relatively lower yields in the range from 27.5–30.5% were evidently caused by the massive slipping of the γ-CDs during the process. Even so, these yields were higher than those any reported loose-fit and/or over-fit γ-CD-based PRs [7,8,10,12].

Characterization of PPRs and PRs

WXRD measurements

In two recent articles [13,14], we reported that attaching PHEMA to two ends of PPO-PEO-PPO via ATRP of HEMA

Table 3: Compositions, GPC data and yields of PR-based multiblock copolymers.

Entry	Molar ratio of PEP40M:γ-CD:MPC		M_n × 10^{-4a}	M_n ×$10^{-4\ b}$	M_w/M_n^b	Yield/%^{c}
	Feed ratio	Found ratio^a				
PR0CD30P	1:0:30	1:0:19	1.23	1.00	1.57	58.9
PR30CD30P	1:30:30	1:5:20	1.91	1.21	1.66	27.5
PR30CD50P	1:30:50	1:6:41	2.66	1.64	1.69	29.4
PR30CD80P	1:30:80	1:8:68	3.72	2.33	1.59	30.5

^{a}Determined by ^{1}H NMR in DMF-d_7/D_2O (1:1, v/v) and DMSO-d_6/D_2O (2:1, v/v). ^{b}Determined by GPC in DMF/H_2O (1:1, v/v) using PEG standards. ^{c}Calculated based on the product weight divided by the raw material weight.

could change its self-assembly process with γ-CDs. Wherein, the γ-CDs were threaded onto and moved over the PHEMA segments to give access to unmatched γ-CD/PHEMA-PPO-PEO-PPO-PHEMA PPRs showing a mixed loose-fit (with PEO) and over-fit (with PHEMA) architecture, instead of the PEO-bent double-chain-stranded tight-fit ones like those of γ-CD/BrPEPBr PPRs [15,16]. However, attaching hydrophobic PMA to PPO-PEO-PPO renders the resulting amphiphilic copolymers able to form unique polymeric micelles in aqueous solution before the self-assembly with γ-CDs, as compared to PHEMA-PPO-PEO-PPO-PHEMA. The morphology of self-assembled aggregates of PMA-PPO-PEO-PPO-PMA in aqueous solution was observed by TEM. As shown in Figure S3, Supporting Information File 1, the aggregates were formed as spherical or "core–shell" micelles or aggregates of 500–800 nm diameter, where the shell-forming PEO bent segments would effectively bury the PMA core and shield it from water. In general, surface hydrophilic γ-CDs cannot pass through the hydrophilic shell into the core of micelles to include the PMA segments. A schematic description of the self-assembly process of γ-CDs with PMA-PPO-PEO-PPO-PMA is illustrated in Scheme 1.

WXRD measurements provide a powerful tool to analyze the supramolecular structure of the self-assemblies, consisting of varying amounts of γ-CDs with PMA-PPO-PEO-PPO-PMA. As shown in Figure 2, different from the cage-type crystal structure of γ-CD [6], a new diffraction peak at 2θ = 7.5° was clearly observed in the diffraction pattern of PEP15CD self-assembled from the macroinitiator BrPEPBr with γ-CDs. This is characteristic of the PEO-bent double-chain-stranded tight-fit PPRs [17]. In the WXRD patterns of all the PPRs, the disappearance of two prominent peaks at 19.2° and 23.3° of the central PEO segment in the pentablock copolymer PEP100M verified their self-assembly with γ-CDs. Surprisingly, these PPRs presented varying diffraction patterns as a function of γ-CD content. For example, at a feed molar ratio 10:1 of γ-CD to guest pentablock copolymer, PEP100M10CD displayed a pattern similar to PEP15CD as well as to those previously reported [13,15]. This indicates that the central PEO segments were favorably bent to pass through the cavity of γ-CDs to give rise to the double-chain-stranded tight-fit PPR. For example, at a feed molar ratio of γ-CD to PEP100M equal to 30:1, PEP100M30CD depicted three broad peaks at 2θ = 12.4°, 17.2° and 21.5°, instead of a peak at 7.5° for the typical PEO-bent double-chain-stranded tight-fit PPR. This particular pattern was similar to previously reported, single-chain-stranded loose-fit PPRs [10-12]. It suggested that with the further increase in the number of added γ-CDs, the resulting PEO-bent double-chain-stranded tight-fit PPRs tended to aggregate and settle out through the hydrogen bonding interaction. This leads to the breakdown of the core–shell micellar structure and the exposure of uncoated PMA chains to water. Under this circumstance, the entrapped γ-CDs began to slip off and return to accommodate the PMA segments, moving over them in a randomly distributed manner along the pentablock copolymer chain. This generated the single-chain-stranded loose-fit PPRs showing no characteristic channel-like tight-fit structure. In comparison to PEP100M10CD and PEP100M30CD, a weak peak at 6.8° and other three main peaks at 2θ = 12.4°, 17.2° and 21.5° also appeared in the diffraction pattern of PEP100M15CD. It was shown that at a feed molar ratio 15:1 of γ-CD to PEP100M, the supramolecular structure of PEP100M15CD changed from the PEO-bent double-chain-stranded tight-fit PPR into the single-chain-stranded loose-fit one.

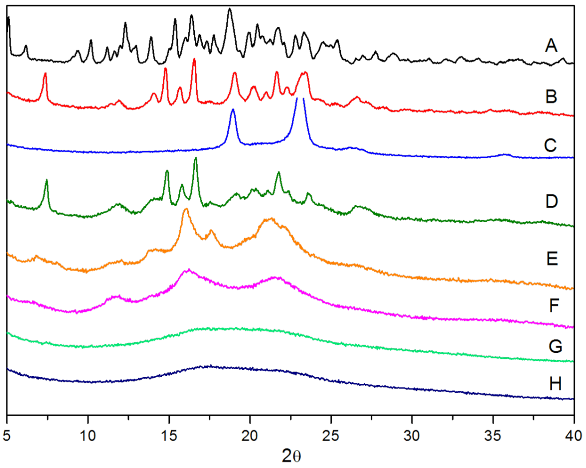

Figure 2: WXRD patterns of γ-CD (A), PEP15CD (B), PEP100M (C), PEP100M10CD (D), PEP100M15CD (E), PEP100M30CD (F), PR30CD50P (G) and PR30CD80P (H).

The WXRD patterns of the resulting PR-based multiblock copolymers are also shown in Figure 2. As can be seen, both PR30CD50P and PR30CD80P exhibited only a single broad diffraction peak, most likely due to those remainimg γ-CDs randomly distributed along the pentablock copolymer chain to form an irregular noncrystalline state. This pattern was also observed in our recent reports [13-15].

^{1}H NMR and GPC analyses

As the PMPC segments in the PRs were insoluble not only in DMF and DMSO but also in water, the ^{1}H NMR spectra were measured in a mixed solution of DMF-d_7/D_2O (1/1, v/v) and DMSO/D_2O (2/1, v/v), respectively, and the results are shown in Figure 3. The ^{1}H NMR spectrum of the heptablock copolymer PR0CD30P is displayed in Figure S4, Supporting Information File 1. As can be seen, the proton resonance peak of γ-CD (CD_1) is not easy to assign in DMF-d_7/D_2O as in

DMSO/D_2O. This suggests that the central PPR segment is soluble and the PMA segments are insoluble in this solvent. Accordingly, the DP of PMPC was determined from the integration area ratio of the proton resonance peaks of methyl groups (a) of MPC repeating units to that of the methylene protons in MPC and MA ($b_1 + b_2$) repeating units, according to Figure 3A. The CD coverage ratios were obtained from the integration area ratio of the proton resonance peaks of γ-CD (CD_1) to that of methyl groups (a) of MPC repeating units from Figure 3B. It was found that only about one-fifth of the added γ-CDs were left on the PMA-PPO-PEO-PPO-PMA main chains after the second ATRP of MPC in this study. This was most

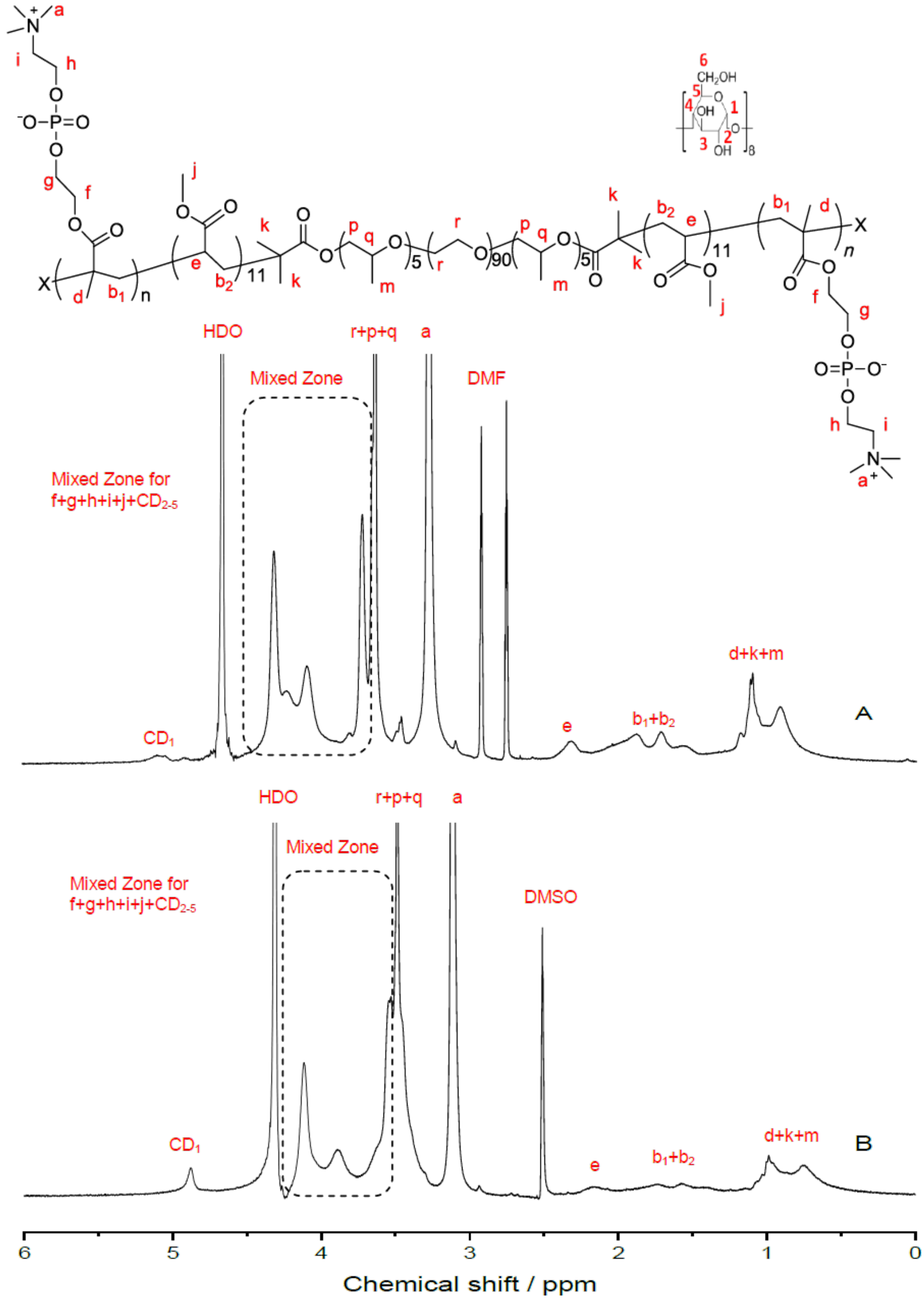

Figure 3: ^{1}H NMR spectra of PR30CD80P in DMF-d_7/D_2O (A) and DMSO-d_6/D_2O (B).

likely due to a relatively smaller cross-sectional area of PMA compared with PHEMA, leading to a lower inclusion complexation stability of PMA-PPO-PEO-PPO-PMA with γ-CDs during the one-pot in situ ATRP of MPC [14].

GPC analysis further confirmed the unique structure of the resultant γ-CD-based PRs. As depicted in Figure 4, the molecular weights were increased with the feed molar ratio of MPC to PEP40M, and all samples exhibited a symmetrical and unimodal GPC curve showing no free γ-CD peak. Although PMA was used as the outer hydrophobic segment to induce the self-aggregation of the pentablock copolymers in aqueous solution, a multimodal molecular weight distribution (which usually results from the addition of methacrylates to the polymers of acrylates) was not shown in the GPC curves of the PR-based multiblock copolymers [18,19]. Given that nearly the same quantity of 5–8 γ-CDs were left after the second ATRP (as determined by ^{1}H NMR), it is suggested that the one-pot endcapping via the in situ ATRP of MPC using Cu(I)Br/Me$_6$TREN as a catalyst successfully converted the γ-CD/PMA-PPO-PEO-PPO-PMA PPRs into the same conformational, mechanically interlocked, PR-based multiblock copolymers.

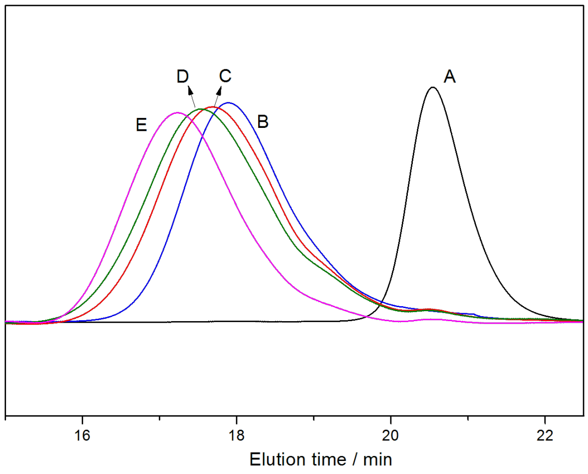

Figure 4: GPC curves of γ-CD (A), PR0CD30P (B), PR30CD30P (C), PR30CD50P (D) and PR30CD80P (E).

^{13}C CP/MAS NMR and 2D NOESY NMR testing

Figure 5 shows the solid-state ^{13}C CP/MAS NMR spectra of the PEP100M15CD PPR sample and γ-CDs. In line with previous research [20], the less symmetric, cyclic conformations of γ-CDs in the uncomplexed crystalline state bring about its spectrum with multiple, clear C1, C4 and C6 resonance peaks. In the test sample, PEP100M15CD, the corresponding carbon reveals a single resonance peak together with the typical resonance peaks from PMA. This clearly suggested that the γ-CDs were threaded in a head-to-head and tail-to-tail fashion onto the PMA-PPO-PEO-PPO-PMA chain. This offered direct evidence, confirming the self-assembly of γ-CDs with PMA-PPO-PEO-PPO-PMA to give rise to PPRs.

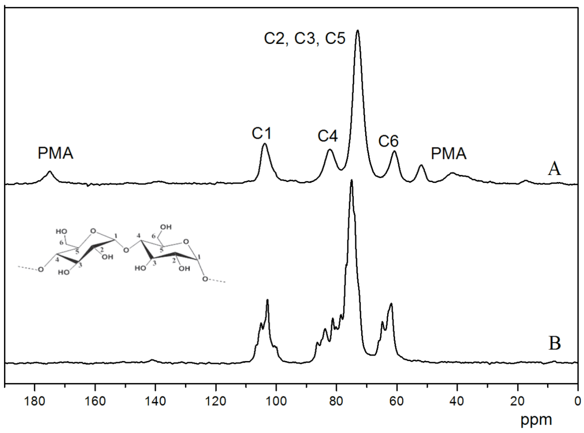

Figure 5: ^{13}C CP/MAS NMR spectra of PEP100M15CD (A) and γ-CD (B).

To further confirm the inclusion complexation structure of γ-CDs with the pentablock copolymers and the preferential location of γ-CDs on the different segments after the second in situ ATRP, 2D ^{1}H NOESY NMR measurements were carried out on the PR sample PR30CD80P (Figure 6). Consistent with ^{1}H NMR and GPC analyses, the correlation of peaks between the interior protons of γ-CDs (CD$_3$ and CD$_5$) and those of MA (b$_2$), PPO (m, p, q) and PEO (r) clearly indicated that host γ-CDs remained for inclusion of the guest pentablock copolymer chain after the one-pot ATRP of MPC. Because this spectrum was taken in DMSO-d_6/D$_2$O, the entrapped γ-CDs showed no bias to be located along a particular segment of the PMA-PPO-PEO-PPO-PMA chain.

FTIR measurements

The FTIR spectra of the PPR and PR samples and their precursors are depicted in Figure 7. The peaks at 1235, 1088 and 788 cm^{-1} are attributed to the stretching vibrations of O–P–O, C–N–C and P–O–C in MPC repeat units, respectively [21]. The wider absorption peak at 584 cm^{-1} (as compared with the uncomplexed γ-CD) and the characteristic peak at 1028 cm^{-1} were visible in the spectra of both PEP100M15CD and PR30CD80P, while the –CH$_2$– vibration absorption peak of PEO at 1350 cm^{-1} disappears in the spectrum of PEP100M15CD. This is due to the restricting and shielding effects from the inner cavity of γ-CDs against the vibration of the corresponding chemical bond [22]. This confirmed that the PMPC segments were successfully attached to two ends of the pentablock polymer to convert γ-CD/PMA-PPO-PEO-PPO-PMA PPRs into the PR-based multiblock copolymers [14,23].

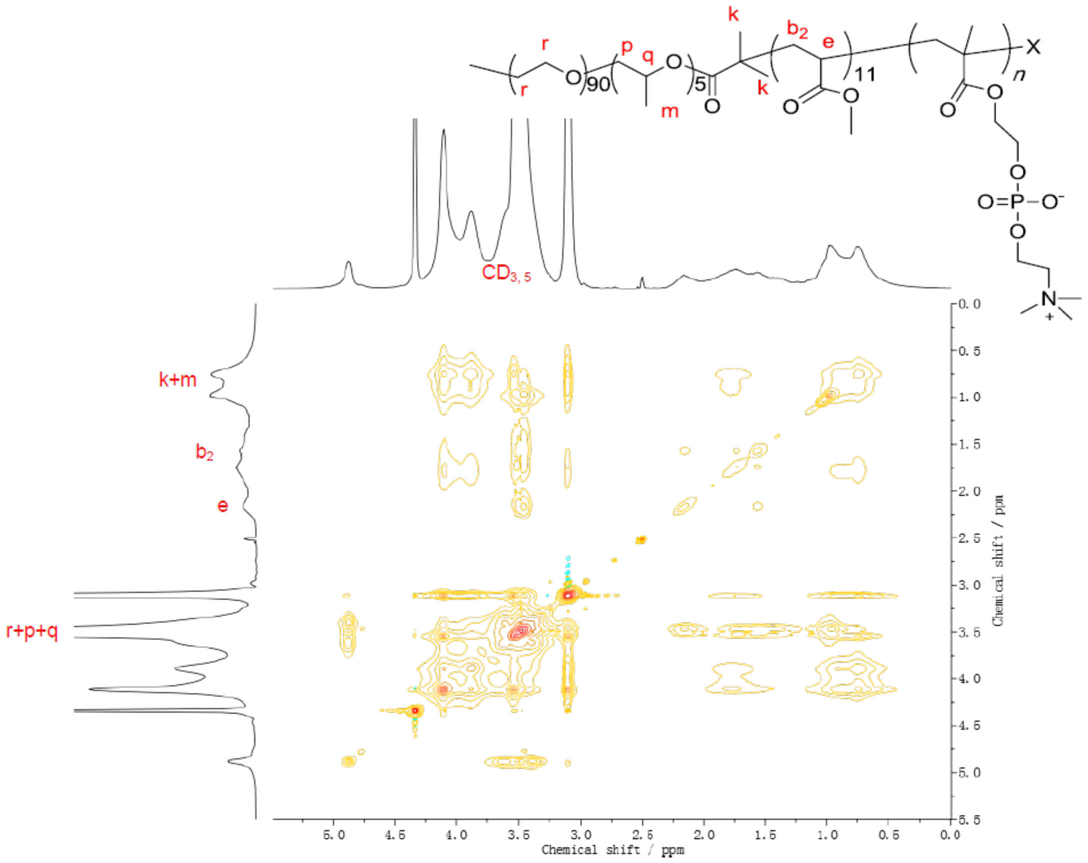

Figure 6: 2D NOESY NMR spectrum of PR30CD80P in DMSO-d_6/D_2O.

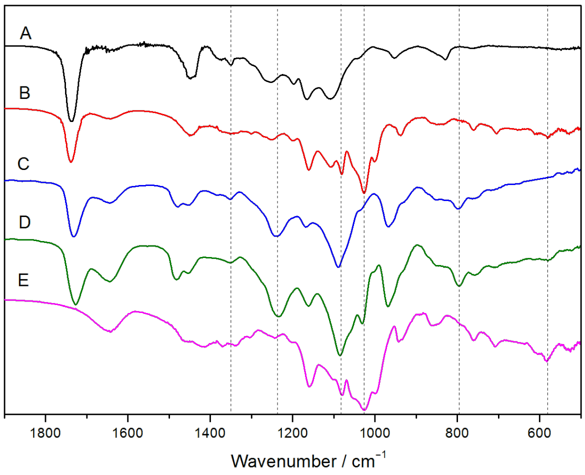

Figure 7: FTIR spectra of PEP100M (A), PEP100M15CD (B), PR0CD30P (C), PR30CD80P (D) and γ-CD (E).

Thermal analysis

TGA analysis was carried out to further confirm the structure of the PPRs. As shown in Figure 8, the free γ-CD began to decompose at about 300 °C and the PEP100M at around 325 °C. Unlike either the pure γ-CD or PEP100M, the PEP100M10CD and PEP100M30CD samples underwent a two-step, thermal degradation process. The thermal weight loss at about 275 °C and 350 °C is attributed to the decomposition of γ-CD and the pentablock polymer chain, respectively. The pentablock copolymers were substantially stabilized by the formation of PPRs. Meanwhile, PEP15CD presented an additional thermal weight loss component starting at about 200 °C, possibly due to the decomposition of 2-bromoisobutyryl ends of the BrPEPBr in a U-shape [13]. Compared with the thermal decomposition of γ-CD, the PPR samples (including PEP15CD) displayed shifted, γ-CD-related thermal decomposition towards lower temperature. This was likely due to the differing architecture of the PPRs self-assembled from PMA-PPO-PEO-PPO-PMA with the varying amount of γ-CDs [10-12].

The DSC measurements of PPRs and PRs were also conducted in this study. As shown in Figure 9, BrPEPBr reveals an endothermic peak at 51.8 °C, corresponding to the melting point of the PEO crystalline phase. As for PEP100M, a lower melting point appeared at 41.8 °C, due to the interference of the PMA blocks attaching to the two ends of PPO-PEO-PPO. However,

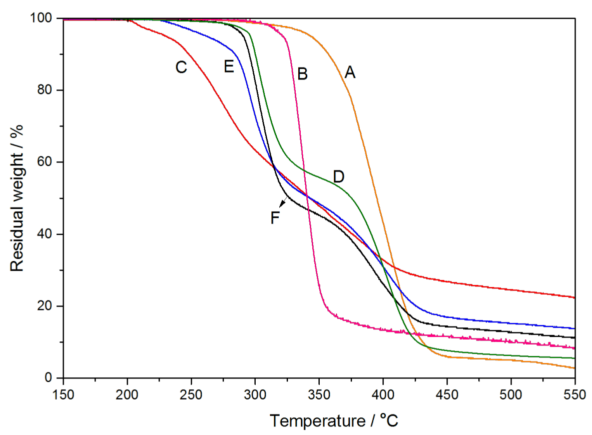

Figure 8: TGA curves of PEP100M (A), γ-CD (B), PEP15CD (C), PEP100M10CD (D), PEP100M15CD (E) and PEP100M30CD (F).

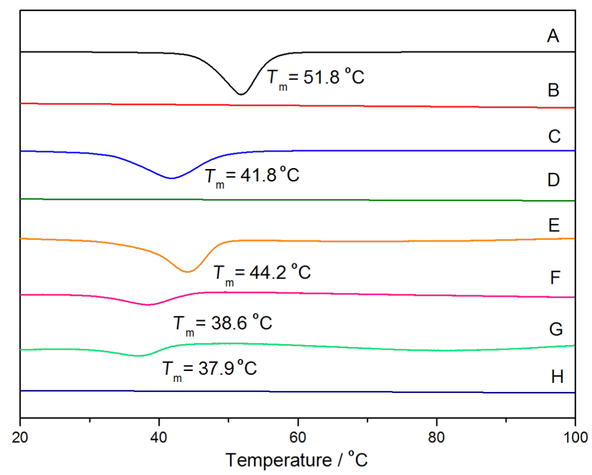

Figure 9: BrPEPBr (A), PEP15CD (B), PEP100M (C), PEP100M15CD (D), PR0CD30P (E), PR30CD50P (F), PR30CD80P (G) and γ-CD (H).

compared with the macroinitiator, the penta-block copolymer and pure γ-CD, the PEP100M15CD and other PPR samples exhibited no endothermic peak in the range from 20 to 100 °C. This clearly indicated that the entrapped γ-CDs restrict the central PEO segment from aggregating to form the crystalline phase [24]. The neat pentablock copolymer PR0CD30P gave rise to an endothermic peak for PEO at 44.2 °C. At the same time, weak endothermic peaks at 38.6°C and 37.9°C were observed in two PR samples, PR30CD50P and PR30CD80P, respectively. Given that nearly the same amount of γ-CDs were left on the polymer chain after the second in situ ATRP, the DP of PMPC segments seemed to exert little effect on the crystalline behavior of the central PEO segment in the PR-based multiblock copolymers. The occurrence of broad, weak endothermic peaks in PR30CD50P and PR30CD80P suggested that the remaining γ-CDs were randomly distributed along the pentablock copolymer chain after endcapping via the one-pot ATRP of MPC.

Conclusion

Novel PPRs were synthesized in high yield from the self-assembly of γ-CDs with PMA-PPO-PEO-PPO-PMAs. It was found that at a lower γ-CD feed ratio, the central PEO segment was preferentially bent to pass through the cavity of γ-CDs to construct double-chain-stranded tight-fit PPRs. By further increasing the feed ratio, the added γ-CDs began to include the PMA segments and move over them in a randomly distributed manner along the pentablock copolymer chain to give rise to single-chain-stranded loose-fit PPRs. Moreover, these single-chain-stranded loose-fit PPRs were endcapped via the second in situ ATRP of MPC into the same conformational PR-based multiblock copolymers. The PPR and PR supramolecular polymers show potential as dynamic-responsive materials, carriers for controlled drug release, biosensors and catalysts.

Experimental

Materials

PPO-PEO-PPO with a central block of 90 PEO units and two flank blocks of 5 PPO units was supplied by Zhejiang Huangma Chemical Industry Group Co., Ltd., China. The average molecular weight (M_n) is 4580 g/mol. Methyl acrylate (MA) was purchased from J&K Company, China, and was used after removal of inhibitors. Both 2-bromoisobutyryl bromide (BIBB) and *N,N,N',N'',N''*-pentamethyldiethylenetriamine (PMDETA) were available from Sigma-Aldrich, USA. γ-Cyclodextrin (γ-CD) and 4-dimethylaminopyridine (DMAP) were supplied by TCI, Japan. Triethylamine (TEA) was purchased from VAS Chemical Reagents Company, China and refluxed with *p*-toluenesulfonyl chloride and distilled. 2-Methacryloyloxyethyl phosphorylcholine (MPC) was supplied by Joy Nature, China and used as received. Tris(2-(dimethylamino)ethyl)amine (Me_6TREN) was obtained from Alfa Aesar, USA. Copper(I) chloride (Cu(I)Cl) and copper(I) bromide (Cu(I)Br) were purified by stirring in hydrochloric acid and acetic acid, respectively, and washed with deionized water, methanol, and ether, then finally dried and then stored under a nitrogen atmosphere. CH_2Cl_2 was stirred with CaH_2 and distilled before use. All other solvents and reagents were of analytical grade.

Synthesis of macroinitiator (BrPEPBr)

The macroinitiator was prepared as follows. PPO-PEO-PPO (2 mmol, 9.16 g) was dissolved in 20 mL CH_2Cl_2 in a 100 mL round-bottom three-necked flask. Thereafter, DMAP (4 mmol, 488 mg) and TEA (4 mmol, 404 mg) dissolved in 10 mL CH_2Cl_2 was added. 15 mL of CH_2Cl_2 containing 1.84 g 2-bromoisobutyryl bromide (8 mmol) was then slowly added to the mixture over 2 h at 0 °C under nitrogen atmosphere. Thereafter, the reaction continued for another 24 h at room temperature. The mixture was dissolved in THF and filtered three times to remove the ammonium salt. Finally, the crude product was precipitated in 500 mL anhydrous ether at 5 °C and then dried under vacuum to give a yield of 81.5%.

Synthesis of PMA-PPO-PEO-PPO-PMA via ATRP

A strategy for the preparation of pentablock copolymer PMA-PPO-PEO-PPO-PMA with a feed molar ratio of BrPEPBr/MA equal to 1:100 was as follows. BrPEPBr (0.2 mmol, 0.976 g) was dissolved in 8 mL of DMF in a sealable Pyrex reactor. Subsequently, 1.72 g MA (20 mmol) and 0.138 g PMDETA (0.8 mmol) were added to the mixture and then quenched in liquid nitrogen. Before 79.2 mg CuCl (0.8 mmol) was added, the system was degassed with three freeze–vacuum–thaw cycles and purged with nitrogen. Then the reactor was sealed under vacuum and the polymerization started under stirring for 48 h at room temperature. Afterwards, the whole content was dissolved in THF and passed over a basic alumina column to remove the Cu salts. Finally, the crude product was precipitated in anhydrous ether and dried under vacuum.

Preparation of BrPEPBr-γ-CD PPR

The saturated aqueous solution of γ-CD (486 mg, 0.375 mmol) was added to 2 mL of an aqueous solution of BrPEPBr (0.025 mmol, 122 mg,) under vigorous stirring, followed by stirring at 25 °C for 1 h at room temperature. A white PPR slurry was formed as a result of the self-assembly of γ-CDs with the macroinitiator. After washing with a small amount of water, white powder products were obtained by freeze-drying after centrifugation.

Preparation of PMA-PPO-PEO-PPO-PMA-γ-CD PPRs

A protocol for the synthesis of PPRs via the self-assembly of PMA-PPO-PEO-PPO-PMA with γ-CDs (maintaining a feed molar ratio of PEP100M/γ-CD at 1:10) was as follows. The saturated aqueous solution of 0.26 g γ-CDs (0.2 mmol) was added to a 1 mL aqueous solution of 0.19 g PEP100M (0.02 mmol). The mixture was stirred for 1 h at room temperature, followed by storage at 6–8 °C in a refrigerator for 24 h. A white gel was formed as a result of the self-assembly of γ-CDs and pentablock copolymer. The gel was washed three times with distilled water and freeze dried to get the PPRs powder products.

One-pot preparation of PRs

A protocol for the one-pot synthesis of PRs by endcapping PPRs via the second in situ ATRP of MPC was as follows. In a sealable Pyrex reactor, the mixture of 0.135 g of PEP40M (0.02 mmol) and 0.778 g of γ-CDs (0.6 mmol) in 3 mL water was stirred for 24 h at room temperature. The predetermined amount of MPC and 0.0184 g of Me_6TREN (0.08 mmol) were added to the resulting suspension of PPRs and then quenched in liquid nitrogen. After the system was degassed with seven freeze–vacuum–thaw cycles and purged with nitrogen, 11.5 mg of CuBr (0.8 mmol) was quickly added. The reactor was sealed under vacuum and the reaction was maintained for 60 h at room temperature. After breaking the reactor, the product was dissolved in DMSO/H_2O (1:1 v/v) and dialyzed against distilled water using a cellulose membrane (MWCO 3500) for 10 days, changing the water every 6 h, and then freeze dried.

Measurements

^{1}H NMR spectra were obtained from a Bruker ARX 400 MHz spectrometer at room temperature with tetramethylsilane (TMS) as the internal standard. The GPC analysis was conducted with a HLC-8320GPC (TOSOH, Japan) instrument at 30 °C at a flow rate of 0.3 mL/min. The solid-state ^{13}C CP/MAS NMR measurements were carried out at 75 MHz with a spinning rate of 5 kHz at room temperature using a Bruker AV-300 NMR spectrometer. The chemical shifts were referred to an external adamantane standard. Wide angle X-ray diffraction (WXRD) patterns were recorded on a Shimadzu XD-D1 X-ray diffractometer with Ni-filtered Cu Kα (1.54 Å) radiation (20 kV, 40 mA). Powder samples were scanned from $2\theta = 4.5–60°$ at a speed of 5°/min. FTIR spectra were measured using a Shimadzu IR Prestige-21 FTIR spectrometer at room temperature using the KBr pellet method. TGA analysis was performed with using a TA SDT 2960 instrument at a heating rate of 10 °C/min from room temperature to 500 °C in a nitrogen atmosphere. DSC measurements were measured on a SHIMADZU DSC-60 differential scanning calorimeter with a scanning temperature range from 20–80 °C at a scanning rate of 10 °C/min. The transmission electron microscopy image was observed using a JEM 1200EX (JEOL) transmission electron microscope operating at 120 KV.

Supporting Information

The Supporting Information File 1 contains ^{1}H NMR spectra of BrPEPBr and PEP100M, GPC curves of BrPEPBr, PEP40M, PEP60M and PEP100M, TEM image of PMA-PPO-PEO-PPO-PMA in water and ^{1}H NMR spectra of PR0CD30P.

Supporting Information File 1

Additional experimental data.
[http://www.beilstein-journals.org/bjoc/content/supplementary/1860-5397-11-247-S1.pdf]

Acknowledgements

The authors acknowledge support from the Natural Science Foundation of China (No. 20974015).

References

1. Harada, A.; Li, J.; Kamachi, M. *Nature* **1994,** *370,* 126–128. doi:10.1038/370126a0
2. Harada, A.; Kamachi, M. *Macromolecules* **1990,** *23,* 2821–2823. doi:10.1021/ma00212a039
3. Jiang, R.; Kong, T.; Ye, L.; Zhang, A.-y.; Feng, Z.-g. *Acta Polym. Sin.* **2015,** *7,* 800–807.
4. Harada, A.; Li, J.; Kamachi, M. *Chem. Lett.* **1993,** *22,* 237–240. doi:10.1246/cl.1993.237
5. Okumura, H.; Kawaguchi, Y.; Harada, A. *Macromolecules* **2001,** *34,* 6338–6343. doi:10.1021/ma010516i
6. Kawaguchi, Y.; Nishiyama, T.; Okada, M.; Kamachi, M.; Harada, A. *Macromolecules* **2000,** *33,* 4472–4477. doi:10.1021/ma992103b
7. Kida, T.; Kikuzawa, A.; Akashi, M. *Chem. Lett.* **2008,** *37,* 1120–1121. doi:10.1246/cl.2008.1120
8. Miura, T.; Kida, T.; Akashi, M. *Macromolecules* **2011,** *44,* 3723–3729. doi:10.1021/ma200257z
9. Tamura, A.; Yui, N. *Chem. Commun.* **2014,** *50,* 13433–13446. doi:10.1039/C4CC03709J
10. Wang, J.; Li, S.; Ye, L.; Zhang, A.-y.; Feng, Z.-g. *Macromol. Rapid Commun.* **2012,** *33,* 1143–1148. doi:10.1002/marc.201200017
11. Takahashi, A.; Katoono, R.; Yui, N. *Macromolecules* **2009,** *42,* 8587–8589. doi:10.1021/ma9022372
12. Jiang, L.; Ye, L.; Zhang, A.-y.; Feng, Z.-g. *Macromol. Chem. Phys.* **2014,** *215,* 1022–1029. doi:10.1002/macp.201400047
13. Kong, T.; Ye, L.; Zhang, A.-y.; Feng, Z.-g. *Beilstein J. Org. Chem.* **2014,** *10,* 2461–2469. doi:10.3762/bjoc.10.257
14. Kong, T.; Lin, J.; Ye, L.; Zhang, A.-y.; Feng, Z.-g. *Polym. Chem.* **2015,** *6,* 5832–5837. doi:10.1039/C5PY00674K
15. Gao, P.; Wang, J.; Ye, L.; Zhang, A.-y.; Feng, Z.-g. *Macromol. Chem. Phys.* **2011,** *212,* 2319–2327. doi:10.1002/macp.201100319
16. Gao, P.; Wang, J.; Wang, P.-J.; Ye, L.; Zhang, A.-y.; Feng, Z.-g. *Macromol. Chem. Phys.* **2012,** *213,* 1532–1539. doi:10.1002/macp.201200105
17. Shuai, X.-T.; Porbeni, F. E.; Wei, M.; Bullions, T.; Tonelli, A. E. *Macromolecules* **2002,** *35,* 2401–2405. doi:10.1021/ma012085+
18. Matyjaszewski, K.; Xia, J. *Chem. Rev.* **2001,** *101,* 2921–2990. doi:10.1021/cr940534g
19. Zhang, X.; Zhu, X.; Tong, X.; Ye, L.; Zhang, A.-Y.; Feng, Z.-G. *J. Polym. Sci., Part A: Polym. Chem.* **2008,** *46,* 5283–5293. doi:10.1002/pola.22856
20. Li, J.; Li, X.; Toh, K. C.; Ni, X.; Zhou, Z.; Leong, K. W. *Macromolecules* **2001,** *34,* 8829–8831. doi:10.1021/ma011129b
21. Xiong, D.; Deng, Y.; Wang, N.; Yang, Y. *Appl. Surf. Sci.* **2014,** *298,* 56–61. doi:10.1016/j.apsusc.2014.01.088
22. Su, Y.-l.; Wang, J.; Liu, H.-z. *Macromolecules* **2002,** *35,* 6426–6431. doi:10.1021/ma0105284
23. Wang, J.; Wang, P.-J.; Gao, P.; Jiang, L.; Li, S.; Feng, Z.-G. *Front. Mater. Sci.* **2011,** *5,* 329–334. doi:10.1007/s11706-011-0144-2
24. Li, J.; Ni, X.; Zhou, Z.; Leong, K. W. *J. Am. Chem. Soc.* **2003,** *125,* 1788–1795. doi:10.1021/ja026623p

License and Terms

BEILSTEIN JOURNAL OF ORGANIC CHEMISTRY

Co-solvation effect on the binding mode of the α-mangostin/β-cyclodextrin inclusion complex

Chompoonut Rungnim[1], Sarunya Phunpee[1], Manaschai Kunaseth[1],
Supawadee Namuangruk[1], Kanin Rungsardthong[2], Thanyada Rungrotmongkol[*,‡3,4,§]
and Uracha Ruktanonchai[*,‡1,¶]

Full Research Paper

Open Access

Address:
[1]National Nanotechnology Center (NANOTEC), National Science and Technology Development Agency (NSTDA), Pathumthani 12120, Thailand, [2]Faculty of Pharmacy Thammasat University, Rangsit Center, Pathumthani 12120 Thailand, [3]Structural and Computational Biology Unit, Department of Biochemistry, Faculty of Science, Chulalongkorn University, Bangkok 10330, Thailand and [4]Ph.D. Program in Bioinformatics and Computational Biology, Faculty of Science, Chulalongkorn University, Bangkok 10330, Thailand

Email:
Thanyada Rungrotmongkol* - t.rungrotmongkol@gmail.com;
Uracha Ruktanonchai* - uracha@nanotec.or.th

* Corresponding author ‡ Equal contributors
§ Fax: +66(0)2218-5418; Tel. +66(0)2218-5426
¶ Fax: +66(0)2564-6985; Tel. +66(0)2564-6552

Keywords:
α-mangostin; β-cyclodextrin; binary complex; inclusion complex

Beilstein J. Org. Chem. **2015,** *11,* 2306–2317.
doi:10.3762/bjoc.11.251

Received: 31 July 2015
Accepted: 06 November 2015
Published: 25 November 2015

This article is part of the Thematic Series "Superstructures with cyclodextrins: Chemistry and applications III".

Guest Editor: G. Wenz

Abstract

Cyclodextrins (CDs) have been extensively utilized as host molecules to enhance the solubility, stability and bioavailability of hydrophobic drug molecules through the formation of inclusion complexes. It was previously reported that the use of co-solvents in such studies may result in ternary (host:guest:co-solvent) complex formation. The objective of this work was to investigate the effect of ethanol as a co-solvent on the inclusion complex formation between α-mangostin (α-MGS) and β-CD, using both experimental and theoretical studies. Experimental phase-solubility studies were carried out in order to assess complex formation, with the mechanism of association being probed using a mathematical model. It was found that α-MGS was poorly soluble at low ethanol concentrations (0–10% v/v), but higher concentrations (10–40% v/v) resulted in better α-MGS solubility at all β-CD concentrations studied (0–10 mM). From the equilibrium constant calculation, the inclusion complex is still a binary complex (1:1), even in the presence of ethanol. The results from our theoretical study confirm that the binding mode is binary complex and the presence of ethanol as co-solvent enhances the solubility of α-MGS with some effects on the binding affinity with β-CD, depending on the concentration employed.

Introduction

Solubilization of otherwise poorly soluble drugs under physiological conditions to improve their bioavailability is challenging, and a requirement for the design and development of effective formulations. There are several ways to favorably enhance the solubility of poorly soluble drugs which include micronization, chemical modification, pH adjustment, complexation [1], co-solvent addition [2-8] and surfactant addition [9]. Complexation is one of the most utilized methods for enhancing the solubility of poorly soluble drugs. Cyclodextrins (CDs) are well-known macrocyclic oligosaccharides that are produced by enzymatic degradation of starch. CDs consist of 6, 7 and 8 α-D-glucopyranose units and are depicted as α-CD, β-CD and γ-CD, respectively. CDs are able to bind non-polar molecules, including poorly soluble drugs, in their hydrophobic cavities to form binary inclusion complexes [10-12]. Inclusion of the drug can result in its enhanced solubility, dissolution rate, bioavailability, and stability (in comparison to the free drug), with controlled release also being possible [13-16]. In addition, co-solvent addition is a well-established method for increasing the equilibrium solubility of non-polar drugs. Recent studies combining co-solvent addition with complexation [2,3,6] have demonstrated that the thermodynamics underlying the interactions between host–guest molecules can be significantly changed in these instances. In these cases, the co-solvent can also occupy the CD cavity in conjunction with the guest (drug) molecules to form CD/guest/co-solvent ternary complexes. In other studies, the co-solvent has been shown to compete with the drug molecules for the entry into the CD cavity, with the result of lower drug loadings (inclusion of drug molecules) in the system. Besides, the co-solvent effect was found as a factor that control anion affinity and selectivity of a neutral anion receptor, bis(cyclopeptide) [17].

Molecular dynamics (MD) simulations can give important insights into the energetics of structural interactions. The hydrated structure of β-CD in aqueous solution [18] and those showing host–guest interactions between the β-CD structure and guest molecules in its inclusion compounds have been reported [19-21]. Moreover, MD simulations of β-CD in water and ethanol mixtures have been performed to investigate the orientation of the co-solvent in the hydrophobic cavity of the β-CD [22]. Recently, Biedermann et al. [23] reviewed the hydrophobic effect of supramolecular complexes from MD simulation studies and emphasized that the non-covalent driving force of high-energy water in the cavity of cyclodextrins, cyclophanes and cucurbiturils was an essential factor for complexation with the guest molecule. MD simulations are therefore a useful technique providing details of the molecular interactions of structural components in different environments (e.g., water or water/co-solvent mixtures) which are often encountered in formulations.

In our previous work [24], the preliminary results of phase solidities of the inclusion complex in ethanol and methanol were reported but the co-solvation effects was not clearly stated. Hence, to fulfill the understanding of such effects, further details of the solvation effects are presented in this work. We experimentally and theoretically study the influence of ethanol as a co-solvent on the complex formation between α-mangostin (α-MGS) and β-CD. Phase solubility studies were carried out in order to assess the formation of those complexes at various β-CD concentrations, with ethanol as a co-solvent. A simple mathematical model was then applied to explain the solubility of α-MGS influenced by the presence of β-CD and ethanol. MD simulations were performed to quantify the strength of inclusion complex formation in terms of binding energy, hydrogen bonding interactions, and displacement analysis.

Materials and methods

Experimental study

Chemicals and reagents

α-Mangostin (purity >90%), isolated from mangosteen pericarp, was obtained from Honsea Sunshine Biotech Co., Ltd. (Guangzhou, China). The α-mangostin reference standard (≥98% purity) was obtained from Sigma-Aldrich (USA). β-CD (Cavamax® W7, pharmaceutical grade, purity >98%) was obtained from Wacker Chemie AG (Bangkok, Thailand). Acetic acid, ethanol, methanol, and acetonitrile were of analytical grade and supplied by Carlo Erba (Rome, Italy). Deionized (DI) water was produced using a Milli-Q Plus system (Millipore, Schwalbach, Germany).

Phase solubility

The phase solubility study was conducted using the Higuchi and Connors method (Higuchi and Connors, 1965). Briefly, α-mangostin (2 g, excess) was added into gas-tight vials containing both β-CD and ethanol. The concentration of β-CD (0 to 10 mM), and ethanol (0 to 40% v/v) was varied in each vial such that a series was produced. The gas-tight vials were shaken using a shaking incubator (Vision Scientific Co., Ltd., Korean) at 25 °C for 48 h to ensure equilibrium was reached. The samples were then passed through a 0.45 μm Nylon filter, and the concentration of dissolved α-mangostin was determined by high-performance liquid chromatography, HPLC, (Waters, model e2695, USA) using the following method. The photodiode array (PDA) detector was set to monitor at a λ_{max} of 320 nm. The chromatographic separation was performed at 25 °C using a C_{18} column (Waters, 250 mm × 4.6 mm, 5 μm). The eluents were composed of 1% acetic acid in DI water as a mobile phase A, and methanol as mobile phase B. The isocratic steps of A and B were set at 10% and 90%, respectively, for 15 min with a total flow rate of 1 mL/min. Sample injection volume was 10 µL. The calibration curve was made at concentrations ranging from 0.001 to 0.1 mg/mL. All samples were prepared in triplicate.

The total drug solubility in the presence of both co-solvent and CD was determined according to Equation 1:

$$[D_{tot}] = [D] + [DL] + [DLC] \quad (1)$$

where $[D_{tot}]$ is the total solubility of the drug, [D] is the concentration of the free drug, [DL] is the concentration of the binary complex, and [DLC] is the concentration of the ternary complex.

According to Equation 2, the concentration of the free drug, [D], can be calculated based on the assumption that complexation has a negligible effect on the amount of free drug. The logarithm of the drug solubility increases linearly with the concentration of co-solvent as described in Equation 3 and co-solvent solubilizing power (σ), the slope of this linear function, depends upon the polarity of both the solute and the solvent.

$$\left[D\right] = \left[D_u\right] \times 10^{\sigma\left[C\right]} \quad (2)$$

$$\log\left[D\right] = \log\left[D_u\right] + \sigma\left[C\right] \quad (3)$$

D_u represents the intrinsic drug solubility, σ is the co-solvent solubilizing power and [C] is the co-solvent concentration.

The concentration of the α-MGS/β-CD binary complex [DL] is directly related to the concentration of free α-MGS [D], the concentration of β-CD, and the apparent binary complexation constant, K_b^{app}, which can be determined according to Equation 4.

$$\left[DL\right] = K_b^{app}\left[D\right]\left[L\right] \quad (4)$$

Furthermore, the apparent binary complexation constant, K_b^{app}, has an association with the co-solvent concentration [C], the intrinsic complexation constant, K_b^{int}, and co-solvent destabilizing power for the binary complex, ρ_b, and can be determined according to Equation 5.

$$K_b^{app} = K_b^{int} \times 10^{-\rho_b\left[C\right]} \quad (5)$$

The concentration of the α-MGS/β-CD/ethanol ternary complex [DLC] is related to the concentration of free α-MGS [D], the concentration of β-CD [L], the co-solvent concentration [C] and the apparent ternary complexation constant, K_t^{app}, as shown in Equation 6.

$$\left[DLC\right] = K_t^{app}\left[D\right]\left[L\right]\left[C\right] \quad (6)$$

K_t^{app} has a correlation with co-solvent destabilizing power for the ternary complex (ρ_t), the intrinsic ternary complexation constant (K_t^{int}) and the concentration of co-solvent [C], as defined in Equation 7.

$$K_t^{app} = K_t^{int} \times 10^{-\rho_t\left[C\right]} \quad (7)$$

From Equation 1, the expression for total solubility of drug $[D_{tot}]$ in the presence of both co-solvent and complexation can be rearranged and expressed as in Equation 8.

$$\begin{aligned}[D_{tot}] = &\left\{[D_u]\times 10^{\sigma[C]}\right\} \\ &+\left\{[D_u]\left\{\left[L\right]K_b^{int}\times 10^{(\sigma-\rho_b)[C]}\right\}\right\} \\ &+\left\{[D_u]\left\{\left[L\right]\left[C\right]K_t^{int}\times 10^{(\sigma-\rho_t)[C]}\right\}\right\}\end{aligned} \quad (8)$$

Theoretical study

Structural preparation for MD simulation

The initial geometry of β-CD was obtained from the PDB databank (3C6G), while the α-MGS structure was extracted from the International Union of Crystallography (KP2293) database, see Figure 1. According to the ChemAxon method [25-27], the calculated pK_a of three hydroxy groups are 7.4 (O6), 7.8 (O3), and 8.2 (O5). For that reason, the α-mangostin was considered as neutral molecule in the MD simulation (pH 7). Parameters for the β-CD were applied using the Glycam-06 force field while the atomic charges and parameters for α-MGS were derived using a restrained electrostatic potential (RESP) charge-fitting procedure as described in the previous studies [28-31]. Details of atom types and partial atomic charges of α-mangostin are enclosed in Supporting Information File 1 (Table S1). The RESP was calculated at the HF/6-31G(d) level of theory using Gaussian 09 [32]. The hydrogen atoms added by the Leap module were minimized by 1000 steps of steepest descent, and followed by 2000 steps of conjugated gradients to remove bad

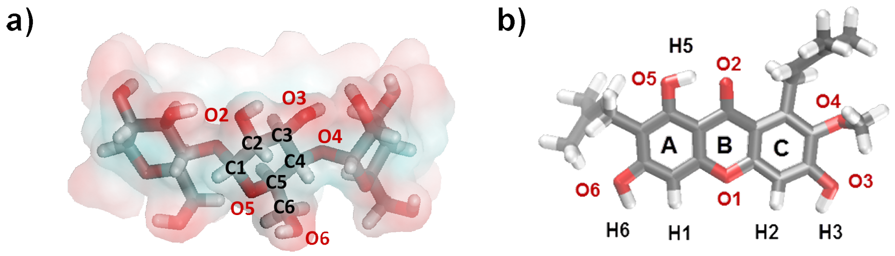

Figure 1: Schematic views of a) β-CD and b) α-mangostin (α-MGS) geometries.

contacts. Then, the relaxed inclusion complexes were solvated by the TIP3P water molecules with a set distance of 15 Å from the system surface. In aqueous solvation, the system consists of 3,100 water molecules within a 45.0 × 45.0 × 45.0 $Å^3$ truncated periodic box. The periodic box size was kept constant for the inclusion complex at all ethanol (EtOH) concentrations (% v/v). Following this, the solvation molecules were added to the solvation box using the PACKMOL package [33]. The number of water and ethanol molecules is given in Table 1.

Table 1: Number of co-solvent molecules in the six simulation systems.

System	No. of water	No. of EtOH
Water	3,100	–
5% v/v EtOH	2,945	48
15% v/v EtOH	2,635	144
30% v/v EtOH	2,170	287
60% v/v EtOH	1,240	574
EtOH	–	957

Details of molecular dynamics simulations

In the present study, all MD simulations were performed using the SANDER module of the Amber10 software package in accordance with the recently reported MD simulations of flavonoid/β-CD inclusion complexes in water [34,35]. The particle-mesh Ewald method with a cut-off distance of 12 Å was employed. The integration time step was 2 fs and the SHAKE algorithm was applied to constrain all bonds attached to hydrogen atoms. Prior to heating, the solvent molecules were only minimized using 3,500 steps of conjugated gradients. The whole system was then heated to 300 K within the 500 steps of relaxation time using the Canonical Ensemble (NVT) algorithm at constant volume up to 1 g/mL of water density. Finally, the MD simulations were performed at 1 atm and 300 K for 20 ns.

The structural dynamics over simulation time were monitored by root mean square displacement (RMSD). The orientation and solvation of α-MGS occupying the β-CD cavity were investigated in terms of structural properties, and the radial distribution function (RDF). The hydrogen bond interactions between α-MGS and β-CD molecules were analyzed using the criteria of (i) distance between the hydrogen donor and acceptor atoms being ≤3.5 Å; and (ii) the angle of the donor-hydrogen-acceptor being ≥120° [36].

Binding free energy calculations

Herein, the binding free energies of α-MGS/β-CD complex were calculated as follows. The ΔG is defined by

$$\Delta G_{\text{bind}} = G^{\alpha\text{-MGS}/\beta\text{-CD}} - G^{\alpha\text{-MGS}} - G^{\beta\text{-CD}} \qquad (9)$$

where each free energy is estimated from

$$\Delta G = \Delta E_{\text{MM}} + \Delta G_{solv} - T\Delta S \qquad (10)$$

The gas phase energy, ΔE_{MM}, is a summation of bonded and non-bonded (electrostatic and van der Waals (vdW)) energies obtained from molecular mechanics calculation. The ΔG_{solv} is solvation free energy. In general, there are several methods for ΔG_{solv} prediction. Some methods calculate the ΔG_{solv} using implicit solvent models such as Generalized Born (GB) [37,38], Poisson–Boltzmann (PB) [39,40] and Reference Interaction Site Model (RISM) [41]. Meanwhile, the other methods such as linear interaction energy (LIE) [42-44] and linear response approximation (LRA) [45-47] calculate the ΔG_{solv} based on a modified linear response to treat electrostatic interactions with an empirical term treating the dispersion interactions. In this work, the ΔG_{solv} was considered as polar and non-polar solvation terms. The polar solvation term is evaluated from the Poisson–Boltzmann (PB) solvation method which is successfully applied in other biological systems [29,34,35,48]. The non-polar contribution is calculated by the solvent-assessable surface area (SASA) as

$$\Delta G_{(non-polar)} = \gamma \cdot \text{SASA} \qquad (11)$$

Where γ was set as 0.0072 kcal/(mol/A^2) [49]. The *TS* term is a solute entropy contribution arising from changes in degrees of freedom (translation, rotation and vibration) of the molecule which can be estimated using the NMODE module in Amber10.

Results and Discussion

Experimental results

Phase solubility results

In this study, the phase solubility method was chosen to investigate the complexation of α-MGS and β-CD in the presence of ethanol [50]. The stoichiometry and formation constant (the equilibrium constant, K_b^{app}) can be obtained from phase solubility diagrams constructed by assessing the effect of the CD concentration on the apparent solubility of α-MGS. Figure 2 shows the α-MGS solubility increasing exponentially with ethanol concentration, as described in Equation 2. The co-solvent solubilizing power (σ, 0.36 M^{-1}) was determined by plotting the logarithm of the α-MGS solubility against co-solvent concentration. The intrinsic solubility (D_u) of α-MGS was determined to be 0.74 mM.

In the absence of ethanol, the solubility of α-MGS increases linearly with increasing β-CD concentration, up to 10 mM. The phase solubility profile can be considered to be of the A_L type [50] with a 1:1 β-CD and α-MGS stoichiometry as evident from the phase solubility diagram. In the absence of co-solvent, K_b^{app} was equal to K_b^{int} (910.91 M^{-1}) and was calculated from the slope and y-intercept of the phase solubility profile.

According to Figure 3, the α-MGS solubility shows a linear correlation with the β-CD concentration. From considering the slope of the curve at various ethanol concentrations, it can be concluded that the solubility of α-MGS in the media containing 0.5% ethanol (% v/v) is higher than the solubility of α-MGS in pure water. This may be due to the ethanol concentration of 0.5% being not sufficient to promote ternary inclusion complex (α-MGS/β-CD/ethanol) formation. Moreover, the solubility of α-MGS decreases with increasing ethanol concentration (0.5 to 10% v/v) as a consequence of the competitive binding of ethanol to the β-CD cavity as suggested from MD simulations [22] and X-ray diffraction [51]. However, greater solubility of α-MGS was observed over a concentration range of 20–40% ethanol. The intrinsic ternary complexation constant, K_t^{int}, could be determined according to Equation 8, and subsequently ρ_b and ρ_t were calculated using nonlinear regression and found to be 0.27 and 0.22 M^{-1}, respectively. The equilibrium constant for binary complex formation (α-MGS/β-CD) was higher than that for ternary complex formation (α-MGS/β-CD/ethanol) (Table 2). Note that no ternary complex was formed for this system. The apparent binary complexation constant, K_b^{app}, as a function of ethanol concentration was calculated and highlighted in Table 3. A slight decrease in complexation constant was found from 910 to 886 M^{-1} as the ethanol concentration increased. This suggests that the addition of ethanol results in increased local polarity around the α-MGS molecule, resulting in the preference for α-MGS to be located partially outside the β-CD cavity.

Theoretical results

MD simulations were performed to investigate the effect of solvent towards the orientation and stability of the binary α-MGS/β-CD inclusion complex at the atomic level. Two

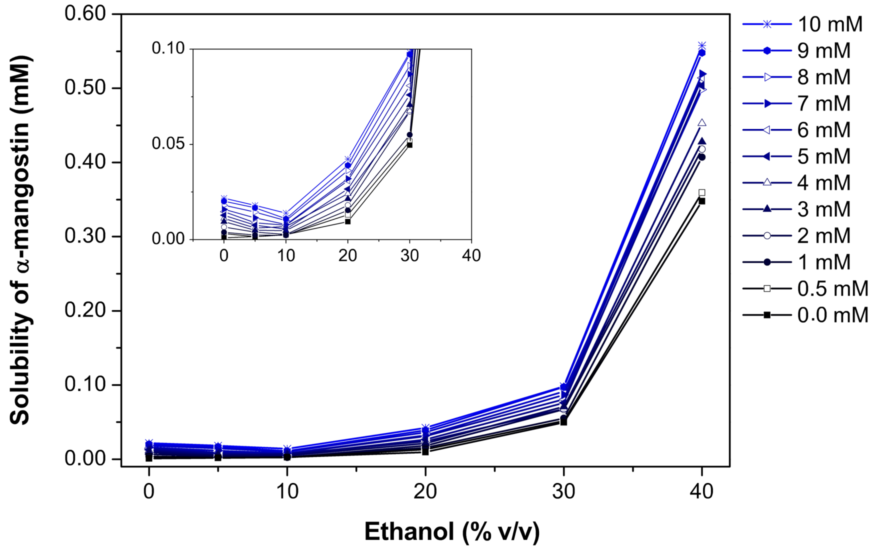

Figure 2: Solubility of α-mangostin as a function of ethanol concentration for different β-CD concentrations.

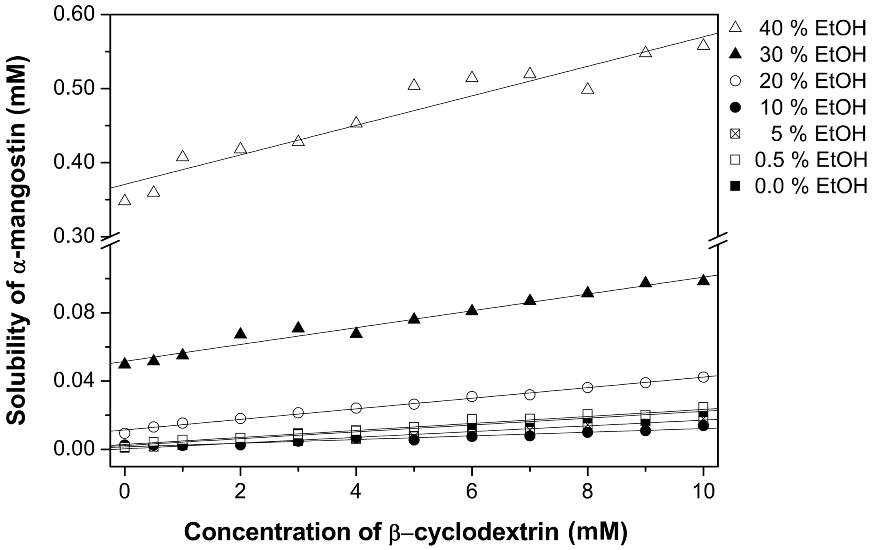

Figure 3: Solubility of α-mangostin as a function of β-CD for different ethanol concentrations.

Table 2: Estimation of solubilization parameters.

Parameters	Values
D_u (mM)	0.74
σ (M^{-1})	0.36
ρ_b (M^{-1})	0.27
ρ_t (M^{-1})	0.22
K_b^{int} (M^{-1})	910.91
K_t^{int} (M^{-2})	1.61

Table 3: The apparent binary complexation constant, K_b^{app}, as a function of ethanol concentration.

Ethanol concentration (% v/v)	K_b^{app} (M^{-1})
0.0	911
0.5	911
5.0	908
10.0	905
20.0	898
30.0	892
40.0	886

conformations of inclusion complexes in water (complexes I and II in Figure S1, Supporting Information File 1) were generated, and subjected to MD simulation for 20 ns. The results implied that the displacement and mobility of the α-MGS trapped within the hydrophobic cavity of β-CD was dependent on interactions between the methoxy group presented on the narrow rim of β-CD, and the 3-methylbut-2-enyl group on the C-ring of α-MGS. Having α-MGS with its C ring located almost outside the cavity (complex II) was a preferable arrangement. On the other hand, in complex I, the secondary rim is wide enough to support two functional groups of the C-ring. Even though α-MGS has three hydroxy groups, no hydrogen bonding between guest and host molecules was detected. Thus, electrostatic interactions may not be the key factor controlling the formation of inclusion complexes; van der Waals interactions could be more important. The MM-PBSA result in Table S2, Supporting Information File 1, confirmed this assumption; the main contribution for α-MGS inclusion arises from van der Waals interactions (ΔE_{vdW}) 7–8 fold higher than for electrostatic interactions (ΔE_{ele}). Through summation of the solvation free energy (ΔG_{solv}) and the entropy term ($T\Delta S$), the predicted binding free energies (ΔG_{bind}) of the inclusion complexes I and II are similar with values of -8.86 ± 3.25 and -9.06 ± 2.87 kcal/mol, respectively. Thus, the steric effect of the α-MGS functional groups influences only the inclusion geometry, but not the binding energy. Further details for MD simulations of the α-MGS/βCD inclusion complex in water solvation system appear in Supporting Information File 1.

Solvation effect on the α-MGS/β-CD inclusion complex

According to the above results, the complex II arrangement of the inclusion complex in water showed slightly higher stability. Hence, this complex was selected as the representative model, and its last snapshot was used as the initial structure for further investigations on the solvation effect by co-solvent on inclusion complex formation. Five MD simulations of the inclusion complex in aqueous solutions with different percentages of ethanol (5, 15, 30, 60 and 100% v/v) were studied for comparison with the experimental results.

System stability

Figure 4 highlights the RMSDs of α-MGS and β-CD for five systems with increasing ethanol concentration, plotted versus simulation time. Notably, the α-MGS inside the β-CD cavity and the β-CD itself, showed more fluctuation when the ethanol percentage was raised. Adding ethanol to the aqueous solution induces greater mobility of both guest and host molecules in the inclusion complex. For a relative comparison of these situations with the inclusion complex in pure water, trajectories within the same range of the last 5 ns for the five systems focused in Figure 4 were further considered.

Displacement of α-mangostin

The α-MGS displacement analysis together with the last snapshot in Figure 5 evidently shows that at low ethanol concentrations (5 and 15% v/v) α-MGS is preferentially positioned inside the hydrophobic cavity of β-CD, similar to that in water (Figure S1, Supporting Information File 1). However, the xanthone core structure of α-MGS is significantly shifted, relative to the complex formed in pure water, through the center of the β-CD cavity and thus only the A ring is partially located at the narrow rim and the 3-methylbutenyl group occupies the cavity at ≥30% v/v ethanol (Figure 5c–e). This situation consequently leads to a weak hydrogen bond (H-bond) formation between the hydroxy group (O^6) on the A ring of α-MGS and the primary hydroxy group (O^6) on the narrow edge of the β-CD (Table 4). The H-bond strength showed an enhancement as a function of alcohol concentration (% H-bond of 32, 60 and 77 for 30, 60 and 100% v/v ethanol, respectively), which likely promoted electrostatic interactions between the α-MGS and β-CD molecules (ΔE_{ele} in Table 5). The data obtained also suggested that, at high alcohol content ≥30% v/v, ethanol greatly stabilized the hydrophobicity of aromatic ring outside the β-CD cavity as it can be seen by the co-solvent accessibility towards the trapped α-MGS (discussed below).

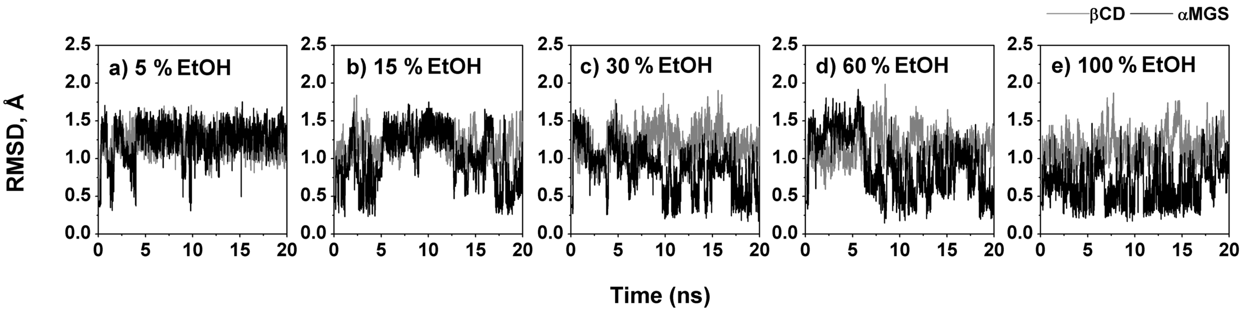

Figure 4: RMSD plots of β-CD (grey) and α-MGS (black) for the five systems with different ethanol percentages.

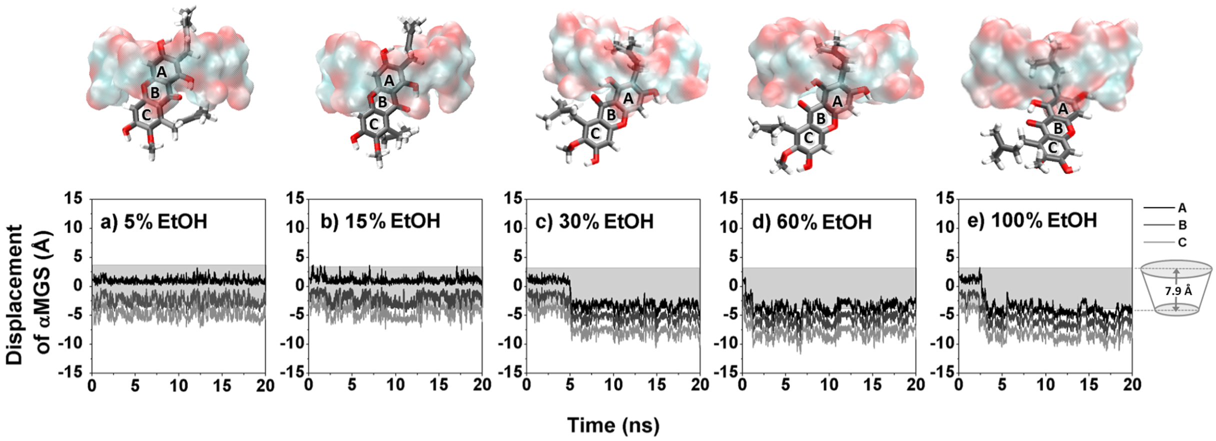

Figure 5: Displacement of the A–C rings of α-MGS with respect to the β-CD center of gravity for five systems having different ethanol percentages a) 5%, b) 15%, c) 30%, d) 60% and e) 100%. The last snapshot of each system is displayed above each graph.

Table 4: Percentage of hydrogen bond (% H-bond) formed between the hydroxy groups of α-MGS and the β-CD molecules, O^6–H^6(α-MGS)···O^6(β-CD), in six inclusion complexes.

System	% H-bond
water	–
5% v/v EtOH	–
15% v/v EtOH	–
30% v/v EtOH	32
60% v/v EtOH	60
EtOH	77

Radial distribution function analysis

To probe the influence of ethanol co-solvent towards α-MGS occupation within the β-CD cavity, the radial distribution function (RDF or $g_{ij}(r)$) was used to monitor the solvation of water and/or ethanol around the α-MGS in the formed inclusion complexes. The $g_{ij}(r)$ was calculated as a function of the ethanol or water oxygen atom j within a spherical radius of r from the α-MGS heteroatom (oxygen atom i). The RDF results of ethanol and water co-solvation are shown in the left and right columns of Figure 6, respectively. The integration number, $n(r)$, of solvent molecules are presented in Table S3 of Supporting Information File 1. RDFs of systems with pure water, and pure

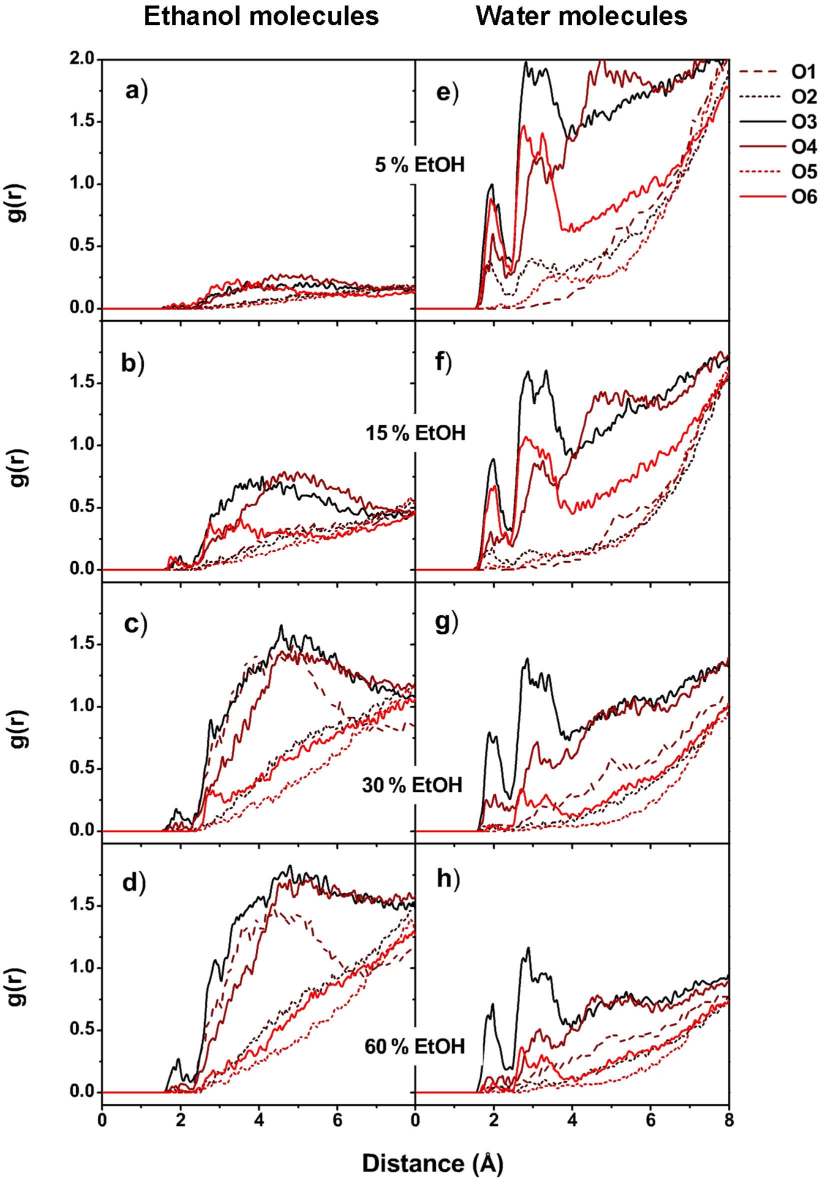

Figure 6: Radial distribution functions (RDF) of (a–d) ethanol, and (e–h) water molecules around the oxygen atoms of α-MGS on complexation with β-CD at different ethanol percentages.

ethanol solvation, are presented in Figure S2 of Supporting Information File 1.

For the systems in water, and with low ethanol concentrations (5 and 15% v/v EtOH), the xanthone ring of the α-MGS is mostly localized within the β-CD cavity, with its functional groups located close to the β-CD rims, as already discussed. Thus, the sharp peaks of water molecules noticeably appear around 2.2 Å and 3.1 Å of the O^2, O^3, O^4 and O^6 atoms of the α-MGS (see Figure 6), which represent the first and second solvation shells with the numbers of solvated water molecules ranked in order of $O^3 > O^6 > O^4 > O^2$. In contrast, no sharp peak for ethanol solvation appeared within ≈3 Å of all six oxygen atoms of α-MGS, suggesting that only a very small amount of ethanol was able to access the mostly entrapped α-MGS at low alcohol concentrations.

At higher alcohol content (≥30% v/v ethanol), the number of water molecules in the first solvation shell around the heteroatoms of α-MGS dramatically decreased, especially for the O^6 and O^2 atoms. This is a result of partial displacement of α-MGS from the β-CD cavity. When the percentage of ethanol solvation increases, only the 3-methylbut-2-enyl group and a portion of the A-ring are located inside the β-CD cavity, whilst the B- and C-rings are almost completely displaced. For this reason, O^6 is shielded by the narrow rim of β-CD while O^1, O^3 and O^4 are exposed to solvent molecules (Figure 7). The first solvation shell of ethanol at 60% v/v concentration appears around 2 Å from O^3 of α-MGS, but the $n(r)$ of ethanol molecules (0.2) is lower than the $n(r)$ of water molecules (0.4) for the same shell as shown in Table S3 of Supporting Information File 1. The number of solvated ethanol molecules increases in the secondary solvation shell (≈3 Å) from O^3, O^1 and O^4 atoms with $n(r)$ values of 2.2, 1.5 and 1.0, respectively. Compared to the $n(r)$ of water molecules in the secondary solvation shell of O^3 (2.5), it is conceivable that, in instances of co-solvation, a lower degree of water solvation is well compensated by the higher accessibility of ethanol molecules to the α-MGS heteroatoms in the secondary solvation shell. It is worth noting that the O^3 atom is the most attractive site for solvation molecules because water and ethanol molecules always solvate around 2 Å from O^3, compared to other oxygen atoms in α-MGS.

Binding energy analysis

Based on the MM-PBSA approach, the binding free energies of the α-MGS/β-CD complexes at various EtOH concentrations were predicted. The decomposition of free energy into additive contributions has potential to provide relationship between structure and binding affinity as well as the solvation effects. Theoretical basis of solvation free energy decomposition and the Free Energy Perturbation (FEP) formalism allowing additive for free-energy contributions arising from different types of interaction were well defined by Bren et al. [52,53]. To evaluate the solvation effect in this work, the binding free energies were decomposed in Table 5.

In line with the hydrogen bond analysis, the binding energy in terms of electronic interactions (ΔE_{ele}) significantly increased from > −5 kcal/mol in pure water and low ethanol concentrations to −8.69, −10.17 and −10.20 kcal/mol in 30, 60 and 100% v/v ethanol. By contrast, the van der Waals energy contribution (ΔE_{vdW}) was reduced by ≈10–15 kcal/mol due to almost total displacement of the α-MGS xanthone ring from the β-CD cavity via the primary rim. However, the magnitude of ΔE_{ele} was lower than ΔE_{vdW}, which is known to be the main factor

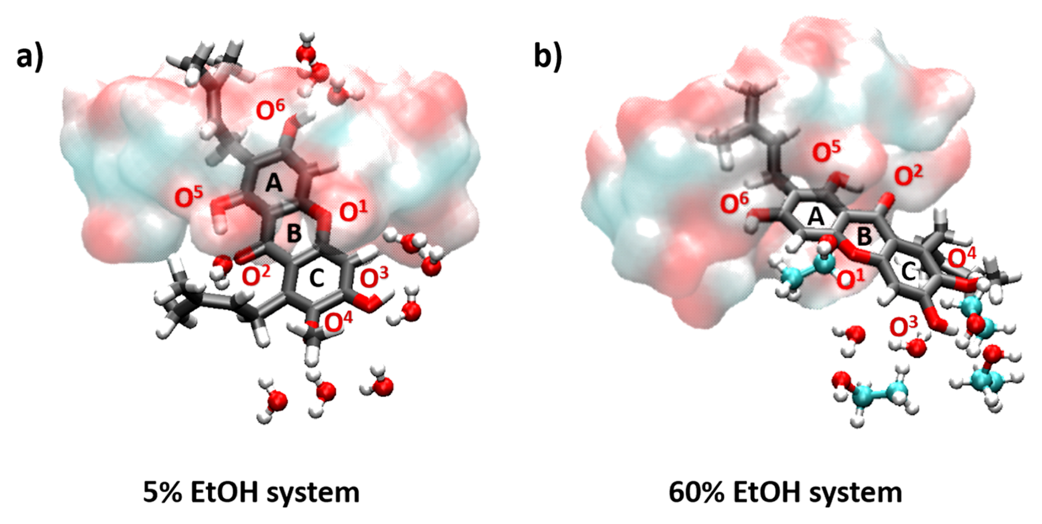

Figure 7: Snapshots of solvation around heteroatoms of α-MGS/β-CD for systems containing 5% and 60% v/v ethanol.

Table 5: MM-PBSA binding free energies (kcal/mol) and their energy components for α-MGS/β-CD complexes at different EtOH concentrations.

		EtOH concentration (% v/v)					
		0%	5%	15%	30%	60%	100%
ΔE_{ele}		−4.61 ± 2.67	−4.30 ± 2.35	−4.99 ± 3.07	−8.69 ± 4.50	−10.17 ± 4.35	−10.20 ± 3.84
ΔE_{vdW}		−37.04 ± 1.93	−37.46 ± 2.55	−36.14 ± 2.53	−28.36 ± 4.43	−26.98 ± 4.10	−22.39 ± 3.72
ΔE_{MM}	(1)	−41.65 ± 3.22	−41.76 ± 3.59	−41.13 ± 4.02	−37.05 ± 5.77	−37.15 ± 5.80	−32.58 ± 5.41
ΔG_{nsolv}		−4.53 ± 0.17	−4.49 ± 0.21	−4.48 ± 0.20	−4.01 ± 0.31	−3.91 ± 0.30	−3.54 ± 0.32
ΔG_{psolv}		23.83 ± 3.80	23.03 ± 3.75	22.21 ± 4.10	18.51 ± 3.57	18.86 ± 3.53	16.70 ± 2.95
ΔG_{solv}	(2)	19.30 ± 3.72	18.54 ± 3.64	17.73 ± 3.99	14.50 ± 3.42	14.94 ± 3.39	13.16 ± 2.75
$\Delta G_{\mathrm{psolv}} + E_{ele}$		19.22 ± 3.00	18.73 ± 3.13	17.22 ± 3.17	9.83 ± 3.3	8.68 ± 3.19	6.50 ± 3.18
$\Delta G_{\mathrm{nsolv}} + E_{vdW}$		−41.57 ± 2.10	−41.95 ± 2.76	−40.62 ± 2.73	−32.37 ± 4.74	−30.89 ± 4.40	−25.93 ± 4.04
$-\mathrm{T}\Delta S$	(3)	13.29 ± 2.72	13.00 ± 2.73	12.88 ± 2.92	13.04 ± 2.44	13.31 ± 3.10	12.46 ± 2.51
$\Delta G_{bind\ \mathrm{(1)+(2)+(3)}}$		−9.06 ± 2.87	−10.21 ± 2.84	−10.51 ± 2.93	−9.51 ± 3.19	−8.90 ± 3.56	−6.96 ± 3.14

governing the stability of CD inclusion complexes [35]. By considering the solvation effect, we found that the presence of ethanol molecules can enhance the solvation energy (ΔG_{solv}) of the inclusion complex, as seen by a reduction in ΔG_{solv} at high ethanol percentages. In contrast, the entropies of all systems were likely similar ($-T\Delta S$ of ≈13 kcal/mol). After combining the interaction energy (1), solvation (2) and entropy (3) terms, the binding affinity of the α-MGS/β-CD complexation at 0–60% v/v ethanol almost steady at the range of −9.06 to −8.90 kcal/mol. This is because increases in ΔE_{MM} are compromised by a lowering of ΔG_{solv}. Moreover, the inclusion complex in pure ethanol is less stable than that in pure water, by ca. 2 kcal/mol. By taken altogether, the addition of ethanol mainly affects the displacement and solvation accessibility of α-MGS in the inclusion complex, rather than its binding affinity in term of the total binding free energy. These results are in line with our experimental study where increasing the ethanol percentage does not dramatically reduce the $K_{\mathrm{b}}^{\mathrm{app}}$ of the binary inclusion complex.

Conclusion

In this study the effect of water/ethanol co-solvation systems on the formation of α-MGS/β-CD complexes has been investigated. From experimental work, a mathematical model was used to explain complex formation in relation to phase solubility. From the equilibrium constant calculation it was found that the inclusion complex is still a binary complex, even in the presence of ethanol. When the ethanol concentration was higher than 10% v/v, the solubility of α-MGS was enhanced. Besides, increasing the ethanol concentration resulted in slight decreases in the α-MGS/β-CD complexation constant. The MD simulation results indicated that the dynamics property of α-MGS in respect to the β-CD cavity axis, the solvent accessibility towards the encapsulated α-MGS and the binding affinity of the inclusion complex depend on the ethanol concentrations. At high ethanol concentrations (>30% v/v), the stability of the hydrophobic aromatic ring of the α-MGS outside the inclusion cavity was promoted resulting in a reduced binding interaction but enhanced solubility of the α-MGS/β-CD inclusion complex. As a compromise between those two factors, interaction energy and solvation free energy, the total binding free energy of the α-MGS/β-CD was slightly reduced when the ethanol percentage was increased. In conclusion, the presence of ethanol enhances the solubility of α-MGS and its inclusion complex, α-MGS/β-CD, with effects on the binding affinity with β-CD being dependent on the co-solvent concentration.

Supporting Information

Supporting Information File 1

Additional data.
[http://www.beilstein-journals.org/bjoc/content/supplementary/1860-5397-11-251-S1.pdf]

Acknowledgements

The authors thank the National Nanotechnology Center (NANOTEC) for financial support. The computer facility of the National e-Science Infrastructure Consortium, Thailand, is also acknowledged. T.R thanks the Thailand Research Fund (IRG578008) and Ratchadaphiseksomphot Endowment Fund from Chulalongkorn University.

References

1. Brewster, M. E.; Vandecruys, R.; Peeters, J.; Neeskens, P.; Verreck, G.; Loftsson, T. *Eur. J. Pharm. Sci.* **2008,** *34,* 94–103. doi:10.1016/j.ejps.2008.02.007

2. Li, P.; Zhao, L.; Yalkowsky, S. H. *J. Pharm. Sci.* **1999,** *88,* 1107–1111. doi:10.1021/js990159d
3. He, Y.; Li, P.; Yalkowsky, S. H. *Int. J. Pharm.* **2003,** *264,* 25–34. doi:10.1016/S0378-5173(03)00389-2
4. Viernstein, H.; Weiss-Greiler, P.; Wolschann, P. *Int. J. Pharm.* **2003,** *256,* 85–94. doi:10.1016/S0378-5173(03)00065-6
5. Reineccius, T. A.; Reineccius, G. A.; Peppard, T. L. *J. Agric. Food Chem.* **2005,** *53,* 388–392. doi:10.1021/jf0488716
6. Li, R.; Quan, P.; Liu, D.-F.; Wei, F.-D.; Zhang, Q.; Xu, Q.-W. *AAPS PharmSciTech* **2009,** *10,* 1137–1144. doi:10.1208/s12249-009-9317-z
7. Belica, S.; Sadowska, M.; Stępniak, A.; Graca, A.; Pałecz, B. *J. Chem. Thermodyn.* **2014,** *69,* 112–117. doi:10.1016/j.jct.2013.10.004
8. Liao, Y.; Bohne, C. *J. Phys. Chem.* **1996,** *100,* 734–743. doi:10.1021/jp951697r
9. Soares-Sobrinho, J. L.; Santos, F. L. A.; Lyra, M. A. M.; Alves, L. D. S.; Rolim, L. A.; Lima, A. A. N.; Nunes, L. C. C.; Soares, M. F. R.; Rolim-Neto, P. J.; Torres-Labandeira, J. J. *Carbohydr. Polym.* **2012,** *89,* 323–330. doi:10.1016/j.carbpol.2012.02.042
10. Rogers, T. L.; Nelsen, A. C.; Hu, J.; Brown, J. N.; Sarkari, M.; Young, T. J.; Johnston, K. P.; Williams, R. O., III. *Eur. J. Pharm. Biopharm.* **2002,** *54,* 271–280. doi:10.1016/S0939-6411(02)00063-2
11. Pralhad, T.; Rajendrakumar, K. *J. Pharm. Biomed. Anal.* **2004,** *34,* 333–339. doi:10.1016/S0731-7085(03)00529-6
12. Messner, M.; Kurkov, S. V.; Palazón, M. M.; Fernández, B. Á.; Brewster, M. E.; Loftsson, T. *Int. J. Pharm.* **2011,** *419,* 322–328. doi:10.1016/j.ijpharm.2011.07.041
13. Li, X.; Jin, Z.; Wang, J. *Food Chem.* **2007,** *103,* 461–466. doi:10.1016/j.foodchem.2006.08.017
14. Ciobanu, A.; Landy, D.; Fourmentin, S. *Food Res. Int.* **2013,** *53,* 110–114. doi:10.1016/j.foodres.2013.03.048
15. Kfoury, M.; Landy, D.; Auezova, L.; Greige-Gerges, H.; Fourmentin, S. *Beilstein J. Org. Chem.* **2014,** *10,* 2322–2331. doi:10.3762/bjoc.10.241
16. Ciobanu, A.; Mallard, I.; Landy, D.; Brabie, G.; Nistor, D.; Fourmentin, S. *Food Chem.* **2013,** *138,* 291–297. doi:10.1016/j.foodchem.2012.10.106
17. Sommer, F.; Kubik, S. *Org. Biomol. Chem.* **2014,** *12,* 8851–8860. doi:10.1039/c4ob01497a
18. Lawtrakul, L.; Viernstein, H.; Wolschann, P. *Int. J. Pharm.* **2003,** *256,* 33–41. doi:10.1016/S0378-5173(03)00060-7
19. Seridi, S.; Seridi, A.; Berredjem, M.; Kadri, M. *J. Mol. Struct.* **2013,** *1052,* 8–16. doi:10.1016/j.molstruc.2013.08.035
20. Lu, Y.; Guo, T.; Qi, J.; Zhang, J.; Wu, W. *AAPS PharmSciTech* **2012,** *13,* 1222–1229. doi:10.1208/s12249-012-9842-z
21. Dinar, K.; Sahra, K.; Seridi, A.; Kadri, M. *Chem. Phys. Lett.* **2014,** *595–596,* 113–120. doi:10.1016/j.cplett.2014.02.004
22. Boonyarattanakalin, K. S.; Wolschann, P.; Lawtrakul, L. *J. Inclusion Phenom. Macrocyclic Chem.* **2011,** *70,* 279–290. doi:10.1007/s10847-010-9913-2
23. Biedermann, F.; Nau, W. M.; Schneider, H.-J. *Angew. Chem., Int. Ed.* **2014,** *53,* 11158–11171. doi:10.1002/anie.201310958
24. Jittamaro, P.; Ruktanonchai, U.; Phunpee, S.; Soottitantawat, A. *Effect of Solvent on the Complex between α-Mangostin and β-Cyclodextrin.* In *International Conference on Chemical, Civil and Material Engineering (ICCCME'2015),* 2015, Bangkok, Thailand.
25. Szegezdi, J.; Csizmadia, F. *Prediction of dissociation constant using microconstants.* In *27th ACS (American Chemical Society) National Meeting* 2004: Anaheim, California.
26. Csizmadia, F.; Tsantili-Kakoulidou, A.; Panderi, I.; Darvas, F. *J. Pharm. Sci.* **1997,** *86,* 865–871. doi:10.1021/js960177k
27. Toure, O.; Dussap, C.-G.; Lebert, A. *Oil Gas Sci. Technol.* **2013,** *68,* 281–297. doi:10.2516/ogst/2012094
28. Meeprasert, A.; Khuntawee, W.; Kamlungsua, K.; Nunthaboot, N.; Rungrotmongkol, T.; Hannongbua, S. *J. Mol. Graphics Modell.* **2012,** *38,* 148–154. doi:10.1016/j.jmgm.2012.06.007
29. Khuntawee, W.; Rungrotmongkol, T.; Hannongbua, S. *J. Chem. Inf. Model.* **2012,** *52,* 76–83. doi:10.1021/ci200304v
30. Bren, U.; Hodošček, M.; Koller, J. *J. Chem. Inf. Model.* **2005,** *45,* 1546–1552. doi:10.1021/ci050151r
31. Udommaneethanakit, T.; Rungrotmongkol, T.; Bren, U.; Frecer, V.; Stanislav, M. *J. Chem. Inf. Model.* **2009,** *49,* 2323–2332. doi:10.1021/ci900277r
32. *Gaussian 09;* Gaussian, Inc.: Wallingford, CT, USA, 2009.
33. Martínez, L.; Andrade, R.; Birgin, E. G.; Martínez, J. M. *J. Comput. Chem.* **2009,** *30,* 2157–2164. doi:10.1002/jcc.21224
34. Sangpheak, W.; Khuntawee, W.; Wolschann, P.; Pongsawasdi, P.; Rungrotmongkol, T. *J. Mol. Graphics Modell.* **2014,** *50,* 10–15. doi:10.1016/j.jmgm.2014.03.001
35. Nutho, B.; Khuntawee, W.; Rungnim, C.; Pongsawasdi, P.; Wolschann, P.; Karpfen, A.; Kungwan, N.; Rungrotmongkol, T. *Beilstein J. Org. Chem.* **2014,** *10,* 2789–2799. doi:10.3762/bjoc.10.296
36. Fabiola, F.; Bertram, R.; Korostelev, A.; Chapman, M. S. *Protein Sci.* **2002,** *11,* 1415–1423. doi:10.1110/ps.4890102
37. Gohlke, H.; Kiel, C.; Case, D. A. *J. Mol. Biol.* **2003,** *330,* 891–913. doi:10.1016/S0022-2836(03)00610-7
38. Hou, T.; Wang, J.; Li, Y.; Wang, W. *J. Comput. Chem.* **2011,** *32,* 866–877. doi:10.1002/jcc.21666
39. Rocchia, W.; Alexov, E.; Honig, B. *J. Phys. Chem. B* **2001,** *105,* 6507–6514. doi:10.1021/jp010454y
40. Rastelli, G.; Del Rio, A.; Degliesposti, G.; Sgobba, M. *J. Comput. Chem.* **2010,** *31,* 797–810. doi:10.1002/jcc.21372
41. Genheden, S.; Luchko, T.; Gusarov, S.; Kovalenko, A.; Ryde, U. *J. Phys. Chem. B* **2010,** *114,* 8505–8516. doi:10.1021/jp101461s
42. Bren, U.; Janežič, D. *J. Chem. Phys.* **2012,** *137,* 024108. doi:10.1063/1.4732514
43. Bren, U.; Fuchs, J. E.; Oostenbrink, C. *Chem. Res. Toxicol.* **2014,** *27,* 2136–2147. doi:10.1021/tx5004062
44. Åqvist, J.; Medina, C.; Samuelsson, J.-E. *Protein Eng.* **1994,** *7,* 385–391. doi:10.1093/protein/7.3.385
45. Bren, U.; Lah, J.; Bren, M.; Martínek, V.; Florián, J. *J. Phys. Chem. B* **2010,** *114,* 2876–2885. doi:10.1021/jp9064246
46. Bren, U.; Oostenbrink, C. *J. Chem. Inf. Model.* **2012,** *52,* 1573–1582. doi:10.1021/ci300118x
47. Lee, F. S.; Chu, Z.-T.; Bolger, M. B.; Warshel, A. *Protein Eng.* **1992,** *5,* 215–228. doi:10.1093/protein/5.3.215
48. Miller, B. R.; McGee, T. D., Jr.; Swails, J. M.; Homeyer, N.; Gohlke, H.; Roitberg, A. E. *J. Chem. Theory Comput.* **2012,** *8,* 3314–3321. doi:10.1021/ct300418h
49. Still, W. C.; Tempczyk, A.; Hawley, R. C.; Hendrickson, T. *J. Am. Chem. Soc.* **1990,** *112,* 6127–6129. doi:10.1021/ja00172a038
50. Higuchi, T.; Connors, K. A. *Adv. Anal. Chem. Instrum.* **1965,** *4,* 117–212.
51. Aree, T.; Chaichit, N. *Carbohydr. Res.* **2003,** *338,* 1581–1589. doi:10.1016/S0008-6215(03)00220-9
52. Bren, U.; Martínek, V.; Florián, J. *J. Phys. Chem. B* **2006,** *110,* 12782–12788. doi:10.1021/jp056623m
53. Bren, M.; Florián, J.; Mavri, J.; Bren, U. *Theor. Chem. Acc.* **2007,** *117,* 535–540. doi:10.1007/s00214-007-0264-z

License and Terms

The definitive version of this article is the electronic one which can be found at:
doi:10.3762/bjoc.11.251

BEILSTEIN JOURNAL OF ORGANIC CHEMISTRY

Preparation of Pickering emulsions through interfacial adsorption by soft cyclodextrin nanogels

Shintaro Kawano[1], Toshiyuki Kida[*2], Mitsuru Akashi[2], Hirofumi Sato[1], Motohiro Shizuma[1] and Daisuke Ono[*1]

Full Research Paper

Address:
[1]Biomaterial and Commodity Chemicals Research Division, Osaka Municipal Technical Research Institute, 1-6-50 Morinomiya, Joto-ku, Osaka 536-8553, Japan and [2]Department of Applied Chemistry, Graduate School of Engineering, Osaka University, Suita, Osaka 565-0871, Japan

Email:
Toshiyuki Kida* - kida@chem.eng.osaka-u.ac.jp; Daisuke Ono* - Daiskono@omtri.or.jp

* Corresponding author

Keywords:
crosslinked cyclodextrin polymer; interfacial adsorption; nanogel; Pickering emulsion

Beilstein J. Org. Chem. **2015,** *11,* 2355–2364.
doi:10.3762/bjoc.11.257

Received: 31 July 2015
Accepted: 10 November 2015
Published: 30 November 2015

This article is part of the Thematic Series "Superstructures with cyclodextrins: Chemistry and applications III".

Guest Editor: G. Wenz

Abstract

Background: Emulsions stabilized by colloidal particles are known as Pickering emulsions. To date, soft microgel particles as well as inorganic and organic particles have been utilized as Pickering emulsifiers. Although cyclodextrin (CD) works as an attractive emulsion stabilizer through the formation of a CD–oil complex at the oil–water interface, a high concentration of CD is normally required. Our research focuses on an effective Pickering emulsifier based on a soft colloidal CD polymer (CD nanogel) with a unique surface-active property.

Results: CD nanogels were prepared by crosslinking heptakis(2,6-di-*O*-methyl)-β-cyclodextrin with phenyl diisocyanate and subsequent immersion of the resulting polymer in water. A dynamic light scattering study shows that primary CD nanogels with 30–50 nm diameter assemble into larger CD nanogels with 120 nm diameter by an increase in the concentration of CD nanogel from 0.01 to 0.1 wt %. The CD nanogel has a surface-active property at the air–water interface, which reduces the surface tension of water. The CD nanogel works as an effective Pickering emulsion stabilizer even at a low concentration (0.1 wt %), forming stable oil-in-water emulsions through interfacial adsorption by the CD nanogels.

Conclusion: Soft CD nanogel particles adsorb at the oil–water interface with an effective coverage by forming a strong interconnected network and form a stable Pickering emulsion. The adsorption property of CD nanogels on the droplet surface has great potential to become new microcapsule building blocks with porous surfaces. These microcapsules may act as stimuli-responsive nanocarriers and nanocontainers.

Introduction

Pickering emulsions, which are emulsions stabilized by colloidal particles instead of conventional low-molecular-weight surfactants [1], are formed through the adsorption of colloidal particles at an oil–water interface to give stable emulsion droplets. Particle adsorption, which depends on the wettability of the particles against the two fluids, is related to the contact angle at the oil–water interface [2].

Although many reports have used inorganic [3,4] or organic particles [5,6] as Pickering emulsifiers, soft microgels, which are colloidal particles composed of swollen crosslinked polymers, have recently been demonstrated as Pickering emulsifiers with pH or thermo-responsive properties [7-9]. Such emulsions have potential in pharmaceutical, food, and cosmetic products. Moreover, emulsions stabilized by stimuli-responsive soft microgels should be applicable as templates to fabricate functional materials such as hollow permeable microcapsules. With regard to biomedical and pharmaceutical fields, emulsifiers derived from natural polymers such as saccharides are attractive compared to Pickering emulsifiers derived from synthetic polymers.

Cyclodextrins (CDs) are cyclic oligosaccharides, which have subnanometer-sized cavities where guest molecules with an appropriate size and shape are incorporated [10]. CDs have been reported to work as emulsion stabilizers [11-14]. Previous studies have shown that CDs can form surface-active inclusion complexes with oil molecules at the oil–water interfaces that can stabilize emulsions, although they do not alter the surface tension of water alone [15].

Only a few papers have reported Pickering emulsions stabilized by CD inclusion complexes. For example, Inoue et al. prepared oil-in-water (O/W) emulsions with α-, β- and γ-CDs using an *n*-alkane/water system [12]. They reported that the most stable emulsion is formed by β-CD–oil complexes when the contact angles are close to 90° at the oil–water interface. Davarpanah et al. examined the relationship between the stability of O/W Pickering emulsions formed through complexation of β-CD with select oil solvents and the interfacial tension at the oil–water interface [13]. Mathapa et al. described the effect of the particle size formed with the CD–oil complex on the stability of the Pickering emulsion [14]. They also reported that “CD colloidosomes” composed of the CD–oil complexes microparticles can be formed by an emulsion template and subsequent core oil removal. These previous works have been limited to preparing Pickering emulsions via the formation of CD–oil complexes at the oil–water interface. Thus, emulsion formation requires a high concentration of CDs and depends on the type of oil solvent.

Our research focuses on a new class of Pickering emulsifiers based on nanometer-sized hydrogel nanoparticles composed of crosslinked CD polymers (hereafter CD nanogels), which have a surface-active property and form stable emulsions at the oil-water interface. Reports on CD nanogels have been increasing in terms of drug delivery systems using the nanoporous cavities of the CDs and hydrogel networks, which can effectively store and release molecules [16,17]. However, to the best of our knowledge, the use of CD nanogels as Pickering emulsifiers has yet to be reported.

We have previously reported urethane-crosslinked CD polymers, which were prepared by reacting heptakis(2,6-di-*O*-methyl)-β-cyclodextrins (DM-β-CDs) with aromatic diisocyanates such as 4,4’-methylenebis(phenyl isocyanate) (MDI) and 1,4-phenylene diisocyanate (PDI) [18]. Although MDI- or PDI-crosslinked DM-β-CD polymers bearing a [MDI or PDI]/[DM-β-CD] feed ratio of more than three has a lipophilic nature, they show a poor hydrophilicity. Controlling the degree of crosslinking should provide an appropriate balance between the hydrophilicity and hydrophobicity, generating an amphiphilic crosslinked CD polymer, which can be dispersed in water as well as in nonpolar solvents. This amphiphilic polymer should realize water-swellable hydrogel nanoparticles containing CDs (CD nanogels). In this paper, we describe the preparation of Pickering emulsions using CD nanogels composed of crosslinked DM-β-CD polymers in water.

Results and Discussion

Preparation and characterization of the CD nanogels

Nanometer-sized CD nanogels were prepared by crosslinking DM-β-CD with PDI and subsequent immersion of the resulting polymers in water (Figure 1). The crosslinking reaction was performed at 70 °C for 24 h (the crosslinker/DM-β-CD feed ratio = 3/1). The resulting crosslinked DM-β-CD/PDI polymer is water soluble. The polymer product was purified by dialysis (molecular weight cut off = 10,000) against water.

A powder of the DM-β-CD/PDI polymer obtained by freeze-drying was easily redispersed in water with the aid of ultrasonication. Previously, we prepared a urethane-crosslinked DM-β-CD/PDI polymer at a higher crosslinker/DM-β-CD feed ratio (>5.0). The resulting polymer forms a submicrometer-sized particle and does not disperse in water [18]. These results reveal that controlling the crosslinking degree gives a polymer with a good colloidal stability in water.

Figure 2 shows the ^{1}H NMR spectra of the DM-β-CD/PDI polymer and DM-β-CD. The peaks of the DM-β-CD and 1,4-

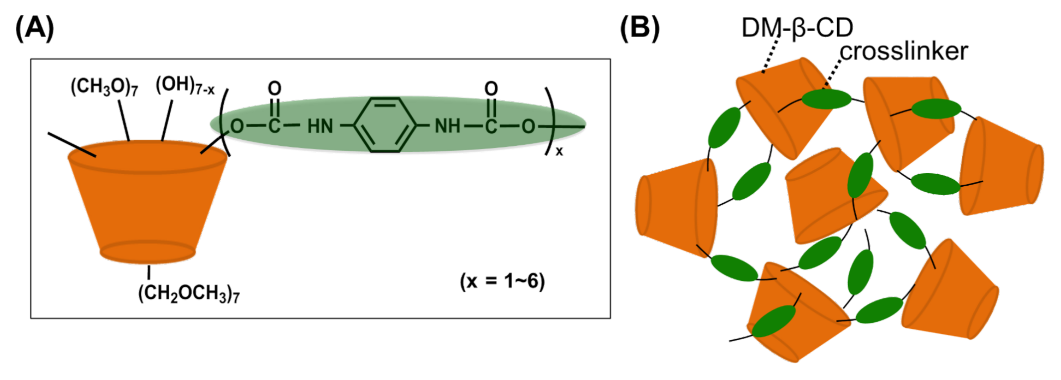

Figure 1: (A) Chemical structure and (B) schematic illustration of DM-β-CD/PDI polymer.

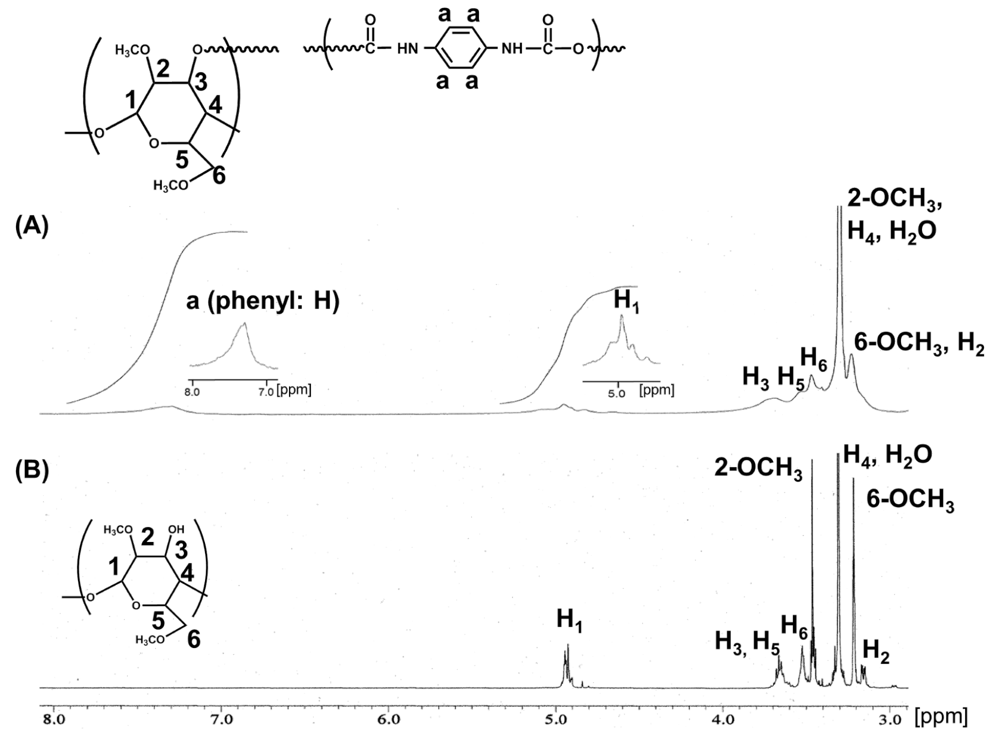

Figure 2: ^{1}H NMR spectra of (A) DM-β-CD/PDI polymer and (B) DM-β-CD in $(CD_3)_2SO$.

phenylene dicarbamyl (PDC) segments are broadened due to the restricted movement of the network linkage of the polymer. The integral ratio of the peaks for the phenyl groups in PDC to the peaks of H_1 protons of DM-β-CD indicates that the PDC/DM-β-CD ratio is two. The appearance of C=O stretching bands from urethane (1714 cm^{-1}) in the FTIR spectrum (Supporting Information File 1, Figure S1) confirms that a urethane-crosslinked polymer is formed. In addition, a O–H stretching band at 3309 cm^{-1} shows that free OH groups remain in the polymer.

The surface charge of the DM-β-CD/PDI polymer nanogels was characterized by measuring the zeta potential of the aqueous solution through electrophoretic analysis at various pH levels. The zeta potential is approximately +2.0 to +4.0 mV for pH 5.0 to 9.0, suggesting that the nanogels have almost neutral surface charges (Figure S2, Supporting Information File 1). Thus, the following study was carried out using CD nanogel solutions without pH control.

The hydrodynamic diameter and size distribution of the CD nanogels were studied using dynamic light scattering (DLS). Figure 3A shows the DLS data of CD nanogel obtained after redispersion of the freeze-dried DM-β-CD/PDI polymer powder in water. The concentration of the CD nanogel was adjusted to

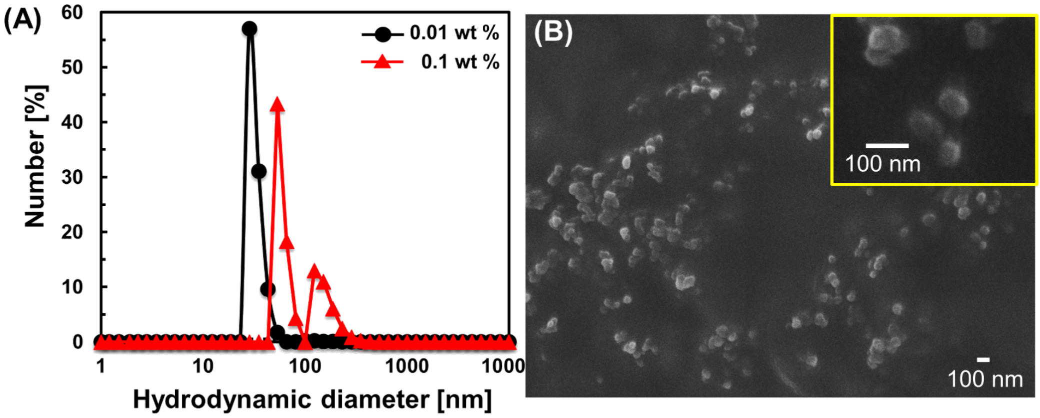

Figure 3: (A) Number-averaged particle size distributions of DM-β-CD/PDI nanogels measured by DLS at concentrations of 0.01 and 0.1 wt % in water. (B) SEM image of DM-β-CD/PDI nanogels. Inset shows the magnified image.

0.01 and 0.1 wt %. At a 0.01 wt % concentration, a unimodal size distribution occurs with a peak at 30 nm diameter. When the concentration of the CD nanogel is increased to 0.1 wt %, a bimodal size distribution is observed and the major peak shifts from a 30 nm (at 0.01 wt %) to 50 nm (at 0.1 wt %) diameter, and a new peak appears at 120 nm diameter. An increase in the particle size of the primary CD nanogel and the appearance of a new peak at a larger diameter (120 nm) may be due to the self-assembly of the primary CD nanogels at 0.1 wt % concentration in water.

The scanning electron microscopy (SEM) measurement was carried out in order to observe the self-assembled nanogel structures. Prior to the observation, the CD nanogel was immediately frozen, using liquid nitrogen, and freeze-dried. The diameters of the spherical particles range from 50 to 100 nm (Figure 3B), confirming the formation of self-assembled CD nanogels in water. The transmission electron microscopy (TEM) images demonstrate that the self-assembled CD nanogels consist of primary CD nanogel cores (Figure S3, Supporting Information File 1).

To investigate the surface activity of CD nanogels, the surface tension of the aqueous solution was measured by the pendant drop method. The surface tensions of the aqueous solutions of DM-β-CD and the DM-β-CD/PDI nanogels at different concentrations are shown in Table 1 and Figure S4 (Supporting Information File 1). The surface tension of the DM-β-CD/PDI nanogel solution remarkably decreases when the concentration increases in the range from 1.0×10^{-3} to 4.0×10^{-2} wt %, indicating that the DM-β-CD/PDI nanogels have the ability to lower surface tension through the adsorption at the air–water interface. Then, the surface tension reaches a plateau, showing that the nanogels self-aggregate in water. A critical aggregation concentration (CAC) was estimated to be 4.0×10^{-2} wt % from the breakpoint of the surface tension vs concentration (on log-scale) curve (Figure S4, Supporting Information File 1). Comparison of the surface tension between the DM-β-CD/PDI nanogel solution and the DM-β-CD solution reveals that DM-β-CD/PDI nanogels show a greater ability to lower surface tension as compared to that of DM-β-CD in the concentration range examined. Moreover, an aqueous solution containing CD nanogels gradually becomes opaque as the CD

Table 1: Surface tensions of aqueous solutions of DM-β-CD/PDI nanogels and DM-β-CD at different concentrations.

	DM-β-CD/PDI polymer		DM-β-CD	
Concentration [wt %]	Surface tension[a] [mN/m]	S.D.[b]	Surface tension[a] [mN/m]	S.D.[b]
1.0×10^{-3}	62.9	2.3	64.4	0.90
1.0×10^{-2}	56.8	0.5	62.4	1.6
5.0×10^{-2}	54.5	0.8	58.5	0.9
1.0×10^{-1}	54.4	1.2	57.5	0.8
5.0×10^{-1}	54.2	1.1	56.1	0.6

[a]Measured after allowing to stand for 1 h. [b]Standard deviation (S.D.) was calculated from the average of the runs.

nanogel concentration increases (>0.1 wt %) possibly due to self-aggregation.

Formation of Pickering emulsions

The DM-β-CD/PDI nanogel functions as a good Pickering emulsifier when a mixture of the aqueous solution (0.1 wt %) with either *n*-dodecane (Figure 4A) or toluene (Figure 4B) is homogenized at 8000 rpm for 1 min. A milky emulsion phase is produced after standing for 24 h when a 50:50 oil/aqueous volume ratio (denote $\Phi_{oil} = 0.5$) is employed.

In each case, stable creaming is visually observed without further phase separation where the lower phase is composed of the CD nanogel aqueous solution. The drop test confirmed the presence of an oil-in-water (denote O/W) emulsion. Upon adding a drop of the emulsion to water, the emulsion disperses well in water. The volume fraction of the emulsion phase was investigated by monitoring the height of the upper oil, emulsion, and lower aqueous phases. When *n*-dodecane was used as an oil phase, the volume fractions for the lower aqueous, emulsion, and the upper oil phases are 0.25, 0.69, and 0.06, respectively (Figure 4A-2). In the case of toluene, the volume fractions for the lower aqueous, emulsion, and the upper oil phases are 0.29, 0.62, and 0.09, respectively (Figure 4B-2). These results show a slight phase separation of the oil from the emulsion phase. It should be noted that reducing a volume ratio of oil ($\Phi_{oil} = 0.3$) does not result in a phase separation for either oil (data not shown).

Optical microscopy observation confirmed the presence of dispersed oil droplets for both O/W emulsions as shown in Figure 4C (for *n*-dodecane) and 4D (for toluene). The emulsion droplets are slightly larger for the *n*-dodecane (35 ± 10 μm) compared to those of toluene (24 ± 5.1 μm). The mean droplet sizes and the corresponding emulsion volume fraction should be related to the Hansen solubility parameter of the oil [19]. Organic solvents possess a solubility parameter, which is manifested from dispersion forces (δ_d), polarity (δ_p), and hydrogen bonding forces (δ_h). Toluene has a relatively higher contribution in terms of δ_p and δ_h compared to *n*-dodecane; these parameters may result in a higher affinity for the interface of toluene and water compared to that of *n*-dodecane and water. Thus, the droplet sizes are slightly smallerer for toluene than that of *n*-dodecane [13], while the emulsion volume fraction, which is correlated to the emulsion stability, is higher for *n*-dodecane than that of toluene. Previous results on the effect of the oil type

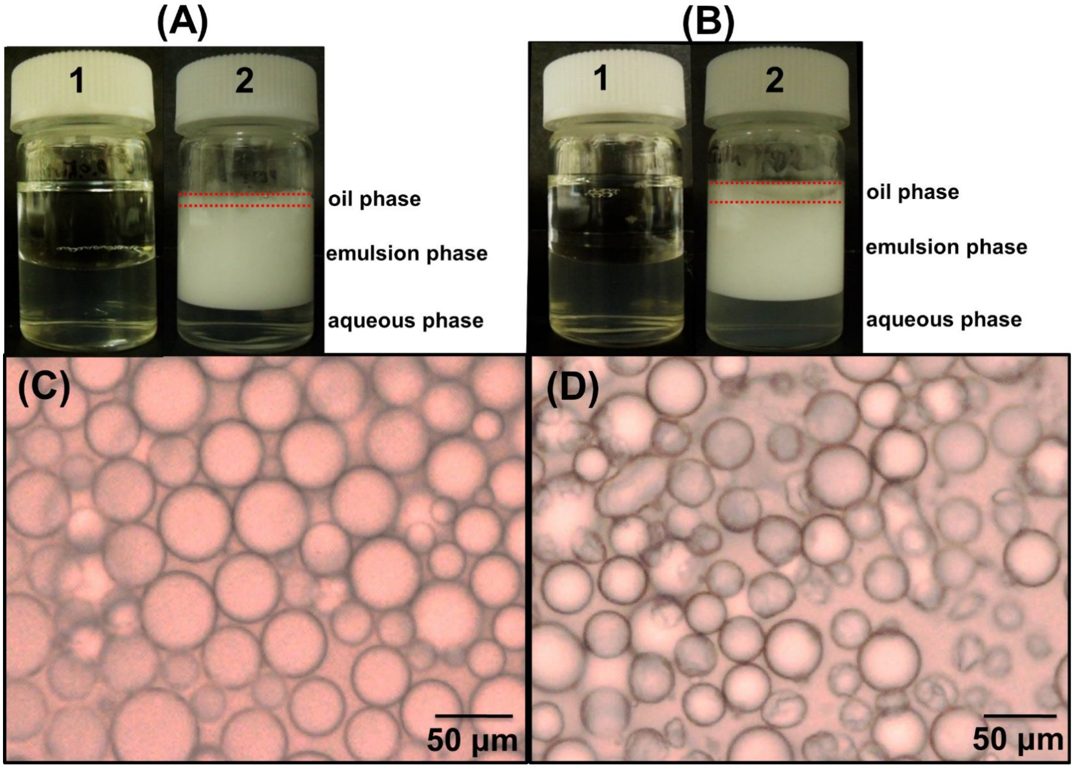

Figure 4: (A,B) Digital photograhs of (1) the initial DM-β-CD/PDI nanogel (0.1 wt %) with (A) *n*-dodecane or (B) toluene added directly to the vial and (2) the *n*-dodecane- or toluene-in-water emulsion stabilized by the DM-β-CD/PDI nanogel after standing for 24 h. Red dotted lines show oil phase boundaries. (C,D) The corresponding optical microscope image for the (C) *n*-dodecane- or (D) toluene-in-water droplets stabilized with the DM-β-CD/PDI nanogel.

when preparing a Pickering emulsion have shown that a relatively nonpolar oil favors the formation of an O/W type emulsion, while a polar oil favors the formation of a W/O type emulsion [20].

The stabilities of the *n*-dodecane- and toluene-in-water emulsions formed by the DM-β-CD/PDI nanogel were studied by varying the CD nanogel concentration (Figure 5A,B). The relationship between the oil droplet diameter and the corresponding CD nanogel concentrations (Figure 5C,D) was also examined. In both oils, when the CD nanogel concentration increases from 0.01 to 0.1 wt %, the emulsion phase volume fractions increase, indicating that the Pickering emulsion becomes more stable. In a concentration range from 0.05 to 0.1 wt %, the change in the emulsion volume fractions is negligible for both oils, suggesting that 0.05 wt % concentration of the CD nanogel is sufficient to inhibit coalescence of the emulsions. Therefore, the mean droplet diameters remain constant in the concentration range from 0.05 to 0.1 wt %. In the case of the 0.01 wt % concentration, the initial emulsion volume fractions are lower and their droplet diameters are higher, indicating a remarkable decrease in the emulsion stabilities for both oils. However, the creamed emulsion phases never become clear, even at a CD nanogel concentration as low as 0.01 wt %.

It should be noted that the DM-β-CD/PDI nanogel realizes the formation of a Pickering emulsion at ten times lower concentrations compared to previous emulsifiers using CDs [12-14]. Moreover, conventional methods depend on the formation of inclusion complexes between the CDs and oil molecules at an interface. The findings herein demonstrate that CD nanogels have efficient adsorption properties at oil–water interfaces to stabilize emulsions. The adsorption properties of CD nanogels, which consist of hydrophilic DM-β-CD and lipophilic benzene parts, may be affected by their hydrophilic and lipophilic balance of the nanogels.

Identification of the CD nanogel assembly at the interface

Adsorption of a CD nanogel at the oil–water interface in the emulsion phase was identified using a fluorescent dye-labeling method. The CD nanogel was labeled with fluorescein isothiocyanate (FITC) in the aqueous phase before emulsification. A Pickering emulsion was prepared by mixing the aqueous dispersion containing FITC labeled-CD nanogels (0.1 wt %) with *n*-dodecane ($\Phi_{\text{oil}} = 0.1$) and subsequent shaking for 1 min. After dilution with water, the emulsion was observed using fluorescence microscopy. Similar oil droplets were observed by optical (Figure 6A) and fluorescence (Figure 6B) microscopy without

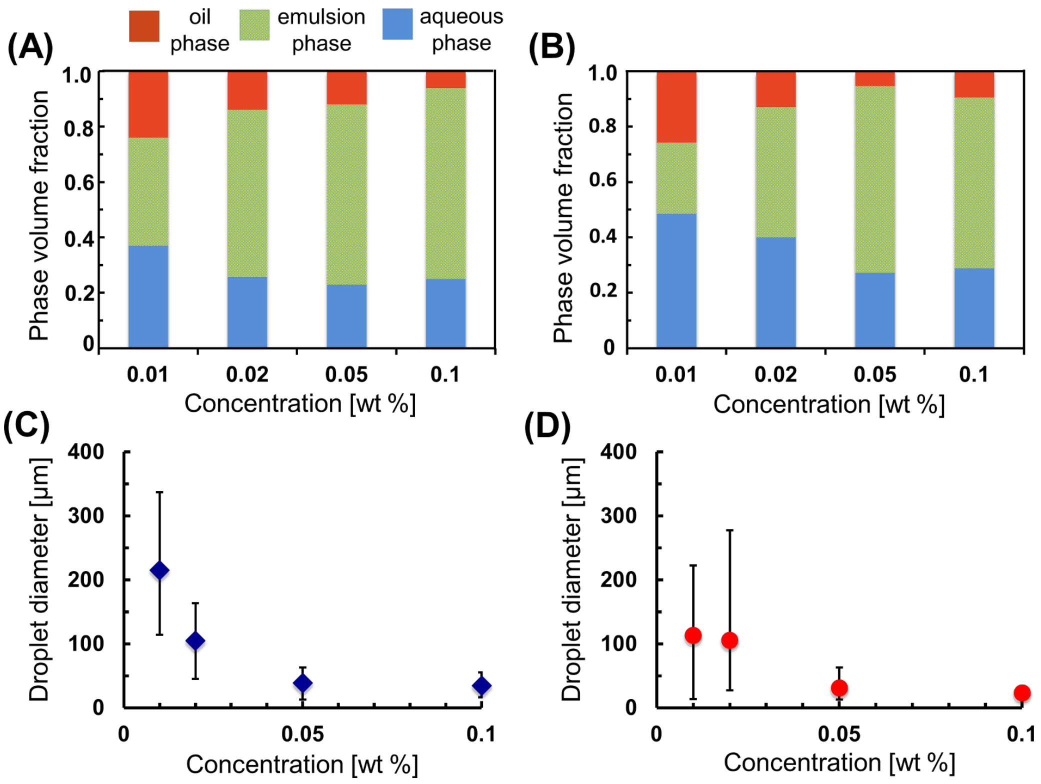

Figure 5: (A,B) Phase volume fractions and (C,D) droplet diameters of *n*-dodecane-(A) or toluene- (B) in-water emulsion stabilized by the DM-β-CD/PDI nanogel at various nanogel concentrations.

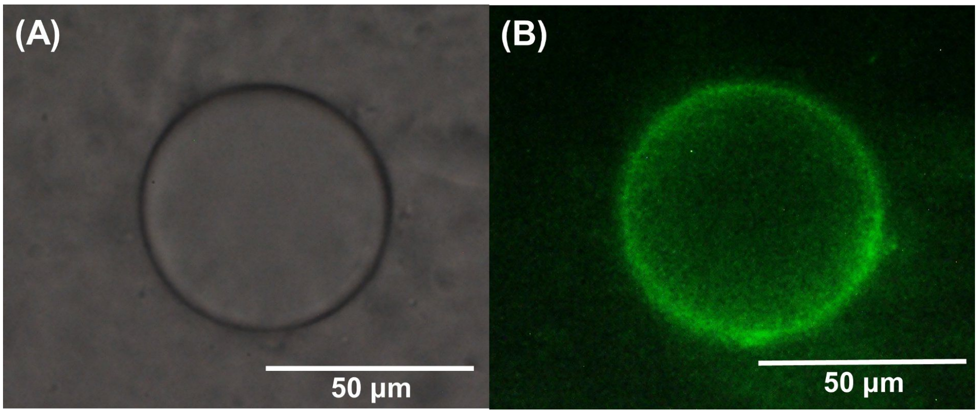

Figure 6: (A) Optical and (B) fluorescence micrographs of the *n*-dodecane-in-water emulsion stabilized by the FITC-labeled DM-β-CD/PDI nanogel before (A) and after (B) observations with the filter sets (excitation wavelength: 470 nm and emission wavelength: >510 nm).

and with a filter set, respectively. The CD nanogels (green) are concentrated at the surface of the oil droplet, confirming that the adsorption of the CD nanogels at the oil–water interface stabilizes the emulsion.

Organization of CD nanogels at the interface

To characterize the interfacial structure and to examine the stability of interfacial assembly of the CD nanogels, laser or scanning microscopy observation was performed after evaporation of the oil droplets. Figure 7A,B show the optical and profile images of the toluene-in-water droplets stabilized by DM-β-CD/PDI nanogel after evaporation of the toluene core. The assembled layer of CD nanogel particles maintains the circular shape of the oil droplet, although the three-dimensional spherical structure collapses and flattens during the drying process. The image appears to have a "deflated balloon" structure, indicating that CD nanogel particles can be fused together via interconnections after adsorption at the oil–water interface.

The "deflated balloon" structures, which consist of a CD nanogel assembly, were also observed after the removal of toluene (Figure S5, Supporting Information File 1). The layer thickness of the CD nanogel assembly was assessed by a cross-sectional histogram using a laser microscope (Figure 7C). The

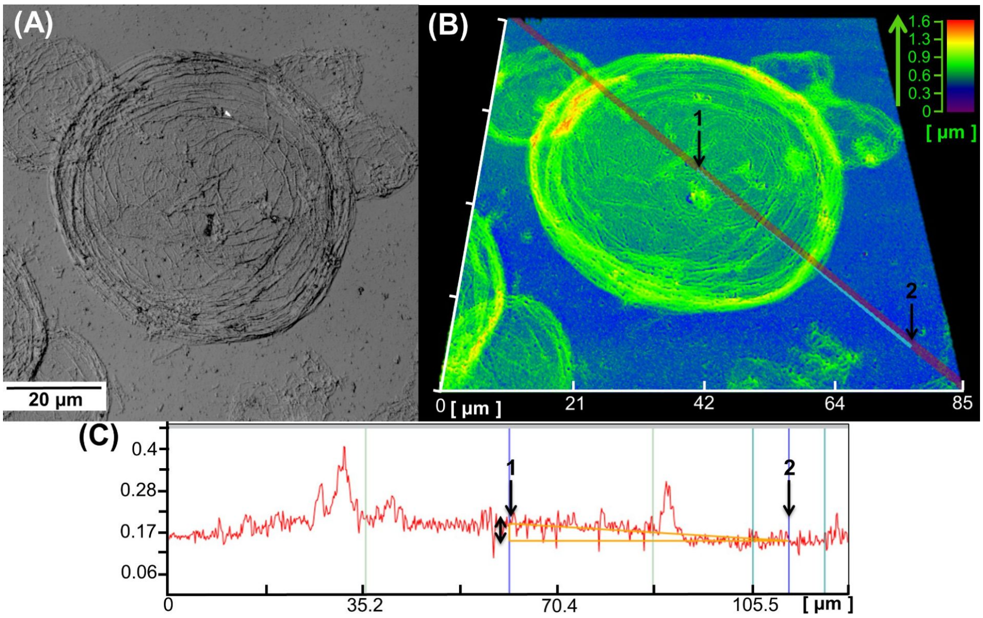

Figure 7: Laser microscope images of the toluene-in-water droplets stabilized by the DM-β-CD/PDI nanogel after evaporation of the toluene cores. (A) Optical image, (B) profile image, and (C) the cross-sectional histogram. Inset arrows and numbers correspond to the orientation for both images (B and C).

estimated layer thickness between the top layer (Figure 7C-1) and the bottom substrate (Figure 7C-2) is about 46 nm, suggesting that the original nanogel particles (30 to 50 nm in diameter) self-assemble at the oil–water interface to form interconnected monolayers. Hence, the Pickering emulsion should be fabricated from the monolayer shell (whose thickness corresponds to the particle diameter) of self-assembled CD nanogels and not a multilayer structure.

The outermost layer of the CD nanogel assembly was observed using SEM. A number of "deflated balloon" structures appear under low magnification (Figure 8A), while a flattened layer is observed in the magnified image due to the fusion of CD nanogel particles (Figure 8B). The spherical CD nanogel particles are easily inter-penetrable [21] and may form a dense interconnected network (Figure 8B). The strong connectivity results in an interfacial layer, which effectively protects the oil droplets from coalescence.

Conclusion

Amphiphilic CD nanogels, which are a new class of soft hydrogel nanoparticles, were prepared by crosslinking DM-β-CDs with PDI followed by the immersion in water. The DLS study shows that the primary CD nanogels (30–50 nm in diameter) assemble into larger ones (120 nm in diameter). These CD nanogels show surface-active properties at the air–water interface and function as an effective Pickering emulsion stabilizer at relatively low concentrations (0.05–0.1 wt %). Due to the adsorption property of CD nanogels on droplets, CD nanogels have potential as new building blocks for microcapsules with porous surfaces and stimuli-responsive nanocarriers in storage and/or release systems.

Experimental

Materials

Heptakis(2,6-di-*O*-methyl)-β-cyclodextrin (DM-β-CD) was purchased from Nacalai Tesque, Inc. (Japan). DM-β-CD was vacuum dried at 80 °C overnight prior to use. Anhydrous *N*,*N*-dimethylformamide (DMF) and 1,4-phenylene diisocyanate (PDI) were purchased from Wako Pure Chemical Industries, Ltd. (Japan). Toluene and *n*-dodecane were purchased from Kanto Chemical Co., Ltd. (Japan). Fluorescein-4-isothiocyanate was purchased from Dojin Chemical Co. Ltd. (Japan). The dialysis membrane with a cellulose tube (molecular weight cut-off of 10 kDa) was purchased from the Japan Medical Science Co. Ltd. (Japan) and stored in a moist environment prior to use. Distilled water was used for the purification process. Ultra pure water (Milli-Q) was used for the redispersed solution and emulsion preparation.

Preparation of CD nanogels

A crosslinked CD polymer was synthesized by reacting DM-β-CD with 1,4-phenylene diisocyanate (PDI) as a crosslinker at a molar feed ratio of diisocyanate to DM-β-CD = 3.0. Dried DM-β-CD (1 g, 0.752 mmol) was reacted with PDI in anhydrous DMF (10 mL) for 12 h at 70 °C under an argon atmosphere. The reaction mixture was dropped into water under ice bath cooling to terminate the reaction. The resulting polymer solution was purified by dialysis for three days using a dialysis membrane to remove unreacted DM-β-CD and PDI. The dialysis water was changed twice daily. Then the aqueous dispersion was lyophilized for three days to yield a white powder as a urethane-crosslinked DM-β-CD polymer. The CD nanogel was prepared by the redispersion of the powder in distilled water with the aid of ultrasonication and stored in a refrigerator until use.

Characterization of CD nanogels

^{1}H NMR spectroscopy

^{1}H NMR spectra were recorded in $(CD_3)_2SO$ using a 600 MHz JEOL RESONANCE; JNM-ECA600, Delta V5 (Japan) and averaged 16 scans at 25 °C. The chemical shifts of protons associated with different carbon atoms were presented in Table S1, Supporting Information File 1.

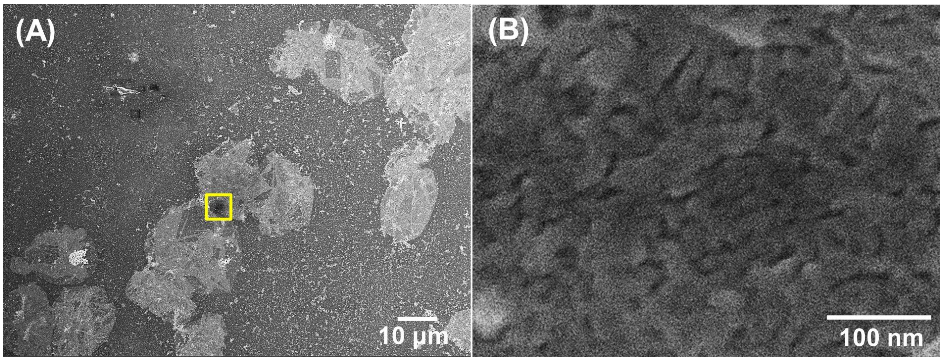

Figure 8: SEM images of the toluene-in-water droplets stabilized by the DM-β-CD/PDI nanogel after evaporation of the toluene core. (B) Magnified image of the square box on (A).

Dynamic light scattering (DLS)

The particle size distribution was measured at 25 °C using DLS6000HL (Otsuka Electronic Co.) equipped with a He-Ne laser (wavelength 632.8 nm). The mean particle diameter was calculated from the diffusion coefficients using the Stokes–Einstein equation. The particle size distribution was estimated from the scattering intensity function using the histogram analysis method, which was performed with the software supplied by the manufacturer. The weight-average distribution corresponding to each particle size was corrected from the scattering intensity, and the number-average distribution was calculated from the values where the weight-average distribution values were divided by the cube of the particle diameter. All measurements were repeated thrice using an appropriate concentration of the CD nanogel aqueous solution. Milli-Q water was used to dilute the solutions, which were ultrafiltered through a 0.8 μm membrane to remove dust.

Electron microscopy

Scanning electron microscopy (SEM) studies were performed using a field emission gun scanning electron microscope (JSM-6700F, JEOL Ltd., Japan) with a beam current of 10 μA at a typical operating voltage of 15 kV. Each Pickering emulsion sample was dried directly onto carbon tape and allowed to dry overnight before being sputter-coated with a thin layer of tungsten. Transmittance electron microscopy (TEM) studies were performed using a JEOL JEM-2100 operating at a voltage of 50 kV in order to clarify the particle morphology. Dilute solutions were prepared and deposited onto a copper grid covered by a carbon membrane at ambient temperature. The electronic contrast of the specimen was enhanced by labeling with ammonium molybdate.

Surface tension

The surface tension of the aqueous solution was measured using a CAX-150 (Kyowa Interface Science Co., Ltd) operating in the pendant drop method. The solution was added to a glass syringe after standing for 1 h at 25 °C. The droplet was prepared just before it fell to the ground. The surface (interfacial) tension (γ) was calculated by ds/de method proposed by Andreas [22], which is expressed as $\gamma = g(D_e)^2\Delta\rho/H$ where g is the gravitational constant, $\Delta\rho$ is the difference between the densities, D_e is the equatorial diameter of the drop, H is a correction factor related to the shape factor of the pendant drop (S). S is defined as $S = D_s/D_e$ where D_s is the drop diameter measured horizontally at a distance D_e away from the apex of the drop. The density between air and water was assumed to be 0.997 g/cm^3. All measurements were repeated thrice using an appropriate concentration of the CD nanogel in the aqueous solution. The standard deviation (S.D.) was calculated from the average of the five runs.

Preparation of a Pickering emulsion

The CD nanogel concentration was adjusted to 0.1 wt % using Milli-Q water. The CD nanogel solution (5.0 mL) was then added to a 13 mL vial, together with the same volume of oil (toluene or *n*-dodecane). The oil/water mixture was homogenized for 1 min using a homogenizer (DIAX 900; Heidolph) at 8000 rpm (25 °C). The resulting emulsion was allowed to stand at 25 °C for 24 h. To confirm the adsorption of the CD nanogels at the oil–water interface in the emulsion, the CD nanogel (0.1 wt %) was labeled with fluorescein-4-isothiocyanate. The aqueous solution of labeled CD nanogel was mixed with *n*-dodecane ($\Phi_{oil} = 0.1$) by hand for 1 min. Then it was allowed to stand for 1 h.

Characterization of the Pickering emulsion

Emulsion stability

The Pickering emulsion stability was evaluated by measuring the volume fraction of the aqueous, emulsion, and oil phases after standing for 24 h. Photographs of the emulsions were taken with a digital camera (FinePix J250, Fujifilm Co., Japan).

Drop test

The emulsion type (o/w or w/o) was confirmed by a drop test. An emulsion droplet was placed into water or oil. If the droplet easily spreads and disperses in water, the emulsion's continuous phase is an aqueous phase. On the other hand, if the droplet remains intact, the continuous phase differs from that of the droplet.

Microscope observations

A drop of the diluted emulsion was placed on a glass slide and viewed using an optical microscope (BX50-DIC, OLYMPUS Co., Japan) equipped with a digital camera (D90, Nikon Co., Japan), which was connected to a laptop PC to record the images. The size distribution of the emulsion droplet was determined by measuring the dimensions of 50 droplets from the images recorded.

Fluorescent microscopy was used to observe the emulsion droplet, which was stabilized by the CD nanogel labeled with fluorescein-4-isothiocyanate (FITC). The FITC-labeled CD nanogel was prepared as follow: FITC aqueous solution (1.0×10^{-5} M) was added to the CD nanogel aqueous solution (5 mg/mL), and the mixture was stirred at ambient temperature for 24 h. The resulting solution was purified by dialysis for three days using a dialysis membrane (molecular weight cut-off of 10 kDa) to remove free FITC. The aqueous dispersion was lyophilized for three days to yield a powder. Finally, the FITC-labeled CD/PDI polymer was dissolved in water. The fluorescence intensity of the FITC-labeled CD nanogels was detected by fluorescent microscopy ($\lambda_{ex} = 495$ nm, $\lambda_{em} = 520$ nm). The observations were carried out with filter sets (ex filter 470–490 nm and abs filter 510–550 nm).

The structure of the Pickering emulsion was observed using a laser microscope (OLS4100; OLYMPUS Co., Japan) under atmospheric conditions. The emulsion solution was directly dropped onto the glass slide and dried at ambient temperature. The observation was conducted with a diode laser at 405 nm.

Supporting Information

Supporting Information File 1

Additional material.
[http://www.beilstein-journals.org/bjoc/content/supplementary/1860-5397-11-257-S1.pdf]

Acknowledgements

This work was supported by Grants-in-Aid for Scientific Research of Japan Society for the Promotion of Science (Grant number 25870402).

References

1. Pickering, S. U. *J. Chem. Soc., Trans.* **1907,** *91,* 2001–2021. doi:10.1039/ct9079102001
2. Finkle, P.; Draper, H. D.; Hildebrand, J. H. *J. Am. Chem. Soc.* **1923,** *45,* 2780–2788. doi:10.1021/ja01665a002
3. Binks, B. P.; Lumsdon, S. O. *Langmuir* **2000,** *16,* 2539–2547. doi:10.1021/la991081j
4. Binks, B. P.; Lumsdon, S. O. *Phys. Chem. Chem. Phys.* **2000,** *2,* 2959–2967. doi:10.1039/b002582h
5. Velev, O. D.; Furusawa, K.; Nagayama, K. *Langmuir* **1996,** *12,* 2374–2384. doi:10.1021/la9506786
6. Aveyard, R.; Clint, J. H.; Nees, D.; Paunov, V. N. *Langmuir* **1999,** *16,* 1969–1979. doi:10.1021/la990887g
7. Ngai, T.; Behrens, S. H.; Auweter, H. *Chem. Commun.* **2005,** 331–333. doi:10.1039/b412330a
8. Ngai, T.; Auweter, H.; Behrens, S. H. *Macromolecules* **2006,** *39,* 8171–8177. doi:10.1021/ma061366k
9. Brugger, B.; Richtering, W. *Langmuir* **2008,** *24,* 7769–7777. doi:10.1021/la800522h
10. Szejtli, J. *Chem. Rev.* **1998,** *98,* 1743–1754. doi:10.1021/cr970022c
11. Shimada, K.; Fujikawa, K.; Yahara, K.; Nakamura, T. *J. Agric. Food Chem.* **1992,** *40,* 945–948. doi:10.1021/jf00018a005
12. Inoue, M.; Hashizaki, K.; Taguchi, H.; Saito, Y. *J. Oleo Sci.* **2009,** *58,* 85–90. doi:10.5650/jos.58.85
13. Davarpanah, L.; Vahabzadeh, F. *Starch/Staerke* **2012,** *64,* 898–913. doi:10.1002/star.201200027
14. Mathapa, B. G.; Paunov, V. N. *Phys. Chem. Chem. Phys.* **2013,** *15,* 17903–17914. doi:10.1039/c3cp52116h
15. Mathapa, B. G.; Paunov, V. N. *J. Mater. Chem. A* **2013,** *1,* 10836–10846. doi:10.1039/c3ta12108a
16. Moya-Ortega, M. D.; Alvarez-Lorenzo, C.; Sigurdsson, H. H.; Concheiro, A.; Loftsson, T. *Carbohydr. Polym.* **2012,** *87,* 2344–2351. doi:10.1016/j.carbpol.2011.11.005
17. Moya-Ortega, M. D.; Alvarez-Lorenzo, C.; Concheiro, A.; Loftsson, T. *Int. J. Pharm.* **2012,** *428,* 152–163. doi:10.1016/j.ijpharm.2012.02.038
18. Kawano, S.; Kida, T.; Miyawaki, K.; Fukuda, Y.; Kato, E.; Nakano, T.; Akashi, M. *Polym. J.* **2015,** *47,* 443–448. doi:10.1038/pj.2015.13
19. Hansen, C. *Hansen Solubility Parameters, A User's Handbook;* CRC Press: Boca Raton, FL, 2000.
20. Binks, B. P.; Clint, J. H. *Langmuir* **2002,** *18,* 1270–1273. doi:10.1021/la011420k
21. Destribats, M.; Lapeyre, V.; Wolfs, M.; Sellier, E.; Leal-Calderon, F.; Ravaine, V.; Schmitt, V. *Soft Matter* **2011,** *7,* 7689–7698. doi:10.1039/c1sm05240c
22. Andreas, J. M.; Hauser, E. A.; Tucker, W. B. *J. Phys. Chem.* **1938,** *42,* 1001–1019. doi:10.1021/j100903a002

License and Terms

BEILSTEIN JOURNAL OF ORGANIC CHEMISTRY

Size-controlled and redox-responsive supramolecular nanoparticles

Raquel Mejia-Ariza‡, Gavin A. Kronig‡ and Jurriaan Huskens*§

Full Research Paper

Open Access

Address:
Molecular NanoFabrication group, MESA+ Institute for Nanotechnology University of Twente, P.O. Box 217, 7500 AE Enschede, The Netherlands

Email:
Jurriaan Huskens* - J.Huskens@utwente.nl

* Corresponding author ‡ Equal contributors
§ Homepage: http://www.utwente.nl/tnw/mnf/

Keywords:
host–guest interactions; nanoparticles; self-assembly; stimulus-responsive; supramolecular chemistry

Beilstein J. Org. Chem. **2015,** *11,* 2388–2399.
doi:10.3762/bjoc.11.260

Received: 28 August 2015
Accepted: 20 November 2015
Published: 01 December 2015

This article is part of the Thematic Series "Superstructures with cyclodextrins: Chemistry and applications III".

Guest Editor: G. Wenz

Abstract

Control over the assembly and disassembly of nanoparticles is pivotal for their use as drug delivery vehicles. Here, we aim to form supramolecular nanoparticles (SNPs) by combining advantages of the reversible assembly properties of SNPs using host–guest interactions and of a stimulus-responsive moiety. The SNPs are composed of a core of positively charged poly(ethylene imine) grafted with β-cyclodextrin (CD) and a positively charged ferrocene (Fc)-terminated poly(amidoamine) dendrimer, with a monovalent stabilizer at the surface. Fc was chosen for its loss of CD-binding properties when oxidizing it to the ferrocenium cation. The ionic strength was shown to play an important role in controlling the aggregate growth. The attractive supramolecular and repulsive electrostatic interactions constitute a balance of forces in this system at low ionic strengths. At higher ionic strengths, the increased charge screening led to a loss of electrostatic repulsion and therefore to faster aggregate growth. A Job plot showed that a 1:1 stoichiometry of host and guest moieties gave the most efficient aggregate growth. Different stabilizers were used to find the optimal stopper to limit the growth. A weaker guest moiety was shown to be less efficient in stabilizing the SNPs. Also steric repulsion is important for achieving SNP stability. SNPs of controlled particle size and good stability (up to seven days) were prepared by fine-tuning the ratio of multivalent and monovalent interactions. Finally, reversibility of the SNPs was confirmed by oxidizing the Fc guest moieties in the core of the SNPs.

Introduction

Self-assembly and molecular recognition are two core concepts underlying supramolecular chemistry. These offer convenient and versatile pathways to nanostructured materials composed of molecular building blocks [1]. This fabrication strategy has been used to form supramolecular nanoparticles (SNPs) in which multiple copies of different building blocks interact via specific, non-covalent interactions [2]. They have the potential to be used in biomedical applications owing to control over their size, their assembly/disassembly, and the modular character for the versatile incorporation of agents aiming for imaging [3], photothermal therapy [4], drug delivery [5-7] and gene delivery [8-10] applications.

Different approaches have been used to form SNPs. Davis et al. showed the formation of SNPs using attractive electrostatic interactions between positively charged β-cyclodextrin (CD)-containing polymers and negatively charged siRNA at the core [8]. Neutral adamantyl-grafted poly(ethylene glycol) (Ad-PEG) was incorporated at the surface to stabilize these SNPs using host–guest interactions between CD and Ad. Tseng et al. studied the formation of SNPs that are assembled solely by host–guest interactions [11,12]. Here, the core is composed of multivalent interactions between positively charged CD-grafted polymers and positively charged poly(amidoamine) (PAMAM) dendrimers, and a monovalent neutral Ad-PEG stopper is introduced at the surface for stabilization. The SNP size was increased by increasing the amount of multivalent guest molecules in the core, while keeping the host and stopper concentration constant and having an excess of stopper to avoid precipitation. Wintgens et al. showed the formation of SNPs by controlling the host–guest ratio and the total concentration of components with a neutral polymer backbone [13]. Recently, our group [2,14,15] formed SNPs by varying the ratio of neutral monovalent stoppers and multivalent, positively charged guest dendrimer. Here, the overall concentration of the building blocks was kept constant while maintaining an equimolar stoichiometry of host and guest moieties. Moreover, our group [16] showed that SNP formation is controlled by a balance of forces between attractive supramolecular and repulsive electrostatic interactions using a multicomponent system based on a linear, negatively charged polymer. The force balance used in the latter approach was only observed with negatively charged polymers at low ionic strengths, and it is not known whether this balance occurs also for positively charged polymers and dendrimers.

In order to use these SNPs for biomedical applications, in particular for drug delivery, a stimulus-responsive self-assembled system is desired for controlled cargo release. Ferrocene (Fc) is a ubiquitous redox-responsive molecule that is associated with a reversible one-electron oxidation to the ferrocenium cation. At the same time, in its reduced state, Fc is a good guest for CD, but the affinity for CD is practically completely lost upon oxidation [17]. Thus, the formed CD-Fc inclusion complex disassembles when the Fc moiety is converted to the ferrocenium cation by electrochemistry [18] or by adding an oxidizing agent [19]. Different studies have employed this concept to form redox-responsive systems applied, for example, in self-healing materials [19], polymeric hydrogels [20,21], voltage-responsive vesicles [22], ultrasentive enzyme sensors [23], and as a plasma membrane protein isolation method [24]. So far, this concept has not been applied to SNPs.

Here, we aim to make SNPs with a redox-switchable assembly/disassembly mechanism. As a proof of concept, we used positively charged CD-grafted poly(ethylene imine) (CD-PEI) as a host, positively charged ferrocene-terminated PAMAM (Fc_8-PAMAM) dendrimer as the multivalent guest and a monovalent stabilizer. Different stabilizers were used such as: Ad-PEG, Fc-terminated poly(ethylene glycol) (Fc-PEG), methoxypoly(ethylene glycol) (mPEG), and Ad-tetraethylene glycol (Ad-TEG). The effect of the following parameters on the formation of these SNPs is investigated: the role of ionic strength on SNP formation, the role of host–guest stoichiometry on the growth rate of the SNPs, and the influence of the affinity of the guest moiety and that of the PEG length of the stabilizer on the SNP stability. The size of the SNPs is controlled by the stoichiometry of the multivalent guest and the monovalent stabilizer. Finally, the reversibility of the SNPs is assessed by studying the influence of oxidation of the Fc moieties.

Results and Discussion

Characterization of building blocks

The positively charged host CD-PEI was synthesized according to earlier reports with slight modifications [25,26]. A reaction between 6-monotosyl-β-cyclodextrin (TsCD) and PEI in DMSO was performed using an excess of triethylamine as a base, followed by purification by dialysis. In order to control the stoichiometry of the host and guest moieties, the number of CDs per PEI was determined using microcalorimetry and NMR. According to the ^1H NMR spectrum, the PEI backbone in the polymer building block CD-PEI is functionalized with, on average, 8 CD units. To assess the CD concentration in a CD-PEI stock solution, a calorimetric titration was performed using CD-PEI as the host and Ad-TEG as a guest, as shown in Figure 1a. Fitting the results by optimizing $\Delta H°$, K and the CD host concentration gave a concentration of 0.39 mg/mL of CD-PEI, which is equivalent to a concentration of 0.088 mM of CD moieties participating in host–guest interactions. The results gave a binding constant (K_a) of 3×10^4 L mol^{-1}. This is slightly lower than the interaction between native CD and Ad-TEG, for which a K_a value of 5×10^4 L mol^{-1} has been determined (see Figure 1b). It can therefore be concluded that the grafting of CD to PEI has a minor effect on the host–guest binding affinity.

The positively charged Fc_8-PAMAM multivalent guest was prepared according to a procedure developed in our group [27]. The positively charged Ad-terminated PAMAM (Ad_8-

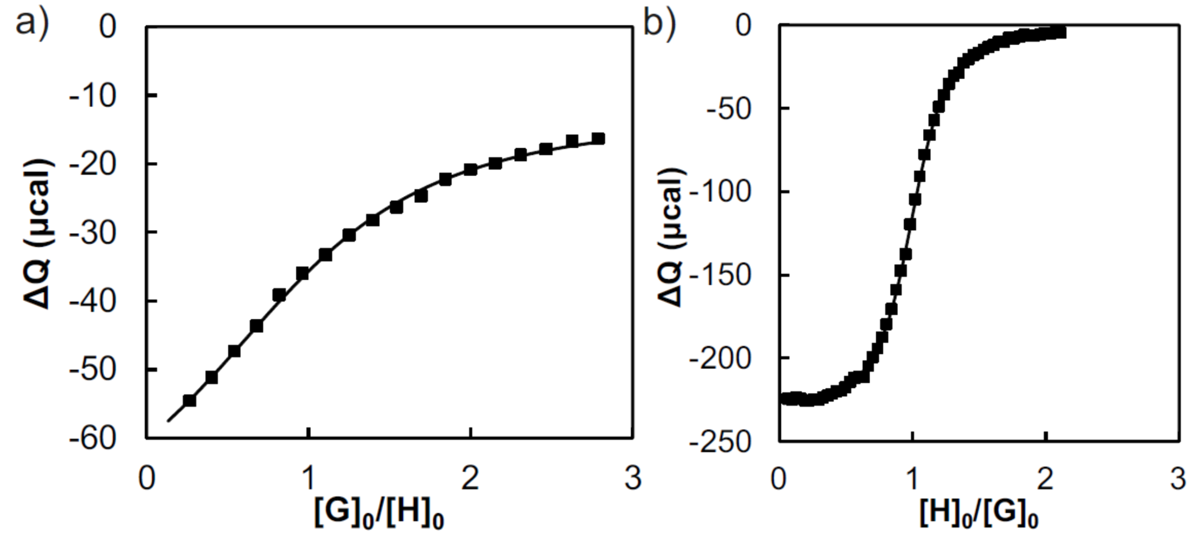

Figure 1: Microcalorimetric titrations of a) CD-PEI (CD concentration of 0.088 mM, cell) with Ad-TEG (1.1 mM, burette) and b) Ad-TEG (1.1 mM, cell) with CD (10 mM; burette). H = host (CD from CD-PEI or native CD) and G = guest (Ad from Ad-TEG). Experimental binding curve (markers) and best fit to a 1:1 model (line).

PAMAM), used as a control, was prepared according to a literature procedure [11]. The neutral Fc-PEG stabilizer was synthesized by a reaction of 1-(chlorocarbonyl)ferrocene with the terminal amino group of methoxypoly(ethylene glycol)amine (M_w = 5000 g/mol) in dichloromethane, using an excess of triethylamine as a base, followed by precipitation from diethyl ether. To evaluate the association constant of the Fc moiety with free CD, and to confirm the degree of functionalization, a calorimetric titration was performed with native CD, as shown in Figure 2. This titration confirmed that nearly 100% of Fc-PEG was formed. The K_a of Fc-PEG with native CD is 1.2×10^3 L mol^{-1}, which is comparable to the binding constant of Fc dendrimers with CD [28].

The neutral stabilizer Ad-PEG was synthesized according to a literature procedure [11], by the reaction of 1-adamantylamine with the succinimidyl ester of carboxymethyl-PEG (M_w = 5000 g/mol) in dichloromethane with an excess of triethylamine.

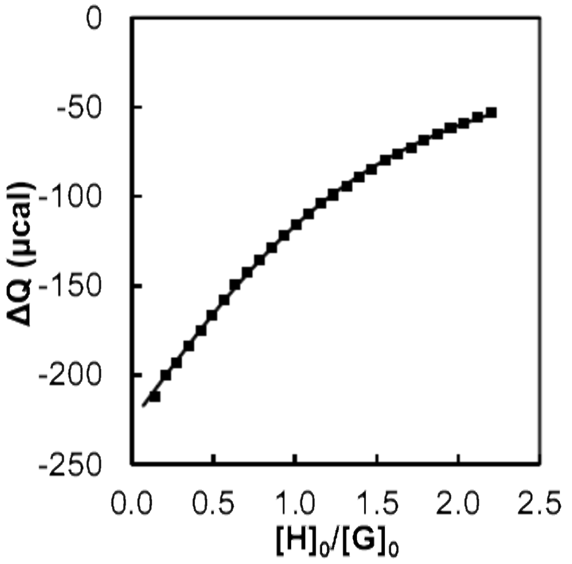

Figure 2: ITC titration of Fc-PEG (1.03 mM; cell) with native CD (10 mM; burette). H = host and G = guest. Experimental binding curve (markers) and best fit to a 1:1 model (line).

Formation and size control of SNPs

Scheme 1a shows the concept of forming SNPs based on host–guest interactions, and the possible or impossible redox-induced disassembly when using Fc or Ad as the guest moiety, respectively. Throughout this study, concentrations of all the building blocks were expressed as the molar concentrations of the monovalent host and guest moieties, i.e., CD, Ad and Fc.

Influence of the ionic strength

The SNPs used here are formed using host–guest interactions between Fc_8-PAMAM and CD-PEI. These molecules have positive charges that can influence the growth by repulsive interactions, which is an additional parameter that can influence the formation of SNPs. Moreover, Fc is used as the guest moiety as its stimulus-responsive properties lead to a triggered assembly/disassembly system. In order to study the influence of ionic strength on SNP formation, we used 0 to 0.2 M NaCl solutions and different guest–host ratios when assembling SNPs from CD-PEI and Fc_8-PAMAM in the absence of stabilizer. SNPs were formed by adding Fc_8-PAMAM (dissolved in

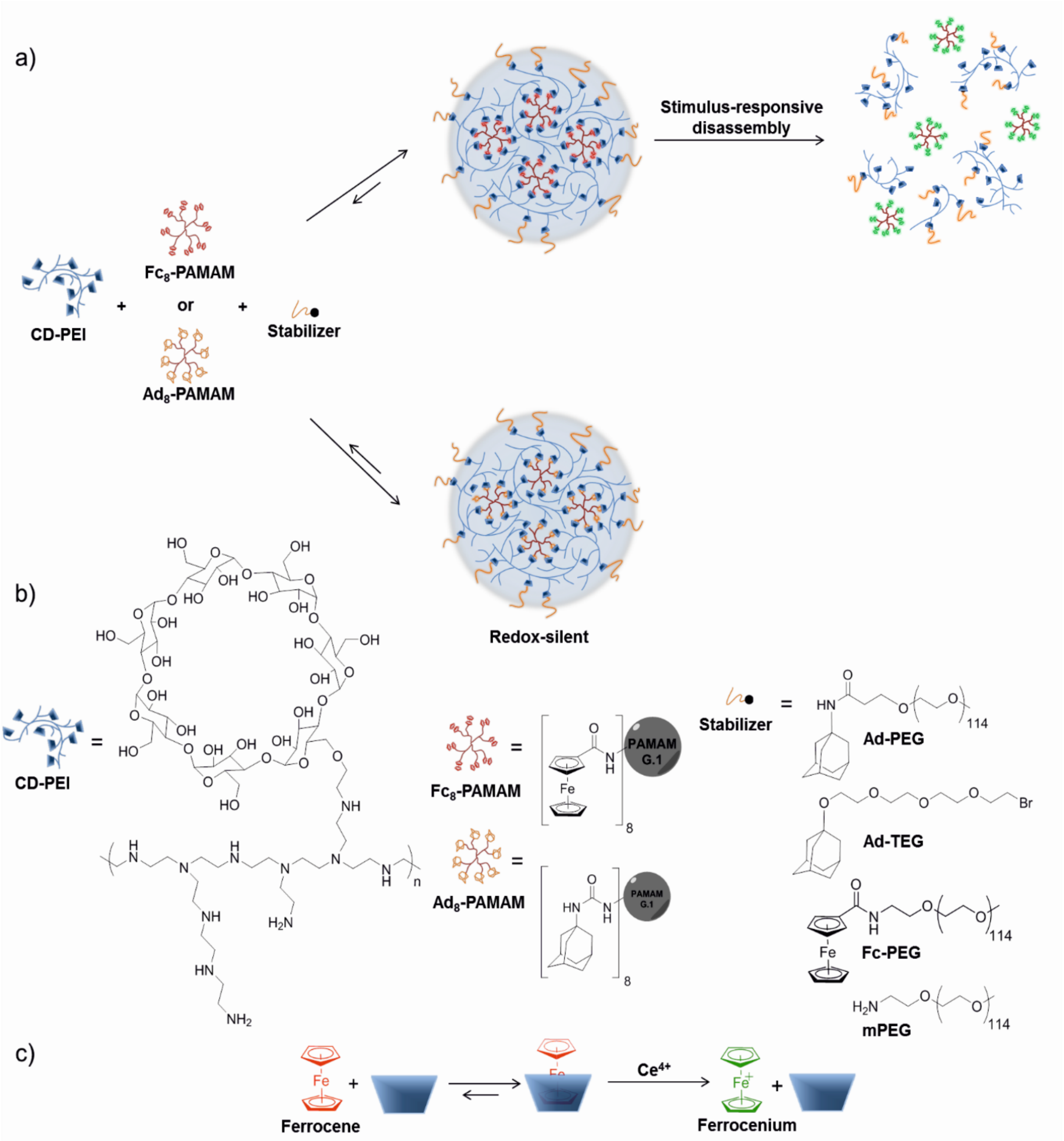

Scheme 1: a) Schematic representation of the supramolecular nanoparticle (SNP) self-assembly and redox-triggered disassembly of the host–guest complex. b) Chemical structures of the building blocks used here. c) Binding of Fc by CD and subsequent dissociation upon oxidation of Fc.

DMSO) to an aqueous solution of CD-PEI ([CD] = 100 µM) in aqueous NaCl solution. To confirm particle formation, SNPs were characterized using DLS and SEM (Figure 3). DLS measurements of the particles in water without salt showed nanoparticles of comparable hydrodynamic diameters (*d*) for the different Fc/CD ratios. The size for 0% Fc (only CD-PEI) was approx. 70 nm, which is attributed to the fact that the concentration of CD-PEI is above its critical aggregation concentration. These results show that the particle size remains similar for the range of Fc/CD ratios shown here (in the absence of salt).

Similar experiments were performed at three different salt concentrations, 0.1, 0.15 and 0.2 M NaCl, while keeping [CD] = 100 µM. Particle formation and growth was observed by DLS after 20 min and 3 h. Figure 4 shows an increase of particle size with increasing salt concentration at ionic strengths above 0.1 M, and the effect is stronger after 3 h, indicating

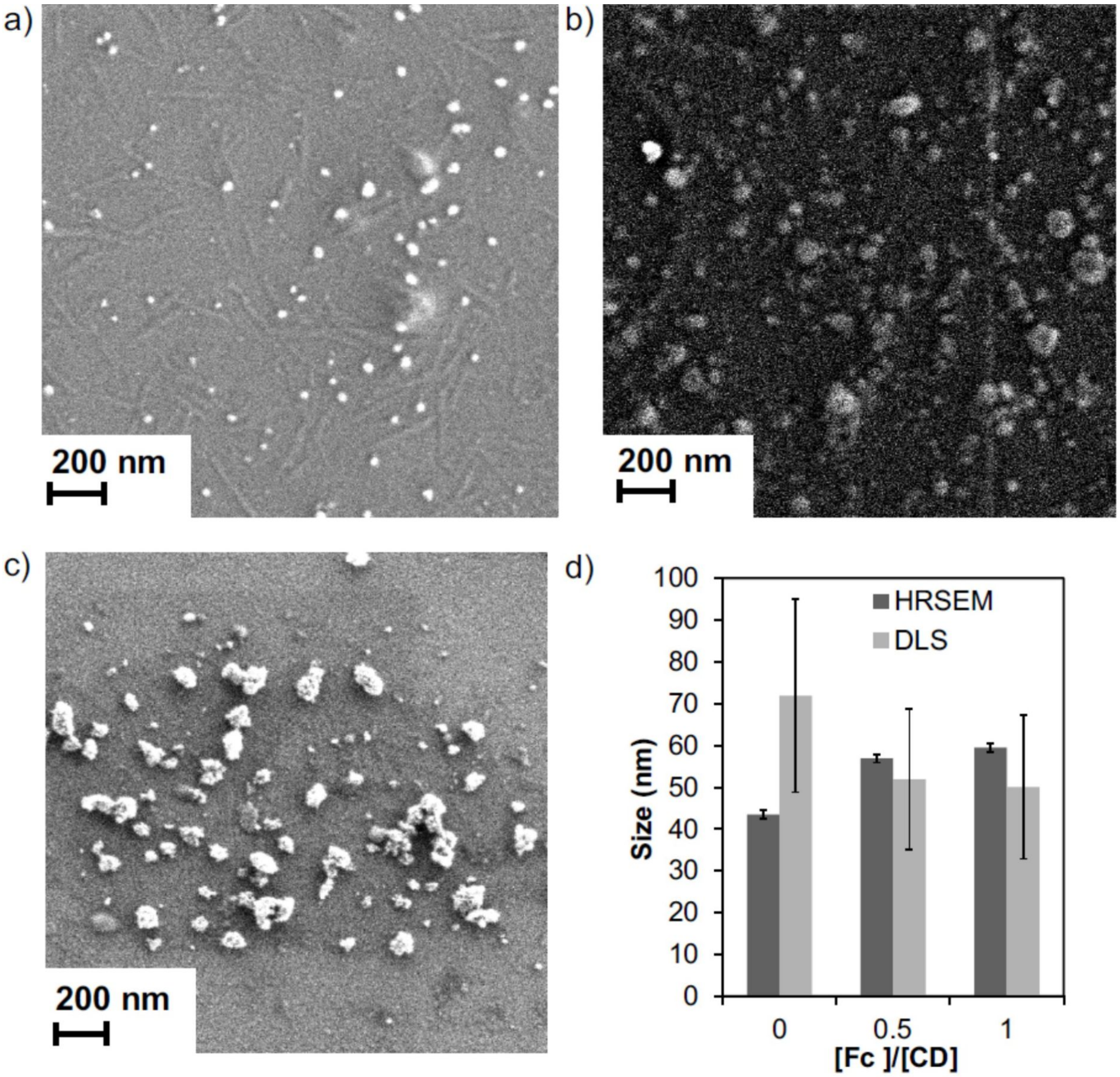

Figure 3: Size determination of SNPs prepared from CD-PEI and Fc_8-PAMAM: SEM images (a–c) of the resulting SNPs as a function of the [Fc]/[CD] ratio (in Fc and CD moieties from Fc_8-PAMAM and CD-PEI, respectively) in aqueous solution (without salt) (a: 0, b: 0.5 and c: 1) used during supramolecular assembly keeping constant the total concentration using [CD] = 100 μM and d) *d* by DLS and size by HRSEM.

a slow growth process. Up to an ionic strength of 0.1 M, however, no change of particle size was apparent.

Both host–guest and electrostatic interactions are at play here. Cyclodextrin host–guest interactions are largely hydrophobic in nature, and their affinity tends to increase slightly at increasing ionic strength. However, because of the already strong and multivalent nature [27,28] of the host–guest interactions at low ionic strengths, we do not expect such affinity differences to lead to the drastic stability differences observed here between the ionic strengths of 0.10 and 0.15 M. Regarding the electrostatic interactions, the Debye screening length is reduced to approx. 1 nm when increasing the ionic strength to 0.1 M. Moreover, zeta potential (ζ) measurements were performed using [CD] = 100 μM (CD is the number of moieties from CD-PEI) and [Fc] = 50 μM (Fc is the number of moieties from Fc_8-PAMAM) at different salt concentrations after 20 min, as shown in Table 1. ζ decreased at increased ionic strengths, and values below 20 mV were observed at ionic strengths of 0.1 M and higher, indicating an absence of colloidal stabilization by charge repulsion at high ionic strength. These results demonstrate, as shown before for negatively charged polymers [16], that the aggregation is due to a loss of electrostatic colloidal stabilization. Thus, a balance between repulsive electrostatic

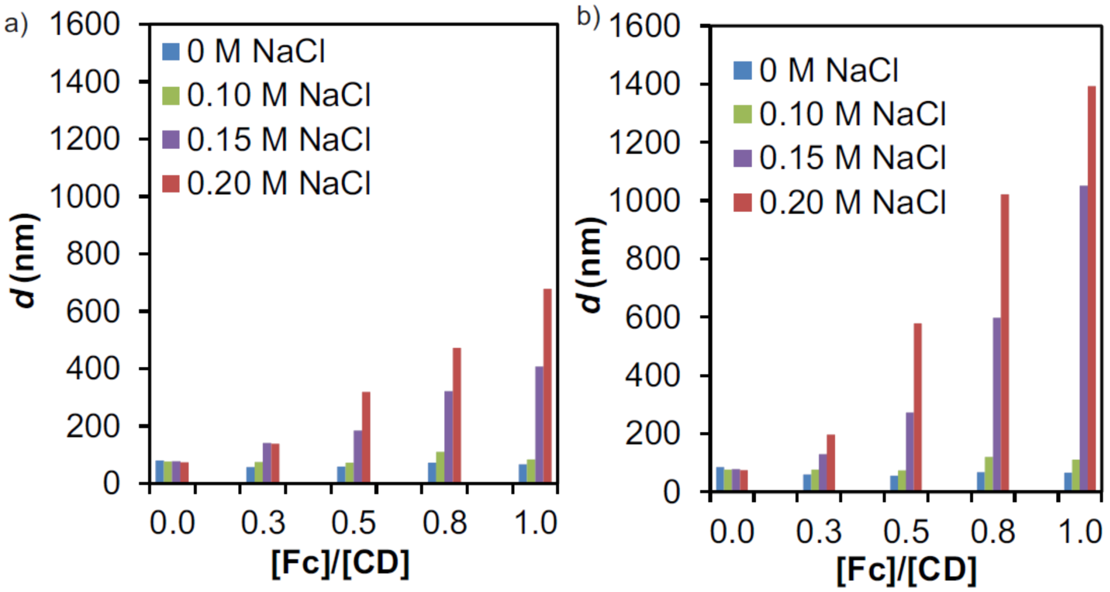

Figure 4: DLS size determination of SNPs prepared from CD-PEI and Fc_8-PAMAM by increasing the [Fc]/[CD] ratio (in Fc and CD moieties from Fc_8-PAMAM and CD-PEI, respectively) at different salt concentrations (0–0.2 M NaCl) keeping constant the total concentration using [CD] = 100 μM after: a) 20 min and b) 3 h.

forces and attractive host–guest interactions exists at low ionic strengths, leading to stable SNPs even in the absence of a stabilizer. At higher ionic strengths, however, the increased charge screening leads to a loss of electrostatic repulsion and therefore to aggregates that grow over time.

Table 1: Hydrodynamic diameters, *d*, and zeta potentials, ζ, measured by DLS of SNPs prepared at increasing salt concentrations (0–0.2 M NaCl) using CD-PEI and Fc_8-PAMAM keeping the total concentration constant at [CD] = 100 μM and [Fc] = 50 μM (in Fc and CD moieties from Fc_8-PAMAM and CD-PEI, respectively).

salt concentration (M)	*d* (nm)	ζ (mV)
0	51	33
0.1	58	17
0.15	247	15
0.20	441	15

Influence of the host–guest stoichiometry on SNP formation

To assess whether all host and guest moieties of CD-PEI and Fc_8-PAMAM are engaged in interactions, a Job plot was performed by varying the host–guest ratio while keeping the sum of the concentrations constant. The SNP growth at high ionic strength was used as a sign of interactions between the multivalent host and guest molecules. When increasing the Fc content to 0.5 (i.e., a host–guest ratio of 1:1), an increase in particle size was observed, but the particle size remained constant as the Fc concentration was increased further (data not shown). Therefore, 2 mM of native CD was added in an attempt to suppress non-specific, hydrophobically driven aggregation at excess Fc moieties. Figure 5a shows, however, a very similar picture, with particle sizes increasing as the Fc fraction was raised from 0 to 0.5, and a plateau of constant size at higher Fc fractions. Apparently, the addition of native CD was insufficient to cap excess free Fc groups, due to a lack of affinity. To verify that this low affinity is the main reason for the continued particle growth observed at Fc contents above 0.5, the Ad dendrimer analog was used as a control. Similar to the Fc case, increase of the Ad fraction up to 0.5 (see Figure 5b) led to an increase of the SNP size. Higher Ad contents in the presence of 2 mM native CD, however, led to a decrease in particle size, indicating that an excess of Ad is efficiently blocked by CD, which is in line with the approx. 30 times higher binding affinity of Ad (see above). Most importantly, this graph (Figure 5) confirms a 1:1 binding stoichiometry of the system. These results demonstrate that SNPs form optimally at a 1:1 stoichiometry at which all available host and guest moieties are simultaneously engaged in host–guest interactions.

Effect of a monovalent stopper

In order to limit particle growth and achieve stabilization, a proper stabilizing agent should be found. The strategy on stoichiometry remains the same as previously described, keeping the host–guest ratio at 1:1 and a high ionic strength of 0.2 M NaCl. Two different parameters were considered to study the effect of a stopper: length and binding affinity. The formation of SNPs was studied using constant concentrations of

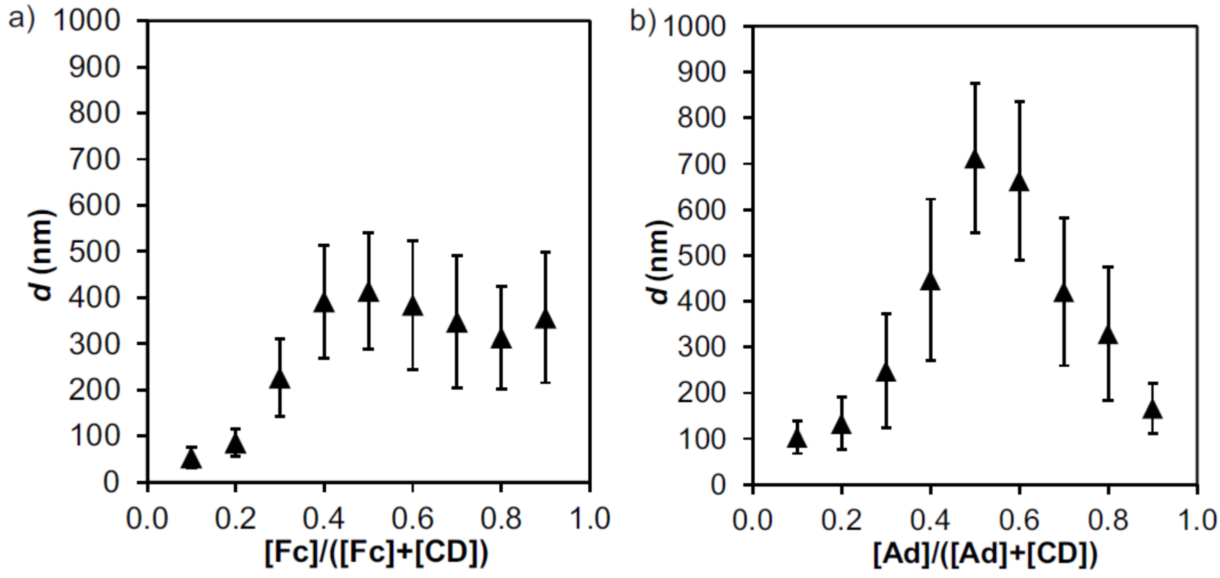

Figure 5: Hydrodynamic diameter, *d*, of SNPs prepared from CD-PEI and Fc_8-PAMAM or Ad_8-PAMAM measured by DLS as a function of the [guest]/([guest] + [CD]) ratio for: a) CD-PEI and Fc_8-PAMAM [CD + Fc] = 50 µM (in CD and Fc moieties), *I* = 0.4 M NaCl, with 2 mM native CD measured after 10 min, and b) CD-PEI and Ad_8-PAMAM [CD + Ad] = 200 µM (in CD and Ad moieties), *I* = 0.2 M NaCl, with 2.0 mM native CD measured after 6 min.

[CD] = 100 µM (CD is the number of moieties from CD-PEI) and [Fc + guest-stabilizer] = 100 µM (Fc is the number of moieties from Fc_8-PAMAM), thus keeping the molecular recognition moieties in a 1:1 stoichiometry ratio. For these experiments, first aqueous solutions of CD-PEI without or with a stabilizer (Ad-PEG, mPEG, Fc-PEG, Ad-TEG; see Scheme 1b) were prepared. Subsequently, Fc_8-PAMAM (dissolved in DMSO) was injected into the respective aqueous solutions. Size tuning of the SNPs was assessed by using two different concentrations of Fc_8-PAMAM dendrimers and stabilizer, while keeping the overall concentration of the guest moieties constant. The formation of SNPs was evaluated by DLS after 20 min and 4 h. Figure 6 shows the strong effect of the use of a stabilizer on the SNP size and, as shown before, that the SNP size is further increased by increasing the fraction of multivalent Fc moieties at the core of the particles. These results show that the smallest sizes and most stable particles were formed when using Ad-PEG as the stabilizer. Larger particles were observed for Fc-PEG than for Ad-PEG, but these also appeared stable (sizes after 20 min and 4 h are similar). The shorter Ad-TEG was less efficient in capping and stabilizing the SNPs compared to polymeric Ad-PEG. Leaving out the guest moiety, by using mPEG as a stabilizer, led to uncontrolled growth as was also observed in the absence of PEG. It should be noted that polymeric PEG derivatives have a critical aggregation constant that can be well below 1 µM [29]. We measured DLS for a 25 µM solution Ad-PEG and observed particles with a size of approx. 85 nm (data not shown), and others have observed sizes of 20–30 nm for different PEG derivatives [29]. However, the sizes reported here (Figure 6) for SNPs are much larger, most likely caused by larger abundance of SNPs compared to PEG aggregates and the higher response of SNPs by DLS. In particular the high similarity of the hydrodynamic sizes between the control (using the non-interacting mPEG) and the SNPs in the absence of stopper shows that the DLS data reported in Figure 6 are not convoluted by PEG aggregates. In summary, these results demonstrate that a guest moiety is important, and that a weaker guest is less efficient in stabilizing the particle. Moreover, steric repulsion by having a long polymer chain present on the stopper is important for achieving SNP stability.

Size control by changing the stoichiometric composition

SNP size control was achieved by changing the stoichiometry of the multivalent guest and the monovalent stabilizer while keeping the overall host–guest ratio constant and equimolar. SNPs were observed by SEM and DLS for all samples as shown in Figure 7. The particle sizes determined by SEM (see Figure 7a–c) with sizes of 49 ± 13 nm (Fc fraction of 0.375), 61 ± 17 nm (Fc fraction of 0.5) and 67 ± 21 nm (Fc fraction of 0.625) were much smaller than those measured by DLS. This can be possibly due to drying effects. Figure 7d–f shows an increasing size with increasing fraction of the multivalent Fc_8-PAMAM and they are stable up to 7 days. In summary, we have demonstrated the formation of stable and size-tunable SNPs by varying the multivalent vs monovalent stoichiometry.

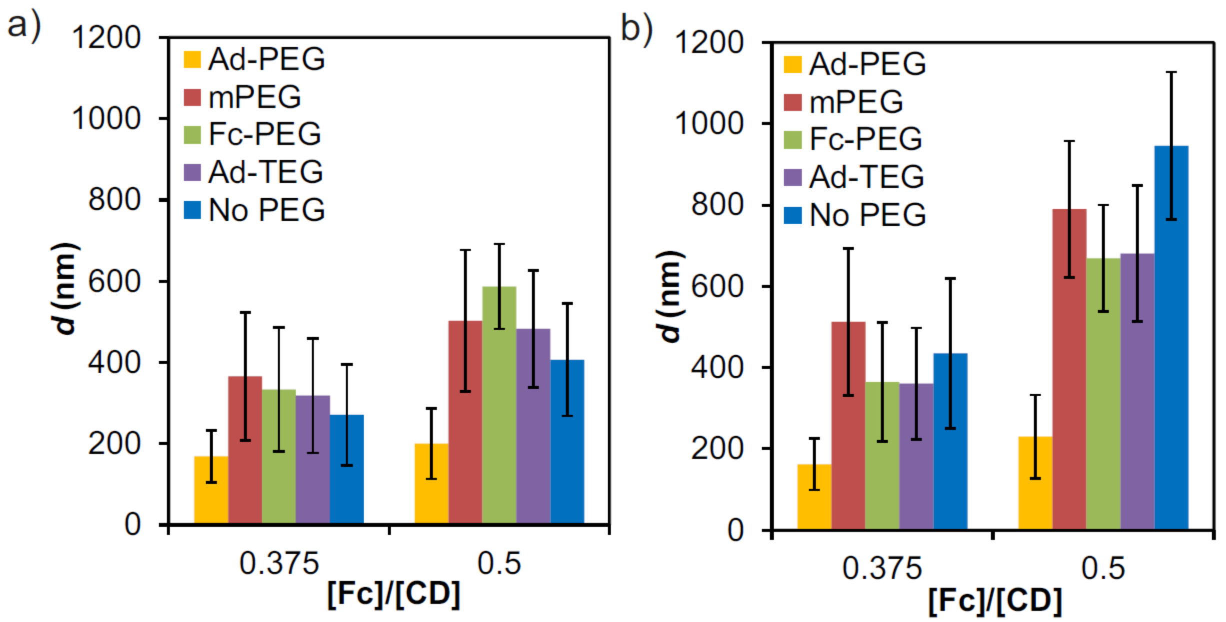

Figure 6: DLS size determinations of SNPs prepared from CD-PEI, Fc_8-PAMAM, in the absence or presence of a monovalent stopper, for two [Fc]/[CD] ratios (in Fc and CD moieties from Fc_8-PAMAM and CD-PEI, respectively) keeping constant both [CD] = [Fc] + [stopper] = 100 uM (where [stopper] is the concentration of the monovalent stopper), using 0.2 M NaCl and different stoppers: Ad-PEG, mPEG (no guest moiety), Fc-PEG, Ad-TEG and without stabilizer after: a) 20 min and b) 4 h.

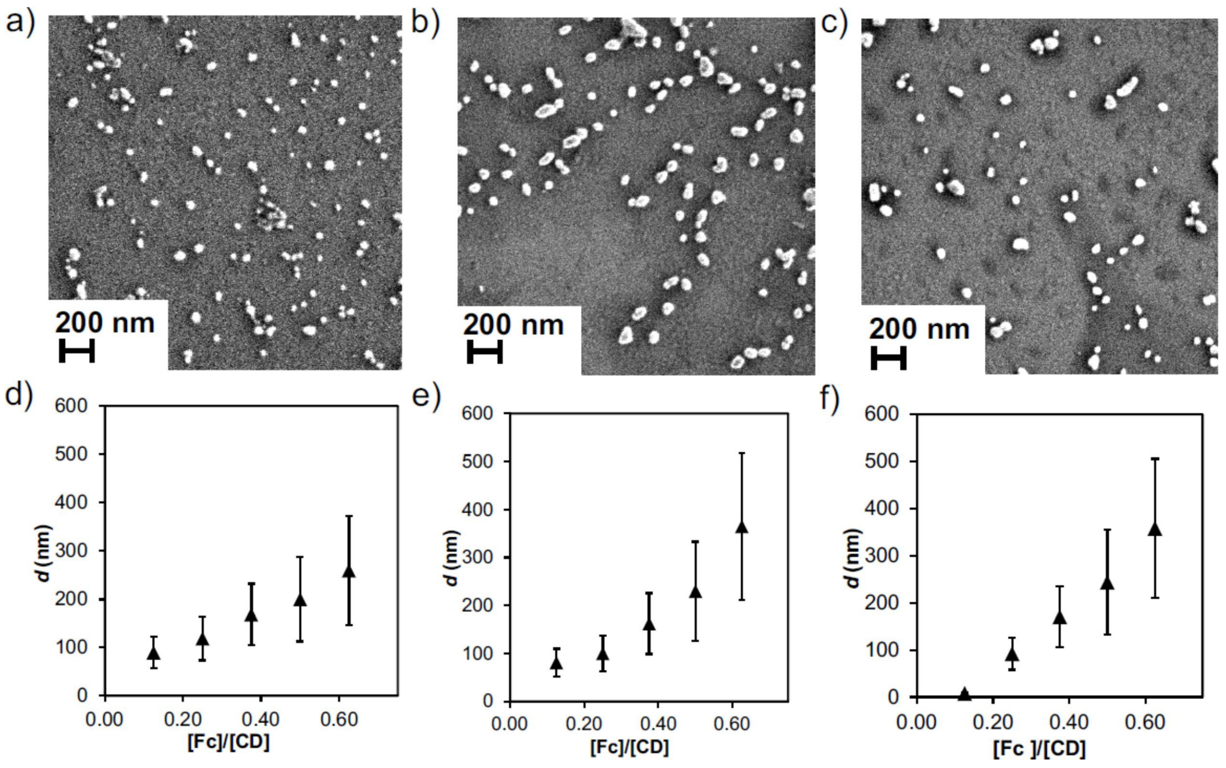

Figure 7: Size determinations of SNPs prepared from CD-PEI, Fc_8-PAMAM and Ad-PEG: SEM images (a–c) of the resulting SNPs by increasing [Fc]/[CD] ratios (in Fc and CD moieties from Fc_8-PAMAM and CD-PEI, respectively) using 0.2 M NaCl (a: 0.375, b: 0.50 and c: 0.625) used during supramolecular assembly using [CD] = 100 μM and CD:(Ad + Fc) stoichiometry, and DLS data (d–f) after: d) 20 min, e) 4 h and f) 7 days.

Stimulus-responsive disassembly by oxidation

The redox-triggered disassembly of the Fc-containing SNPs (see Scheme 1a) makes use of the redox-responsive properties of Fc and the resulting loss of binding affinity for CD upon oxidation of Fc to the ferrocenium cation. We chose Ce^{4+} as the oxidizing agent to perform the disassembly experiments because of its proven effectiveness in a Fc/CD system similar to ours [30]. SNPs composed of CD-PEI, Fc_8-PAMAM and Ad-PEG were formed using a ratio of CD/(Ad + Fc) = 1:1. The hydrodynamic diameter *d* by DLS was found to be 210 nm. Directly thereafter, a small volume of a Ce^{4+} stock solution was injected into the sample (Ce/Fc = 10). The SNP size was then monitored by DLS over time as shown in Figure 8a before (red) and after addition of Ce^{4+} (green) at 10 min. These results show a quick breakdown of the aggregates in the first 20 min. Sizes measured thereafter resemble the size measured for CD-PEI only. To prove that particle disassembly requires the redox-active Fc group, a similar experiment was performed using the redox-silent Ad_8-PAMAM dendrimer (see Scheme 1a) as a control. SNPs composed of CD-PEI, Ad_8-PAMAM and Ad-PEG were formed using [CD] = 100 µM (CD is the number of moieties from CD-PEI), [Ad] = 37.5 µM (Ad is the number of moieties coming from Ad_8-PAMAM) and [Ad] = 62.5 µM (from Ad-PEG) in 0.2 M NaCl. A size of $d \approx 150$ nm was measured by DLS. Figure 8b shows the hydrodynamic diameter of these aggregates over time before (red) and after addition of Ce^{4+} (green) at 10 min. These results shows that the Ad-based SNPs do not disassemble in the presence of oxidant. Therefore we conclude that Fc groups are needed to equip the SNPs with a triggered disassembly mechanism, attributed to the oxidation of the Fc groups of Fc_8-PAMAM to the ferrocenium cation resulting in decomplexation of the guest groups and concomitant loss of multivalent links between the CD-PEI units in the SNPs.

Conclusion

In conclusion, we have developed a strategy to form supramolecular nanoparticles using a redox-active host–guest complex as the interaction motif. The size of the resulting nanoparticles was controlled by different parameters, and SNP disassembly was achieved by using oxidation of the redox-active Fc moiety as the trigger. For the first time, we have shown that using positively charged building blocks, the size and stability of the supramolecular nanoparticles depend on a balance between repulsive electrostatic interactions between the charged building blocks and attractive host–guest interactions between the multivalent guest-functionalized dendrimers and host-functionalized polymers. At higher ionic strengths, the increased charge screening led to a loss of electrostatic repulsion and therefore to larger aggregates. Optimal self-assembly of the multivalent components was observed at a 1:1 stoichiometry of the host/guest moieties. A stabilizer with high binding affinity and sufficient steric repulsion is needed to obtain stable and

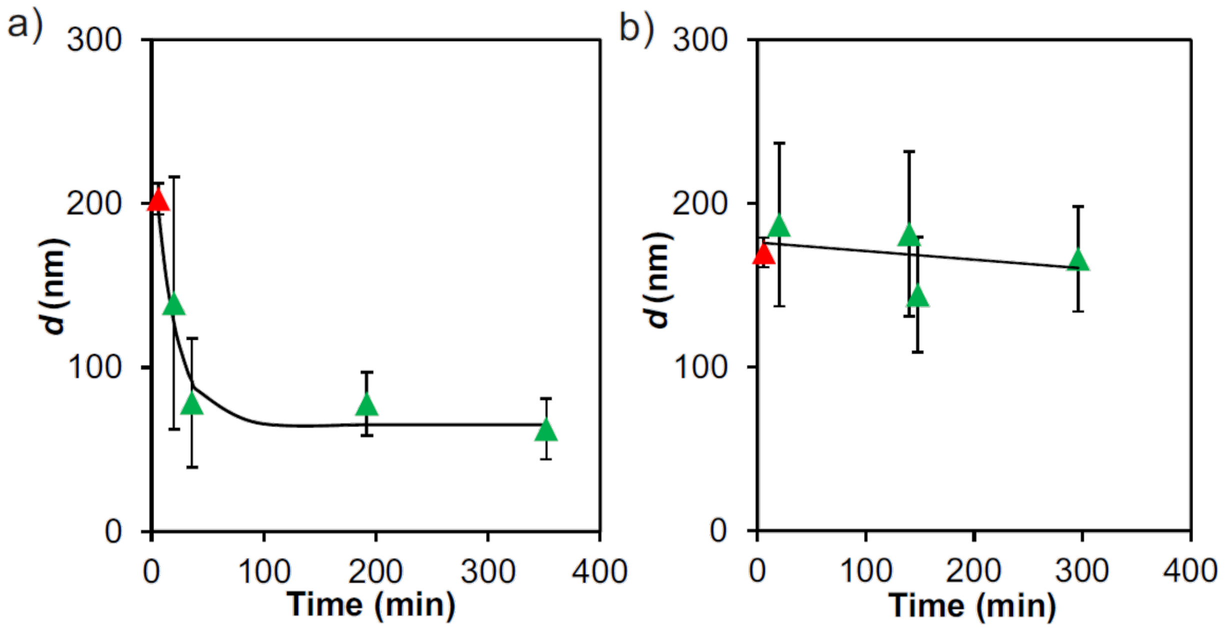

Figure 8: DLS size determination before (red) and after the addition of the oxidant agent Ce^{4+} (green) for as-prepared SNPs: a) [CD] = 100 µM (in CD moieties from CD-PEI) [Fc] = 50 µM (in Fc moieties from Fc_8-PAMAM) and [Ad] = 50 µM (from Ad-PEG) and b) [CD] = 100 µM and [Ad] = 37.5 µM (in Ad moieties from Ad_8-PAMAM) and [Ad] = 62.5 µM (from Ad-PEG) (control) in 0.2 M NaCl. 10 equiv of Ce^{4+}relative to Fc was added to the SNPs. Experimental *d* measurements (markers) and trendlines (line, guide to the eye).

small particles, thus Ad-PEG was observed to be the optimal stopper. Variation of the mono- to multivalent guest ratio provided a range of SNP sizes, and the SNPs were stable up to 7 days. The particles were successfully disassembled using a chemical oxidant. The understanding of the forces involved in SNP formation, and control over their stability and responsive character makes these SNPs a promising candidate for developing a drug delivery vehicle where control over the drug encapsulation and release can be achieved.

Experimental

Materials

Reagents and solvents were purchased from Sigma-Aldrich and used as received without further purification, unless noted otherwise. Millipore water with a resistivity of 18.2 MΩ cm at 25 °C was used in all the experiments. The amine-terminated poly(amido amine) dendrimer was purchased from Symo-Chem and received as a solution in methanol (20% w/w).

Synthetic procedures

The 6-monotosyl-β-cyclodextrin was synthesized according to a literature procedure [31]. The multivalent Fc_8-PAMAM was prepared according to a procedure developed in our group [28]. Syntheses of Ad_8-PAMAM and Ad-PEG (M_w = 5000 g/mol) were performed according to literature procedures [11], as well as Ad-TEG [32].

Synthesis of CD-PEI

The procedure for preparing the β-CD-functionalized PEI polymer was based on a literature procedure [11]. DMSO was freshly distilled under argon. Then, to a solution of branched poly(ethylene imine) [$M_w \approx$ 10,000 g/mol] (250 mg, 0.025 mmol) dissolved in 45 mL DMSO under argon at 60 °C, a solution of 6-monotosyl-β-cyclodextrin (1.4 g, 1.1 mmol) and 0.5 mL triethylamine in 35 mL of DMSO was added slowly under argon by using a syringe while stirring. The resulting solution was stirred at 60 °C for three days under argon. The solution was cooled to room temperature and diluted with 40 mL deionized water with a resulting pH of 10.9. The solution was transferred to a Spectra/Por MWCO 6–8 kD membrane and dialyzed against water for 4 days. The dialyzed solutions were filtered over paper and lyophilized to afford 189 mg of a fluffy, near-white solid. ^{1}H NMR (400 MHz, D_2O) δ (ppm) 5.39–5.05 (br, 7H, C1H of CD), 3.87–3.56 (m, 42.1, C2-6H of CD), 3.5–2.2 (br, 115.6, OCH_2 of PEI).

Synthesis of Fc-PEG

Methoxypoly(ethylene glycol)amine (M_w = 5000 g/mol; 250 mg, 0.050 mmol) and 0.2 mL triethylamine was dissolved in 15 mL CH_2Cl_2 under argon in a 100 mL one-necked round-bottom flask. While stirring, a solution of ferrocenoyl chloride (500 mg, 2.0 mmol) in 15 mL dichloromethane was added dropwise by using a syringe. The mixture was allowed to stir overnight at room temperature under argon. The solvent was removed leaving an orange residue. The residue was dissolved in 20 mL chloroform. The chloroform mixture was washed with 10 mL aqueous saturated $NaHCO_3$ solution after which the organic layer was dried using $MgSO_4$. After filtration over paper, the solvent was removed by evaporation and the remaining precipitate was redissolved in 2 mL chloroform. The chloroform solution was added dropwise to 40 mL of diethyl ether, giving immediate precipitation of a yellow solid, which was filtrated and dried in a vacuum oven at 40 °C overnight. This yielded 136 mg of a slightly yellow solid. ^{1}H NMR (400 MHz, D_2O) δ (ppm) 4.78 (m, 2H, Fc), 4.53 (t, 2H, Fc), 4.28 (s, 5H, Fc), 3.85 (t, 2H, CH_2CH_2NHCO), 3.50 (t, 2H, CH_2NHCO), 3.36 (s, 3H, OCH_3).

Methods

Supramolecular nanoparticle assembly as a function of ionic strength

For the preparation of SNPs as a function of ionic strength (0–0.2 M NaCl), aqueous solutions of CD-PEI and NaCl and Fc_8-PAMAM in DMSO were prepared before mixing. The concentration of CD-PEI was kept constant. As an example, for preparing a solution of 50% Fc entities derived from the Fc dendrimer in 0.1 M NaCl, first 100 µL of aqueous CD-PEI solution (500 µM in CD moieties), 60 µL of aqueous NaCl solution (833.3 mM) and 340 µL of water were mixed for 30 s. After mixing, 7.5 µL of Fc_8-PAMAM solution in DMSO (3336 µM in Fc moieties) was injected to the previous solution while sonicating.

Job plot using Fc_8-PAMAM

For the preparation of SNPs using 0.4 M NaCl, an aqueous solution of CD-PEI, free CD, NaCl and a solution of Fc_8-PAMAM in DMSO were prepared before mixing. The concentration of total moieties was kept constant at 50 µM. As an example, for preparing a solution of 50% Fc entities (25 µM) derived from the Fc dendrimer, first 125 µL of aqueous CD-PEI/free CD solution (100 µM in CD moieties; 2 mM free CD), 240 µL of aqueous NaCl/free CD solution (833.3 mM NaCl; 2 mM free CD) and 135 µL of aqueous free CD solution (2 mM), were mixed for 30 s. After mixing, 7.5 µL of Fc_8-PAMAM solution in DMSO (1664 µM in Fc moieties) was injected to the previous solution while sonicating.

Job plot using Ad_8-PAMAM

For the preparation of SNPs using 0.2 M NaCl, aqueous solution of CD-PEI, free CD, NaCl and solution of Ad_8-PAMAM in DMSO were prepared before mixing. The concentration of total moieties was kept constant at 200 µM. As an example, for preparing a solution of 50% Ad entities (100 µM) derived from the Ad dendrimer, first 125 µL of aqueous CD-PEI/free CD solution (400 µM in CD moieties; 2 mM free CD), 120 µL of aqueous NaCl/free CD solution (833.3 mM NaCl; 2 mM free CD) and 255 µL of aqueous free CD solution (2 mM), were mixed for 30 s. After mixing, 7.5 µL of Ad_8-PAMAM solution in DMSO (6664 µM in Ad moieties) was injected to the previous solution while sonicating.

Supramolecular nanoparticle assembly as a function of different stoppers

For the preparation of SNPs using 0.2 M NaCl as a function of stoppers at two different Fc fractions, various aqueous solutions of CD-PEI, PEG modified (Ad-TEG, Ad-PEG (M_w = 5000 g/mol), Fc-PEG (M_w = 5000 g/mol), mPEG (M_w = 5000 g/mol) and using two different concentrations of Fc_8-PAMAM in DMSO were prepared. The concentration of CD-PEI was kept the same. As an example, for preparing a solution of 50% Fc entities derived from the Fc dendrimer using Ad-PEG, first 100 µL of aqueous CD-PEI solution (500 µM in CD moieties), 100 µL of aqueous Ad-PEG solution (250 µM), 120 µL of aqueous NaCl solution (833.3 mM) and 180 µL of DI water were mixed for 30 s. After mixing, 7.5 µL of Fc_8-PAMAM solution in DMSO (3336 µM in Fc moieties) was injected to the previous solution while sonicating.

Supramolecular nanoparticle assembly as a function of increasing multivalent guest

For the preparation of SNPs in 0.2 M NaCl various aqueous solution of CD-PEI and Ad-PEG and Fc_8-PAMAM in DMSO were prepared before mixing. The concentration of CD-PEI was kept the same. As an example, preparing a solution of 50% Fc entities derived from the Fc dendrimer, first 100 µL of aqueous CD-PEI solution (500 µM in CD moieties), 100 µL of aqueous Ad-PEG solution (250 µM), 120 µL of aqueous NaCl solution (833.3 mM) and 180 µL of DI-water were mixed for 30 s. After mixing, 7.5 µL of Fc_8-PAMAM solution in DMSO (3336 µM in Fc moieties) was injected to the previous solution while sonicating.

Triggered disassembly of SNPs

To evaluate the redox responsiveness of the particles, SNPs containing [CD] = 100 µM (in CD moieties from CD-PEI), [Fc] = 50 µM (in Fc from Fc_8-PAMAM) and [Ad] = 50 µM (from Ad-PEG) were prepared in 0.4 M NaCl solution. The *d* was measured over time after the injection of Ce^{4+} (10 equiv of Ce^{4+} relative to Fc was added to the SNPs). To evaluate whether the SNP disassembly was due to the oxidation of the ferrocene groups, SNPs containing [CD] = 100 µM (in CD moieties from CD-PEI), [Ad] = 37.5 µM (in Ad from Ad_8-PAMAM) and [Ad] = 62.5 µM (from Ad-PEG) were prepared in 0.2 M NaCl. The *d* was measured over time after the injection of Ce^{4+} (10 equiv of Ce^{4+} relative to Ad was added to the SNPs).

Equipment

Dynamic light scattering (DLS)

Hydrodynamic diameters and zeta potentials were measured on a Zetasizer NanoZS (Malvern Instrument Ltd, Malvern, United Kingdom) at 20 °C, with a laser wavelength of 633 nm and a scattering angle of 173°.

High resolution scanning electron microscopy (HR-SEM)

All SEM images were taken with a Carl Zeiss Merlin scanning electron microscope. The samples were prepared by drop-casting 10 µL of a SNP solution onto a silicon wafer. After 60 s, excess of water was removed by filter paper. The particle dimensions are obtained from SEM images with ImageJ software. For each sample at least 100 particles were measured.

Calorimetric analysis

Calorimetric titrations were performed at 25 °C using a Microcal VP-ITC titration microcalorimeter. Sample solutions were prepared in Millipore water.

NMR spectroscopy

^1H NMR spectra was recorded on a Bruker 400 MHz NMR spectrometer. ^1H chemical shift value, 400 MHz is reported as δ using the residual solvent signal as internal standard at ≈22 °C.

Mass spectrometry

Mass analysis was done using matrix-assisted laser desorption ionization (MALDI) on a Waters Synapt G1 using 2,5-dihydroxybenzoic acid as the matrix.

Acknowledgements

This research was supported by the Council for Chemical Sciences of the Netherlands Organization for Scientific Research (NWO-CW, Vici grant 700.58.443 to J.H.). We gratefully thank Laura Grana Suarez for the synthesis of Ad_8-PAMAM and Ad-PEG, Carmen Stoffelen for the synthesis of Ad-TEG, and Regine Van der Hee for the mass measurements. Alejandro Mendez Ardoy and Rian Ruhl are acknowledged for their help and fruitful discussions and Mark A. Smithers for HR-SEM imaging.

References

1. Chen, K.-J.; Garcia, M. A.; Wang, H.; Tseng, H.-R. *Supramolecular Chemistry;* John Wiley & Sons, Ltd, 2012; pp 1–16.
2. Stoffelen, C.; Huskens, J. *Chem. Commun.* **2013,** *49,* 6740–6742. doi:10.1039/c3cc43045f

3. Chen, K.-J.; Wolahan, S. M.; Wang, H.; Hsu, C.-H.; Chang, H.-W.; Durazo, A.; Hwang, L.-P.; Garcia, M. A.; Jiang, Z. K.; Wu, L.; Lin, Y.-Y.; Tseng, H.-R. *Biomaterials* **2011,** *32,* 2160–2165. doi:10.1016/j.biomaterials.2010.11.043
4. Wang, S. T.; Chen, K. J.; Wu, T. H.; Wang, H.; Lin, W. Y.; Ohashi, M.; Chiou, P. Y.; Tseng, H.-R. *Angew. Chem., Int. Ed.* **2010,** *49,* 3777–3781. doi:10.1002/anie.201000062
5. Chen, K.-J.; Tang, L.; Garcia, M. A.; Wang, H.; Lu, H.; Lin, W.-Y.; Hou, S.; Yin, Q.; Shen, C. K. F.; Cheng, J.; Tseng, H.-R. *Biomaterials* **2012,** *33,* 1162–1169. doi:10.1016/j.biomaterials.2011.10.044
6. Lee, J.-H.; Chen, K.-J.; Noh, S.-H.; Garcia, M. A.; Wang, H.; Lin, W.-Y.; Jeong, H.; Kong, B. J.; Stout, D. B.; Cheon, J.; Tseng, H.-R. *Angew. Chem., Int. Ed.* **2013,** *52,* 4384–4388. doi:10.1002/anie.201207721
7. Liu, Y.; Wang, H.; Kamei, K.-i.; Yan, M.; Chen, K.-J.; Yuan, Q.; Shi, L.; Lu, Y.; Tseng, H.-R. *Angew. Chem., Int. Ed.* **2011,** *50,* 3058–3062. doi:10.1002/anie.201005740
8. Davis, M. E. *Mol. Pharmaceutics* **2009,** *6,* 659–668. doi:10.1021/mp900015y
9. Wang, H.; Chen, K.-J.; Wang, S.; Ohashi, M.; Kamei, K.-i.; Sun, J.; Ha, J. H.; Liu, K.; Tseng, H.-R. *Chem. Commun.* **2010,** *46,* 1851–1853. doi:10.1039/b923711a
10. Wang, H.; Liu, K.; Chen, K. J.; Lu, Y. J.; Wang, S. T.; Lin, W. Y.; Guo, F.; Kamei, K. I.; Chen, Y. C.; Ohashi, M.; Wang, M. W.; Garcia, M. A.; Zhao, X. Z.; Shen, C. K. F.; Tseng, H. R. *ACS Nano* **2010,** *4,* 6235–6243. doi:10.1021/nn101908e
11. Wang, H.; Wang, S.; Su, H.; Chen, K.-J.; Armijo, A. L.; Lin, W.-Y.; Wang, Y.; Sun, J.; Kamei, K.-i.; Czernin, J.; Radu, C. G.; Tseng, H.-R. *Angew. Chem., Int. Ed.* **2009,** *48,* 4344–4348. doi:10.1002/anie.200900063
12. Mejia-Ariza, R.; Huskens, J. *J. Mater. Chem. B* **2014,** *2,* 210–216. doi:10.1039/C3TB21228A
13. Wintgens, V.; Nielsen, T. T.; Larsen, K. L.; Amiel, C. *Macromol. Biosci.* **2011,** *11,* 1254–1263. doi:10.1002/mabi.201100097
14. Stoffelen, C.; Munirathinam, R.; Verboom, W.; Huskens, J. *Mater. Horiz.* **2014,** *1,* 595–601. doi:10.1039/C4MH00103F
15. Stoffelen, C.; Voskuhl, J.; Jonkheijm, P.; Huskens, J. *Angew. Chem., Int. Ed.* **2014,** *53,* 3400–3404. doi:10.1002/anie.201310829
16. Grana Suarez, L.; Verboom, W.; Huskens, J. *Chem. Commun.* **2014,** *50,* 7280–7282. doi:10.1039/C4CC03136A
17. Harada, A.; Takahashi, S. *J. Inclusion Phenom.* **1984,** *2,* 791–798. doi:10.1007/BF00662247
18. Kaifer, A. E. *Acc. Chem. Res.* **1998,** *32,* 62–71. doi:10.1021/ar970335u
19. Nakahata, M.; Takashima, Y.; Yamaguchi, H.; Harada, A. *Nat. Commun.* **2011,** *2,* 511. doi:10.1038/ncomms1521
20. Nakahata, M.; Takashima, Y.; Harada, A. *Angew. Chem., Int. Ed.* **2014,** *53,* 3617–3621. doi:10.1002/anie.201310295
21. Du, P.; Liu, J.; Chen, G.; Jiang, M. *Langmuir* **2011,** *27,* 9602–9608. doi:10.1021/la201843z
22. Yan, Q.; Yuan, J.; Cai, Z.; Xin, Y.; Kang, Y.; Yin, Y. *J. Am. Chem. Soc.* **2010,** *132,* 9268–9270. doi:10.1021/ja1027502
23. de laRica, R.; Fratila, R. M.; Szarpak, A.; Huskens, J.; Velders, A. H. *Angew. Chem., Int. Ed.* **2011,** *50,* 5704–5706. doi:10.1002/anie.201008189
24. Lee, D.-W.; Park, K. M.; Banerjee, M.; Ha, S. H.; Lee, T.; Suh, K.; Paul, S.; Jung, H.; Kim, J.; Selvapalam, N.; Ryu, S. H.; Kim, K. *Nat. Chem.* **2011,** *3,* 154–159. doi:10.1038/nchem.928
25. Pun, S. H.; Bellocq, N. C.; Liu, A.; Jensen, G.; Machemer, T.; Quijano, E.; Schluep, T.; Wen, S.; Engler, H.; Heidel, J.; Davis, M. E. *Bioconjugate Chem.* **2004,** *15,* 831–840. doi:10.1021/bc049891g
26. Shen, J.; Kim, H.-C.; Su, H.; Wang, F.; Wolfram, J.; Kirui, D.; Mai, J.; Mu, C.; Ji, L.-N.; Mao, Z.-W.; Shen, H. *Theranostics* **2014,** *4,* 487–497. doi:10.7150/thno.8263
27. Nijhuis, C. A.; Yu, F.; Knoll, W.; Huskens, J.; Reinhoudt, D. N. *Langmuir* **2005,** *21,* 7866–7876. doi:10.1021/la051156l
28. Nijhuis, C. A.; Huskens, J.; Reinhoudt, D. N. *J. Am. Chem. Soc.* **2004,** *126,* 12266–12267. doi:10.1021/ja048271n
29. Lu, J.; Huang, Y.; Zhao, W.; Marquez, R. T.; Meng, X.; Li, J.; Gao, X.; Venkataramanan, R.; Wang, Z.; Li, S. *Biomaterials* **2013,** *34,* 1591–1600. doi:10.1016/j.biomaterials.2012.10.073
30. Nakahata, M.; Takashima, Y.; Hashidzume, A.; Harada, A. *Angew. Chem., Int. Ed.* **2013,** *52,* 5731–5735. doi:10.1002/anie.201300862
31. Djedaini-Pilard, F.; Gosnat, M.; Steinbruckner, S.; Dalbiez, J. P.; Crini, G.; Perly, B.; Gadelle, A. In *Proceedings of the Ninth International Symposium on Cyclodextrins,* Santiago de Compostela, Spain, May 31–June 3, 1998; Labandeira, J. J. T.; Vila-Jato, J. L., Eds.; Springer: Netherlands, 1999; pp 73–76.
32. Mulder, A.; Onclin, S.; Péter, M.; Hoogenboom, J. P.; Beijleveld, H.; ter Maat, J.; García-Parajó, M. F.; Ravoo, B. J.; Huskens, J.; van Hulst, N. F.; Reinhoudt, D. N. *Small* **2005,** *1,* 242–253. doi:10.1002/smll.200400063

License and Terms

The definitive version of this article is the electronic one which can be found at:
doi:10.3762/bjoc.11.260

BEILSTEIN JOURNAL OF ORGANIC CHEMISTRY

Aggregation behaviour of amphiphilic cyclodextrins: the nucleation stage by atomistic molecular dynamics simulations

Giuseppina Raffaini[*1,2,§], Antonino Mazzaglia[3] and Fabio Ganazzoli[1,2]

Full Research Paper

Open Access

Address:
[1]Dipartimento di Chimica, Materiali e Ingegneria Chimica 'G. Natta', Politecnico di Milano, via L. Mancinelli 7, 20131 Milano, Italy, [2]Unità Politecnico, INSTM, piazza Leonardo da Vinci 32, 20133 Milano, Italy and [3]CNR-ISMN Istituto per lo Studio dei Materiali Nanostrutturati, c/o Dipartimento di Scienze Chimiche, Biologiche, Farmaceutiche ed Ambientali dell'Università di Messina, Via F. Stagno d'Alcontres 31, 98166 Messina, Italy

Email:
Giuseppina Raffaini[*] - giuseppina.raffaini@polimi.it

* Corresponding author
§ Tel. +39-0223993068; Fax +39-0223993081

Keywords:
aggregation; amphiphilic cyclodextrins; micelles; molecular dynamics simulations; nanoparticles; self-assembly

Beilstein J. Org. Chem. **2015,** *11,* 2459–2473.
doi:10.3762/bjoc.11.267

Received: 30 July 2015
Accepted: 19 November 2015
Published: 07 December 2015

This article is part of the Thematic Series "Superstructures with cyclodextrins: Chemistry and applications III".

Guest Editor: G. Wenz

Abstract

Amphiphilically modified cyclodextrins may form various supramolecular aggregates. Here we report a theoretical study of the aggregation of a few amphiphilic cyclodextrins carrying hydrophobic thioalkyl groups and hydrophilic ethylene glycol moieties at opposite rims, focusing on the initial nucleation stage in an apolar solvent and in water. The study is based on atomistic molecular dynamics methods with a "bottom up" approach that can provide important information about the initial aggregates of few molecules. The focus is on the interaction pattern of amphiphilic cyclodextrin (aCD), which may interact by mutual inclusion of the substituent groups in the hydrophobic cavity of neighbouring molecules or by dispersion interactions at their lateral surface. We suggest that these aggregates can also form the nucleation stage of larger systems as well as the building blocks of micelles, vesicle, membranes, or generally nanoparticles thus opening new perspectives in the design of aggregates correlating their structures with the pharmaceutical properties.

Introduction

Inclusion complexes with supramolecular structures formed by native or modified cyclodextrins (CDs) are attracting an increasing attention [1-8], including also the new polymeric CD nanogels [9] and nanosponges [10-13]. Over the past twenty years, amphiphilic cyclodextrins (aCD) formed with α-, β-, or γ-CD have given rise to a wide interest in the scientific community because of their versatility both as drug carriers [11,14,15] and as self-assembling systems for molecular recognition [16-18]. Different research groups investigated the aCD behaviour in solution, elucidating their nanostructures and physicochemical behaviour, including the temperature- and concentration-dependence of the supramolecular structures, or the pH dependence of water solubility, so as to improve our understanding of their activity as drug delivery systems [19,20] and of the biological fate of the assemblies [21,22]. The balance between the hydrophobic and the polar groups on the two CD rims modulates the formation of micelles, vesicles, nanospheres (or dense aggregates), and nanocapsules [1]. In particular, non-ionic aCD obtained from β-CD modified with hydrophobic thioalkyl chains (H groups in the following) at the primary rim and short polar PEG oligomers (P groups) at the secondary rim form micelles and micellar clusters that are increasingly dispersible in water when functionalized with thioalkyl C2 or C6 chains [23,24] (see Scheme 1), or vesicles with C12 or C16 chains, respectively [17,22].

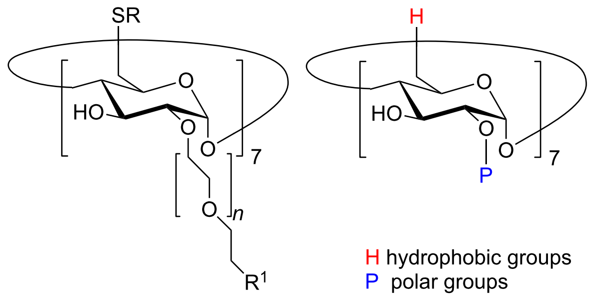

1: R = C_2H_5 R^1 = OH *n* = 0–1
2: R = C_6H_{13} R^1 = OH *n* = 0–1

Scheme 1: Structure of an aCD functionalized with hydrophobic thioalkyl C2 (R = C_2H_5) or C6 (R = C_6H_{13}) chains at the primary rim (hydrophobic H groups) and polar oligoethylene glycol ($-OCH_2CH_2-)_n$ chains at the secondary rim (polar P groups).

Potential applications of non-ionic aCD as anticancer and antiviral drug nanocarriers were recently reported [14], while analogue cationic aCD with terminal short amino-PEG at the secondary rim form nanoassemblies which entrap photosensitizers for photoactivated therapy [25] or DNA for gene delivery [26-30]. The potential of aCD is strengthened by their ability to selectively recognize cells by exposing receptor-targeting groups on the surface of the nanoassembly [30]. Because of these promising results, we have begun to investigate the aggregation behaviour of an aCD model compound by atomistic computer simulation to clarify the early stages of self-assembly, in particular the aCD interactions in the nucleation stage, and give insights on the structure of the embryonic building blocks of the aCD's supramolecular nanosystems. We also note that in the case of a kinetic control of aggregation taking place by sequential interaction of further aCD, the nature of these embryonic building blocks may affect the structure and stability of the larger aggregates.

Some papers already reported simulation studies of CD aggregates, or better dimers, in water in the presence of hydrophobic or at least amphiphilic moieties, such as ionic [31] and non-ionic [32-34] surfactants assuming a preassembled state with the hydrophobic chains threading through one or two native CDs (see also the non-covalent super-amphiphilic complexes described in [33,34]), or of the unbiased aggregation process of two larger CDs encapsulating C_{60} [35]. Other studies considered again preassembled micelles, such as for instance the wormlike micelles formed by the cetyltrimethylammonium cations, investigated at various salt concentrations to assess their stability against rupture in smaller spherical micelles [36], or more recently a bilayer of aCDs functionalized through an anthraquinone moiety mimicking a small portion of a whole vesicle [37]. Otherwise, coarse-grained Monte Carlo simulations in two dimensions modelled the self-assembly of aCD [38]. It should be underlined, however, that in the atomistic simulations a manually pre-assembled system was generally assumed, while the spontaneous formation of supramolecular aggregates was seldom, if ever, considered, apart from the above-mentioned reference [35]. To improve our understanding of the factors driving the formation of aCD molecular assemblies, we describe in this paper an atomistic molecular dynamics investigation of a model compound of a non-ionic aCD extensively studied experimentally [23,24]. The aim of the present work is to describe the first aggregation step that eventually leads to formation of a micelle or more generally of a large aggregate that may be held together through the interaction both within the cavity and, at the outer surface, by a combination of dispersion and dipolar interactions and of hydrogen bonds, adopting throughout a "bottom up" atomistic description.

The modelled system consists of an amphiphilic β-CD of Scheme 1 carrying hydrophobic H groups at the primary rim (R = C_2H_5) and polar P groups at the secondary rim with *n* = 0 (R^1 = OH), simply denoted in the following as the model aCD. The simulations used molecular mechanics (MM) and molecular dynamics (MD) methods, and were carried out both in vacuo, to mimic a non-polar and weakly interacting solvent, and in explicit water, using a box of water molecules with periodic boundary conditions (PBC). While MM methods involve energy minimizations of the simulated systems with respect to all the atomic coordinates, the MD methods describe the time evolution of the whole system at the chosen temperature, according to Newton's equation of motion, thus following the kinetics of a process and the system equilibration, within the accessible simulation time. As previously done [35,39-42], we employ a standard simulation protocol subsequently adopted also by other groups [43]: First we carry out an initial energy minimization of trial geometries mimicking a random approach of the molecules in solution, and then we perform MD runs of these geometries until equilibrium, monitored inter alia through the system energy and its components, and through the intermolecular separations, is achieved. Eventually, we carry out final optimizations of different conformations saved during the MD runs after equilibration to determine the interaction energy and the system geometry, either in the most stable final state or in some largely populated geometry met within the dynamic run in order to characterize the main features of the (pseudo) equilibrium nucleation states.

In the following, after the methodological section, we first discuss the conformation of the isolated molecule of the model compound to determine the intramolecular conformation in vacuo and in water. We then model the interaction between two molecules in vacuo and in water considering three different mutual orientations variously facing the H and P groups to have information about the stability of the contacts among the hydrophobic and/or the polar substituents. Afterwards, we study more briefly the interaction among four molecules, mentioning also some preliminary results of larger systems. The final section summarizes the main results with an outlook to future work.

Simulation Method

The simulations were performed with InsightII/Discover 2000 [44], using the consistent valence force field CVFF [45] as previously done [35,39,40,46]. The geometry of the model aCD, generated with the available templates of InsightII, was subjected to an MD run in vacuo and in explicit water at 300 K, and finally optimized up to an energy gradient lower than 4×10^{-3} kJ mol^{-1} Å^{-1}. The aggregate formation was modelled by placing the appropriate number of molecules in different trial arrangements (see later), so that the different CD rims could face one another. The hydrated systems were modelled after adding a large number of water molecules at the local density of 1 g cm^{-3} in prismatic cells of appropriate size, adopting periodic boundary conditions (constant-volume conditions). These molecules were then modelled exactly in the same way as the solute molecules. After an initial geometry optimization, the resulting adducts were subjected to independent MD runs and final geometry optimizations considering in vacuo many different geometries saved during the MD run, and in water the final configuration at equilibrium (the simulation length, dependent on the system size, will be mentioned in the text). The dynamic equations were integrated using the Verlet algorithm [47] with a time step of 1 fs at a temperature of 300 K, controlled through the Berendsen thermostat [48], and the instantaneous coordinates were periodically saved for further analysis. The system equilibration was monitored by the time change of the total and potential energy of the system and of its components, and of relevant intermolecular distances, in particular those between the centres of mass of the interacting macrocycles. Based on these equilibration criteria, the MD runs were carried out for different lengths. The simulations in explicit water were often shorter than in vacuo due to the much larger computational burden of a fully hydrated system, so that much lengthier rearrangements cannot be ruled out. On the other hand, system thermalization is significantly faster in water than in vacuo due to the random collisions with the solvent molecules, which compensates in part the difference in the length of the MD runs.

The geometries periodically sampled in the MD runs were analysed through the pair distribution function $g_{ij}(r)$, or PDF, as described for instance in [49]. This function gives the probability density of finding atoms *j* at a distance *r* from atoms *i*, and is defined here in the non-normalized form as

$$g_{ij}\left(r\right) = \frac{d\left\langle N_{ij}\left(r\right)\right\rangle}{dV\left(r\right)} \tag{1}$$

where $d\left\langle N_{ij}\left(r\right)\right\rangle$ is the average number of times the *j* atoms are comprised in a spherical shell of thickness *dr* at a distance *r* from atoms *i* within an MD run. Thus, $g_{ij}(r)$ yields the average non-normalized probability of finding of atoms *j* in the shell volume $dV(r)$ at a distance between *r* and $r + \mathrm{d}r$ from atoms *i*, giving an immediate picture of the local density of *j* atoms due to specific interactions.

Results and Discussion

The isolated molecule in vacuo and in explicit water

Using the above-mentioned simulation protocol proposed by some of us [39-42], we first studied the isolated aCD molecule. After the initial minimization, the MD run at room temperature lasting for 5 ns, and the final optimizations of 200 snapshots saved along the trajectory, we obtained the most stable geometry in vacuo. The simulations show a weak clustering of the hydrophobic thioalkyl groups and an extensive pattern of hydrogen bonds at the polar rim involving the adjacent OH groups (Figure 1a), yielding a cylindrical molecular shape with similar diameters of the two rims. This shape is qualitatively displayed by the internal molecular cavity shown in Figure 1a, and quantitatively revealed by the similarity of the pair distribution function PDF of the glycosidic oxygens on the macrocycle and of the S atoms carrying the H chain as a function of their distance from the macrocycle centre of mass (c.o.m.), shown in Figure 2a. In particular, these distances roughly fluctuate around a similar average value, with a similar shoulder at larger separation. We further note for the later discussion that the surface accessible to the solvent (Figure 1a)

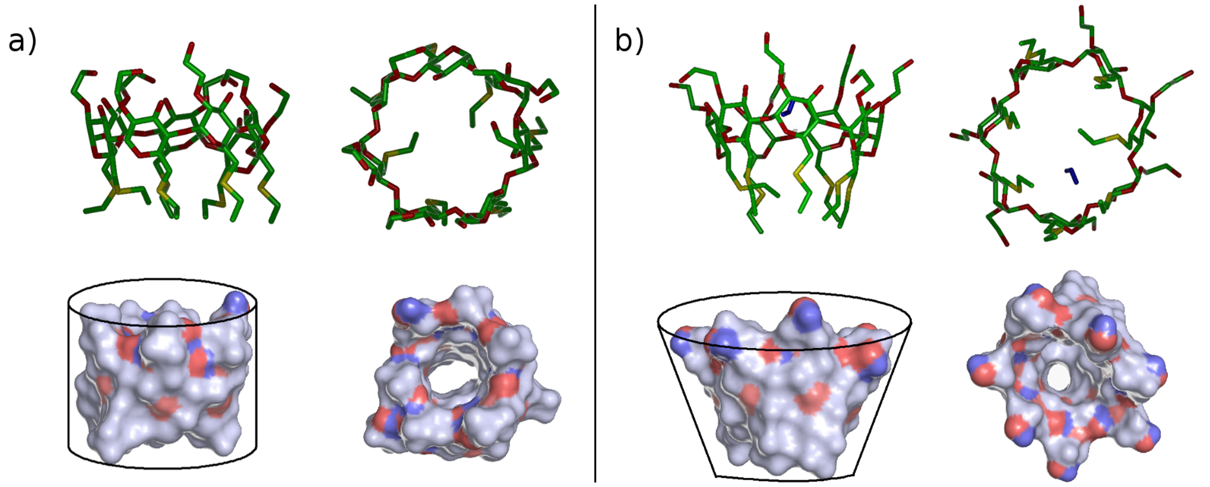

Figure 1: The final optimized geometry of the aCD molecule in vacuo (panel a) and in explicit water (panel b) viewed sideways (at left) and from above the polar groups (at right). In each panel, the upper part shows the line drawing of the molecule (carbons are in green, oxygens in red, and the sulfur atoms of the H chain in yellow, while the hydrogens were omitted for clarity) and the lower part the surface accessible to the solvent, considered as a spherical probe with the radius of 1.4 Å (the electrically neutral part of the molecule is in grey, the negative areas of the oxygens are in red and the positive ones of the hydroxy hydrogens in blue). In part b, we also show a water molecule entering the cavity to replace another one present at the beginning of the MD run (see text).

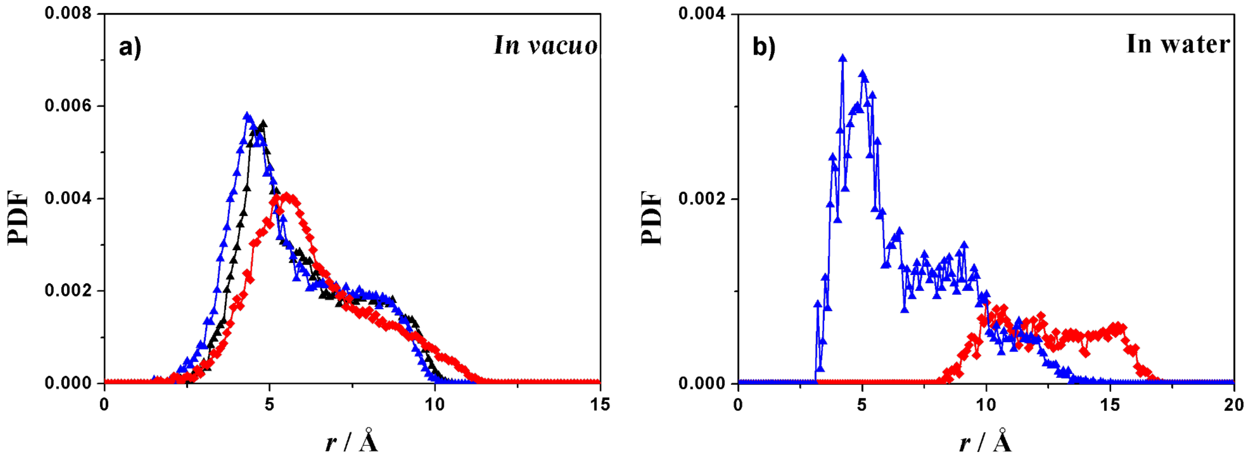

Figure 2: Some relevant PDF's calculated along the runs for the isolated aCD. a) The PDF of the glycosidic oxygens (black and blue symbols) of the polar secondary rim and of the S atoms (red symbols) of the hydrophobic primary rim as a function of their separation from the macrocycle c.o.m. in vacuo. b) The PDF of the glycosidic oxygens carrying the P chains (red symbols), and of the S atoms carrying the H chains (blue symbols) as a function of their separation from the macrocycle c.o.m in water.

amounts to 1266 Å^2, and the radius of gyration R_g (defined as the mass-weighted root-mean-square distance of the system atoms from their common c.o.m.) to 6.97 Å.

A somewhat different geometry is achieved in explicit water (Figure 1b), where a cubic cell with a size of 33.0 Å was adopted with 1091 water molecules and the MD run lasted for 500 ps, in view of the much faster relaxation due to the random collisions with the solvent. Here, the aCD assumes the typical truncated-cone shape taken by cyclodextrins in the solid state, but in the present case this feature is further enhanced by the clustering of the H chains in order to minimize the exposed surface. The PDF is again most useful to characterize the molecular shape induced by the environment. This feature can be seen in the PDF of the glycosidic oxygens of the macrocycle and of the S atoms plotted as before as a function of their distance from the macrocycle c.o.m. in Figure 2b, showing that the glycosidic oxygens at the secondary rim are much further from the c.o.m. that the S atoms carrying the H chains, which strongly cluster to minimize their contact with the water molecules. In this way, the macrocycle also achieves a large opening of the secondary rim so as to maximize the P-chain hydration.

It should also be noted that there is a small cluster of five water molecules trapped into the cavity, and quite isolated from the bulk water, with a pattern rather similar to what found in the native β-CD [46]. Interestingly, also in this case there is a dynamic equilibrium involving the water molecules initially clustered within the hydrophobic CD cavity that are replaced by other molecules entering the cavity from the bulk water during the MD run. An example of this exchange process is shown by the trajectories (reported in Figure 3) of two water molecules in terms of the distance between their oxygen atoms and the c.o.m. of the hosting aCD plotted as a function of time: one of them is a water molecule entering the cavity (the water molecule evidenced in Figure 1b), while the other one is a water molecule initially comprised within the cavity that escapes to the outer bulk water. Moreover, the PDF of the atoms of the water molecules as a function of their distance from the macrocycle c.o.m. (see Figure 4) show that the cavity is populated throughout the MD runs, even though by different molecules.

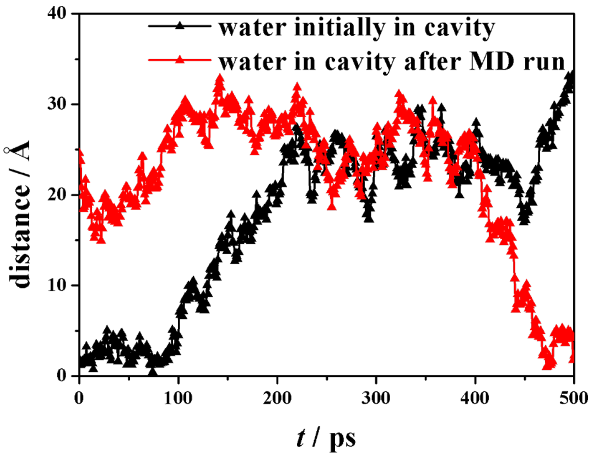

Figure 3: The distance between the oxygen atoms of two water molecules and the c.o.m. of the aCD plotted as a function of time calculated during the 500 ps MD run. One water molecule initially within the cavity escapes to bulk water (black symbols), being replaced by another one within the MD run (red symbols).

In conclusion, in water the apolar H groups significantly cluster so as to minimize the contact with the environment, whereas the hydrophilic P groups show a marked opening to enhance their hydration. The ellipsoidal distortion of the macrocycle caused by the above mentioned interactions should also be noted. As a result, in water the surface accessible to the solvent is equal to 1358 Å^2, while the radius of gyration R_g increases to 7.30 Å, with values significantly larger than what is obtained in vacuo (or in an apolar solvent).

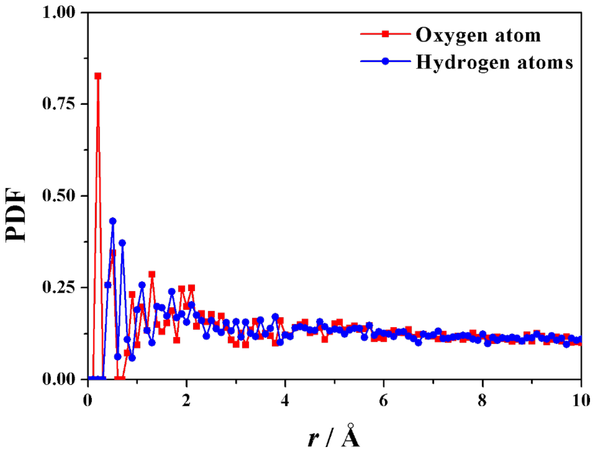

Figure 4: The PDF of the oxygen and of the hydrogen atoms of the water molecules (in red and in blue, respectively) plotted as a function of their distance from the aCD macrocycle c.o.m. calculated during the 500 ps MD run.

The interaction between two molecules

Simulations in vacuo

The pairwise interaction between two amphiphilic CDs was investigated by facing two aCD molecules through their H groups, through one H and one P group, or through their P groups as shown in Figure 5, using the most stable optimized geometry obtained in vacuo.

The initial minimizations in vacuo yield a relatively weak interaction for the H–H arrangement involving the hydrophobic H groups through dispersive interactions, a stronger interaction in the P–P arrangement involving the polar P groups through mainly dipolar interactions and possible hydrogen bonds, and an even stronger interaction in the H–P arrangement, even though the additional stabilization only amounts to about 3 kJ/mol. It should be noted that while a P–P interaction may allow for intermolecular hydrogen bonds among the terminal OH groups, in the P–H arrangement a slightly larger number of intramolecular hydrogen bonds is actually present together with some shallow self-inclusion of two H groups. Moreover, the H–P arrangement does allow for a significant optimization of the dispersive interactions through partial inclusion of some H groups in the hydrophobic cavity of the other molecule. Significant changes are however achieved within the MD runs in vacuo lasting 30 ns, which allow for possible major rearrangements of the two molecules, as indeed found in the fully optimized geometries shown in Figure 6 at left. In particular, the H–H and H–P initial arrangements display an almost complete rotation and/or a noticeable tilt of one molecule with respect to the other one (Figure 6a and Figure 6b, respectively) leading in both cases to some favourable H–P interactions. The most stable geometry was found after the MD runs and final

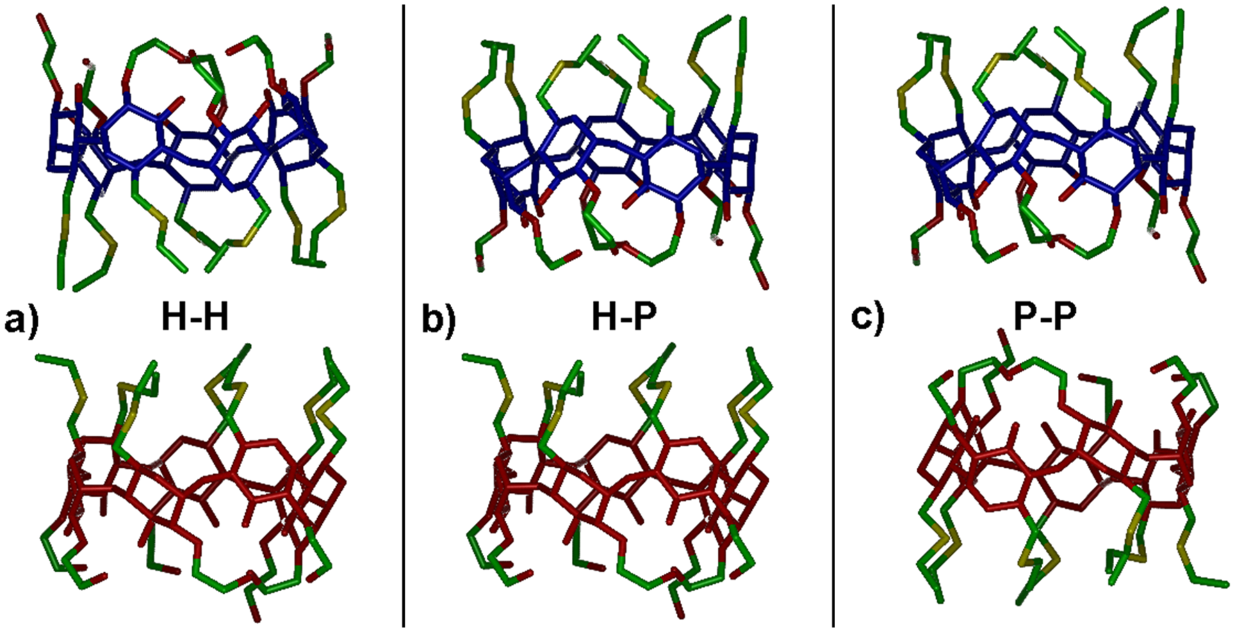

Figure 5: The pairwise initial arrangements of two amphiphilic molecules that face the two hydrophobic H groups, the hydrophobic H and the polar P groups, and the two polar P groups, from left to right in the order. The colour codes are as in Figure 1, while the macrocycles of the two aCD molecules are shown in blue and red for clarity.

optimization of many instantaneous snapshots (100 snapshots taken at equilibrium in the final 10 ns when all the monitored quantities fluctuate around a constant average value) starting from the initial P–P geometry, which involves an interaction among the two polar groups. In this way, the two molecules can form seven intermolecular hydrogen bonds (in addition to the intramolecular ones) and optimize the dipolar interactions (Figure 6c) with the largest interaction energy, in absolute value, and the smallest radius of gyration but the largest surface accessible to the solvent (see Figure S1 of the Supporting Information File 1) as shown in Table 1. Here and in the following, the interaction energy is defined as $E_{\mathrm{int}} = E_{\mathrm{aggr}} - nE_{\mathrm{isol}}$, where E_{aggr} is the energy of the aggregate formed by n molecules and E_{isol} the energy of the isolated molecule. Interestingly, in this geometry the aggregate also shows a larger surface accessible to the solvent than in the other arrangements (see Table 1).

The two higher-energy geometries do not show major differences, since both have a favourable interaction of the P groups of one molecule with the H groups and with part of the lateral surface of the other molecule. Moreover, in either case there is inclusion of two H groups of one molecule in the hydrophobic cavity of the second one, and four intermolecular hydrogen bonds. In particular, the initial H–H arrangement yielded the final geometry of Figure 6a, with an interaction energy (see Table 1) intermediate between the most (Figure 6c) and the least stable one having the H–P arrangement (Figure 6b) due to somewhat weaker dipolar interactions of the latter one.

Table 1: Interaction energies.

Starting arrangement	In vacuo			In water		
	E_{int} (kJ/mol)	R_g (Å)	Accessible surface (Å^2)	E_{pot}[a] (kJ/mol)	R_g (Å)	Accessible surface (Å^2)
H–H	−251	8.17	1799	0	10.09	2333
H–P	−242	8.11	1771	54	9.74	2424
P–P	−266	7.94	1848	176	8.51	2112

[a] These are the average potential energies within the MD run with respect to the lowest one.

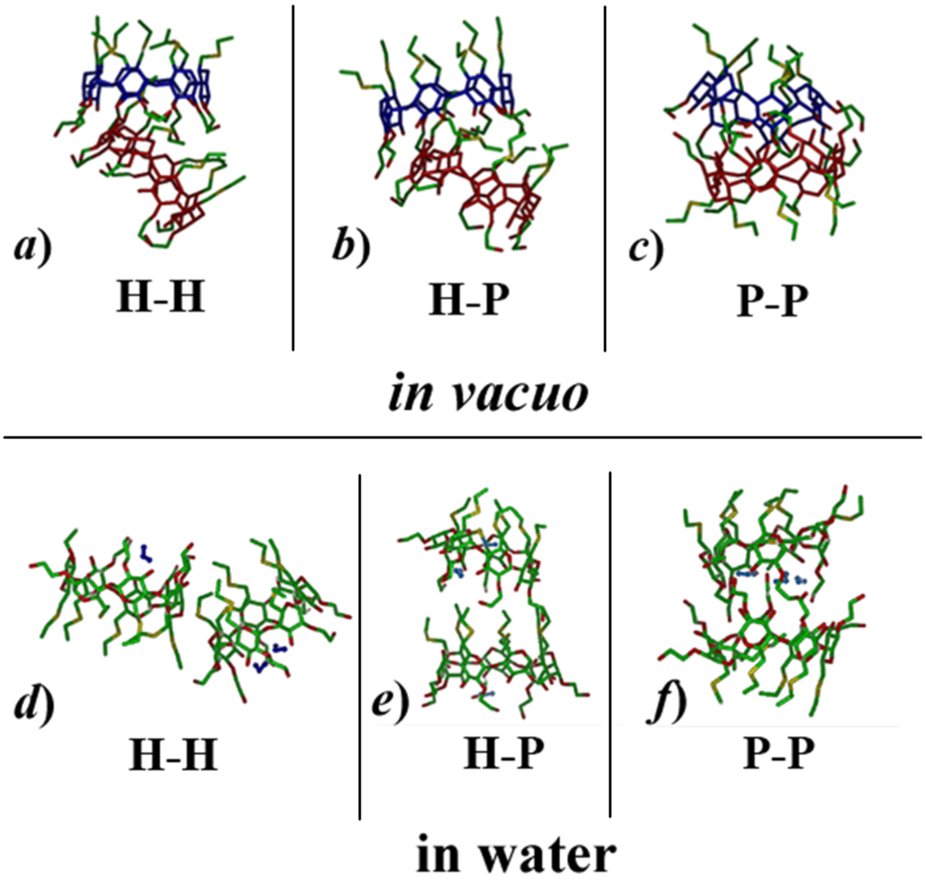

Figure 6: Final optimized geometries at equilibrium after the 30 ns MD runs obtained both in vacuo and in water. The Figure shows a line drawing of the dimeric aggregates (the hydrogen atoms were omitted for clarity). The atom colour codes are the same as in Figure 1.

Simulations in water

The simulations in explicit water were carried out starting again from the initial arrangements shown in Figure 5 within a tetragonal cell with axes equal to 38 Å × 38 Å × 48 Å and 2086 water molecules. In water, the interaction between two amphiphilic β-CD is definitely weaker than in vacuo because of the competing interaction of the polar groups with the water molecules. In the initial minimizations, only minor changes were observed, mainly involving some clustering and partial shielding of the H groups to minimize contact with water. After the MD runs, only relatively loose aggregates were obtained, their optimized geometry being shown in Figure 6. The geometry of Figure 6d is the most stable one, as inferred by the potential energy averaged after equilibration within the final 350 ps of a preliminary dynamic trajectory lasting for 500 ps, while the geometries shown in Figure 6e and 6f have a higher average potential energy, as shown in Table 1. Further dynamic runs were carried out for a total of 30 ns to check for the robustness and stability of these geometries, but we did not detect any major change, neither in the potential energy, nor in the mutual arrangements of the two aCD (or more precisely in the distance between the centers of mass of the two aCD), which can require a longer simulation time to achieve equilibrium by small local rearrangements than potential energy. Accordingly, the initial interaction geometry kinetically traps the adducts in a deep local potential energy minimum, which may drive and affect the subsequent growth after addition of further molecules.

On the other hand, full optimization of the final snapshots produced as the minimum energy conformation the geometry of Figure 6e, even though the energy values of the optimized arrangements can be largely affected by the presence of the random, glassy arrangement of the water molecules trapped in some local energy minimum. The geometry of the aCD pair involves a weak interaction between a few P and H groups of the two molecules, producing a relatively open aggregate with a large surface accessible to the solvent shown in Supporting Information File 1, Figure S1 (see Table 1). Interestingly, the squared value of the radius of gyration is close to, though still smaller than, twice the squared radius of gyration of the isolated molecule in water, stressing again the relatively poor clustering of this dimeric aggregate. An analogous optimization for the other starting arrangements yielded the geometries shown in Figure 6d and Figure 6f. However, in the former case the aggregate has a quite large size, as shown by its radius of gyration, indicative again of a weak interaction with a quite large surface exposed to the water solvent, whereas in the latter case it has a significantly smaller radius of gyration and an even smaller exposed surface (see Table 1 and Supporting Information File 1, Figure S1). It must be pointed out that the size of the last arrangement could suggest stronger intermolecular interactions than in the previous cases mediated by the water molecules entrapped by the P groups, but this arrangement is not the most stable one in view of its higher energy, related in turn with the presence of H groups exposed to water.

The interaction among four molecules

Simulations in vacuo

The stability of larger aggregates was then investigated considering four molecules interacting in different relative orientations. In the starting arrangements, the four molecules can interact through a) the four H groups, b) the four P groups, or c) two P groups, one H group and a side surface, thus being essentially placed at random (first row of Figure 7). The initial minimizations already produced significant interactions among the molecules, which approached one another with only minor

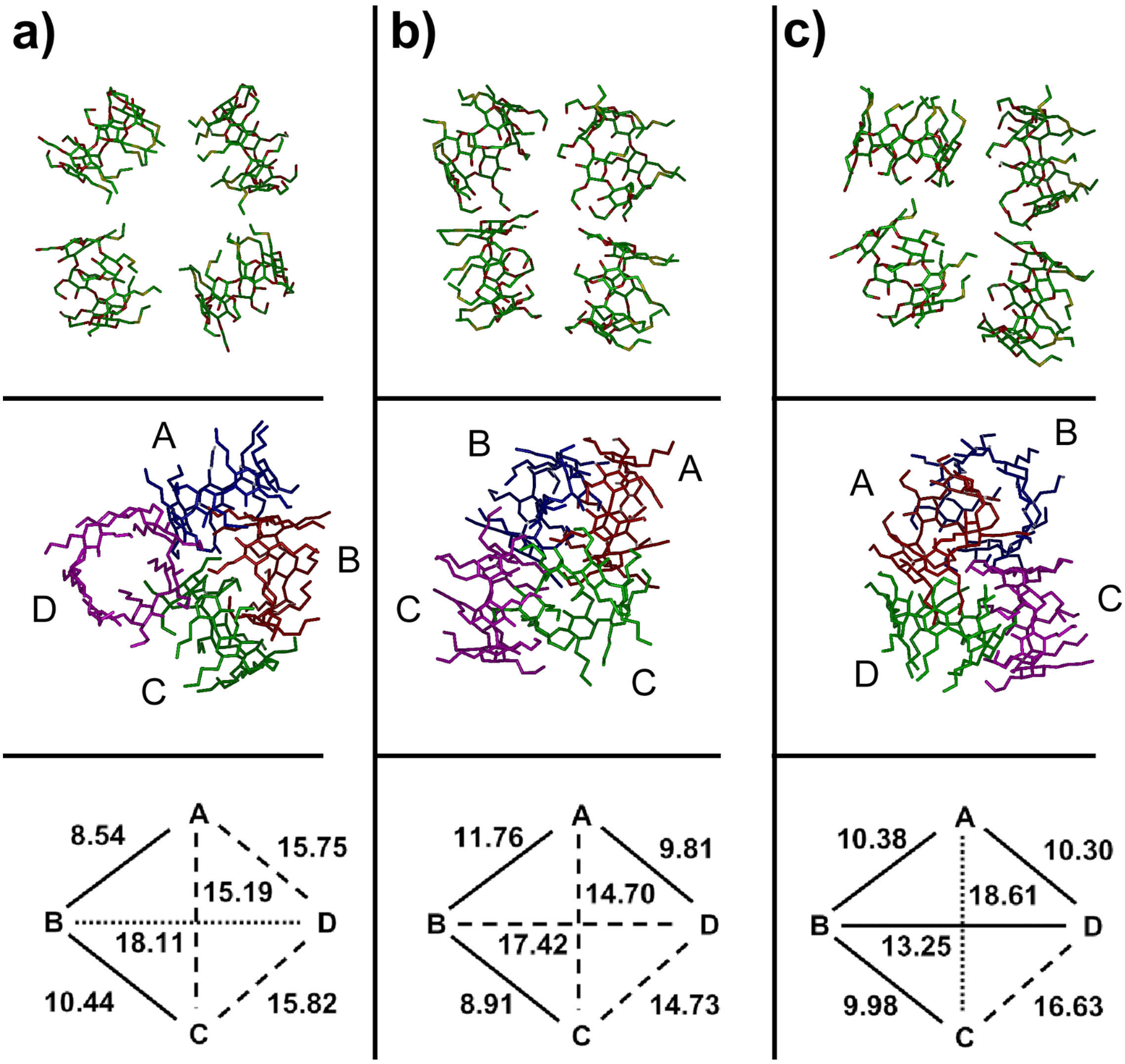

Figure 7: The starting arrangements (a–c) of the four α-CD molecules (top row) and the final arrangement after the MD run and the final optimization in vacuo (second row). The bottom row shows a schematic pattern of the distances (in Å) between the centres of mass of the four macrocycles averaged over the last 10 ns of the MD run (out of a total of 30 ns). The solid lines indicate the short distances (<14 Å), the dashed lines the longer distances (in the range between 14 and 18 Å) and the dotted lines the still larger separations (>18 Å). In general the standard errors of the mean are ≤0.01 Å, while the standard deviation around the mean are in the range ±(0.3–0.5) Å.

changes. The interactions energies turned out to be quite significant, and increasingly larger in the above-mentioned order, with weaker interactions among the H groups only due to dispersion forces in case a, and stronger interactions in cases b and c due to the presence of intermolecular hydrogen bonds and dipolar interactions.

The subsequent MD runs of these geometries, each lasting for 30 ns, led in some cases to significant rearrangements, always producing single aggregates where the four molecules are kept together by different combinations of dispersion forces, dipolar interactions and hydrogen bonds. However, there are small but significant differences in the aggregation pattern, as it is already evident from simple inspection of the final optimized geometries of Figure 7. The most stable state arrived in cases a and b of Figure 7 approximately shows the same stability in vacuo, as shown by their interaction energies reported in Table 2. However, the aggregation patterns are very different, with important implications for the interactions of larger clusters. In fact, in the case of Figure 7a the MD run leads to large rearrangements such that one molecule (molecule B in Figure 7) undergoes a complete rotation in order to optimize its intermolecular interactions through inclusion of two of its P groups in the hydrophobic cavity of two neighbouring molecules (molecules A and C), thus acting as a bridge between them, showing also self-inclusion of one of its H groups. As a result, three molecules are quite close to one another, whereas the fourth one (molecule D) is farther away, being connected more loosely to the other ones through a few intermolecular hydrogen bonds.

To better classify these aggregates, let us conveniently denote as closer molecules those showing a distance d between their c.o.m. smaller than 14 Å, i.e., roughly twice the value of the radius of gyration of the isolated molecule, and farther molecules those with a larger d. These distances are graphically shown in the fourth row of Figure 7, where the thick lines denote the separation between the closer molecules ($d < 14$ Å), the dashed lines the slightly longer distances (14 Å $< d < 18$ Å), and the dotted lines the farther molecules ($d > 18$ Å). In case of Figure 7a, molecule D is somewhat farther away, as implied by the d values involving it. Accordingly, we may denote this as a 3 + 1 aggregate, and in fact the whole system has a relatively large R_g value and a large surface accessible to the solvent (see Table 2 and Supporting Information File 1, Figure S2).

The case of Figure 7b has about the same stability, as said before, due to a different combination of dispersion interactions and hydrogen bonds. In this case, in fact, molecule D shows both self-inclusion of a P group and inclusion of another, adjacent P group in the cavity of the neighbouring molecule A. Moreover, molecule B includes one of its P groups in the cavity of molecule C, forming also a hydrogen bond with a glycosidic oxygen of the latter macrocycle. Accordingly, this aggregate could be identified as a tight 2 + 2 cluster held together by intermolecular hydrogen bonds between two pairs of molecules, but it may also be denoted as a veritable 4 cluster in view of the small value of the radius of gyration (10.59 Å, see Table 2) and of the distances d shown in Figure 7 showing that all the molecules are quite close together. Correspondingly, in this arrangement the surface exposed to the solvent is also quite small (see again Table 2 and Supporting Information File 1, Figure S2). Finally, case 7c shows the most stable aggregate with the largest E_{int}, in absolute value (see Table 2) due to strong interactions with mutual inclusion of H and P groups in neighbouring macrocycles. Thus, in addition to a shallow self-inclusion of an H group, molecule B of Figure 7c shows inclusion of one H group in the macrocycle of C, and of two H groups in the macrocycle of A. Moreover, molecule A shows inclusion of one P group within the macrocycle of D. Thanks also to the intermolecular hydrogen bonds, involving molecules A and D, and molecules B and C, the aggregation leads to rather short distances among the c.o.m. of the closer molecules, as shown in the last row of Figure 7, so that this is again a 4 cluster. On the other hand, this inclusion pattern leads a more “open” aggregate, in view of the quite long A–C separation, producing a quite large radius of gyration and a relatively large exposed surface, as shown in Table 2 and Supporting Information File 1, Figure S2. As a conclusion of this paragraph, we point out that if the E_{int} values for the aggregates of four molecules are normalized by the number of interacting molecules, we get quite larger values (in absolute value) than for two molecules, though not by a factor of six (the number of pairwise interactions among four molecules). Such a result suggests cooperative effects favouring larger clusters compared to smaller ones, even though the four molecules cannot simultaneously optimize all the possible pairwise interactions for steric reasons.

Table 2: Solvent-accessible surface.

Starting arrangement[a]	In vacuo		
	E_{int} (kJ/mol)	R_g (Å)	Accessible surface (Å^2)
a	−678	11.26	3541
b	−679	10.59	3139
c	−731	11.05	3381

[a]The three arrangements are labelled as indicated in Figure 7.

Simulations in water

The simulations in water of larger systems of aCD in water are computationally more demanding, and accordingly here we only report our preliminary results, already providing interesting information, deferring to a future paper a more detailed analysis. The simulation of four aCD in water was carried out in a large cubic cell with an axis equal to 60 Å and 6806 water molecules starting with the arrangement shown in Figure 7a where the H groups point towards the common centre of mass. This arrangement somehow shields the hydrophobic chains from water while exposing the polar chains to water, but since we obtained rather soon an interaction pattern similar to what obtained in vacuo with four molecules and also in water with eight molecules, we did not consider the other arrangements of Figure 7 for brevity. In fact, the final, optimized geometry achieved in water after an MD run of 1 ns, shows a strong interaction between two molecules (molecules A and D in Figure 8), as shown by the the short distance between the centers of mass of their macrocycles. These molecules are somewhat off-axis so as to optimize the interactions between their H groups that tightly inter-digitate, with a mutual shallow inclusion of a few of them into the cavity of the facing molecule. Furthermore, there is a looser side interaction of a third molecule (molecule B in Figure 8), interacting with the A and D molecules through dispersion interactions involving a few H groups of the B molecule and the P groups of the A molecule. An even looser interaction with these molecules is shown by the fourth one (molecule C in Figure 8), which anyway is sufficient to keep it aligned with molecule B along an axis passing through average planes formed by the CD macrocycles. The weakness of this interaction can also be gauged by the conformation of the latter molecule that closely matches the shape of the isolated molecule in water, both for the tight clustering of the H groups to minimize the hydrated surface and for the wide opening of the P groups to maximize their hydration. In conclusion, even though one could denote this arrangement as a 2 + 1 + 1 aggregate, it is best described as a 3 + 1 aggregate. There is a further observation supporting this conclusion. In fact, the radius of gyration of the whole cluster is much larger than in vacuo, amounting to 13.43 Å. On the other hand, the cluster formed by the closer molecules (A, B and D in Figure 5) has a radius of gyration of 11.71 Å, but the surface exposed to the solvent is quite small (see Supporting Information File 1, Figure S3), amounting to 3154 Å^2. Even though the size of this cluster is still larger than the value obtained in vacuo for the whole aggregate of four molecules, it favourably compares with the values of the two clusters of three molecules achieved in water with a larger system, as described in the next section.

The embryonic micelle: random aggregation of eight molecules

Simulations in vacuo

In order to better investigate the early stage of the nucleation of larger aggregates or possibly veritable micelles formed by the amphiphilic CDs, we first investigated the association behaviour of eight molecules in vacuo to model an apolar, weakly interacting solvent. To this purpose, we randomly placed the molecules with an unbiased arrangement in a cubic cell with a size of 61.5 Å using periodic boundary conditions (Figure 9a).

The initial minimization already yielded a very large, but relatively loose aggregate. In the subsequent MD run lasting for 15 ns, such an aggregate turned out to be quite stable, further enhancing the intermolecular interactions. The final, optimized geometry is shown in Figure 9b: the eight molecules do strongly interact both through the intermolecular hydrogen bonds and through mutual inclusion of the side chains in the cavity of

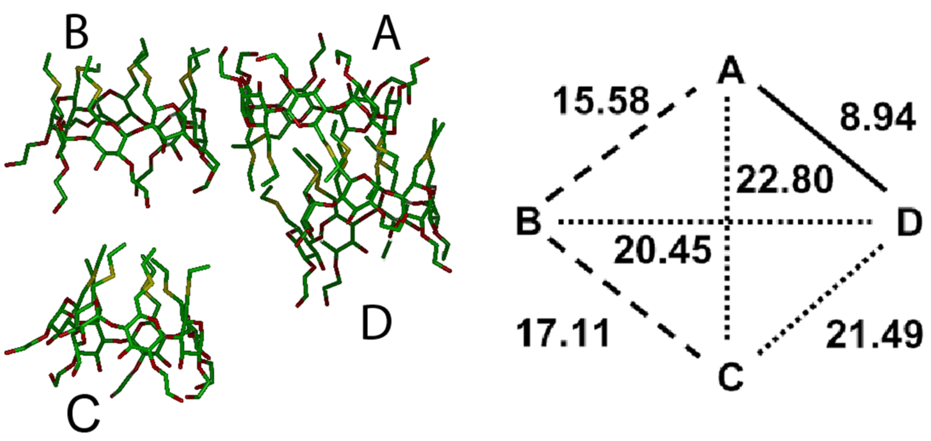

Figure 8: The optimized geometry achieved by four aCD molecules in water by four molecules after the MD run. The line drawing of the aggregate (at left) and a schematic pattern of the distances (in Å, at right) between the centres of mass of the four macrocycles is shown (see Figure 7 for more details).

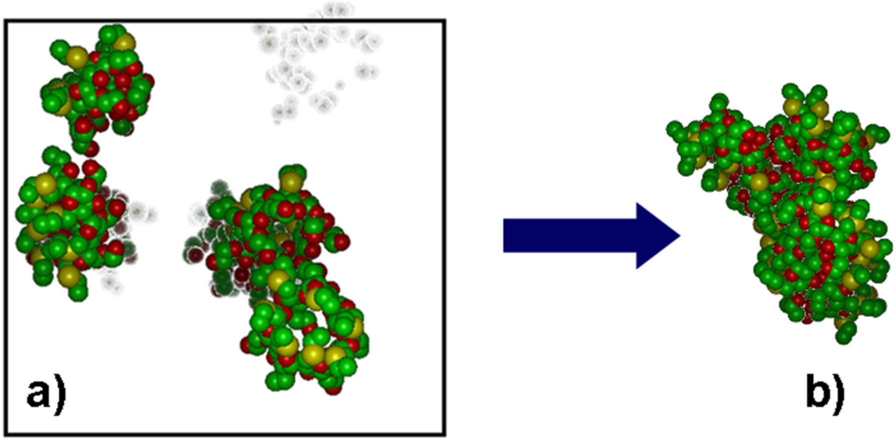

Figure 9: a) The initial random arrangement of eight molecules of the model aCD in a space-filling representation within the simulation box (note that the overlap of the molecules is only apparent). b) The optimized geometry of the aggregate formed by eight molecules of the model aCD in vacuo. The hydrogen atoms were omitted for clarity, while the atoms colour code is the same as in the line drawings of Figure 1.

adjacent molecules, basically repeating on a larger scale the interaction pattern of smaller aggregates. Also, the radius of gyration of the whole aggregate has a relatively small value $R_g = 13.55$ Å. Interestingly, this value is slightly less than twice the value of the single molecule, 6.96 Å, and since the volume pervaded by a molecule or an aggregate scales as $R_g{}^3$, it turns out that the volume of the aggregate is somewhat less than eight times the volume of the single molecule thanks to the attractive intermolecular interactions.

Simulations in water

The simulations in explicit water adopted the same starting arrangement as in vacuo into the same periodic cell, which required the presence of 6250 solvent molecules to achieve the bulk water density. In water, the initial minimization led to a very poor clustering of a few molecules, not yet corresponding to a real aggregate. The subsequent MD runs produced some rearrangements which could thus form veritable, although still loose aggregates, which however did not show any tendency to coalesce into larger ones. After 2 ns of simulation time, the system appeared to have achieved a (pseudo) equilibrium state, as monitored through the system energy and intermolecular distances within each formed aggregate. In this case, the whole system comprised two aggregates, each formed by three molecules and denoted in the following as clusters A and B (see Figure 10), quite similar to the aggregate formed by molecules A, B, D in Figure 8, together with two isolated molecules.

Cluster A presents inclusion of a P group of one molecule in the cavity of a second, neighbouring molecule, while the third one

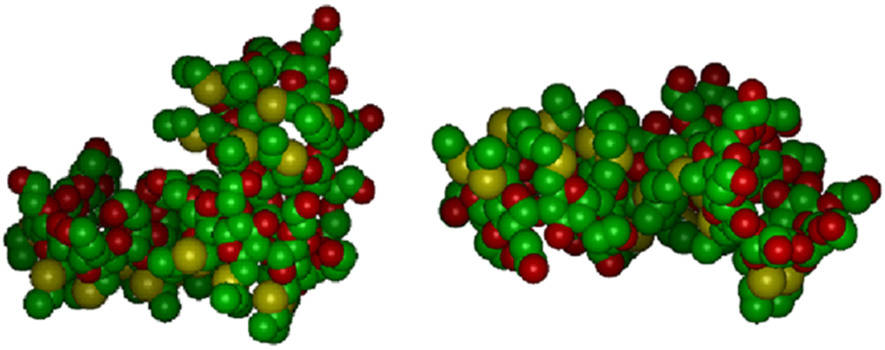

Figure 10: The two aggregates obtained in water, each comprising three molecules of the model aCD, cluster A (at left) and cluster B (at right) in a space-filling representation. The hydrogen atoms were omitted for clarity, while the atoms colour code is the same as in the line drawings of Figure 1.

interacts with the latter through dipolar and dispersive interactions at their lateral surfaces. It is interesting to note that in this cluster the S atoms of the H groups tend to be close to the c.o.m. of the aggregate during the MD run, as shown by the PDF of Figure 11. Moreover, the P groups, and in particular the secondary hydroxyl groups of the macrocycles and the terminal ones of the P groups tend to stay in the outer region to enhance the overall hydration. On the other hand, no inclusion is present in cluster B, where the three molecules are held together by dipolar and dispersion interactions taking only place at their outer surfaces. Note that this nanostructure could be viewed as the building block of a vesicle surface [37]. In any case, the radius of gyration of the two clusters are essentially equal, since they amount to 12.01 Å and 12.09 Å, respectively, showing again the relatively loose association achieved in water in this stage. It should be stressed, however, that these values are only marginally larger than the value of 11.71 Å achieved in water for the aggregate of the three closer molecules discussed in the previous section. This result suggests that this cluster size is indeed quite favourable in this initial pseudo equilibrium aggregation stage that may persist for quite a long time.

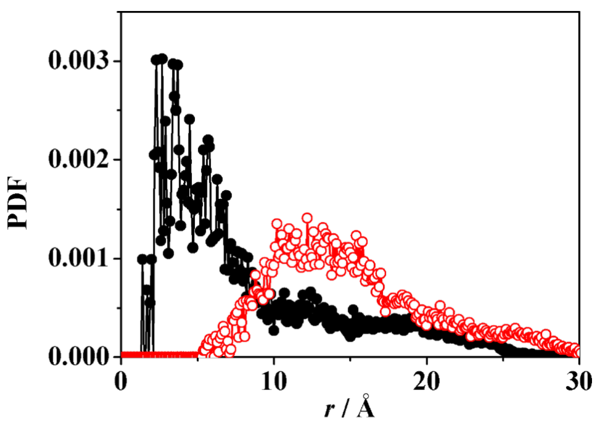

Figure 11: The PDF of the S atoms of the H groups at the primary rim (black symbols) and of the oxygen atoms of the hydroxyl groups at the secondary rim and in the P groups (red symbols) in cluster A plotted as a function of their distance *r* from the cluster c.o.m.

The aggregation process led to an apparent equilibration, as suggested inter alia by the lack of change in the potential and van der Waals energy of the whole system in the last half of the MD run (see Figure 12). Of course much lengthier processes cannot be ruled out: in fact, in view of the small size of these aggregates and of the simulations carried out in vacuo with four and eight molecules, the present results only describe the embryonic stage of aggregation, separated from later stages by some free energy barrier, mainly due to configurational entropy. On the other hand, taken together the present results in water may provide some clues about the possible kinetics of aggregation: at first there is the fast formation of small clusters comprising few molecules, followed by the further aggregation of these cluster with may add individual molecules but also coalesce more slowly because of their smaller diffusivity related in turn with their larger size.

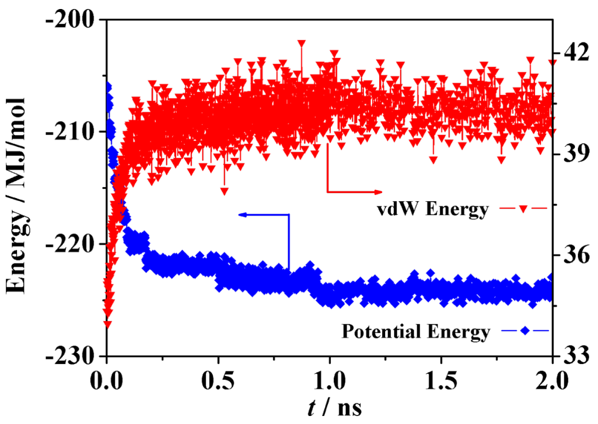

Figure 12: The time change of the potential energy and of the van der Waals energy due to the dispersion and covolume interactions in the MD run of eight molecules of the model aCD in water, showing the apparent equilibration after about 1 ns.

The MD run in water yielded also an increase of the intermolecular order, as shown by the change in the pair distribution function PDF of Figure 13a within the initial part of the MD run. In particular, in the PDF the first peak centred at about 8 Å from the common c.o.m. within the initial 200 ps of the MD run suggests that a few molecules cluster near it, while other farther molecules lead to a broad distribution of distances roughly centred at 18 Å, indicating also a large and independent molecular mobility. Later on, within the following 300 ps the PDF shows a broad first peak at about 6–7 Å from the common centre of mass, followed by a second well-defined peak at about 17 Å and then a broad shoulder at larger distances. These features suggest the embryonic formation of a more structured system corresponding to the formation of clusters A and B.

As for the system hydration, it can be described through the PDF of the water molecules (or equivalently of their oxygen atoms) as a function of their distance *r* from the atoms of the two clusters, shown in Figure 13b. The first peak at about *r* = 1.7 Å is due to the O–H$\cdots$O$_W$ hydrogen bonds of the hydroxy groups of the cluster with the water oxygens (indicated as O$_W$), while the two peaks or shoulders at about *r* = 2.9 Å and 3.7 Å are mainly due to the O$\cdots$O$_W$ non-bonded distances of the two first hydration shells. Note also the slightly larger value of the PDF for the cluster B due to its more “open” shape that produced an effectively larger accessible surface for the solvent.

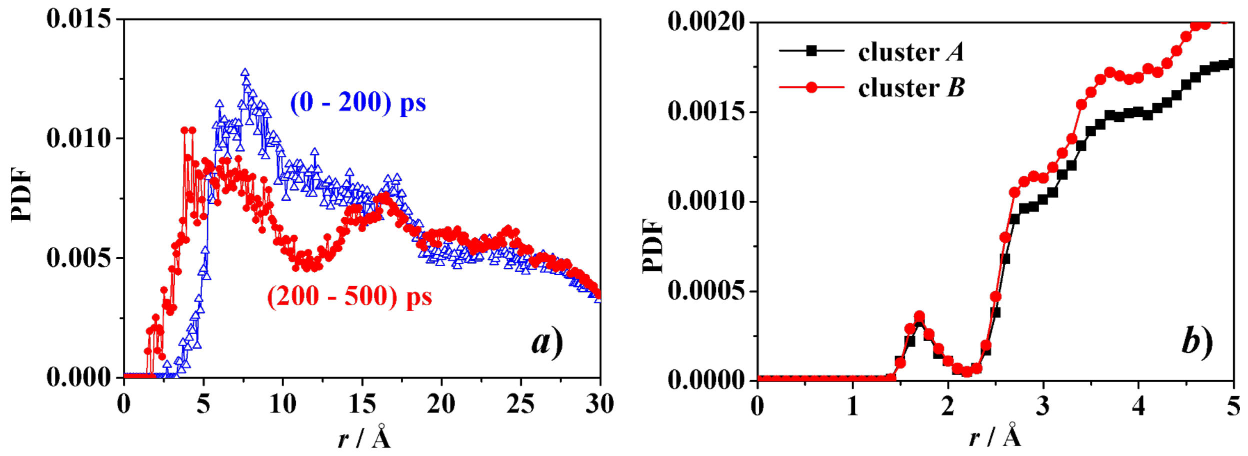

Figure 13: a) The PDF of the eight molecules of the model aCD in water as a function of their distance *r* from the common c.o.m. b) The pair distribution function of the water molecules (more precisely, of their oxygen atoms) as a function of their distance from the atoms belonging to each of the two clusters of three molecules (see Figure 10).

Conclusion

The supramolecular aggregation of molecules is an important phenomenon determined both by their interactions in a specific environment (hence on their concentration and on the solvent) and by their shape, which may preferentially determine stable mesophases, ranging from micelles to membranes, or even liquid crystals. It is well-known that the shape and the interactions among native or modified cyclodextrins can drive specific packing in the solid state, but also in solutions these factors are crucial in driving the nucleation and then the large-scale aggregation, inducing the observed arrangements of micelles and/or vesicles and/or nanospheres. It is in general very difficult to model and understand at the atomistic level these events, but theoretical studies based on molecular mechanics and molecular dynamics simulations can yield a most useful “bottom up” approach to model amphiphilic cyclodextrins that may interact in vacuo or in water.

The simulation results reported in the present paper show that non-ionic amphiphilic β-CD (aCD) carrying short hydrophobic (thioethyl) and polar (ethylene oxide) substituents at opposite rims can aggregate with a relatively complex interaction pattern. In fact, the hydrophobic H groups and the polar P groups may compete for either self or mutual inclusion in their own or in a neighbouring hydrophobic cavity. Such patterns were monitored by MD simulations in vacuo and in water, which suggest that all these interactions are present, at least in the embryonic aggregation stage, while the expulsion of a few water molecules clustered within the hydrophobic cavities of the aCD entropically favours the process. Interestingly, the simulations in explicit water suggest the clusters of three molecules of the model aCD are quite robust, and may coexist with isolated molecules for a while (at least for nanoseconds, according to the present preliminary simulations), whereas the simulations in vacuo suggest the relative fast formation of larger aggregates comprising all the molecules included in the simulations. While specific solvation effects cannot be ruled out, we point out that in vacuo all kinetic processes are much faster than in explicit water because of the lack of the solvent viscosity (the random collisions with the water molecules). Accordingly, the results obtained in vacuo suggest that larger aggregates might eventually form in water as well, possibly with unlike arrangements, so that the present results give a picture of the early nucleation stage of the larger aggregates that are experimentally observed. Note also in this context that our results suggest also the presence of robust, though metastable arrangements that may persist also after addition of further aCD molecules, with similar but unlike interaction geometries.

It should be noted that a qualitatively similar pattern was indeed experimentally observed in particular by light scattering studies [24]. In fact, the observed scattered intensity obtained for an aCD similar to compound **1** of Scheme 1 but with a longer polar chain with $n = 1$ (on the average), could be well interpreted as due to the diffusive behaviour of isolated molecules, of small micelles of a few molecules and of much larger aggregates that coexist at equilibrium, even though no quantitative comparison can be made with the present results obtained for a model compound. It should be added that in the same paper [24] the presence of the small micelles and of the larger aggregates was independently confirmed by small-angle X-ray and dynamic light scattering experiments, respectively. We further note that aCD with longer alkyl chains (compound **2** of Scheme 1, data not shown) did not show the presence of isolated molecules in equilibrium with small micelles and larger clusters [24]. In this case, the aCD would show a relatively more hydrophobic nature than our model aCD. We can thus speculate that mutual inclusion of the polar chains in the cavity of neighbouring molecules as found in the present paper would be more unlikely because of the enhanced hydrophobic interactions among the alkyl chains: their cooperative effect would then favour the micelle formation *vs.* the isolated molecules in spite of the entropy loss entailed by the clustering process.

As a final remark, we point out that with atomistic MM and MD methods we can model the first nucleation steps which may take place both in apolar solvent and in water in terms of the geometry of the aggregates and of their interaction energy in a given solvent. In the proposed approach the different shapes assumed by aCD and the non-covalent interactions with the solvent may lead to different macro-aggregates, either micelles or bilayer, or vesicles and nanospheres at appropriate concentrations. In the recent past, some of these structures have been selected to yield versatile and reliable carriers for drug delivery [3,50], and even for molecular recognition of polymers [51]. In this scenario, the proposed study can open new perspectives in the design of aggregates and correlate their structures with the physico-chemical properties.

Supporting Information

Supporting Information File 1

Pictures of the surface accessible to the solvent for the aggregates of two and four aCD molecules.
[http://www.beilstein-journals.org/bjoc/content/supplementary/1860-5397-11-267-S1.pdf]

Acknowledgments

Financial support of MERIT-FIRB RBNE08YYBM (CNRISMN) and EuroBioSAS-OP-009 (ICS project) are gratefully acknowledged. We also gratefully acknowledge the financial support from MIUR – FIRB Futuro in Ricerca 2008 (RBFR08XH0H).

References

1. Bilensoy, E.; Hincal, A. A. *Expert Opin. Drug Delivery* **2009,** *6,* 1161–1173. doi:10.1517/17425240903222218
2. Roux, M.; Perly, B.; Djedaïni-Pilard, F. *Eur. Biophys. J.* **2007,** *36,* 861–867. doi:10.1007/s00249-007-0207-6
3. Zhang, J.; Ma, P. X. *Adv. Drug Delivery Rev.* **2013,** *65,* 1215–1233. doi:10.1016/j.addr.2013.05.001
4. Choisnard, L.; Gèze, A.; Putaux, J.-L.; Wong, Y.-S.; Wouessidjewe, D. *Biomacromolecules* **2006,** *7,* 515–520. doi:10.1021/bm0507655
5. Sallas, F.; Darcy, R. *Eur. J. Org. Chem.* **2008,** 957–969. doi:10.1002/ejoc.200700933
6. Harada, A. *Acc. Chem. Res.* **2001,** *34,* 456–464. doi:10.1021/ar000174l
7. Li, J.; Loh, X. J. *Adv. Drug Delivery Rev.* **2008,** *60,* 1000–1017. doi:10.1016/j.addr.2008.02.011
8. Silva, O. F.; Fernández, M. A.; Pennie, S. L.; Gil, R. R.; de Rossi, R. H. *Langmuir* **2008,** *24,* 3718–3726. doi:10.1021/la702962f
9. Moya-Ortega, M. D.; Alvarez-Lorenzo, C.; Concheiro, A.; Loftsson, T. *Int. J. Pharm.* **2012,** *428,* 152–163. doi:10.1016/j.ijpharm.2012.02.038
10. Trotta, F.; Tumiatti, W.; Cavalli, R.; Roggero, C. M.; Mognetti, B.; Berta Nicolao, G. Pat. WO 09/003656, 2009.
11. Thatiparti, T. R.; Shoffstall, A. J.; von Recum, H. A. *Biomaterials* **2010,** *31,* 2335–2347. doi:10.1016/j.biomaterials.2009.11.087
12. Raffaini, G.; Ganazzoli, F.; Mele, A.; Castiglione, F. *J. Inclusion Phenom. Macrocyclic Chem.* **2013,** *75,* 263–268. doi:10.1007/s10847-012-0126-8
13. Bolmal, U. B.; Manvi, F. V.; Rajkumar, K.; Palla, S. S.; Paladugu, A.; Reddy, K. R. *Int. J. Pharm. Sci. Nanotechnol.* **2013,** *6,* 1934–1944.
14. Perret, F.; Parrot-Lopez, H. In *Cyclodextrins in Pharmaceutics, Cosmetics, and Biomedicine: Current and Future Industrial Applications;* Bilensoy, E., Ed.; John Wiley & Sons, Inc.: Hoboken, NJ, USA, 2011; pp 197–233.
And references therein.
15. Choisnard, L.; Gèze, A.; Vanhaverbeke, C.; Yaméogo, J. B. G.; Putaux, J.-L.; Brasme, B.; Jullien, L.; Boullanger, S.; Elfakir, C.; Wouessidjewe, D. *Biomacromolecules* **2011,** *12,* 3031–3038. doi:10.1021/bm2006664
16. Jiang, L.; Yan, Y.; Huang, J. *Adv. Colloid Interface Sci.* **2011,** *169,* 13–25. doi:10.1016/j.cis.2011.07.002
17. Voskuhl, J.; Ravoo, B. J. *Chem. Soc. Rev.* **2009,** *38,* 495–505. doi:10.1039/B803782P
18. Parrot-Lopez, H.; Ling, C. C.; Zhang, P.; Baszkin, A.; Albrecht, G.; de Rango, C.; Coleman, A. W. *J. Am. Chem. Soc.* **1992,** *114,* 5479–5480. doi:10.1021/ja00039a100
19. Memisoglu-Bilensoy, E.; Vural, I.; Bochot, A.; Renoir, J. M.; Duchene, D.; Hıncal, A. A. *J. Controlled Release* **2005,** *104,* 489–496. doi:10.1016/j.jconrel.2005.03.006
20. Yaméogo, J. B. G.; Gèze, A.; Choisnard, L.; Putaux, J.-L.; Gansané, A.; Sirima, S. B.; Semdé, R.; Wouessidjewe, D. *Eur. J. Pharm. Biopharm.* **2012,** *80,* 508–517. doi:10.1016/j.ejpb.2011.12.007
21. Mazzaglia, A.; Valerio, A.; Micali, N.; Villari, V.; Quaglia, F.; Castriciano, M. A.; Monsù Scolaro, L.; Giuffrè, M.; Siracusano, G.; Sciortino, M. T. *Chem. Commun.* **2011,** *47,* 9140–9142. doi:10.1039/C1CC12821C
22. Quaglia, F.; Ostacolo, L.; Mazzaglia, A.; Villari, V.; Zaccaria, D.; Sciortino, M. T. *Biomaterials* **2009,** *30,* 374–382. doi:10.1016/j.biomaterials.2008.09.035
23. Mazzaglia, A.; Ravoo, B. J.; Darcy, R.; Gambadauro, P.; Mallamace, F. *Langmuir* **2002,** *18,* 1945–1948. doi:10.1021/la015626x
24. Lombardo, D.; Longo, A.; Darcy, R.; Mazzaglia, A. *Langmuir* **2004,** *20,* 1057–1064. doi:10.1021/la035370q
25. Ferro, S.; Jori, G.; Sortino, S.; Stancanelli, S.; Nikolov, P.; Tognon, G.; Ricchelli, F.; Mazzaglia, A. *Biomacromolecules* **2009,** *10,* 2592–2600. doi:10.1021/bm900533r
26. Villari, V.; Mazzaglia, A.; Darcy, R.; O'Driscoll, C. M.; Micali, N. *Biomacromolecules* **2013,** *14,* 811–817. doi:10.1021/bm3018609
27. Croyle, M. A.; Roessler, B. J.; Hsu, C. P.; Sun, R.; Amidon, G. L. *Pharm. Res.* **1998,** *15,* 1348–1355. doi:10.1023/A:1011985101580
28. Redenti, E.; Pietra, C.; Gerloczy, A.; Szente, L. *Adv. Drug Delivery Rev.* **2001,** *53,* 235–244. doi:10.1016/S0169-409X(01)00230-7

29. Jessel, N.; Oulad-Abdelghani, M.; Meyer, F.; Lavalle, P.; Haîkel, Y.; Schaaf, P.; Voegel, J.-C. *Proc. Natl. Acad. Sci. U. S. A.* **2006,** *103,* 8618–8621. doi:10.1073/pnas.0508246103
30. Díaz-Moscoso, A.; Guilloteau, N.; Bienvenu, C.; Méndez-Ardoy, A.; Jiménez Blanco, J. L.; Benito, J. M.; Le Gourriérec, L.; Di Giorgio, C.; Vierling, P.; Defaye, J.; Mellet, C. O.; García Fernández, J. M. *Biomaterials* **2011,** *32,* 7263–7273. doi:10.1016/j.biomaterials.2011.06.025
31. Brocos, P.; Díaz-Vergara, N.; Banquy, X.; Pérez-Casas, S.; Costas, M.; Piñeiro, A. *J. Phys. Chem. B* **2010,** *114,* 12455–12467. doi:10.1021/jp103223u
32. Piñeiro, A.; Banquy, X.; Pérez-Casas, S.; Tovar, E.; García, A.; Villa, A.; Amigo, A.; Mark, A. E.; Costas, M. *J. Phys. Chem. B* **2007,** *111,* 4383–4392. doi:10.1021/jp0688815
33. Mouria-Bellabdelli, F.; Potier, J.; Bouterfas, M.; Cavrot, J.-P.; Sayede, A.; Menuel, S.; Monflier, E.; Machut-Binkowski, C. *Colloids Surf., A* **2012,** *415,* 380–387. doi:10.1016/j.colsurfa.2012.09.033
34. Messner, M.; Kurkov, S. V.; Jansook, P.; Loftsson, T. *Int. J. Pharm.* **2010,** *387,* 199–208. doi:10.1016/j.ijpharm.2009.11.035
35. Raffaini, G.; Ganazzoli, F. *J. Phys. Chem. B* **2010,** *114,* 7133–7139. doi:10.1021/jp911812j
36. Wang, Z.; Larson, R. G. *J. Phys. Chem. B* **2009,** *113,* 13697–13710. doi:10.1021/jp901576e
37. Sun, T.; Guo, Q.; Zhang, C.; Hao, J.; Xing, P.; Su, J.; Li, S.; Hao, A.; Liu, G. *Langmuir* **2012,** *28,* 8625–8636. doi:10.1021/la301497t
38. Patti, A.; Ramsch, R.; Marsà, C. S. *J. Phys. Chem. B* **2012,** *116,* 2687–2695. doi:10.1021/jp212448q
39. Raffaini, G.; Ganazzoli, F.; Malpezzi, L.; Fuganti, C.; Fronza, G.; Panzeri, W.; Mele, A. *J. Phys. Chem. B* **2009,** *113,* 9110–9122. doi:10.1021/jp901581e
40. Raffaini, G.; Ganazzoli, F. *J. Inclusion Phenom. Macrocyclic Chem.* **2007,** *57,* 683–688. doi:10.1007/s10847-006-9265-0
41. Mele, A.; Raffaini, G.; Ganazzoli, F.; Juza, V.; Schurig, V. *Carbohydr. Res.* **2003,** *338,* 625–635. doi:10.1016/S0008-6215(02)00493-7
42. Raffaini, G.; Melone, L.; Punta, C. *Chem. Commun.* **2013,** *49,* 7567–7570. doi:10.1039/C3CC90254D
43. Anand, R.; Ottani, S.; Manoli, F.; Manet, I.; Monti, S. *RSC Adv.* **2012,** *2,* 2346–2357. doi:10.1039/c2ra01221a
44. *InsightII;* Accelrys Inc.: San Diego, CA, 2000, http://www.accelrys.com/. See also the URL.
45. Dauber-Osguthorpe, P.; Roberts, V. A.; Osguthorpe, D. J.; Wolff, J.; Genest, M.; Hagler, A. T. *Proteins: Struct., Funct., Genet.* **1988,** *4,* 31–47. doi:10.1002/prot.340040106
46. Raffaini, G.; Ganazzoli, F. *Chem. Phys.* **2007,** *333,* 128–134. doi:10.1016/j.chemphys.2007.01.015
47. Verlet, L. *Phys. Rev.* **1967,** *159,* 98–103. doi:10.1103/PhysRev.159.98
48. Berendsen, H. J. C.; Postma, J. P. M.; van Gunsteren, W. F.; Di Nola, A.; Haak, J. R. *J. Chem. Phys.* **1984,** *81,* 3684–3690. doi:10.1063/1.448118
49. Raffaini, G.; Ganazzoli, F. *Phys. Chem. Chem. Phys.* **2006,** *8,* 2765–2772. doi:10.1039/B604540E
50. Challa, R.; Ahuja, A.; Ali, J.; Khar, R. K. *AAPS PharmSciTech* **2005,** *6,* E329–E357. doi:10.1208/pt060243
51. Ravoo, B. J.; Jacquier, J.-C.; Wenz, G. *Angew. Chem., Int. Ed.* **2003,** *42,* 2066–2070. doi:10.1002/anie.200350923

License and Terms

BEILSTEIN JOURNAL OF ORGANIC CHEMISTRY

Inclusion complexes of 2-methoxyestradiol with dimethylated and permethylated β-cyclodextrins: models for cyclodextrin–steroid interaction

Mino R. Caira*, Susan A. Bourne, Halima Samsodien and Vincent J. Smith

Full Research Paper

Open Access

Address:
Centre for Supramolecular Chemistry Research (CSCR), Department of Chemistry, University of Cape Town, Rondebosch 7701, South Africa

Email:
Mino R. Caira* - Mino.Caira@uct.ac.za

* Corresponding author

Keywords:
complexation; cyclodextrin; 2-methoxyestradiol; solubility; X-ray diffraction

Beilstein J. Org. Chem. **2015,** *11,* 2616–2630.
doi:10.3762/bjoc.11.281

Received: 30 September 2015
Accepted: 02 December 2015
Published: 16 December 2015

This article is part of the Thematic Series "Superstructures with cyclodextrins: Chemistry and applications III".

Guest Editor: G. Wenz

Abstract

The interaction between the potent anticancer agent 2-methoxyestradiol (2ME) and a series of cyclodextrins (CDs) was investigated in the solid state using thermal analysis and X-ray diffraction, while the possibility of enhancing its poor aqueous solubility with CDs was probed by means of equilibrium solubility and dissolution rate measurements. Single crystal X-ray diffraction studies of the inclusion complexes between 2ME and the derivatised cyclodextrins heptakis(2,6-di-*O*-methyl)-β-CD (DIMEB) and heptakis(2,3,6-tri-*O*-methyl)-β-CD (TRIMEB) revealed for the first time the nature of the encapsulation of a bioactive steroid by representative CD host molecules. Inclusion complexation invariably involves insertion of the D-ring of 2ME from the secondary side of each CD molecule, with the 17-OH group generally hydrogen bonding to a host glycosidic oxygen atom within the CD cavity, while the A-ring and part of the B-ring of 2ME protrude from the secondary side. In the case of the TRIMEB·2ME complex, there is evidence that complexation proceeds with mutual conformational adaptation of host and guest molecules. The aqueous solubility of 2ME was significantly enhanced by CDs, with DIMEB, TRIMEB, randomly methylated β-CD and hydroxypropyl-β-CD being the most effective hosts. The 2:1 host–guest β-CD inclusion complex, prepared by two methods, yielded very rapid dissolution in water at 37 °C relative to untreated 2ME, attaining complete dissolution within 15 minutes (co-precipitated complex) and 45 minutes (complex from kneading).

Introduction

This report focuses on the modes of inclusion of the anticancer agent 2-methoxyestradiol (2ME, Figure 1) in the host cyclodextrins (CDs) heptakis(2,6-di-*O*-methyl)-β-CD (DIMEB) and heptakis(2,3,6-tri-*O*-methyl)-β-CD (TRIMEB) in the solid state. The structures to be described are the first for crystalline CD inclusion complexes of a representative bioactive steroid and as such, their molecular structures shed some light on the nature of cyclodextrin-steroid interactions, including the phenomenon of 'mutually induced fit' accompanying complexation. This feature, while commonly observed in protein–ligand recognition and selection, is rare for small molecule structures [1]. In addition to the solid-state results detailed below, we report original data on the use of CDs to enhance the aqeous solubility of 2ME.

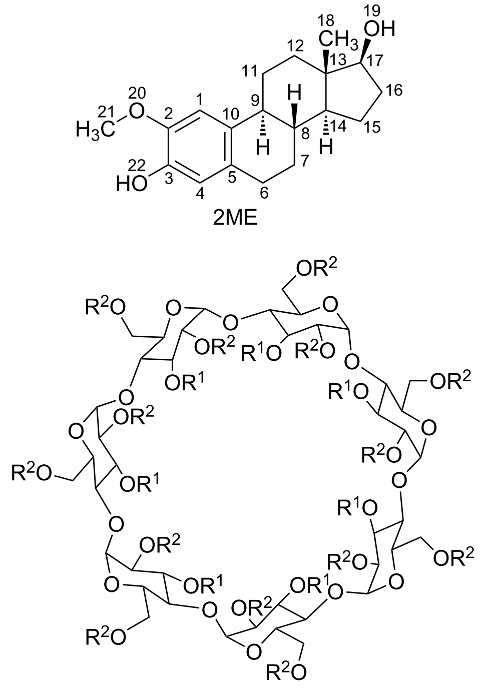

R^1 = H, R^2 = Me (DIMEB); R^1 = R^2 = Me (TRIMEB)

Figure 1: Chemical structures of 2-methoxyestradiol (top) and the derivatised CDs DIMEB and TRIMEB (bottom).

The title steroid, originally identified as an endogenous metabolite of the most common estrogen hormone, 17β-estradiol, has been intensively studied owing to its proven potent antiangiogenic, antiproliferative and antitumoral activities [2,3]. However, its poor bioavailability has retarded its development as a drug [4,5]. Although recent reports of ongoing clinical trials with 2ME continue to appear [6,7], attention has shifted towards its more promising derivatives, such as 2-methoxyestradiol-3,17-di,*O*-bis-sulfamate (2MES), with higher potency and improved pharmacokinetic properties [8]. Nevertheless, as noted in our recent report on some aspects of the solid-state chemistry of 2ME and 2MES [9] several new indications for 2ME in the area of anticancer therapy, in particular, coupled with the well-established low toxicity of underivatised 2ME, have revived interest in this compound [9,10], providing ongoing motivation for increasing its poor bioavailability. We therefore embarked on a study of 2ME [11] with the objectives of investigating both the interactions between CD molecules and 2ME in the solid-state as well as the effects of CDs on the aqueous solubility of 2ME, neither of these aspects having been given significant attention in the literature. Encapsulation of poorly soluble drug molecules by CDs with the aim of enhancing drug bioavailability has been practised for over four decades, the first demonstration of both in vivo and in vitro effects of complexation on drug release having been reported in the early 1970s [12,13]. Steroid hormones were among the first bioactive compounds whose aqueous solubilities were shown to be significantly enhanced via CD inclusion. For example, in an early study by Uekama et al. [14], the interactions between 18 steroid hormones and the native cyclodextrins α-, β- and γ-CD in aqueous solution were investigated to gain insight into CD–steroid interaction modes and the stability of the resulting inclusion complexes. These researchers also used Fourier transform infrared spectroscopy (FTIR), thermal analysis and powder X-ray diffraction (PXRD) to infer the existence of solid native CD–steroid inclusion complexes, some of them having host–guest stoichiometric ratios of 2:1 and 3:2 with β-CD and γ-CD, respectively. An early attempt to acquire basic structural information from PXRD data for crystalline inclusion complexes of β-CD with a series of pregnanes as guests led to the estimation of crystal unit cell parameters [15], from which the authors inferred a 'channel cyclindrical structure' as a possible arrangement in the crystalline state. However, no definitive structural studies were subsequently published. Our search in the Cambridge Structural Database [16] for CD complex structures revealed two reported crystal structures containing the rocuronium ion, a well-known neuromuscular blocking agent consisting of a steroid nucleus that is highly functionalised [17], this species being encapsulated by specially designed CD derivatives [per-6-deoxy-per-6-carboxyethylsulfanyl-γ-CD and 6-perdeoxy-6-per(4-carboxylatophenyl)thio-γ-CD] capable of accommodating such a large guest species. While being of significant interest in the context of modern anaesthesia [18], this more exotic supramolecular construct does not serve to illustrate CD–steroidal interactions that might be associated with the vast majority of bioactive steroids and our search further revealed that no representative CD–steroid structures containing more common CDs and steroidal guests (e.g., cortisone, prednisolone, estradiol, or their derivatives) have been reported hitherto. Very recently, an account of the crystal structure of a host comprising a γ-CD duplex system connected by two disulfide bonds that forms stable complexes with steroids appeared [19]. However, no crystal structure of any of its inclusion complexes was reported.

Finally, the lack of published studies on the potential for CDs to improve the aqueous solubility of 2ME also prompted our study of this pharmaceutically relevant aspect of the bioactive compound. Here, we report original data that reflect significant solubility enhancements for 2ME effected by a range of CDs as well as comparative dissolution data in aqueous medium to highlight the potential advantages for further development of 2ME.

Results and Discussion

Interaction between 2ME and native CDs

Initial studies focused on possible isolation of solid inclusion complexes of 2ME with the native cyclodextrins α-, β- and γ-CD. Following neat co-grinding of each CD and 2ME (1 h, 1:1 molar ratios) and kneading (1 h with water as medium, CD-2ME ratios 1:1 and 2:1), PXRD traces of the products were recorded. These revealed that physical mixtures resulted in all cases but one, namely kneading β-CD and 2ME in a 2:1 molar ratio, where inclusion complexation definitely occurred. This was deduced by comparing the experimental PXRD trace of the product with that of an isostructural inclusion complex, namely the β-CD complex of 4-*tert*-butylbenzyl alcohol (CSD refcode KOFJEU [16]), and finding a reasonable match [20]. This procedure also enabled correct prediction of the space group ($C222_1$) of the complex and the approximate unit cell dimensions ($a \approx 19.2$, $b \approx 24.4$, $c \approx 32.8$ Å), results which were subsequently confirmed by a single crystal X-ray diffraction study of the same phase obtained via the co-precipitation method. (Relevant PXRD traces and single crystal data are provided in Supporting Information File 1). Further routine characterization of the β-CD complex of 2ME by UV spectrophotometry (at $\lambda = 198.5$ nm in MeOH/water 50:50 v/v) coupled with thermogravimetric anlysis (TGA) data (8.8 ± 0.4% one-step mass loss in the range 30–150 °C, $n = 3$) yielded the host–guest stoichiometry (2:1) and crystal water content (12.6 ± 0.6 water molecules per complex unit) respectively, and hence the complex formula $(\beta\text{-CD})_2\cdot2\text{ME}\cdot(12.6 \pm 0.6)\text{H}_2\text{O}$. X-ray crystal structure solution by isomorphous replacement, using as trial model the host molecule coordinates of KOFJEU, led to successful refinement of the host framework but the included 2ME molecule, located within the ‘cage’ provided by the well known hydrogen-bonded β-CD dimeric unit, was severely disordered and no details of its mode of inclusion could be deduced from difference electron-density syntheses. However, despite this deficiency, the inclusion complex was chemically well-defined and hence met the criterion for subsequent solubility studies.

Interaction between 2ME and the amorphous CD derivatives RAMEB and HPBCD

PXRD, differential scanning calorimetry (DSC) and FTIR methods were employed to investigate the products of kneading between crystalline 2ME and these amorphous host compounds. (Relevant PXRD traces, DSC traces and FTIR spectra are provided in the Supporting Information File 1). In each case, kneading an equimolar physical mixture of the respective host and 2ME produced an amorphous phase, as evidenced by a PXRD pattern devoid of peaks characteristic of the crystalline component 2ME. Consistent with this, no melting endotherm for 2ME was observed in DSC traces of these preparations, whereas the traces of the corresponding CD-2ME physical mixtures revealed fusion of 2ME at a peak temperature of 188 °C (reported mp 187 °C [9]). Definitive inclusion complex formation between 2ME and both of the host molecules was finally confirmed by comparing the FTIR spectrum of pure 2ME with those of the pure CD and the putative CD-2ME inclusion complexes prepared by kneading; characteristic bands for 2ME (at 1600, 2861, 2903, 3179 and 3413 cm^{-1}) were seen to either undergo significant shifts or be masked by broad bands of the hosts RAMEB and HPBCD in the spectra of the materials prepared by kneading.

Preparation and preliminary characterization of crystalline inclusion complexes between 2ME and the hosts DIMEB and TRIMEB

Hot stage microscopy (HSM) was employed for preliminary investigation of single crystals of a putative inclusion complex between 2ME and DIMEB, prepared using the co-precipitation method. (Details of the thermal analysis of the DIMEB complex of 2ME are provided in the Supporting Information File 1). The crystals, immersed in silicone oil and heated from 30 °C at 10 K/min, were initially clear. Bubbles appearing at ≈80 °C indicated commencement of the release of included water. This process appeared to be continuous, posing difficulty in estimating the temperature corresponding to complete dehydration. The anhydrous phase began to discolour at ≈290 °C, indicating the onset of slow decomposition. Vigorous bubbling and the dark brown colour that developed at ≈400 °C signified the onset of rapid final complex decomposition. Corresponding to these events, the DSC trace displayed an endotherm for dehydration in the approximate range 54–105 °C (peak temperature 80 °C), and a sequence of two small endotherms, a large exotherm, and a small endotherm, all of them spanning the range ≈255–350 °C, attributed to final dehydration and the onset of complex decomposition. The absence of any endothermic effect for the fusion of pure 2ME was consistent with inclusion complex formation. A PXRD trace of the material did not match any of those generated for known polymorphs of the pure host DIMEB [16], again supporting the formation of an inclusion complex between DIMEB and 2ME.

As for the characterization of the β-CD·2ME complex described above, single crystals of the putative DIMEB complex were dissolved in a MeOH/water medium and UV spectrophotometric analysis yielded a host–guest ratio of 1:1. Together with the TGA estimate of water content (5.3 ± 0.3%, $n = 3$), the complex formula DIMEB·2ME·$(5.5 \pm 0.3)H_2O$ was indicated.

A putative inclusion complex between 2ME and the fully methylated host TRIMEB was prepared by the co-precipitation method and initially examined by HSM. (Details of the thermal analysis of the TRIMEB complex of 2ME are provided in Supporting Information File 1). Upon heating the crystals under silicone oil, no dehydration was evident and the material melted at 170 °C. Decomposition, indicated by the molten complex turning brown, commenced at ≈350 °C. The melting point in this case is significantly higher than those reported for the pure host TRIMEB in different crystal forms (148 and 157 °C [21]), supporting the presence of a complex between 2ME and TRIMEB. PXRD subsequently confirmed the presence of a new crystalline phase. TGA indicated no significant mass loss over the interval 30–260 °C while the DSC trace displayed only an endotherm of fusion with a peak temperature of 170 °C. Finally, a 1:1 TRIMEB/2ME complex ratio was indicated from UV spectrophotometric measurements of a solution of dissolved single crystals.

Definitive structural information for crystalline inclusion complexes between 2ME and the hosts DIMEB and TRIMEB

Since the unit cell dimensions of the two inclusion complexes had no counterparts in the Cambridge Crystallographic Database [16], structure solution by isomorphous replacement was not possible. Both crystal structures were therefore solved ab initio by direct methods using the program SHELXD [22]. Model development involved successive difference Fourier syntheses and iterative refinement by the full-matrix least-squares technique using SHELXH [22]. With only a single complex unit DIMEB·2ME in the crystal asymmetric unit, structure solution was fairly straightforward. However, the structure determination and refinement of the TRIMEB inclusion complex proved to be considerably more challenging due to the presence of four TRIMEB·2ME units (A–D) in the asymmetric unit. Table 1 summarises the crystal data and refinement details for the two complexes.

Salient features of the mode of inclusion of the steroid molecule 2ME in the host DIMEB molecule and complex crystal packing are shown in Figure 2. In the complex, the DIMEB molecule maintains the ‘round’ conformation that is generally observed for this CD, this feature being effected by the ‘belt’ of intramolecular O2(n)–H···O3($n-1$) hydrogen bonds [23] that link contiguous glucose rings (Figure 2a) and for which the seven relevant O···O distances span the narrow range 2.771(5)–2.883(6) Å (see Table S1 in Supporting Information File 1). The set of seven glycosidic oxygen atoms comprising the so-called ‘O4-heptagon’ has a high degree of planarity, with a root-mean-square deviation (RMSD) from the least-squares plane of only 0.06 Å. Guest inclusion involves entry of the D-ring terminus of the 2ME molecule from the wider (secondary) side of the DIMEB molecule and location of this ring near the narrower (primary) side. Maximal penetration of the D-ring into the CD cavity places atom O19 of the 17-OH group at a distance of ≈0.7 Å above the mean plane of the O4-heptagon, where it engages in a hydrogen bond with one of the host glycosidic oxygen atoms (O19–H···O4G2, with O···O 3.195(6) Å and angle O–H···O 151°). This interaction is complemented by a weaker C–H···O19 hydrogen bond (not shown) involving a host methine group donor (C5G2–H···O19, with C···O 3.280(7) Å and angle C–H···O 143°). A side-view of the complex unit (Figure 2b) in space-filling representation reveals that essentially only the A-ring of the 2ME molecule protrudes significantly from the host secondary side, while the sectioned view (Figure 2c) indicates that the steroid molecule appears to be ‘wedged’ into the CD cavity to its maximal extent. The mean plane of the O4-heptagon and that of the 2ME molecule intersect at ≈84°, this nearly perpendicular relationship being expected under the constraint of the belt of intramolecular hydrogen bonds on the secondary rim of the DIMEB molecule that limits its conformational flexibility, which in turn restricts the orientation of the steroid molecule within the host cavity.

Quantitative indications that the host molecule maintains a fairly symmetrical shape while accommodating the 2ME molecule include the narrow ranges in parameters that measure distortion in CD molecules [24]. These include the radii (r) of the O4-heptagon, i.e., the distances from the O4-heptagon centroid to each of the O4 atoms (range 5.02–5.12 Å), the glycosidic O4(n)···O4(n+1) distances, D (range 4.36–4.42 Å), and the O4($n-1$)···O4(n)···O4(n+1) angles (a) (range 126.6–129.6°). On the other hand, the ‘tilt angle’ parameter (τ_2), measured as the angle between the plane containing atoms O4(n), C4(n), C1(n) and O4(n+1) of a given ring and the O4-heptagon mean plane, shows some variation, albeit narrow (range 8.8–14.4°), as the host accommodates the steroid molecule. (A full listing of these and other parameters is provided in Supporting Information File 1). To assess the extent of possible host molecule distortion that the inclusion of a molecule of 2ME in DIMEB might produce, the above tilt angle range for the seven glucose residues in the complex was compared with the ranges calculated for crystalline forms of DIMEB containing either no guest or water molecules only [16]. Interestingly, these ranges span a significantly wider range than that quoted above, namely −5.1–34.6° for anhydrous DIMEB (CSD refcode ZULQAY),

Table 1: Crystal data, data collection parameters and refinement details.

abbreviated formulae	DIMEB·2ME·5.3H_2O	TRIMEB·2ME
complex formula	$C_{56}H_{98}O_{35}$·$C_{19}H_{26}O_3$·5.3H_2O	$C_{63}H_{112}O_{35}$·$C_{19}H_{26}O_3$
formula wt. / g mol^{-1}	1729.23	1731.92
crystal system	monoclinic	triclinic
space group	$P2_1$	$P1$
a / (Å)	13.5514(1)	14.1675(2)
b / (Å)	24.3921(2)	23.7963(3)
c / (Å)	13.7237(1)	28.2467(4)
α / (°)	90.0	85.380(1)
β / (°)	97.047(1)	86.395(1)
γ / (°)	90.0	73.836(1)
V / ($Å^3$)	4502.06(6)	9108.6(2)
Z	2	4
D_c / (Mg m^{-3})	1.276	1.263
μ (MoKα) / (mm^{-1})	0.105	0.099
F (000)	1862	3736
data collection temp. / K	173(2)	173(2)
crystal size / (mm)	0.22 × 0.29 × 0.32	0.18 × 0.23 × 0.26
range scanned θ / °	1.00 – 25.35	1.00 – 24.71
index ranges ±h, ±k, ±l	−16:16; −29:28; −16:16	−16:16; −28:28; −33:33
reflections (total)	15799	62723
independent reflections	15799	62722
reflections with I > 2σ(I)	13657	38538
completeness (%)	99.0	98.8
no. of parameters	1088	3654
goodness-of-fit, S	1.028	1.023
R_1 [$I > 2\sigma(I)$]	0.0817	0.0853
wR on F^2	0.2266	0.2324
weighting scheme a, b in $w = 1/[\sigma^2(F_o^2) + (aP)^2 + (bP)]$	0.1665 , 2.8047	0.0960, 16.0732
$(\Delta/\sigma)_{mean}$	< 0.001	0.001
Δρ excursions / e $Å^{-3}$	−0.63 and 0.85	−0.42 and 0.83
CCDC deposition no.	CCDC 1428344	CCDC 1428345

3.6–24.3° for DIMEB dihydrate (CEQCUW) and 2.8–27.6° for DIMEB pentadecahydrate (CSD refcode BOYFOK04), confirming that complexation between 2ME and DIMEB does not cause untoward host distortion, but is instead associated with a more symmetrical macrocyclic shape.

On the the primary side of the DIMEB molecule, three of the torsion angles O5–C5–C6–O6 (*ω*) are (+)-*gauche* and four are (−)-*gauche*, while six of the C5–C6–O6–C9 torsion angles have a *trans* orientation, the exception being that for glucose G5, where the orientation is (+)-*gauche*. This combination results in the methoxymethyl chains on the primary side of the DIMEB molecule being significantly extended and thus providing space directly above the included 2ME molecule (Figure 2d and Figure 2e) that accommodates six components of disordered water molecules. The remaining four components reside outside the DIMEB cavity, where they engage in hydrogen bonding with oxygen atoms on the periphery of the host molecule.

Comparison of the conformation of the encapsulated 2ME molecule and that of the same molecule in its own crystal structure [9] shows that there is minimal difference, with a RMSD of only 0.084 Å and a maximum deviation between two equivalent atoms of 0.202 Å. (A graphical overlay of the molecules appears in the Supporting Information File 1). Thus, in the DIMEB inclusion complex, the steroid skeleton retains the same conformation as that recently observed in the crystal of 2ME, as well as in crystals of the solvated phase 2ME·$(CHCl_3)_2$ and the sulfamoylated derivative of 2ME, namely 2-methoxyestradiol-3,17-di,*O*-bis-sulfamate [9], the A-ring being planar (aromatic), the B-, C- and D-rings being a half-chair, a chair and a twist form (twisted on C13–C14) respectively. Thus, no

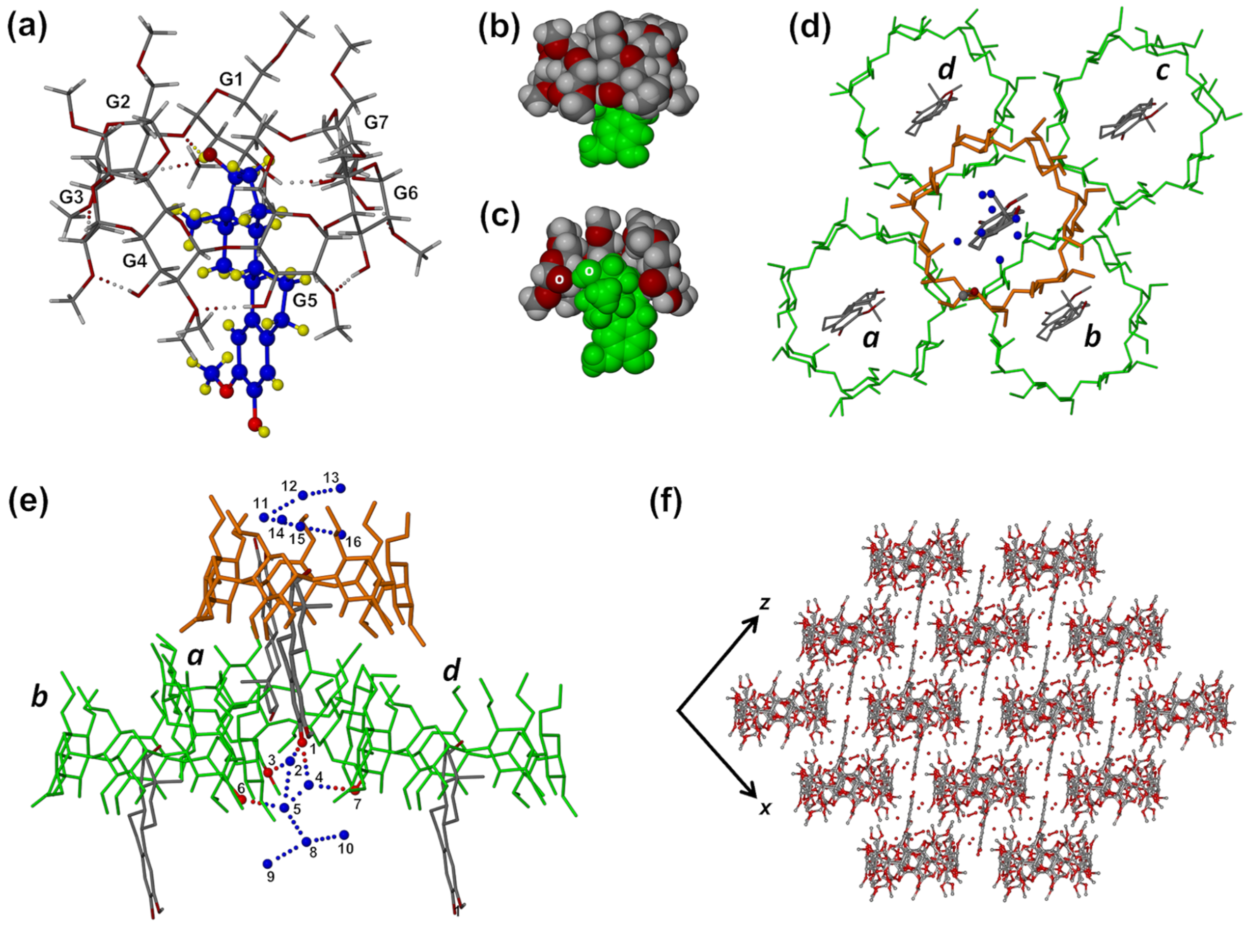

Figure 2: The mode of inclusion of 2ME in the DIMEB cavity (a), space-filling side view of the complex with the 2ME molecule in green (b) and cutaway view (c), location of the A-ring of 2ME protruding from the central DIMEB complex unit (orange) within the space created by the quartet of displaced neighbouring host molecules (d), H-bonding between the representative A-ring hydroxy group –O22–H and three neighbouring CD units mediated by water molecules (blue spheres) (e), and the extended packing arrangement viewed along [10] (f).

significant distortions of the host or guest conformations are evident as a result of inclusion of the 2ME molecule in the host DIMEB.

Protrusion of the A-ring of the 2ME molecule from the secondary side of the DIMEB host molecule leads to a unique crystal packing arrangement, details of which are shown in Figure 2d–f. The A-ring of the 2ME molecule in the central complex unit (Figure 2d) is located in an interstitial pocket at the juncture of four neighbouring complex units *a*–*d* in a layer below. As shown in Figure 2e, the A-ring phenolic group –O22–H is hydrogen bonded to a network of water oxygen atoms (blue spheres), three of which act as bridges to the three neighbouring CD molecules (see Table S2 in Supporting Information File 1, for the atom label key, all relevant O···O distances and symmetry operators). In summary, the phenolic group oxygen atom (labelled 1) is hydrogen bonded to water oxygens 2 and 4, which respectively hydrogen bond to O6G2 (3) of host molecule *a* and O3G7 (7) of host molecule *d*. Finally, the water cluster is hydrogen bonded to atom O3G4 (6) of host molecule *b* via water oxygen atom O2 (5). The A-ring is thus strongly tethered within the interstitial pocket. From Figure 2e it is also evident that the water clusters are located in the regions near the two hydrophilic terminals of the steroid molecule (namely the phenolic groups –O22–H on the A-ring and –O19–H on the D-ring). Each 2ME molecule is thus isolated from other 2ME molecules primarily by encapsulation within the DIMEB cavity, but also by hydrogen bonded water clusters that ‘cap’ the terminal rings. The unique layering that results in the extended crystal structure is shown in Figure 2f, a view along the [010] direction.

Methylation of the DIMEB molecule at the 3-position results in fully methylated β-CD (TRIMEB), the second crystalline derivatised CD investigated here for its potential to include the steroid 2ME. Permethylation of DIMEB has the drastic effect of eliminating the belt of O2(*n*)–H···O3(*n−1*) hydrogen bonds observed in that host molecule, so that the conformational constraints described above no longer apply to the resulting host TRIMEB. This indicates the distinct possibility of differences arising in the modes of inclusion of 2ME in TRIMEB relative to that observed in DIMEB, and this was indeed confirmed, as detailed below.

Whereas the crystal asymmetric unit of the DIMEB complex of 2ME comprises only a single (hydrated) DIMEB·2ME complex unit, the asymmetric unit in the crystal of the inclusion complex between TRIMEB and 2ME (TRIMEB·2ME), consists of four distinct 1:1 host–guest units, shown in the stereoview of Figure 3. Since the space group is *P*1, the asymmetric unit corresponds to the full unit cell content, implying also that each of the complex units A–D is unique, being unrelated to any other by crystallographic symmetry elements.

What is immediately evident from Figure 3 is that the gross features of the mode of 2ME inclusion appear to be essentially the same in all four complex units, the guest molecule entering the secondary side of the TRIMEB molecule, with the D-ring penetrating the cavity maximally, and with both the A-ring as well as a portion of the B-ring protruding from the host secondary side. Further examination of the arrangement of the complex units in Figure 3, however, indicates that the units A and B are very similar in structure and that they are spatially related by a translation of ≈*b*/2, the same translational relationship applying to the pair of complex units C and D. This feature of a 'pseudo-cell' having one or more lattice dimensions close to one-half of the true periodicity is common, and is often induced when a crystal initially at ambient temperature is cooled for X-ray data-collection. In the case of the TRIMEB·2ME complex, however, the unit cell dimensions of the crystal determined initially at 21 °C corresponded with those recorded at −100 °C, the temperature of the data-collection. During attempts to solve the structure, the presence of such a 'pseudo-cell' for the TRIMEB·2ME crystal was predicted from a preliminary examination of the X-ray diffraction pattern, which showed that the reciprocal lattice layers *hkl* with $k = 2n$ had significantly higher intensities than those with $k = 2n + 1$ (see Supporting Information File 1 for images of representative reciprocal lattice levels). Within the above temperature range, therefore, there are discernible structural differences among the four TRIMEB·2ME complex units, as detailed below, such differences being of interest in the context of 'mutually induced fitting' of host and guest during complexation [1].

Complex units A and B of TRIMEB·2ME, related by a pseudo-translation of ≈*b*/2, have nearly identical structural features, namely common TRIMEB host conformations and lack of host disorder, apparent twofold disorder of the 2ME methylene group at C6 (site-occupancy factors, s.o.f.s, 0.56 and 0.63 for the respective major components) and essentially the same mode of guest inclusion. (A full listing of these and other parameters is provided in Supporting Information File 1). A least-squares overlay of the host molecules A and B (see Supporting Information, File 1) yields a RMSD of only 0.157 Å and a maximum deviation between two equivalent atoms of 0.649 Å. In both cases, the phenolic group –O19–H of 2ME is hydrogen bonded to a common glycosidic oxygen atom, with O···O distances and O–H···O angles having values of 3.064(6) Å and

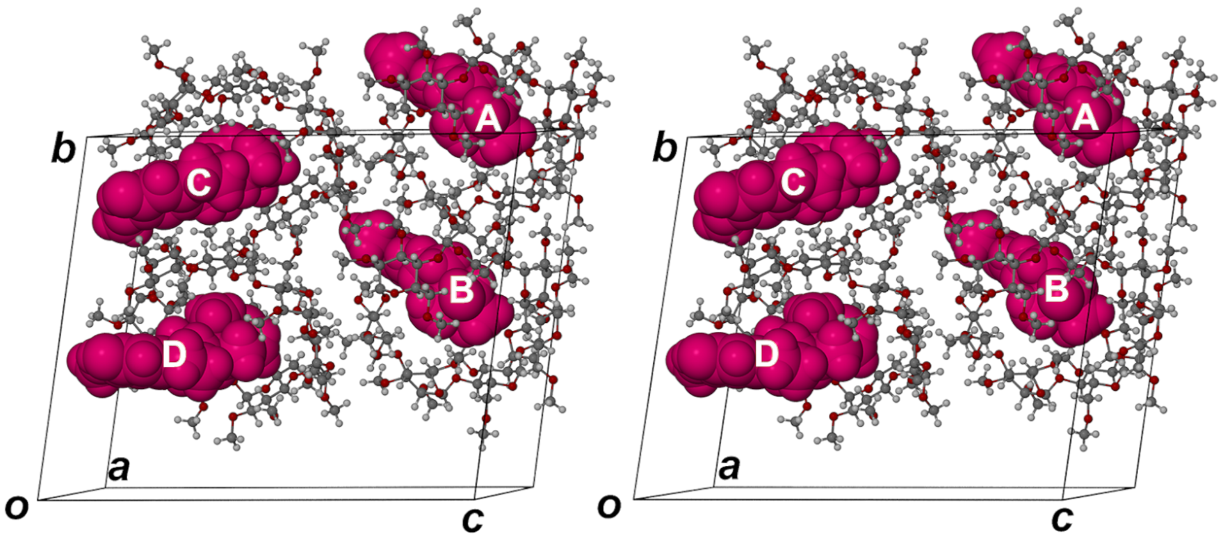

Figure 3: Stereoview of the asymmetric unit in the crystal of the inclusion complex TRIMEB•2ME, with the host TRIMEB molecules drawn in ball-and-stick representation and the guest 2ME molecules (magenta) in space-filling mode.

169° respectively for complex unit A, and 3.186(6) Å and 170° for unit B. Figure 4a, featuring complex unit A as representative, illustrates in space-filling mode the nature of the common guest inclusion mode in complex units A and B. This involves encapsulation of the C- and D-rings of 2ME within the host cavity while the A- and B-rings protrude from the secondary side of the TRIMEB molecule. The hydrogen bond that links the host and guest molecules is indicated in the cutaway view of Figure 4a.

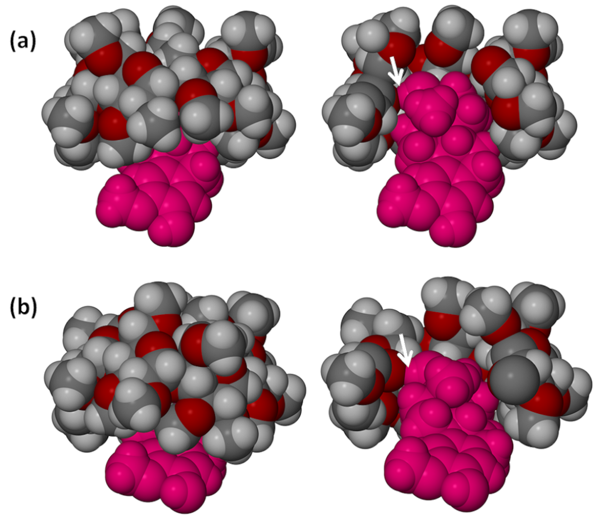

Figure 4: Space-filling images of complex unit A (as representative of units A and B) (a) and complex unit C (b) of TRIMEB·2ME. The images on the left show guest residues (magenta) protruding from the secondary side of the host molecule while the images on the right are cutaway views highlighting the common (guest)O19–H···O4(host) hydrogen bond, indicated by arrows.

In contrast to the symmetrical host in the DIMEB·2ME complex, where the $–C5–CH_2–O–CH_3$ residues on the primary side of the host are fully extended and the tilt angles of the glucose rings are not severe, the strong tilting of the glucose rings of the TRIMEB·2ME complex results in several of these residues being in close contact. This results in steric crowding of the primary methoxy groups, creating a bowl-like surface on the host primary side above the D-ring of the included 2ME molecule. Such a bowl-like surface was first observed for the host DIMEB [25] and was subsequently observed in numerous inclusion complexes of TRIMEB as well [16].

The host molecules in complex units C and D (also displaced by ≈*b*/2) are nearly isostructural, but differ significantly from the isostructural pair A and B, as indicated by the conformational parameters described earlier. The least-squares overlay of host molecules C and D reveals several differences in the torsional parameters of the primary methoxy residues (see Figure S15, Supporting Information File 1), which result in a RMSD of 0.819 Å and a maximum deviation of 3.417 Å between two terminal methoxy carbon atoms. Figure 4b illustrates in space-filling mode the inclusion of 2ME in host molecule C as representative. Guest inclusion again involves hydrogen bonding between the phenolic group O19–H and a host glycosidic O4 atom (O···O 2.894(6) Å). This is evident in the cutaway diagram in Figure 4b.

Complex unit C is unique in having neither host nor guest disorder and complex unit D also shows a unique feature, namely disorder in both the C- and D-rings of the 2ME molecule, which is thus present as two conformers in the ratio 0.61:0.39. One consequence of this is that there are two distinct positions for the O19–H phenolic group, each conformer forming a hydrogen bond with a different TRIMEB acceptor oxygen atom. Further details of this disorder and its implications are given below.

Another very significant feature is evident from comparing the structures of the TRIMEB·2ME and DIMEB·2ME complexes, namely the inclination of the mean plane of the included steroidal guest molecule relative to the mean O4-plane of the respective host molecule as reference (Figure 5). The interplanar angles listed in the caption contrast the relatively ‘shallow’ entry of the 2ME molecule into the secondary side of hosts A and B of TRIMEB with its nearly ‘vertical’ entry into the host DIMEB. Furthermore, the corresponding parameters for inclusion of 2ME in the TRIMEB hosts C and D are in the narrow range ≈45–49°, i.e., significantly different from the ≈60–61° observed for inclusion in TRIMEB host molecules A and B. Thus, inclusion of the 2ME molecule into the secondary sides of hosts C and D is even more ‘shallow’ than it is for the hosts A and B, consistent with the finding that these pairs of host molecules have significantly different conformations.

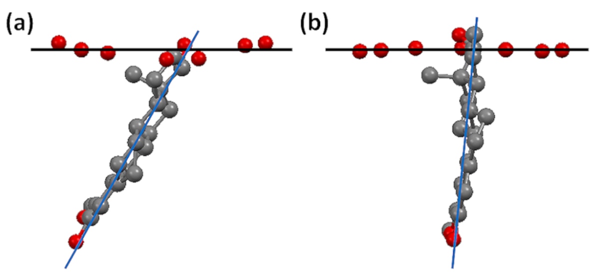

Figure 5: Inclination of the mean plane of the included 2ME molecule relative to the O4-heptagon of the host molecule in (a) complex unit A of TRIMEB·2ME, (b) the complex DIMEB·2ME. The respective interplanar angles are ≈60° and ≈84°.

The steroid molecules included in the respective complex units A–D are shown in Figure 6 where each is overlayed on the

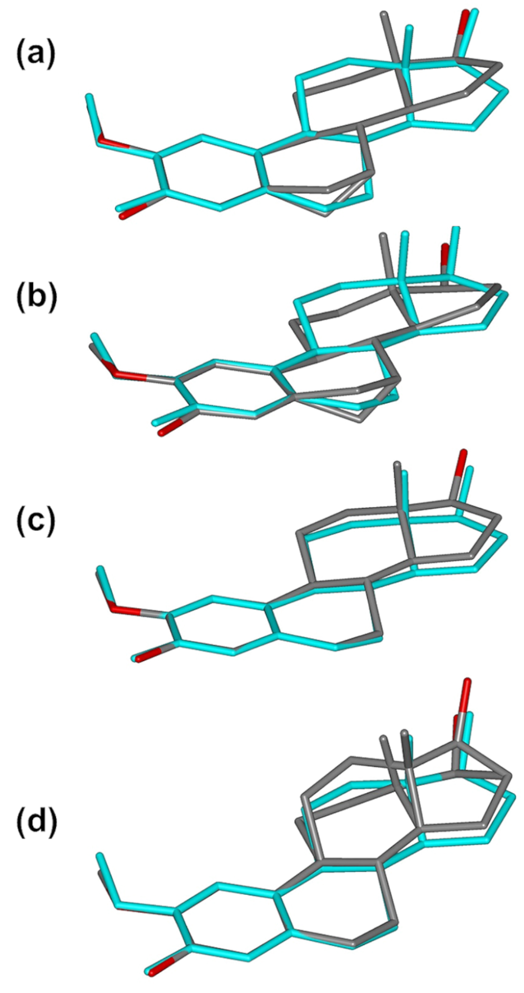

Figure 6: Overlay of the steroid nucleus of 2ME (blue) in its own crystal with the refined models (grey) of the four molecules of 2ME in the complex units A (a), B (b), C (c), D (d) of TRIMEB·2ME.

steroid nucleus taken from the crystal structure of 2ME alone [9], the comparison being based on maximum overlap of the A-ring (aromatic) atoms in each case. In the 2ME molecule itself, as the common reference, the B–D ring conformations are a half-chair (B-ring), a chair (C-ring) and a twist-form, twisted on C13–C14 (D-ring) [9]. The refined guest models in Figure 6a and Figure 6b are virtually identical, mirroring the close similarity of the conformations of their respective host molecules in complex units A and B. The methylene carbon atom C6 on ring B showed abnormally high thermal motion which could not be modelled satisfactorily with anisotropic displacement parameters; it was therefore treated as a ‘split’ atom, resulting in s.o.f. ratios of 0.44:0.56 and 0.37:0.63 for the disordered components of the C6-methylene group in 2ME molecules A and B. (In these cases, if the two discrete positions indicated for C6 were to be considered for this group, the B-ring conformations would resemble a chair and a twist-boat form, rather than a half-chair).

Ring C adopts a chair conformation (Figure 6a and Figure 6b), while the D-ring is a twist form (twisted on C13-C14). The net result is that the modelled 2ME molecules in complex units A and B have a conformation which is significantly distorted relative to that of the 2ME molecule in its own crystal.

As shown in Figure 6c, the modelled 2ME molecule in complex unit C of the TRIMEB·2ME structure is unique in displaying no evidence of disorder, with the conformations of the B-, C- and D-rings being a half-chair, a chair and a twist form (twist on C13–C14) respectively. While the individual ring conformations correspond with those of 2ME in its own crystal, the overall conformations are clearly not identical, but very close. The conformation of the refined 2ME model in Figure 6c is also very close to that of the 2ME molecule in the DIMEB·2ME complex, with a least-squares fit having a RMSD vaue of 0.083 Å and a maximum atomic deviation of 0.161 Å (see Supporting Information File 1 for graphical overlay).

It was noted above that the least-squares overlay of host molecules A and B yielded a considerably smaller RMSD (0.157 Å) than the overlay of host molecules C and D (0.819 Å). Accordingly, the conformation of the modelled 2ME molecule in complex unit D differs from that in complex unit C. Specifically, in complex unit D (Figure 6d) the steroid molecule displays significant disorder of both the C- and D-rings, the C-ring adopting as major component the chair form (s.o.f. 0.61) and as minor component a slightly twisted chair (s.o.f. 0.39), while the D-ring adopts as major component a twist-form (twisted on C13D–C14D) and as minor component an envelope (flap on C17F) with respective s.o.f.s as for ring C. An interesting consequence of the presence of two guest conformers in complex unit D is that the disordered components of the 17-OH group are separated by ≈1.5 Å, one as the major component (s.o.f. 0.61) and the other as the minor, with s.o.f. 0.39 and these –OH groups are donors in different guest–host hydrogen bonds. This feature is illustrated in Figure 7, where the respective H-bonds indicated are as follows: **1** – (major component O19D)–H···O6D5 with O···O 3.07(1) Å and O–H···O angle 152°; **2** – (minor component O19F)-H···O4D5 with O···O 2.96(2) Å and O-H···O angle 172°.

The structures of the hydrated DIMEB·2ME and the TRIMEB·2ME complexes presented here illustrate for the first time details of the encapsulation of a ‘classical’ steroidal molecule by cyclodextrin hosts. In addition, from the variety of host and guest conformations observed in the TRIMEB·2ME complex, even in one crystal, it is evident that complex formation

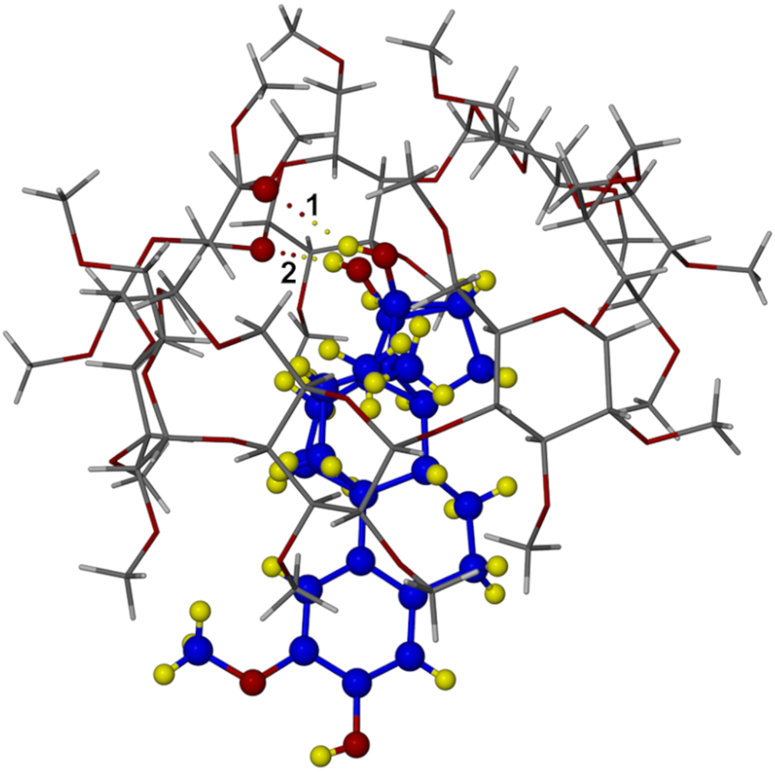

Figure 7: The TRIMEB·2ME complex unit D with two distinct (guest)O19-H···O(host) hydrogen bonds highlighted. To distinguish the host and guest, C and H atoms of 2ME are coloured blue and yellow respectively.

involves some degree of 'mutually induced fit' of host and guest [1,26].

Enhancement of the solubility of 2ME by selected CDs

One of the objectives of our study of the anticancer agent 2ME was to investigate methods of improving its aqueous solubility (S_o = 0.005 mg/cm^3 at 25 °C [9]) which might in turn enhance its poor bioavailability [4,5]. A factor which limited investigation to the relatively simple initial analysis reported here was the prohibitive cost of synthesis of 2ME and hence the paucity of material available. This precluded our carrying out, e.g., full phase-solubility analyses, which would have yielded additional information such as the values of the association constants for complex formation in solution. Thus instead, the simpler expedient of determining the solubility of 2ME in a series of aqueous solutions of both native and derivatised cyclodextrins of known concentrations (typically 2% m/v) was initially employed in order to estimate solubility enhancement factors (S_{CD}/S_o, where S_{CD} is the solubility of 2ME in the CD solution at the same temperature). This parameter has been used previously to gauge the ability of a range of CDs to solubilise drugs with poor aqueous solubility [27]. The cyclodextrins employed and the resulting apparent solubilities relative to that of 2ME in water are summarised in Table 2.

Interestingly, with the exception of TriEtBCD, all of the CDs tested yielded some improvement in 2ME solubility. Of the native CDs, γ-CD was the most efficient solubiliser for 2ME, a result which is consistent with earlier studies for a variety of steroidal guests [28]. However, the best enhancement was achieved with the derivatised CDs DIMEB, RAMEB, HPBCD and TRIMEB. As γ-CD, RAMEB and HPBCD are more pharmaceutically acceptable [29], they therefore appear to be media with potential use in medicinal applications requiring elevated concentrations of 2ME.

Comparative dissolution rate studies at 37 °C using the rotating basket method with samples in gelatin capsules were also carried out for pure 2ME and various preparations containing β-CD and 2ME (Figure 8), namely the hydrated 2:1 inclusion complex obtained by co-precipitation, two physical mixtures (pm) of β-CD and 2ME (molar ratios 1:1 and 2:1), and the hydrated 2:1 inclusion complex obtained by kneading (kn). Of all the preparations tested, 2ME in the form of its β-CD inclusion complex, prepared by both co-precipitation and kneading,

Table 2: Solubility enhancement factors[a] for 2ME with various cyclodextrins at 25 °C.

cyclodextrin	CD solution concentration (% *m*/*v*)	solubility enhancement factor S_{CD}/S_o
α-CD	2	7.5
β-CD	2	10
γ-CD	2	86
RAMEB (randomly methylated β-CD)	2	156
DIMEB (heptakis(2,6-di-*O*-methyl)-β-CD)	2	256
TRIMEB (heptakis(2,3,6-tri-*O*-methyl)-β-CD)	2	23
HPBCD (hydroxypropyl-β-CD)	2	88
TRIMEA (hexakis(2,3,6-tri-*O*-methyl)-α-CD)	0.5	4
TriAcBCD (triacetyl-β-CD)	0.002	8
TriAcGCD (triacetyl-γ-CD)	0.0025	2
TriEtGCD (triethyl-γ-CD)	0.002	0.84

[a]All experimental data were compared with those for a control and were based on triplicate measurements.

yielded the most rapid and complete dissolution, the times for attaining the 100% level being 15 and 45 minutes, respectively. This performance significantly outweighed that of the untreated 2ME, for which the percentage dissolved attained a maximum level of only 25–32% after 15 minutes. The dissolution of 2ME from physical mixtures of β-CD and 2ME was evidently hindered by the presence of the cyclodextrin, an effect that increased with the concentration of β-CD present.

Comparative dissolution profiles were also recorded for 2ME in physical mixtures with the native cyclodextrins β- and γ-CD as well as RAMEB and HPBCD (Supporting Information File 1). While only 30% of untreated 2ME dissolved in water after 20 minutes, the equimolar γ-CD/2ME physical mixture yielded a value of ≈55% during the same period. Furthermore, after three hours, the level had risen to 80%. In contrast, the other CD/2ME mixtures produced relatively small effects on the release of 2ME. It was concluded that the γ-CD/2ME physical mixture had potential as a vehicle for formulation of a controlled release form of 2ME.

Finally, it was considered of interest to compare the dissolution profile of the inclusion complex $(\beta\text{-CD})_2\cdot 2ME$ (shown in Figure 8 to be very favourable) with those for a series of

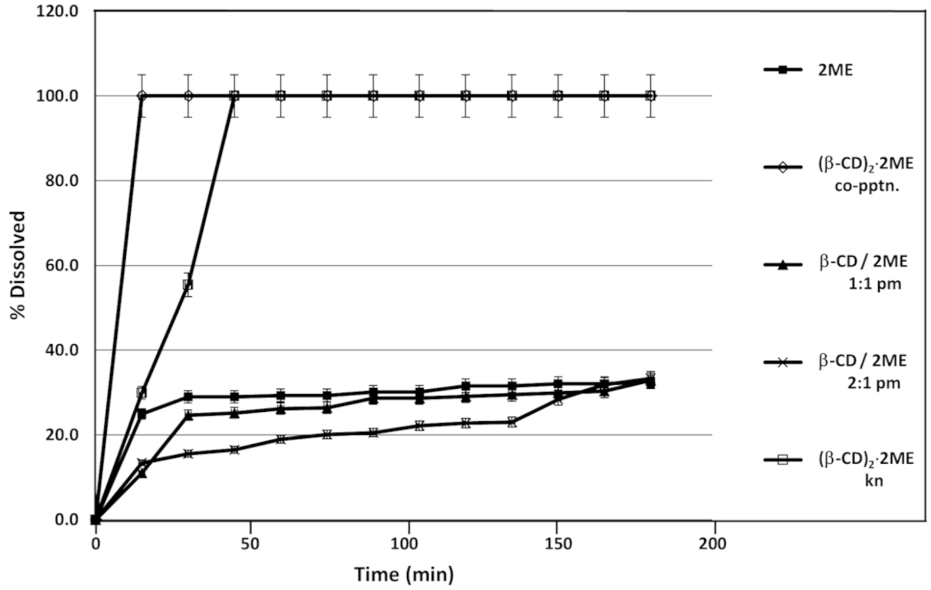

Figure 8: Dissolution profiles in water at 37 °C for untreated 2ME and various β-CD-containing preparations of 2ME.

2ME/CD samples resulting from kneading (kn) (Supporting Information File 1). This series included the products of kneading in 1:1 molar ratios each of the combinations 2ME with α-CD, with β-CD and with γ-CD, as well as the 1:1 inclusion complexes HPBCD·2ME and RAMEB·2ME. All of these preparations led to rapid dissolution of 2ME. In particular, both the γ-CD/2ME and the RAMEB/2ME samples resulted in 100% of the 2ME concentration being attained 15 min after the commencement of the dissolution run, as found also for the complex $(\beta\text{-CD})_2 \cdot 2\text{ME}$. All of these preparations displayed superior dissolution characteristics to those of untreated 2ME, only 30% of which dissolved in the same medium within 20 minutes.

Conclusion

Single crystal X-ray diffraction has revealed the modes of inclusion of the potent anticancer agent 2-methoxyestradiol (2ME) in two representative host CD molecules, one of them (DIMEB) having restricted conformational flexibility owing to cooperative intramolecular O–H···O hydrogen bonding that maintains the round shape of the macrocycle, and the other (TRIMEB) lacking this facility and hence having access to significantly greater conformational freedom. Accordingly, in the case of the complex DIMEB·2ME, while the host molecule is relatively undistorted on inclusion of 2ME, the guest molecule maintains the conformation that it displays in its own crystal structure. Instead, in the case of the TRIMEB·2ME complex, the four independent 1:1 host–guest units in the crystal display a variety of host distortions as well as guest conformational variation, reflecting a mutually induced fit accompanying complexation. The phenomenon of mutually induced fit was highlighted previously by Mavridis et al. for per-derivatised CDs and especially in the case of TRIMEB [30]. The TRIMEB·2ME complex is thus another example of a synthetic system that displays host–guest adaptation on complexation, complementing our recently reported analogous observations for inclusion complexes between methylated CDs and the antioxidant *trans*-resveratrol [26]. Hydrogen bonding between the 17-OH group of 2ME and glycosidic (O4) oxygen atoms within the cavity of the host CDs generally occurs, while in unit D of the TRIMEB complex, where there are two 17-OH disorder components, the major component hydrogen bonds to a host methoxy O6 atom and the minor to a host glycosidic oxygen atom. The results presented here are of general interest in the context of CD–steroid interaction, with special reference to estranes that contain a 17-OH function (e.g., the estrogen sex hormone 17β-estradiol).

Previous studies of the anticancer activities of 2ME have indicated that its low aqueous solubility and rapid metabolism lead to poor bioavailability [4,5]. However, the effect of various CDs on the aqueous solubility of 2ME has hitherto not been assessed. In this study, we have shown via a variety of in vitro experiments that CDs can enhance 2ME aqueous solubility very significantly and conclude that they warrant consideration as potential vehicles for facilitating both further biological testing of 2ME in anticancer studies as well as the development of alternative dosage forms of 2ME.

Experimental

Materials

2-Methoxyestradiol (2ME, $C_{19}H_{26}O_3$) was generously provided by Shimoda Biotech (Pty) Ltd (Port Elizabeth, South Africa). Synthesis of the sample of 2ME from commercially available 17β-estradiol was reported earlier [9]. The following cyclodextrins (CDs) were purchased from Cyclolab (Budapest, Hungary) and were used as received: α-CD, β-CD, γ-CD, hexakis(2,3,6-tri-*O*-methyl)-α-CD, heptakis-(2,6-di-*O*-methyl)-β-CD, heptakis(2,3,6-tri-*O*-methyl)-β-CD, randomly methylated β-CD, heptakis(2,3,6-tri-*O*-ethyl)-β-CD, heptakis(2,3,6-tri-*O*-acetyl)-β-CD and octakis(2,3,6-tri-*O*-acetyl)-γ-CD. All other materials and solvents used were of analytical reagent grade.

Complex preparation

The inclusion complex $(\beta\text{-CD})_2 \cdot 2\text{ME} \cdot 12.6\text{H}_2\text{O}$ was generated within 45–60 min via the manual kneading technique with the host and guest in a 2:1 molar ratio and using only water as liquid medium. The same crystalline phase was obtained by co-precipitation, which involved vigorous stirring at 60 °C of an aqueous solution containing the host and guest in a 2:1 molar ratio. Slow cooling yielded single crystals of the inclusion complex. Complexation between 2ME and the amorphous hosts RAMEB and HPBCD was achieved by kneading (as above) but with a 1:1 host–guest molar ratio.

The crystalline inclusion complex DIMEB·2ME was prepared as follows. A 44.00 mg (0.033 mmol) sample of DIMEB and 10 mg (0.033 mmol) of 2ME were placed in 3 cm^3 of distilled water and the suspension was stirred vigorously over a period of 24 h at ambient temperature (18–25 °C). The resulting solution was filtered (0.45 μm nylon microfilter) and then placed on a hot plate set at 60 °C. After several days, large block-like single crystals appeared and were harvested for analysis. Identical procedures were successfully employed to isolate single block-like crystals of the TRIMEB inclusion complex of 2ME, TRIMEB·2ME, the only difference being the mass of the host compound TRIMEB (44.27 mg, 0.033 mmol).

Thermal analysis

HSM was performed on a Linkam TH MS600 hot stage connected to a Linkam TP92 temperature control unit. Images were captured by a real-time Sony Digital Hyper HAD colour video camera coupled to a Nikon SMZ-10 stereoscopic microscope. The Soft Imaging system, analySIS [31] was used to process the images.

For TGA a Mettler Toledo TGA/SDTA851e instrument was employed with a nitrogen gas purge (flow rate 30 cm^3/min). Indium (mp 156.6 °C) and aluminium (mp 660.3 °C) were used for all calibrations. Accurately weighed samples (mass range 2–5 mg) were placed in an open porcelain pan and were heated at 10 K/min.

For DSC studies, a Perkin-Elmer PC-7 series thermal analysis system was used, with a a nitrogen gas purge (flow rate 30 cm^3/min). Temperature calibration was achieved using the onset temperatures of fusion of indium (156.6 °C) and zinc (419.5 °C). The heat flow calibration was based on the value of ΔH of fusion of indium (28.62 J/g). Samples in the form of fine powders (mass range 2–5 mg) were sealed in crimped, vented aluminium pans and were heated at 10 K/min, with a sealed, empty pan as reference.

FTIR spectroscopy

A Perkin-Elmer 100 FTIR instrument fitted with UATR and controlled with Spectrum® software for sample analysis was used to record the infrared spectra of crystalline and amorphous powders in the range 400–4000 cm^{-1}.

UV–visible spectrophotometry

Spectra were recorded on a Beckman DU® 640 series UV–vis spectrophotometer operating at a scan rate of 1200 nm/min over the range 190–450 nm with solutions for analysis placed in 2 mm quartz cuvettes. For CD inclusion compounds of 2ME, host–guest stoichiometries were determined at the absorption maximum for the bioactive compound (λ_{max} = 198.5 nm) in methanol/water (1:1 v/v) solution. This instrument was also used for solubility and dissolution rate assays (details below).

Single crystal X-ray diffraction analysis

Intensity data were collected on a Nonius Kappa CCD diffractometer using graphite-monochromated Mo Kα-radiation (λ = 0.71073 Å), with each crystal coated in Paratone oil (Exxon Chemical Co., TX, USA), mounted on a cryoloop and cooled to 173(2) K in a constant stream of nitrogen vapour (Oxford Cryostream, UK).

Due to the fact that both the DIMEB·2ME and the TRIMEB·2ME inclusion complexes had no previously published isostructural counterparts [16], their structures were solved using ab initio direct methods (program SHELXD [22]) and their refinement by full-matrix least-squares followed with program SHELXH-97 [22] operating under the X-Seed interface [32]. For the DIMEB·2ME structure, with a single complex formula unit DIMEB·2ME in the asymmetric unit, all non-H atoms refined anisotropically except O19 on the D-ring of the 2ME molecule, two disordered methyl groups and several partial water molecules that resulted from the 5.3 water molecules per complex unit being located over ten sites. The former showed excessive thermal motion that was not amenable to standard anisotropic treatment while the disordered water oxygen atoms did not warrant anisotropic treatment. A minor, but unexpected feature of the DIMEB inclusion complex, was partial methylation of the O3-H hydroxy group of the host glucose ring G1 (s.o.f. = 0.5 for the resulting $-CH_3$ residue). While this contribution did not lead to any abnormally short intermolecular contacts, such a contact was observed elsewhere, specifically between a disordered methyl group component (s.o.f. 0.5) on residue G6 and a methyl group on glucose residue G7 of a neighbouring host molecule. This necessitated reduction of the s.o.f. of the latter methyl group from 1.0 to 0.5. The net effect was that despite partial methylation of O3–H on G1, appropriate modelling of disordered residues resulted in retention of the nominal formula for the DIMEB molecule, namely $C_{56}H_{98}O_{35}$. The structure of TRIMEB·2ME, with four distinct complex units in the asymmetric unit, was modelled with anisotropic thermal parameters for all atoms except (a) the carbon atoms of the glucose rings, which refined with relatively low values for their U_{iso} values (range 0.024–0.053 $Å^2$) and showed no evidence of anisotropic motion in difference Fourier syntheses, and (b) ten atoms of the 2ME molecules with partial occupation. Despite the resulting significant reduction in the number of U_{ij} least-squares parameters, the final structural model was based on full-matrix refinement of as many as 3644 parameters. Hydrogen atoms were sought in difference Fourier syntheses and a large proportion of these could be located. All of the H atoms were included in idealised positions in a riding model with U_{iso} values in the range 1.2–1.5 times those of their parent atoms. Further details of the data-reduction and least-squares refinements for the complexes appear in the CIF files. CCDC 1428344 and 1428345 contain the supplementary crystallographic data for this paper. These data can be obtained free of charge at http://www.ccdc.cam.ac.uk/products/csd/request/ [or from the Cambridge Crystallographic Data Centre (CCDC), 12 Union Road, Cambridge CB2 1EZ, UK; fax: +44(0)1223-336033; email: deposit@ccdc.cam.ac.uk].

Solubility and dissolution rate measurements

Aqueous solutions of a series of native and derivatised CDs with pre-determined fixed concentrations were prepared at 25 °C. Following their saturation with 2ME, assaying of the 2ME concentration in the filtered solutions was performed using UV spectrophotometry at 198 nm, with solutions appropriately diluted to ensure that the absorbance values were in the range 0 to 1. A standard calibration curve of absorbance as a function of 2ME concentration was employed. Solubility enhancement factors for the steroid were calculated as S_{CD}/S_o, where S_{CD} is the maximum concentration of 2ME in each CD solution in mg/cm^3 and S_o is the aqueous solubility of 2ME in water at 25 °C (viz. 0.005 mg/cm^3 at 25 °C).

Dissolution studies were carried out using the rotating basket method with samples in gelatin capsules and employing the procedures and instruments we described previously [9]. Recording of dissolution profiles was performed in triplicate. UV spectrophotometric anaysis of 2ME followed the procedure already described above. Analysis of variance (ANOVA) methods were used to discriminate dissolution profiles.

Supporting Information

Supporting Information File 1

Additional data.
[http://www.beilstein-journals.org/bjoc/content/supplementary/1860-5397-11-281-S1.pdf]

Acknowledgements

Members of the Centre for Supramolecular Chemistry Research who were involved in the study reported here express their thanks to the National Research Foundation (Pretoria) and the University of Cape Town for research support. Any opinion, findings and conclusions or recommendations expressed in this material are those of the authors and therefore the NRF does not accept any liability in that regard.

References

1. Sawada, T.; Hisada, H.; Fujita, M. *J. Am. Chem. Soc.* **2014,** *136,* 4449–4451. doi:10.1021/ja500376x
2. Dubey, R. K.; Imthurn, B.; Jackson, E. K. *Endocrinology* **2007,** *148,* 4125–4127. doi:10.1210/en.2007-0514
3. Verenich, S.; Gerk, P. M. *Mol. Pharmaceutics* **2010,** *7,* 2030–2039. doi:10.1021/mp100190f
4. LaVallee, T. M.; Burke, P. A.; Swartz, G. M.; Hamel, E.; Agoston, G. E.; Shah, J.; Suwandi, L.; Hanson, A. D.; Fogler, W. E.; Sidor, C. F.; Treston, A. M. *Mol. Cancer Ther.* **2008,** *7,* 1472–1482. doi:10.1158/1535-7163.MCT-08-0107
5. Peyrat, J.-F.; Brion, J.-D.; Alami, M. *Curr. Med. Chem.* **2012,** *19,* 4142–4156. doi:10.2174/092986712802430072
6. Kulke, M. H.; Chan, J. A.; Meyerhardt, J. A.; Zhu, A.; Abrams, T. A.; Blaszkowsky, L. S.; Regan, E.; Sidor, C.; Fuchs, C. S. *Cancer Chemother. Pharmacol.* **2011,** *68,* 293–300. doi:10.1007/s00280-010-1478-7
7. Bruce, J. Y.; Eickhoff, J.; Pili, R.; Logan, T.; Carducci, M.; Arnott, J.; Treston, A.; Wilding, G.; Liu, G. *Invest. New Drugs* **2012,** *30,* 794–802. doi:10.1007/s10637-010-9618-9
8. Leese, M. P.; Leblond, B.; Smith, A.; Newman, S. P.; Di Fiore, A.; De Simone, G.; Supuran, C. T.; Purohit, A.; Reed, M. J.; Potter, B. V. L. *J. Med. Chem.* **2006,** *49,* 7683–7696. doi:10.1021/jm060705x
9. Caira, M. R.; Bourne, S. A.; Samsodien, H. *J. Pharm. Sci.* **2015,** *104,* 3418–3425. doi:10.1002/jps.24545
10. Pinto, M. P.; Medina, R. A.; Owen, G. I. *Horm. Cancer* **2014,** *5,* 274–283. doi:10.1007/s12672-014-0181-2
11. Samsodien, H. Supramolecular derivatives of selected bioactive compounds: a physicochemical study. Ph.D. Thesis, Department of Chemistry, University of Cape Town, Dec 2010.
12. Frömming, K.-H.; Weyermann, I. *Arch. Pharm.* **1972,** *305,* 290–299. doi:10.1002/ardp.19723050412
13. Frömming, K.-H.; Weyermann, I. *Arzneim. Forsch.* **1973,** *23,* 424–426.
14. Uekama, K.; Fujinaga, T.; Hirayama, F.; Otagiri, M.; Yamasaki, M. *Int. J. Pharm.* **1982,** *10,* 1–15. doi:10.1016/0378-5173(82)90057-6
15. Vergeichik, Y. N.; Kompantseva, Y. V.; Gavrilin, M. V.; Ovcharenko, L. P. *Khim.-Farm. Zh.* **1993,** *27,* 58–59.
16. *Cambridge Structural Database and Cambridge Structural Database system,* Version 5.36; Cambridge Crystallographic Data Centre, University Chemical Laboratory: Cambridge, United Kingdom, 2015.
17. Bom, A.; Bradley, M.; Cameron, K.; Clark, J. K.; van Egmond, J.; Feilden, H.; MacLean, E. J.; Muir, A. W.; Palin, R.; Rees, D. C.; Zhang, M.-Q. *Angew. Chem., Int. Ed.* **2002,** *41,* 265–270. doi:10.1002/1521-3773(20020118)41:2<265::AID-ANIE265>3.0.CO;2-Q
18. de Boer, H. D. *J. Crit. Care* **2009,** *24,* 36–42. doi:10.1016/j.jcrc.2008.08.004
19. Volkov, S.; Kumprecht, L.; Buděšínský, M.; Lepšík, M.; Dušek, M.; Kraus, T. *Org. Biomol. Chem.* **2015,** *13,* 2980–2985. doi:10.1039/C4OB02464H
20. Caira, M. R. *Rev. Roum. Chim.* **2001,** *46,* 371–386.
21. Caira, M. R.; Bourne, S. A.; Mhlongo, W. T.; Dean, P. M. *Chem. Commun.* **2004,** 2216–2217. doi:10.1039/B408660K
22. Sheldrick, G. M. *Acta Crystallogr., Sect. A* **2008,** *64,* 112–122. doi:10.1107/S0108767307043930
23. Aree, T.; Saenger, W.; Leibnitz, P.; Hoier, H. *Carbohydr. Res.* **1999,** *315,* 199–205. doi:10.1016/S0008-6215(99)00033-6
24. Sanger, W. In *Inclusion Compounds;* Davies, J. L.; Atwood, J. E. D.; MacNicol, D. D., Eds.; Academic Press: London, United Kingdom, 1984; Vol. 2, pp 231–259.
25. Steiner, T.; Saenger, W. *Carbohydr. Res.* **1995,** *275,* 73–82. doi:10.1016/0008-6215(95)00148-M
26. Trollope, L.; Cruickshank, D. L.; Noonan, T.; Bourne, S. A.; Sorrenti, M.; Catenacci, L.; Caira, M. R. *Beilstein J. Org. Chem.* **2014,** *10,* 3136–3151. doi:10.3762/bjoc.10.331
27. Frömming, K.-H.; Szejtli, J. *Cyclodextrins in Pharmacy;* Topics in Inclusion Science, Vol. 5; Springer: Berlin, Germany, 1994; pp 22–23. doi:10.1007/978-94-015-8277-3
28. Schmid, G. Chapter 1. In *New Trends in Cyclodextrins and Derivatives;* Duchêne, D., Ed.; Editions de Santé: Paris, France, 1991; pp 40–41.
29. European Medicines Agency, Committee for Human Medicinal Products (CHMP). Draft Report EMA/CHMP/333892/2013: Background review for cyclodextrins used as excipients. http://www.ema.europa.eu/docs/en_GB/document_library/Report/2014/12/WC500177936.pdf (accessed Sept 26, 2015).
30. Makedonopoulou, S.; Yannakopoulou, K.; Mentzafos, D.; Lamzin, V.; Popov, A.; Mavridis, I. M. *Acta Crystallogr.* **2001,** *B57,* 399–409. doi:10.1107/S0108768101001963
31. *Digital Solutions for Imaging and Microscopy,* Version 3.1 for Windows; Soft Imaging System GmbH, 2000.

32. Barbour, L. J. *J. Supramol. Chem.* **2001,** *1,* 189–191. doi:10.1016/S1472-7862(02)00030-8

License and Terms

BEILSTEIN JOURNAL OF ORGANIC CHEMISTRY

Synthesis and photophysical characteristics of polyfluorene polyrotaxanes

Aurica Farcas*[1], Giulia Tregnago[2], Ana-Maria Resmerita[1], Pierre-Henri Aubert[3] and Franco Cacialli*[2]

Full Research Paper

Open Access

Address:
[1]Supramolecular Chemistry Group, "Petru Poni" Institute of Macromolecular Chemistry, Grigore Ghica Voda Alley, 700487-Iasi, Romania, [2]London Centre for Nanotechnology and Department of Physics and Astronomy University College London, Gower Street, London WC1E 6BT, UK and [3]Laboratoire de Physicochimie des Polymères et des Interfaces (EA 2528), Institut des Matériaux, Université de Cergy-Pontoise, F-95031 Cergy-Pontoise Cedex, France

Email:
Aurica Farcas* - afarcas@icmpp.ro;
Franco Cacialli* - f.cacialli@ucl.ac.uk

* Corresponding author

Keywords:
energy band gaps; fluorescence lifetimes; permethylated cyclodextrins; polyfluorene; polyrotaxanes

Beilstein J. Org. Chem. **2015,** *11,* 2677–2688.
doi:10.3762/bjoc.11.288

Received: 31 August 2015
Accepted: 04 December 2015
Published: 21 December 2015

This article is part of the Thematic Series "Superstructures with cyclodextrins: Chemistry and applications III".

Guest Editor: G. Wenz

Abstract

Two alternating polyfluorene polyrotaxanes (**3·TM-βCD** and **3·TM-γCD**) have been synthesized by the coupling of 2,7-dibromofluorene encapsulated into 2,3,6-tri-*O*-methyl-β- or γ-cyclodextrin (TM-βCD, TM-γCD) cavities with 9,9-dioctylfluorene-2,7-diboronic acid bis(1,3-propanediol) ester. Their optical, electrochemical and morphological properties have been evaluated and compared to those of the non-rotaxane counterpart **3**. The influence of TM-βCD or TM-γCD encapsulation on the thermal stability, solubility in common organic solvents, film forming ability was also investigated. Polyrotaxane **3·TM-βCD** exhibits a hypsochromic shift, while **3·TM-γCD** displays a bathochromic with respect to the non-rotaxane **3** counterpart. For the diluted $CHCl_3$ solutions the fluorescence lifetimes of all compounds follow a mono-exponential decay with a time constant of ≈0.6 ns. At higher concentration the fluorescence decay remains mono-exponential for **3·TM-βCD** and polymers **3**, with a lifetime $\tau = 0.7$ ns and 0.8 ns, whereas the **3·TM-γCD** polyrotaxane shows a bi-exponential decay consisting of a main component (with a weight of 98% of the total luminescence) with a relatively short decay constant of $\tau_1 = 0.7$ ns and a minor component with a longer lifetime of $\tau_2 = 5.4$ ns (2%). The electrochemical band gap (ΔE_g) of **3·TM-βCD** polyrotaxane is smaller than that of **3·TM-γCD** and **3**, respectively. The lower ΔE_g value for **3·TM-βCD** suggests that the encapsulation has a greater effect on the reduction process, which affects the LUMO energy level value. Based on AFM analysis, **3·TM-βCD** and **3·TM-γCD** polyrotaxane compounds exhibit a granular morphology with lower dispersity and smaller roughness exponent of the film surfaces in comparison with those of the neat copolymer **3**.

Introduction

Over the last decades, conjugated polymers (CPs) have been actively investigated as an alternative to conventional inorganic materials in many electronic applications due to their low cost and easy processability [1-6]. Among the various CPs, polyfluorenes (PFs) have been intensively studied as emitting materials owing to their pure blue emission [7-11]. However, some major drawbacks for their use are their high ionization potential associated with low photoluminescence (PL) efficiency, their rather large band gap and facile photochemical degradation [12,13]. Different strategies have been employed in view to reduce these undesirable effects, e.g., the synthesis of copolymers [14-17], block copolymers [18], the introduction of donor (D) and acceptor (A) moieties [19-21], or bulky substituents at the C-9 position of the fluorene units [22-24], incorporating PF moieties into zeolites [25], nanochannels [26], or by wrapping with amylose [27]. The past decade has witnessed remarkable innovations and progress in polymer science, including the field of supramolecular science as a complementary field, which offers great opportunity for new concepts, new materials with unique properties, and novel practical applications. The construction of polyrotaxane architectures has an impact on the polymer-chain behavior and subsequently generates smart functional polymeric materials [28-31]. Polyrotaxanes with conjugated polymers have attracted considerable attention over the last decades due to their architectures and topologies, but mostly because they provide an efficient strategy to achieve an “insulation” of individual molecular wires [30]. Additionally, the synthesis of such structures makes it possible to tune a large number of physicochemical properties of conjugated polymers [16-20,26-38]. The first step in the preparation of conjugated polyrotaxanes is the threading of macrocyclic compounds (hosts) onto linear chains (guests), when a thermodynamically unstable inclusion complex (IC) is obtained. A wide variety of host molecules have the ability to encapsulate the π-conjugated backbones into their cavities based on intermolecular interactions, and thus leading to ICs. Cyclodextrins (CDs) are by far the most intensively investigated macrocyclic molecules in the synthesis of such supramolecular architectures [39]. The second most investigated group of host molecules in the synthesis of conjugated polyrotaxanes is comprised of chemically-modified CDs. They are less hydrophilic than native CDs, and should exhibit a significantly increased ability to bind aromatic guests through ionic, ion-dipole, as well as hydrophobic interactions. CD liphophilic derivatives are more soluble in non-polar solvents and water and exhibit lower propensity to aggregate than native CDs [40-42]. Considering that larger hydrophobic CD surfaces can lead to increased interactions with the hydrophobic aromatic guest, several types of permodified CD derivatives, such as 2,3,6-tri-*O*-methyl-βCD (TM-βCD) or 2,3,6-tri-*O*-methyl-γCD (TM-γCD) have been synthesized in the course of our investigations.

With a view to better understand the influence of TM-βCD and TM-γCD encapsulations on the photophysical properties of PF, poly[2,7-(9,9-dioctylfluorene)-*alt*-2,7-fluorene/TM-βCD)] (**3·TM-βCD**) and poly[2,7-(9,9-dioctylfluorene)-*alt*-2,7-fluorene/TM-γCD)] (**3·TM-γCD**) polyrotaxanes have been synthesized. Thus, **3·TM-βCD** and **3·TM-γCD** have been obtained through the Suzuki cross-coupling reaction of 2,7-dibromofluorene (**1**) encapsulated into TM-βCD or TM-γCD cavities (**1·TM-βCD** and **1·TM-γCD)** with 9,9-dioctylfluorene-2,7-diboronic acid bis(1,3-propanediol) ester (**2**), as bulky stopper units [43]. The thermal, surface morphology, optical as well electrochemical characteristics of both polyrotaxanes were compared to those of the non-threaded **3** counterpart, Scheme 1.

Results and Discussion

In continuation of our interest on the exploration of photophysical properties of PF copolymers by supramolecular encapsulation, we have performed the present study by using liphophylic CD derivatives, such as TM-βCD and TM-γCD instead native β- or γCD [43-45], or TMS-γCD [46]. Therefore, **3·TM-βCD** and **3·TM-γCD** polyrotaxanes were synthesized by Suzuki coupling of **1** being in the form of its IC (**1·TM-βCD** or **1·TM-γCD)** with **2** followed by the termination of the growing chains by bromobenzene, Scheme 1. To have the reference the neat copolymer **3** was also synthesized by coupling **1** with **2** under similar reaction conditions (Scheme 1).

TM-βCD and TM-γCD macrocyclic molecules were prepared according to previously reported procedures [47]. **1·TM-βCD** and **1·TM-γCD** were synthesized in water by using a 2:1 molar ratio of macrocycles and monomer **1**. The synthesis of **1·TM-βCD** or **1·TM-γCD** in polar protic solvents is driven by hydrophobic interactions in combination with electrostatic, van der Waals or π–π interactions. In comparison, in polar aprotic solvents such as DMF, THF relies mostly on host–guest specific interactions, such as dispersion or dipole–dipole interactions.

As results of the encapsulation into TM-βCD and TM-γCD cavities compared to native CDs [43-45], i.e., the use of toluene as solvent medium instead of a 3:1 v/v toluene/DMF mixture led to compounds soluble in toluene, THF, CH_2Cl_2 (DCM), and $CHCl_3$. **3·TM-βCD** due to its higher coverage showed 7% water solubility. In addition, better optical quality films could be prepared by spin-coating from **3·TM-βCD** and **3·TM-γCD** THF, DCM, and $CHCl_3$ solutions.

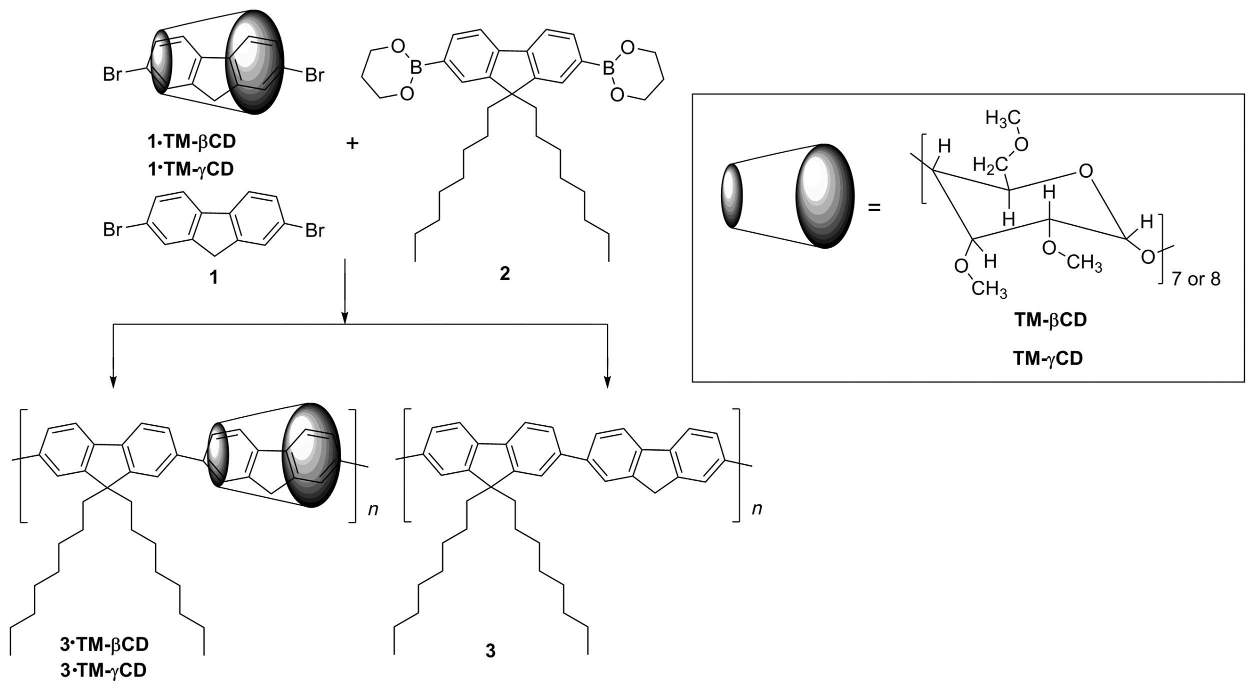

Scheme 1: Synthetic route of **3·TM-βCD** and **3·TM-γCD** polyrotaxanes, and the non-rotaxane counterpart **3**.

The investigated guest **1** proved binding ability to the hosts TM-βCD and TM-γCD, according to our determination of constant stability (K_s), which was performed by UV–vis absorption in $CHCl_3$. Changes in the absorption intensity of **1** at 321 nm in the presence of increasing concentrations of TM-βCD or TM-γCD provides the values of K_s, Figures S1 and S2 in Supporting Information File 1. The analysis data shows that K_s could be approximately around 580 ± 100 and 160 ± 30 M^{-1} for **1·TM-βCD** and **1·TM-γCD**, respectively. K_s values of TM-βCD encapsulation were higher than that of TM-γCD, due to its more favorable dimensional compatibility.

Characterization of these compounds has been performed using FTIR and NMR spectroscopy. Figure S3 in Supporting Information File 1 gives the FTIR spectra of both polyrotaxanes and the reference **3**. FTIR of encapsulated compounds **3·TM-βCD** and **3·TM-γCD** reveals a distinct vibration peaks located in 1159–1042 cm^{-1} region due to the presence of TM-βCD or TM-γCD, whereas the reference **3** does not show any absorption peaks in this interval. Consequently, the disappearance of the characteristic peaks in 1159–1042 cm^{-1} region in the FTIR spectrum of reference **3** evidences the presence of macrocycles on **3·TM-βCD** and **3·TM-γCD**, well consistent with ^1H NMR results.

As expected, the ^1H NMR spectrum of **3·TM-βCD** polyrotaxane exhibits correlation peaks of both H3 and H5 protons of TM-βCD with those methylene protons (H_d) protons of monomer **2**, and all the characteristic protons have been identified, Figure 1. Figures S4–S7 in Supporting Information File 1 show the ^1H NMR and ^{13}C NMR spectra of **3·TM-γCD** and the reference **3**.

The resonance peak of the d proton from monomer **2** is upfield shifted by more than 0.06 ppm in the polyrotaxane **3·TM-βCD** compared to those of the non-rotaxane **3** counterpart, as shown in Figure 1 and Figure S4 in Supporting Information File 1. The resonance peaks of a–c and a'–c' protons of **3·TM-βCD** rotaxane copolymer are also upfield shifted by 0.05 ppm as compared to those of the non-rotaxane homologue, while all protons of the TM-βCD macrocycle are shifted by more than 0.07 ppm. Comparing the integrals of d' protons from monomer **1** to those corresponding to H1 protons of TM-βCD, the average number of coverage per repeating unit has been calculated. By using the ratio of the integrated area of the H1 from TM-βCD (5.13–5.12 ppm, $I_{H\text{-}1}$) and the methylene proton peaks of the monomer **1** (4.11–4.09 ppm, $I_{d'}$); $(I_{H\text{-}1}/7)/(I_{d'}/2)$ the coverage ratio was found to be of about 0.26 (i.e., ca. 26% coverage) suggesting that about every three structural unit was threaded with TM-βCD macrocycle. However, compared with native CD [43,45], ^1H NMR results suggest poor hydrophobic–hydrophobic interactions of molecule **1** towards TM-βCD. Unfortunately, as a consequence of the low K_s of **1·TM-γCD**, the polyrotaxane **3·TM-γCD** presented only 11% coverage. The physical properties of the investigated copolymers are listed in Table 1.

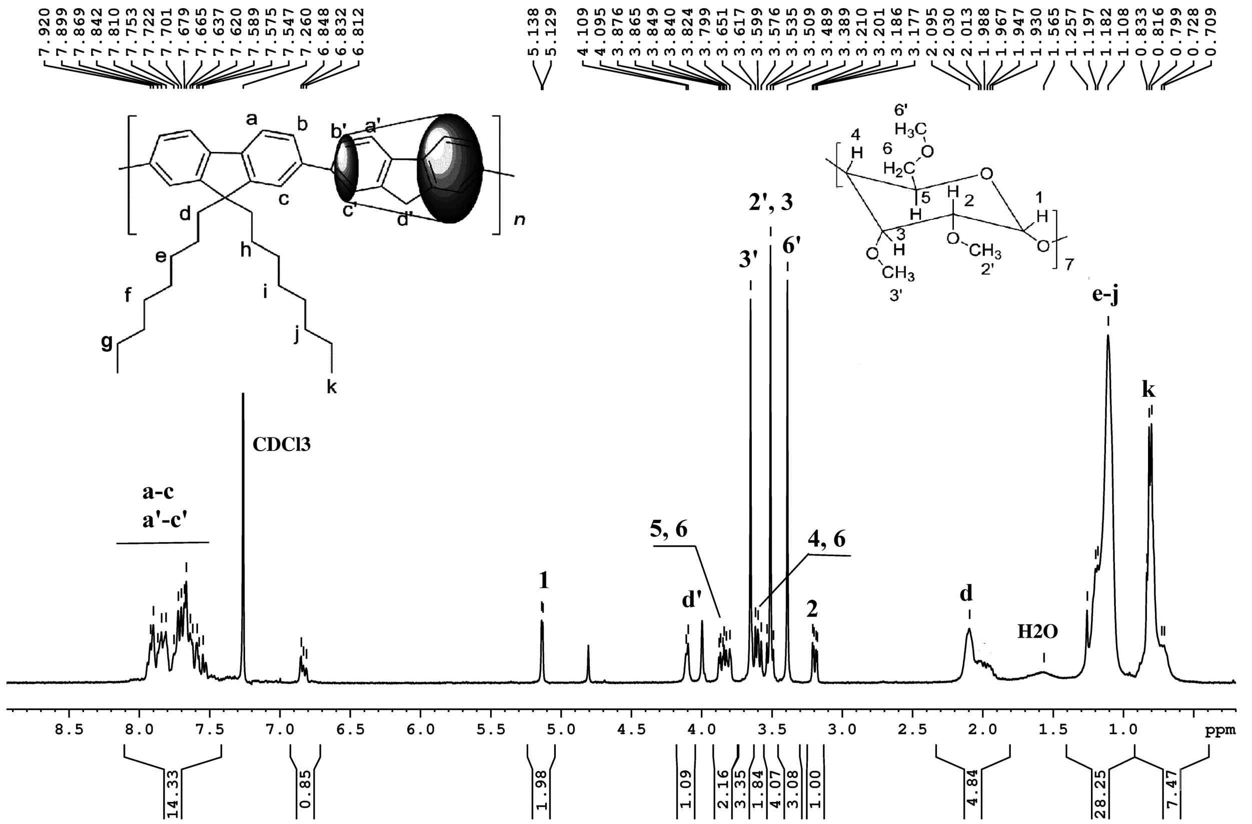

Figure 1: ^{1}H NMR spectrum of the polyrotaxane **3·TM-βCD** copolymer in $CDCl_3$.

Table 1: Physicochemical characteristics of **3**, **3·TM-βCD** and **3·TM-γCD**.

Sample	M_n[a]	M_w/M_n[b]	Coverage[c] (%)	T_g[d] (°C)
3	27900	1.83	—	88
3·TM-βCD	24300	1.94	26	104
3·TM-γCD	20100	2.24	11	96

[a]Number average molecular weight determined by GPC, THF, Polystyrene (Pst) standards. [b]Polydispersity index. [c]Average number of macrocycles /structural units, determined from ^{1}H NMR analysis. [d]Glass-transition temperature estimated from the second-heating DSC measurements.

The polydispersity index (M_w/M_n) and molecular weight distributions (M_n) of polymers obtained by gel permeation chromatography (GPC) analysis using Pst standards and THF as eluent, are presented in Table 1. Two things should be noted here concerning the lower M_n of **3·TM-βCD** and **3·TM-γCD** polyrotaxanes than that of the neat copolymer **3**. Firstly, the less ability of ester groups from molecule **2** to partially penetrate the macrocyclic cavities in the condensation reaction due to the sterical hindrance of methyl groups [48]. Secondly, could be assigned to the differences of the hydrodynamic radii of the polyrotaxane rod-like backbones and standards. Furthermore, the polarity and backbone stiffness of polyrotaxanes can deviate strongly from those of Pst. The higher M_w/M_n of **3·TM-βCD** and **3·TM-γCD** polyrotaxanes than that of **3** non-rotaxane sample was assigned to the different content of threaded TM-βCD or TM-γCD on the copolymer chains (see incomplete coverage determined by ^{1}H NMR).

The thermal properties of the copolymers were evaluated by differential scanning calorimetry (DSC) and thermogravimetric analysis (TGA). All copolymers showed only glass-transitions (T_g) and not any exothermal crystallization peak characteristic of polymers containing 9,9-dioctyl-2,7-fluorene units (PFO) [49], Figure 2.

The non-rotaxane copolymer **3** has a T_g at 88 °C. The T_g value increases for **3·TM-γCD** and **3·TM-βCD** to 96 °C and 104 °C, with respect to that of the non-rotaxane counterpart. The threading of **1** backbone through the cavities gives a more rigid copolymer structures with increased T_g, as results of its encapsulation, Table 1. It should be mentioned, that increased threading leads to a higher T_g of the resulting **3·TM-βCD** polyrotaxane. The thermal stability of the copolymers was also investigated by TGA (not shown) and the TGA data revealed that all polymers were stable up to about 300 °C.

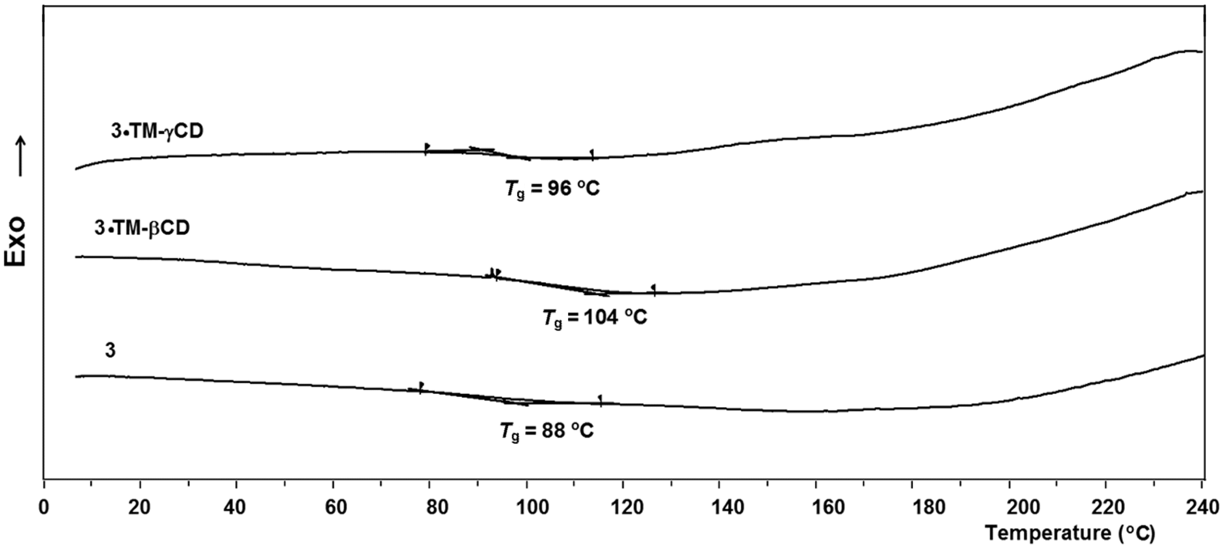

Figure 2: DSC traces on second heating scan of **3**, **3·TM-βCD** and **3·TM-γCD** compounds.

The absorption spectra of **3·TM-βCD** and **3·TM-γCD** polyrotaxanes and the unthreaded **3** counterpart at a concentration of 10^{-1} mg·mL^{-1} in $CHCl_3$ are reported in Figure 3a. The non-rotaxane **3** copolymer shows a featureless band peaking at 374 nm. Upon encapsulation with the TM-βCD, we note a hypsochromic shift of about 7 nm that can be attributed to a reduction of intermolecular interactions and/or a variation of the polarity when the PF core is inside the macrocycles' cavity. The **3·TM-γCD** polyrotaxane copolymer, instead, displays a red-shift of about 8 nm thereby suggesting the presence of some intrachain species. We consider such a red-shift however, not to be sufficient to infer the presence of fluorenone defects [24], although clear spectroscopic signature of the presence of such species can be gleaned from time-resolved photoluminescence efficiency (PL) experiments.

The PL spectra of the copolymers in $CHCl_3$ solutions at a concentration of 10^{-1} mg·mL^{-1} are reported in Figure 3b. The emission of the non-rotaxane **3** copolymer shows three vibronic components at about 418, 435 and 460 nm. The intensity of the 0–1 fluorescence band (435 nm) for diluted $CHCl_3$ solution is the most intense. At the same concentration, **3·TM-βCD** exhibited a slight blue-shift (2 nm) of the emission. The ratio of the emission intensity of the 0–0 transition for **3·TM-βCD** is higher than that of the 0–1 transition, contrary to what we observe for the non-rotaxane **3** counterpart. Such trends suggest that the encapsulation with the macrocycle TM-βCD acts to reduce intermolecular interactions, in agreement with previous reported results [50]. Interestingly, **3·TM-γCD** shows a much stronger 0–1 transition than the 0–0 one, as the non-rotaxane copolymer **3**, which might be indicative of some aggregation even though

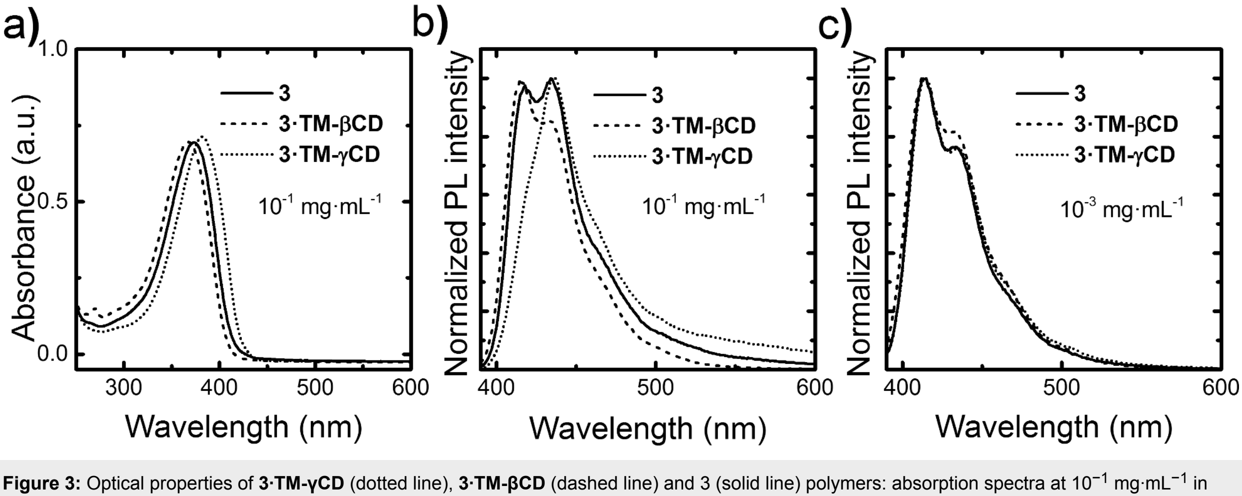

Figure 3: Optical properties of **3·TM-γCD** (dotted line), **3·TM-βCD** (dashed line) and 3 (solid line) polymers: absorption spectra at 10^{-1} mg·mL^{-1} in $CHCl_3$ (a), and normalized emission spectra at 10^{-1} mg·mL^{-1} and 10^{-3} mg·mL^{-1} in $CHCl_3$, (b) and (c), respectively.

we do not observe a strong tail in the 500–600 nm regions (apart from the minor red-shift mentioned earlier). We also note that such TM-γCD threaded polyrotaxanes and the unthreaded polymer have a similar PL emissions with the 0–0 the most intense transition for diluted solutions (10^{-3} mg·mL^{-1} in $CHCl_3$), as reported in Figure 3c. It appears that TM-βCDs are much more effective than TM-γCD at suppressing intermolecular interactions upon an increase of the polymer concentration. Such interpretation is also corroborated by the time-resolved PL spectroscopy. Indeed, we find that the temporal decays for the diluted solutions are mono-exponential with a time constant of ≈0.6 ns for the polyrotaxanes and the non-rotaxane polymer at a concentration of 10^{-3} mg·mL^{-1} in $CHCl_3$. However, at a concentration of 10^{-1} mg·mL^{-1} in $CHCl_3$, while the decay is still mono-exponential for **3** and **3·TM-βCD** polymers ($\tau \approx 0.7$ ns and 0.8 ns, respectively), **3·TM-γCD** polymer shows a bi-exponential decay with τ of 0.7 ns and 5.4 ns, with relative weights of 98 and 2%, respectively. The longer τ for the **3·TM-γCD** polyrotaxane is consistent with "interchain states". While these do not dominate the luminescence of the materials (the longer lifetime only accounts for 2% of the total PL weight), they are plausible, considered the significantly bigger size of the γCD**,** which might favor both unthreading of the cores, or even accommodation of more than one core unit within the macrocycles cavities. Poor suppression of interchain interactions by γCD had already been observed in the case of diphenylenevinylene rotaxanes, and it is therefore not surprising that we observe similar effects [33].

Interestingly, we measure a photoluminescence quantum efficiency (PLQE) of 66 ± 7% for the **3·TM-γCD**, 56 ± 6% for the **3·TM-βCD** and 46 ± 5% for the reference **3** polymer. Given the relatively large errors in these measurements the only conclusion we can draw is that the unthreaded materials is slightly less efficient than **3·TM-γCD**, but we consider we should not try to read too much into the difference in PL efficiency between **3·TM-γCD** and **3·TM-βCD**.

With a view to understand the factors that control the charge transport within and between conjugated macromolecular chains and the macrocycles, **3**, **3·TM-βCD** and **3·TM-γCD** were electrochemically investigated by cyclic voltammetry (CV), Figure 4 and the results are summarized in Table 2. The $E_{\text{p,onset}}$ and $E_{\text{n,onset}}$ values allow the estimation of the ionization potential (IP), electron affinity (EA) and energy band gap (ΔE_g) using ferrocene (Fc) as reference [51]. The IP, EA energy levels and ΔE_g were calculated according to Equations 1–3 [52,53].

$$E_{\text{HOMO}}(\sim \text{IP}) = -\text{e}\left(E_{\text{p,onset}} - 0.44\right) - 4.80\ (\text{eV}) \quad (1)$$

$$E_{\text{LUMO}}(\sim \text{EA}) = -\text{e}\left(E_{\text{n,onset}} - 0.44\right) - 4.80\ (\text{eV}) \quad (2)$$

$$\Delta E_g = (\text{EA} - \text{IP})\ (\text{eV}) \quad (3)$$

where: −4.80 eV represents the position of the Fc^+/Fc redox couple in the energetic diagram [51]; +0.44 V is the redox potential of Fc^+/Fc vs Ag.

As indicated in Table 2, during the *n*-doping process, polyrotaxane **3·TM-βCD** is reduced at a lower potential (−1.71 V) compared to the neat copolymer **3**, and the polyrotaxane **3·TM-γCD**, whose reduction potentials are attained at −1.79 V, and −2.02 V, respectively. The encapsulation of monomer **1** into TM-βCD or TM-γCD cavities appears to have a greater effect on the LUMO energy levels of **3·TM-βCD** and **3·TM-γCD** polyrotaxanes. Furthermore, these results suggest that TM-βCD may impose a more constrictive environment for the monomer **1** than TM-γCD, due to its smaller inner cavity diameter. Consequently there is the possibility for TM-γCD to move along on the monomer **1** backbone, until the stopper groups and these displacements to affect the LUMO energy level of the resulting **3·TM-γCD** polyrotaxane, see Table 2. By contrast, TM-βCD which is more localized on the monomer **1** backbone do not influence the LUMO energy level of **3·TM-βCD** compared to the reference **3**. Obviously, the LUMO energy value is responsible for the low value of ΔE_g in the case of **3·TM-βCD** polyrotaxane. Note that the redox behaviors of the investigated polyrotaxanes have a similar origin with those of the reference copolymer **3**. Close inspection of the electrochemical results suggest that all three investigated compounds exhibit typical semi-conducting properties, i.e., an insulating behavior in a wide range of potential between *n*- and *p*-doping processes.

As shown by the CV in Figure 4, **3·TM-βCD** exhibited three reduction peaks in the first CV scan at 0.0 V (very small), −1.0 V and at −1.8 V, respectively. The last one corresponds to the *n*-doping process. The peaks from 0.0 V and −1.0 V could be associated with the trapping of ionic charges into the polymer when the polymer returns to its neutral (insulating) state after the first CV scan, as previously reported [20]. Furthermore, these results suggest that the reduction process of **3·TM-βCD** displays a semi-reversible behavior.

The HOMO/LUMO energy levels in combination with the electronic potentials of the anodic indium tin oxide (ITO) glass substrate (−4.75 eV) and cathodic aluminum (−2.2 eV), prove that the investigated compounds are electrochemically accessible as electron-transporting materials for fabrication of organic light-emitting diodes (OLEDs) [54], Figure 4d.

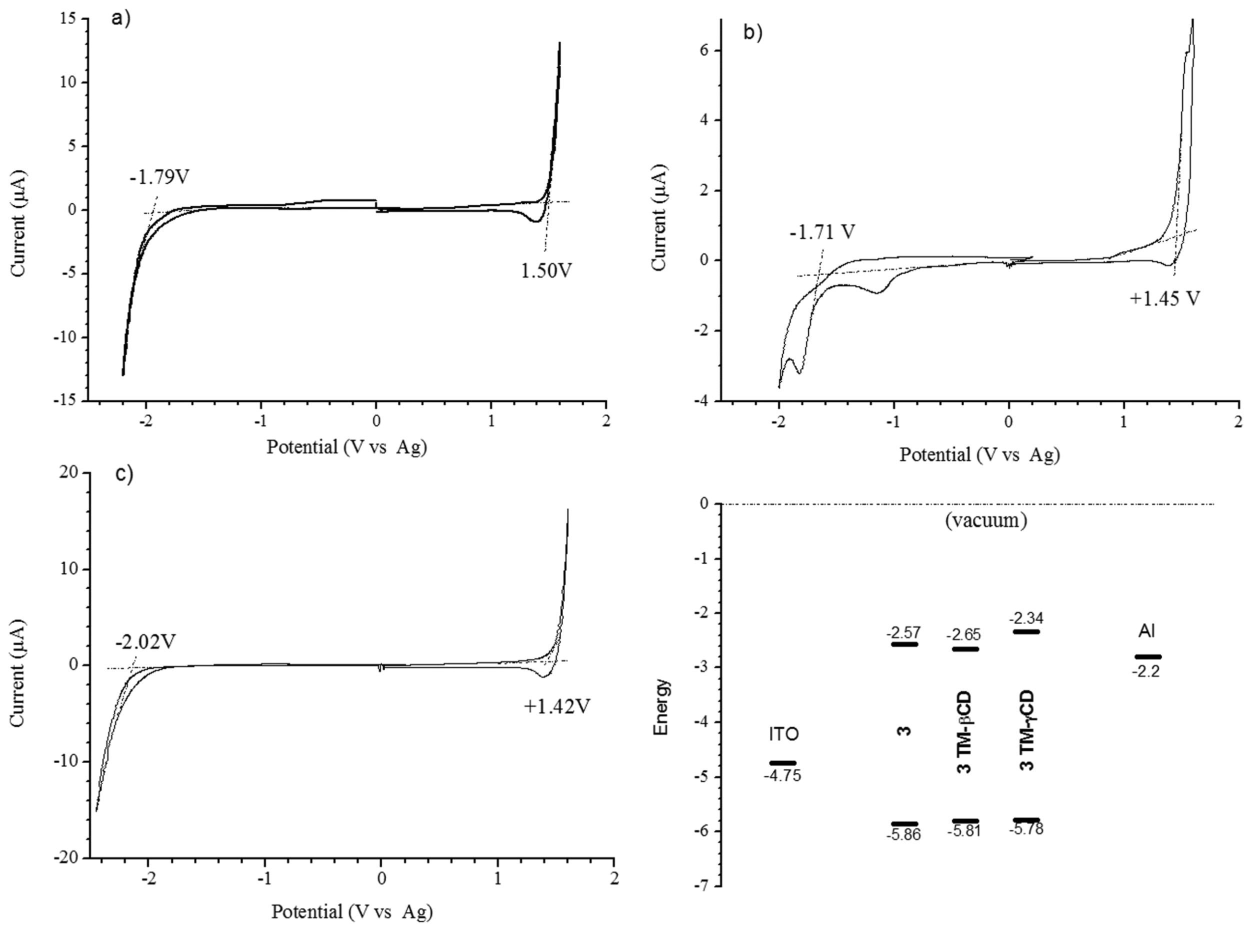

Figure 4: CV of **3** (a), **3·TM-βCD** (b) and **3·TM-γCD** (c) in 0.1 M tetrabutylammonium perchlorate (TBAClO$_4$)/ACN solution at scan rate 20 mV·s^{-1} and HOMO/LUMO energetic levels in addition to the work function of ITO (anode) and Al (cathode) (d).

Table 2: The electrochemical data for **3**, **3·TM-βCD** and **3·TM-γCD** copolymers.

Sample	**3**	**3·TM-βCD**	**3·TM-γCD**
Oxidation^a ($E_{p,onset}$) (V)	1.5	1.45	1.42
Reduction^b ($E_{n,onset}$) (V)	−1.79	−1.71	−2.02
E_{HOMO} ≈ IP^c (eV)	−5.86	−5.81	−5.78
E_{LUMO} ≈ EA^d(eV)	−2.57	−2.65	−2.34
ΔE_g^{e}(eV)	3.29	3.16	3.44

^{a}Oxidation onset potentials. ^{b}Reduction onset potentials. ^{c}$E_{HOMO} = -e(E_{p,onset} - 0.44) - 4.80$. ^{d}$E_{LUMO} = -e\ (E_{n,onset} - 0.44) - 4.80$ (eV). ^{e}Electrochemical band gap ($\Delta E_g = E_{LUMO} - E_{HOMO}$).

To gain further insights into the effect of macrocyclic encapsulations, it is also important to investigate the influence of the nature of host molecules on the induced chemical changes of the **3·TM-βCD** and **3·TM-γCD** polyrotaxane surfaces. Advancing contact angles (θ) values of water (polar) and diiodomethane (apolar) have been obtained for spin-coated copolymer films, Table 3. The smaller value of θ in water for **3·TM-γCD** (87°) with respect to the non-rotaxane counterpart **3** (100°) reflects its higher hydrophilicity attributed to TM-γCD encapsulation. A different behavior is observed for **3·TM-βCD** which prevented any contact angle measurements. This phenomenon should be attributed to the better dissolution of the spin-coated film of **3·TM-βCD** in water. As can be seen from Table 3, quite similar values were obtained in diiodomethane for the reference **3** and **3·TM-γCD** polyrotaxane. These results are typical of surfaces covered with a close packing of hydro-

Table 3: Advancing contact angle of water and diiodometane measured on spin-coated film of compounds.

Sample	θ(°)[a]	θ(°)[b]
3	100.1 ± 1.9	49.9 ± 0.3
3·TM-βCD	—[c]	43.5 ± 0.7
3·TM-γCD	87.3 ± 1.7	48.4 ± 0.8

[a] Water advancing contact angle. [b] Diiodomethane advancing contact angle. [c] Due to the dissolution of the spin-coated film, water advancing contact angles prevented any contact angle measurements.

carbon chains [55]. In contrast, a lower θ value is observed for **3·TM-βCD.** Such phenomenon represents a significant contribution of TM-βCD high coverage.

To further explore the effect of the TM-βCD and TM-γCD encapsulations, the surface topography of the copolymers was also investigated by atomic force microscopy (AFM) analysis. Some representative images obtained for the non-rotaxane **3**, **3·TM-βCD** and **3·TM-γCD** polyrotaxanes over 3 × 3 µm^2 areas, are shown in Figure 5 and the results are summarized in Table 4.

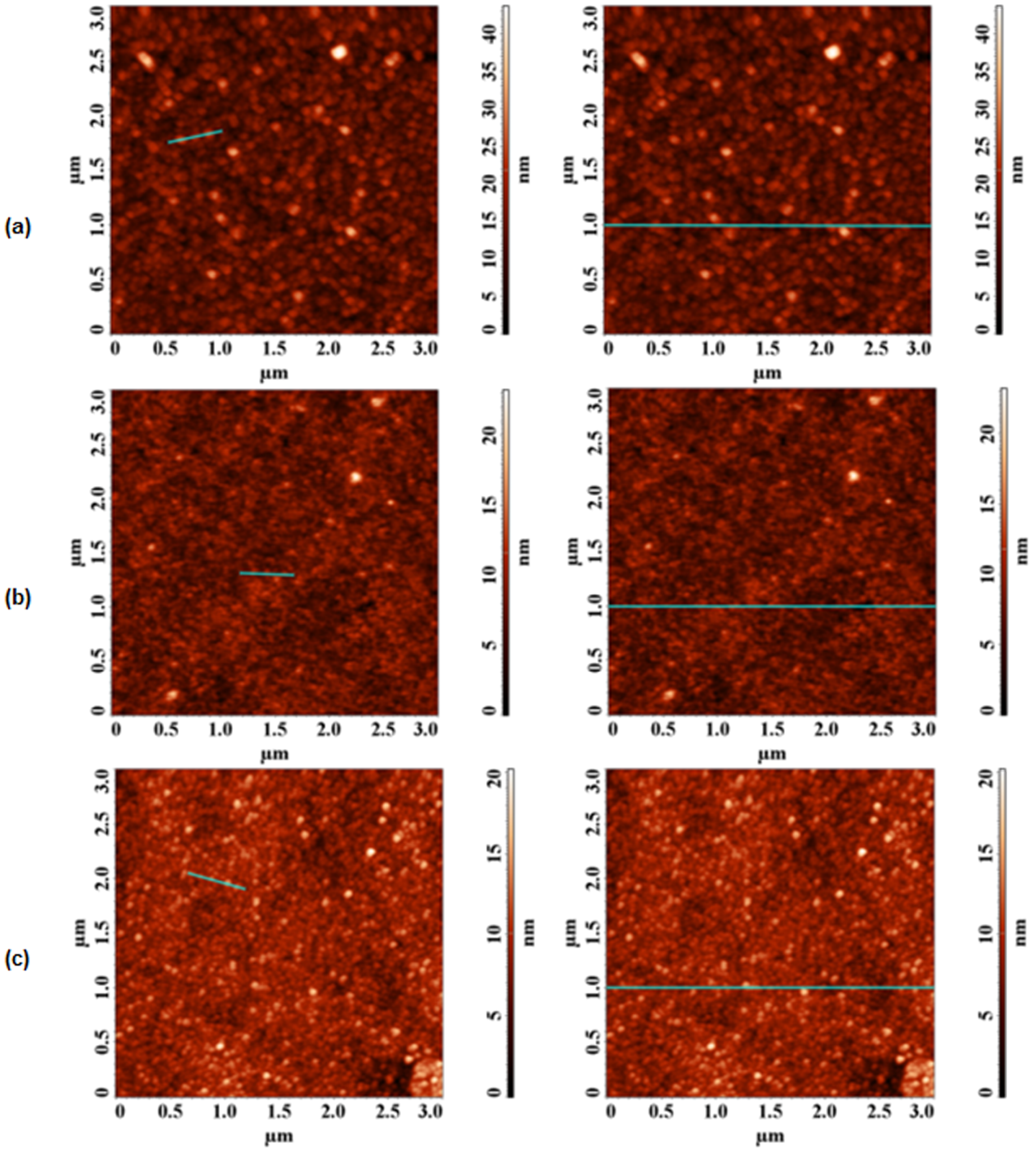

Figure 5: Representative AFM images obtained over 3 × 3 µm^2 areas of the non-rotaxane **3** (a), **3·TM-βCD** (b) and **3·TM-γCD** (c) polyrotaxanes.

Table 4: Roughness and grains parameters collected from 3 × 3 μm^2 AFM images of **3**, **3·TM-βCD** and **3·TM-γCD** thin films.

Sample	Surface roughness		
	Sy (nm)[a]	*Sq* (nm)[b]	*Sa* (nm) [c]
3	43.7	3.73	2.73
3·TM-βCD	21.3	1.76	1.35
3·TM-γCD	23.2	1.85	1.42

[a]Peak to valley height. [b]Root mean square roughness. [c]Average roughness.

As can be seen from Figure 5, the polyrotaxane film surfaces displayed granular morphologies with lower root mean square roughness *(Sq)* and average roughness (*Sa*) surface parameters compared to that of the non-rotaxane counterpart **3**. It should be note that the lower *Sq* and *Sa* values provide microscopic evidence of the changes in the surface topography of the encapsulated compounds.

Taking into account all the information obtained from AFM analysis, it can be concluded that the lower surface parameters clearly evidenced that the encapsulation with chemically-modified CDs leads to better film forming ability with a smoother surface.

Conclusion

TM-βCD or TM-γCD encapsulations of PF backbones lead to distinct improvements in the solubility and transparency of the solid films, increased glass-transition temperatures, enhancements of the surface characteristics. The optical investigations confirmed that the encapsulated compounds exhibited higher PLQE and fluorescence lifetimes. These complex architectures showed interesting electrochemical characteristics, which were consistent with optical and surface morphological results. The slightly lower ΔE_g value for **3·TM-βCD** suggests that the encapsulation have a greater effect on the reduction process, which affects the LUMO values. In addition, HUMO/LUMO energy levels proved that all copolymers are electrochemically accessible in an electroluminescence configuration cell. The present study is significantly valuable and informative as a method to built new conjugated polyrotaxanes by using permodified CD derivatives. Development of new polyrotaxane architectures should be beneficial especially in the field of materials for the generation of active layers in organic electronic devices.

Experimental

Materials and methods

1, **2**, tetrakis(triphenylphosphine)palladium(0) [$Pd(PPh_3)_4$], β- and γCD, bromobenzene (Br–Ph), dimethylformamide (DMF), dimethyl sulfoxide (DMSO), and quinine sulfate dehydrate in 0.5 M sulfuric acid were purchased from (Sigma-Aldrich) and used as received. $TBAClO_4$ for electrochemical analysis (99.0%) (Fluka) was used without further purification. Acetonitrile (ACN) (Fischer), DCM, $CHCl_3$, toluene and all other solvents were purchased from commercial sources (Sigma-Aldrich, Fisher) and used without further purification.

^{1}H NMR spectra have been recorded on a Bruker Avance DRX 400 MHz instrument equipped with a 5 mm QNP direct detection probe and z-gradients. Spectra have been recorded in $CDCl_3$ at room temperature. The chemical shifts are reported as δ values (ppm) relative to the residual peak of the solvent. The FTIR (KBr pellets) spectra were obtained on a Bruker Vertex 70 spectrophotometer. The molecular weights of copolymers were determined by GPC in THF by using a Water Associates 440 instrument and polystyrene (Pst) calibrating standards. DSC was performed with a Mettler Toledo DSC-12E calorimeter with two repeated heating–cooling cycles at a heating rate of 5 °C·min^{-1} under N_2 atmosphere. TGA analysis was performed under constant nitrogen flow (20 mL·min^{-1}) with a heating rate of 10 °C·min^{-1} using a Mettler Toledo TGA/SDTA 851e balance. UV–vis and fluorescence spectra in $CHCl_3$ solutions were performed using **3**, **3·TM-βCD** and **3·TM-γCD** with the same concentration (either 10^{-1} mg·mL^{-1} or 10^{-3} mg·mL^{-1}) of the **3** cores without macrocyclic molecules. Time-resolved photoluminescence (PL) measurements were performed with a time-correlated single photon counting (TCSPC) spectrometer previously reported [17]. The PLQE was estimated by comparison with a solution of quinine sulfate dehydrate in 0.5 M sulfuric acid of known quantum efficiency, 56 ± 5%.

CVs were carried out in a three-electrode cell in which Pt (1 mm diameter) was used as a working electrode, a Pt wire as counter-electrode and an Ag wire as pseudo-reference electrode. A $TBAClO_4$ solution (0.1 M) in anhydrous ACN was used as the supporting electrolyte. The set-up was introduced into a glove box and controlled by AUTOLAB PGSTAT 101 (Ecochemie) using NOVA software. The pseudo-reference was calibrated with a 10^{-3} M of Fc solution in ACN. The polymer samples were drop-casted onto the working electrode from a concentrated DCM solution and studied in the interval −2.5 and +2.0 V vs Ag wire. Cathodic and anodic scans were performed independently.

The surface profiles of copolymers films were evaluated by AFM measurements. AFM were performed in the tapping mode, using a Solver PRO-M scanning probe microscope (NTMDT, Russia) with commercially available NSG10 cantilever. Films were prepared onto mica substrates by spin-coating from $CHCl_3$ solution at 3000 rpm for 60 s on a

WS-400B-6NPP-Lite Single Wafer Spin Processor (Laurel Technologies Corporation, USA). Scan areas of 3 × 3 μm^2, were analyzed with a resolution of 512 × 512 pixels. Advancing and receding contact angle measurements were performed by using the drop shape analysis profile device equipped with a tiltable plane (DSA-P, Kruss, Germany). Ultrapure water (Millipore, resistivity = 18 MΩ·cm) or a diiodomethane drop was first deposited on the sample using a variable volume micropipette. The drop volume was set to 15 µL for water and 10 µL for diiodomethane. In order to perform dynamic contact angle measurements, the sample surface sustaining the drop was tilted at a constant speed (1 $deg \cdot s^{-1}$) and the images of the drop simultaneously recorded. The advancing contact angle was measured at the front edge of the drop, just before the triple line starts moving. The angle was obtained using the tangent of the drop profile at the triple line. For each sample, contact angles were measured on four samples and three drops per sample. The reported contact angle values correspond to the average of all measurements with an error bar corresponding to the standard deviation.

Synthesis of 2,3,6-tri-*O*-methyl-CD (TM-βCD) and 2,3,6-tri-*O*-methyl-CD (TM-γCD): TM-βCD and TM-γCD as macrocyclic molecules were synthesized according to previously reported procedure [47,48].

Synthesis of 1·TM-βCD: To prepare **1·TM-βCD** inclusion complex, 0.572 g (0.4 mmol) of TM-βCD were dissolved in water (5.0 mL) and 0.067 g (0.2 mmol) of **2** were added. The mixture was stirred at room temperature under nitrogen atmosphere for 48 h to give a turbid dispersion. The water was removed by lyophilization and the complex, as a white powder was used for the preparation of **1·TM-βCD**. The synthesis of the inclusion complex **1·TM-γCD** was performed under similar experimental conditions as those used for the preparation of the **1·TM-βCD** inclusion complex, except (0.654 g, 0.4 mmol) of TM-γCD was used instead of TM-βCD.

Synthesis of 3·TM-βCD and 3·TM-γCD polyrotaxane copolymers: **1·TM-βCD** (0.639 g, 0.2 mmol) and **2** (0.115 g, 0.2 mmol) were dissolved into 6 mL of toluene in a flask under argon (Ar) protection. The mixture was flushed with Ar several times, and then 1.5 mL of a 3 M solution of sodium carbonate (Na_2CO_3) and 18.2 mg of $(Ph_3P)_4Pd(0)$, as catalyst dissolved in 4 mL of degassed toluene were added into the flask. The solution was flushed with Ar again for another three times, and the reaction mixture was protected against light. The oil bath was heated to 90 °C, and the reaction mixture was stirred for 72 h. Then, an excess of 0.005 g (0.01 mmol) of monomer **2** dissolved in 3 mL of toluene was added and the reaction was continued for 12 h. Finally, 1.0 µL of Br-Ph was added as end-capper of the copolymer chain and the reaction was continued overnight. After cooling, the mixture was poured into water and extracted with toluene. The organic extracts were washed with water and dried over magnesium sulfate ($MgSO_4$). The toluene solution was concentrated by rotary evaporation and precipitated in CH_3OH. The solid was filtered, dried and purified by Soxhlet extraction with methanol and acetone in succession to remove the oligomers. The polymer was further purified by reprecipitation from concentrated $CHCl_3$ solution with methanol, collected by centrifugation and vacuum dried at 60 °C to afford **3·TM-βCD** (128 mg, 18.8% yield) as a yellow-brownish solid. ^1H NMR (400 MHz, $CDCl_3$) 7.92–7.55 (m, Ha–d and a'–d'), 6.85–6.81 (m, Ph), 5.13 (d, *J* = 3.6 Hz, 7H, C(1)H), 4.11–4.09 (m, Hg'), 3.88–3.80 (m, 14H, C(5)H, C(6)H), 3.65 (s, 21H, O(3')-CH_3), 3.62–3.58 (m, 14H, C(4)H, C(6)H), 3.54–3.49 (m, 28H, C(3)H, O(2')-CH_3), 3.39 (s, 21H, O(6')-CH_3), 3.19 (dd, *J* = 3.6 Hz, 7H, C(2)H), 2.10–1.93 (m, Hh), 1.26–1.11 (m, Hi-n), 0.83–0.71 (m, Ho); FTIR (KBr, cm^{-1}): 3433, 2927, 2853, 1724, 1614, 1459, 1410, 1357, 1159, 1091, 1042, 968, 875, 813 cm^{-1}; GPC (THF, Pst standard): M_n = 24300 $g \cdot mol^{-1}$, M_w/M_n = 1.94.

3·TM-γCD was synthesized by similar experimental conditions as described for **3·TM-βCD**, except that TM-γCD was used instead of TM-βCD. **3·TM-γCD** polyrotaxane was also obtained as a yellow-brownish solid in a 24.7% yield. ^1H NMR (400 MHz, $CDCl_3$) 7.92–7.38 (m, Ha–d and a'–d'), 6.91 (s, Ph), 5.26–5.02 (m, 7H, C(1)H), 4.1–3.25 (m, Hg', C(2–6)H, O(2',3',6')-CH_3), 2.11 (s, Hh), 1.11 (s, Hi–n), 0.81 (s, Ho); ^{13}C NMR (100 MHz, $CDCl_3$) 151.79–140.10 (C c, e, f, c', e', f'), 132.18–120.21 (C a, b, d, a', b', d'), 98.09 (C1), 82.11 (C2, 4), 71.04 (C5,6), 61.07–59.02 (C 2', 3', 6'), 55.41 (C g), 40.49 (C h), 37.18 (Cg'), 31.79 (Ci), 30.05–29.20 (Cj–m), 22.59 (Cn), 14.02 (Co); FTIR (KBr, cm^{-1}): 3416, 3058, 2923, 2850, 1634, 1610, 1457, 1405, 1373, 1291, 1095, 888, 810, cm^{-1}; GPC (THF, Pst standard): M_n = 20100 $g \cdot mol^{-1}$, M_w/M_n = 2.24.

Synthesis of the non-rotaxane 3 copolymer: The non-rotaxane copolymer **3** was synthesized under similar experimental conditions as those described for **3·TM-βCD** or **3·TM-γCD** polyrotaxanes, except that free monomer **1** was used instead of **1·TM-βCD** or **1·TM-γCD**. The crude polymer **3** was collected by filtration and then extracted with a Soxhlet extractor using methanol and acetone. Further the solid was redissolved in $CHCl_3$, precipitated with methanol, collected by filtration and vacuum dried at 50 °C. The copolymer was obtained as an orange solid in a yield of 47.8%. ^1H NMR (400 MHz, $CDCl_3$) 7.98–7.39 (m, Ha–d and a'–d'), 6.93–6.87 (m, Ph), 4.14–4.06 (m, Hg'), 2.16 (s, Hh), 1.16 (s, Hi–n), 0.86 (s, Ho); ^{13}C NMR (100 MHz, $CDCl_3$) 151.77–140.05 (C c, e, f, c', e', f'), 128.79–120.24 (C a, b, d, a', b', d'), 55.37 (Cg), 40.47 (Ch), 37.18 (Cg’), 31.79 (Ci), 30.04–29.21 (Cj–m), 22.60 (Cn), 14.06 (Co); FTIR (KBr, cm^{-1}): 3438, 3024, 2954, 2922, 2850, 1605, 1457, 1405, 1378, 1261,1196, 1092, 1023, 810 cm^{-1}; GPC (THF, Pst standard): M_n = 27900 g·mol^{-1}, M_w/M_n = 1.83.

Supporting Information

Supporting Information File 1

Characterization data of the compounds: The stability constant, FTIR, ^{1}H NMR and ^{13}C NMR spectra of the investigated copolymers.
[http://www.beilstein-journals.org/bjoc/content/supplementary/1860-5397-11-288-S1.pdf]

Acknowledgements

This research was supported by a grant of the Romanian National Authority for Scientific Research, CNCS – UEFISCDI, project number PN-II-ID-PCE-2011-3-0035. A. F. acknowledges financial support from Institute d`Etude Avancees (IEA), University of Cergy-Pontoise, France. Also, we are grateful to Prof. Sophie Cantin for advancing contact angles of water and diiodomethane measurements. We also thank the EC Seventh Framework Programme (FP7/2007-2013) under Grant Agreement No. 264694 (GENIUS), the EU Horizon 2020 Research and Innovation Programme under Grant Agreement N. 643238 (SYNCHRONICS), as well as the Royal Society and the EPSRC. FC is a Royal Society Wolfson Research Merit Award holder.

References

1. Chen, H.-Y.; Hou, J.; Zhang, S.; Liang, Y.; Yang, G.; Yang, Y.; Yu, L.; Wu, Y.; Li, G. *Nat. Photonics* **2009,** *3,* 649–653. doi:10.1038/nphoton.2009.192
2. Xue, J. *Polym. Rev.* **2010,** *50,* 411–419. doi:10.1080/15583724.2010.515766
3. Liang, Y.; Yu, L. *Polym. Rev.* **2010,** *50,* 454–473. doi:10.1080/15583724.2010.515765
4. Facchetti, A. *Chem. Mater.* **2011,** *23,* 733–758. doi:10.1021/cm102419z
5. Brédas, J.-L.; Norton, J. E.; Cornil, J.; Coropceanu, V. *Acc. Chem. Res.* **2009,** *42,* 1691–1699. doi:10.1021/ar900099h
6. Allard, S.; Forster, M.; Souharce, B.; Thiem, H.; Scherf, U. *Angew. Chem., Int. Ed.* **2008,** *47,* 4070–4098. doi:10.1002/anie.200701920
7. Leclerc, M. *J. Polym. Sci., Part A: Polym. Chem.* **2001,** *39,* 2867–2873. doi:10.1002/pola.1266
8. Ramsdale, C. M.; Barker, J. A.; Arias, A. C.; MacKenzie, J. D.; Friend, R. H.; Greenham, N. C. *J. Appl. Phys.* **2002,** *92,* 4266–4270. doi:10.1063/1.1506385
9. Xia, R.; Heliotis, G.; Bradley, D. D. C. *Appl. Phys. Lett.* **2003,** *82,* 3599–3601. doi:10.1063/1.1576906
10. Vasilopoulou, M.; Palilis, L. C.; Botsialas, A.; Georgiadou, D. G.; Bayiati, P.; Vourdas, N.; Petrou, P. S.; Pistolis, G.; Stathopoulos, N. A.; Argitis, P. *Phys. Status Solidi C* **2008,** *5,* 3658–3662. doi:10.1002/pssc.200780214
11. Inganäs, O.; Zhang, F.; Andersson, M. R. *Acc. Chem. Res.* **2009,** *42,* 1731–1739. doi:10.1021/ar900073s
12. Scherf, U.; List, E. J. W. *Adv. Mater.* **2002,** *14,* 477–487. doi:10.1002/1521-4095(20020404)14:7<477::AID-ADMA477>3.0.CO;2-9
13. Grimsdale, A. C.; Chan, K. L.; Martin, R. E.; Jokisz, P. G.; Holmes, A. B. *Chem. Rev.* **2009,** *109,* 897–1091. doi:10.1021/cr000013v
14. Lee, S. K.; Ahn, T.; Cho, N. S.; Lee, J.-I.; Jung, Y. K.; Lee, J.; Shim, H. K. *J. Polym. Sci., Part A: Polym. Chem.* **2007,** *45,* 1199–1209. doi:10.1002/pola.21892
15. Zhu, Y.; Gibbons, K. M.; Kulkarni, A. P.; Jenekhe, S. A. *Macromolecules* **2007,** *40,* 804–813. doi:10.1021/ma062445z
16. Farcas, A.; Resmerita, A.-M.; Stefanache, A.; Balan, M.; Harabagiu, V. *Beilstein J. Org. Chem.* **2012,** *8,* 1505–1514. doi:10.3762/bjoc.8.170
17. Farcas, A.; Tregnago, G.; Resmerita, A.-M.; Taleb Dehkordi, S.; Cantin, S.; Goubard, F.; Aubert, P.-H.; Cacialli, F. *J. Polym. Sci., Part A: Polym. Chem.* **2014,** *52,* 460–471. doi:10.1002/pola.27034
18. Jahanfar, M.; Tan, Y.; Tsuchiya, K.; Shimomura, T.; Ogino, K. *Open J. Org. Polym. Mater.* **2013,** *3,* 41–45. doi:10.4236/ojopm.2013.32007
19. Farcas, A.; Resmerita, A.-M.; Aubert, P.-H.; Stoica, I.; Farcas, F.; Airinei, A. *Beilstein J. Org. Chem.* **2014,** *10,* 2145–2156. doi:10.3762/bjoc.10.222
20. Farcas, A.; Janietz, S.; Harabagiu, V.; Guegan, P.; Aubert, P.-H. *J. Polym. Sci., Part A: Polym. Chem.* **2013,** *51,* 1672–1683. doi:10.1002/pola.26546
21. Mativetsky, J. M.; Kastler, M.; Savage, R. C.; Gentilini, D.; Palma, M.; Pisula, W.; Müllen, K.; Samorí, P. *Adv. Funct. Mater.* **2009,** *19,* 2486–2494. doi:10.1002/adfm.200900366
22. Chu, Z.; Wang, D.; Zhang, C.; Fan, X.; Tang, Y.; Chen, L.; Zou, D. *Macromol. Rapid Commun.* **2009,** *30,* 1745–1750. doi:10.1002/marc.200900268
23. Yang, C.; Song, H.-S.; Liu, D.-B. *J. Mater. Sci.* **2013,** *48,* 6719–6727. doi:10.1007/s10853-013-7473-8
24. Lim, S.-F.; Friend, R. H.; Rees, I. D.; Li, J.; Ma, Y.; Robinson, K.; Holmes, A. B.; Hennebicq, E.; Beljonne, F.; Cacialli, F. *Adv. Funct. Mater.* **2005,** *15,* 981–988. doi:10.1002/adfm.200400457
25. Calzaferri, G.; Huber, S.; Mass, H.; Minkowski, C. *Angew. Chem., Int. Ed.* **2003,** *42,* 3732–3758. doi:10.1002/anie.200300570
26. Sozzani, P.; Comotti, A.; Bracco, S.; Simonutti, R. *Angew. Chem., Int. Ed.* **2004,** *43,* 2792–2797. doi:10.1002/anie.200353479
27. Frampton, M. J.; Claridge, T. D. W.; Latini, G.; Broveli, S.; Cacialli, F.; Anderson, H. L. *Chem. Commun.* **2008,** 2797–2799. doi:10.1039/b803335h
28. Cacialli, F.; Wilson, J. S.; Michels, J. J.; Daniel, C.; Silva, C.; Friend, R. H.; Severin, N.; Samorì, P.; Rabe, J. P.; O'Connell, M. J.; Taylor, P. N.; Anderson, H. L. *Nat. Mater.* **2002,** *1,* 160–164. doi:10.1038/nmat750
29. Wenz, G.; Han, B.-H.; Müller, A. *Chem. Rev.* **2006,** *106,* 782–817. doi:10.1021/cr970027+
30. Frampton, M. J.; Anderson, H. L. *Angew. Chem., Int. Ed.* **2007,** *46,* 1028–1064. doi:10.1002/anie.200601780

31. Harada, A.; Hashidzume, A.; Yamaguchi, H.; Takashima, Y. *Chem. Rev.* **2009,** *109,* 5974–6023. doi:10.1021/cr9000622
32. Petrozza, A.; Brovelli, S.; Michels, J. J.; Anderson, H. L.; Friend, R. H.; Silva, C.; Cacialli, F. *Adv. Mater.* **2008,** *20,* 3218–3223. doi:10.1002/adma.200800007
33. Oddy, F. E.; Brovelli, S.; Stone, M. T.; Klotz, E. J. F.; Cacialli, F.; Anderson, H. L. *J. Mater. Chem.* **2009,** *19,* 2846–2852. doi:10.1039/b821950h
34. Farcas, A.; Jarroux, N.; Ghosh, I.; Guégan, P.; Nau, W. M.; Harabagiu, V. *Macromol. Chem. Phys.* **2009,** *210,* 1440–1449. doi:10.1002/macp.200900140
35. Zalewski, L.; Wykes, M.; Brovelli, S.; Bonini, M.; Breiner, T.; Kastler, M.; Dötz, F.; Beljonne, D.; Anderson, H. L.; Cacialli, F.; Samorì, P. *Chem. – Eur. J.* **2010,** *16,* 3933–3941. doi:10.1002/chem.200903353
36. Zalewski, L.; Brovelli, S.; Bonini, M.; Mativetsky, J. M.; Wykes, M.; Orgiu, E.; Breiner, T.; Kastler, M.; Dötz, F.; Meinardi, F.; Anderson, H. L.; Beljonne, D.; Cacialli, F.; Samorì, P. *Adv. Funct. Mater.* **2011,** *21,* 834–844. doi:10.1002/adfm.201001135
37. Farcas, A.; Ghosh, I.; Nau, W. M. *Chem. Phys. Lett.* **2012,** *535,* 120–125. doi:10.1016/j.cplett.2012.03.069
38. Brovelli, S.; Sforazzini, G.; Serri, M.; Winroth, G.; Suzuki, K.; Meinardi, F.; Anderson, H. L.; Cacialli, F. *Adv. Funct. Mater.* **2012,** *22,* 4284–4291. doi:10.1002/adfm.201200786
39. Szejtli, J. *Chem. Rev.* **1998,** *98,* 1743–1753. doi:10.1021/cr970022c
40. Dsouza, R. N.; Pischel, U.; Nau, W. M. *Chem. Rev.* **2011,** *111,* 7941–7980. doi:10.1021/cr200213s
41. Wenz, G. *Adv. Polym. Sci.* **2009,** *222,* 204–254. doi:10.1007/12_2008_13
42. González-Gaitano, G.; Rodríguez, P.; Isasi, J. R.; Fuentes, M.; Tardajos, G.; Sánchez, M. *J. Inclusion Phenom. Macrocyclic Chem.* **2002,** *44,* 101–105. doi:10.1023/A:1023065823358
43. Farcas, A.; Jarroux, N.; Guégan, P.; Fifere, A.; Pinteala, M.; Harabagiu, V. *J. Appl. Polym. Sci.* **2008,** *110,* 2384–2392. doi:10.1002/app.28760
44. Farcas, A.; Ghosh, I.; Jarroux, N.; Harabagiu, V.; Guégan, P.; Nau, W. M. *Chem. Phys. Lett.* **2008,** *465,* 96–101. doi:10.1016/j.cplett.2008.09.058
45. Farcas, A.; Jarroux, N.; Harabagiu, V.; Guégan, P. *Eur. Polym. J.* **2009,** *45,* 795–803. doi:10.1016/j.eurpolymj.2008.11.047
46. Farcas, A.; Jarroux, N.; Guegan, P.; Harabagiu, V.; Melnig, V. *J. Optoelectron. Adv. Mater.* **2007,** *9,* 3484–3488.
47. Nakazono, K.; Takashima, T.; Arai, T.; Koyama, Y.; Takata, T. *Macromolecules* **2010,** *43,* 691–696. doi:10.1021/ma902161d
48. Stefanache, A.; Silion, M.; Stoica, I.; Fifere, A.; Harabagiu, V.; Farcas, A. *Eur. Polym. J.* **2014,** *50,* 223–234. doi:10.1016/j.eurpolymj.2013.11.001
49. Chen, S. H.; Su, A. C.; Su, C. H. *Macromolecules* **2005,** *38,* 379–385. doi:10.1021/ma048162t
50. Brovelli, S.; Meinardi, F.; Winroth, G.; Fenwick, O.; Sforazzini, G.; Frampton, M. J.; Zalewski, L.; Levitt, J. A.; Marinello, F.; Schiavuta, P.; Suhling, K.; Anderson, H. L.; Cacialli, F. *Adv. Funct. Mater.* **2010,** *20,* 272–280. doi:10.1002/adfm.200901764
51. Liu, B.; Yu, W. -L.; Lai, Y.-H.; Huang, W. *Chem. Mater.* **2001,** *13,* 1984–1991. doi:10.1021/cm0007048
52. de Leeuw, D. M.; Simenon, M. M. J.; Brown, A. R.; Einerhand, R. E. F. *Synth. Met.* **1997,** *87,* 53–59. doi:10.1016/S0379-6779(97)80097-5
53. Metri, N.; Sallenave, X.; Plesse, C.; Beouch, L.; Aubert, P.-H.; Goubard, F.; Chevrot, C.; Sini, G. *J. Phys. Chem. C* **2012,** *116,* 3765–3772. doi:10.1021/jp2098872
54. Al-Ibrahim, M.; Roth, H.-K.; Schroedner, M.; Konkin, A.; Zhokhavets, U.; Gobsch, G.; Scharff, P.; Sensfuss, S. *Org. Electron.* **2005,** *6,* 65–77. doi:10.1016/j.orgel.2005.02.004
55. Cantin, S.; Bouteau, M.; Benhabib, F.; Perrot, F. *Colloids Surf., A* **2006,** *276,* 107–115. doi:10.1016/j.colsurfa.2005.10.025

License and Terms

The definitive version of this article is the electronic one which can be found at:
doi:10.3762/bjoc.11.288

BEILSTEIN JOURNAL OF ORGANIC CHEMISTRY

Physical properties and biological activities of hesperetin and naringenin in complex with methylated β-cyclodextrin

Waratchada Sangpheak[1], Jintawee Kicuntod[1], Roswitha Schuster[2], Thanyada Rungrotmongkol[1,3], Peter Wolschann[1,2,4], Nawee Kungwan[5], Helmut Viernstein[2], Monika Mueller[*2] and Piamsook Pongsawasdi[*6,§]

Full Research Paper

Open Access

Address:
[1]Structural and Computational Biology Unit, Department of Biochemistry, Faculty of Science, Chulalongkorn University, Bangkok 10330, Thailand, [2]Department of Pharmaceutical Technology and Biopharmaceutics, University of Vienna, Vienna 1090, Austria, [3]Ph.D. Program in Bioinformatics and Computational Biology, Faculty of Science, Chulalongkorn University, Bangkok 10330, Thailand, [4]Institute of Theoretical Chemistry, University of Vienna, Vienna 1090, Austria, [5]Department of Chemistry, Faculty of Science, Chiang Mai University, Chiang Mai, 50200, Thailand and [6]Starch and Cyclodextrin Research Unit, Department of Biochemistry, Faculty of Science, Chulalongkorn University, Bangkok 10330, Thailand

Email:
Monika Mueller* - monika.mueller@univie.ac.at;
Piamsook Pongsawasdi* - piamsook.p@chula.ac.th

* Corresponding author
§ Tel: +66 2 2185423; Fax: + 66 2 2185418

Keywords:
binding energy; bioactivity; cyclodextrins; hesperetin; naringenin

Beilstein J. Org. Chem. **2015,** *11,* 2763–2773.
doi:10.3762/bjoc.11.297

Received: 31 July 2015
Accepted: 02 December 2015
Published: 29 December 2015

This article is part of the Thematic Series "Superstructures with cyclodextrins: Chemistry and applications III".

Guest Editor: G. Wenz

Abstract

The aim of this work is to improve physical properties and biological activities of the two flavanones hesperetin and naringenin by complexation with β-cyclodextrin (β-CD) and its methylated derivatives (2,6-di-*O*-methyl-β-cyclodextrin, DM-β-CD and randomly methylated-β-CD, RAMEB). The free energies of inclusion complexes between hesperetin with cyclodextrins (β-CD and DM-β-CD) were theoretically investigated by molecular dynamics simulation. The free energy values obtained suggested a more stable inclusion complex with DM-β-CD. The vdW force is the main guest–host interaction when hesperetin binds with CDs. The phase solubility diagram showed the formation of a soluble complex of A_L type, with higher increase in solubility and stability when hesperetin and naringenin were complexed with RAMEB. Solid complexes were prepared by freeze-drying, and the data from differential scanning calorimetry (DSC) confirmed the formation of inclusion complexes. The data obtained by the dissolution method showed that complexation with RAMEB resulted in a better release of both flavanones to aqueous solution. The flavanones-β-CD/DM-β-CD complexes demonstrated a similar or a slight increase in anti-inflammatory activity and cytotoxicity towards three different cancer cell lines. The overall results suggested that solubilities and bioactivities of both flavanones were increased by complexation with methylated β-CDs.

Introduction

Flavonoids are secondary metabolites found in fruits, vegetables, grains, roots, bark, stems, flowers, and especially in tea and wine [1]. More than 5,000 naturally occurring different flavonoids have been identified [2], including flavonols, flavones, flavanones, anthocyanidins, isoflavones, and dihydroflavonols. They possess many beneficial biological properties, i.e., free radical scavenging activity [3], cardioprotective action [4], antibacterial and antiviral activities [5]. Two flavonoids in the class of flavanones, hesperetin and naringenin (chemical structures in Figure 1), can be extracted from citrus fruits such as lemon, grapefruit and orange. Several reports on biological effects of hesperetin and naringenin have been found [6], including blood lipid- and cholesterol-lowering effects [7-9], anti-inflammatory [10-13] and anticancer [14-16] activities, improved microcirculation, recovery of venous ulcers, inhibition of chronic venous insufficiency and hemorrhoids, and prevention of post-operative thromboembolism [17]. Hesperetin can inhibit chemically induced mammary [18], urinary bladder [19], colon carcinogenesis in laboratory animals [20-22], and proliferation of breast cancer cells (MCF-7) [23,24]. Naringenin has the ability to hinder a tumor growth on various human cancer cell lines [25], and acts as an inhibitor that blocks basal and insulin-stimulated glucose uptake in breast cancer cells [26]. Additionally, naringenin reduces the incidence of hormone-responsive cancer [27]. In spite of having several benefits, the use of these flavonoids is frequently limited by their low water solubility and stability with a consequence of exerting rather low biological activity.

The natural β-cyclodextrin (β-CD) is a cyclic oligosaccharide consisting of seven D-glucopyranose units linked by α-(1,4)-glycosidic bonds. It contains a highly hydrophobic central cavity and the hydrophilic outer surface. The 2,6-di-*O*-methyl-β-cyclodextrin (DM-β-CD), a commercially available β-CD derivative, is obtained by methylation of the hydroxy groups at C2 and C6 of all glucose units, thus having the degree of substitution of 2.0. While the randomly methylated-β-cyclodextrin (RAMEB) prepared with the average degree of substitution of 1.8, being fully methylated at C6 but partial at C2 and C3 positions (Figure 1) [28]. Cyclodextrin complexation is at present highly relevant to various branches of industry, including pharmaceutical, medicine, cosmetics, food and agriculture [29]. β-CD and its derivatives have been widely used to increase the water solubility, stability, and consequent bioavailability of poorly water soluble drugs [30-32], such as β-CD in complex with piroxicam [33] and etodolac [34] and DM-β-CD in complex with camptothesin [35], chloramphenicol [36] and paclitaxel [37]. DM-β-CD has been found to improve the insulin absorption via pulmonary administration [38], and to stimulate nasal insulin absorption with a reduction of the serious nasal toxicity [39].

In the present work, we aimed to improve physical properties and biological activities of hesperetin and naringenin through complexation with cyclodextrins. Computational tools (molecular dynamics simulation) were adopted to first predict the stability of flavanones/CDs inclusion complexes. Consequently,

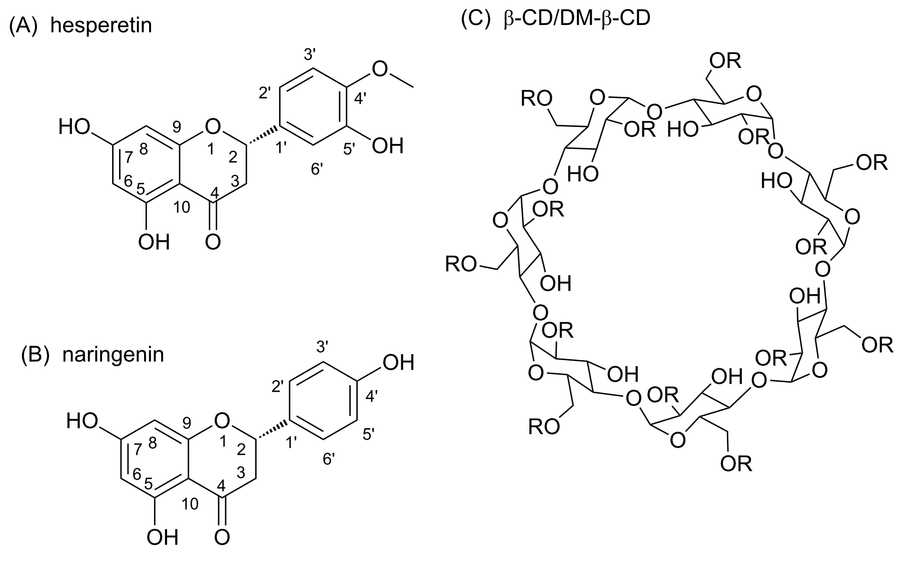

Figure 1: Structures of (A) hesperetin, (B) naringenin and (C) the two cyclodextrins: β-CD and DM-β-CD with the –H and $–CH_3$ substitutions on –R groups, respectively. For DM-β-CD, substitution by $–CH_3$ is at OH of C2 and C6 while for RAMEB, full substitution is found at OH of C6 but partial at C2 and C3 of each glucose unit.

the experimental phase solubility and dissolution study of flavanones were studied. The formed inclusion complexes were analyzed by DSC. The anti-inflammatory activity of inclusion complexes and the free flavanones were determined by investigating the secretion of certain cytokines in lipopolysaccharide (LPS)-stimulated macrophages. In addition, the cytotoxic activity on CaCo-2, HeLa and MCF-7 carcinoma cell lines of inclusion complexes was also determined.

Results and Discussion

The binding free energy of inclusion complexes between naringenin with β-CD and DM-β-CD has been previously reported by our group [40]. In the present work, we reported the binding study of hesperetin with the two cyclodextrins. Furthermore, the physical properties of both flavanones when complexation with β-CD and RAMEB were investigated, the RAMEB was used in this part to save the experimental cost and with the anticipation that RAMEB and DM-β-CD should not give much difference to these properties. However, in the third part whereby biological activities were examined, the two flavanones complexing with β-CD and DM-β-CD were used since the different degree of methylation might exert significant effect on the result as previously reported [28].

Binding free energy of inclusion complexes

Root mean square displacements (RMSDs) for all atoms of the complex, cyclodextrin and hesperetin in respect with those of initial structures (Figure S1, Supporting Information File 1) suggested that the three independent simulations of β-CD (A1–A3) and DM-β-CD (B1–B3) complexes had reached equilibration at 25 ns. The 30 MD snapshots from the last 55 ns of each simulation was selected for binding free energy calculations in accordance with the naringenin/CDs complexes [40].

In this study, we applied a molecular mechanics and continuum solvation method to estimate the binding free energies, or calculate the free energies of molecules in solution (ΔG_{bind}) using the MM-PBSA/GBSA method. The free energy decomposition of each complex in terms of gas phase energy (ΔE_{MM}) including ΔE_{ele} and ΔE_{vdw} energies, solvation free energy (ΔG_{sol}) and entropic term ($T\Delta S$) is shown in Table 1. It seems that both flavanones interacted with cyclodextrins through van der Waals (vdW) force 2 to 5-fold stronger than electrostatic interaction. The ΔE_{vdw} and ΔE_{ele} of hesperetin/β-CD and hesperetin/DM-β-CD were −23.58 and −31.30 kcal·mol^{-1} and −9.95 and −5.90 kcal·mol^{-1}, respectively (Table 1). For naringenin/β-CD and naringenin/DM-β-CD, the ΔE_{vdW} values were −25.69 and −29.71 kcal·mol^{-1} while ΔE_{ele} values were −4.09 and −4.73 kcal·mol^{-1}, respectively [40] (Supporting Information File 1). Thus, the vdW interaction played an important role in forming the inclusion complex. The obtained information was in good agreement with previous studies in which the hydrophobic interaction was found to be the main driving force for flavanones–CD inclusion complexes [40,41]. For the summation of entropic and solvation terms, both MM/PBSA and MM/GBSA methods predicted that the binding free energy of hesperetin/DM-β-CD was by ≈7.6 kcal·mol^{-1} lower than that of hesperetin/β-CD, and a better binding of naringenin in the cavity of DM-β-CD than in that of β-CD by ≈4.6 kcal·mol^{-1} was suggested [40]. Nevertheless, the MM-PBSA/GBSA binding free energies of the two inclusion complexes might be overestimated due to MM energy. To correct this energy section, the same set of 25 to 80 MD snapshots was carried out by the single point DFT M062X/6-31+g (d,p) calculation in this study. The results of QM/PBSA and QM/GBSA binding free energies were in agreement with MM/PBSA and MM/GBSA energies. The experimental ΔG values showed the same trend with values from molecular dynamics simulation that complexing with DM-β-CD was more effective than with β-CD, and the values obtained were in good agreement with the previous report [42]. These results suggested that both flavanones bind to and interact with DM-β-CD stronger than with β-CD.

Table 1: MM-PBSA/GBSA binding free energies (kcal/mol) and energy components between hesperetin and β-CD/DM-β-CD complexes in comparison to experimental values.

energy (kcal/mol)	hesperetin/β-CD	hesperetin/DM-β-CD
ΔE_{ele}	−9.95 ± 0.73	−5.90 ± 0.46
ΔE_{vdW}	−23.58 ± 2.97	−31.30 ± 0.44
ΔE_{MM}	−33.86 ± 3.23	−38.23 ± 0.60
ΔE_{QM}	−28.80 ± 0.03	−31.33 ± 0.03
$T\Delta S$	−12.46 ± 0.37	−11.27 ± 0.07
$\Delta G_{\text{sol (PBSA)}}$	15.08 ± 1.78	12.42 ± 2.73
$\Delta G_{\text{sol (GBSA)}}$	14.14 ± 1.71	12.79 ± 2.10
$\Delta G_{\text{MM-PBSA}}$	−6.32 ± 1.08	−14.54 ± 2.06
$\Delta G_{\text{MM-GBSA}}$	−7.25 ± 1.15	−14.17 ± 1.30
$\Delta G_{\text{QM-PBSA}}$	−1.26 ± 1.38	−7.64 ± 2.69
$\Delta G_{\text{QM-GBSA}}$	−2.20 ± 1.37	−7.27 ± 2.06
$\Delta G_{\text{experiment}}$	−3.50	−4.27

Phase solubility studies

The phase-solubility diagrams for the hesperetin/CD and naringenin/CD complexes at different temperatures are shown in Figure 2. The linear relationship of the plots for all complexes, suggested the typical A_L-type of the phase solubility profiles with the 1:1 molar ratio of soluble guest and host inclusion complexes [43]. This finding agrees with the previous study which reported complexation between these two flavanones with β-CD [42]. We here found that the aqueous solubility of hesperetin and naringenin were remarkably increased approxi-

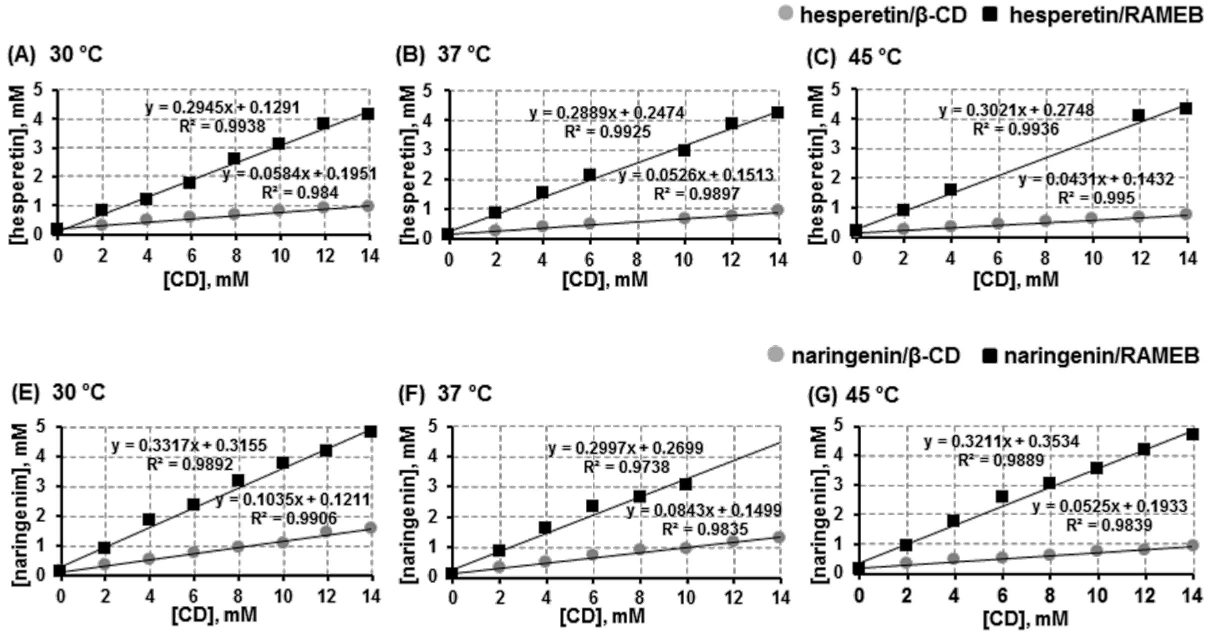

Figure 2: Phase solubility study of hesperetin (upper panel) and naringenin (lower panel) with β-CD or RAMEB in water at 30 °C, 37 °C and 45 °C.

mately 10 and 40 times by the solubilizing effects of β-CD and RAMEB. Thus, the solubility of both flavanones in the presence of CDs followed the order of RAMEB > β-CD, reflecting an enhancement of binding and solubility of both flavanones.

A previous report by Yang et al. showed a similar result, methylated-β-CDs gave a much better solubilization effect on naringenin than β-CD [31]. The solubility of the naringenin/CD complex was increased to approximately 1.34, 1.60 and 1.52 mg/mL by complexing with β-CD, DM-β-CD and TM-β-CD (trimethyl-β-CD), respectively, while the solubility of free naringenin was 4.38 µg/mL. The methyl substitution plays an important role in balancing the CD water solubility and its complexing ability [44].

It was previously reported that increasing the degree of methylation up to an optimum level improves the CD aqueous solubility, and the binding of guests to CDs is increased by increasing the surface area of binding [41,45-47]. However, beyond the optimum level, the steric hindrances of the host molecule impair CD complexing efficiency or capacity. The summarized data for stability constants (K_c) of the hesperetin/CD and naringenin/CD complexes at different temperatures are shown in Table 2. The stability constant (K_c) was determined from the linear part of the phase solubility diagram assuming a 1:1 complex. The solubility of flavanone in the absence of cyclodextrin can be estimated from the intercept of the plot between the concentration of flavanone and cyclodextrin. It was observed that the stability constant (K_c) of the complexes was affected by temperature, the decrease in temperature resulted in the increase in the K_c value. These findings are in accordance with the work of Tommasini et al. which reported the stability of hesperetin and naringenin complexes with β-CD at different temperatures in the range of 15–45 °C [42]. The temperature parameter contributes to the strength of the interaction between the host and guest molecules in complex formation. Size matching of the host and guest molecules also dominates complex stability. Our results showed that the binding constants for

Table 2: Stability constants (K_c) of hesperetin/CD complex and naringenin/CD complex at different temperature.

temperature (°C)	K_c (M^{-1})			
	hesperetin/β-CD	hesperetin/RAMEB	naringenin/β-CD	naringenin/RAMEB
30	339.2	1289.3	425.0	1015.5
37	249.9	1030.5	367.8	999.9
45	195.6	1000.2	203.0	892.7

the complexation of both flavanones with RAMEB were higher than those for β-CD. This suggested that the RAMEB complex was more stable than the β-CD system; the result showed the same trend of advantage of the methyl derivative as in the binding free energy obtained from calculation using the computational method (Table 1). From the result on the binding energy, the vdW energy was about six-fold greater than the electrostatic energy in both of the CDs complexes (Table 1 for hesperetin and Table S1, Supporting Information File 1 for naringenin). This implied that the complex stability was mainly governed by the vdW interaction.

DSC analysis

To investigate the solid inclusion complex obtained by freeze-drying (Figure 3D and E) and kneading methods (Figure 3F and G), DSC measurements were performed. The thermogram revealed information about the thermal properties of the starting free materials (flavanones, β-CD and RAMEB) compared with those inclusion complexes. The melting endothermic peaks are characteristic of each of the free compounds: hesperetin at 234.5 °C (Figure 3C), β-CD at 117.7 °C (Figure 3A), RAMEB at 73.8 °C (Figure 3B) and naringenin at 256.7 °C were determined. In case of the complexes obtained from freeze-drying, the endothermic peaks of free hesperetin and naringenin disappeared, simultaneously with the appearance of a new peak at 157.4 and 141.9 °C for hesperetin/β-CD and hesperetin/RAMEB, respectively (see also Figure 3D and E, left panel). Naringenin/β-CD and naringenin/RAMEB systems showed a new peak at 145.5 and 150.5 °C, respectively (Figure 3D and E, right panel). The complete inclusion complexes were thus observed for the system obtained by freeze-drying. In contrast, the kneading method resulted in a shift to lower temperatures of the flavanones's melting points in the thermogram of the complexes. In addition, there were peaks that could be ascribed to some flavanones/CD interaction [48]. The result suggested that the kneading method yielded incomplete inclusion complexes.

Dissolution study

Reports of release studies of several guest/drug molecules, e.g., ampelopsis, simvastatin, ketoconazole and famotidine can be found in literature [49-52]. For dissolution studies of the two flavanones, Tommasini and co-workers reported the dissolution profiles of hesperetin, naringenin and their β-CD complexes in buffer solutions at different pH [42]. They found that the dissolution of the hesperetin complex rapidly increases within 30 minutes at pH 1.5 while the highest amount of dissolved drug was observed at pH 8.0. It was also found that naringenin showed almost the same behavior.

The dissolution of the solid complexes of the two flavanones and cyclodextrins formed by freeze-drying at a 1:1 molar ratio was determined in this study. The dissolution diagram of the free guests, hesperetin and naringenin, and their inclusion complexes in water at 37 °C are shown in Figure 4. The free form of hesperetin or naringenin exhibited poor dissolution owing to their hydrophobicity. It can be observed that the dissolution of the two flavanones was enhanced significantly when

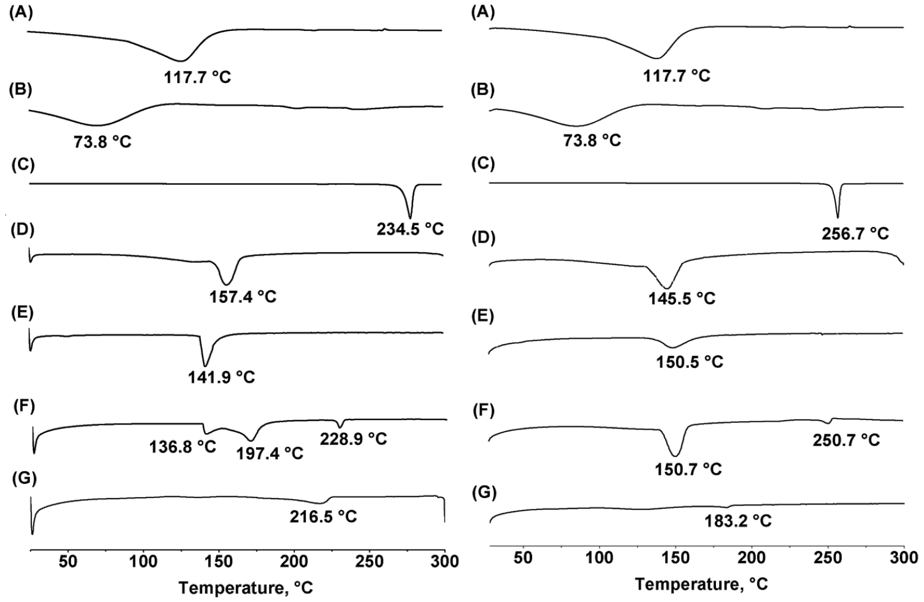

Figure 3: DSC thermograms of hesperetin (left) and naringenin (right) (A) β-CD, (B) RAMEB, (C) Free flavanones, (D and E) flavanones/β-CD and flavanones/RAMEB complexes, respectively, prepared by freeze-drying, (F and G) flavanones/β-CD and flavanones/RAMEB complexes, respectively, prepared by the kneading method.

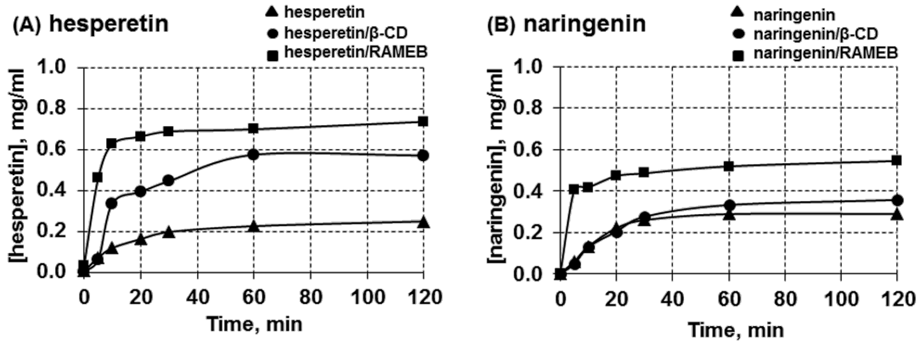

Figure 4: The dissolution diagram at 37 °C in water of the free flavanones and their complexes. (A) hesperetin and (B) naringenin. Complex formation was by freeze-drying.

they formed complexes with cyclodextrins. Both free and inclusion complexes of hesperetin and naringenin were dissolved with high rate for the first 10 minutes. When compared the dissolved amounts of free hesperetin, β-CD complex and RAMEB complex after 10 minutes, the amounts of dissolved hesperetin were 0.11, 0.33 and 0.63 mg/mL, respectively. For free naringenin, naringenin/β-CD and naringenin/RAMEB complexes, the amounts of dissolved naringenin were 0.13, 0.13 and 0.42 mg/mL. As effect of the type of the carrier host, it was concluded that the RAMEB system showed a dissolution rate higher than the inclusion complex with β-CD. The dissolved amount of both free and hesperetin complexes increased significantly within 30 minutes. Naringenin showed almost the same behavior, as the greatest solubilization occurs within 30 minutes as well. These results were in good agreement with a previous report [42] in which the dissolution of hesperetin and naringenin complexed with β-CD was studied. The improved dissolution rate observed may be due to the increase in solubility, as well as a decrease in the crystallinity of guest molecules, brought about by complexation with CDs [53].

Cytokine levels in response to treatment with inclusion complexes of flavanones

To investigate the anti-inflammatory effect of the inclusion complexes compared to free compounds, we used LPS-stimulated macrophages for testing the change of interleukin (IL)-6 secretion. The anti-inflammatory effects of flavanones and their inclusion complexes are shown in Figure 5. Secretion of the IL-6 was significantly inhibited by naringenin, naringenin/β-CD and naringenin/DM-β-CD (at least 30%) at 0.1 and 0.05 mM, however, the free and complex form gave a similar result. These findings support previous studies of Mueller and co-workers [54], who showed a comparable effect of naringenin. Bodet and co-workers [55] studied the anti-inflammatory effect of naringenin in macrophages and ex vivo in human whole-blood models. They found that naringenin at high concentrations (25 and 50 µg/mL) significantly reduced the amount of secreted IL-6. In case of hesperetin and their complexes, a reduction of IL-6 secretion by at least 20% at 0.1 and 0.05 mM concentration was found. It is clearly seen that the inclusion complexes of hesperetin at 0.1 mM were more effective than free hesperetin,

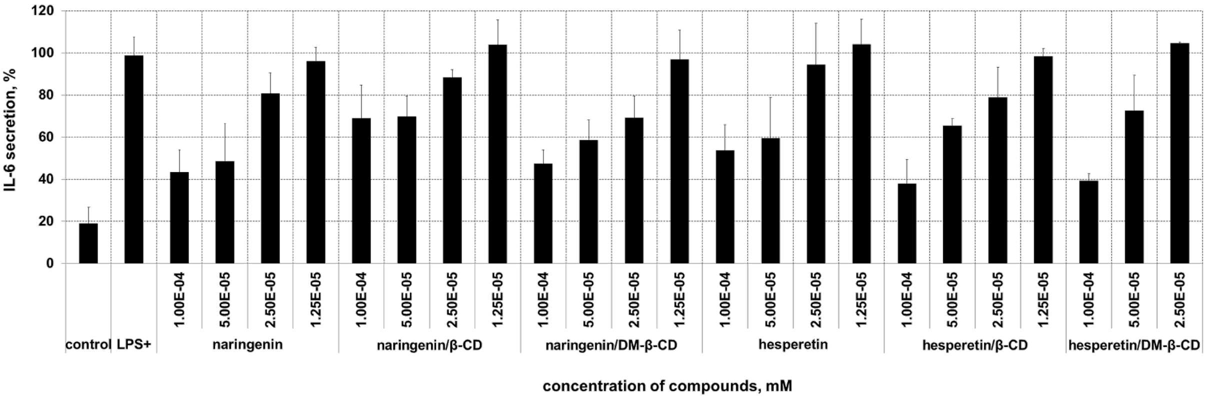

Figure 5: The influence of flavanones and their complexes on IL-6 secretion from LPS-stimulated macrophages.

but only at low concentration, the β-CD complex showed a slightly better effect than the DM-β-CD complex. Complexation of nonpolar drugs with cyclodextrins is known to be beneficial for pharmaceutical research due to the possibility to increase water solubility, stability and bioavailability of those drugs [56,57]. In such a way, the bioavailability of genistein was found to be increased by complexation with CDs [58].

Cytotoxicity to cancer cell lines

The cytotoxicity of flavanones and their inclusion complexes against three cancer cell lines (CaCo-2, HeLa and MCF-7) has been determined by MTT assay which measures the metabolic activity and thus viability of cells based on their ability to reduce the tetrazolium substrate to formazan. For the breast cancer cell line (MCF-7), naringenin and their complexes exhibited cytotoxic effects when compared to the control (Figure 6A). This result is consistent with a previous study of Harmon et al. who suggested that naringenin inhibits the proliferation of MCF-7 cells via impaired glucose uptake [26]. Krishnakumar et al. showed the cytotoxic effects between naringenin and naringenin-loaded nanoparticles which exhibited significant cytotoxicity at high concentrations (30, 40 and 50 µg/mL) [59]. At low concentration (0.025 mM), naringenin complexed with DM-β-CD exerted a higher effect on MCF-7 and HeLa cells than free naringenin. However, for CaCo-2 cells, the effect of the naringenin complex was similar to that of the free form (Figure 6C). In case of hesperetin and its complexes, a significant effect on the cell viability on MCF-7, HeLa and CaCo-2 cells was shown at concentrations of 0.1 and 0.5 mM (Figure 6A–C).

Conclusion

A more stable complexation of hesperetin/DM-β-CD over the β-CD complex was supported by binding free energy calculation, with the vdW force as the main interaction for the inclusion complex. RAMEB gave a higher increase in aqueous solu-

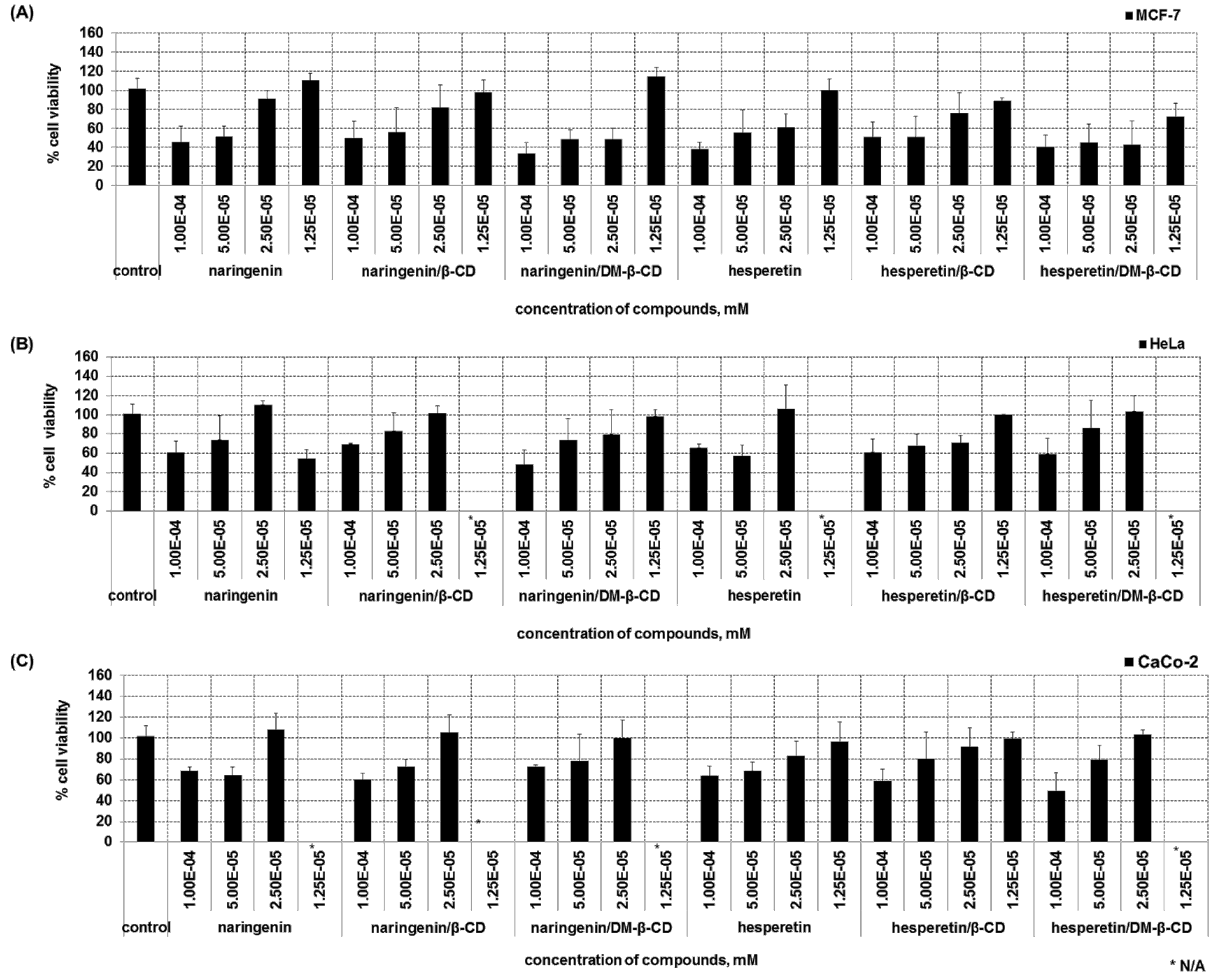

Figure 6: Cytotoxicity of free flavanones and their inclusion complexes on different cancer cell lines.

bility and stability of hesperetin and narengenin than β-CD. The stability constant of the inclusion complexes decreased with an increase in temperature. The dissolution of the complexes was increased with a faster dissolution rate than the free flavanones, the RAMEB complex was better dissolved. Naringenin, hesperetin and their inclusion complexes exhibited anti-inflammatory activity as indicated by the reduction of the secretion of the pro-inflammatory IL-6. No significant difference was found in the activity of free and complexed naringenin whereas for hesperetin the anti-inflammatory effect could be slightly increased. The flavanones and their inclusion complexes effectively exerted cytotoxic effects towards cancer cell lines. Complexation mostly leads to a slightly increased effect.

Experimental

Materials

Hesperetin was purchased from Cayman Chemicals (Ann Arbor, MI, USA) and β-CD and RAMEB were purchased from Wako Pure Chemical Industries (Osaka, Japan), respectively. Naringenin, DM-β-CD, dimethyl sulfoxide (DMSO), sodium dodecyl sulfate (SDS), thiazolyl blue (MTT), compounds for phosphate buffer saline (PBS) and lipopolysaccharides (LPS) from *Escherichia coli* O111:B4 were obtained from Sigma-Aldrich (Darmstadt, Germany). Dulbecco's Modified Eagle's Medium (DMEM) was obtained from Life Technologies (Carlsbad, CA, USA). Anti-Mouse IL-6 was purchased from eBioscience Inc. (San Diego, CA, USA). Human colon cancer (Caco-2) cells, breast cancer (MCF-7) cells and human cervical carcinoma (HeLa) cells were obtained from the American Type Cell Culture Collection (ATCC), USA.

Methods

Binding free energy calculation

Molecular dynamics (MD) simulations with periodic boundary condition were performed on the three best docked structures of the hesperetin/CDs complexes (Figure 7) similar to our previous studies on naringenin/CDs complexes [40,60] using the Amber 12 software package [61]. Note that the docked structures were resulted from the CDOCKER module implemented in Accelrys Discovery Studio 2.5 (Accelrys, Inc.). The Glycam-06 bimolecular force field was applied on the cyclodextrins, while the partial atomic charges and parameters of hesperetin were developed by the standard procedure [32,62,63]. Using a truncated octahedral box, the SPC water molecules were solvated with a spacing distance of 12 Å from the complex surface. Each system was heated up to 298 K within 100 ps and followed by the 80 ns simulation with NPT ensemble at the same temperature, 1 atm and time step of 2 fs. The non-bonded interaction was truncated within a 12 Å cutoff distance. The particle-mesh of Ewald's method [64] was used for adequate treatment of the long-range electrostatic interactions with 12 Å cutoff. All bond lengths involving hydrogen atoms were constrained by SHAKE [32]. The coordinates were recorded every 500 steps for analysis. The MM- and QM-PBSA/GBSA calculations were conducted to estimate the binding free energy of the inclusion complex [40,60]. For QM calculation, the single point M06-2X/

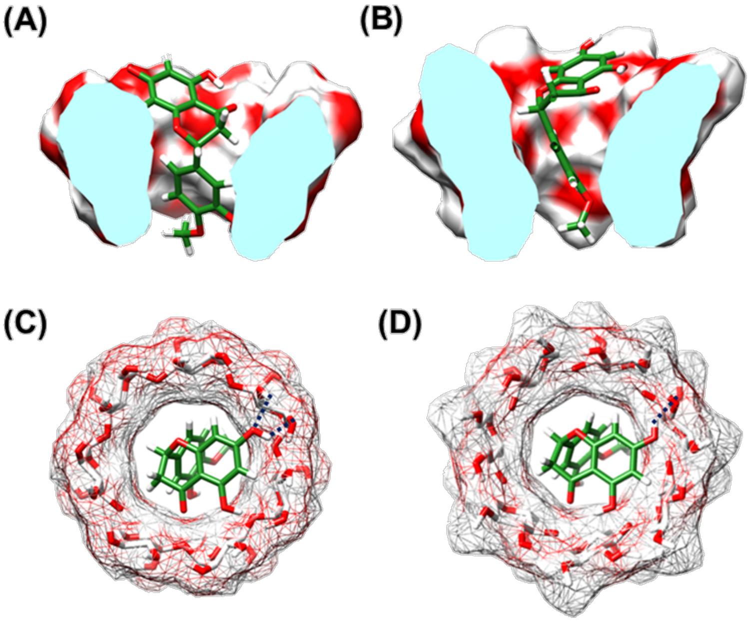

Figure 7: The docked orientations of hesperetin in the hydrophobic cavity of (A) β-CD and (B) DM-β-CD and top views of the CD hydrophobic cavity and H-bond showing (C) phenyl ring inserted into β-CD's cavity (D) phenyl ring inserted into DM-β-CD's cavity.

6-31+G** level of theory including the empirical dispersion correction energy [46] was treated on the same set of structures of inclusion complex, cyclodextrin and hesperetin using Gaussian09 program package [65].

Phase solubility studies

Phase solubility studies were carried out according to Higuchi and Connors [43]. Excess amount of flavanones were added to a series of 0–14 mM concentration of cyclodextrin (β-CD and RAMEB) solutions. The mixtures were shaken at 30 ± 0.5, 37 ± 0.5 and 45 ± 0.5 °C for 72 hours in a water bath shaker. After equilibrium, the samples were centrifuged at 12,000 rpm for 15 minutes; then the solubility was determined by measuring the absorbance at 256 nm using a DU650 UV visible spectrophotometer. The apparent stability constant K_c was calculated from the phase solubility diagram by means of Equation 1.

$$K_c = \frac{Slope}{[S_0(1 - slope)]} \quad (1)$$

Inclusion complexation preparation

The inclusion complex of flavanones/CDs (β-CD and RAMEB) in a 1:1 molar ratio was prepared by freeze-drying. Each compound was accurately weighed, then dissolved in distilled water (10 mL) and sealed in a flask. The mixture was stirred magnetically at room temperature for 24 hours. Subsequently, the solution was filtered through a 0.45 μm pore size filter, frozen overnight and then lyophilized (LYO-LAB, Lyophilization Systems, Inc USA) over the period of 24 hours. The dried powder was stored in desiccators for further use.

Differential scanning calorimetry (DSC) analysis

The differential scanning calorimetry (DSC, Netzsch, 204 F1 Phoenix) was used for recording DSC thermograms of the free hesperetin and naringenin and the inclusion complexes with β-CD and RAMEB. The thermal behavior was studied by heating samples (2–5 mg) in closed aluminum crimped pans at a rate of 10 °C min^{-1} between a temperature range of 25 to 250 °C for both hesperetin and naringenin [42].

Dissolution study

Dissolution studies of all samples were carried out in 20 mL of distilled water. Hesperetin or naringenin and its solid complexes with β-CD and RAMEB (5 mg) were added in distilled water, and shaken at 37 °C, 1 mL was withdrawn for analysis of the hesperetin or naringenin content at different time intervals (0, 5, 10, 20, 30, 60 and 120 minutes). The sample was diluted to appropriate concentration, and analyzed for absorbance at 286 nm by high-performance liquid chromatography (HPLC, Waters 600, USA). The dissolution studies were performed in triplicate.

Determination of biological activity of flavanones

Preparation of free compound and their complexes: Stock solutions of 100 mM of free compounds were prepared in water. Inclusion complexes of hesperetin and naringenin with β-CD and DM-β-CD were prepared by freeze drying and diluted with distilled water to a final concentration of 100 mM.

Anti-inflammatory assay: Macrophages (RAW 264.7, ATCC) were used to examine the effect of free compounds and their inclusion complexes on inflammation as described previously [59]. Cells were seeded at a density of 2×10^6 cells per well in 24 well plates, and incubated at 37 °C for 24 hours. After that, samples were added to obtain a final concentration of 0.1, 0.05 and 0.025 mM preincubated for 3 hours and then a final concentration of 1 μg/mL of LPS was added. The cells were incubated for a further 24 hours at 37 °C. On the following day, the media supernatant was removed, centrifuged and stored at −20 °C prior to analysis by ELISA. The negative control experiments were cells untreated with LPS and the positive control experiments were cells incubated with LPS only. An enzyme linked immunosorbent assay (ELISA) was used for the determination of the concentration of secreted IL-6 of the cells in the supernatant. All incubation steps were performed at room temperature according to the manufacturer´s protocol (eBiosciences, Santa Clara, CA, USA). The absorbance was measured at 450 nm and corrected by background absorbance at 570 nm, using a Genios Pro microplate reader (Tecan, Crailsheim, Germany). After removing the supernatant for ELISA analysis, the cells were incubated with MTT (0.5 mg/mL) for 3 hours at 37 °C. Then, the cells were lysed using 10% SDS in 0.01 N HCl. To monitor cell viability, secreted cytokine levels were measured at the suitable cell density. The absorbance at 570 nm was measured for the formazan product and corrected by the absorbance at a reference wavelength of 690 nm, using a Genios Pro microplate reader. Positive control was performed using cells incubated with LPS only and was set at 100%. All experiments were performed in three separate measurements and the results are shown as mean with error bars representing the standard deviation.

Cytotoxicity towards cancer cell lines: An MTT assay was performed to determine the cell viability and thus the cytotoxicity of the test compounds towards three different cancer cell lines (HeLa, CaCo-2, MCF-7). Cells were seeded into 96-well plates at a density of 2×10^6 cells/mL and incubated for 24 hours under normal culture conditions. On the next day, test substances were added and the cells were incubated for another 24 hours. Then, 10 μL MTT solution was added, incubated for

2 hours and cells were lysed. The absorption was measured at 570 nm with correction for background at 690 nm as described above, using an Infinite M200 microplate reader. The amount of cells of the positive control (cells only incubated with DMEM) was defined as 100%. The results from the test substances were calculated as a percentage of the positive control. All experiments were separately performed in triplicate and the results are shown as mean with error bars representing the standard deviation.

Supporting Information

Supporting Information File 1

Additional data.
[http://www.beilstein-journals.org/bjoc/content/supplementary/1860-5397-11-297-S1.pdf]

Acknowledgements

This study was supported by the Ratchadaphiseksomphot Endowment Fund of the Chulalongkorn University (CU) (CU-58-013-FW), and the Thailand Research Fund (IRG5780008). T. R. acknowledges the TRF Research Grant for New Scholars (MRG5580223). W. S. thanks Thailand Graduate Institute of Science and Technology (TGIST Grant No. TG-55-09-58-052D). J. K. received the Scholarship from Graduate School, CU to commemorate the 72nd anniversary of His Majesty King Bhumibol Adulyadej, and the 90thAnniversary of CU Fund (Ratchadaphiseksomphot Endowment Fund). P. W. thanks CU for a short-term visit grant. The ASIA-Uninet short-term research grant is acknowledged. Special thanks go also to the Computational Chemistry Unit Cell (CCUC), the Vienna Scientific Cluster (VSC-2), the Starch and Cyclodextrin Research Unit of the CU and the Department of Pharmaceutical Technology and Biopharmaceutics, University of Vienna, for providing facilities, computing resources and helpful support.

References

1. Middleton, E., Jr. Effect of plant flavonoids on immune and inflammatory cell function. *Flavonoids in the Living System;* Springer: Berlin, Germany, 1998; pp 175–182.
2. Harborne, J. B.; Williams, C. A. *Phytochemistry* **2000,** *55,* 481–504. doi:10.1016/S0031-9422(00)00235-1
3. Kandaswami, C.; Middleton, E., Jr. Free radical scavenging and antioxidant activity of plant flavonoids. *Free radicals in diagnostic medicine;* Springer: Berlin, Germany, 1994; pp 351–376.
4. Cook, N. C.; Samman, S. *J. Nutr. Biochem.* **1996,** *7,* 66–76. doi:10.1016/S0955-2863(95)00168-9
5. Marín, L.; Miguélez, E. M.; Villar, C. J.; Lombó, F. *BioMed Res. Int.* **2015,** *2015,* No. 905215. doi:10.1155/2015/905215
6. Vinson, J. A.; Liang, X.; Proch, J.; Hontz, B. A.; Dancel, J.; Sandone, N. Polyphenol antioxidants in citrus juices: in vitro and in vivo studies relevant to heart disease. In *Flavonoids in Cell Function;* Buslig, B. S.; Manthey, J. A., Eds.; Kluwer Academic: New York, NY, U.S.A., 2002; pp 113–122.
7. Borradaile, N. M.; Carroll, K. K.; Kurowska, E. M. *Lipids* **1999,** *34,* 591–598.
8. Lee, S. H.; Park, Y. B.; Bae, K. H.; Bok, H.; Kwon, Y. K.; Lee, E. S.; Choi, M. S. *Ann. Nutr. Metab.* **1999,** *43,* 173–180. doi:10.1159/000012783
9. Santos, K. F. R.; de Oliveira, T. T.; Nagem, T. J.; Pinto, A. S.; Oliveira, M. G. A. *Pharmacol. Res.* **1999,** *40,* 493–496. doi:10.1006/phrs.1999.0556
10. Aswar, M.; Kute, P.; Mahajan, S.; Mahajan, U.; Nerurkar, G.; Aswar, U. *Pharmacol., Biochem. Behav.* **2014,** *124,* 101–107. doi:10.1016/j.pbb.2014.05.013
11. Kim, H. P.; Son, K. H.; Chang, H. W.; Kang, S. S. *J. Pharm. Sci.* **2004,** *96,* 229–245. doi:10.1254/jphs.CRJ04003X
12. YYang, H.-L.; Chen, S.-C.; Senthil Kumar, K. J.; Yu, K.-N.; Lee Chao, P.-D.; Tsai, S.-Y.; Hou, Y.-C.; Hseu, Y.-C. *J. Agric. Food Chem.* **2012,** *60,* 522–532. doi:10.1021/jf2040675
13. Yang, Y.-L.; Hsu, H.-T.; Wang, K.-H.; Han, C.-Y.; Chen, C.-M.; Chen, C.-M.; Ko, W.-C. *J. Biomed. Sci. (London, U. K.)* **2011,** *18,* 84. doi:10.1186/1423-0127-18-84
14. Lopez-Lazaro, M. *Curr. Med. Chem.: Anti-Cancer Agents* **2002,** *2,* 691–714. doi:10.2174/1568011023353714
15. Ren, W.; Qiao, Z.; Wang, H.; Zhu, L.; Zhang, L. *Med. Res. Rev.* **2003,** *23,* 519–534.
16. Ghosal, A.; Satoh, H.; Thomas, P. E.; Bush, E.; Moore, D. *Drug Metab. Dispos.* **1996,** *24,* 940–947.
17. Kanaze, F. I.; Gabrieli, C.; Kokkalou, E.; Georgarakis, M.; Niopas, I. *J. Pharm. Biomed. Anal.* **2003,** *33,* 243–249. doi:10.1016/S0731-7085(03)00289-9
18. So, F. V.; Guthrie, N.; Chambers, A. F.; Moussa, M.; Carroll, K. K. *Nutr. Cancer* **1996,** *26,* 167–181. doi:10.1080/01635589609514473
19. Yang, M.; Tanaka, T.; Hirose, Y.; Deguchi, T.; Mori, H.; Kawada, Y. *Int. J. Cancer* **1997,** *73,* 719–724. doi:10.1002/(sici)1097-0215(19971127)73:5<719::aid-ijc18>3.0.co;2-0
20. Tanaka, T.; Makita, H.; Kawabata, K.; Mori, H.; Kakumoto, M.; Satoh, K.; Hara, A.; Sumida, T.; Ogawa, H. *Carcinogenesis* **1997,** *18,* 957–965. doi:10.1093/carcin/18.5.957
21. Miyagi, Y.; Om, A. S.; Chee, K. M.; Bennink, M. R. *Nutr. Cancer* **2000,** *36,* 224–229. doi:10.1207/S15327914NC3602_12
22. Aranganathan, S.; Selvam, J. P.; Nalini, N. *Invest. New Drugs* **2009,** *27,* 203–213. doi:10.1007/s10637-008-9158-8
23. Choi, E. J. *Nutr. Cancer* **2007,** *59,* 115–119.
24. So, F. V.; Guthrie, N.; Chambers, A. F.; Carroll, K. K. *Cancer Lett.* **1997,** *112,* 127–133. doi:10.1016/S0304-3835(96)04557-0
25. Kanno, S.-i.; Tomizawa, A.; Hiura, T.; Osanai, Y.; Shouji, A.; Ujibe, M.; Ohtake, T.; Kimura, K.; Ishikawa, M. *Biol. Pharm. Bull.* **2005,** *28,* 527–530. doi:10.1248/bpb.28.527
26. Harmon, A. W.; Patel, Y. M. *Breast Cancer Res. Treat.* **2004,** *85,* 103–110. doi:10.1023/B:BREA.0000025397.56192.e2
27. Bulzomi, P.; Bolli, A.; Galluzzo, P.; Leone, S.; Acconcia, F.; Marino, M. *IUBMB Life* **2010,** *62,* 51–60. doi:10.1002/iub.279
28. Legrand, F.-X.; Sauthier, M.; Flahaut, C.; Hachani, J.; Elfakir, C.; Fourmentin, S.; Tilloy, S.; Monflier, E. *J. Mol. Catal. A: Chem.* **2009,** *303,* 72–77. doi:10.1016/j.molcata.2008.12.017
29. Rajewski, R. A.; Stella, V. J. *J. Pharm. Sci.* **1996,** *85,* 1142–1169. doi:10.1021/js960075u

30. Ficarra, R.; Tommasini, S.; Raneri, D.; Calabrò, M. L.; Di Bella, M. R.; Rustichelli, C.; Gamberini, M. C.; Ficarra, P. *J. Pharm. Biomed. Anal.* **2002,** *29,* 1005–1014. doi:10.1016/S0731-7085(02)00141-3
31. Yang, L.-J.; Ma, S.-X.; Zhou, S.-Y.; Chen, W.; Yuan, M.-W.; Yin, Y.-Q.; Yang, X.-D. *Carbohydr. Polym.* **2013,** *98,* 861–869. doi:10.1016/j.carbpol.2013.07.010
32. Kaiyawet, N.; Rungrotmongkol, T.; Hannongbua, S. *J. Chem. Inf. Model.* **2013,** *53,* 1315–1323. doi:10.1021/ci400131y
33. Dalmora, M. E. A.; Oliveira, A. G. *Int. J. Pharm.* **1999,** *184,* 157–164. doi:10.1016/S0378-5173(99)00099-X
34. Milić-Aškrabić, J.; Rajić, D. S.; Tasić, Lj.; Djurić, S.; Kása, P.; Pintye-hódi, K. *Drug Dev. Ind. Pharm.* **1997,** *23,* 1123–1129. doi:10.3109/03639049709150503
35. Kang, J.; Kumar, V.; Yang, D.; Chowdhury, P. R.; Hohl, R. J. *Eur. J. Pharm. Sci.* **2002,** *15,* 163–170. doi:10.1016/S0928-0987(01)00214-7
36. Shi, J.-H.; Zhou, Y.-F. *Spectrochim. Acta, Part A* **2011,** *83,* 570–574. doi:10.1016/j.saa.2011.09.005
37. Choi, S. G.; Lee, S.-E.; Kang, B.-S.; Ng, C. L.; Davaa, E.; Park, J.-S. *PLoS One* **2014,** *9,* e109090. doi:10.1371/journal.pone.0109090
38. Hussain, A.; Yang, T.; Zaghloul, A.-A.; Ahsan, F. *Pharm. Res.* **2003,** *20,* 1551–1557.
39. Merkus, F. W. H. M.; Verhoef, J. C.; Marttin, E.; Romeijn, S. G.; van der Kuy, P. H. M.; Hermens, W. A. J. J.; Schipper, N. G. M. *Adv. Drug Delivery Rev.* **1999,** *36,* 41–57. doi:10.1016/S0169-409X(98)00054-4
40. Sangpheak, W.; Khuntawee, W.; Wolschann, P.; Pongsawasdi, P.; Rungrotmongkol, T. *J. Mol. Graphics Modell.* **2014,** *50,* 10–15. doi:10.1016/j.jmgm.2014.03.001
41. Liu, B.; Li, W.; Nguyen, T. A.; Zhao, J. *Food Chem.* **2012,** *134,* 926–932. doi:10.1016/j.foodchem.2012.02.207
42. Tommasini, S.; Raneri, D.; Ficarra, R.; Calabrò, M. L.; Stancanelli, R.; Ficarra, P. *J. Pharm. Biomed. Anal.* **2004,** *35,* 379–387. doi:10.1016/S0731-7085(03)00647-2
43. Higuchi, T.; Connors, K. A. Advances in Analytical Chemistry and Instrumentation. *Phase Solubility Studies;* 1965; pp 117–212.
44. Challa, R.; Ahuja, A.; Ali, J.; Khar, R. K. *AAPS PharmSciTech* **2005,** *6,* E329–E357. doi:10.1208/pt060243
45. Jullian, C.; Moyano, L.; Yañez, C.; Olea-Azar, C. *Spectrochim. Acta, Part A* **2007,** *67,* 230–234. doi:10.1016/j.saa.2006.07.006
46. Yuan, C.; Jin, Z.; Li, X. *Food Chem.* **2008,** *106,* 50–55. doi:10.1016/j.foodchem.2007.05.045
47. Johnson, L. V.; Walsh, M. L.; Chen, L. B. *Proc. Natl. Acad. Sci. U. S. A.* **1980,** *77,* 990–994. doi:10.1073/pnas.77.2.990
48. Zingone, G.; Rubessa, F. *Int. J. Pharm.* **2005,** *291,* 3–10. doi:10.1016/j.ijpharm.2004.11.013
49. Hassan, M. A.; Suleiman, M. S.; Najib, N. M. *Int. J. Pharm.* **1990,** *58,* 19–24. doi:10.1016/0378-5173(90)90282-9
50. Esclusa-Diaz, M. T.; Guimaraens-Méndez, M.; Pérez-Marcos, M. B.; Vila-Jato, J. L.; Torres-Labandeira, J. J. *Int. J. Pharm.* **1996,** *143,* 203–210. doi:10.1016/S0378-5173(96)04704-7
51. Ruan, L.-P.; Yu, B.-Y.; Fu, G.-M.; Zhu, D.-n. *J. Pharm. Biomed. Anal.* **2005,** *38,* 457–464. doi:10.1016/j.jpba.2005.01.030
52. Jun, S. W.; Kim, M.-S.; Kim, J.-S.; Park, H. J.; Lee, S.; Woo, J.-S.; Hwang, S.-J. *Eur. J. Pharm. Biopharm.* **2007,** *66,* 413–421. doi:10.1016/j.ejpb.2006.11.013
53. Erden, N.; Çelebi, N. *Int. J. Pharm.* **1988,** *48,* 83–89. doi:10.1016/0378-5173(88)90250-5
54. Mueller, M.; Hobiger, S.; Jungbauer, A. *Food Chem.* **2010,** *122,* 987–996. doi:10.1016/j.foodchem.2010.03.041
55. Bodet, C.; La, V. D.; Epifano, F.; Grenier, D. *J. Periodontal Res.* **2008,** *43,* 400–407. doi:10.1111/j.1600-0765.2007.01055.x
56. Rasheed, A.; Ashok Kumar, C. K.; Sravanthi, V. V. N. S. S. *Sci. Pharm.* **2008,** *76,* 567–598. doi:10.3797/scipharm.0808-05
57. Stancanelli, R.; Mazzaglia, A.; Tommasini, S.; Calabrò, M. L.; Villari, V.; Guardo, M.; Ficarra, P.; Ficarra, R. *J. Pharm. Biomed. Anal.* **2007,** *44,* 980–984. doi:10.1016/j.jpba.2007.03.025
58. Daruházi, Á. E.; Szente, L.; Balogh, B.; Mátyus, P.; Béni, S.; Takács, M.; Gergely, A.; Horváth, P.; Szőke, É.; Lemberkovics, É. *J. Pharm. Biomed. Anal.* **2008,** *48,* 636–640. doi:10.1016/j.jpba.2008.06.007
59. Krishnakumar, N.; Sulfikkarali, N.; RajendraPrasad, N.; Karthikeyan, S. *Biomed. Prev. Nutr.* **2011,** *1,* 223–231. doi:10.1016/j.bionut.2011.09.003
60. Nutho, B.; Khuntawee, W.; Rungnim, C.; Pongsawasdi, P.; Wolschann, P.; Karpfen, A.; Kungwan, N.; Rungrotmongkol, T. *Beilstein J. Org. Chem.* **2014,** *10,* 2789–2799. doi:10.3762/bjoc.10.296
61. Walker, R. C.; Crowley, M. F.; Case, D. A. *J. Comput. Chem.* **2008,** *29,* 1019–1031. doi:10.1002/jcc.20857
62. Khuntawee, W.; Rungrotmongkol, T.; Hannongbua, S. *J. Chem. Inf. Model.* **2011,** *52,* 76–83. doi:10.1021/ci200304v
63. Meeprasert, A.; Khuntawee, W.; Kamlungsua, K.; Nunthaboot, N.; Rungrotmongkol, T.; Hannongbua, S. *J. Mol. Graphics Modell.* **2012,** *38,* 148–154. doi:10.1016/j.jmgm.2012.06.007
64. Luty, B. A.; van Gunsteren, W. F. *J. Phys. Chem.* **1996,** *100,* 2581–2587. doi:10.1021/jp9518623
65. Alecu, I.; Zheng, J.; Zhao, Y.; Truhlar, D. G. *J. Chem. Theory Comput.* **2010,** *6,* 2872–2887. doi:10.1021/ct100326h

License and Terms

The definitive version of this article is the electronic one which can be found at:
doi:10.3762/bjoc.11.297

BEILSTEIN JOURNAL OF ORGANIC CHEMISTRY

Polydisperse methyl β-cyclodextrin–epichlorohydrin polymers: variable contact time ^{13}C CP-MAS solid-state NMR characterization

Isabelle Mallard[1], Davy Baudelet[1,2,3], Franca Castiglione[4], Monica Ferro[4], Walter Panzeri[5], Enzio Ragg[6] and Andrea Mele[*4,5,§]

Full Research Paper

Open Access

Address:
[1]ULCO, UCEIV, F-59140 Dunkerque, France, [2]UCLille, EA GRIIOT (4481), Laboratoire de Pharmacochimie, HEI, 13 rue de Toul, F-59046 Lille, France, [3]UFR Pharmacie, EA GRIIOT (4481), Laboratoire de Chimie Analytique, BP 83, F-59006 Lille, France, [4]Dipartimento di Chimica, Materiali ed Ingegneria Chimica 'G. Natta' Politecnico di Milano, Piazza L. da Vinci 32, I-20133 Milano, Italy, [5]CNR-ICRM, Via L. Mancinelli 7, I-20131 Milano, Italy and [6]Dipartimento di Scienze Molecolari Agroalimentari, Università di Milano, Via Celoria, 2 I-20133 Milano, Italy

Email:
Andrea Mele[*] - andrea.mele@polimi.it

* Corresponding author
§ Tel.: 39-02-23993006; Fax: 39-02-23993180

Keywords:
dynamic cross-polarization; epichlorohydrin; imprinted; insoluble CRYSMEB polymers; solid-state NMR spectroscopy

Beilstein J. Org. Chem. **2015,** *11,* 2785–2794.
doi:10.3762/bjoc.11.299

Received: 22 July 2015
Accepted: 14 December 2015
Published: 30 December 2015

This article is part of the Thematic Series "Superstructures with cyclodextrins: Chemistry and applications III".

Guest Editor: G. Wenz

Abstract

The polymerization of partially methylated β-cyclodextrin (CRYSMEB) with epichlorohydrin was carried out in the presence of a known amount of toluene as imprinting agent. Three different preparations (D1, D2 and D3) of imprinted polymers were obtained and characterized by solid-state ^{13}C NMR spectroscopy under cross-polarization magic angle spinning (CP-MAS) conditions. The polymers were prepared by using the same synthetic conditions but with different molar ratios of imprinting agent/monomer, leading to morphologically equivalent materials but with different absorption properties. The main purpose of the work was to find a suitable spectroscopic descriptor accounting for the different imprinting process in three homogeneous polymeric networks. The polymers were characterized by studying the kinetics of the cross-polarization process. This approach is based on variable contact time CP-MAS spectra, referred to as VCP-MAS. The analysis of the VCP-MAS spectra provided two relaxation parameters: T_{CH} (the CP time constant) and $T_{1\rho}$ (the proton spin-lattice relaxation time in the rotating frame). The results and the analysis presented in the paper pointed out that T_{CH} is sensitive to the imprinting process, showing variations related to the toluene/cyclodextrin molar ratio used for the preparation of the materials. Conversely, the observed values of $T_{1\rho}$ did not show dramatic variations with the imprinting protocol, but rather confirmed that the three polymers are morphologically similar. Thus the combined use of T_{CH} and $T_{1\rho}$ can be helpful for the characterization and fine tuning of imprinted polymeric matrices.

Introduction

Cyclodextrin polymers are a subject of great interest because of their use in pharmaceutical industry [1,2], analytical chemistry [3-5], wastewater treatment [6] and food industry [7-9]. Water-insoluble β-cyclodextrin (β-CD) polymers [10] have been widely described to remove organic pollutants [6,11-13] and heavy metals [14] from water. The most efficient method for the synthesis of insoluble polymers is to use di- or polyfunctional linkers with monomers of cyclodextrins. Different effective crosslinkers have been reported in the literature such as epichlorohydrin [15,16], isocyanates [17,18], polycarboxylic acids [19,20] and anhydrides [21]. Following a slightly different approach, Trotta [18] and his group demonstrated that polymerization of cyclodextrins with a variety of synthetic equivalents of di- and tetracarboxylic acids provides an easy, efficient and environmentally sustainable route to highly cross-linked, nanoporous polymers commonly referred to as cyclodextrin nanosponges.

One of the most frequently used crosslinker for insoluble polymers is epichlorohydrin (EP). In this case, the reaction of β-CD with EP requires very strong alkaline conditions to achieve deprotonation of the hydroxyl groups. Then, EP reacts with the alkoxide to form intra- or inter-ether linkages.

We previously proposed the synthesis [22] of soluble and insoluble polymers of a partially secondary rim methylated β-CD (DS = 4.9) commonly called CRYSMEB. In this previous paper, we described the synthesis of imprinted polymers. The imprinting technique is based on interactions between a template and a suitable functional monomer during the prepolymerization process. Once the template is removed, the resulting product is a cross-linked copolymer matrix with specific recognition sites for the template molecule.

As a matter of fact, high-resolution solid-state NMR is a powerful tool to characterize the structure of polymers [23,24] and to study their dynamics [25,26]. Crini has reported previously a solid-state NMR spectroscopy study [27,28] of β-cyclodextrin polymers. At this time, no discussion concerning the NMR spectroscopic characterization of insoluble imprinted CRYSMEB polymers has been reported.

The main purpose of these measurements was to explore possible applications of solid-state NMR spectroscopy for the characterization, at the atomic level, of polymers obtained from polydisperse crystalline methyl β-CD (CRYSMEB) and epichlorohydrin in the presence of a guest molecule. Particular emphasis is devoted to the determination of possible experimental descriptors able to distinguish polymers obtained with the same synthetic route but in the presence of different amounts of imprinting agent, as in the present case. We herein propose an approach based on solid-state ^{13}C NMR techniques such as variable contact time cross-polarization magic angle spinning with dipolar decoupling (VCP-MAS) to describe these new materials. The dynamics of cross-polarization can be conveniently exploited to fingerprint the new materials and to provide information for tailored synthesis.

Results and Discussion

The molecular imprinting technique allows the introduction of a molecular memory for drugs [29,30] or volatile organic compounds [31,32]. This selective recognition in shape, size and chemical functionality is achieved due to the presence of the target molecule during the polymerization process (Scheme 1).

Initially the target molecules form a complex with the cyclodextrin followed by a copolymerization of the imprinted

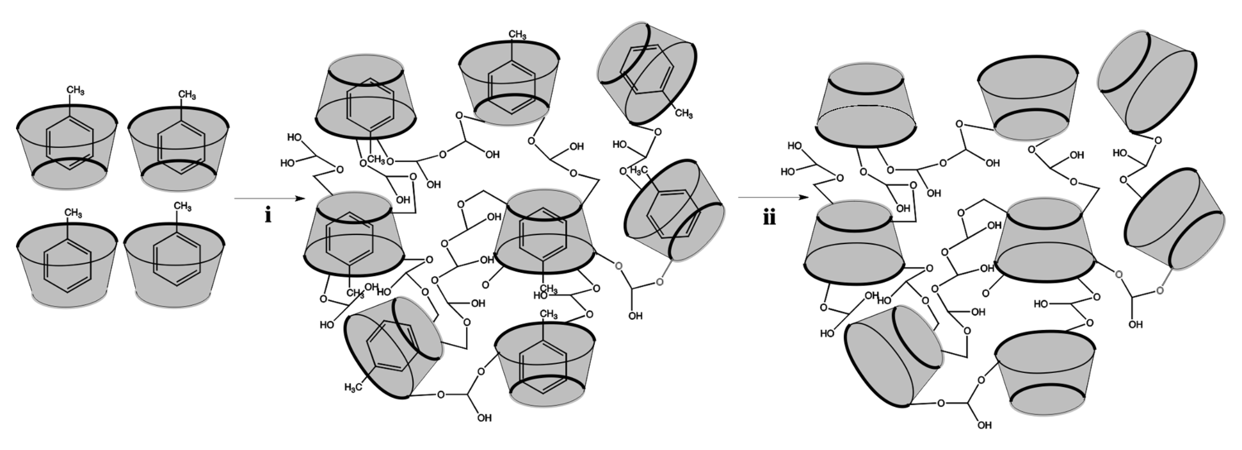

Scheme 1: Schematic representation of molecular imprinting technique. i) Polymerization process with toluene-imprinted CRYSMEB and epichlorohydrin, ii) toluene removal.

monomers with the crosslinker. The template introduces highly specific sites into the polymeric network and, after removal of the target the polymer is able to rebind the molecule with high selectivity.

Polymers of CRYSMEB were synthesized according to the procedure of Mallard Favier [22]. Our synthetic protocol was chosen to employ a larger ratio of crosslinker to functional monomer to get insoluble polymers. The deprotonation was carried out in aqueous basic media and imprinting was performed in toluene for 20 min before the polymerization process. After the introduction of toluene, a clear solution was systematically observed. The absence of light diffraction, as expected in the case of toluene aggregation, was controlled by recording the UV–vis absorption spectra in the visible region (400–700 nm), outside the absorption range of toluene. As flattened signals with absorbances close to zero were obtained for all of the mixtures, one can conclude that toluene was dissolved quantitatively in the aqueous phase. Different molar ratios of toluene/CD were used as reported in Table 1. Toluene was chosen as a template for a paradigmatic representative of aromatic organic compounds. The combination of the two parameters such as the value of the binding constant between toluene and β-CD ($K_f = 158\ M^{-1}$) [33] and the high volatility of toluene leads to the conclusion that toluene is a good template for imprinting reactions. According to Ritter [34], the CD–toluene complex fosters mainly the formation of linear polymers instead of globular polymers and the linear polymer network promotes a more efficient guest binding due to a more effective accessibility of the cavity. These points allow an easy removal of toluene by simple drying in the oven under vacuum. Additionally, the control of the polymer growth leading to linear polymer network provided a sufficiently regular system for the interpretation of the NMR results.

Table 1: Experimental conditions for the synthesis of polymer.[a]

Polymer	EP/CD	Toluene/CD
D1	40/1	1/4
D2	40/1	4/1
D3	40/1	3/1

[a] Ratios are molar ratios.

Due to the experimental conditions such as high NaOH concentration, high EP/CD ratio and high temperature [15,35], the polymerization process leads exclusively to insoluble cross-linked polymers after EP addition. It should be mentioned that the formation of intralinked bonds between hydroxyl groups and epichlorohydrin was reduced due to the presence of methyl groups in the outer CD cavity. Under the reaction conditions used (33% NaOH, EP/CD= 40 and *T* = 60 °C), gel formation [36] was observed, and the template had no effect on the gel point. Indeed the polymerization process provided insoluble cross-linked polymers without any apparent interference due to the presence of the template during the synthesis.

FTIR analysis

A first inspection of the spectroscopic characteristic of D1, D2 and D3 was achieved by FTIR. The infrared spectra of the samples, including reference CRYSMEB, were recorded and are depicted in Figure 1. The fingerprint peaks of the glucopyranose rings were reflected specifically in all polymer spectra: the C–O–C stretching vibration at 1040 cm^{-1}, the stretching vibration for the aliphatic CH_2 at 2900 cm^{-1} and the OH stretching vibration between 3700 and 3000 cm^{-1}. As a consequence of the crosslinking process with EP, the spectra of D1, D2 and D3 exhibited a new stretching vibration assigned to CH_2 groups at 2970 cm^{-1}, and a scissoring bending vibration at 1400 cm^{-1}. The presence of these more intense bands indicates that EP reacted with the hydroxyl groups. The characteristic water vibration band at around 1650 cm^{-1}, assigned to the δHOH bending mode, present in the CRYSMEB spectrum, was indeed absent in the spectra of the polymers. All spectral features observed for the polymers D1, D2 and D3 were in agreement with the results obtained by Orpecio and Evans [37] for β-cyclodextrin–epichlorohydrin polymers.

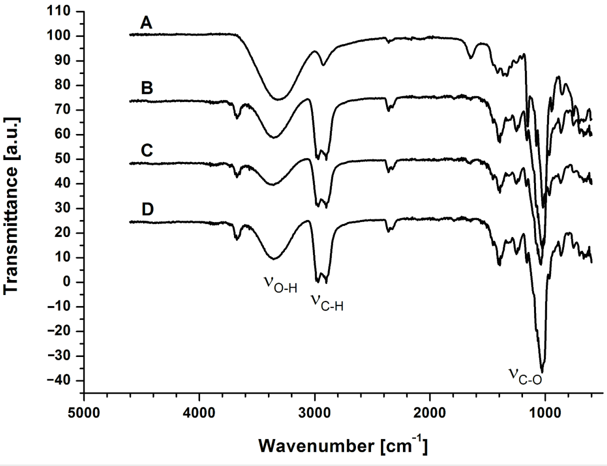

Figure 1: FTIR spectra of (A): native CRYSMEB, (B): D3 (toluene/CD 3:1), (C): D2 (toluene/CD 4:1), and (D): D1 (toluene/CD 1:4) polymers.

Powder X-ray diffraction spectra

The starting monomer, CRYSMEB and all polymers D1, D2 and D3 were analyzed by X-ray powder diffraction. Figure 2 shows, as an example, the X-ray powder diffraction (XRPD) profiles of CRYSMEB and polymer D1. The upper trace clearly displays the typical halos of the amorphous material. This finding was indeed unexpected, as the starting material was supposed to show non-negligible crystallinity. Similar patterns are observed for D1, as shown in the bottom trace. The diffraction profiles of D2 and D3 were very similar to that obtained for D1 and are not reported here. In all the cases the polymeric material was completely amorphous. However, all the XRPD of D1–D3 samples show a shape of the amorphous profile modified with respect to that of pure CRYSMEB.

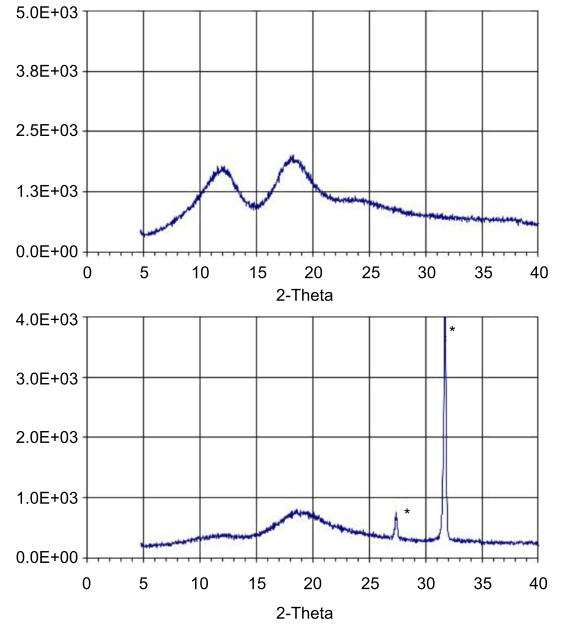

Figure 2: Top: XRPD pattern for CRYSMEB. Bottom: XRPD pattern for D1 polymer. The diffraction peaks denoted with an asterisk at 2θ = 27.48° and 31.7° are due to the presence of traces of residual NaCl. The assignment was confirmed by collecting the XRDP in the 4–100° range of 2θ and comparing the experimental profile with the literature pattern of pure NaCl.

NMR analysis

NMR analysis was carried out by ^{13}C {^{1}H} solid-state CP-MAS NMR techniques and the experimental spectra of the three samples are shown in Figure 3. The chemical shift range is 50–110 ppm, which is characteristic for the β-CD moiety. The assignment of the polymer resonances is based on the reported values for the crystalline permethylated β-CD. Four carbon resonances due to the glucose unit are observed for all samples and are reported from larger to smaller chemical shift values: C(1), C(4), [C(5), C(3) and C(2)], and C(6). The CH_2–CH signals of epichlorohydrin are overlapped with the β-CD resonances, and only the signal at 64 ppm can be assigned to the epichlorohydrin moiety [22]. In general all resonances mainly appear as broad single peaks.

No chemical shift changes were observed in the spectra for D1, D2 and D3, indicating that no major structural modifications occurred when the amount of the guest molecule toluene is varied. The line width of the spectral bands in the ^{13}C CP-MAS NMR spectra can be qualitatively associated with the crystallinity of the samples: the more crystalline the sample is the sharper are the peaks. However, in the present case the XRPD analysis (vide supra) ruled out any crystalline character of the polymers. Thus, the higher resolution obtained for the sample D3 with respect to D2 and D1 (see top trace in Figure 3), represents an empirical finding. Indeed, all signals in the spectrum of sample D3 are sharper than the corresponding peaks in the spectra of the other two samples, as can be seen considering the peak at 64 ppm which is assigned to epichlorohydrin.

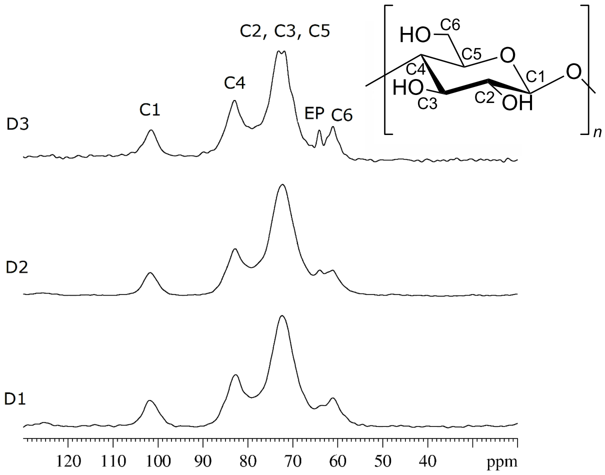

Figure 3: ^{13}C {^{1}H} CP-MAS spectra of polymers D1, D2 and D3. Peak assignment is given in the upper trace.

For comparison, a sample of native CRYSMEB was also analyzed. The ^{13}C {^{1}H} CP-MAS spectrum is reported in Figure 4 together with the spectrum of the D3 polymer. The

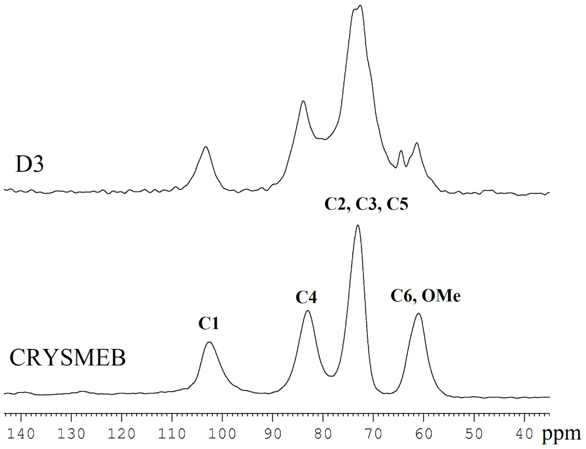

Figure 4: ^{13}C {^{1}H} CP-MAS spectra of native CRYSMEB and polymer D3. Peak assignment is given on CRYSMEB spectrum.

comparison of the two experimental spectra reveals that no chemical shift variations are observed. Consequently, no relevant structural modification occurs on the β-CD moiety during the polymerization process.

Dynamics of cross polarization – theoretical description

Important features of the dynamic behavior of a material can be extracted from solid-state NMR data by the analysis of the dynamics of the cross-polarization process.

Cross-polarization from abundant spins ^{1}H to dilute spins ^{13}C is a double resonance technique mainly used to improve the lower ^{13}C sensitivity. If the nuclei are close in space, some dipolar magnetic interactions are established. The nuclei coupled in such a way may transfer polarization from the abundant to the dilute spin (cross-polarization, CP) provided the so called Hartmann–Hahn matching condition if fulfilled. Under CP conditions, a significant sensitivity enhancement of the dilute spin (^{13}C) is achieved. The efficiency of CP depends on structural and dynamic factors, related to the sample under investigation. In particular, the internuclear distances and the dynamics of the functional groups are factors affecting the process. Thus, CP provides both structural information (the chemical connectivity) and dynamic insights (the overall molecular dynamics in the solid state). Pines et al. [38] were the first to discuss the effect of different types of motion – such as molecular conformational changes, molecular reorientation and macroscopic sample rotation – on the CP process. Later, the influence of molecular motion on the heteronuclear polarization rate was investigated in several studies [39].

The dynamics of cross-polarization can be explored by performing several experiments with increasing CP contact time and usually it is theoretically described in the 'fast regime approximation' according to the thermodynamic model developed by Mehring [40]. At the early stage of CP, the ^{13}C magnetization is polarized, arising from the ^{1}H–^{13}C heteronuclear dipolar interactions through ^{1}H reservoirs. Here the growth of the spin magnetization is governed by the cross-polarization rate constant, T_{CH}^{-1}. At long contact times, the ^{13}C magnetization follows an exponential decay described by the proton relaxation time in a rotating frame, $T_{1\rho}$. The combination of these factors leads to the general law for signal intensity reported in Equation 1:

$$I(t) = I_0\left[1-\exp^{-t/T_{CH}}\right]\exp^{-t/T_{1\rho}} \qquad (1)$$

Equation 1 describes the time evolution of the CP intensity *I(t)* as a function of the contact time *t* [38]. The intensity behavior is dictated by two different time constants: T_{CH} and $T_{1\rho}$, the former affecting the initial part of the curve, the latter driving the final decay. When the two relaxation times deviate by at least two orders of magnitude, it is possible to resolve $T_{1\rho}$ and T_{CH} parameters separately from the logarithmic plot of the CP intensity against the contact time.

The CP rate constant T_{CH}^{-1} can be easily extracted from the build-up curves and contains structural and dynamical information. This parameter mainly depends on the number of H atoms attached to a given C atom and on the mobility of the functional group. Thus, a fast cross-polarization process is generally detected in systems containing many H atoms in the proximity of the observed ^{13}C nucleus due to the strong dipolar H–C interaction. Additionally, the molecular motion influences the CP rate as well, thus allowing information about molecules that are entrapped or confined within a porous system. In summary, both the H–C distances and the flexibility of the functional groups contribute to the rate of cross-polarization.

Dynamics of cross polarization – experimental results

The CP magnetization transfer build-up curves were monitored using a constant CP level at various contact times *t*, ranging from 35 μs up to 9 ms. The one-dimensional ^{13}C CP-MAS spectra were acquired at the constant MAS rate of 10 kHz for all samples D1, D2, D3 (the spectra of D3 is shown in Figure 5), and native CRYSMEB to test the applicability of this measurement to the samples.

The CP build-up curves for all carbon atoms of CRYSMEB are reported in Figure 6 and the results observed for the polymers D1 and D3 are shown in Figure 7 as an example. In all cases the typical CP dynamics profile was obtained, where the short-time exponential rise of the curves is put down to the ^{1}H–^{13}C polarization-transfer process due to the residual carbon–proton dipolar interactions, in turn quantified by T_{CH}. On the other hand, the intensity decay after reaching the saturation level mainly originates from the ^{1}H spin–lattice relaxation in the rotating frame ($T_{1\rho}$). Both regimes are well-defined within the contact time range chosen in our experiments.

T_{CH} Contact times: The CP rate ($1/T_{CH}$) under spin-locking conditions is determined by the ^{1}H and ^{13}C relaxation behavior and the effective strength of the dipolar interaction (which is derived from both the C–H distance and molecular motion). The experimental data at short CP times for polymer D1 are illustrated in Figure 8. The plot expanded scale allows to highlight the signals intensities growth in the range of 0–100 μs. A similar behavior is observed for the other polymers D2 and D3.

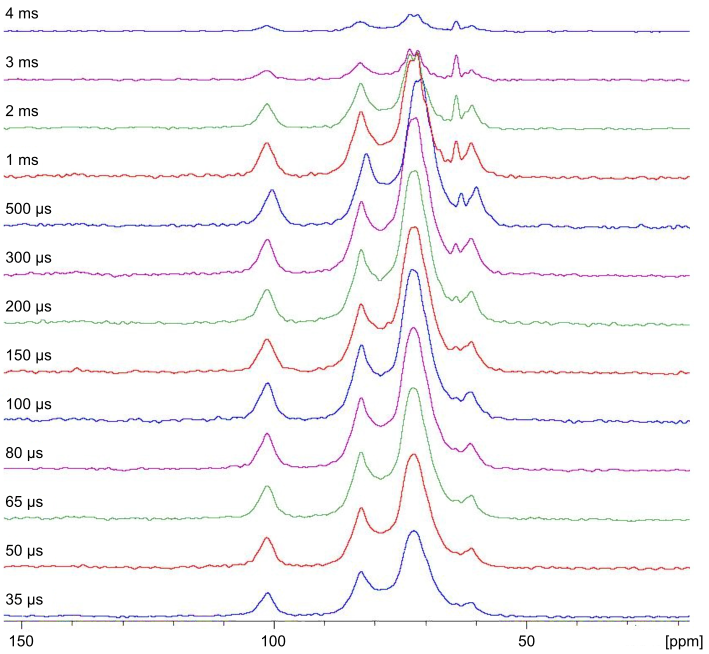

Figure 5: 1D ^{13}C CP/MAS spectra of polymer D3 as a function of the contact time varying from 35 µs to 4 ms.

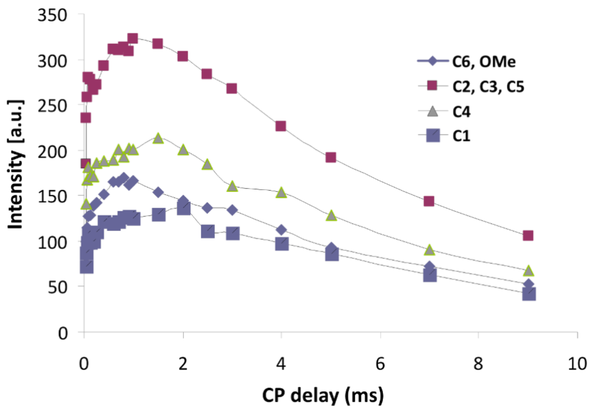

Figure 6: Cross-polymerization (CP) build-up curve of the ^{13}C resonances with variable contact times for the CRYSMEB sample.

The maximum of the curve is observed in the range of 0.8–2 ms for the native CRYSMEB sample (see Figure 6), while shorter contact times (<0.9 ms) are observed for all polymers (see Figure 7). This indicates, in the latter cases, a highly efficient magnetization transfer. This is consistent with a rigid molecular frame, as expected in a cross-linked polymer. As a consequence of such molecular stiffness, strong heteronuclear dipolar interactions are established and facilitate an effective magnetization transfer from the proton to various carbon atoms. A good line-shape fitting was obtained for all carbons of the sugar ring (C1–C5) and C6 for CRYSMEB, while for the three polymers the C6 signal is strongly overlapped with the epichlorohydrin resonances, consequently this line was not analyzed. The T_{CH} values extracted from fitting the exponential rise of the magnetization build-up curves are listed in Table 2 for all studied samples.

First of all we propose analyzing the data for comparing the monomer with the three polymers. This can be done by comparing the data present in the columns 3, 5, 7 and 9 of Table 2. For the CRYSMEB moiety all the carbon atoms show similar T_{CH} values (Table 2, column 3). Similar results are observed for the three polymers, as shown by the values of columns 5, 7 and 9 in the order. For polymers D1 and D3, the T_{CH} values of the β-CD sugar moiety are decreased with respect to that observed for native CRYSMEB, while for polymer D2 the opposite trend is observed. The emerging overall picture is that the polymerization can significantly change the response of the cyclodextrin macro-ring C atoms to the cross-polarization with respect to the pristine CRYSMEB. In detail, the sugar ring C atoms show T_{CH} values correlated to the molar ratio of cyclodextrin to toluene. The observed trend T_{CH} (D2) > T_{CH} (CRYSMEB) > T_{CH} (D3) > T_{CH} (D1) indicates that the increasing amount of toluene used in the polymerization reaction is likely to generate a progressively more loosely packed polymer network that requires longer contact times for the cross-polarization to be effective. It is also interesting to note that the range of variation of T_{CH} values is sufficiently broad to allow for an efficient discrimination among polymers imprinted

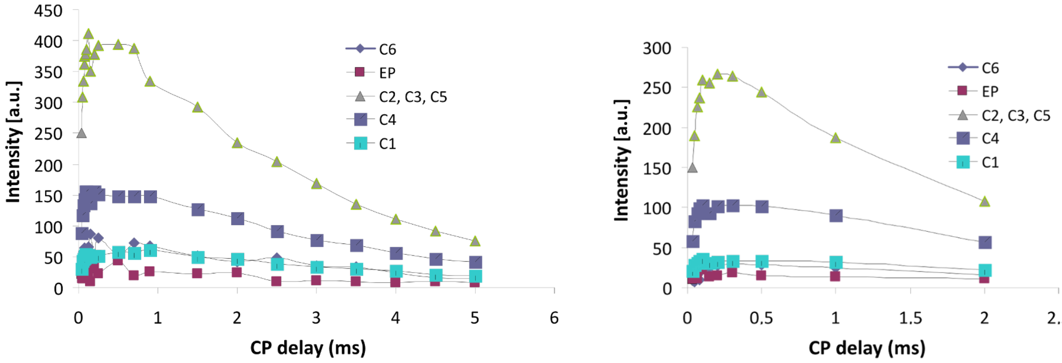

Figure 7: Cross-polymerization (CP) build-up curve of the ^{13}C resonances with variable contact time for polymers D1 (left) and D3 (right).

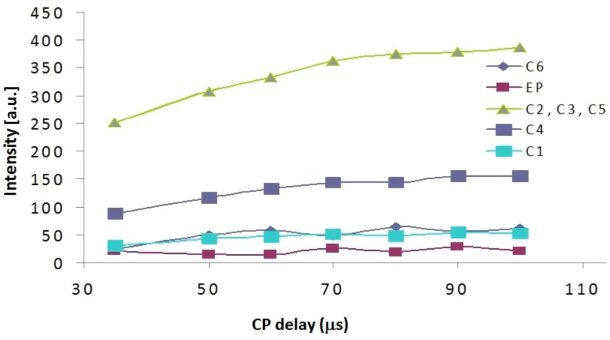

Figure 8: CP build-up curves of the ^{13}C resonances with cross-polymerization in the range 0–100 μs for polymer D1.

with close amounts of the imprinting agent. The polymer growth in the presence of increasing amounts of toluene leaves empty voids influencing the cross-polarization rate in terms of average C–H distances, H atoms density in the proximity of the observed C and the local dynamics. The data thus point out that T_{CH} can be used as a descriptor to differentiate polymers with the same chemical structure and not showing any spectral differences, as shown by the spectra of Figure 3 where no chemical shift variations can be detected, but indeed differently imprinted by toluene.

$T_{1\rho}$ Relaxation times: Proton $T_{1\rho}$ via a resolved carbon resonance provides information on the relative mobility of the H atoms in the molecular frame and whether regions of morphological heterogeneity exist or not. At this stage, it is important to stress two points: i) $T_{1\rho}$ describes the relaxation time of the ^1H nuclei, and thus it is sensitive to hydrogen parameters only, including, as an example, the hydration state. Conversely, the previously reported and discussed T_{CH} values depend on the mutual C–H distance and H atoms' density in the proximity of a given C atom; ii) $T_{1\rho}$ and T_{CH} span a different time scale, the former in milliseconds, the latter in microseconds.

We have analyzed the magnetization decay for the three polymer samples D1, D2, D3 and the native CRYSMEB. The semi logarithmic plot of I/I_0 against CP contact time in the range of 1–5 ms shows a linear behavior and $1/T_{1\rho}$ is the slope of the linear fit. The relaxation curves can be represented by a single exponential indicating that any segmental motion inside the polymeric frame can be ruled out. The results are reported in Table 2. All H atoms attached to β-CD carbons of the three polymers exhibit a rapid $T_{1\rho}$ relaxation compared to the corresponding H atoms of the native CRYSMEB. This fact is in line with the results previously observed in the case of cyclodextrin nanosponges [41]. A striking feature from the data in Table 2 is

Table 2: ^{13}C Chemical shifts (ppm), T_{CH} values (in μs) and ^1H spin-lattice relaxation in the rotating frame ($T_{1\rho}$ in ms) of the carbon atoms of CRYSMEB and the polymers D1, D2 and D3.

		CRYSMEB		Polymer, D1		Polymer, D2		Polymer, D3	
Peak	Chemical shift (ppm)	T_{CH} (μs)	$T_{1\rho}$ (ms)	T_{CH} (μs)	$T_{1\rho}$ (ms)	T_{CH} (μs)	$T_{1\rho}$ (ms)	T_{CH} (μs)	$T_{1\rho}$ (ms)
C1	101.4	140.1	6.5	72.4	3.5	160.9	3.6	96.5	3.3
C4	82.7	105.9	6.5	71.2	3.1	173.7	2.9	88.6	2.5
C2, C3, C5	72.3	144.8	6.6	96.5	2.6	160.9	2.4	96.5	1.8
C6	61.1	114.3	6.8	n.d.	3.5	n.d.	1.9	n.d.	2.7
EP	64.2			n.d.	2.5	n.d.	1.7	n.d.	3.6

that the values of $T_{1\rho}$ for all the H atoms of the three polymers are basically the same, with no particular variation related to structure or the synthetic route. In particular, it seems that the imprinting process has no effect on the $T_{1\rho}$ relaxation values. These findings thus point out that the three polymers are morphologically homogeneous and do not show conformational heterogeneity. As a consequence, the simultaneous determination of both values T_{CH} and $T_{1\rho}$ provides complementary information on the effect of the imprinting process and on the overall dynamic behavior of the materials.

Conclusion

The current study was carried out in order to investigate the structure of insoluble imprinted CRYSMEB polymers using ^{13}C solid-state NMR spectroscopy techniques. The proper characterization of these materials in view of their application as selective sorbent for aromatic pollutants necessarily passes through the assessment of the effect of the imprinting process on the polymeric structure. The CP-MAS NMR spectra showed that the three polymers share the same chemical structure, as no apparent chemical shift and line-shape differences are detectable from the ^{13}C CP-MAS NMR spectra. The study of the kinetics of the cross-polarization process allowed us to determine, for a large collection of C atoms of all the systems, the T_{CH} and $T_{1\rho}$ parameters. A clear-cut physical interpretation of the numerical values derived from our experiments requires the formulation of a dynamic model of the polymers, which is not attempted here and, more importantly, not crucial for the main goal of this work: the formulation of an easy and efficient numerical descriptor accounting for the effect of the imprinting agent in the final materials. Indeed, the combined analysis of T_{CH} and $T_{1\rho}$ provides a fingerprinting discrimination of the three polymeric materials here discussed, D1, D2 and D3. T_{CH} variations were found to be nicely associated to the molar ratio of toluene/CRYSMEB (i.e. imprinting agent/monomer), with longer times related to a larger quantity of toluene and, reasonably, to the presence of the imprinted voids in the polymer frame. Conversely, the values of $T_{1\rho}$ measured for the H atoms attached to the observed C of the polymers did not reveal any significant variation, either within the same polymer or in comparison with the homologous H atoms of the other polymers. This latter point confirms that the polymer synthesis provides homogeneous materials, without micro-heterogeneities or remarkable morphology changes. We are currently extending this methodology – the combined use of T_{CH} and $T_{1\rho}$ – in order to provide a general approach for the characterization of the imprinting features of this class of sorbent materials.

CP-MAS NMR spectra of CRYSMEB-EP polymers can be easily collected providing sufficient resolution for assignment of C signals. The exploration of the dynamic behavior and the molecular morphology of the examined systems is, on our opinion, the most innovative and original feature of the investigation. Indeed, the solid-state NMR parameters (i.e. chemical shift, efficiency of cross-polarization and ^{1}H $T_{1\rho}$ relaxation time) indicate that the addition of toluene leads to a swollen polymer framework and an increase in molecular mobility (as shown by the increased T_{CH}).

The T_{CH} parameter for the various C atoms and for the different batches of polymers could be taken as fingerprint indicator. Moreover, it would be interesting studying a system in which the guest molecules are actually entrapped inside the cross-linked polymer. In this case, the dynamics of the guest could provide precious information on the state of the included molecule inside the polymer network.

Experimental

Chemicals

Toluene, sodium hydroxide and epichlorohydrin were purchased from Aldrich and were used as received. CRYSMEB (DS = 4.9) was provided by Roquette Frères (Lestrem, France).

Materials and instruments

Fourier-transform infrared (FTIR) absorption spectra were recorded using a FTIR Equinox 55 Bruker spectrometer equipped with an ATR module, in the range of 4000–500 cm^{-1} and a resolution of 2 cm^{-1}. The dissolution of toluene in the aqueous phase was analyzed by UV–vis spectroscopy (Perkin-Elmer lambda 2S spectrophotometer). X-ray powder diffraction in the 2θ range of 4.7–40° (step size 0.02°; time per step 0.04 s, slits 0.6–8 mm, 30 KV × 10 mA, PSD 3) were collected on a Bruker AXS D2 Phaser diffractometer equipped with LinxEye detector and in Bragg–Brentano geometry, using Cu Kα radiation (λ = 1.54060 Å) with a Ni filter. The data were collected in open air and with a quartz monocrystal zero background sample holder with 0.2 mm depth. Solid-state CP-MAS ^{13}C NMR spectra were recorded on a Bruker Avance 600 spectrometer, operating at a frequency of 150.9 MHz and equipped with a MAS probe head. The powder sample was inserted in a 4 mm zirconia rotor and spun in air at 10 kHz speed. The conventional ^{13}C spectra were recorded with a proton 90° pulse length of 4 μs, a contact time of 1 ms and 4 s as recycle delay time. Each free induction decay (FID) was acquired with 512 scans and a sweep width of 250 ppm. The TPPM ^{1}H decoupling sequence [30] was used during the acquisition period. CP build-up curves were recorded by increasing the length of the contact pulse from 35 μs to 9 ms. This was done in steps of 35 μs at short times, while for times longer than 250 μs the value of the increment was progressively increased. All the experiments were performed at 298 K. The data analysis was performed using the OriginPro software (9.0 version). The NMR spectra were deconvoluted using OriginPro software (9.0 version). Each peak was approximated by a Gaussian function curve fitting analysis.

General procedure for the preparation of the cyclodextrin polymers

Imprinted polymers were synthesized by a one-step condensation polymerization analogous to that described in [22]. Sodium hydroxide (5 g) was dissolved in water (15 g) and heated under stirring at 60 °C. CRYSMEB (5 g) was added slowly to the solution. Toluene was introduced as template and kept under stirring during 20 min. Then 20 mL of epichlorohydrin were added drop wise to the stirred solution at a rate of about 2 mL every 15 min. At the end of addition, the reaction mixture was kept at 60 °C for 4 h and the polymers were obtained in the gel state. After crushing with ethanol and washing with various solvents, the polymers were dried under vacuum.

References

1. Davis, M. E.; Brewster, M. E. *Nat. Rev. Drug Discovery* **2004,** *3,* 1023. doi:10.1038/nrd1576
2. Gidwani, B.; Vyas, A. *Colloids Surf., B* **2014,** *114,* 130. doi:10.1016/j.colsurfb.2013.09.035
3. Yu, J. C.; Jiang, Z.-T.; Liu, H.-Y.; Yu, J.; Zhang, L. *Anal. Chim. Acta* **2003,** *477,* 93. doi:10.1016/S0003-2670(02)01411-3
4. Crini, G.; Morcellet, M. *J. Sep. Sci.* **2002,** *25,* 789. doi:10.1002/1615-9314(20020901)25:13<789::AID-JSSC789>3.0.CO;2-J
5. De Klerck, K.; Mangelings, D.; Vander Heyden, Y. *J. Pharm. Biomed. Anal.* **2012,** *69,* 77. doi:10.1016/j.jpba.2012.01.021
6. Sancey, B.; Trunfio, G.; Charles, J.; Badot, P.-M.; Crini, G. *J. Inclusion Phenom. Macrocyclic Chem.* **2011,** *70,* 315. doi:10.1007/s10847-010-9841-1
7. Ciobanu, A.; Mallard, I.; Landy, A.; Brabie, G.; Nistor, D.; Fourmentin, S. *Food Chem.* **2013,** *138,* 291. doi:10.1016/j.foodchem.2012.10.106
8. Ciobanu, A.; Mallard, I.; Landy, A.; Brabie, G.; Nistor, D.; Fourmentin, S. *Carbohydr. Polym.* **2012,** *87,* 1963. doi:10.1016/j.carbpol.2011.10.005
9. Gazpio, C.; Sánchez, M.; Isasi, J. R.; Vélaz, I.; Martín, C.; Martínez-Ohárriz, C.; Zornoza, A. *Carbohydr. Polym.* **2008,** *71,* 140. doi:10.1016/j.carbpol.2007.06.007
10. Morin-Crini, N.; Crini, G. *Prog. Polym. Sci.* **2013,** *38,* 344. doi:10.1016/j.progpolymsci.2012.06.005
11. Mamba, B. B.; Krause, R. W.; Malefetse, T. J.; Nxumalo, E. N. *Environ. Chem. Lett.* **2007,** *5,* 79. doi:10.1007/s10311-006-0082-x
12. Mele, A.; Castiglione, F.; Malpezzi, L.; Ganazzoli, F.; Raffaini, G.; Trotta, F.; Rossi, B.; Fontana, A.; Giunchi, G. *J. Inclusion Phenom. Macrocyclic Chem.* **2011,** *69,* 403. doi:10.1007/s10847-010-9772-x
13. Crini, G.; Bertini, S.; Torri, G.; Naggi, A.; Sforzini, D.; Vecchi, C.; Janus, L.; Lekchiri, Y.; Morcellet, M. *J. Appl. Polym. Sci.* **1998,** *68,* 1973. doi:10.1002/(SICI)1097-4628(19980620)68:12<1973::AID-APP11>3.0.CO;2-T
14. Li, N.; Wei, X.; Mei, Z.; Xiong, X.; Chen, S.; Ye, M.; Ding, S. *Carbohydr. Res.* **2011,** *346,* 1721. doi:10.1016/j.carres.2011.05.027
15. Renard, E.; Barnathan, G.; Deratani, A.; Sebille, B. *Macromol. Symp.* **1997,** *122,* 229. doi:10.1002/masy.19971220136
16. Vélaz, I.; Isasi, J. R.; Sánchez, M.; Uzqueda, M.; Ponchel, G. *J. Inclusion Phenom. Macrocyclic Chem.* **2007,** *57,* 65. doi:10.1007/s10847-006-9221-z
17. Wilson, L. D.; Mohamed, M. H.; Headly, J. V. *J. Colloid Interface Sci.* **2011,** *357,* 215. doi:10.1016/j.jcis.2011.01.081
18. Trotta, F.; Zanetti, M.; Cavalli, R. *Beilstein J. Org. Chem.* **2012,** *8,* 2091. doi:10.3762/bjoc.8.235
19. Zhao, D.; Zhao, L.; Zhu, C.; Tian, Z.; Shen, X. *Carbohydr. Polym.* **2009,** *78,* 125. doi:10.1016/j.carbpol.2009.04.022
20. Zhao, D.; Zhao, L.; Zhu, C.-S.; Huang, W.-Q.; Hu, J.-L. *J. Inclusion Phenom. Macrocyclic Chem.* **2009,** *63,* 195. doi:10.1007/s10847-008-9507-4
21. Girek, T.; Kozlowski, C. A.; Koziol, J. J.; Walkowiak, W.; Korus, I. *Carbohydr. Polym.* **2005,** *59,* 211. doi:10.1016/j.carbpol.2004.09.011
22. Mallard Favier, I.; Baudelet, D.; Fourmentin, S. *J. Inclusion Phenom. Macrocyclic Chem.* **2011,** *69,* 433. doi:10.1007/s10847-010-9776-6
23. Komoroski, R. A. *High Resolution NMR-Spectroscopy of Synthetic Polymers in Bulk;* Wiley-VCH: Weinheim, Germany, 1986.
24. Ngono-Ravache, Y.; Foray, M.-F.; Bardet, M. *Polym. Adv. Technol.* **2001,** *12,* 515. doi:10.1002/pat.112
25. Bovey, F. A.; Mirau, P. A. *NMR of polymers;* Academic Press: New York, NY, U.S.A., 1996.
26. Schmidt-Rohr, K.; Clauss, J.; Spiess, H. W. *Macromolecules* **1992,** *25,* 3273. doi:10.1021/ma00038a037
27. Crini, G.; Cosentino, C.; Bertini, S.; Naggi, A.; Torri, G.; Vecchi, C.; Janus, L.; Morcellet, M. *Carbohydr. Res.* **1998,** *308,* 37. doi:10.1016/S0008-6215(98)00077-9
28. Crini, G.; Bourdonneau, M.; Martel, B.; Piotto, M.; Morcellet, M.; Richert, T.; Vebrel, J.; Torri, G.; Morin, N. *J. Appl. Polym. Sci.* **2000,** *75,* 1288. doi:10.1002/(SICI)1097-4628(20000307)75:10<1288::AID-APP10>3.0.CO;2-J
29. Deng, Y.; Cheng, C.; Quin, X.; Xian, X.; Alford, T. T.; Choi, H. W.; Tsow, F.; Forzani, E. S. *Sens. Actuators, B* **2015,** *211,* 25. doi:10.1016/j.snb.2015.01.068
30. Tominaga, Y.; Kubo, T.; Yasuda, K.; Kato, K.; Hosoya, K. *Microporous Mesoporous Mater.* **2012,** *156,* 161.
31. Figueiredo, L.; Erny, G. L.; Santos, L.; Alves, A. *Talanta* **2016,** *146,* 754. doi:10.1016/j.talanta.2015.06.027
32. Zhang, H. *Polymer* **2014,** *55,* 699.
33. Fourmentin, S.; Ciobanu, A.; Landy, D.; Wenz, G. *Beilstein J. Org. Chem.* **2013,** *9,* 1185. doi:10.3762/bjoc.9.133
34. Koopmans, C.; Ritter, H. *Macromolecules* **2008,** *41,* 7418. doi:10.1021/ma801202f
35. Romo, A.; Peñas, F. J.; Sevillano, X.; Isasi, J. R. *J. Appl. Polym. Sci.* **2006,** *100,* 3393. doi:10.1002/app23778
36. Renard, E.; Deratani, A.; Volet, G.; Sebille, B. *Eur. Polym. J.* **1997,** *33,* 49. doi:10.1016/S0014-3057(96)00123-1
37. Orprecio, R.; Evans, C. H. *J. Appl. Polym. Sci.* **2003,** *90,* 2103. doi:10.1002/app.12818
38. Pines, A.; Gibby, M. G.; Waugh, J. S. *J. Chem. Phys.* **1973,** *59,* 569. doi:10.1063/1.1680061
39. Kolodziejski, W.; Klinowski, J. *Chem. Rev.* **2002,** *102,* 613. doi:10.1021/cr000060n

40. Mehring, M. *Principles of high resolution NMR in solids;* Springer: Berlin, Germany, 1983.
41. Castiglione, F.; Crupi, V.; Majolino, D.; Mele, A.; Panzeri, W.; Rossi, B.; Trotta, F.; Venuti, V. *J. Inclusion Phenom. Macrocyclic Chem.* **2013,** *75,* 247. doi:10.1007/s10847-012-0106-z

License and Terms

BEILSTEIN JOURNAL OF ORGANIC CHEMISTRY

Determination of formation constants and structural characterization of cyclodextrin inclusion complexes with two phenolic isomers: carvacrol and thymol

Miriana Kfoury[1,2], David Landy[2], Steven Ruellan[2], Lizette Auezova[1],
Hélène Greige-Gerges[1] and Sophie Fourmentin[*2]

Full Research Paper

Address:
[1]Bioactive Molecules Research Group, Doctoral School of Science and Technology, Department of Chemistry and Biochemistry, Faculty of Sciences, section II, Lebanese University, Lebanon and [2]Unité de Chimie Environnementale et Interactions sur le Vivant (UCEIV, EA 4492), ULCO, F-59140 Dunkerque, France

Email:
Sophie Fourmentin* - lamotte@univ-littoral.fr

* Corresponding author

Keywords:
cyclodextrins; DOSY-NMR; formation constant; molecular modeling; solubility

Beilstein J. Org. Chem. **2016,** *12,* 29–42.
doi:10.3762/bjoc.12.5

Received: 29 October 2015
Accepted: 17 December 2015
Published: 08 January 2016

This article is part of the Thematic Series "Superstructures with cyclodextrins: Chemistry and applications III".

Guest Editor: E. Monflier

Abstract

Carvacrol and thymol have been widely studied for their ability to control food spoilage and to extend shelf-life of food products due to their antimicrobial and antioxidant activities. However, they suffer from poor aqueous solubility and pronounced flavoring ability that limit their application in food systems. These drawbacks could be surpassed by encapsulation in cyclodextrins (CDs). Applications of their inclusion complexes with CDs were reported without investigating the inclusion phenomenon in deep. In this study, inclusion complexes were characterized in terms of formation constants (K_f), complexation efficiency (CE), CD:guest molar ratio and increase in bulk formulation by using an UV–visible competitive method, phase solubility studies as well as ^{1}H and DOSY ^{1}H NMR titration experiments. For the first time, a new algorithmic treatment that combines the chemical shifts and diffusion coefficients variations for all guest protons was applied to calculate K_f. The position of the hydroxy group in carvacrol and thymol did not affect the stoichiometry of the inclusion complexes but led to a different binding stability with CDs. 2D ROESY NMR experiments were also performed to prove the encapsulation and illustrate the stable 3D conformation of the inclusion complexes. The structural investigation was accomplished with molecular modeling studies. Finally, the radical scavenging activity of carvacrol and thymol was evaluated by the ABTS radical scavenging assay. An improvement of this activity was observed upon encapsulation. Taken together, these results evidence that the encapsulation in CDs could be valuable for applications of carvacrol and thymol in food.

Introduction

Carvacrol (2-methyl-5-(1-methylethyl)phenol, **1**) and thymol (5-methyl-2-(1-methylethyl)phenol, **2**) are monoterpenic phenol isomers (Figure 1) produced by several aromatic plants (oregano, thyme, savory, marjoram, etc.) [1]. They are generally recognized as safe (GRAS), approved by the US Food and Drug Administration for human consumption and included by the Council of Europe in the list of food flavorings [1,2].

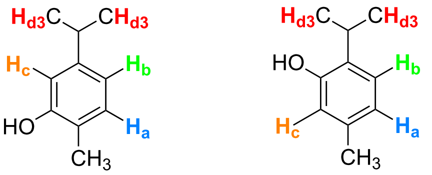

Carvacrol (**1**)
logP^a = 3.81
V = 249.53 Å^3

Thymol (**2**)
logP^a = 3.34
V = 257.25 Å^3

Figure 1: Chemical structures, log*P* values and molecular volumes (*V*) of carvacrol (**1**) and thymol (**2**). ^{a}http://www.molinspiration.com/cgi-bin/properties. $V = M/d$NA, with M: molecular weight, d: density, NA: Avogadro's number.

These phenols are traditionally used at low concentrations as flavoring agents in food [3] and do not have any mutagenic or genotoxic effects [1]. They are cited by the European Commission among the essential oils components registered for use as flavoring in foodstuffs [2,4]. Recently, essential oils have received a growing attention as natural preservatives [5,6] especially in active packaging material for increasing the shelf-life of food products [7,8]. This is due to their potent activity against a broad range of natural spoilage bacteria, fungi and foodborne pathogens [9,10] as well as their pronounced antioxidant effect [11,12]. Consequently, they could be employed as alternatives to synthetic antioxidants such as butylated hydroxytoluene (BHT) or butylated hydroxyanisole (BHA), suspected to be carcinogenic [13,14]. However, the major drawbacks for their use in food are their low aqueous solubility that limits their homogenous dispersion and their contact with pathogens [15], their susceptibility for loss during storage or heat treatement [16] and their relatively high flavor impact and low flavor threshold that lead to the deterioration of food organoleptic quality [4]. Encapsulation in cyclodextrins (CDs) could overcome these limitations. Indeed, CDs have the ability to increase the solubility, protect encapsulated guests against a harmful environment, prevent interactions with food matrix components, generate controlled release systems, reduce off note development and maintain the true aromatic profile of the food [17-20]. CDs are crystalline, homogenous, non-hygroscopic cyclic oligosaccharides. The common native CDs contain 6, 7 and 8 D-(+)-glucopyranose units bound together by α(1→4) linkages and are referred to as α-, β- and γ-CDs [21]. The chair conformation of the glucose units results in a truncated shape of CDs with an external hydrophilic surface and a hydrophobic internal cavity that allows the encapsulation of hydrophobic guests by the formation of inclusion complexes. The substitution of hydroxy groups present on the rims of the torus leads to the production of CD derivatives with increased solubility and enhanced complexation ability [22-24].

Despite that several studies attempted to examine CD/**1** and CD/**2** inclusion complexes [25-33], little is known about the strength of interactions and the difference in the recognition ability of CDs for both isomers. Indeed, only the formation constant (K_f) of the inclusion complex HP-β-CD/**2** (hydroxypropylated-β-CD/**2**) has been reported in literature [28].

Therefore, the present study aimed to determine the ability of CDs to encapsulate and solubilize **1** and **2**. The stoichiometry and K_f values of CD/**1** and CD/**2** inclusion complexes were determined using a competitive UV–visible method, phase solubility studies as well as ^1H and DOSY ^1H NMR titration experiments. An algorithmic treatment was applied to NMR results to calculate K_f values. This algorithm is the first attempt that associates numerous signals (chemical shifts and diffusions coefficients variations) from several entities of the guest molecule (different guest protons) simultaneously to calculate one K_f value. Then, 2D ROESY NMR was carried out to prove the encapsulation as well as to investigate the geometry of inclusion complexes. NMR studies were completed by molecular modeling investigations to illustrate the most energetically favorable conformation of inclusion complexes. Finally, the effect of encapsulation on the antioxidant properties of **1** and **2** was evaluated using the ABTS radical cation assay.

Results and Discussion

UV–visible competitive studies

Stoichiometries and K_f values of inclusion complexes of **1** and **2** with six CDs (α-CD, β-CD, γ-CD, hydroxypropylated-β-CD (HP-β-CD), randomly methylated β-CD (RAMEB) and a low methylated-β-CD (CRYSMEB)) were determined by an UV–visible competitive method using methyl orange (MO) as competitor [34]. Firstly, K_f values of CD/MO inclusion complexes were determined and were consistent with the literature [35]. Then, the competition method was applied. Variations in the absorbance spectra of MO were in good agreement with an 1:1 (CD:guest) stoichiometry proving that all studied CD/**1** and CD/**2** inclusion complexes present an 1:1 stoichiometry. This is coherent with generally observed results for aromatic monoterpenes [17,18,28]. K_f values (Table 1) were calculated based on the absorbance variations using an algorithmic treatment. Only a K_f value of the HP-β-CD/**2** inclusion complex, determined by fluorescence spectroscopy, was found in the literature (1400 M^{-1}) [28]. The obtained K_f value is in good agreement with our results (Table 1).

Table 1: Formation constants K_f (M^{-1}) of CD/carvacrol (**1**) and CD/thymol (**2**) inclusion complexes determined by the competitive UV–visible method at 25 °C.

K_f (M^{-1})	Carvacrol (**1**)	Thymol (**2**)
α-CD	454	107
β-CD	2620	1467
γ-CD	999	233
HP-β-CD	2154	1488
RAMEB	3564	3337
CRYSMEB	2421	2386

Compounds **1** and **2** differ only by the position of the hydroxy group on the aromatic cycle (Figure 1). Results showed that encapsulation of **1** and **2** occurred with all the six CDs. Nonetheless, both phenols were more readily recognized by β-CD and its derivatives as compared to α-CD and γ-CD. Our findings could be strengthened by the fact that the vigor of binding is highly influenced by the complementarity between guest and CD cavity. Molecules with aromatic ring structures would fit better within the β-CD cavity.

When comparing the performance of β-CD derivatives to the native CD, we observed a decline in the K_f value of HP-β-CD/**1** as compared to β-CD/**1** (the decrease in the K_f value of CRYSMEB/**1** was not significant <10%). This could be explained by the steric hindrance of the hydroxypropyl groups of HP-β-CD during the inclusion of **1** inside the cavity. RAMEB gave the most stable inclusion complexes with both **1** and **2**. This is due to that the methoxy groups of RAMEB are small and do not lead to a significant steric hindrance and that the methylation of β-CD hydroxy groups increases the hydrophobic character of the cavity which strengthen its binding to guests.

Concerning the influence of the position of the hydroxy group of **1** and **2** on their recognition by CDs, the former allowed the formation of relatively more stable inclusion complexes as demonstrated by higher K_f values. A tight steric complementarity between CD and guest is crucial to allow the formation of a stable inclusion complex. This is mainly controlled by the chemical structure of the encapsulated guest. K_f values generally increase for guests with an isopropyl moiety. Indeed, *p*-cymene [36] showed higher K_f values than toluene [37]. However, the comparison of K_f values for **1**, **2** and *p*-cymene with β-CDs showed that K_f values for **1** and *p*-cymene were similar while a decrease in the binding interactions for **2** was observed. Both **1** and **2** have a hydroxy group in addition to *p*-cymene. Thus, the decline in the K_f values observed for **2** could be attributed to the enhanced steric hindrance caused by the *ortho* position of the hydroxy group (Figure 1).

Moreover, **1** presents a relatively superior hydrophobic character than **2,** as expressed by log*P* values (Figure 1), which additionally reinforces hydrophobic interactions with the apolar CD cavity.

Phase solubility studies

Phase solubility studies are widely used to evaluate the ability of CDs to increase the aqueous solubility of the guests. They also lead to the determination of diverse parameters involved in complex formation such as K_f value, complexation efficiency (CE), optimal molar ratio for solid inclusion complex prepration and increase in formulation bulk [38].

K_f values obtained by UV–visible competitive studies showed that β-CD and its derivatives form more stable inclusion complexes with **1** and **2** than α-CD and γ-CD. Moreover, HP-β-CD is the only β-CD derivative cited in the FDA's list of Inactive Pharmaceutical Ingredients among the studied derivatives [39] and it previously showed a good solubilizing effect for natural aromas [18]. Consequently, phase solubility studies were performed only with β-CD and HP-β-CD. Results obtained with **1** and **2** at 25 °C are illustrated in Figure 2.

The aqueous solubility of **1** and **2** increased whith CD concentration. A_L-type profiles were obtained with HP-β-CD while B-type profiles were observed in the case of β-CD with both monoterpenes. This could be attributed to the limited aqueous solubility of inclusion complexes obtained between β-CD and poorly soluble guests leading to their precipitation [38]. The slopes of A_L-type and the linear segment of B-type profiles were less than one indicating the formation of 1:1 inclusion complexes in accordance with UV–visible results. K_f values were consequently calculated and were in good agreement with those obtained by the competitive UV–visible method. However, for both phenols, HP-β-CD did not give lower K_f values compared to β-CD as observed with the UV–visible competitive method. This could be explained by the better solubilizing potential of the β-CD derivative compared to the native one. Indeed, K_f values obtained from phase solubility profiles are generally apparent values that combine several effects on the guest solubility: inclusion complexation, self-association of poorly soluble guests, self-aggregation of CD:guest complexes, as well as non-inclusion interaction and micelles formation [38].

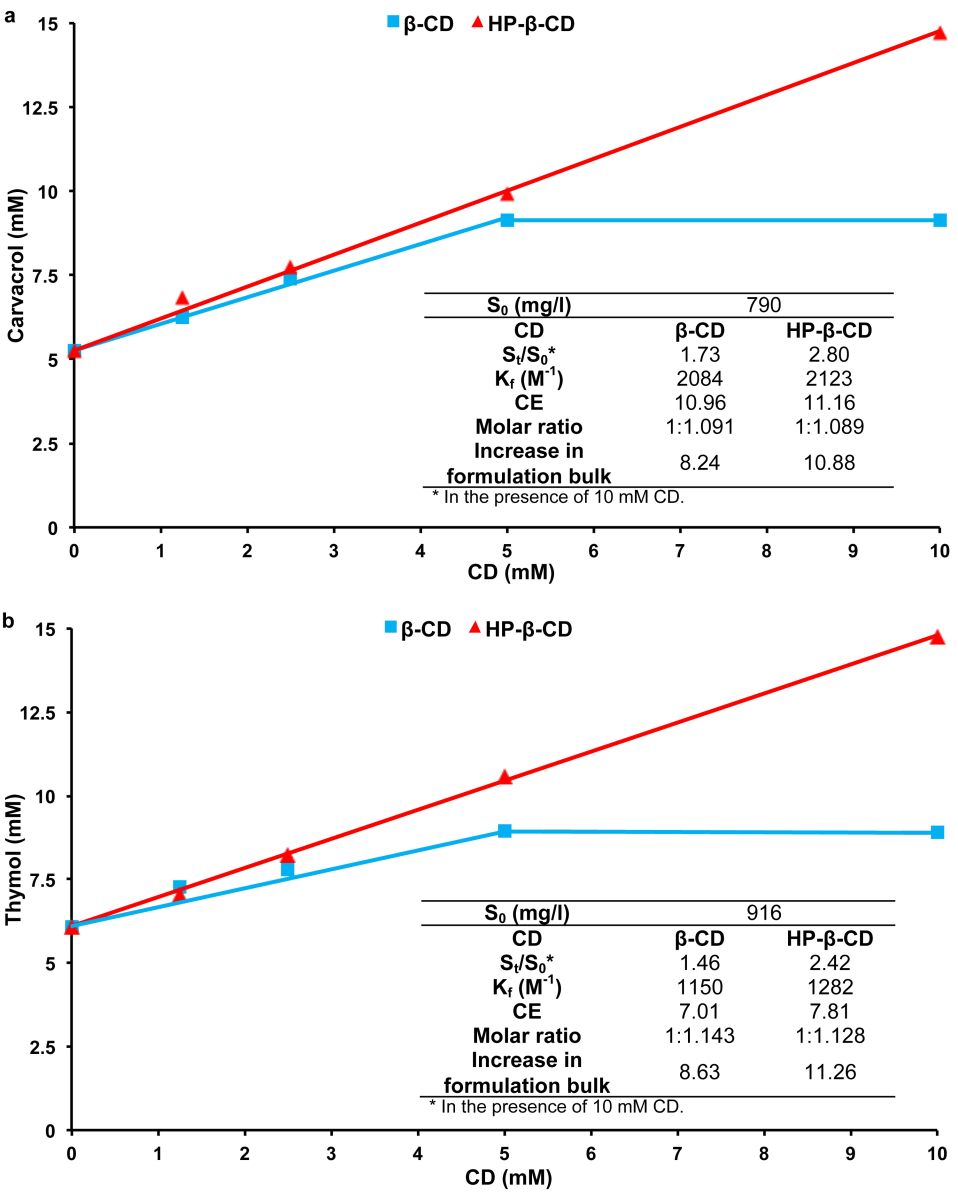

S_0 (mg/l)	790	
CD	**β-CD**	**HP-β-CD**
S_t/S_0*	1.73	2.80
K_f (M^{-1})	2084	2123
CE	10.96	11.16
Molar ratio	1:1.091	1:1.089
Increase in formulation bulk	8.24	10.88

* In the presence of 10 mM CD.

S_0 (mg/l)	916	
CD	**β-CD**	**HP-β-CD**
S_t/S_0*	1.46	2.42
K_f (M^{-1})	1150	1282
CE	7.01	7.81
Molar ratio	1:1.143	1:1.128
Increase in formulation bulk	8.63	11.26

* In the presence of 10 mM CD.

Figure 2: Phase solubility profiles of (a) CD/carvacrol (**1**) and (b) CD/thymol (**2**) inclusion complexes. Inset: Values of formation constants (K_f), solubility enhancement ratio (S_t/S_0), complexation efficiency (CE), optimum molar ratio and increase in formulation bulk of each guest.

The solubilizing potential (S_t/S_0) of CDs was more important for **1** than **2** (Figure 2). This could be attributed to the lower intrinsic solubility of **1** as compared to its isomer. Results are in good agreement with the literature [18] where authors showed that solubilizing potential of CDs increased with the decrease in guest’s solubility.

For both phenols, CE and solubility enhancement were more important for HP-β-CD (Figure 2) confirming that β-CD derivatives are better solubilizers than native β-CD [18,38]. Optimal guest:CD ratios for solid inclusion complexes preparation as well as the increase in formulation bulks were subsequently calculated based on CE values and are presented in Figure 2. HP-β-CD led to a larger increase in the formulation bulk than the parent β-CD due to its greater molecular weight. Relatively high CE values were obtained. It has been reported that guests possessing log*P* between 1 and 4 frequently show good CE values in accordance with our findings [38]. High CE values and reasonable formulation bulk increase suggested that inclusion complexes of **1** and **2** could be potentially used in a solid dosage form for storage or further applications for both phenols [38].

NMR spectroscopy

NMR spectroscopy has been widely employed to investigate CD inclusion complexes [40,41]. It is one of the most complete spectroscopic techniques because it allows a clear distinction between inclusion and other possible external interaction processes. Moreover, it gives direct information on the three-dimensional structure of inclusion complexes [42]. The protons of **1** and **2** are named according to Figure 1.

^{1}H and DOSY ^{1}H NMR titration experiments

Generally, hydrogen atoms of CD and guest are affected by the inclusion resulting in a displacement of their chemical shifts (δ) and diffusion coefficients (D). ^{1}H and DOSY ^{1}H NMR spectra were recorded for free guests (**1** and **2**), pure β-CD (host) and for their inclusion complexes with guest/β-CD ratios ranging from 0.4 to 4. The concentration of guest was kept constant at 2 mM while the concentration of β-CD varied from 0.5 to 5 mM. The chemical shifts (δ) of β-CD protons in the free and complexed states are summarized in Table 2 at equimolar CD/guest ratios.

Table 2: ^{1}H Chemical shifts (δ, ppm) corresponding to β-CD protons in the free and complexed states in the presence of equimolar amounts of either carvacrol (**1**) or thymol (**2**).

β-CD ^{1}H	Free	β-CD/carvacrol (**1**)		β-CD/thymol (**2**)	
	δ	δ	Δδ	δ	Δδ
H-1	5.11	5.08	−0.03	5.09	−0.02
H-2	3.70	3.67	−0.03	3.67	−0.03
H-3	4.00	3.93	−0.07	3.95	−0.05
H-4	3.62	3.61	−0.01	3.61	−0.01
H-5	3.89	3.76	−0.13	3.80	−0.09
H-6	3.91	3.83	−0.08	3.83	−0.08

A positive sign of Δδ ppm shows a downfield displacement and a negative sign an upfield displacement ($\Delta\delta = \delta_{\text{complex}} - \delta_{\text{free}}$).

The protons of the guest molecules were also affected by encapsulation. The chemical shifts (δ) and D of **1** and **2** protons at the different guest/CD ratios are tabulated in Table 3 and Table 4.

We note that no new peak appeared in the inclusion complexes spectra. This indicated that the inclusion of **1** and **2** in CD is a fast exchange process that takes place on the NMR timescale.

Table 3: Diffusion coefficients (*D*, 10^{-10} m^2/s) and chemical shifts (δ, ppm) of carvacrol (**1**) protons in the presence of different β-CD concentrations.

β-CD (mM)	H_a		H_b		H_c		H_d	
	D	δ	D	δ	D	δ	D	δ
0	6.800	7.188	6.680	6.880	6.670	6.843	6.750	1.228
0.5	6.200	7.156	6.340	6.843	6.230	6.806	6.100	1.248
1.0	5.310	7.122	5.250	6.806	5.360	6.771	5.380	1.258
1.5	4.820	7.101	4.780	6.783	4.870	6.749	4.840	1.268
2.0	4.570	7.084	4.540	6.766	4.540	6.733	4.530	1.276
2.5	4.210	7.068	4.180	6.749	4.150	6.716	4.150	1.285
5.0	3.440	7.035	3.460	6.713	3.380	6.681	3.360	1.302

Table 4: Diffusion coefficients (*D*, 10^{-10} m^2/s) and chemical shifts (δ, ppm) of thymol (**2**) protons in the presence of different β-CD concentrations.

β-CD (mM)	H_b		H_a		H_c		H_d	
	D	δ	D	δ	D	δ	D	δ
0	6.880	7.261	6.870	6.854	6.830	6.791	6.760	1.203
0.5	6.080	7.219	6.120	6.806	6.110	6.780	6.070	1.212
1.0	5.630	7.185	5.710	6.785	5.570	6.770	5.550	1.222
1.5	5.180	7.152	5.320	6.734	5.100	6.764	5.010	1.231
2.0	4.610	7.132	4.760	6.711	4.740	6.759	4.780	1.235
2.5	4.240	7.108	4.210	6.684	4.170	6.752	4.370	1.239
5.0	3.580	7.063	3.650	6.632	3.620	6.742	3.630	1.251

In the presence of either **1** or **2**, the protons of β-CD underwent changes in their chemical shifts (δ) (Table 2). The upfield shifts of H-1, H-2 and H-4 protons of β-CD were marginal as compared to those observed for H-3, H-5 and H-6. This indicated that both guests only interact with the inner cavity of CD. Moreover, the clear upfield shift of the H-6 proton of CD could be explained by the deep insertion of guests and showed that interactions occurred between **1** and **2** protons and the narrow side of CD due to steric hindrance. Particularly, the shift of H-3, H-5 and H-6 to higher magnetic fields could be attributed to magnetic anisotropy effects due to their location near to the aromatic ring of the guests which is rich in π-electrons [43].

The protons of **1** and **2** were also affected by the presence of β-CD (Table 3 and Table 4). A progressive upfield shift of the aromatic protons (H_a, H_b and H_c) of **1** and **2** was observed when increasing the CD concentration. Other protons of the guest showed progressive downfield shifts with less pronounced magnitude than those observed for the aromatic protons.

This upfield shift indicated that the aromatic protons of **1** and **2** are mainly involved in the hydrophobic interactions with the interior of the CD cavity [44,45]. Additionally, this revealed some conformational changes generated by the inclusion of **1** and **2** in the CD. The downfield shift observed for other guests' protons is due to a variation in the polarity of their micro-environment when **1** and **2** are inside the CD cavity [46]. This also indicated a shielding effect due to the interactions between guest and CD [47], particularly by van der Waals interactions [48].

These observations suggested that the whole guest molecule is involved in the binding process to CD with the aromatic cycle of both **1** and **2** playing the prominent role in the inclusion process and being embedded in the center of the CD cavity near to oxygen atoms.

DOSY experiments also reveal the intermolecular interactions in solution by observing the variation in the intrinsic diffusion coefficients (*D*) of compounds upon interactions. The *D* values of **1** and **2** protons at the different guest/CD ratios are given in Table 3 and Table 4. The results for the 2 mM solutions of β-CD, guests (**1** and **2**) and the corresponding inclusion complexes are graphically depicted in the 2D DOSY plot in Figure 3. In these spectra, the f1 dimension shows the diffusion coefficient expressed as log*D* and the f2 stands for the chemical shift (δ). f1 is specific for each molecule thus moieties that belong to the same entity will appear in the same f1 row.

CD and guests possess their own *D* values in the free state. *D* is directly related to the molecular weight and size of each molecule. The guests molecules presented higher *D* values than CD in agreement with the fact that the guests are smaller than CD [49]. During the DOSY experiments for β-CD/**1** and β-CD/**2** inclusion complexes, *D* values of β-CD were relatively unaffected by the presence of neither **1** nor **2**. This is due to the small relative mass changes between the free and the complexed macrocycle. Meanwhile, the *D* values of both encapsulated **1** and **2** decreased (Table 3, Table 4 and Figure 3). This proved that **1** and **2** are included in the CD cavity and diffuse slowly.

Finally, variation of chemical shifts (Δδ) and diffusion coefficients (Δ*D*) were plotted as a function of CD concentration for both guests (Figure 4). A global analysis was applied to determine the host/guest affinity. A unique K_f, together with the maximum shifts of each signal, were used to fit simultaneously theoretical and experimental data for all considered Δδ and Δ*D*.

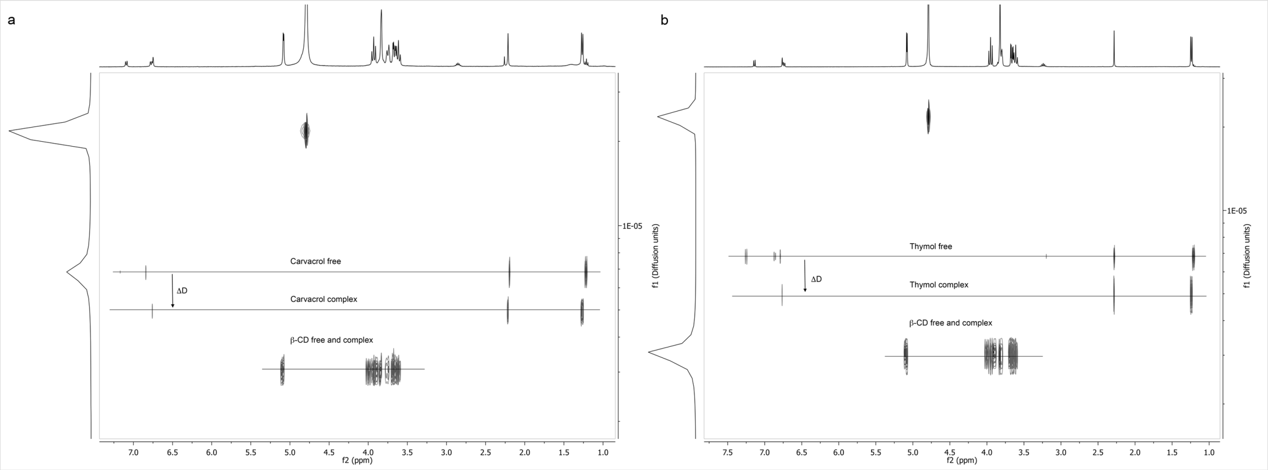

Figure 3: 2D DOSY NMR spectra of (a) β-CD, carvacrol (**1**) and β-CD/carvacrol (**1**) inclusion complex and (b) β-CD, thymol (**2**) and β-CD/thymol (**2**) inclusion complex.

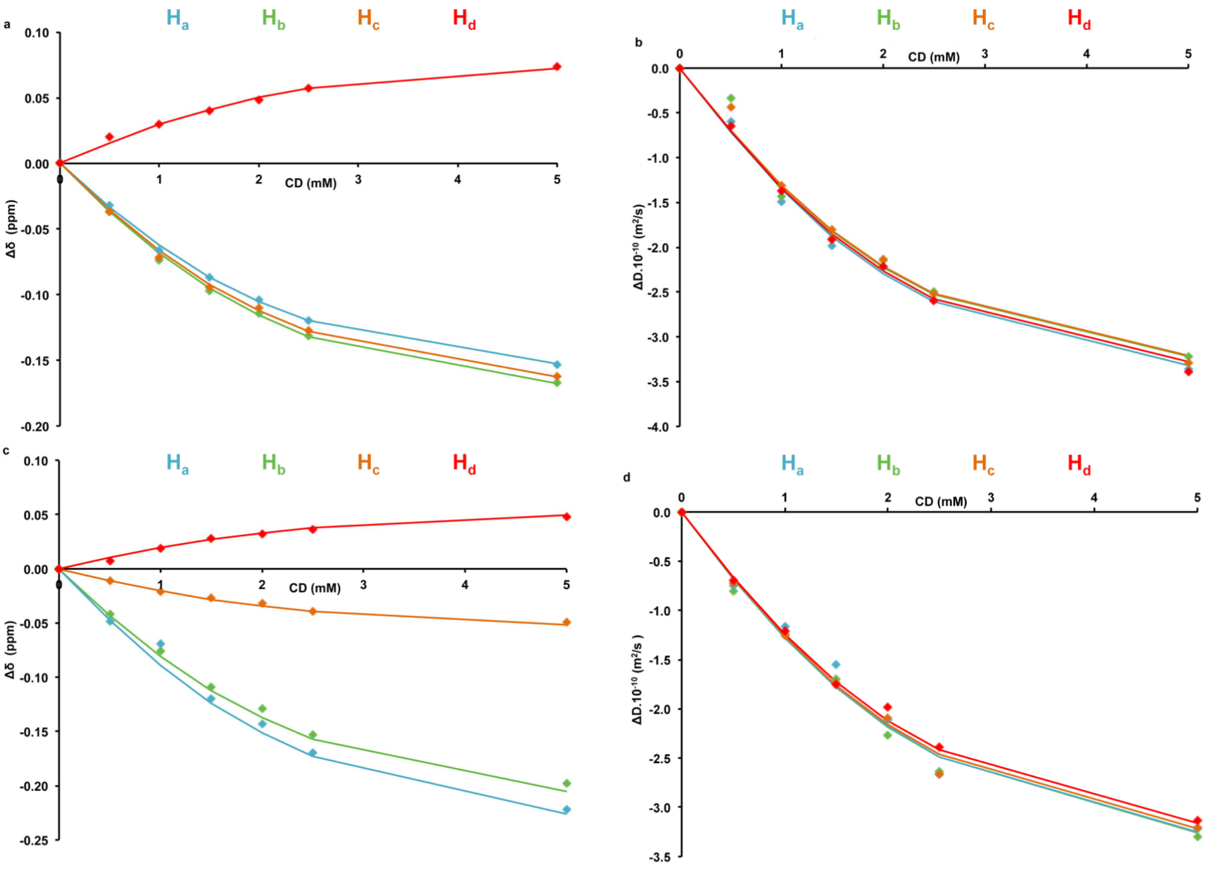

Figure 4: Representation of chemical shifts variations (Δδ) of a) carvacrol (**1**) and c) thymol (**2**) protons and diffusion coefficients variations (ΔD) of b) carvacrol (**1**) and d) thymol (**2**) protons with various β-CD concentrations. Experimental results are represented as filled diamonds and theoretical data are illustrated as solid lines.

The obtained K_f values for β-CD/**1** and β-CD/**2** were equal to 1736 M^{-1} and 1344 M^{-1}, respectively. These values are consistent with the UV–visible competitive method and phase solubility studies.

2D ROESY NMR

2D ROESY spectroscopy is a very useful technique for describing the real structure of CD inclusion complexes and indicating the exact positioning of guest inside the CD cavity. It is based on the observation of the nuclear Overhauser effect (NOE) between the protons of the guest and that of the CD that take action in the inclusion process [42]. The presence of NOE cross correlation peaks between the protons of guest and CD indicates space couplings and confirms that protons are close in space (<4Å).

We performed 2D ROESY experiments for inclusion complexes of both β-CD/**1** and β-CD/**2** prepared at equimolar ratios. Partial contour plots of the ROESY spectra of inclusion complexes are shown in Figure 5 and Figure 6 for **1** and **2**, respectively.

First, the absence of any NOE cross correlation peaks between **1** and **2** protons and H-1, H-2 and H-4 protons of β-CD ruled out any significant interaction between guests and the external surface of β-CD at equilibrium in agreement with ^{1}H NMR results.

For both guests, ROESY spectra showed two important sets of intermolecular cross-peaks. The first was observed between β-CD cavity protons (H-3 and H-5) and aromatic protons of **1** and **2** (H_a, H_b and H_c) and was stronger than the second one between the protons of the β-CD cavity and those of the methyl and isopropyl groups of **1** and **2**. This confirmed that, for both guests, the aromatic ring was deeply included in the β-CD cavity and that encapsulation occurred mainly through interactions with their phenyl moiety. But, it also pointed out that other guests' protons are involved in the complexation.

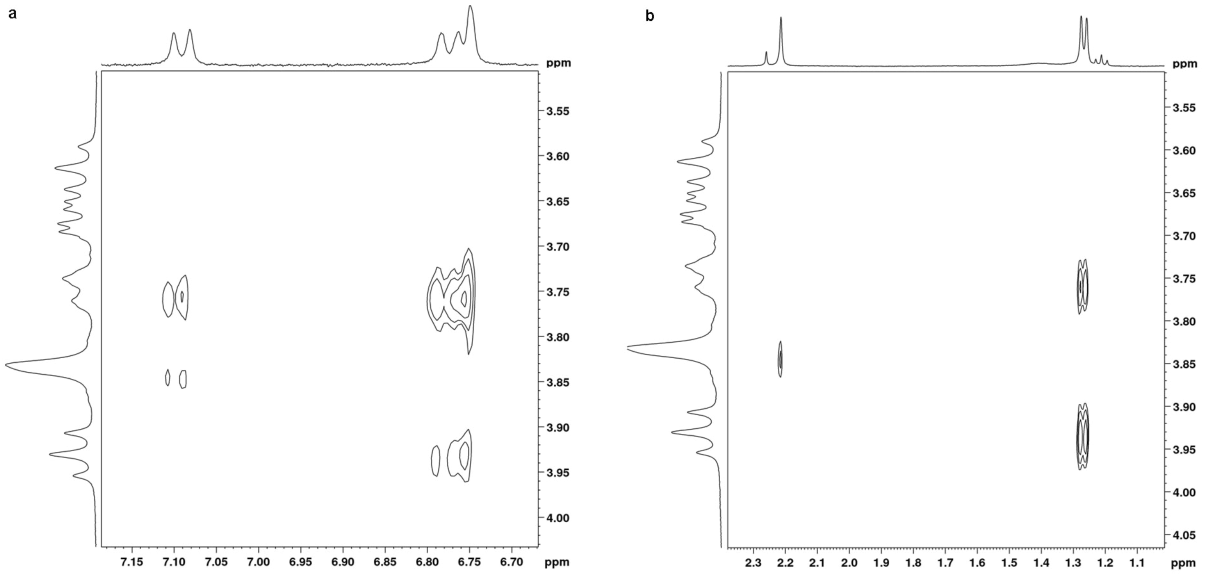

Figure 5: 2D ROESY plots of β-CD/carvacrol (**1**) complex in D_2O showing the NOEs between the H-3 and H-5 protons of β-CD and (a) the aromatic protons and (b) the aliphatic protons of carvacrol (**1**).

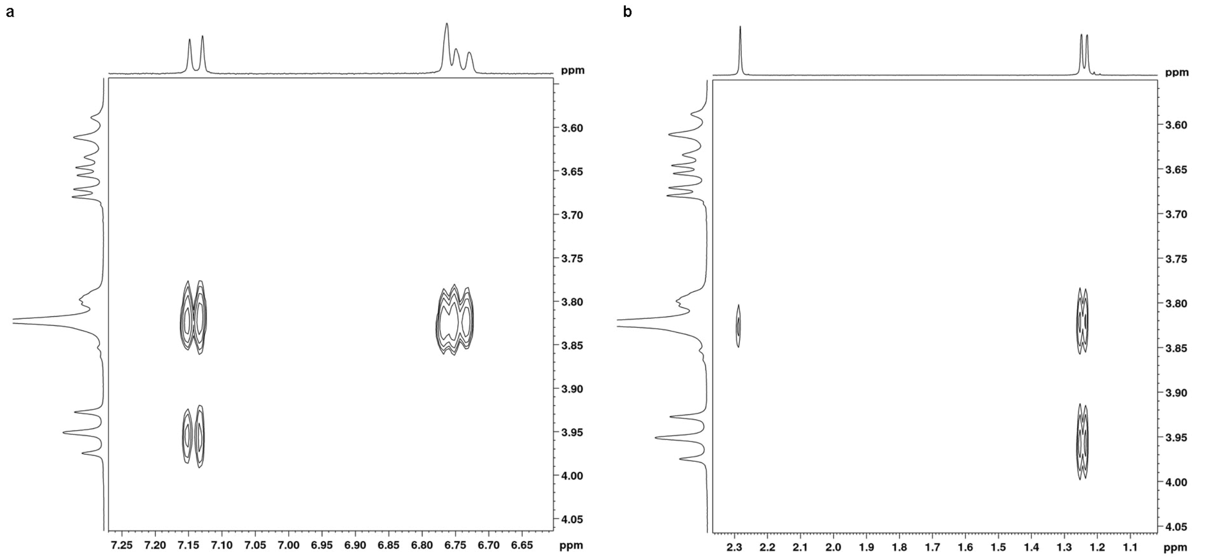

Figure 6: 2D ROESY plots of β-CD/thymol (**2**) complex in D_2O showing the NOEs between the H-3 and H-5 protons of β-CD and (a) the aromatic protons and (b) the aliphatic protons of thymol (**2**).

We can particularly see that H_b and H_c protons of **1** showed NOE cross peaks with both cavity protons while the H-a proton of **1** displayed NOE correlation peaks only with the H-5 proton of the CD cavity. Also, NOE cross peaks were observed between the H_a and H_c protons of **2** and both CD cavity protons but the H_b proton of **2** exhibited NOE correlations only with the H-5 proton of the CD cavity. This indicated that the H_a proton of **1** and H_b proton of **2** are oriented toward the narrower primary rim of β-CD.

Moreover, non-aromatic (aliphatic) protons of both **1** and **2** also revealed cross correlation peaks with CD protons. NOE cross peaks were observed between the protons of the isopropyl group of the guests and both protons H-3 and H-5. This indicated a partial penetration of the isopropyl group into the CD cavity. Moreover, the H-6 proton of β-CD showed cross peaks only with the protons of the methyl group of both **1** and **2** but not with those of the isopropyl moiety. This showed that, for both guests, the methyl group is pointed towards the primary narrower rim of the CD host.

According to these observations, it became possible to estimate the orientation of **1** and **2** inside the β-CD cavity: the methyl group of both guests is oriented toward the narrower rim of the CD cavity whereas the isopropyl moiety points to the wider rim.

Molecular modeling

A molecular modeling study was performed to rationalize the NMR results, find out the most probable conformations of the inclusion complexes in solution and illustrate their 3D structures. The most stable inclusion complexes conformers, presenting the weakest relative binding energies (Δ*E*) values, are illustrated in Figure 7.

Firstly, results showed that **1** and **2** could form inclusion complexes with β-CD with the aromatic cycle embedded inside the lipophilic cavity. This supported the fact that hydrophobic forces play a leading role in inclusion complex formation. Although Δ*E* values clearly illustrate the stability of each inclusion complex, it has to be underlined that such theoretical energies cannot be directly compared to K_f values, as the entropic part of the inclusion phenomena is not simulated.

In addition, the applied conformational research method showed that different conformers probably co-exist, since various structures with Δ*E* values quite close to those of the most stable conformers were obtained for both guests. On a structural point of view, these results are also consistent with the experimental NMR data showing that the most stable conformers for β-CD/**1** and β-CD/**2** resulted from a preferential inclusion mode; guests penetrate the CD via their methyl moiety and the isopropyl group of both is pointed to the secondary wider rim.

It is interesting to note that the H_c proton of **2** protruds outside the cavity (Figure 7). This might result from the fact that the hydroxy group of **2** comes close to the primary hydroxy groups of CD to form hydrogen bonds that further stabilize the inclusion complex. This leads to the projection of the H_c proton of **2** outside the cavity. This observation could explain why, during the ^{1}H NMR titration experiments, the H_c proton of **2** showed less pronounced chemical shift variations (Δδ) (Figure 4) upon encapsulation as compared to H_a and H_b protons.

Radical scavenging activity

Both compounds **1** and **2** are described as potent free-radical scavengers [29]. Moreover, it is well accepted that a wide variety of essential oils possess important antioxidant activities due to their high content in **1** and **2** [50]. In this work, the effect of encapsulation on the antioxidant activity of **1** and **2** was evaluated. The ABTS$^{•+}$ assay is commonly applied to determine the antioxidant activity of CD inclusion complexes [51-54]. We performed this test to determine the radical scavenging ability of **1** and **2** as well as the activity of their corresponding β-CD and HP-β-CD inclusion complexes. Trolox was used as reference and the results were expressed as Trolox equivalent antioxidant capacity TEAC (μmol Trolox/g of guest).

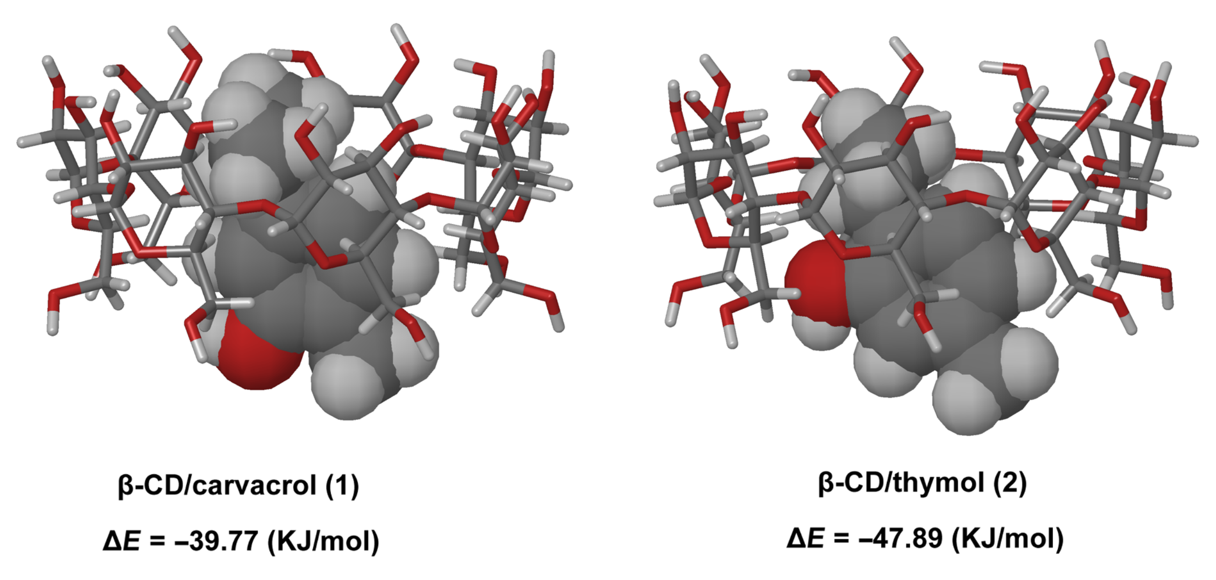

Figure 7: Representation of the most stable CD/guest inclusion complex conformers.

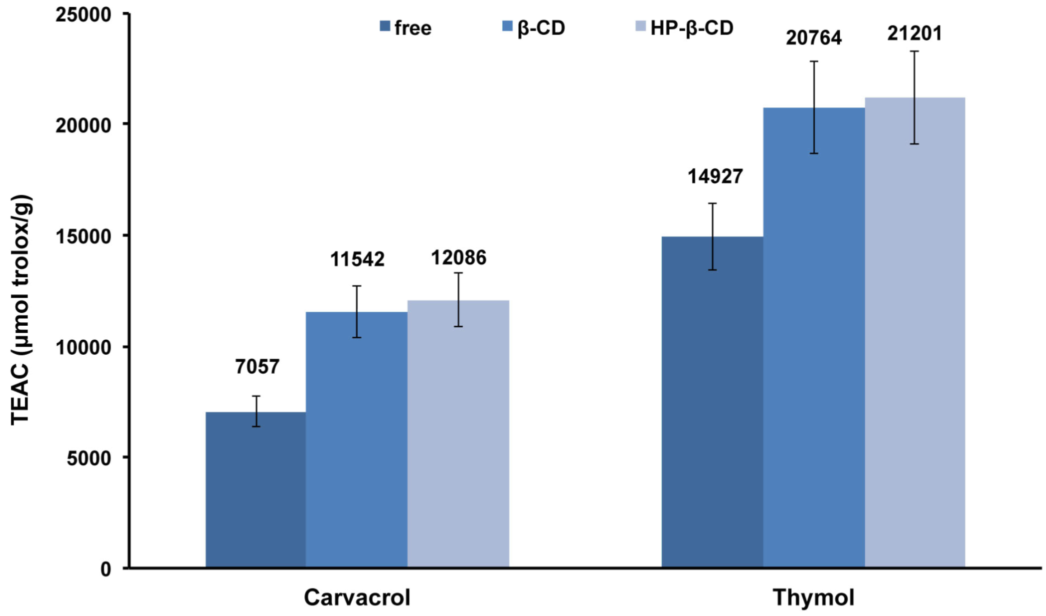

Figure 8: Effects of β-CD and HP-β-CD on the TEAC (µmol Trolox/ g of guest) of carvacrol (**1**) and thymol (**2**) by using ABTS$^{•+}$ assay.

As can be seen in Figure 8, both phenols exhibited anti-ABTS$^{•+}$ scavenging activity with **2** being more potent. This could be attributed to the difference in the position of aromatic cycle substituents, which affects the stability of the resulted phenoxyl radical upon reaction of guest with ABTS$^{•+}$. Similar TEAC value for **1** was reported in the literature [32].

We should note that a decrease of ABTS$^{•+}$ absorbance was observed when the assay was carried out with CDs alone. This fact could be attributed to the inclusion of ABTS$^{•+}$ inside the CD cavity in agreement with literature [51]. We then compared the activity of **1** and **2** to their corresponding inclusion complexes. As we can see in Figure 8, inclusion complexes showed higher radical scavenging activities than free molecules. The increased antioxidant activity could be attributed to the encapsulation of **1** and **2** in CDs [51]. Inclusion in CD cavity could protect and stabilize the formed phenoxyl radicals after reaction with ABTS$^{•+}$ leading to an enhanced activity by delaying its oxidation. It has been also demonstrated that CDs could act as secondary antioxidants and improve the activity of antioxidants [55]. Altogether data indicated that CDs could increase the half-life of antioxidant compounds and broaden their applications.

Conclusion

In this work, we clearly demonstrated that CDs could successfully encapsulate **1** and **2**. Experimental and theoretical results showed that all inclusion complexes have a 1:1 CD:guest stoichiometry and that the molecular structure of the guest affected its binding ability to CD. K_f values determined by an UV–visible competitive method, phase solubilty studies and ^{1}H and DOSY ^{1}H NMR titration experiments were consistent. 2D NMR and molecular modeling studies revealed the geometry of the most stable inclusion complexes. Encapsulation of **1** and **2** in CDs made them more soluble in aqueous systems than their free forms and improved their radical scavenging activity. Thus, CD/**1** and CD/**2** inclusion complexes could be used in food formulations as flavoring and antioxidant agents.

Experimental

Materials

Carvacrol (**1**), thymol (**2**), Trolox and $K_2S_2O_8$ were purchased from Aldrich. Methyl orange (MO) was purchased from Acros Organics. CRYSMEB (DS = 4.9) was provided from Roquette Frères (Lestrem, France), α-CD, β-CD, γ-CD, HP-β-CD (DS = 5.6) and RAMEB (DS = 12.6) were purchased from Wacker-Chemie (Lyon, France). All products were of analytical grade and were used as received. Distilled deionized water was used all over the study.

UV–visible competitive studies

Formation constants (K_f) values of inclusion complexes were determined by an UV–visible competitive method (or spectral displacement method) using the azo dye competitor MO [34].

This method requires a previous determination of K_f values of CD/MO inclusion complexes by a direct titration method. The competitive method was applied by adding **1** and **2** to a solution containing known concentrations of CD and MO. This addition induced an absorbance increment leading to the assessment of K_f values for the CD/**1** or CD/**2** inclusion complexes. The MO concentration was fixed to 0.1 mM and spectra were recorded between 520–530 nm with a 1 cm thick quartz cuvette using an UV–visible dual-beam spectrophotometer (Perkin Elmer Lambda 2S) at 25 °C. MO shows optimal differences in absorbance in this wavelength range between its free and complexed forms. Aiming to avoid any spectral influence of diffraction phenomena, the K_f values were calculated using an algorithmic treatment applied to the first derivatives of UV spectra. Experiments were done in triplicate.

Phase solubility studies

Phase solubility studies were carried out as described by Higuchi and Connors [56]. Excess amounts of **1** or **2** were added to 1 mL of CD solution at different concentrations ranging from 0 to 10 mM. The obtained mixtures were shaken at 25 °C for 24 h then filtered through a 0.45 µm cellulose filter. The concentrations of **1** or **2** in the filtrate were determined spectrophotometrically at 275 and 277 nm, respectively. Phase solubility profiles were obtained by plotting the solubility of **1** or **2** as a function of CD concentration. The K_f value of each inclusion complex was calculated from the linear segment of the corresponding phase solubility profile using the following equation:

$$K_f = \frac{\text{slope}}{S_0\ (1-\text{slope})} \tag{1}$$

where S_0 is the intrinsic solubility of **1** or **2** when no CD was added and the slope is the slope of the phase solubility profile. The solubilizing capacity of CD was estimated by the complexation efficiency (CE) parameter. CE was calculated from the slope of the phase solubility profile and is equal to the complex to the free CD concentrations ratio:

$$\text{CE} = S_0 \times K_f = \frac{[\text{CD/guest}]}{[\text{CD}]} = \frac{\text{slope}}{1-\text{slope}} \tag{2}$$

where [CD/guest] is the concentration of the dissolved inclusion complex and [CD] is the concentration of free CD. Consequently, the CE allowed the evaluation of guest:CD optimal preparation ratio as follows:

$$\text{guest:CD} = 1 : \left(1 + \frac{\text{slope}}{1-\text{slope}}\right) \tag{3}$$

The correlation between CE and the molecular weights of CD or guest leads to the evaluation of the increase in formulation bulk that can be calculated as follows:

$$\text{increase in fomulation bulk} = \frac{MW_{\text{CD}}}{MW_{\text{guest}}} \times \left(1 + \frac{1}{\text{CE}}\right) \tag{4}$$

where MW_{CD} and MW_{guest} are the molecular weights of CD and guest, respectively. All preparations and experiments were done in triplicate.

NMR experiments

All NMR experiments were carried out in D_2O (4.79 ppm) and were recorded on a Bruker Avance III spectrometer at 400 MHz (9.4 T), equipped with a multinuclear *z*-gradient BBFO probe head capable of producing magnetic field pulse gradients in the *z*-direction of 48.15 G·cm^{-1}. Throughout all experiments, the probe temperature was maintained at 300 K and standard 5 mm NMR tubes were used. The ^{1}H spectra were recorded by averaging 32 scans, with a digital resolution of 0.30 Hz. ^{1}H NMR spectra were recorded for six samples containing mixtures of β-CD and guests with guest/β-CD molar ratios ranging from 0.4 to 4.

2D NMR experiments were carried out for inclusion complexes prepared by mixing β-CD and guest in a 1:1 molar ratio at a concentration of 2 mM.

2D ROESY spectra were acquired with a mixing time of 600 ms during spin-lock with 64 scans using the States-TPPI method with a 1024 K time domain in F2 and 256 experiments in F1.

2D DOSY spectra were performed using the bipolar longitudinal eddy current delay (BPPLED – bipolar pulsed field gradient longitudinal eddy delay) pulse sequence. The pulse gradients were incremented in 16 steps from 2 to 98% of the maximum gradient strength in a linear ramp. Diffusion times and gradient pulse durations were optimized for each experiment in order to achieve a 95% decrease in resonance intensity at the largest gradient amplitude: Typically, diffusion time between 75 and 300 ms, gradient strength between 0.55 and 3 ms, spoil gradient strength of 0.6 ms, and longitudinal eddy current of 5 ms. After Fourier transformation, phase and baseline correction, the diffusion dimension of the 2D DOSY spectra was processed by means of the Bruker Dynamics Center software (version 2.1.9). The diffusion constants were calculated by exponential fitting of the data belonging to individual columns of the 2D matrix. The software gave the mean value of the diffusion coefficient.

The K_f values were obtained by global analyses of ^{1}H and DOSY ^{1}H data, using a non-linear treatment. Briefly, for each prepared solution, the inclusion complex concentration may be expressed as follows for a 1:1 stoichiometry:

$$[\mathrm{CD/G}] = -\frac{1}{2}\sqrt{\left(\frac{1}{K_\mathrm{f}}+[\mathrm{CD}]_\mathrm{T}+[\mathrm{G}]_\mathrm{T}\right)^2 - 4[\mathrm{CD}]_\mathrm{T}[\mathrm{G}]_\mathrm{T}} + \frac{1}{2}\left(\frac{1}{K_\mathrm{f}}+[\mathrm{CD}]_\mathrm{T}+[\mathrm{G}]_\mathrm{T}\right) \quad (5)$$

With [CD/G], [CD] and [G] being the complex, CD and Guest concentrations, respectively. The subscript $_\mathrm{T}$ stands for total.

Then, the variation of chemical shifts (Δδ) and diffusion coefficients (Δ*D*) were calculated according to:

$$\Delta\delta = \Delta\delta_\mathrm{complex} \times \frac{[\mathrm{CD/G}]}{[\mathrm{G}]_\mathrm{T}} \quad (6)$$

$$\Delta D = \Delta D_\mathrm{complex} \times \frac{[\mathrm{CD/G}]}{[\mathrm{G}]_\mathrm{T}} \quad (7)$$

With $\Delta\delta_\mathrm{complex}$ and $\Delta D_\mathrm{complex}$ being respectively the chemical shift variation and the diffusion coefficient variation, between the free and complexed forms of the guest.

The squared differences between theoretical and experimental data are then summed over all solutions and over all guests' ^{1}H and DOSY signals. These Δδ and Δ*D* differences are weighted relatively to each other in order that chemical shift (δ) and *D* generate equal sum of squared differences, in such a way that both signals contribute significantly to the determination of K_f. A Newton–Raphson procedure finally minimizes the sum of the squared differences by varying the unique K_f value and each $\Delta\delta_\mathrm{complex}$ and $\Delta D_\mathrm{complex}$.

Molecular modeling

The determination of possible inclusion complex conformations was carried out by a conformational Monte Carlo research method using the MMFFs force field in the presence of water (GB/SA implicit model) with the generation of 5000 conformations (FMNR conjugate gradient minimization convergence fixed to 0.01 kJ Å^{-1} mol^{-1}). Prior to docking and simulations, the structures of **1** or **2** were constructed manually and minimized. The host β-CD structure was a non-distorted symmetrical shell that was maintained rigid during the conformational search. Guests **1** or **2** were allowed to freely rotate and translate during the search. The total energy difference (Δ*E*, kJ/mol) between inclusion complexes and the sum of their individual components (CD and **1** or CD and **2**) in their optimized fundamental states was calculated for the most stable conformers. Δ*E* was used as the theoretical parameter to evaluate the complexation energy of the inclusion complex.

ABTS radical scavenging method

The ABTS (2,2'-azino-bis(3-ethylbenzothiazoline-6-sulfonic acid) radical cation (ABTS$^{\bullet+}$) scavenging method was used to determine the radical scavenging potency of free and encapsulated **1** and **2**. This method relies on the capacity of an antioxidant to scavenge and reduce ABTS$^{\bullet+}$ into its colorless reduced state. The ABTS$^{\bullet+}$ was generated by reacting the ABTS salt (7 mM) with $K_2S_2O_8$ (2.45 mM) in water at room temperature in the dark for 12–16 h. A diluted ABTS$^{\bullet+}$ solution was then prepared in water to obtain an initial absorbance of 0.75 ± 0.2 at 730 nm using an UV–visible dual-beam spectrophotometer (Perkin Elmer Lambda 2S) with a 1 cm thick quartz cuvette. Aliquots of free and encapsulated **1** or **2** were added to 2 mL of ABTS$^{\bullet+}$ containing solutions. The solutions were shaken in the dark for 1 hour at 25 ± 0.1 °C. The absorbance was measured at 730 nm. Blank samples contained ABTS$^{\bullet+}$ alone or in the presence of 10 mM of CD. The radical scavenging activity was expressed as Trolox equivalents TEAC (µmol Trolox/g of G) by using a Trolox calibration curve prepared for a concentration range of 2.5–25 µM. All analyses were done in triplicate.

References

1. Llana-Ruiz-Cabello, M.; Pichardo, S.; Maisanaba, S.; Puerto, M.; Prieto, A. I.; Gutiérrez-Praena, D.; Jos, A.; Cameán, A. M. *Food Chem. Toxicol.* **2015,** *81,* 9–27. doi:10.1016/j.fct.2015.03.030
2. Hyldgaard, M.; Mygind, T.; Meyer, R. L. *Front. Microbiol.* **2012,** *3,* No. 12. doi:10.3389/fmicb.2012.00012
3. Zotti, M.; Colaianna, M.; Morgese, M. G.; Tucci, P.; Schiavone, S.; Avato, P.; Trabace, L. *Molecules* **2013,** *18,* 6161–6172. doi:10.3390/molecules18066161
4. Burt, S. *Int. J. Food Microbiol.* **2004,** *94,* 223–253. doi:10.1016/j.ijfoodmicro.2004.03.022
5. Chavan, P. S.; Tupe, S. G. *Food Control* **2014,** *46,* 115–120. doi:10.1016/j.foodcont.2014.05.007
6. Zheng, L.; Bae, Y. M.; Jung, K. S.; Heu, S.; Lee, S. Y. *Food Control* **2013,** *32,* 665–672. doi:10.1016/j.foodcont.2013.01.009
7. Gutiérrez, L.; Escudero, A.; Batlle, R.; Nerín, C. *J. Agric. Food Chem.* **2009,** *57,* 8564–8571. doi:10.1021/jf901459e
8. Kuorwel, K. K.; Cran, M. J.; Sonneveld, K.; Miltz, J.; Bigger, S. W. *Packag. Technol. Sci.* **2014,** *27,* 49–58. doi:10.1002/pts.2003
9. Klein, G.; Rüben, C.; Upmann, M. *Curr. Microbiol.* **2013,** *67,* 200–208. doi:10.1007/s00284-013-0354-1
10. Suntres, Z. E.; Coccimiglio, J.; Alipour, M. *Crit. Rev. Food Sci. Nutr.* **2015,** *55,* 304–318. doi:10.1080/10408398.2011.653458
11. Brewer, M. S. *Compr. Rev. Food Sci. Food Saf.* **2011,** *10,* 221–247. doi:10.1111/j.1541-4337.2011.00156.x
12. Quiroga, P. R.; Asensio, C. M.; Nepote, V. *J. Sci. Food Agric.* **2015,** *95,* 471–479. doi:10.1002/jsfa.6744
13. Grice, H. C. *Food Chem. Toxicol.* **1988,** *26,* 717–723. doi:10.1016/0278-6915(88)90072-5

14. Witschi, H. P. *Food Chem. Toxicol.* **1986,** *24,* 1127–1230. doi:10.1016/0278-6915(86)90298-X
15. Mastelić, J.; Jerković, I.; Blažević, I.; Poljak-Blaži, M.; Borović, S.; Ivančić-Baće, I.; Smrěcki, V.; Žarković, N.; Brčić-Kostic, K.; Vikić-Topić, D.; Müller, N. *J. Agric. Food Chem.* **2008,** *56,* 3989–3996. doi:10.1021/jf073272v
16. Locci, E.; Lai, S.; Piras, A.; Marongiu, B.; Lai, A. *Chem. Biodiversity* **2004,** *1,* 1354–1366. doi:10.1002/cbdv.200490098
17. Kfoury, M.; Auezova, L.; Ruellan, S.; Greige-Gerges, H.; Fourmentin, S. *Carbohydr. Polym.* **2015,** *118,* 156–164. doi:10.1016/j.carbpol.2014.10.073
18. Kfoury, M.; Landy, D.; Auezova, L.; Greige-Gerges, H.; Fourmentin, S. *Beilstein J. Org. Chem.* **2014,** *10,* 2322–2331. doi:10.3762/bjoc.10.241
19. Marques, H. M. C. *Flavour Fragrance J.* **2010,** *25,* 313–326. doi:10.1002/ffj.2019
20. Szente, L.; Szejtli, J. *Trends Food Sci. Technol.* **2004,** *15,* 137–142. doi:10.1016/j.tifs.2003.09.019
21. Szejtli, J. *Chem. Rev.* **1998,** *98,* 1743–1753. doi:10.1021/cr970022c
22. Del Valle, E. M. M. *Process Biochem.* **2004,** *39,* 1033–1046. doi:10.1016/S0032-9592(03)00258-9
23. Szente, L.; Szejtli, J. *Adv. Drug Delivery Rev.* **1999,** *36,* 17–28. doi:10.1016/S0169-409X(98)00092-1
24. Schmidt, B. V. K. J.; Hetzer, M.; Ritter, H.; Barner-Kowollik, C. *Prog. Polym. Sci.* **2014,** *39,* 235–249. doi:10.1016/j.progpolymsci.2013.09.006
25. Bethanis, K.; Tzamalis, P.; Tsorteki, F.; Kokkinou, A.; Christoforides, E.; Mentzafos, D. *J. Inclusion Phenom. Macrocyclic Chem.* **2013,** *77,* 163–173. doi:10.1007/s10847-012-0230-9
26. Guimarães, A. G.; Oliveira, M. A.; Alves, R. D. S.; Menezes, P. D. P.; Serafini, M. R.; De Souza Araújo, A. A.; Bezerra, D. P.; Quintans, L. J. *Chem.-Biol. Interact.* **2015,** *227,* 69–76. doi:10.1016/j.cbi.2014.12.020
27. Kamimura, J. A.; Santos, E. H.; Hill, L. E.; Gomes, C. L. *LWT–Food Sci. Technol.* **2014,** *57,* 701–709. doi:10.1016/j.lwt.2014.02.014
28. Kfoury, M.; Auezova, L.; Fourmentin, S.; Greige-Gerges, H. *J. Inclusion Phenom. Macrocyclic Chem.* **2014,** *80,* 51–60. doi:10.1007/s10847-014-0385-7
29. Miguel, M. G.; Dandlen, S. A.; Figueiredo, A. C.; Pedro, L. G.; Barroso, J. G.; Marques, M. H. *Acta Hortic.* **2010,** *853,* 363–368. doi:10.17660/ActaHortic.2010.853.44
30. Mulinacci, N.; Melani, F.; Vincieri, F. F.; Mazzi, G.; Romani, A. *Int. J. Pharm.* **1996,** *128,* 81–88. doi:10.1016/0378-5173(95)04224-5
31. Nieddu, M.; Rassu, G.; Boatto, G.; Bosi, P.; Trevisi, P.; Giunchedi, P.; Carta, A.; Gavini, E. *Carbohydr. Polym.* **2014,** *102,* 393–399. doi:10.1016/j.carbpol.2013.10.084
32. Santos, E. H.; Kamimura, J. A.; Hill, L. E.; Gomes, C. L. *LWT–Food Sci. Technol.* **2015,** *60,* 583–592. doi:10.1016/j.lwt.2014.08.046
33. Tao, F.; Hill, L. E.; Peng, Y.; Gomes, C. L. *LWT–Food Sci. Technol.* **2014,** *59,* 247–255. doi:10.1016/j.lwt.2014.05.037
34. Caron, L.; Tilloy, S.; Monflier, E.; Wieruszeski, J.-M.; Lippens, G.; Landy, D.; Fourmentin, S.; Surpateanu, G. *J. Inclusion Phenom. Macrocyclic Chem.* **2000,** *38,* 361–379. doi:10.1023/A:1008165110579
35. Decock, G.; Fourmentin, S.; Surpateanu, G. G.; Landy, D.; Decock, P.; Surpateanu, G. *Supramol. Chem.* **2006,** *18,* 477–482. doi:10.1080/10610270600665749
36. Ciobanu, A.; Landy, D.; Fourmentin, S. *Food Res. Int.* **2013,** *53,* 110–114. doi:10.1016/j.foodres.2013.03.048
37. Fourmentin, S.; Ciobanu, A.; Landy, D.; Wenz, G. *Beilstein J. Org. Chem.* **2013,** *9,* 1185–1191. doi:10.3762/bjoc.9.133
38. Loftsson, T.; Hreinsdóttir, D.; Másson, M. *J. Inclusion Phenom. Macrocyclic Chem.* **2007,** *57,* 545–552. doi:10.1007/s10847-006-9247-2
39. Kurkov, S. V.; Loftsson, T. *Int. J. Pharm.* **2013,** *453,* 167–180. doi:10.1016/j.ijpharm.2012.06.055
40. Kfoury, M.; Auezova, L.; Greige-Gerges, H.; Ruellan, S.; Fourmentin, S. *Food Chem.* **2014,** *164,* 454–461. doi:10.1016/j.foodchem.2014.05.052
41. Schneider, H. J.; Hacket, F.; Rüdiger, V.; Ikeda, H. *Chem. Rev.* **1998,** *98,* 1755–1786. doi:10.1021/cr970019t
42. Mura, P. *J. Pharm. Biomed. Anal.* **2014,** *101,* 238–250. doi:10.1016/j.jpba.2014.02.022
43. Fernandes, C. M.; Carvalho, R. A.; Pereira da Costa, S.; Veiga, F. J. B. *Eur. J. Pharm. Sci.* **2003,** *18,* 285–296.
44. Sun, D.-Z.; Li, L.; Qiu, X.-M.; Liu, F.; Yin, B.-L. *Int. J. Pharm.* **2006,** *313,* 7–13. doi:10.1016/j.ijpharm.2006.02.020
45. Ribeiro, L.; Carvalho, R. A.; Ferreira, D. C.; Veiga, F. J. B. *Eur. J. Pharm. Sci.* **2005,** *24,* 1–13. doi:10.1016/j.ejps.2004.09.003
46. Djedaini, F.; Sheng Zhao, L.; Perly, B.; Wouessidjewe, D. *J. Pharm. Sci.* **1990,** *79,* 643–646. doi:10.1002/jps.2600790721
47. Chen, M.; Diao, G.; Zhang, E. *Chemosphere* **2006,** *63,* 522–529. doi:10.1016/j.chemosphere.2005.08.033
48. Veiga, F. J. B.; Fernandes, C. M.; Carvalho, R. A.; Geraldes, C. F. G. C. *Chem. Pharm. Bull.* **2001,** *49,* 1251–1256. doi:10.1248/cpb.49.1251
49. Jullian, C.; Miranda, S.; Zapata-Torres, G.; Mendizábal, F.; Olea-Azar, C. *Bioorg. Med. Chem.* **2007,** *15,* 3217–3224. doi:10.1016/j.bmc.2007.02.035
50. Srinivasan, K. *Crit. Rev. Food Sci. Nutr.* **2014,** *54,* 352–372. doi:10.1080/10408398.2011.585525
51. Lucas-Abellán, C.; Mercader-Ros, M. T.; Zafrilla, M. P.; Gabaldón, J. A.; Núñez-Delicado, E. *Food Chem. Toxicol.* **2011,** *49,* 1255–1260. doi:10.1016/j.fct.2011.03.004
52. Li, S.; Yue, J.; Zhou, W.; Li, L. *J. Inclusion Phenom. Macrocyclic Chem.* **2015,** *82,* 453–460. doi:10.1007/s10847-015-0516-9
53. Gharibzahedi, S. M. T.; Razavi, S. H.; Mousavi, M. *Carbohydr. Polym.* **2014,** *101,* 1147–1153. doi:10.1016/j.carbpol.2013.10.074
54. Chakraborty, S.; Basu, S.; Lahiri, A.; Basak, S. *J. Mol. Struct.* **2010,** *977,* 180–188. doi:10.1016/j.molstruc.2010.05.030
55. López-Nicolás, J. M.; Pérez-López, A. J.; Carbonell-Barrachina, Á.; García-Carmona, F. *J. Agric. Food Chem.* **2007,** *55,* 5312–5319. doi:10.1021/jf070499h
56. Higuchi, T.; Connors, A. K. Phase-Solubility Techniques. In *Advances in Analytical Chemistry and Instrumentation;* Reilly, C. N., Ed.; Wiley-Interscience: New York, 1965; Vol. 4, pp 117–212.

License and Terms

BEILSTEIN JOURNAL OF ORGANIC CHEMISTRY

Supramolecular polymer assembly in aqueous solution arising from cyclodextrin host–guest complexation

Jie Wang[1], Zhiqiang Qiu[1], Yiming Wang[1], Li Li[1], Xuhong Guo[*1], Duc-Truc Pham[2], Stephen F. Lincoln[*2] and Robert K. Prud'homme[3]

Review

Address:
[1]State Key Laboratory of Chemical Engineering, East China University of Science and Technology, Shanghai 200237, China, [2]Departmant of Chemistry, University of Adelaide, Adelaide, SA 5005, Australia and [3]Department of Chemical Engineering, Princeton University, Princeton, NJ 08544, USA

Email:
Xuhong Guo[*] - guoxuhong@ecust.edu.cn; Stephen F. Lincoln[*] - stephen.lincoln@adelaide.edu.au

* Corresponding author

Keywords:
cyclodextrin; host–guest; polymer; smart-material; supramolecular

Beilstein J. Org. Chem. **2016,** *12,* 50–72.
doi:10.3762/bjoc.12.7

Received: 27 August 2015
Accepted: 11 December 2015
Published: 12 January 2016

This article is part of the Thematic Series "Superstructures with cyclodextrins: Chemistry and applications III".

Guest Editor: G. Wenz

Abstract

The employment of cyclodextrin host–guest complexation to construct supramolecular assemblies with an emphasis on polymer networks is reviewed. The main driving force for this supramolecular assembly is host–guest complexation between cyclodextrin hosts and guest groups either of which may be discrete molecular species or substituents on a polymer backbone. The effects of such complexation on properties at the molecular and macroscopic levels are discussed. It is shown that cyclodextrin complexation may be used to design functional polymer materials with tailorable properties, especially for photo-, pH-, thermo- and redox-responsiveness and self-healing.

Introduction

Supramolecular assembly driven by associative forces including hydrogen bonding, coordinate bonding, electrostatic interactions and hydrophobic interactions is ubiquitous in nature. This is exemplified by the use of DNA and RNA complementarity [1,2] and polypeptide helix formation [3,4] to produce three-dimensional structures and materials with specific biofunctionality. Similar interactions may be utilized in the construction of functional materials. This is demonstrated in supramolecular assemblies based on cyclodextrin host–guest complexation which have attracted considerable interest through their applications in enzyme technology [5], chemical sensors [6] and drug delivery [7-9].

As discussed in a range of reviews [10-14] and books [15-18], cyclodextrins are naturally occurring cyclic oligosaccharides which are also produced industrially through the enzymatic metabolism of starch and related compounds. The enzymes used are cyclodextrin glucosyltransferases which are produced by several microorganisms including *Bacillus macerans* and *Bacillus circulans*. The most common cyclodextrins are α-, β- and γ-cyclodextrin (α-, β- and γ-CD) which consist of 6, 7 and 8 α-1,4-linked D-glucopyranose subunits, respectively. Stabilized by intramolecular hydrogen bonds, cyclodextrins form truncated toroidal structures with different internal annular diameters but the same depth of 7.9 Å (Figure 1, Table 1) [19]. The primary hydroxy groups are located on the C6 carbons of the D-glucopyranose subunits and delineate the narrower, or primary, face of the torus and the secondary hydroxy groups are located on the C2 and C3 carbons and delineate the wider, or secondary, face. While the hydroxy groups on both cyclodextrin faces hydrogen bond with water in aqueous solution, the interior of the annulus is hydrophobic and selectively complexes hydrophobic guest species to form host–guest complexes, or inclusion compounds. The host–guest complexes formed by cyclodextrins and their hydrophobic guests, which range from small molecules to polymer substituents and sections of polymer chains, have been widely studied and utilized as building blocks in supramolecular structures and functional materials. These are exemplified by catenanes [20,21], rotaxanes [21-25], polyrotaxanes [24-29], polymers and polymer networks [12,22,26,30-34].

The focus of this review is on recent developments in the construction of supramolecular assemblies and polymer networks in water based on host–guest complexation between cyclodextrin hosts and discrete molecular entities and polymer substituents acting as guests. (Whilst the cyclodextrin torus is shown in a variety of ways in the literature, only the internal outline of the annulus is shown for uniformity and simplicity in this review.)

Review

1 Host–guest complexation between cyclodextrins and guest-substituted polymers

1.1 Modulation of hydrophobic interactions

Hydrophobic interactions of water soluble polymers substituted with either terminal hydrophobic substituents alone or multiple hydrophobic substituents along the polymer backbone result in aqueous solutions with tunable viscosities, diffusion characteristics and relaxation times whilst lacking undesirable thickening effects [35,36]. The extent of such hydrophobic interaction may be controlled by either the type or density of hydrophobic groups [36,37]. Alternatively, similar control may be effected through additives exemplified by a range of molecular species, salts and surfactants [38-40]. Among such additives are cyclodextrins which can disrupt the interactions between hydrophobic substituents rendering a solution viscous by forming host–guest complexes with individual hydrophobic substituents and thereby lower solution viscosity [41-44]. This process may be reversed by adding competing hydrophobes

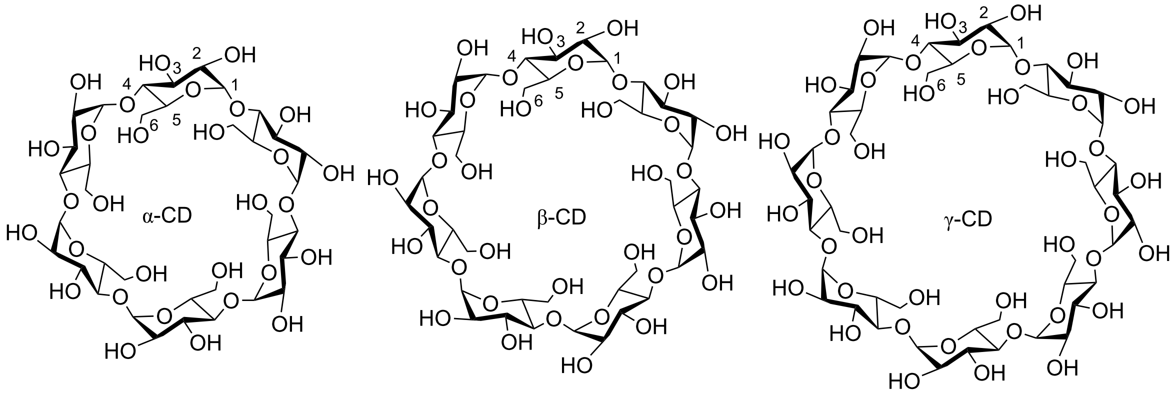

Figure 1: Structures of α-, β- and γ-CD. Individual carbon atom numbering is shown for one D-glucopyranose subunit in each structure.

Table 1: Physical propertices of cyclodextrins [19].

CD	Number of D-glucopyranose subunits	Molecular weight, g/mol	Solubility in water (298.2 K), g/100 cm^3	Narrow and wide face annular diameters, Å	Depth of annulus, Å
α-	6	972	14.5	4.7–5.3	7.9
β-	7	1135	1.85	6.0–6.5	7.9
γ-	8	1297	23.2	7.5–8.3	7.9

which complex cyclodextrins more strongly than the hydrophobic substituents to restore solution viscosity [45,46].

1.2 Host–guest complexation of hydrophobic substituents in polymers

Hydrophobic associations in aqueous solution between either terminal or multiple hydrophobic substituents along the backbone of a polymer, which generate the high viscosity of associative thickeners, may be disrupted by cyclodextrin host–guest complexation of these substituents (Figure 2) [41-49]. Thus, in 1998, Zhang et al. reported that the viscosity of an aqueous solution of perfluorocarbon-substituted poly(ethylene glycol) was decreased through the addition of β-CD due to host–guest complexation as observed by ^{19}F NMR spectroscopy [47]. Subsequently, Islam et al. observed the host–guest complexation of the linear alkyl substituents n-C_8H_{17}, n-$C_{16}H_{33}$ and n-$C_{20}H_{41}$ of hydrophobically substituted alkali-soluble emulsion (HASE) polymers by methylated β-CD using gel permeation chromatography and light scattering methods [48]. In 2002, Karlson et al. found that hydrophobic association among the hydrophobic substituents of substituted poly(ethylene glycol) was disrupted by host–guest complexation by methylated α-CD [42]; as was a similar association by the hydrophobic substituents of substituted ethyl(hydroxyethyl) cellulose by α-CD, β-CD and their methylated analogs [49].

Guo et al. have shown that the viscosity of aqueous solutions 0.5 wt % in 2% n-$C_{12}H_{25}$, n-$C_{14}H_{29}$ or n-$C_{18}H_{37}$ randomly substituted poly(acrylate) (PAAddn, PAAtdn and PAAodn, respectively) is significantly decreased upon addition of α-, β- or γ-CD due to decreased hydrophobic interaction between the n-alkyl substituents because of their cyclodextrin host–guest complexation [46]. Due to the differences in annular size (Table 1), the hydrophobe complexing abilities of α-, β- and γ-CD differ [44-46]. At low PAAodn 0.5 wt % concentration in aqueous solution, the viscosity decreases substantially to a minimum value at either 1:1 α-CD, β-CD or γ-CD host to n-$C_{18}H_{37}$ guest substituent mole ratio (Figure 3) [46]. This minimum viscosity value decreases on going from α-CD to γ-CD due to the stronger complexation of a single n-$C_{18}H_{37}$ substituent with increasing size of the cyclodextrin annulus.

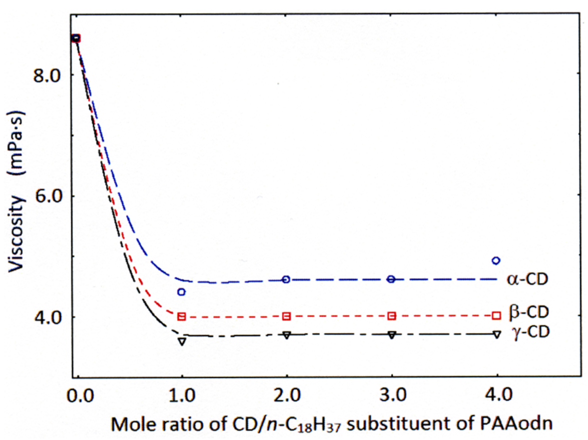

Figure 3: Decrease of aqueous solution viscosity at a shear rate of 50 s^{-1} due to α-CD (circles), β-CD (rectangles) and γ-CD (triangles) host–guest complexation of n-$C_{18}H_{37}$ substituents competing with n-$C_{18}H_{37}$ hydrophobic interactions in the randomly substituted poly(acrylate), PAAodn, 0.5 wt % aqueous solution (0.10 M NaCl, pH 7.0). Adapted with permission from [46]. Copyright (2008) American Chemical Society.

At a higher PAAodn concentration (2 wt %), the viscosity behavior changes with the increase in the cyclodextrin mole ratio (Figure 4) [46]. Thus, at a 1:1 α-CD:n-$C_{18}H_{37}$ mole ratio the solution viscosity decreases by almost a half and the viscosity profile is little changed (Figure 4a). This is consistent

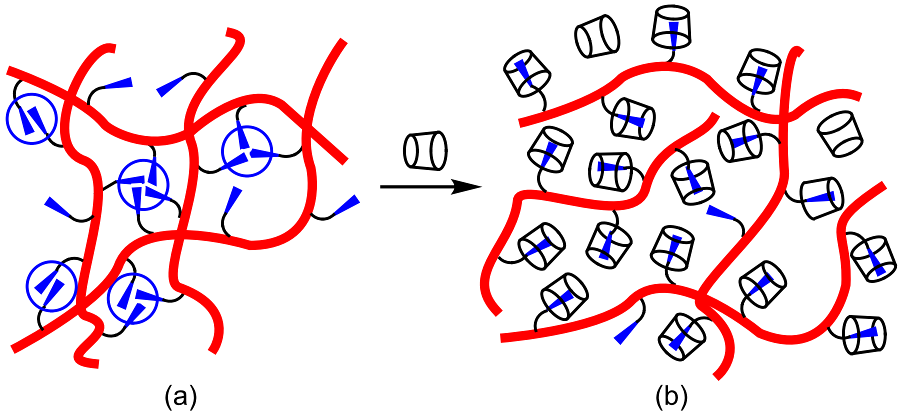

Figure 2: Associations of hydrophobic substituents (circled) (a) and their disruption through host–guest complexation by cyclodextrins (b).

with n-$C_{18}H_{37}$ partially protruding from the narrow α-CD annulus such that residual hydrophobic interactions occur between n-$C_{18}H_{37}$ substituents and substantial viscosity is retained. However, when the α-CD:n-$C_{18}H_{37}$ mole ratio increases to 2:1 the viscosity decreases by almost three orders of magnitude and further addition of α-CD has little effect. This is consistent with a 2:1 2α-CD:n-$C_{18}H_{37}$ host guest stoichiometry being assumed where two α-CD thread onto a single n-$C_{18}H_{37}$ substituent such that interaction between substituents decreases greatly. In contrast, at 1:1 β-CD:n-$C_{18}H_{37}$ mole ratio the solution viscosity decreases greatly and further addition of β-CD has only a small effect (Figure 4b). This is consistent with a β-CD:n-$C_{18}H_{37}$ host–guest stoichiometry dominating and n-$C_{18}H_{37}$ folding inside the larger β-CD annulus such that little residual interaction between the n-$C_{18}H_{37}$ hydrophobic substituents occurs. Nevertheless, the expected shear thickening occurs with increasing shear rate in the presence of both α-CD and β-CD. The effect of addition of γ-CD is quite different and probably reflects the effect of a 1:1 γ·CD:n-$C_{18}H_{37}$ host–guest stoichiometry dominating at low to moderate shear rates (Figure 4c). At higher shear rates, a γ-CD/2n-$C_{18}H_{37}$ host–guest stoichiometry in which the large γ-CD annulus accommodates two n-$C_{18}H_{37}$ from adjacent PAAodn chains becomes increasingly significant and shear thickening occurs.

1.3 Recovery of hydrophobic association

Hydrophobic associations in substituted polymer solutions may be recovered by adding other guest species which form more stable cyclodextrin host–guest complexes than the polymer substituents do [41,45,46,50]. Thus, Khan et al. used nonionic surfactants based on poly(ethylene glycol) to recover the hydrophobic associations in hydrophobically substituted alkali-soluble emulsion (HASE) polymers complexed by α-CD and β-CD [41]. (It should be noted that association occurs between hydrophobically substituted polymers in aqueous solution and that this may be decreased by the addition of surfactants as shown by Prud'homme et al. for hydrophobically substituted hydroxyethyl cellulose [51].) Guo et al. showed that the addition of sodium dodecyl sulfate (SDS) to 2 wt % aqueous PAAodn in which the α-CD:n-$C_{18}H_{37}$ mole ratio is 2:1 to make the mole ratios of SDS:α-CD:n-$C_{18}H_{37}$ 1:2:1 and 2:2:1 causes viscosity to closely approach and to exceed that of 2 wt % aqueous PAAodn, respectively (Figure 5a) [45,46]. Further addition of SDS causes solution viscosity to decrease. This is consistent with α-CD complexing SDS more strongly than n-$C_{18}H_{37}$ such that hydrophobic interactions between PAAodn are restored in the 1:2:1 and 2:2:1 solutions while at higher SDS ratios SDS dominated micelles form which disrupt interpolymer chain interactions [37,40,51]. Similar additions of SDS to the 2:1 β-CD:n-$C_{18}H_{37}$ solution restores the hydrophobic

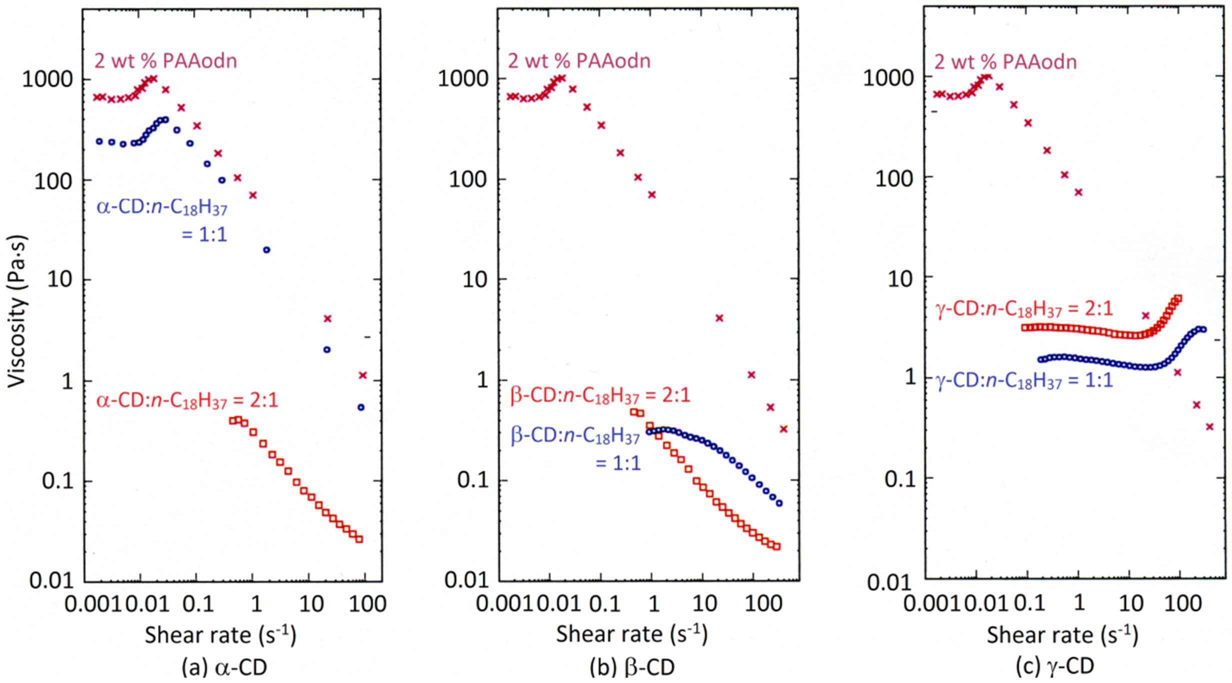

(a) α-CD (b) β-CD (c) γ-CD

Figure 4: The effect of (a) α-CD, (b) β-CD and (c) γ-CD on the hydrophobic interactions between n-$C_{18}H_{37}$ substituents of 2% randomly substituted poly(acrylate), PAAodn, in 2 wt % aqueous solution (0.10 M NaCl, pH 7.0) as indicated by shear rate. The data sets refer to 2 wt % PAAodn alone (crosses), and where cyclodextrin to n-$C_{18}H_{37}$ substituent mole ratios are: 1:1 (circles) and 2:1 (rectangles). Adapted with permission from [46]. Copyright (2008) American Chemical Society.

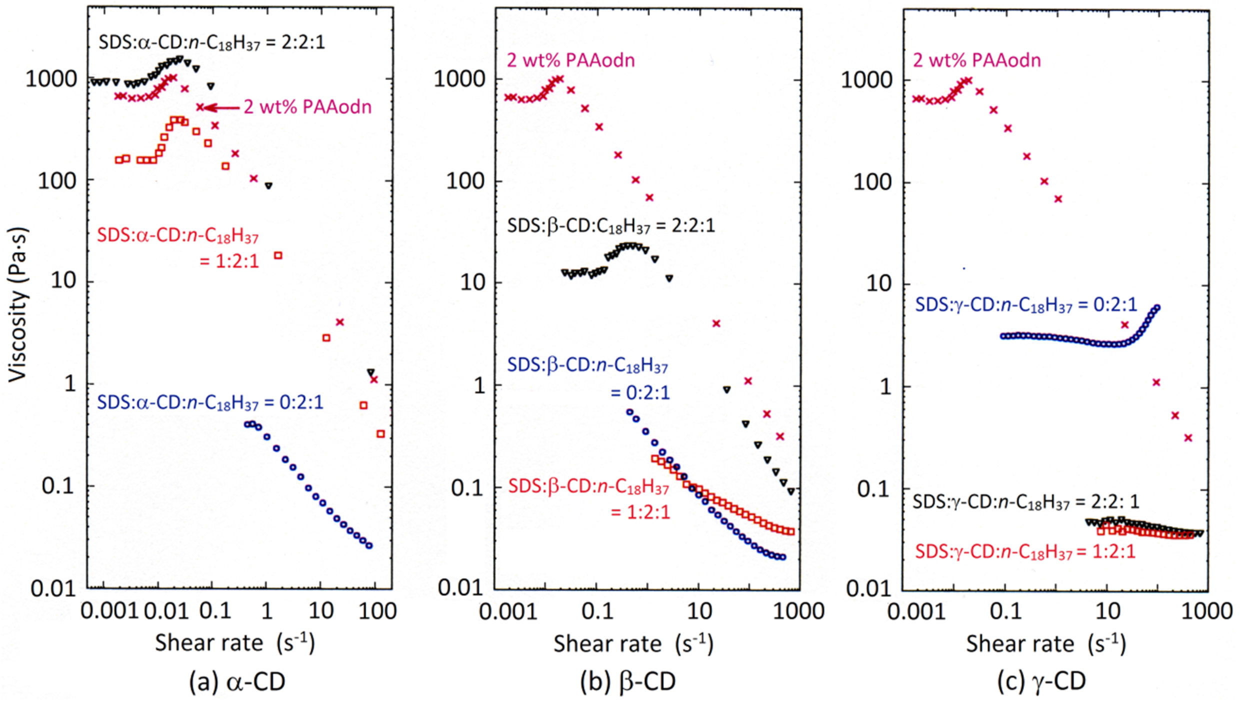

Figure 5: The effect of SDS addition on viscosity shear rate dependence for 2 wt % aqueous PAAodn solutions containing (a) α-CD, (b) β-CD and (c) γ-CD with a molar ratio of CD to n-$C_{18}H_{37}$ = 2:1 (0.10 M NaCl, pH 7.0). Data sets are shown for 2 wt % PAAodn alone (crosses) and for the ratios: SDS:CD:n-$C_{18}H_{37}$ = 0:2:1 (circles), SDS:CD:n-$C_{18}H_{37}$ = 1:2:1 (rectangles) and SDS:CD:n-$C_{18}H_{37}$ = 2:2:1 (triangles). Adapted with permission from [46]. Copyright (2008) American Chemical Society.

interactions between PAAodn and viscosity but to a lesser extent than for the 2:1 α-CD:n-$C_{18}H_{37}$ solution consistent with the n-$C_{18}H_{37}$ substituents competing more effectively with SDS in host–guest complexation with β-CD (Figure 5b). Addition of SDS decreases viscosity and removes the shear thickening observed for the 2:1 γ-CD:n-$C_{18}H_{37}$ solution probably as a result of the larger γ-CD simultaneously complexing both n-$C_{18}H_{37}$ and SDS such that complexation of two n-$C_{18}H_{37}$ by γ-CD is minimized (Figure 5c).

2 Network assembly by cyclodextrin- and guest-substituted polymers

The ability of cyclodextrins to complex hydrophobic guests in aqueous solution may be used to greatly extend supramolecular and polymer chemistry when cyclodextrins and hydrophobes are substituted onto water-soluble polymer backbones. The host–guest complexes formed between the cyclodextrin and hydrophobic substituents represent very specific interactions between polymer chains which may be exploited to modulate the polymer networks formed and the viscosities of their aqueous solutions.

2.1 Construction of polymer networks

The formation of a polymer network through host–guest complexation between cyclodextrin and hydrophobic substituents on different polymer chains is illustrated in a general manner in Figure 6. Such network formation is exemplified by the research of Wenz et al. in which mixtures of poly(maleic acid)-*co*-(isobutene) copolymers substituted with either β-CD or 4-*tert*-butylanilide form viscous aqueous solutions as host–guest complexation between these substituents form a polymer network [52,53]. Gosselet et al. [54,55] and Cammas et al. [56], respectively, mixed the adamantyl-substituted *N*,*N*-dimethylacrylamide hydroxyethylmethacrylate and β-malic acid-co-ethyladamantyl β-malate copolymers with β-CD-substituted-epichlorohydrin copolymers to obtain highly viscous solutions as a result of polymer network formation occurring through host–guest complexation between the β-CD and adamantyl substituents of the polymers.

Guo et al. prepared substituted poly(acrylate) networks through host–guest complexation between either the α-CD or β-CD substituents of PAAα-CD and PAAβ-CD and the n-$C_{18}H_{37}$ substituents of PAAodn [44], and also the 1-(2-aminoethyl)amido-β-CD (β-CDen) and 1-(2-aminoethyl)amidoadmantyl (ADen) substituents on the substituted poly(acrylate)s PAAβ-CDen and PAAADen, respectively [57]. The host–guest complexations between the cyclodextrin substituents and both n-$C_{18}H_{37}$ and ADen substituents in PAAodn and PAAADen, respectively, have a 1:1 stoichiometry. In both cases, the solu-

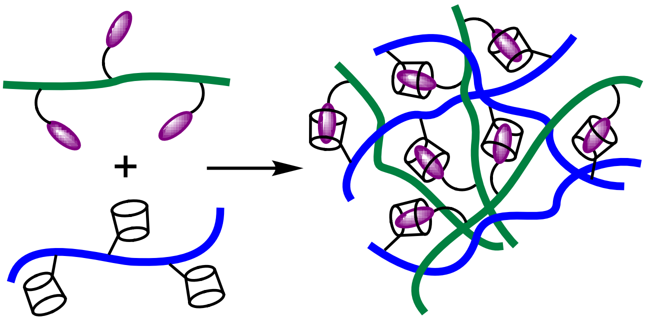

Figure 6: Host–guest complexation between polymers with cyclodextrin and hydrophobic substituents.

tion viscosity reaches a maximum when the host:guest substituent ratio is 1:1 and decreases when one substituent concentration exceeds the other as the substituted poly(acrylate) in excess concentration decreases the overall participation in network formation and thereby lowers solution viscosity (Figure 7a and b).

In principle these are good model systems to quantitatively test theories of polymer association exemplified by the studies of Tanaka and Edwards [58] and Rubinstein et al. [59-62]. However, matching experiment to theory remains a considerable challenge as associative polymer networks can incorporate clusters each containing 10–30 hydrophobic substituents depending on the polymer concentration as shown by the fluorescence studies of Winnik et al. [63-65].

2.2 Comparison of guests

Cyclodextrin host–guest complexation of guest species in aqueous solutions is largely driven by van der Waals and hydrophobic interactions between the interior of the cyclodextrin annulus and the guest with dehydration of both substantially influencing the thermodynamics of the process [66]. As a result, the guest often exhibits a substantial change in its UV–vis, fluorescence and ^{1}H NMR spectra upon complexation, and there is usually a significant enthalpy change. Consequently, UV–vis [67], fluorescence [68] and ^{1}H NMR [69]

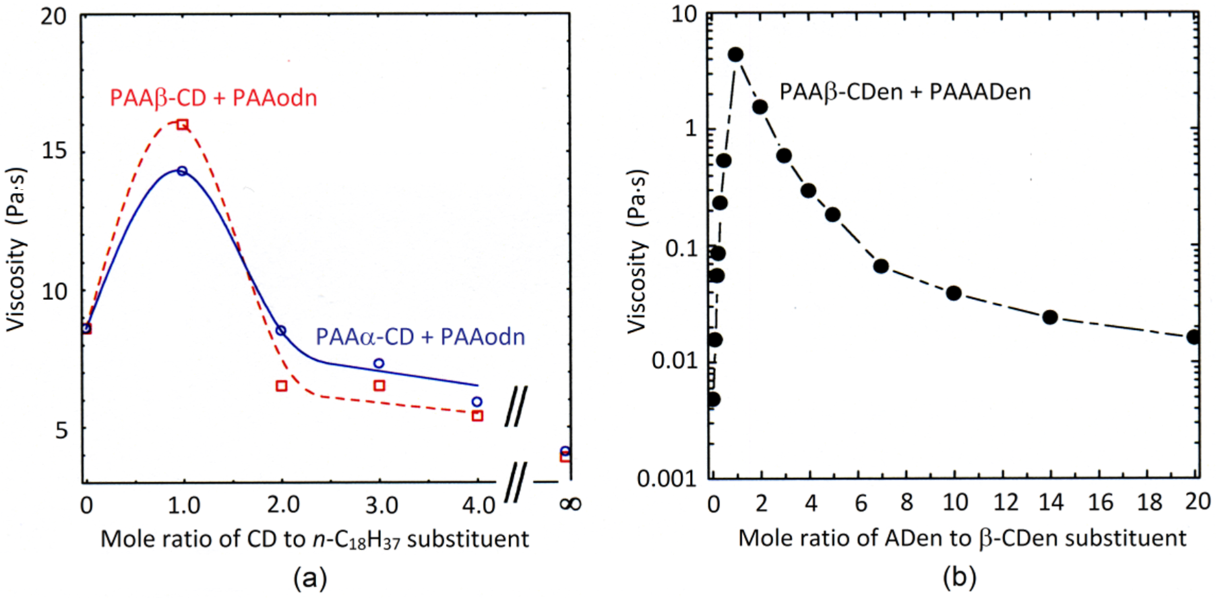

Figure 7: Variation of viscosity with mole ratio of CD substituents to hydrophobic substituents on poly(acrylate), PAA. (a) 0.5 wt % aqueous solutions of, respectively, 2.5 and 2.1% α-CD and β-CD randomly substituted PAA (PAAα-CD and PAAβ-CD) and n-$C_{18}H_{37}$ 3% randomly substituted PAA (PAAodn) [44]. Adapted with permission from [44]. Copyright (2005) American Chemical Society. (b) 2.0 wt % aqueous solution of 2.9% β-CDen randomly substituted PAA (PAAβ-CDen) and 3.0% ADen randomly substituted PAA (PAAADen) [57]. Adapted with permission from [57]. Copyright (2008) American Chemical Society.

spectroscopy and isothermal titrimetry calorimetry, ITC [52,70], are frequently used in characterizing host–guest complexation. When viscosity changes occur because of host–guest complexation, rheology may be used to characterize such complexation [71]. Some examples of aqueous polymer systems characterized by these techniques appear in Table 2.

2.3 Effect of substituent tether length in substituted polymers

Host–guest complexation in substituted polymer systems is substantially affected by the length of the tether through which either the cyclodextrin or hydrophobe is attached to the polymer backbone. This also affects the extent of intramolecular interactions between substituents in a single polymer chain and of intermolecular interactions between substituents in adjacent polymer chains. Consequently, the strength of interaction between the substituted poly(acrylates)s is substantially controlled by the variation in occurrence of intra- and intermolecular host–guest complexation between the β-CD substituents tethered by amido, diacylamino-1,6-hexyl and diacylamino-1,12-dodecyl tethers in the respective substituted poly(acrylate)s, PAAβ-CD, PAAβ-CDhn and PAAβ-CDddn, and the similarly tethered adamantyl (AD) substituents in the PAAAD, PAAADhn and PAAADddn substituted poly(acrylate)s shown in Figure 8 [72]. The substituent tether length largely controls the relative importance of the intra- and intermolecular complexation modes and also the extent to which the adamantyl substituent and its tether and the β-CD tether compete for host–guest complexation in the β-CD substituent annulus to form interchain linkages in the polymer network as shown by 2D ^{1}H NMR spectroscopy. Rheological studies show that as its length shortens the tether is less able to compete for β-CD substituent annular occupancy, and that the coincident increase in steric interactions with the poly(acrylate) backbone also inhibits intermolecular host–guest complexation [72,73].

3 Polymer network assembly through covalently-linked cyclodextrins

The simplest covalently-linked cyclodextrins are dimers which may act as ditopic hosts due to the presence of the two cyclodextrin annuli. Thus, such dimers may be used to form cross-links through the complexation of hydrophobic substituents on adjacent polymer chains and thereby generate a polymer network and hydrogel [74,75]. Variation of the length of the covalent-linker in the cyclodextrin dimer and of the tether between the hydrophobic substituents and the polymer backbone can substantially affect the host–guest interactions as is illustrated by studies of β-CD dimers and adamantyl-substituted poly(acrylate)s (Figure 9) [76]. (A similar situation also prevails for covalently-linked β-CD trimers as shown by Lincoln et al. [77].) The longer succinamide linker in 66β-CD_2su engenders higher viscosities than does the shorter urea linker in 66β-CD_2ur probably because steric hindrance between the adjacent adamantyl-substituted poly(acrylate) chains is greater when 66β-CD_2ur forms a cross-link [76]. (The 66 prefix in 66β-CD_2su and 66β-CD_2ur indicates that the succinamide and urea linkers are attached to the C6 carbon in a D-glucopyranose subunit of each β-CD.) The increasing length of the adamantyl tether from amido to hexylamido in PAAAD and PAAADhn progressively decreases steric hindrance between the poly(acrylate) backbones and facilitates host–guest complexation such that polymer network formation strengthens. Competition between the adamantyl group and its hexyl tether for complexation in the annuli of 66β-CD_2su also occurs (Figure 9). Interestingly, as length increases further to twelve methylene groups in the dodecyl tether in PAAADddn, a partic-

Table 2: Host–guest complexation systems, complexation constants and methodologies.

Polymer backbone	Guest substituent	Host	K (M^{-1})	Method
poly(acrylate)	azobenzene	3α-CD[a]	140	UV–vis [67]
poly(acrylate)	azobenzene	6α-CD[a]	12000	UV–vis [67]
poly(acrylamide)	(1-naphthyl)methyl	6β-CD[a]	77	fluorescence [68]
poly(acrylamide)	(2-naphthyl)methyl	6β-CD[a]	190	fluorescence [68]
poly(methacrylamide)	tryptophan	α-CD[b]	30	^{1}H NMR [69]
poly(methacrylamide)	tryptophan	β-CD[b]	83	^{1}H NMR [69]
poly(methacrylamide)	tryptophan	γ-CD[b]	11	^{1}H NMR [69]
poly(maleate)-*co*-(isobutene)	4-*tert*-butylphenyl	3β-CD[a]	25900	ITC [52]
poly(acrylate)	adamantyl	6β-CD[a]	3020	ITC [70]
HASE polymer	$C_{22}H_{45}$	α-CD[b]	11100	rheology [71]
HASE polymer	$C_{22}H_{45}$	β-CD[b]	1890	rheology [71]

[a]The 3α-CD, 6α-CD and 6β-CD substituents are tethered to the polymer backbone through the 3C carbon of a single D-glucopyranose subunit in the first case, and through the C6 carbon in the second and third cases. [b]Free cyclodextrin.

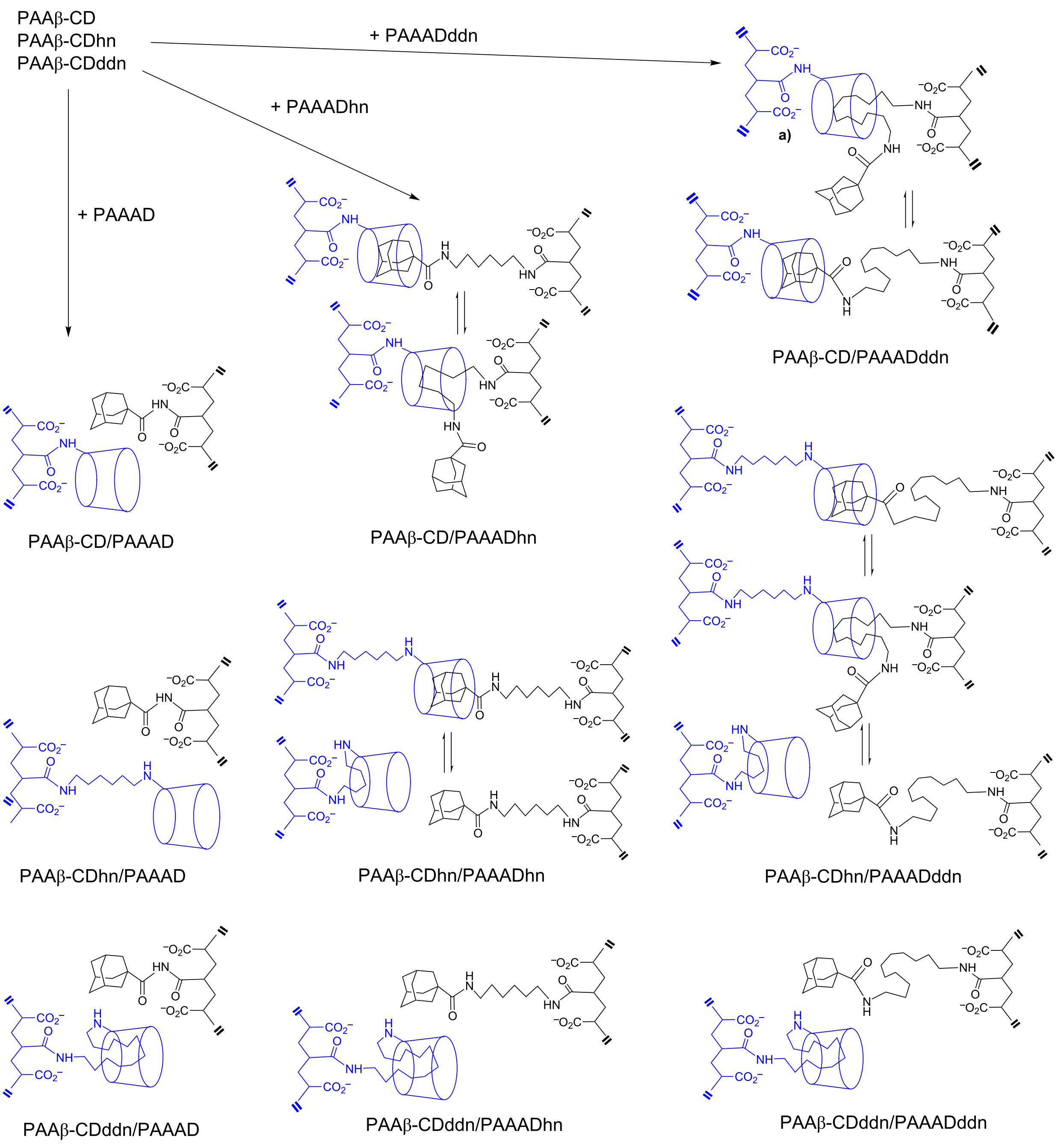

Figure 8: Illustration of the competitive intermolecular host–guest complexation of either the adamantyl substituent or the tethers of the adamantyl and β-CD substituents in a range of substituted poly(acrylate) systems. In each case β-CD is tethered to the PAA backbone through a C6 carbon in a D-glucopyranose subunit of each β-CD. Reproduced with permission from [72]. Copyright (2010) Wiley-VCH.

ularly marked decrease in the viscosity of the hydrogel formed with 66β-CD$_2$ur occurs by comparison with that formed with PAAADhn. This may be partly attributed to the increased flexibility allowed by the longer tether in the polymer network formed when host–guest complexation occurs.

In earlier studies, Auzély-Vetly et al. reported the substitution of chitosan (molecular weight 195 kDa) with adamantyl groups and characterized their complexation in the β-CD annuli of a singly octamethylene-linked β-CD dimer **b** and a doubly octamethylene-linked β-CD dimer **c** (Figure 10a, b and c) [78]

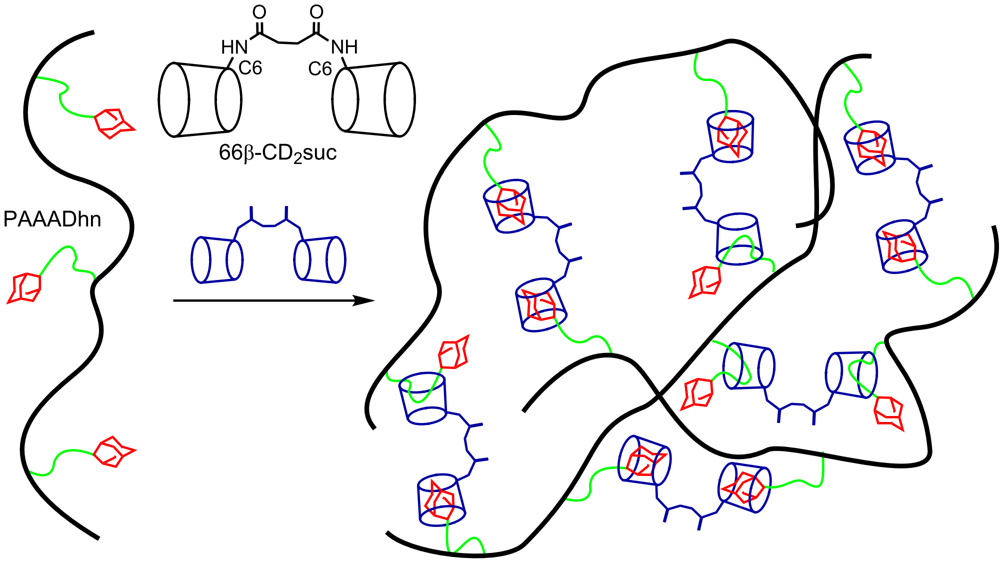

Figure 9: Competitive host–guest complexations in which either the adamantyl substituent (red) or the *n*-hexyl tether (green) of PAAADhn is the guest in the 66β-CD_2suc annuli to form a hydrogel network [76].

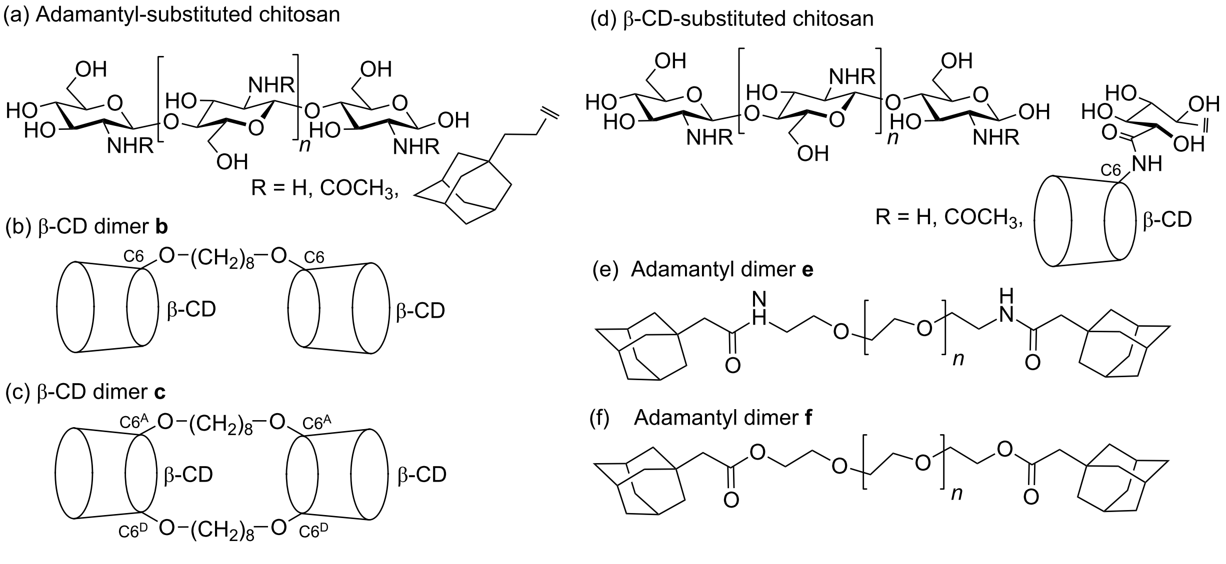

Figure 10: (a) Substituted chitosan in which acyl- and adamantyl-substitution is 5% and 12 %, respectively. (b) Octylmethylene-linked β-CD dimer **b** where substitution is at C6 for each β-CD. (c) Octymethylene-linked β-CD dimer **c** where substitution is at $C6^A$ and $C6^D$ for each β-CD [78] (d) Substituted chitosan in which acyl- and β-CD-substitution is 12% and 10%, respectively. (e) Diaminopolyethyleneglycol-linked adamantyl dimer **e**. (f) Polyethyleneglycol-linked adamantyl dimer **f** [81].

and related β-CD [79,80] dimers in aqueous solution. It was determined from ITC experiments that while β-CD formed a 1:1 host–guest complex with adamantane carboxylate, only one annulus of the β-CD dimer **b** and β-CD dimer **c** complexed adamantane carboxylate on average. This was attributed to aggregation of the dimers as a consequence of their amphiphilic nature, complexation of the octamethylene linker in the β-CD dimer annuli, and hydrogen bonding interactions between their β-CD annuli. The 1:1 complexation constants, $10^{-4}K_{11}$ = 7.96, 2.32 and 26.42 M^{-1} in aqueous solution at 298.2 K for β-CD and the β-CD dimer **b** and the β-CD dimer **c**, respectively, where the greater β-CD dimer **c** complex stability was attributed to the greater hydrophobicity arising from the two octamethylene linkers. Rheological studies of aqueous solutions of adamantyl-substituted chitosan showed a moderate increase in viscosity with increase in β-CD dimer **b** concentration at a constant substituted-chitosan concentration consistent with the formation of cross-links forming through ditopic complexation by the β-CD dimer **b** of adamantyl substituents on adjacent chitosan chains. A much greater increase in viscosity was observed when the β-CD dimer **c** was employed consistent with its greater rigidity derived from the twin octamethylene linkers enhancing interchain cross-link formation.

Interesting variations on the above complexation studies are those relating to β-CD-substituted chitosan and the diamino-poly(ethylene glycol)-linked adamantyl dimer **e** and the poly(ethylene glycol)-linked adamantyl dimer **f**, in which the linker molecular weight is either 3.4 or 20 kDa in each case, shown in Figure 10d, e and f, respectively [81]. Rheological studies of aqueous solutions of β-CD-substituted chitosan show increased viscosity in the presence of adamantyl dimers **e** and **f** consistent with the formation of cross-links forming through complexation of the adamantyl groups of the dimers by β-CD substituents on adjacent chitosan chains.

4 Threading cyclodextrins onto polymer backbones

Since the report of host–guest complexation between α-CD and poly(ethylene glycol) (PEG) by Harada and Kamachi in 1990 [82], a variety of pseudo-polyrotaxanes and polyrotaxanes formed through host–guest complexation between cyclodextrins and linear polymers have been reported [83], some of which form hydrogels [84,85]. In particular, hydrogels formed by PEG and cyclodextrins have been investigated intensively because of the biocompatibility of their components. Interestingly, local crystallization of the polyrotaxane threaded cyclodextrins, sometimes called molecular necklaces [86], may form cross-links and polymer networks in aqueous solution. In 1994, Li et al. reported the formation of hydrogels based on the host–guest complexation between α-CD and high molecular weight PEG [87]. They found the hydrogel melting temperature to increase with increase in PEG length and α-CD concentration and to decrease with increase in PEG concentration consistent with the threading of varying numbers of α-CD onto the PEG. It was also observed that X-ray powder diffraction patterns of the powdered frozen hydrogel were consistent with the formation of localized regions where the α-CD/PEG pseudo-polyrotaxanes crystallized to form interchain links within the hydrogel. Similar conclusions were reached from another X-ray powder diffraction study of frozen α-CD/PEG hydrogels formed with PEG of 8, 20 and 600 kDa molecular weights [87]. The accompanying rheological and differential scanning calorimetric studies were also consistent with the localized crystallization of α-CD/PEG pseudo-polyrotaxanes forming interchain cross-links in the hydrogel.

Low molecular weight <2 kDa PEG forms crystalline precipitates in aqueous solutions in the presence of α-CD largely because multiple α-CD thread onto the PEG chain such that the uncomplexed portions of the PEG chains are too short for significant interchain interaction to form a water soluble network [82,86,88]. However, when a hydrophobic adamantyl group is substituted onto one end of a low molecular weight PEG chain to form amphiphilic AD-PEG, it is found that the adamantyl substituents aggregate in aqueous solution to form a micelle and that subsequent addition of α-CD leads to the formation of a supramolecular hydrogel as shown in Figure 11 [88]. The driving force for gelation is a combination of the hydrophobic aggregation of the adamantyl substituents and the aggregation of the α-CD complexed portions of the AD-PEG chains. Part of the interest in these low molecular weight polymer systems arises because they are able to pass through the kidney membrane [89] and are consequently of interest as components of drug-delivery systems [89,90].

A hydrogel formed through the initial formation of micelles of poly(ethylene glycol)-*b*-poly(acrylate), PEG-*b*-PAA, copolymer and the widely used anticancer drug cis-diamminedichloroplatinum(II), cisplatin [91], and subsequent host–guest complexation by α-CD has been developed by Zhu et al. (Figure 12) [92]. In the first stage, the two chloro ligands on the four-coordinate square-planar platinum(II) center of cisplatin are displaced by PEG-*b*-PAA carboxylate groups to produce PEG-*b*-PAA-cisplatin micelles. Addition of α-CD results in host–guest complexation of the PEG segments of PEG-*b*-PAA and subsequent aggregation of these α-CD-complexed PEG molecular necklace segments to form a network and a supramolecular hydrogel. Because the interactions between the α-CD-complexed PEG segments forming cross-links are non-covalent and quite weak, their aggregations can be broken by applying shear force such that the reversibility of the solution/hydrogel transition is observed in rheological experiments. In vitro tests show that the PEG-*b*-PAA/cisplatin hydrogel has a sustained cisplatin release over three days and that it has a high cytotoxity towards human bladder carcinoma EJ cells.

5 Responsive smart materials

Cyclodextrin host–guest chemistry is characterized by an ever-expanding range of host and guests, some of which undergo structural and interaction variations in response to stimuli as exemplified by photo-, pH-, temperature- and redox-responsive changes. Consequently, cyclodextrins have generated a range of stimuli-responsive materials collectively called "smart ma-

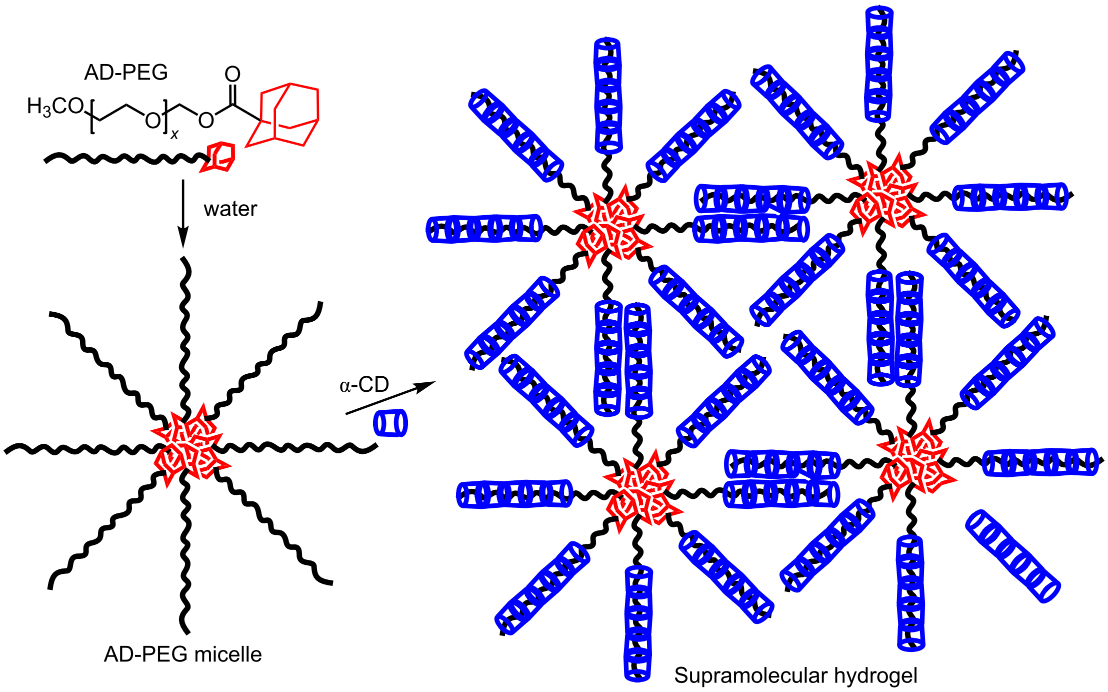

Figure 11: The formation of a AD-PEG micelle followed by the formation of a AD-PEG/α-CD supramolecular hydrogel in aqueous solution [88].

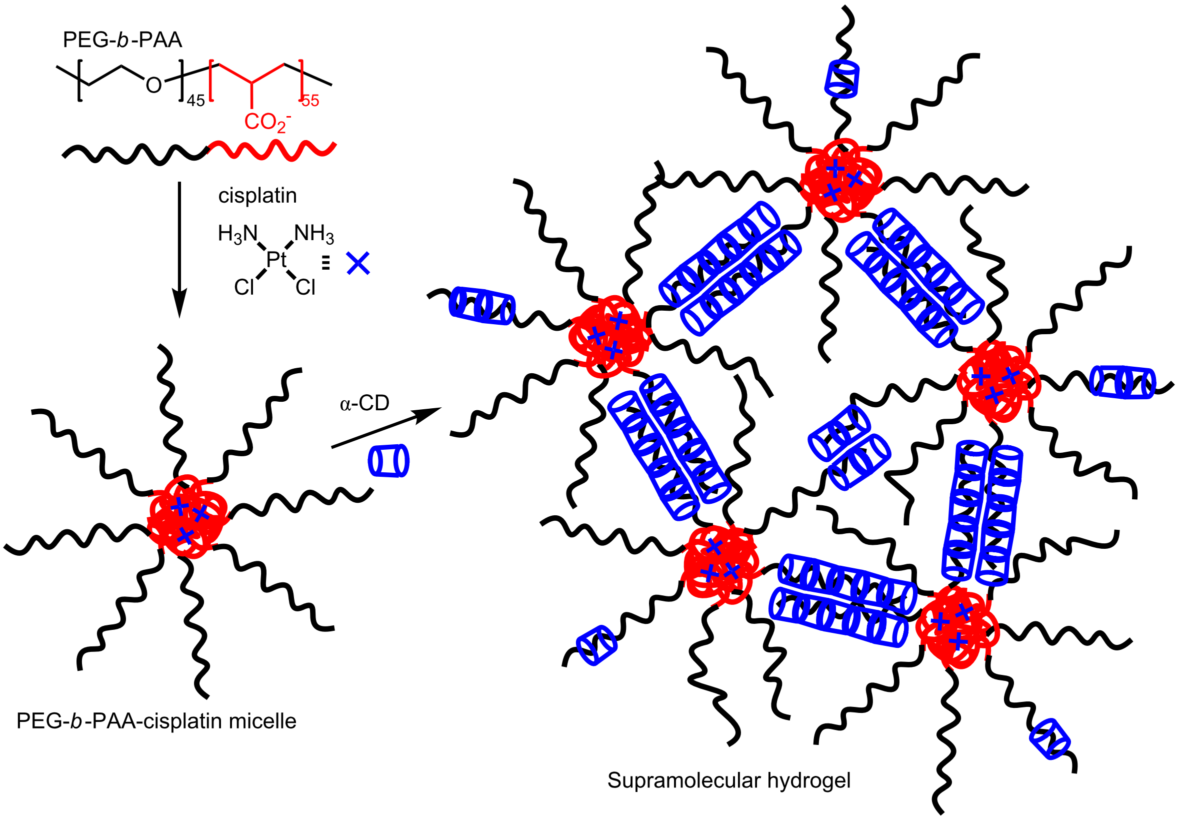

Figure 12: Interaction of PEG-*b*-PAA block copolymer with *cis*-diamminedichloroplatinum(II), cisplatin, to form a PEG-*b*-PAA-cisplatin micelle followed by the addition of α-CD to form a supramolecular hydrogel [92].

terials". These include "self-healing materials" which after being disrupted can recover their former state through host–guest interactions. Some examples of these materials are now discussed.

5.1 Photo-responsive materials

Among the better known photo-responsive small molecules are azobenzene and its derivatives which isomerize from *trans* to *cis* and from *cis* to *trans* under irradiation with UV and visible light, respectively, and are potentially components of photo-responsive materials. In 2005, Harada et al. constructed a photo-responsive dodecyl substituted poly(acrylate), PAAddn, hydrogel system which depends on α-CD complexing *trans*-4,4'-azodibenzoic acid but not its *cis* isomer as seen in Figure 13 [93]. Thus, alone PAAddn forms a hydrogel due to the hydrophobic interchain interactions of its dodecyl substituents. However, upon addition of α-CD the dodecyl substituents are complexed and the hydrogel is disrupted to give a free-flowing solution. The addition of *trans*-4,4'-azobenzene carboxylate to this solution results in the preferential formation of the α-CD·*trans*-4,4'-azobenzene carboxylate host–guest complex and the PAAddn hydrogel reforms. Irradiation at 335 nm causes *trans*-4,4'-azobenzene carboxylate to photo-isomerize to the *cis* isomer which is too sterically hindered to form a stable α-CD complex, and the dodecyl substituents of PAAddn are once again complexed by α-CD and the hydrogel disaggregates. This last step is reversible though irradiation at >440 nm such that the equilibria may be switched to and fro by irradiating at 350 nm, when the viscosity rises to ~3 × 10^3 Pa·s, and >440 nm when the viscosity decreases to ~2 × 10^{-2} Pa·s.

Harada et al. also constructed two other photo-responsive hydrogels from a 2.7% azobenzene-substituted poly(acrylate), PAAAzo, and two α-CD-substituted poly(acrylates) in which α-CD is substituted onto the poly(acrylate) backbone through either the C3- or C6-carbon of a D-glucopyranose subunit, PAA3α-CD and PAA6α-CD, respectively, which are 1.6 and 2.2% substituted (Figure 14) [67]. The PAA3α-CD/PAAAzo and PAA6α-CD/PAAAzo host–guest complexation between the α-CD and azobenzene substituents are characterized by complexation constants, $K = 1.4 \times 10^2$ and 1.2×10^4 M^{-1}, respectively. Under visible light the viscosities of PAA3α-CD/PAAAzo and PAA6α-CD/PAAAzo are 6.5 × 10^{-1} and 2.5 × 10^2 Pa·s at 298.2 K, respectively, and upon ultraviolet radiation these values decrease ten-fold and increase two-fold reversibly, respectively (Figure 15). This reflects the lesser

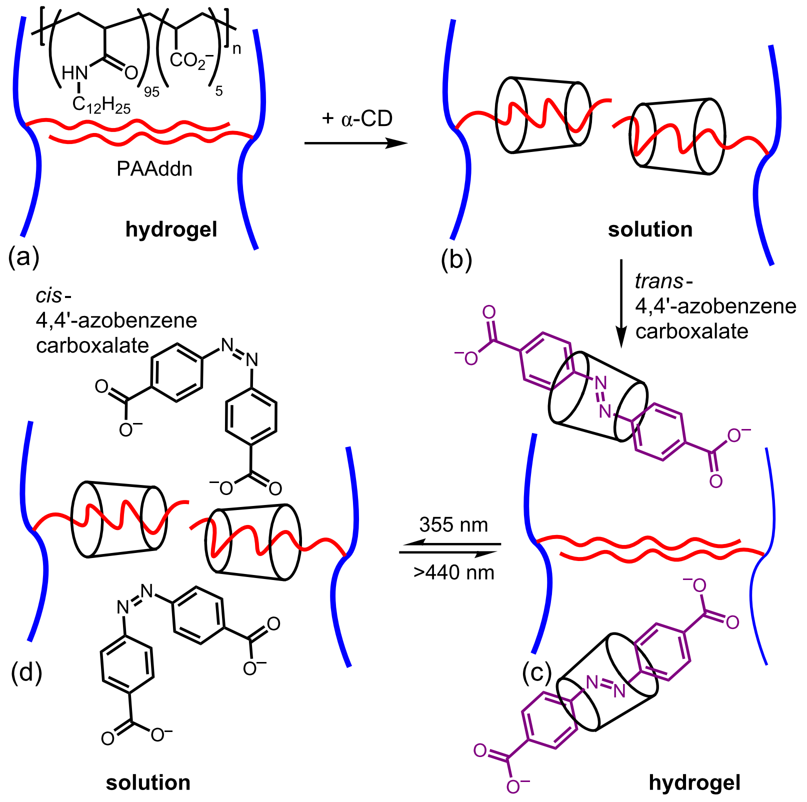

Figure 13: Solution to hydrogel transitions (a)–(d) for a PAAddn segment in the presence of competitive photo-responsive complexation of the dodecyl substituent by α-CD and *E*- or *trans*-4,4'-azobenzene carboxylate and its *Z*- or *cis*-isomer in basic aqueous solution [93].

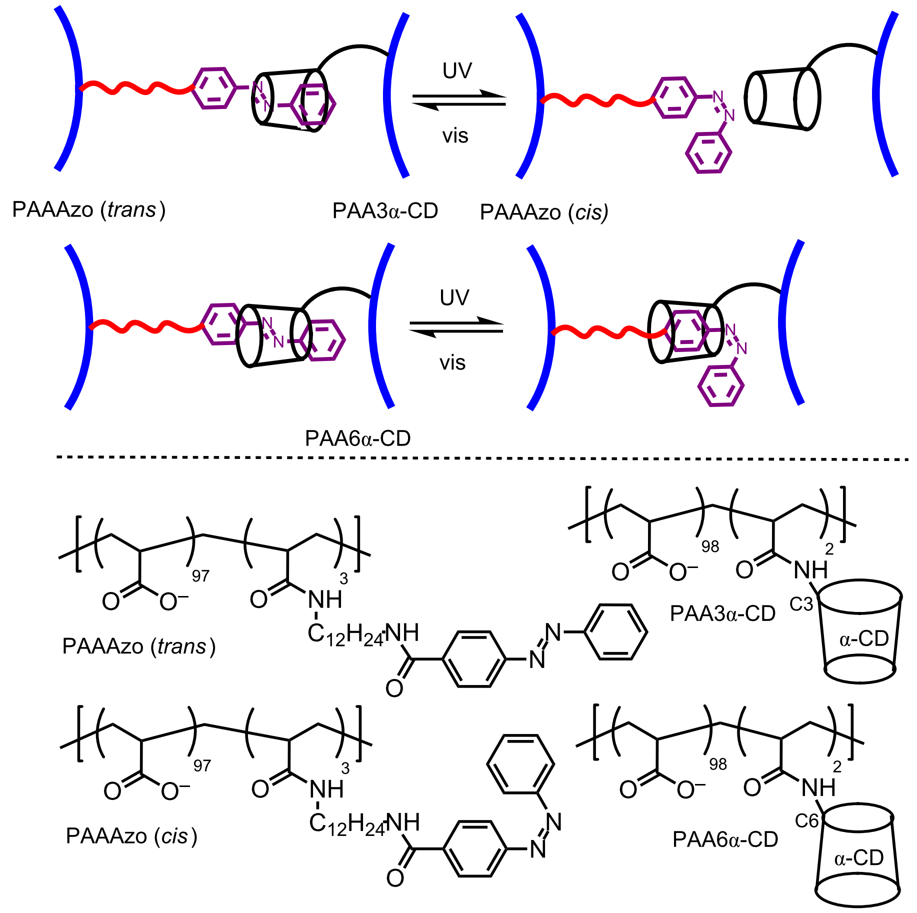

Figure 14: Structures of the poly(acrylate)-based polymers PAAAzo (*trans*), PAAAzo (*cis*), PAA3α-CD and PAA6α-CD, and the effects of the stereochemistry and photo-isomerism of the diazo substituents of PAA3β-CD and PAA6β-CD on their host–guest complexation by the α-CD substituents of PAA3α-CD and PAA6α-CD [67].

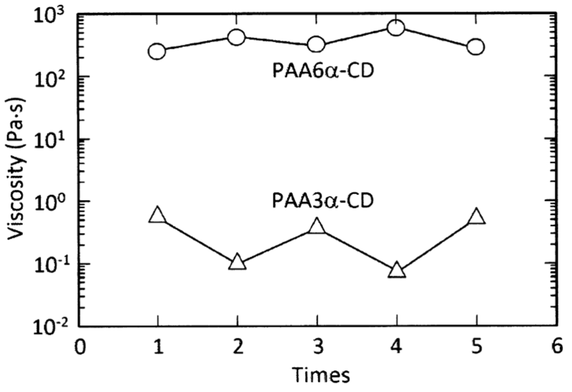

Figure 15: Variation of viscosity of a PAA6α-CD/PAAAzo solution (circles) and a PAA3α-CD/PAAAzo solution (triangles) during repetitive irradiations. For PAA3α-CD/PAAAzo the low and high viscosity values are attained after UV and visible irradiation, respectively, and vice versa for PAA6α-CD/PAAAzo. Adapted with permission from [67]. Copyright (2006) American Chemical Society.

ability of the 3α-CD substituent to complex either the *trans*- or *cis*-azobenzene substituent by comparison with the 6α-CD substituent because of the difference in steric constraint caused by the tether attachment at either the C3 or C6-carbon of a D-glucopyranose subunit, respectively.

A study by Hu et al. of azobenzene-substituted hydroxypropyl methylcellulose (azo-HPMC) polymers shows that the azobenzene substituents are reversibly photo-isomerized from the *trans* to *cis* configurations and vice-versa by ultra-violet and visible radiation, respectively, and that the corresponding solution to hydrogel transition temperatures are 299.7 K and 309.7 K for 10 g L^{-1} azo-HMPC in aqueous 0.5 M NaCl [94]. This is attributed to the *trans*-azobenzene substituents undergoing hydrophobic stacking more effectively than the less planar and more polar *cis*-azobenzene substituents. However, when 3×10^{-2} M^{-1} α-CD is present the solution to hydrogel transition temperatures increase to 330.2 K and 322.2 K for azo-HMPC bearing *trans*- and *cis*-azobenzene substituents, respectively. Host–guest complexation by α-CD eliminates the possibility of hydrophobic stacking between the *trans*-azobenzene substitu-ents, but the *cis*-azobenzene substituents are not significantly complexed by α-CD and can undergo some hydrophobic stacking. In addition the relatively hydrophilic exterior of α-CD minimizes any hydrophobic attraction between the α-CD-complexed *trans*-azobenzene substituents. The solution to hydrogel transition temperature is also dependent on the extent of azobenzene substitution of azo-HMPC and the concentration of α-CD.

Another notable example of a photo-responsive hydrogel activated by the photo-isomerism of azobenzene substituents has been provided by Zhao and Stoddart [95]. In this case the *trans* azobenzene substituents of a substituted poly(acrylate) are complexed by β-CD substituted at the C3 carbon of a D-glucopyranose subunit with deoxycholic acid, and hydrophobic association between them form interchain cross-links and a hydrogel. Upon irradiation at 355 nm, *trans* to *cis* photo-isomerization of the azobenzene substituents occurs, its β-CD complexation dissociates, the deoxycholic acid moieties complex within the β-CD annuli and the hydrogel network disassociates. This process is reversible through irradiation at 450 nm.

5.2. pH-Responsive materials

In 2007, Yui et al. reported a pH-responsive polymer system in which the simultaneous host–guest complexation by γ-CD of two of the 3.4 kDa average molecular weight poly(ethylene glycol)-*b*-poly(ethylamine) strands substituted onto the dextran backbone of a poly(ethylene glycol)-*b*-poly(ethylamine)-*g*-dextran copolymer, PEG-PEI-dex, is considered to form the network underlying the supramolecular hydrogel formed in aqueous solution at pH 10 as shown in Figure 16a [96]. (The PEG-PEI-dex concentration is 3 wt % and the ratio of the concentration of γ-CD to the repeating PEI-PEI unit is 1:4.) The addition of γ-CD to the PEG-PEI-dex solution causes viscosity to rise from ~10^{-1} to 10^{2} Pa·s at pH 10. Upon lowering the PEG-PEI-dex/γ-CD solution pH to 4, under which conditions all of the PEI secondary amine groups are protonated, solution viscosity decreases by three orders of magnitude consistent with

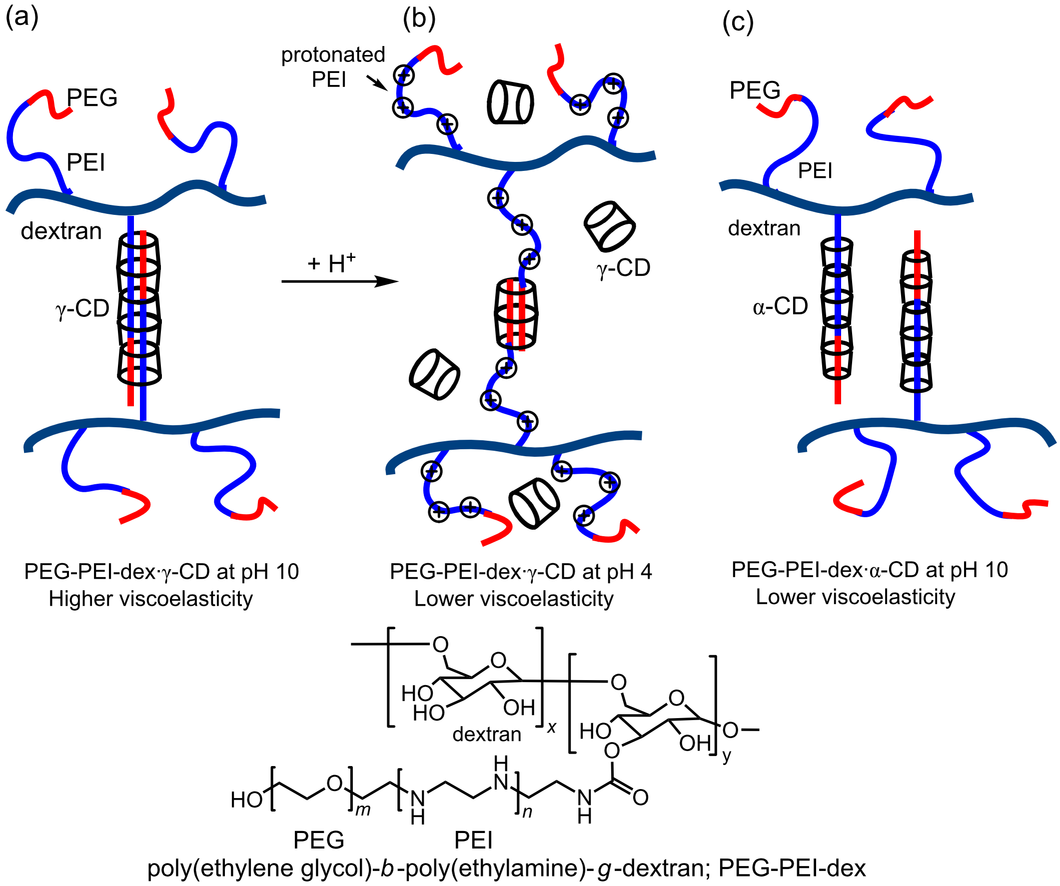

Figure 16: The structures proposed for the poly(ethylene glycol)-*b*-poly(ethylamine)-*g*-dextran·γ-CD, PEG-PEI-dex·γ-CD, supramolecular hydrogel at (a) pH 10 and (b) its much lower viscoelastic protonated form at pH 4. The proposed structure of the PEG-PEI-dex·α-CD at pH 10 is shown in (c) [96].

a loosening of the hydrogel network in which probably only the PEG segments of PEG-PEI-dex/γ-CD are complexed by γ-CD (Figure 16b).

In contrast, when α-CD is added to a PEG-PEI-dex solution at pH 10 under the same conditions as for the addition of γ-CD, there is little change in viscosity consistent with the smaller α-CD annulus only accommodating a single PEG-PEI strand in its host–guest complex and consequently not forming a cross-link between PEG-PEI-dex chains. However, under different conditions, when several α-CD thread onto a single polymer chain to form a polyrotaxane they may aggregate in a localized crystalline state to effectively form cross-links between the polyrotaxanes in a hydrogel network [97-99].

A group of pH-responsive hydrogels which comprises four adamantyl-substituted polyacrylamides, in which the adamantyl tether varies in length, and either a linear or a globular β-CD polymer in which the β-CD are cross-linked with epichlorohydrin has been reported by Koopmans and Ritter et al. [100]. The hydrogel viscosities vary substantially with the concentrations of the two polymers and the length of the adamantyl tether. Thus, when the tether length between the adamantyl substituents and the polymer backbone increases progressively from a single amido group through -CONH(CH)$_2$CONH-, to -CONH(CH)$_5$CONH- to -CONH(CH)$_{11}$CONH- the zero-shear viscosities in the presence of the linear β-CD host polymer vary in the sequence 3.63, 1007, 354.8 and 138.3 Pa·s at 293.2 K and pH 7 (when both polymer concentrations are 50 mg/L). When the tether consists only of an amido group the adamantyl substituents are too crowded by the polymer backbone to complex strongly with the β-CD substituents. An increase in tether length to -CONH(CH)$_2$CONH-, maximizes the host–guest complexation and retains substantial stiffness in the hydrogel. When the tether further lengthens to -CONH(CH)$_5$CONH- and -CONH(CH)$_{11}$CONH- host–guest complexation is unlikely to be hindered, but the increase in tether length decreases the hydrogel stiffness proportionately. In the pH range 4–6, the zero-shear viscosity of the hydrogel formed from the adamantyl polymer with the -CONH(CH)$_5$CONH- tether and the globular β-CD polymer shows little variation. However, zero-shear viscosity doubles at pH 10 consistent with deprotonation of the adamantyl polymer which results in an increase in its volume, as shown by the increase in the hydrodynamic diameter of the adamantyl polymer alone from 3.12 nm at pH 6 to 4.85 nm at pH 10. This allows more adamantyl substituents to be complexed by the β-CD substituents of the β-CD-substituted polymer such that the aggregation of the hydrogel network increases.

5.3 Thermo-responsive materials

In 2006, Kataoka et al. showed that an aqueous solution of the poly(ethylene glycol) polyrotaxane with adamantyl end-substituents (Figure 17) changes from a solution of single

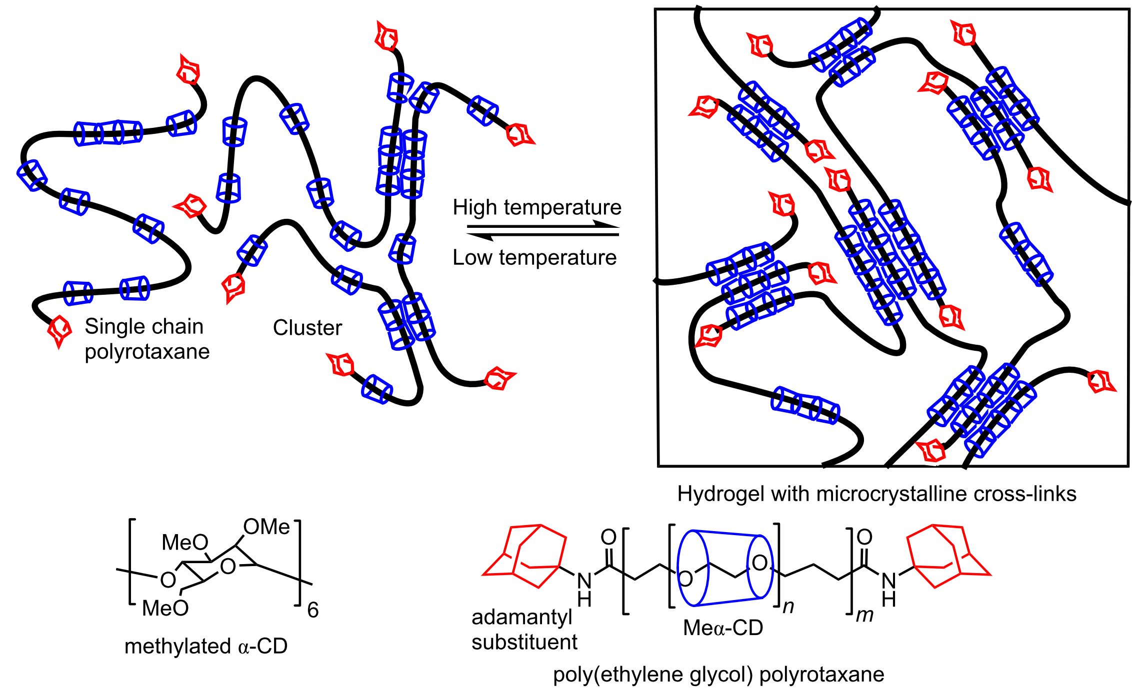

Figure 17: Structure of poly(ethylene glycol) polyrotaxane with adamantyl end substituents, and its temperature dependent equilibrium between the solution and hydrogel states [101].

chains and small clusters of polyrotaxanes at low temperature to an elastic hydrogel containing microcrystalline aggregates of the methylated-α-CD components of the hydrogel at higher temperatures using differential scanning microcalorimetry, rheology, X-ray diffractometry and ^{1}H NMR spectroscopy [101]. The average molecular weight of the poly(ethylene glycol) component of the polyrotaxane was 35 kDa and it was estimated that there were ≈110 methylated-α-CD threaded onto each polyrotaxane chain. At low temperatures, hydrophobic interactions among the methylated α-CD result in forming small clusters and, with increase in temperature, these clusters grow into stable crystal-like structures such that the hydrogel functions similarly to a block copolymer with hard segments composed of micro-crystalline methylated α-CD and softer segments composed of polyethylene glycol in the hydrogel.

The preparations of the copolymers of either *N*,*N*-dimethylacrylamide (DMAA) or *N*-isopropylacrylamine (NIPAAM) with 1-adamantylacrylamide, and of the copolymer of NIPAAM with 6-acryloylaminohexanoic acid in which the ratio of the acrylamide units to adamantyl subunits is 20:1 have been reported by Ritter et al. [102]. They find that the viscosity of 50 g/L aqueous solutions of the three copolymers increases greatly within seconds after mixing with a β-CD dimer (Figure 18) to form stable hydrogels through ditopic host–guest complexation of the adamantyl substituents forming cross-links between the copolymer chains. The DMAA-based adamantyl-substituted copolymer/β-CD dimer hydrogel shows no turbity change in the range of 283.2–363.2 K probably because it is the least hydrophobic of the three polymers. In contrast, those of the two NIPAAM-based adamantyl-substituted/β-CD dimer hydrogels show temperature dependent turbidity with cloud points at 287.2 K and 288.9 K with increase in polymer backbone to adamantyl tether length. These compare with cloud points of 296.2 K and 294.2 K for the two respective NIPAAM-based adamantyl-substituted copolymers alone.

A related study involves the copolymer of isopropylacrylamine and methacrylated β-CD (a) in Figure 19 and the complexation of the anions of the ionic liquids 1-butyl-3-vinylimidazolium-adamantanecarboxylate, -bis(trifluoromethylsulfonylamide and –nonafluorobutansulfonate, (b’), (c’) and (d’), respectively in Figure 19, by the β-CD substituent of the copolymer to form the copolymer complexes (b), (c) and (d) [103]. (β-Cyclodextrin forms 1:1 host–guest complexes with (b’), (c’) and (d’) to give complexes characterized by complexation constants $10^{-3}K_{11}$ = 5.3, 21.0 and 8.1 M^{-1} in aqueous solution at 298.2 K [104].) The three copolymer complexes (b)–(d) are effectively pseudopolyanions and this has interesting behavioral consequences. Thus, turbidity measurements in aqueous solution show the cloud point for (a) to be 309.2 K whereas those of (b) and (c) are 316.2 K and 326.2 K, respectively. These increases are attributed to an increase in hydrophilicity caused by the anionic carboxylate and sulfonate groups protruding from the β-CD annuli and interacting with water. However, in (d) the negative charge is located in the centers of the β-CD annuli and there is no enhancement of interaction with water and the cloud point occurs at 307.2 K.

Light-scattering studies show the hydrodynamic diameters of (a)–(d) to be 15.1, 11.5, 9.8 and 16.5 nm in water at 298.2 K. The decrease in hydrodynamic diameter from (a) to (b) and (c) is attributable to simultaneous ion-pairing between the 1-butyl-3-vinylimidazolium cations and either the anionic carboxylate or sulfonate groups causing overall attraction between the host–guest complex substituents of (b) and (c) and a decrease in polymer coil size by comparison with (a). Conversely, the location of the negative charges in the centers of the β-CD annuli of

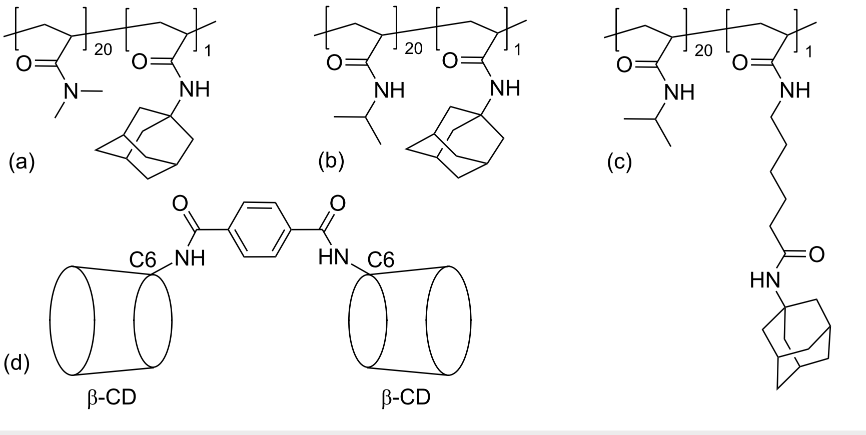

Figure 18: Copolymers of either (a) *N*,*N*-dimethylacrylamide (DMAA) or (b) *N*-isopropylacrylamine (NIPAAM) with 1-adamantylacrylamide, and (c) copolymer of NIPAAM with 6-acryloylaminohexanoic acid [102]. (d) The β-CD dimer in which substitution is at the C6 carbon of a D-glucopyranose subunit of each β-CD.

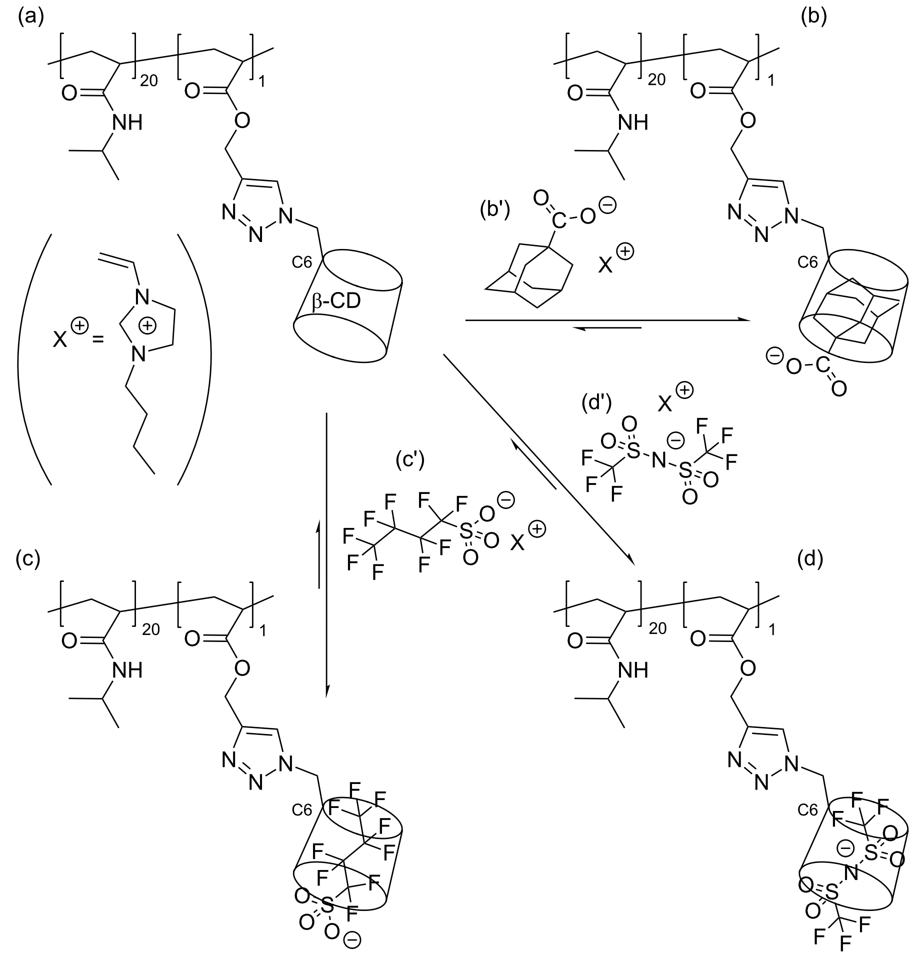

Figure 19: The copolymer of isopropylacrylamine and methacrylated β-CD (a) and its complexation of the anions of the ionic liquids 1-butyl-3-vinylimidazolium-adamantanecarboxylate, -bis(trifluoromethyl sulfonyl amide and -nonafluorobutansulfonate, (b'), (c') and (d'), respectively to give the copolymer complexes (b), (c) and (d) [103].

(d) decreases ion-pairing and repulsion between the 1-butyl-3-vinylimidazolium cations slightly increases polymer coil size by comparison with (a).

5.4 Redox-responsive materials

Redox-responsive hydrogel systems have potential applications as environmentally benign electro-functional materials. Such systems require a redox couple as a central component. One such system is that in which the oxidation states of iron are 0 and I in ferrocenecarboxalate, $[Fe^0(C_5H_5)(C_5H_5CO_2^-)]^-$ (FCA^-) and $[Fe^I(C_5H_5)(C_5H_5CO_2^-)]$ (FCA), respectively, whose interactions with β-CD in basic aqueous solution were studied by Evans et al. in 1985 [105]. A 1:1 β-CD·FCA^- host–guest complex characterized by a complexation constant $K = 2.2 \times 10^3\ M^{-1}$ at 293.2 K forms, but β-CD·FCA has a much lower $K \leq 20\ M^{-1}$. Thus, the oxidation state of iron determines the relative stabilities of β-CD·FCA^- and β-CD·FCA. Conjointly, these complexes may potentially be used as an electrochemical switch in a supramolecular system.

In 2006, Harada et al. realized this potential in a redox-responsive hydrogel system constructed from β-CD, PAAddn and FCA^- (Figure 20) [106]. The hydrophobic association between the *n*-dodecyl substituents, n-$C_{12}H_{25}$, produces cross-links between PAAddn chains and the formation of a PAAddn hydrogel. Addition of β-CD results in a strong complexation of the dodecyl substituents and a free flowing solution. Subsequent addition of FCA^- (Fe(0)) results in preferential complexation between β-CD and FCA^- such that the PAAddn hydrogel reforms. This situation is reversed upon oxidation of FCA^- with sodium hypochlorite to FCA (Fe(I)) which is complexed much less strongly by β-CD than are the dodecyl substituents of PAAddn.

An interesting variation on the redox chemistry of ferrocene in polymer systems was presented by Zhu et al. who attached ferrocene, FC, as a substituent to branched poly(ethylene imine), BPEI, through reaction with ferrocenecarboxaldehyde to give the ferrocene substituted polymer, BPEI-FC [107].

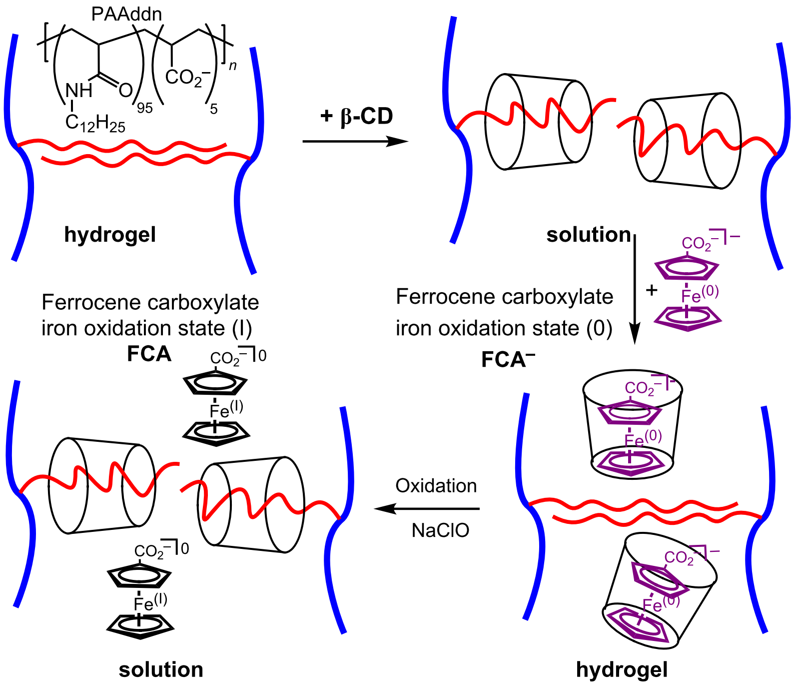

Figure 20: Solution to hydrogel transitions for two segments of PAAddn in the presence of β-CD and change in the ferrocenecarboxylate oxidation state in basic aqueous solution [106].

Aqueous solutions of this polymer are about ten times more viscous than the precursor BPEI polymer as a consequence of the enhancement of polymer chain association because of the hydrophobicity of the ferrocene substituents of BPEI-FC. However, this viscosity is greatly deceased upon the addition of β-CD because host–guest complexation of ferrocene masks its hydrophobicity and the hydrophilic exterior of the complexing β-CD much decreases association between the polymer chains. The same effect occurs when hydrogen peroxide is added to aqueous BPEI-FC and the ferrocene iron(0) is oxidized to ferrocene iron(I). With iron in oxidation state I, the ferrocene substituents assume uni-positive charges and consequently aggregate weakly with a corresponding decrease in solution viscosity.

5.5 Self-healing systems

Because of their ability to form host–guest complexes in water, cyclodextrins have attracted attention as components of self-healing materials. Thus, Harada et al. constructed self-healing supramolecular hydrogels from poly(acrylamide) substituted with both cyclodextrins and aliphatic substituents. This is exemplified by one such system in which the radical copolymerization of aqueous acrylamide, acrylamide substituted β-CD and *N*-adamantyl-acrylamide gives a β-CD- and adamantyl-substituted poly(acrylamide) which forms a hydrogel as shown in Figure 21 [108]. When a portion of the hydrogel is cut in two and both halves are brought back into close contact, the cut rapidly self-heals as β-CD/adamantyl host–guest complexation re-establishes inter-polymer chain links between the two halves. A similar situation occurs with the analogous polymer in which β-CD and the adamantyl substituents in Figure 21 are replaced by α-CD and *n*-butyl substituents, respectively.

Subsequently, Tian et al. reported the formation of a self-healing polymeric hydrogel based on the host–guest interaction between the β-CD substituents of an acrylamide-based polymer, poly-β-CD, and the α-bromonaphthalene substituents of a second acrylamide-based polymer, poly-α-BrNp (Figure 22) [109]. A hydrogel forms rapidly when aqueous solutions of poly-β-CD and poly-α-BrNP are mixed. When a solid sample of this hydrogel is cut in two, it rapidly self-heals within a minute through reforming host–guest complexes between the β-CD and α-bromonaphthalene substituents of poly-β-CD and poly-α-BrNP. Another interesting aspect is that because the α-bromonaphthalene substituents occupy the hydrophobic β-CD annuli in the hydrogel, UV radiation induces room temperature phosphorescence which, in combination with the self-healing properties of the hydrogel, may lead to some interesting applications.

The change of oxidation state of polymer substituent ferrocene iron(0) to more hydrophilic ferrocenium iron(I) can also result in interesting self-healing characteristics as is the case for the hydrogel formed between randomly β-CD substituted

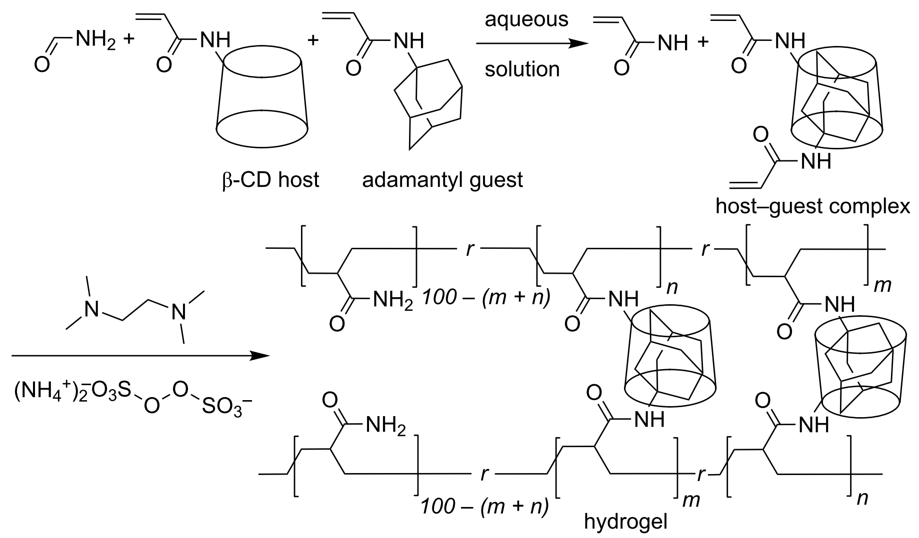

Figure 21: Preparation of a β-CD and adamantyl substituted acrylamide polymer hydrogel involving host–guest complexation between their β-CD and adamantyl substituents [108].

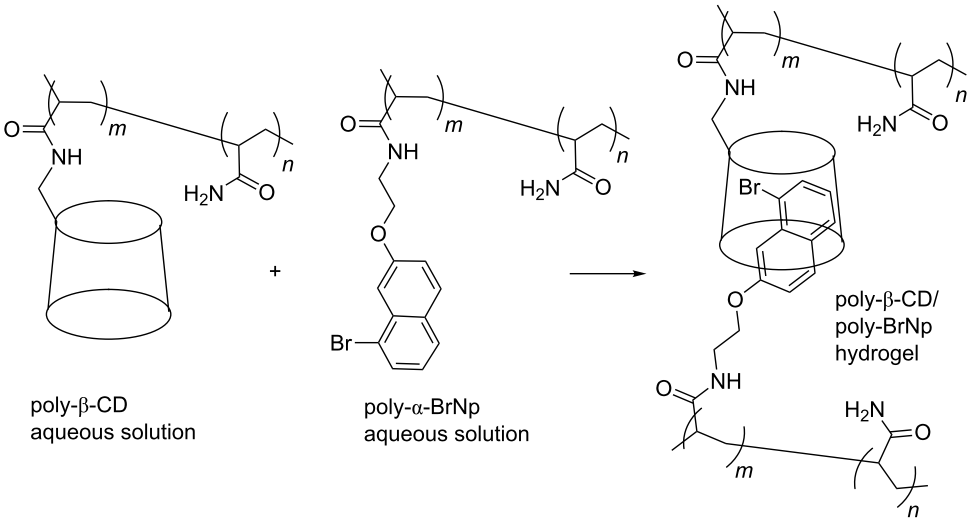

Figure 22: Aqueous solutions of the polymers poly-β-CD and poly-α-BrNP form the poly-β-CD/poly-α-BrNP hydrogel [109].

poly(acrylate), PAA-6β-CD and randomly ferrocenyl substituted poly(acrylate), PAA-Fc shown as (a) and (b), respectively in Figure 23 [110]. Thus, in aqueous solution the β-CD substituents of PAA-6β-CD complex the ferrocenyl substituents of PAA-Fc to form the hydrogel (c) which reverts to a solution of polymer chains when the hydrophobic ferrocenyl substituents of PAA-Fc are oxidized by sodium perchlorate to hydrophilic ferrocenium substituents. This oxidation may be reversed with glutathione to reform the hydrogel. At the macroscopic level a hydrogel cube may be cut in halves which when pressed together re-establish host–guest complexation of the ferrocenyl substituents by the β-CD substituents to self-heal. This self-healing may be controlled by addition of sodium perchlorate solution to the cut surface, whereby oxidation of the ferrocenyl substituent prevents self-healing. Subsequent addition of glutathione solution to the same surface reverses this situation and the self-healing properties are restored.

The simultaneous substitution of a host and two different guest substituents onto a single polymer presents opportunities for variations in self-healing properties to be incorporated as has been explored by Harada et al. with the β-CD, adamantyl and ferrocenyl substituted poly(acrylamide) (pAAm) and poly(*N*-isopropylacrylamide) (pNiPAAM) hydrogels shown in

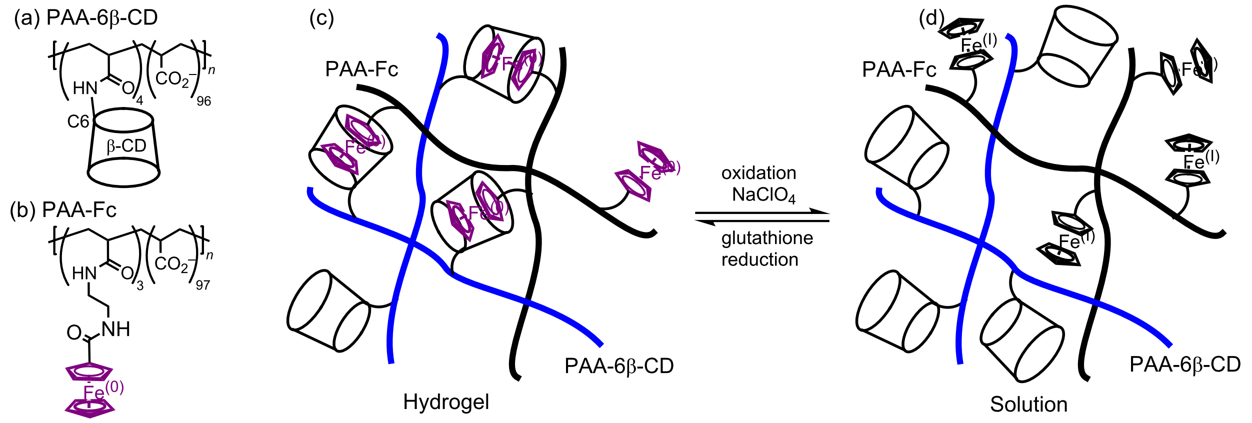

Figure 23: (a) Randomly β-CD substituted poly(acrylate), PAA-6β-CD. (b) Randomly ferrocenyl substituted poly(acrylate), PAA-Fc. (c) PAA-6β-CD/PAA-Fc hydrogel. (d) PAA-6β-CD/PAA-Fc solution after ferrocenyl iron(0) oxidation to ferrocenium iron(I) [110].

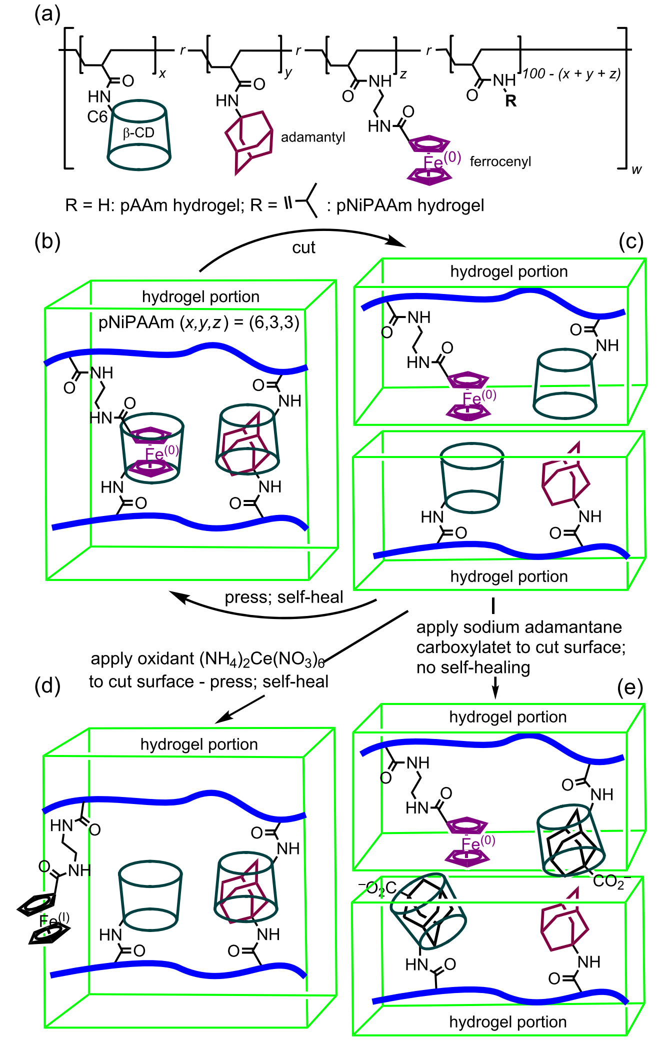

Figure 24: (a) The β-CD, adamantyl and ferrocenyl substituted pAAm and pNiPAAM polymers. (b) The β-CD, adamantyl and ferrocenyl substituted pNiPAAM hydrogel where the substituent mol % ratio *x*:*y*:*z* is 6:3:3. (c) Cutting of a hydrogel cube and self-healing of the two halves after pressing together. (d) Oxidation of the ferrocenyl (Fe(0)) substituent to positively charged ferrocenium (Fe(I)) through oxidation with $(NH_4)_2Ce(NO_3)_6$ on the surfaces of the halves followed by pressing and self-healing. (e) Addition of sodium adamantane carboxylate to the surfaces of the halves results in competitive host–guest complexation and an absence of self-healing [111].

Figure 24 [111]. Thus, a cube of (pNiPAAM) where the mol % ratio of β-CD to adamantyl to ferrocenyl substituents is 6:3:3 may be cut into halves and upon pressing the halves together self-healing occurs through host–guest complexation ((b) and (c)). However, if one of the cut surfaces is treated with $(NH_4)_2Ce(NO_3)_6$ oxidation of iron(0) in the ferrocenyl substituent to iron(I) renders the resulting ferrocenium substituent hydrophilic such that it does not complex in the β-CD substituent annulus ((c) and (d)). Nevertheless, upon pressing the two halves together self-healing still occurs through β-CD substituent/adamantyl substituent complexation. Finally, if adamantane carboxylate is applied to one of the cut surfaces in sufficient quantity and the two halves are pressed together, competitive β-CD substituent/adamantane carboxylate complexation prevents self-healing ((c) and (e)). The properties of this hydrogel can also be utilized in controlling expansion and contraction and shape memory. The practical applications which potentially flow at the macroscopic level from such host–guest chemistry are substantial [112-114].

Conclusion and Perspective

In this brief review it is shown that there is a plethora of routes to supramolecular polymer networks in aqueous solution based on cyclodextrin host–guest complexation. Through variations in this supramolecular chemistry at the molecular level macroscopic properties may be tailored to give smart-materials possessing stimuli responsive characteristics exemplified by photo-, pH-, thermo-, and redox-responsivity and self-healing. Inevitably, many more novel polymer network systems incorporating cyclodextrins will appear; some of which will find exciting applications.

Acknowledgements

This work was supported by the NSFC Grants 51403062, 51273063 and 20774030, the Fundamental Research Funds for the Central Universities, China Postdoctoral Science Foundation (2013M541485), 111 Project Grant (B08021) and the Australian Research Council Grant DP110103177.

References

1. Shih, W. M.; Quispe, J. D.; Joyce, G. F. *Nature* **2004,** *427,* 618–621. doi:10.1038/nature02307
2. O'Connell, M. R.; Oakes, B. L.; Sternberg, S. H.; East-Seletsky, A.; Kaplan, M.; Doudna, J. A. *Nature* **2014,** *516,* 263–266. doi:10.1038/nature13769
3. Greber, B. J.; Boehringer, D.; Leitner, A.; Bieri, P.; Voigts-Hoffmann, F.; Erzberger, J. P.; Leibundgut, M.; Aebersold, R.; Ban, N. *Nature* **2014,** *505,* 515–519. doi:10.1038/nature12890
4. Breedveld, V.; Nowak, A. P.; Sato, J.; Deming, T. J.; Pine, D. J. *Macromolecules* **2004,** *37,* 3943–3953. doi:10.1021/ma049885f
5. Villalonga, R.; Cao, R.; Fragoso, A. *Chem. Rev.* **2007,** *107,* 3088–3116. doi:10.1021/cr050253g
6. Ogoshi, T.; Harada, A. *Sensors* **2008,** *8,* 4961–4982. doi:10.3390/s8084961
7. Hirayama, F.; Uekama, K. *Adv. Drug Delivery Rev.* **1999,** *36,* 125–141. doi:10.1016/S0169-409X(98)00058-1
8. Li, J.; Loh, X. J. *Adv. Drug Delivery Rev.* **2008,** *60,* 1000–1017. doi:10.1016/j.addr.2008.02.011
9. Tiwari, G.; Tiwari, R.; Rai, A. K. *J. Pharm. BioAllied Sci.* **2010,** *2,* 72–79. doi:10.4103/0975-7406.67003
10. Wenz, G. *Angew. Chem., Int. Ed. Engl.* **1994,** *33,* 803–822. doi:10.1002/anie.199408031
11. Szejtli, J. *Chem. Rev.* **1998,** *98,* 1743–1754. doi:10.1021/cr970022c
12. Huang, L.; Tonelli, A. E. J. *J. Macromol. Sci., Polym. Rev.* **1998,** *38,* 781–837. doi:10.1080/15583729808546037
13. Harper, J. B.; Easton, C. J.; Lincoln, S. F. *Curr. Org. Chem.* **2000,** *4,* 429–454. doi:10.2174/1385272003376247
14. Mosinger, J.; Tománková, V.; Němcová, I.; Zýka, J. *Anal. Lett.* **2001,** *34,* 1979–2004. doi:10.1081/AL-100106834
15. Bender, M. L.; Komiyama, M. *Cyclodextrin Chemistry;* Springer-Verlag: Berlin, Germany, 1978.
16. Szejtli, J.; Osa, T., Eds. *Comprehensive Supramolecular Chemistry;* Pergamon: Oxford, 1996.
17. Easton, C. J.; Lincoln, S. F. *Modified Cyclodextrins: Scaffolds and Templates for Supramolecular Chemistry;* Imperial College Press: London, 1999.
18. Lincoln, S. F.; Pham, D.-T. Cyclodextrins: From Nature to Nanotechnology. In *Supramolecular Chemistry: From Molecules to Nanomaterials;* Gale, P. A.; Steed, J. W., Eds.; John Wiley & Sons Ltd.: Chichester, UK, 2012; pp 955–982.
19. Saenger, W.; Jacob, J.; Gessler, K.; Steiner, T.; Hoffmann, D.; Sanbe, H.; Koizumi, K.; Smith, S. M.; Takaha, T. *Chem. Rev.* **1998,** *98,* 1787–1802. doi:10.1021/cr9700181
20. Nepogodiev, S. A.; Stoddart, J. F. *Chem. Rev.* **1998,** *98,* 1959–1976. doi:10.1021/cr970049w
21. Harada, A. *Acc. Chem. Res.* **2001,** *34,* 456–464. doi:10.1021/ar000174l
22. Harada, A. *J. Polym. Sci., Part A: Polym. Chem.* **2006,** *44,* 5113–5119. doi:10.1002/pola.21618
23. Tian, H.; Wang, Q.-C. *Chem. Soc. Rev.* **2006,** *35,* 361–374. doi:10.1039/B512178G
24. Huang, F.; Gibson, H. W. *Prog. Polym. Sci.* **2005,** *30,* 982–1018. doi:10.1016/j.progpolymsci.2005.07.003
25. Qu, D.-H.; Wang, Q.-C.; Ma, X.; Tian, H. *Chem. – Eur. J.* **2005,** *11,* 5929–5937. doi:10.1002/chem.200401313
26. Harada, A.; Hashidzume, A.; Takashima, Y. *Adv. Polym. Sci.* **2006,** *201,* 1–43. doi:10.1007/12_056
27. Nelson, A.; Belitsky, J. M.; Vidal, S.; Joiner, C. S.; Baum, L. G.; Stoddart, J. F. *J. Am. Chem. Soc.* **2004,** *126,* 11914–11922. doi:10.1021/ja0491073
28. Loethen, S.; Kim, J.-M.; Thompson, D. H. *Polym. Rev.* **2007,** *47,* 383–418. doi:10.1080/15583720701455145
29. Araki, J.; Ito, K. *Soft Matter* **2007,** *3,* 1456–1473. doi:10.1039/B705688E
30. Yagai, S.; Kitamura, A. *Chem. Soc. Rev.* **2008,** *37,* 1520–1529. doi:10.1039/B703092B
31. Tonelli, A. E. *Polymer* **2008,** *49,* 1725–1736. doi:10.1016/j.polymer.2007.12.003
32. Takata, T. *Polym. J.* **2006,** *38,* 1–20. doi:10.1295/polymj.38.1
33. van de Manakker, F.; Vermonden, T.; van Nostrum, C. F.; Hennink, W. E. *Biomacromolecules* **2009,** *10,* 3157–3175. doi:10.1021/bm901065f

34. Jia, Y.-G.; Zhu, X. X. *Chem. Mater.* **2015,** *27,* 387–393. doi:10.1021/cm5041584
35. Tae, G.; Kornfield, J. A.; Hubbell, J. A.; Johannsmann, D.; Hogen-Esch, T. E. *Macromolecules* **2001,** *34,* 6409–6419. doi:10.1021/ma0107511
36. Tae, G.; Kornfield, J. A.; Hubbell, J. A.; Lal, J. *Macromolecules* **2002,** *35,* 4448–4457. doi:10.1021/ma011809e
37. McCormick, C. L.; Nonaka, T.; Johnson, C. B. *Polymer* **1988,** *29,* 731–739. doi:10.1016/0032-3861(88)90092-4
38. Xie, X.; Hogen-Esch, T. E. *Macromolecules* **1996,** *29,* 1734–1745. doi:10.1021/ma950687l
39. Huynh, C. T.; Nguyen, M. K.; Lee, D. S. *Macromolecules* **2011,** *44,* 6629–6636. doi:10.1021/ma201261m
40. Iliopoulos, I. *Curr. Opin. Colloid Interface Sci.* **1998,** *3,* 493–498. doi:10.1016/S1359-0294(98)80023-X
41. Abdala, A. A.; Tonelli, A. E.; Khan, S. A. *Macromolecules* **2003,** *36,* 7833–7841. doi:10.1021/ma034173v
42. Karlson, L.; Thuresson, K.; Lindman, B. *Langmuir* **2002,** *18,* 9028–9034. doi:10.1021/la026040t
43. Tsianou, M.; Alexandridis, P. *Langmuir* **1999,** *15,* 8105–8112. doi:10.1021/la990701d
44. Guo, X.; Abdala, A. A.; May, B. L.; Lincoln, S. F.; Khan, S. A.; Prud'homme, R. K. *Macromolecules* **2005,** *38,* 3037–3040. doi:10.1021/ma050071o
45. Guo, X.; Abdala, A. A.; May, B. L.; Lincoln, S. F.; Khan, S. A.; Prud'homme, R. K. *Polymer* **2006,** *47,* 2976–2983. doi:10.1016/j.polymer.2006.03.006
46. Li, L.; Guo, X.; Fu, L.; Prud'homme, R. K.; Lincoln, S. F. *Langmuir* **2008,** *24,* 8290–8296. doi:10.1021/la800859w
47. Zhang, H.; Hogen-Esch, T. E.; Boschet, F.; Margaillan, A. *Langmuir* **1998,** *14,* 4972–4977. doi:10.1021/la971030r
48. Islam, M. F.; Jenkins, R. D.; Bassett, D. R.; Lau, W.; Ou-Yang, H. D. *Macromolecules* **2000,** *33,* 2480–2485. doi:10.1021/ma9907845
49. Karlson, L.; Thuresson, K.; Lindman, B. *Carbohydr. Polym.* **2002,** *50,* 219–226. doi:10.1016/S0144-8617(02)00036-X
50. Talwar, S.; Harding, J.; Oleson, K. R.; Khan, S. A. *Langmuir* **2009,** *25,* 794–802. doi:10.1021/la803056e
51. Panmai, S.; Prud'homme, R. K.; Peiffer, D. G.; Jockusch, S.; Turro, N. J. *Langmuir* **2002,** *18,* 3860–3864. doi:10.1021/la020165g
52. Weickenmeier, M.; Wenz, G.; Huff, J. *Macromol. Rapid Commun.* **1997,** *18,* 1117–1123. doi:10.1002/marc.1997.030181216
53. Wenz, G.; Weickenmeier, M.; Huff, J. *ACS Symp. Ser.* **2000,** *765,* 271–283.
54. Gosselet, N. M.; Borie, C.; Amiel, C.; Sebille, B. *J. Dispersion Sci. Technol.* **1998,** *19,* 805–820. doi:10.1080/01932699808913216
55. Gosselet, N. M.; Beucler, F.; Renard, E.; Amiel, C.; Sebille, B. *Colloids Surf., A* **1999,** *155,* 177–188. doi:10.1016/S0927-7757(99)00026-6
56. Moine, L.; Cammas, S.; Amiel, C.; Renard, E.; Sébille, B.; Guérin, P. *Macromol. Symp.* **1998,** *130,* 45–52. doi:10.1002/masy.19981300105
57. Li, L.; Guo, X.; Wang, J.; Liu, P.; Prud'homme, R. K.; May, B. L.; Lincoln, S. F. *Macromolecules* **2008,** *41,* 8677–8681. doi:10.1021/ma8020147
58. Tanaka, F.; Edwards, S. F. *Macromolecules* **1992,** *25,* 1516–1523. doi:10.1021/ma00031a024
59. Rubinstein, M.; Semenov, A. N. *Macromolecules* **2001,** *34,* 1058–1068. doi:10.1021/ma0013049
60. Semenov, A. N.; Rubinstein, M. *Macromolecules* **1998,** *31,* 1373–1385. doi:10.1021/ma970616h
61. Rubinstein, M.; Semenov, A. N. *Macromolecules* **1998,** *31,* 1386–1397. doi:10.1021/ma970617+
62. Rubinstein, M.; Dobrynin, A. V. *Curr. Opin. Colloid Interface Sci.* **1999,** *4,* 83–87. doi:10.1016/S1359-0294(99)00013-8
63. Horiuchi, K.; Rharbi, Y.; Spiro, J. G.; Yekta, A.; Winnik, M. A.; Jenkins, R. D.; Bassett, D. R. *Langmuir* **1999,** *15,* 1644–1650. doi:10.1021/la9806653
64. Yekta, A.; Xu, B.; Duhamel, J.; Adiwidjaja, H.; Winnik, M. A. *Macromolecules* **1995,** *28,* 956–966. doi:10.1021/ma00108a025
65. Yekta, A.; Duhamel, J.; Brochard, P.; Adiwidjaja, H.; Winnik, M. A. *Macromolecules* **1993,** *26,* 1829–1836. doi:10.1021/ma00060a006
66. Rekharsky, M. V.; Inoue, Y. *Chem. Rev.* **1998,** *98,* 1875–1918. doi:10.1021/cr970015o
67. Tomatsu, I.; Hashidzume, A.; Harada, A. *J. Am. Chem. Soc.* **2006,** *128,* 2226–2227. doi:10.1021/ja058345a
68. Hashidzume, A.; Ito, F.; Tomatsu, I.; Harada, A. *Macromol. Rapid Commun.* **2005,** *26,* 1151–1154. doi:10.1002/marc.200500253
69. Hashidzume, A.; Harada, A. *Polymer* **2006,** *47,* 3448–3454. doi:10.1016/j.polymer.2006.03.040
70. Wang, J.; Pham, D.-T.; Guo, X.; Li, L.; Lincoln, S. F.; Luo, Z.; Ke, H.; Zheng, L.; Prud'homme, R. K. *Ind. Eng. Chem. Res.* **2010,** *49,* 609–612. doi:10.1021/ie901178q
71. Mahammad, S.; Roberts, G. W.; Khan, S. A. *Soft Matter* **2007,** *3,* 1185–1193. doi:10.1039/B700167C
72. Guo, X.; Wang, J.; Li, L.; Pham, D.-T.; Clements, P.; Lincoln, S. F.; May, B. L.; Chen, Q.; Zheng, L.; Prud'homme, R. K. *Macromol. Rapid Commun.* **2010,** *31,* 300–304. doi:10.1002/marc.200900560
73. Guo, X.; Wang, J.; Li, L.; Pham, D.-T.; Clements, P.; Lincoln, S. F.; May, B. L.; Chen, Q.; Zheng, L.; Prud'homme, R. K. *J. Polym. Sci., Part B: Polym. Phys.* **2010,** *48,* 1818–1825. doi:10.1002/polb.22052
74. Wang, J.; Xu, Y.; Wang, Y.; Liu, J.; Xu, J.; Li, L.; Nguyen, H.-T.; Pham, D.-T.; Lincoln, S. F.; Guo, X. *RSC Adv.* **2015,** *5,* 46067–46073. doi:10.1039/C5RA06163F
75. Pham, D.-T.; Nguyen, H.-T.; Lincoln, S. F.; Wang, J.; Guo, X.; Easton, C. J.; Prud'homme, R. K. *J. Polym. Sci., Part A: Polym. Chem.* **2015,** *53,* 1278–1286. doi:10.1002/pola.27563
76. Guo, X.; Wang, J.; Li, L.; Chen, Q.; Zheng, L.; Pham, D.-T.; Lincoln, S. F.; May, B. L.; Prud'homme, R. K.; Easton, C. J. *AIChE J.* **2010,** *56,* 3021–3024. doi:10.1002/aic.12206
    In this reference the positions of Schemes 1 and 2 are interchanged, and the captions to Figures 1, 2 and 3 are interchanged with those of Figures 3, 1 and 2, respectively.
77. Nguyen, H.-T.; Pham, D.-T.; Lincoln, S. F.; Wang, J.; Guo, X.; Easton, C. J.; Prud'homme, R. K. *Polym. Chem.* **2013,** *4,* 820–829. doi:10.1039/C2PY20746J
78. Lecourt, T.; Sinay, P.; Chassenieux, C.; Rinaudo, M.; Auzély-Vetly, R. *Macromolecules* **2004,** *37,* 4635–4642. doi:10.1021/ma049822x
79. Bistri-Aslanoff, O.; Blériot, Y.; Auzely-Velty, R.; Sollogoub, M. *Org. Biomol. Chem.* **2010,** *8,* 3437–3443. doi:10.1039/c001531h
80. Bistri, O.; Mazeau, K.; Auzély-Velty, R.; Sollogoub, M. *Chem. – Eur. J.* **2007,** *13,* 8847–8857. doi:10.1002/chem.200700800
81. Auzély-Vetly, R.; Rinaudo, M. *Macromolecules* **2002,** *35,* 7955–7962. doi:10.1021/ma020664o
82. Harada, A.; Kamachi, M. *Macromolecules* **1990,** *23,* 2821–2823. doi:10.1021/ma00212a039

83. Fujita, H.; Ooya, T.; Yui, N. *Macromolecules* **1999,** *32,* 2534–2541. doi:10.1021/ma9814550
84. Okumura, Y.; Ito, K. *Adv. Mater.* **2001,** *13,* 485–487. doi:10.1002/1521-4095(200104)13:7<485::AID-ADMA485>3.0.CO;2-T
85. Karino, T.; Okumura, Y.; Ito, K.; Shibayama, M. *Macromolecules* **2004,** *37,* 6177–6182. doi:10.1021/ma049598b
86. Harada, A.; Li, J.; Kamachi, M. *Nature* **1992,** *356,* 325–327. doi:10.1038/356325a0
87. Li, J.; Harada, A.; Kamachi, M. *Polym. J.* **1994,** *26,* 1019–1026. doi:10.1295/polymj.26.1019
88. Guo, M.; Jiang, M.; Pispas, S.; Yu, W.; Zhou, C. *Macromolecules* **2008,** *41,* 9744–9749. doi:10.1021/ma801975s
89. Jeong, B.; Bae, Y. H.; Lee, D. S.; Kim, S. W. *Nature* **1997,** *388,* 860–862. doi:10.1038/42218
90. Li, J.; Li, X.; Ni, X.; Wang, X.; Li, H.; Leong, K. W. *Biomaterials* **2006,** *27,* 4132–4140. doi:10.1016/j.biomaterials.2006.03.025
91. Siddik, Z. H. *Oncogene* **2003,** *22,* 7265–7279. doi:10.1038/sj.onc.1206933
92. Zhu, W.; Li, Y.; Liu, L.; Chen, Y.; Wang, C.; Xi, F. *Biomacromolecules* **2010,** *11,* 3086–3092. doi:10.1021/bm100889j
93. Tomatsu, I.; Hashidzume, A.; Harada, A. *Macromolecules* **2005,** *38,* 5223–5227. doi:10.1021/ma050670v
94. Zheng, P.; Hu, X.; Zhao, X.; Li, L.; Tam, K. C.; Gan, L. H. *Macromol. Rapid Commun.* **2004,** *25,* 678–682. doi:10.1002/marc.200300123
95. Zhao, Y.-L.; Stoddart, J. F. *Langmuir* **2009,** *25,* 8442–8446. doi:10.1021/la804316u
96. Joung, Y.-K.; Ooya, T.; Yamaguchi, M.; Yui, N. *Adv. Mater.* **2007,** *19,* 396–400. doi:10.1002/adma.200600604
97. Huh, K. M.; Ooya, T.; Lee, W. K.; Sasaki, S.; Kwon, I. C.; Jeong, S. Y.; Yui, N. *Macromolecules* **2001,** *34,* 8657–8662. doi:10.1021/ma0106649
98. Choi, H. S.; Kontani, K.; Huh, K. M.; Sasaki, S.; Ooya, T.; Lee, W. K.; Yui, N. *Macromol. Biosci.* **2002,** *2,* 298–303. doi:10.1002/1616-5195(200208)2:6<298::AID-MABI298>3.0.CO;2-#
99. Choi, H. S.; Yamamoto, K.; Ooya, T.; Yui, N. *ChemPhysChem* **2005,** *6,* 1081–1086. doi:10.1002/cphc.200400598
100. Koopmans, C.; Ritter, H. *Macromolecules* **2008,** *41,* 7418–7422. doi:10.1021/ma801202f
101. Kataoka, T.; Kidowaki, M.; Zhao, C.; Minamikawa, H.; Shimizu, T.; Ito, K. *J. Phys. Chem. B* **2006,** *110,* 24377–24383. doi:10.1021/jp0649246
102. Kretschmann, O.; Choi, S. W.; Miyauchi, M.; Tomatsu, I.; Harada, A.; Ritter, H. *Angew. Chem., Int. Ed.* **2006,** *45,* 4361–4365. doi:10.1002/anie.200504539
103. Amajjahe, S.; Choi, S.; Munteanu, M.; Ritter, H. *Angew. Chem., Int. Ed.* **2008,** *47,* 3435–3437. doi:10.1002/anie.200704995
104. Amajjahe, S.; Ritter, H. *Macromolecules* **2008,** *41,* 716–718. doi:10.1021/ma702271p
105. Matsue, T.; Evans, D. H.; Osa, T.; Kobayashi, N. *J. Am. Chem. Soc.* **1985,** *107,* 3411–3417. doi:10.1021/ja00298a003
106. Tomatsu, I.; Hashidzume, A.; Harada, A. *Macromol. Rapid Commun.* **2006,** *27,* 238–241. doi:10.1002/marc.200500793
107. Zhu, L.; Shangguan, Y.; Sun, Y.; Ji, J.; Zheng, Q. *Soft Matter* **2010,** *6,* 5541–5546. doi:10.1039/c0sm00246a
108. Kakuta, T.; Takashima, Y.; Nakahata, M.; Otsubo, M.; Yamaguchi, H.; Harada, A. *Adv. Mater.* **2013,** *25,* 2849–2853. doi:10.1002/adma.201205321
109. Chen, H.; Ma, X.; Wu, S.; Tian, H. *Angew. Chem., Int. Ed.* **2014,** *53,* 14149–14152. doi:10.1002/anie.201407402
110. Nakahata, M.; Takashima, Y.; Yamaguchi, H.; Harada, A. *Nat. Commun.* **2011,** *2,* No. 511. doi:10.1038/ncomms1521
111. Miyamae, K.; Nakahata, M.; Takashima, Y.; Harada, A. *Angew. Chem., Int. Ed.* **2015,** *54,* 8984–8987. doi:10.1002/anie.201502957
112. Harada, A.; Takashima, Y.; Nakahata, M. *Acc. Chem. Res.* **2014,** *47,* 2128–2140. doi:10.1021/ar500109h
113. Kakuta, T.; Takashima, Y.; Sano, T.; Nakamura, T.; Kobayashi, Y.; Yamaguchi, H.; Harada, A. *Macromolecules* **2015,** *48,* 732–738. doi:10.1021/ma502316d
114. Nakahata, M.; Takashima, Y.; Harada, A. *Macromol. Rapid Commun.* **2015**. doi:10.1002/marc.201500473

License and Terms

The definitive version of this article is the electronic one which can be found at:
doi:10.3762/bjoc.12.7

BEILSTEIN JOURNAL OF ORGANIC CHEMISTRY

Aggregation behavior of amphiphilic cyclodextrins in a nonpolar solvent: evidence of large-scale structures by atomistic molecular dynamics simulations and solution studies

Giuseppina Raffaini*[1,§], Fabio Ganazzoli[1] and Antonino Mazzaglia[2]

Full Research Paper

Open Access

Address:
[1]Dipartimento di Chimica, Materiali e Ingegneria Chimica ‘G. Natta’, Politecnico di Milano, via Mancinelli 7, 20131 Milano, Italy, and [2]CNR-ISMN Istituto per lo Studio dei Materiali Nanostrutturati, c/o Dipartimento di Scienze Chimiche, Biologiche, Farmaceutiche ed Ambientali dell’Università di Messina, V. le F. Stagno d'Alcontres 31, 98166 Messina, Italy

Email:
Giuseppina Raffaini* - giuseppina.raffaini@polimi.it

* Corresponding author
§ Tel. +39-0223993068; Fax +39-0223993081

Keywords:
aggregation; amphiphilic cyclodextrins; molecular dynamics; nanoparticles; self-assembly; simulations

Beilstein J. Org. Chem. **2016,** *12,* 73–80.
doi:10.3762/bjoc.12.8

Received: 30 October 2015
Accepted: 28 December 2015
Published: 14 January 2016

This article is part of the Thematic Series "Superstructures with cyclodextrins: Chemistry and applications III".

Guest Editor: E. Monflier

Abstract

Chemically modified cyclodextrins carrying both hydrophobic and hydrophilic substituents may form supramolecular aggregates or nanostructures of great interest. These systems have been usually investigated and characterized in water for their potential use as nanocarriers for drug delivery, but they can also aggregate in apolar solvents, as shown in the present paper through atomistic molecular dynamics simulations and dynamic light scattering measurements. The simulations, carried out with a large number of molecules in vacuo adopting an unbiased bottom-up approach, suggest the formation of bidimensional structures with characteristic length scales of the order of 10 nm, although some of these sizes are possibly affected by the assumed periodicity of the simulation cell, in particular at longer lengths. In any case, these nanostructures are stable at least from the kinetic viewpoint for relatively long times thanks to the large number of intermolecular interactions of dipolar and dispersive nature. The dynamic light scattering experiments indicate the presence of aggregates with a hydrodynamic radius of the order of 80 nm and a relatively modest polydispersity, even though smaller nanometer-sized aggregates cannot be fully ruled out. Taken together, these simulation and experimental results indicate that amphiphilically modified cyclodextrins do also form large-scale nanoaggregates even in apolar solvents.

Introduction

Amphiphilic cyclodextrins (aCD) are a class of molecules highly investigated for their self-assembly properties and inherent potential applications [1,2]. In particular, the modification with thioalkyl chains in the primary rim and oligoethylene glycol chains in the secondary rim and, consequently, their hydrophobic–hydrophilic balance (Scheme 1) modulates the formation of differently sized and shaped nanoconstructs as membrane models for molecular recognition [3] or nanocarriers for drug delivery [4]. In the recent past, the aggregation behavior of aCD was investigated in water, getting insights on the structures of free nanoassemblies [5,6] or in combination with therapeutic agents [7]. However, in some stages of preparation and investigation of nanoconstructs based on aCD, the dissolution in organic nonpolar solvent is mandatory to prepare stable nanoemulsions [4,8], thin films [9] or organic dispersions for spectroscopic characterization of aCD unimers [10].

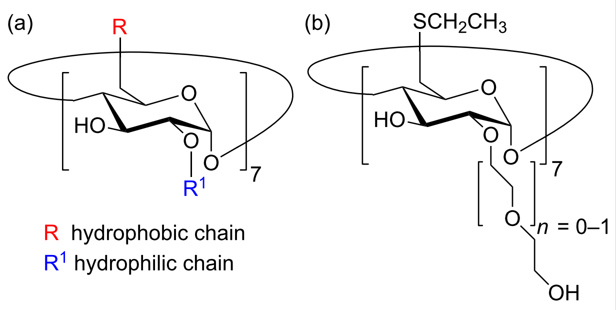

Scheme 1: (a) Typical structure of aCD bearing hydrophobic chains (R) at the primary side and hydrophilic chain (R^1) at secondary side; (b) peculiar structures of aCD (SC2OH) utilized in this study (n = 0, atomistic investigation; n = 1, solution studies).

In a previous paper ([11], henceforth referred to as paper I) we investigated the interaction pattern of these aCD both in vacuo and in explicit water considering at first the isolated molecule, and then the interaction among two or four molecules (and some preliminary results with eight molecules) in different starting arrangement to understand the possible interaction geometries and their relative stability. In this way, we could propose various robust arrangements that could be fully stable within the simulation time at room temperature, suggesting that different metastable states could coexist together with the thermodynamically most stable ones and that kinetic control of the initial aggregation stage could easily take place. In particular, these simulations carried out with relatively small systems comprising a few molecules allowed us to assess that the driving force for aggregation was due to a synergy of different contributions. In particular, we found that the R^1 chains (see Scheme 1: these chains were denoted as polar, or P, chains in paper I [11]) could show inclusion within the cavity of the molecule they belong to or of a neighboring molecule thanks to both dispersive and dipolar interactions and possibly with a few hydrogen bonds that may involve the glycosidic oxygen atoms. Moreover, one or two R chains (see again Scheme 1: these chains were indicated as hydrophobic, or H, chains in paper I [11]) could also show both self-inclusion and mutual inclusion within the hydrophobic cavity of their own molecule or of an adjacent one thanks to favorable dispersive interactions. We also found many cases of interactions among parts of the lateral surfaces of two or more molecules that may help forming extended structures possibly involving many more molecules than considered in paper I [11] largely due again to dispersive interactions but also to some dipolar interaction close to the secondary rim. Note that the latter interaction strength is somewhat weaker than that due to self- or mutual inclusion of a side chain in an aCD cavity, but still we found that it is strong enough to hold together a molecule to a cluster of other two or three, and that these interactions at the lateral surface could be enhanced in larger systems if the aCD is fully surrounded by other molecules. As a conclusion of this paragraph, it should also be noted however that overall we found relatively few hydrogen bonds stabilizing the aggregates of few molecules even in the simulations carried out in vacuo.

In the present paper we report full results about systems comprising eight molecules of the same aCD modelled in paper I [11] with n = 0 for computational simplicity, and new results about much larger systems (namely with sixty-four aCD molecules) modelled in vacuo, which can be taken as an approximation of a nonpolar and weakly interacting solvent, together with some experimental results obtained from a dichloromethane solution of SC2OH with n = 1 (see Scheme 1B). The pioneering knowledge acquired at this stage about the simulated aggregation of the simplest SC2OH (n = 0), could be utilized in perspective in a future investigation on similar aCD with $n > 0$.

In the following, we discuss our simulation and experimental results in the order, and then the simulation methodology and the dynamic light scattering procedure in the Experimental section.

Results and Discussion

Atomistic simulations of the formation of large aggregates

As summarized in the Introduction, in paper I [11] we investigated somewhat in detail the interaction pattern among two or four aCD, and mentioned some preliminary results obtained with eight molecules. Let us know describe more in detail the formation of larger aggregates that may correspond to the systems present in a nonpolar solvent, beginning with the aggregates obtained in the two independent simulations carried out with eight molecules randomly placed in vacuo in a periodic simulation cell. In either case, after the initial minimizations the eight molecules clustered in a single but still relatively loose aggregate. In the subsequent long MD run that was eventually carried out for a total of 100 ns, the two aggregates obtained by these preliminary energy minimizations turned out to be quite stable, enhancing the intermolecular interactions by relatively small local displacements, producing tighter clusters with an intermolecular interaction pattern essentially reproducing on a larger scale the pattern described in paper I [11] for two and four aCD and summarized in the Introduction. Such results were obtained for both replicas of eight molecules randomly placed in the periodic simulation cell, but the aggregate geometries turned out to be somewhat different. In fact, in one case we obtained a cluster with an elongated shape, fully isolated from its periodic images in the neighboring cells, as shown in Figure 1. In this case, the aggregate could be described as forming a prolate ellipsoid with a semi-major axis having a length of about 21.0 Å, and a semi-minor axis of about 14.5 Å. Another feature that can be noticed in Figure 1 is that the exposed hydroxy groups tend to cluster together more than the hydrophobic alkyl groups bound to the sulfur atoms (shown in yellow) because of the hydrogen bonds they form.

On the other hand, in the other case we obtained a more elongated cluster spanning the whole cell length, thus forming a continuous array along the *z* direction in the projections shown in Figure 2 if we consider its periodic images. In this case, the lateral size of the aggregate is somewhat poorly defined due to the presence of surface grooves of different size, but a good estimate of the radius of the array (if the latter is roughly viewed as a cylinder) amounts to about 14 Å. The potential energy averaged in the last part of the MD run when no change was detected in the energy components (i.e., the intramolecular terms, the van der Waals component and the electrostatic one due to the dipolar interactions) showed that the first aggregate is more stable than the other one by about 1.32 ± 0.19 MJ, where the ± sign refers to the value calculated from the standard deviations of the average potential energy values due to the thermal fluctuations. However, the very large stability of each aggregate within the MD run indicates that both are very robust conformations that may form at least for kinetic reasons and persist for a long time.

From the conformational viewpoint, it is also interesting to notice that the thioethyl chains, linked to the primary rim of the macrocycle at the C6 carbon through the sulfur atoms shown in yellow in Figure 1 and Figure 2, tend to stay at the aggregate envelope, thus allowing the hydrophilic chains to better interact among themselves through dipolar interactions and hydrogen bonds. Figure 1 and Figure 2 still show that many oxygen atoms of the polar groups, shown in red, are exposed to vacuum (or a nonpolar solvent, in practice) and thus their interactions are not completely optimized, even though the hydroxy groups comprising them may form many hydrogen bonds among themselves. On the other hand, the polar chains and the molecular

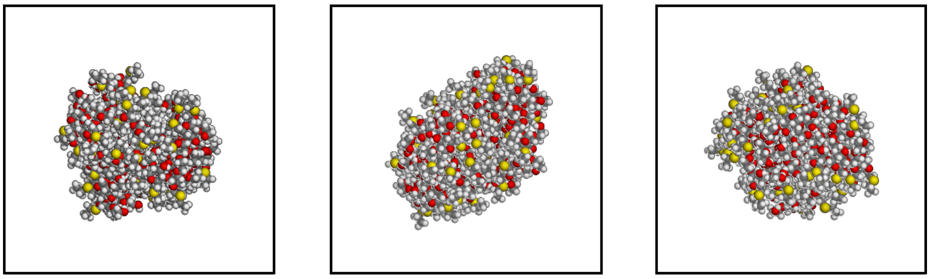

Figure 1: The aggregate of eight molecules of the aCD of Scheme 1 with *n* = 0, obtained from the first trial random arrangement of eight molecules in a periodic cell after the MD run of 100 ns. The three projections are taken along the cell *x*-axis, the *y*-axis, and the *z*-axis from left to right.

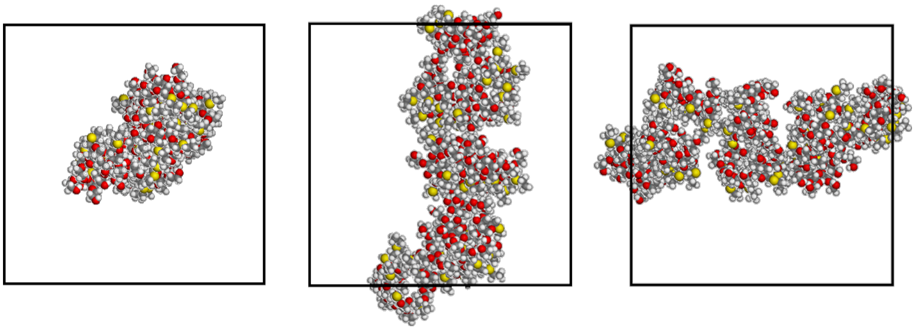

Figure 2: The aggregate of eight molecules of the aCD of Scheme 1 with *n* = 0, obtained from the second trial random arrangement of eight molecules in a periodic cell after the MD run of 100 ns. The three projections are taken along the cell *z*-axis, the *y*-axis, and the *x*-axis from left to right.

hydroxy groups may become trapped at the aggregate envelope for kinetic reasons, while any large-scale rearrangement might become increasingly difficult with an increasing aggregate size.

In order to model larger systems, thus containing more molecules while keeping their concentration constant, we then constructed a supercell by duplicating the *x*-, *y*- and *z*-axes of the final optimized cell with eight molecules for both replicas. In this way, we obtained another cubic cell having edges of 123.0 Å and a volume equal to eight times the original one, while the total number of molecules is sixty-four, i.e., eight times their original value. These sixty-four molecules were initially related to the previous eight ones by translational symmetry, as it can be seen in the starting arrangements displayed in Figure 3 and Figure 4, but afterward they were treated as fully independent molecules.

Note that in the larger cell in one case the cluster of eight molecules is simply periodically repeated eight times, while in the other one the elongated structure initially present (see Figure 2) give rise to four parallel arrays, again repeated periodically. The preliminary energy minimization of these two systems led to only minor changes, so that the periodic repetition within the larger cell is largely preserved. Long MD simulations (50 ns) of these two systems with a total of sixty-four molecules produced significant rearrangements with the formation of extended structures with a long-range connectivity due to intermolecular non-bonded interactions again reproducing those previously mentioned.

The first of these extended structures is shown in Figure 5 along the three orthogonal *x*-, *y*-, *z*-directions, and considering the cell periodicity it consists of a bicontinuous structure in two dimensions with pores of different sizes that may be denoted as nanopores and mesopores. The size and possibly even the presence of these pores may be however affected by the cell periodicity, just as the ordering in arrays suggested in one case (Figure 2) for eight aCD molecules (see also Figure 4 for the starting arrangement of the sixty-four molecules that still display the previously assumed three-dimensional periodicity) yielded a more complicated bidimensional structure after the MD runs.

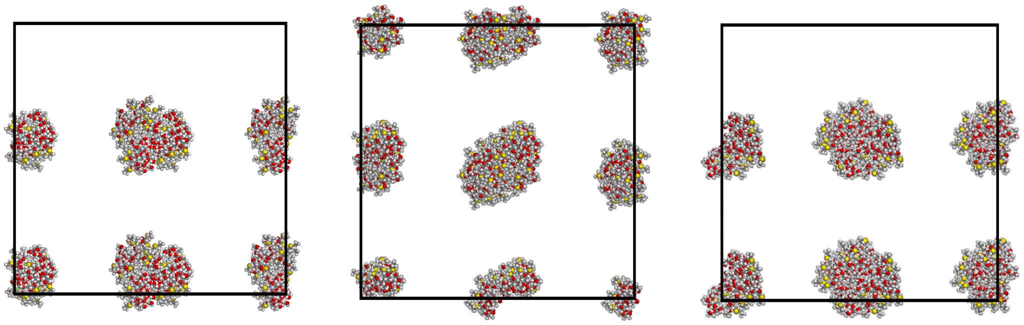

Figure 3: The first trial starting arrangement of sixty-four molecules within the large cell of 123.0 Å, symmetrically arranged in eight clusters each comprising eight molecules as obtained in the previous run with the smaller cell of 61.5 Å. The three projections are taken along the cell *x*-axis, the *y*-axis, and the *z*-axis from left to right. Due to the assumed cell periodicity, some clusters at the cell edges are apparently split in two smaller clusters, but they actually form eight clusters when the larger cell periodicity is taken into account.

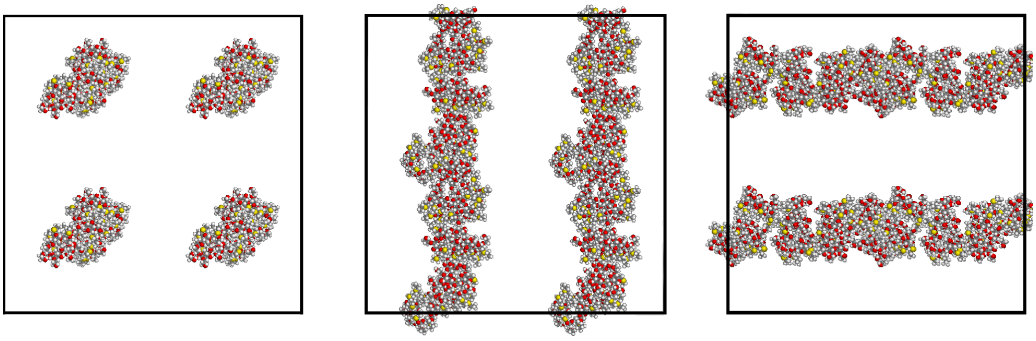

Figure 4: The second trial starting arrangement of sixty-four molecules within the large cell of 123.0 Å, symmetrically arranged in four parallel arrays along the *z*-axis of the projections, and each comprising twice the eight molecules of Figure 2 as obtained in the previous run with the smaller cell of 61.5 Å. The three projections are taken along the cell *z*-axis, the *y*-axis, and the *x*-axis from left to right.

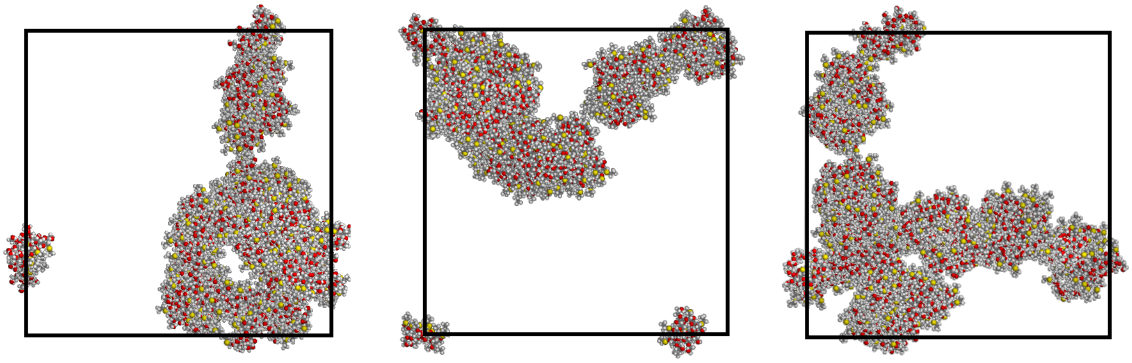

Figure 5: The first final arrangement of sixty-four molecules within the large periodic cell of 123.0 Å after an MD run of 50 ns viewed along the *z*-, *y*-, *x*-directions (from left to right). Due to the cell periodicity, some molecules at the cell edges are apparently separated from the whole clusters to which they belong.

In this arrangement, the aggregate could be described as formed by a solid torus producing the nanopore (Figure 5 at left) and by two elongated arrays defining the mesopores, taking into account the cell periodicity. The size of this aggregate is given by the outer diameter of the solid torus of about 76 Å, and by the nanopore diameter it defines of 14 Å, whereas the apparent size of the mesopores amount to about 90 Å.

While the suggested existence of extended two-dimensional structures is supported by the simulations of the second case discussed in the next paragraph, an even larger number of independent molecules of the order of some hundreds could better clarify the issue of possible artefacts in the structural details due to the assumed periodicity. Such huge simulations are however very demanding both in terms of the number of atoms and in terms of the simulation times that would be required to let the system relax to the (pseudo) equilibrium state, so that they are in practice outside our current possibilities.

The second case mentioned before of sixty-four aCD molecules in the larger periodic cell produced at the end of the MD run the extended bidimensional structure shown in Figure 6, also in this case viewed along the three orthogonal *x*-, *y*-, *z*-directions. It is evident that in this case the initial four arrays of molecules (see Figure 4) have coalesced in two very close arrays (see the central panel of Figure 6) that may also be described as a continuous sheet in two dimensions with a minor central gap having a width of almost 10 Å, or a veritable membrane roughly parallel to one face of the periodic simulation box. The sheet thickness amounts to about 24 Å, on the average, as seen in the *x*-, *y*-projection of Figure 6 (left panel), and shows a sort of sinusoidal, or undulating profile, so that the apparent thickness appears to be larger than 34 Å in the rotated view along the *x*-axis. It should be noted that Figure 6 suggests the presence of a weakly undulating, infinite membrane. However, this pattern could also be somehow affected by the cell periodicity, and we cannot rule out the possibility that the arrangement shown in Figure 6 is but a portion of the surface of a much larger vesicle having a diameter of several tens of nanometres.

Let us finally point out that both arrangements are quite robust, in that they persist for a large part of the 50 ns MD run. On the other hand, from the thermodynamic viewpoint the calculated stability of the two arrangements of sixty-four molecules is

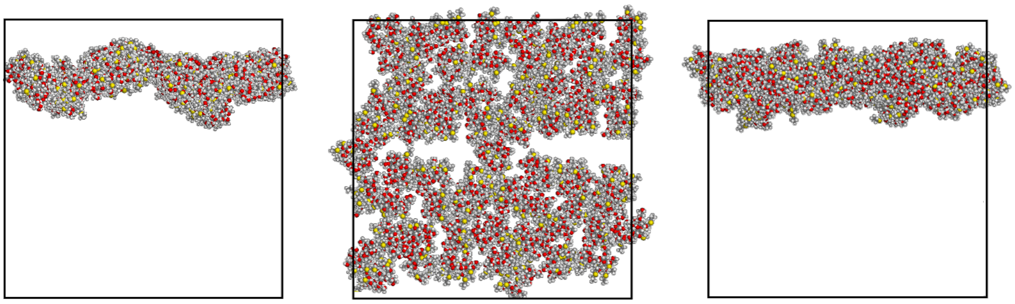

Figure 6: The second final arrangement of sixty-four molecules within the large periodic cell of 123.0 Å after an MD run of 50 ns viewed along the *z*-, *y*-, *x*-directions (from left to right). The flat membrane with a minor central gap is clearly seen in the central panel.

quite different, as it can be seen for instance through the potential energy of the aggregates. Also in this case, the first aggregate shown in Figure 5 has a lower potential energy, as obtained by the values average over the last part of the MD run. The amount of overall stabilization account for 9.37 ± 0.53 MJ, where the ± sign has the same meaning as before. It is also of interest to note that the larger number of molecules induces anyway an additional stabilization due to the number of pairwise interactions that increase their number and importance more than simply proportionally to the number of molecules.

Dynamic light scattering

Dynamic light scattering (DLS) measurements were carried out on SC2OH (Scheme 1B, $n = 1$) dispersion in nonpolar solvent (CH_2Cl_2). Figure 7 shows the monomodal hydrodynamic radii distribution obtained by using CONTIN inversion algorithm and Mie scattering normalization. As a result of the cumulant analysis [12], DLS evidences the presence of aggregates with ≈80 nm hydrodynamic radius (R_H) and a polydispersity index of 0.2. Furthermore, as the technique is highly sensitive to the aggregates presence, it was not possible to exclude the presence of even nanometric-sized clusters apart from the bigger aggregates [13].

Conclusion

Amphiphilic cyclodextrins (aCD) are almost invariably investigated in a water environment for their potential use in nanomedicine, as pointed out in the Introduction, even though the use of nonpolar solvents could also be relevant for preparative or characterization purposes. In the present work, we report an investigation by means of dynamic light scattering on the aggregation properties of the compound shown in Scheme 1b ($n = 1$), dissolved in an apolar solvent and an atomistic Molecular Dynamics study of a model compound ($n = 0$ in Scheme 1) carried out in vacuo. In particular, the latter approach aims to model the bottom-up aggregation of the model aCD molecules, an approach that was started in [11], where the local details of the interaction among a few molecules were investigated. Here the atomistic modelling study takes in account an increasingly large number of molecules in vacuo, taken as an approximation of a nonpolar and weakly interacting solvent, modelled in a cell with periodic boundary conditions. Two fully independent long MD runs of increasingly large systems comprising up to sixty-four molecules suggest the presence of large-scale two-dimensional structures at length scales of more than 10 nm, comprising either relatively uniform membranes or a nano- and mesoporous mesh.

Dynamic light scattering investigations show that, indeed also in a nonpolar solvent such as dichloromethane, these amphiphilic cyclodextrins give rise to quite well defined aggregates, or nanostructures, having a hydrodynamic radius of about 80 nm and a relatively modest polydispersity. This result obtained with a slightly different compound cannot be directly compared with the results of the atomistic simulations that suggest the presence of extended bidimensional structures on scales of the order of about 10 nm, possibly affected however to some extent, or potentially even driven, by the assumed periodicity of the simulation cell having a size of 12.3 nm. However, it is interesting to speculate that the longer length of the hydrophilic chains in the experimental system may lead to strong dipolar interactions favoring the formation of larger and

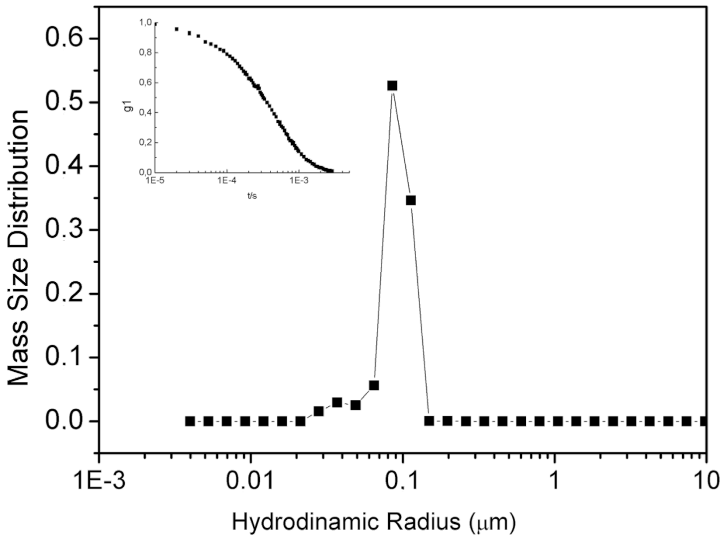

Figure 7: R_H distribution by CONTIN (and Mie scattering normalization) analysis of SC2OH dispersion (2 mg mL^{-1}) in dichloromethane. The inset shows the correspondent scattered electric field autocorrelation function at scattering angle of 90°.

more compact structures compared to what predicted by the atomistic simulations. Such issue could be resolved by very long molecular simulations considering huge numbers of molecules with longer chains, unfortunately outside the current computational possibilities. As a final remark, we point out that atomistic simulations can model in detail the interaction pattern of molecules such as the amphiphilic cyclodextrins, as already noted in [11], but they can also provide a description of larger systems comprising tens or possibly a few hundreds of molecules, even though with an increasingly larger simulation burden.

Experimental

Simulation method

The simulations were performed with InsightII/Discover 2000 and Materials Studio [14], using the consistent valence force field CVFF [15] as previously done [16-19]. The preparation and optimization of the isolated molecule of the aCD shown in Scheme 1 ($n = 0$) was already described in paper I [11], were we also described in detail the aggregates formed by two and four molecules, and more briefly those containing eight molecules. The formation of larger aggregates discussed in the present paper was modelled by creating two independent replicas of a similar starting system obtained by randomly placing eight molecules within a cubic cell with a size of 61.5 Å using periodic boundary conditions (constant-volume conditions). After an initial geometry optimization, for both replicas the resulting adduct(s) were subjected to a long MD runs lasting for 100 ns and final geometry optimizations. In order to model even larger systems, we first duplicated the periodic cell of each replica in the three directions, obtaining a cell with twice the length of each axis (i.e., 123.0 Å), hence a volume and a number of molecules (a total of sixty-four aCD) that were both eight times as large as in the previous cell. For these larger systems, a subsequent MD run was carried out for 50 ns in each case, even though an apparent equilibration based on the time change of the potential energy was apparently achieved roughly after the first 2 ns. The dynamic equations were integrated using the Verlet algorithm with a time step of 1 fs at a temperature of 300 K, controlled through the Berendsen thermostat, and the instantaneous coordinates were periodically saved for further analysis. All the energy minimizations where carried out with the conjugate gradient method up to an energy gradient lower than 4×10^{-3} kJ mol^{-1} Å^{-1}.

Sample preparation and dynamic light scattering

Heptakis (2-oligo(ethylene oxide)-6-ethylthio)-β-CD (SC2OH, M_w (14EO) = 2061 Da, EO = ethylene oxide units) was synthesized in agreement with the reported procedure [20]. SC2OH was dispersed in CH_2Cl_2 (Romil Super Pure, Sigma-Aldrich) and studied at 2 mg mL^{-1} concentration. The dispersion was centrifuged at 3000 rpm (10 min) to remove dust and air bubbles. Dynamic light scattering (DLS) measurements were carried out on a homemade apparatus by using a duplicated Nd:YAG laser source ($\lambda = 532.0$ nm) at a power of 50 mW, at a scattering angle of 90°. The scattered light, collected in a self-beating mode, was analysed using a Malvern 4700 correlator in homodyne configuration, which builds up the normalized intensity autocorrelation function [12].

Acknowledgements

We thank Dr. Norberto Micali (IPCF-CNR) for DLS measurements. Financial support of MERIT-FIRB RBNE08YYBM (CNRISMN) is gratefully acknowledged. We also gratefully acknowledge the financial support from MIUR – FIRB Futuro in Ricerca 2008 (RBFR08XH0H).

References

1. Perret, F.; Parrot-Lopez, H. Amphiphilic Cyclodextrins: Synthesis and Characterization. In *Cyclodextrins in Pharmaceutics, Cosmetics, and Biomedicine: Current and Future Industrial Applications;* Bilensoy, E., Ed.; John Wiley & Sons, Inc.: Hoboken, NJ, U.S.A., 2011; pp 197–233.
2. Bilensoy, E.; Hincal, A. A. *Expert Opin. Drug Delivery* **2009,** *6,* 1161–1173. doi:10.1517/17425240903222218
3. Versluis, F.; Voskuhl, J.; Vos, J.; Friedrich, H.; Ravoo, B. J.; Bomans, P. H. H.; Stuart, M. C. A.; Sommerdijk, N. A. J. M.; Kros, A. *Soft Matter* **2014,** *10,* 9746–9751. doi:10.1039/C4SM01801J
4. Quaglia, F.; Ostacolo, L.; Mazzaglia, A.; Villari, V.; Zaccaria, D.; Sciortino, M. T. *Biomaterials* **2009,** *30,* 374–382. doi:10.1016/j.biomaterials.2008.09.035
5. Mazzaglia, A.; Ravoo, B. J.; Darcy, R.; Gambadauro, P.; Mallamace, F. *Langmuir* **2002,** *18,* 1945–1948. doi:10.1021/la015626x
6. Lombardo, D.; Longo, A.; Darcy, R.; Mazzaglia, A. *Langmuir* **2004,** *20,* 1057–1064. doi:10.1021/la035370q
7. Mazzaglia, A.; Angelini, N.; Lombardo, D.; Micali, N.; Patanè, S.; Villari, V.; Monsù Scolaro, L. *J. Phys. Chem. B* **2005,** *109,* 7258–7265. doi:10.1021/jp0501998
8. Stancanelli, R.; Guardo, M.; Cannavá, C.; Guglielmo, G.; Ficarra, P.; Villari, V.; Micali, N.; Mazzaglia, A. *J. Pharm. Sci.* **2010,** *99,* 3141–3149. doi:10.1002/jps.22065
9. Valli, L.; Giancane, G.; Mazzaglia, A.; Monsù Scolaro, L.; Conoci, S.; Sortino, S. *J. Mater. Chem.* **2007,** 1660–1663. doi:10.1039/b703067c
10. Conte, C.; Scala, A.; Siracusano, G.; Leone, N.; Patanè, S.; Ungaro, F.; Miro, A.; Sciortino, M. T.; Quaglia, F.; Mazzaglia, A. *RSC Adv.* **2014,** *4,* 43903–43911. doi:10.1039/C4RA07847K
11. Raffaini, G.; Mazzaglia, A.; Ganazzoli, F. *Beilstein J. Org. Chem.* **2015,** *11,* 2459–2473. doi:10.3762/bjoc.11.267
12. Villari, V.; Micali, N. *J. Pharm. Sci.* **2008,** *97,* 1703–1730. doi:10.1002/jps.21067
13. D'Urso, A.; Cristaldi, D. A.; Fragalà, M. E.; Gattuso, G.; Pappalardo, A.; Villari, V.; Micali, N.; Pappalardo, S.; Parisi, M. F.; Purrello, R. *Chem. – Eur. J.* **2010,** *16,* 10439–10446. doi:10.1002/chem.201000803
14. *InsightII 2000 and Materials Sudio;* Accelrys Inc.: San Diego, CA, U.S.A..
    See also the URL http://www.accelrys.com/

15. Dauber-Osguthorpe, P.; Roberts, V. A.; Osguthorpe, D. J.; Wolff, J.; Genest, M.; Hagler, A. T. *Proteins: Struct., Funct., Genet.* **1988,** *4,* 31–47. doi:10.1002/prot.340040106
16. Raffaini, G.; Ganazzoli, F. *J. Phys. Chem. B* **2010,** *114,* 7133–7139. doi:10.1021/jp911812j
17. Raffaini, G.; Ganazzoli, F.; Malpezzi, L.; Fuganti, C.; Fronza, G.; Panzeri, W.; Mele, A. *J. Phys. Chem. B* **2009,** *113,* 9110–9122. doi:10.1021/jp901581e
18. Raffaini, G.; Ganazzoli, F. *J. Inclusion Phenom. Macrocyclic Chem.* **2007,** *57,* 683–688. doi:10.1007/s10847-006-9265-0
19. Raffaini, G.; Ganazzoli, F. *Chem. Phys.* **2007,** *333,* 128–134. doi:10.1016/j.chemphys.2007.01.015
20. Mazzaglia, A.; Donohue, R.; Ravoo, B. J.; Darcy, R. *Eur. J. Org. Chem.* **2001,** 1715–1721. doi:10.1002/1099-0690(200105)2001:9<1715::AID-EJOC1715>3.0.CO;2-A

License and Terms

The definitive version of this article is the electronic one which can be found at:
doi:10.3762/bjoc.12.8

BEILSTEIN JOURNAL OF ORGANIC CHEMISTRY

Supramolecular structures based on regioisomers of cinnamyl-α-cyclodextrins – new media for capillary separation techniques

Gabor Benkovics[1,2], Ondrej Hodek[3], Martina Havlikova[3], Zuzana Bosakova[3], Pavel Coufal[3], Milo Malanga[2], Eva Fenyvesi[2], Andras Darcsi[4], Szabolcs Beni[4] and Jindrich Jindrich*[1]

Full Research Paper

Address:
[1]Department of Organic Chemistry, Faculty of Science, Charles University in Prague, Hlavova 8, 128 43, Prague 2, Czech Republic, [2]CycloLab, Cyclodextrin R&D Ltd, Budapest, H-1097 Illatos út 7, Hungary, [3]Department of Analytical Chemistry, Faculty of Science, Charles University in Prague, Hlavova 8, 128 43, Prague 2, Czech Republic and [4]Department of Pharmacognosy, Semmelweis University, Budapest, H-1085 Üllői út 26, Hungary

Email:
Jindrich Jindrich* - jindrich@natur.cuni.cz

* Corresponding author

Keywords:
capillary electrophoresis; cyclodextrin derivatives; mono-cinnamyl; regioisomers; supramolecular structures

Beilstein J. Org. Chem. **2016,** *12,* 97–109.
doi:10.3762/bjoc.12.11

Received: 31 October 2015
Accepted: 28 December 2015
Published: 19 January 2016

This article is part of the Thematic Series "Superstructures with cyclodextrins: Chemistry and applications III".

Guest Editor: E. Monflier

Abstract

This work focuses on the preparation and application of supramolecular structures based on mono-cinnamyl-α-cyclodextrins (Cin-α-CD). Pure regioisomers of Cin-α-CD having the cinnamyl moiety at the 2-*O*- or at the 3-*O*-position, respectively, were prepared, characterized and applied in capillary electrophoresis as additives to the background electrolyte. These new monomer units with a potential to self-organize into supramolecular structures were synthesized via a straightforward one-step synthetic procedure and purified using preparative reversed-phase chromatography allowing a large scale separation of the regioisomers. The ability of the monomers to self-assemble was proved by various methods including NMR spectroscopy and dynamic light scattering (DLS). The light scattering experiments showed that the monomer units have distinguishable ability to form supramolecular structures in different solvents and the size distribution of the aggregates in water can be easily modulated using different external stimuli, such as temperature or competitive guest molecules. The obtained results indicated that the two regioisomers of Cin-α-CD formed different supramolecular assemblies highlighting the fact that the position of the cinnamyl group plays an important role in the intermolecular complex formation.

Introduction

Supramolecular polymers (SP) are aggregates of monomer units held together by non-covalent interactions, such as electrostatic interactions, coordination bonds, hydrogen bonds, hydrophobic interactions and host–guest interactions [1]. Their formation is spontaneous and reversible by self-assembly of the monomer units. Because of this special non-covalent intermolecular bonding, the formation and decomposition of the SP is at thermodynamic equilibrium, which means that the polymer growth or the destruction of the polymer chain can be adjusted by external stimuli. This reversibility makes SPs promising functional materials and gives them the potential to be easily processed, recycled or applied as self-healing materials. Recently much attention has been focused on the preparation and application of SPs and the most promising systems have already found their field of application ranging from cosmetics, printing, personal care to plastic industry. However their use as separation media in separation science remained an unexplored area [2].

The recent work focused on the preparation of supramolecular structures based on cyclodextrin (CD) [3] derivatives and on their application as chiral separation environment in capillary separation techniques. CDs are widely used in capillary separation techniques mainly as chiral selectors, but a common CD-based chiral selector does not form any superstructures and hence, may interact only with the analytes [4]. In comparison, the totally new type of molecular discriminators based on SPs generates superstructures (i.e., polymers) which also interact with analytes and moreover, exist and move as an entire aggregate in the separation environment. This character of the SPs brings an evident benefit in recognition, discrimination and consequently separation of analytes. Another advantage of the SP-based separation environment comes from the stimuli-responsivity of the system, which means that by adjusting different conditions of separation (temperature, ionic strength, pH, organic co-solvent concentration) it is possible to modulate the characteristics of the supramolecular assembly. The increasing or decreasing size of the SP will result in changed sieving effects, different selector–analyte interactions and in modulated separation selectivity.

CDs have been used as the host component for the construction of various interesting supramolecular structures such as pseudorotaxanes, rotaxanes, supramolecular dimers, oligomers and even polymers [5]. Modification of the parent CD molecule with an apolar substituent, which can form an inclusion complex with the CD's cavity results in a conjugate with an ability to self-associate into supramolecular assemblies in polar solvents. The formation of these structures is based mainly on intermolecular host–guest interactions between the hydrophobic interior of the CD in one conjugate and between the apolar substituent of another conjugate. Earlier studies however pointed out that the size matching between the covalently attached guest part and the CD's cavity is not the only requirement for the effective SP formation. In the case of 6-*O*-monobenzoyl-β-CD, for example, the direct attachment of the phenyl moiety to the CD rim did not result in intermolecular complex formation [6]. On the other hand too long and flexible spacers between the host and the guest moiety favored the self-inclusion process of the guest part to the parent CD's cavity [6,7]. These findings showed that a compromise in the flexibility and in the length of the spacer has to be found for efficient formation of intermolecular complexes. Inspired by these works our approach towards SPs was based on the preparation of monocinnamyl-α-CDs, where the rigid double bond in the cinnamyl (Cin) moiety should prevent the self-inclusion of the phenyl ring to the CD cavity and prefer the formation of intermolecular complexes in polar solvents.

The conjugation of the cinnamoyl (Cio) moiety with α- and β-CD through amide and ester linkages was already reported by Harada et al. [8,9]. These monosubstituted derivatives formed different types of supramolecular assemblies (dimers, cyclic oligomers, linear polymers) in water depending on the position of the cinnamoyl moiety on the CD rim. It was also experimentally proven that the cavity of the CD shows distinguishable inclusion affinities towards different substrates, even to homologues and isomers. A self-sorting complex formation ability was described for the two regioisomers of monocinnamoyl-α-CD (Cio-α-CD) [9]. While the 2-Cio-α-CD isomer formed an insoluble double-threaded supramolecular dimer in water, the 3-Cio-α-CD formed a soluble supramolecular oligomer in the same solvent. The mixture of both regioisomers led to the formation of a self-sorting oligomeric system, where only the heterosupramolecular interactions between the two isomers were present but the homosupramolecular interactions between the same species were missing. This work clearly demonstrates that the intermolecular complex formation is a regioselective process where the CD cavity can differentiate between the positional isomers which will result in different aggregation behavior of the regioisomers.

Based on this knowledge our aim was to prepare pure regioisomers of cinnamyl-appended α-CD, to test and compare the ability of different regioisomers to form supramolecular structures and to investigate their application as additives to the background electrolyte in capillary separation techniques. Because this application requires chemically stable conjugates, we decided to prepare conjugates where the guest molecule is bound to the CD by a stable ether bond instead of the labile ester bond. This led us to the family of Cin-α-CD. The complete set of peracetylated regioisomers of Cin-α-CD was previously prepared and characterized by our research group, but our attempts to separate the single 2-*O*- and 3-*O*-regioisomers without further modification were unsuccessful [10]. In order to isolate the single regioisomers using this published method, exhaustive per-*O*-acetylation of the mixture of regioisomers, chromatographic separation of the per-*O*-acetylated derivatives and the de-*O*-acetylation of the separated per-*O*-acetylated regioisomers would be necessary. This three-step reaction procedure makes the large scale preparation of the single regioisomers expensive and time-consuming. For α-CD we were not able to achieve the high regiospecificity of the monocinnamylation which we described for β-CD earlier [11]. In the case of β-CD the only monosubstituted isomer obtained was 3-*O*-Cin-β-CD in 30% isolated yield. This result was explained by a highly regioselective complexation of the alkylation reagent into β-CD, which obviously does not take place with α-CD and only mixtures of regioisomers are formed.

Herein, we report on a straightforward one-step synthetic methodology using preparative reversed-phase chromatography with water–methanol gradient elution for the separation of the regioisomers of Cin-α-CD.

Results and Discussion

The two regioisomers of Cin-α-CD were synthesized via direct alkylation of α-CD (**1**) in DMSO, using NaH as a base for the deprotonation of the secondary OH groups of the α-CD and cinnamyl bromide as an alkylating agent. The reaction resulted in a multicomponent mixture of unreacted α-CD, monosubstituted α-CD and disubstituted α-CD. From this mixture of compounds the pure 2-*O*-Cin-α-CD (**2**) and 3-*O*-Cin-α-CD (**3**) were isolated in one run by preparative reversed-phase chromatography using a water–methanol step gradient elution. This modified procedure allowed us to prepare the two regioisomers of Cin-α-CD in gram-scale which was required for the detailed characterization of their aggregation ability and for their application in capillary electrophoresis (CE). The monosubstituted products were characterized by ESI mass spectrometry, ^{1}H NMR and ^{13}C NMR spectroscopy.

The two regioisomers could be unambiguously distinguished and characterized by cross-linking the data of ^{1}H NMR, ^{13}C NMR, COSY, TOCSY, DEPT-ed-HSQC and HMBC. As an example, the elucidation of the regioisomer **2** is discussed here. The allylic proton signals can be detected in a separated region of the ^{1}H proton spectrum around 4.47 ppm (see proton A in Figure SI 1, Supporting Information File 1). These frequencies can be also easily identified in the DEPT-ed-HSQC spectrum of the compound (see A in Figure SI 3, Supporting Information File 1). The DEPT-ed-HSQC spectrum clearly shows that the compound is unsubstituted at the C6 position, since the characteristic peaks of the two magnetically non-equivalent proton (C6-Ha and C6-Hb), typical for C6 substitution [12] are not detectable in the spectrum. As a consequence the compound is C2- or C3-monosubstituted (the monosubstitution has also been proven by MS). Analyzing the HMBC spectrum (Figure SI 4, Supporting Information File 1), crosspeaks between the allylic protons (4.47 ppm) and a CD-related carbon at 81.38 ppm can be detected (see the black circle in Figure SI 4, Supporting Information File 1). This carbon resonance (81.38 ppm) can either belong to C2’ or C3’ of the glucose unit bearing the cinnamyl substituent (otherwise the crosspeak would not be present in the HMBC spectrum). The frequency of this carbon (and of the correlated proton at 3.57 ppm) can be also detected in the DEPT-ed-HSQC spectrum (see C2’ in Figure SI 3, Supporting Information File 1). Finally, the COSY spectrum clarifies that the carbon at 81.38 ppm corresponds to C2’ since the crosspeak with the anomeric resonance can be detected (see the black circles in Figure SI 5, Supporting Information File 1). This set of data proves unambiguously that the compound is the 2-*O*-Cin-α-CD. A schematic representation of the spectral evidences used for the identification of the cinnamyl position is shown in Figure 1.

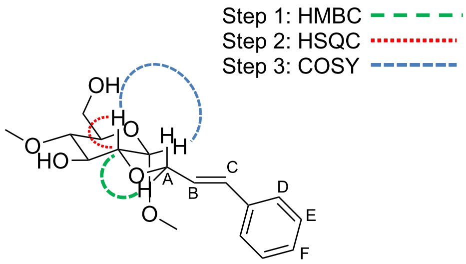

Figure 1: Example of elucidation of 2D NMR spectra of 2-*O*-Cin-α-CD.

Supramolecular structures of 2-*O*-Cin-α-CD and 3-*O*-Cin-α-CD characterized by 2D rotating frame Overhauser effect spectroscopy (ROESY)

2-*O*-Cin-α-CD and 3-*O*-Cin-α-CD are well soluble in water; therefore the supramolecular structures of both regioisomers were first investigated in D_2O solutions. When the cinnamyl moiety is included in the CD cavity thus forming intermolecular complexes or self-included intramolecular species, the 2D ROESY spectrum shows this interaction as NOE crosspeaks between the inner hydrogens (H3 and H5) of the CD cavity and between the aromatic or double bond hydrogens of the cinnamyl moiety.

In the spectra of both regioisomers intense correlations were observed between the phenyl protons (7.2–7.5 ppm) and the protons of the CD cavity (3.6–4.1 ppm) (red circles in Figure 2) proving that the phenyl part is located in the CD cavity.

These correlations were observed for both inner proton region at 3.6–3.8 ppm for protons H5 (red dashed line in Figure 3) and 3.8–4.1 for protons H3 (black dashed line in Figure 3) indicating, that the cinnamyl moiety penetrated deeply into the CD cavity. Less intense cross-correlation was found for the two protons from the double bond region of the cinnamyl moiety (6.2–6.7 ppm, black circles in Figure 2), but their presence indicates that the double bond is also situated in the close proximity of the cavity and therefore contributing to the host−guest interaction. More detailed study of the ROESY spectra (see Figure 3) provided relevant information about the mode of the host–guest interaction.

Important differences can be observed between the interactions of the two double bond protons (B and C in Figure 3) with the cavity. In the 2D ROESY spectra of both regioisomers proton C interacts with both cavity protons (H3 and H5), indicating that proton C is penetrated into the cavity, on the other hand proton B shows interaction only with H3 but there is no interaction with H5 (red circle in Figure 3), suggesting that the linker in the host–guest complex is closer to the wider rim of the CD. The aromatic protons D, E and F of the isomer **2** also interact differently with the two inner protons of the cavity. While protons D and E show cross-correlation with both protons, proton F interacts only with H5 but it does not interact with proton H3 (black circle in Figure 3). These observations altogether leave us with only one possible mode of interaction, which is the inclusion of the cinnamyl moiety to the cavity from the secondary side (side close to the H3 protons) and not from the primary side (side close to the H5 protons) of the CD’s cavity.

The 2D ROESY spectra of the two regioisomers are comparable, (for 2D ROESY spectra of 3-*O*-Cin-α-CD see Figure SI 13 and Figure SI 14 in Supporting Information File 1) showing that in both cases the cinnamyl group is located inside the CD cavity and in both molecules this inclusion phenomenon takes place from the secondary side of the CD cavity.

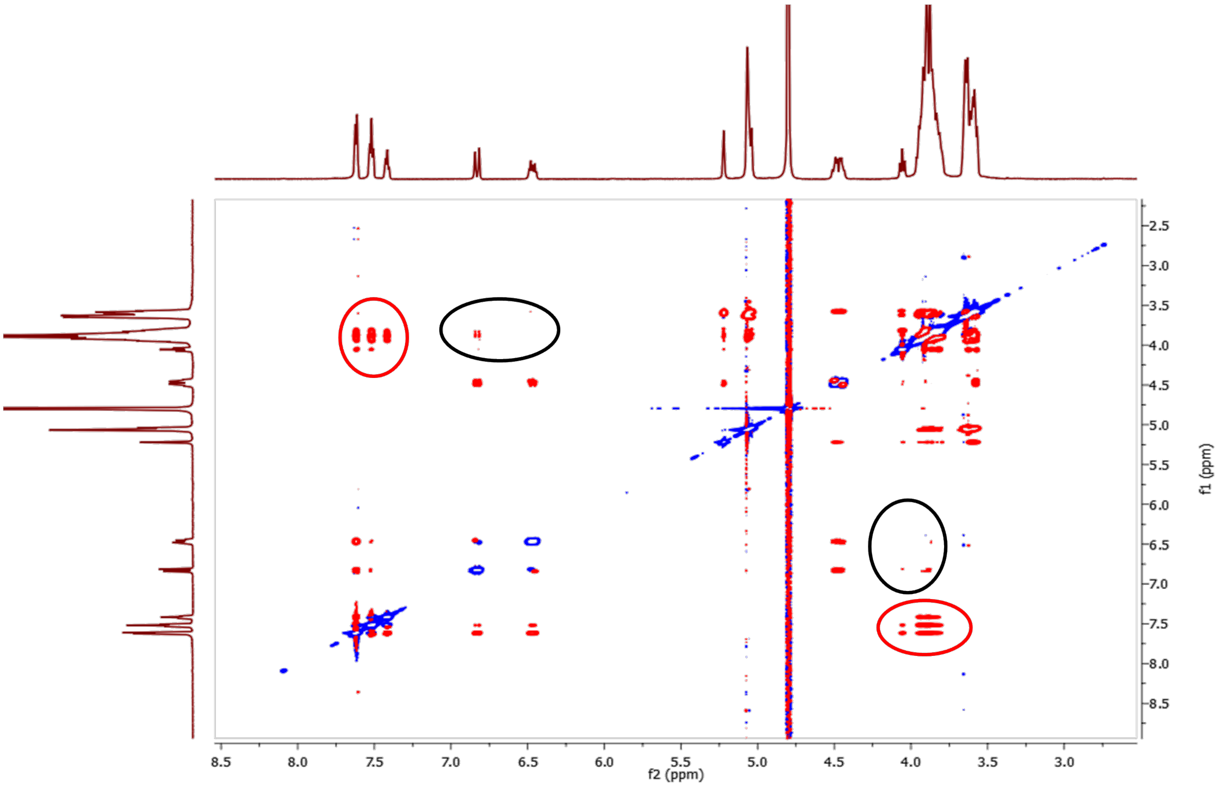

Figure 2: 2D ROESY spectrum of 2-*O*-Cin-α-CD in D_2O at 25 °C at 24 mM concentration.

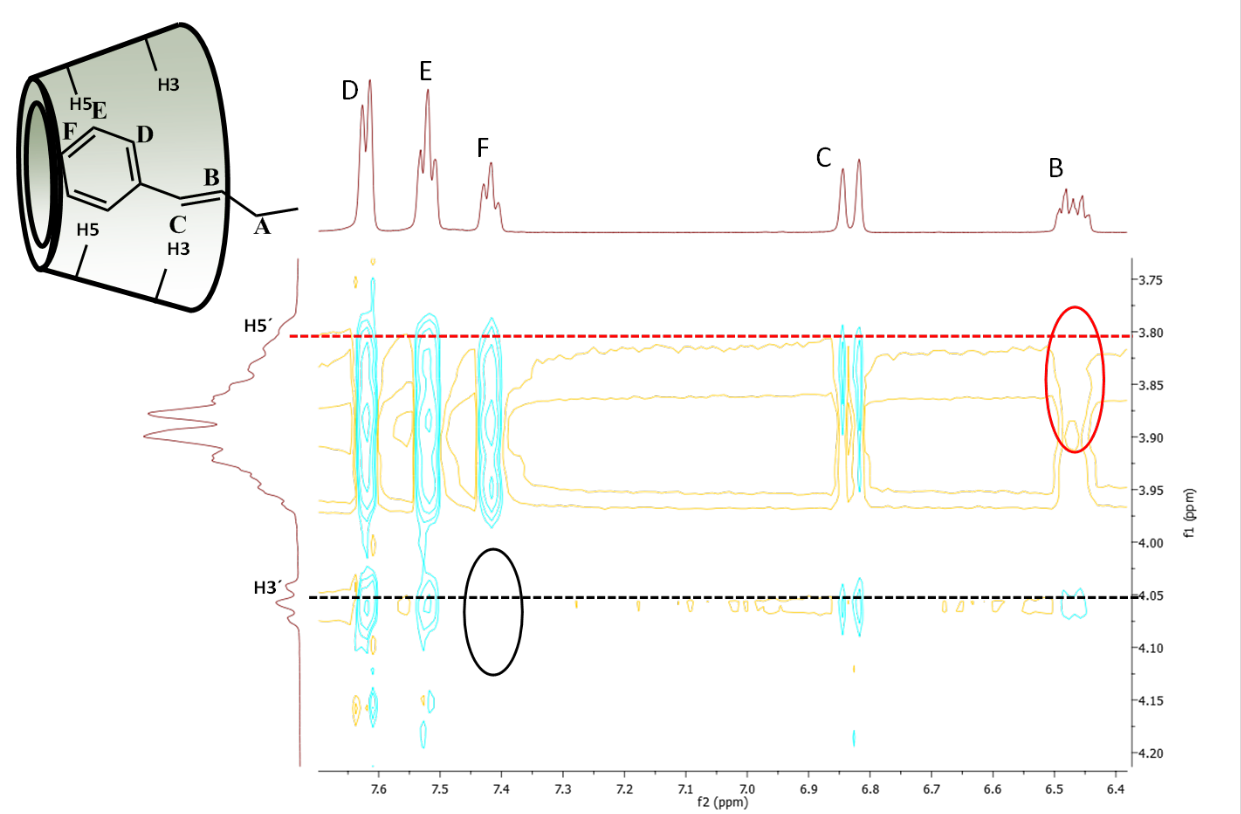

Figure 3: Expansion of the 2D ROESY spectrum of 2-*O*-Cin-α-CD indicating the geometric arrangement.

Supramolecular structures of 2-*O*-Cin-α-CD and 3-*O*-Cin-α-CD characterized by a ^{1}H NMR dilution experiment

The observed NOE signals proved the close spatial proximity of the inner protons of the CD cavity and the aromatic and double bond protons of the cinnamyl moiety. However these experimental evidences do not unambiguously confirm the existence of the intermolecular interaction, because self-inclusion processes cannot be excluded. In order to prove our assumption that the NOE correlations arise from the intermolecular host–guest interactions, the systems were further investigated using a series of ^{1}H NMR spectra recorded at different concentrations. The chemical shifts of ^{1}H resonances of both regioisomers changed as a function of concentration, although those recorded in DMSO-d_6 were concentration-independent.

These results indicate that both regioisomers are capable forming intermolecular complexes in D_2O solution, but they are in non-aggregated state in DMSO-d_6. In the case of the isomer **2** downfield shifts in the aromatic and double bond region were observed when the concentration was changed gradually from 1.5 mM to 24 mM (Figure 4). Further increase in the concentration did not result in additional peak shifts, which means that the system stabilized at around 24 mM concentration and even if the concentration was increased dramatically (up to 96 mM) the chemical environment of the aromatic/double bond protons did not change significantly (Figure 4).

The increasing concentration also influenced the ^{1}H NMR spectrum of the isomer **3**, showing that the 3-*O* derivative also forms intermolecular complexes, but surprisingly the concentration change had an opposite effect compared to the isomer **2** (Figure 5). The double bond protons (protons B and C in Figure 5) and the resonances of the proton at the *para* position of the cinnamyl moiety (proton F in Figure 5) were monotonously shifted towards lower frequency and did not show any plateau when the concentration was increased gradually from 1.5 mM to 96 mM. It was also surprising that the the *orto* and *meta* protons (protons D and E), which showed intense correlations in the 2D ROESY spectra (Figure SI 13 and SI 14, Supporting Information File 1), did not exhibit concentration-dependent chemical shift differences (Figure 5).

In conclusion, the observed concentration-dependent chemical shift changes in the aromatic and double bond region unequivocally prove the intermolecular interactions in the case of both regioisomers and clearly show that these two regioisomers form supramolecular structures in a different manner.

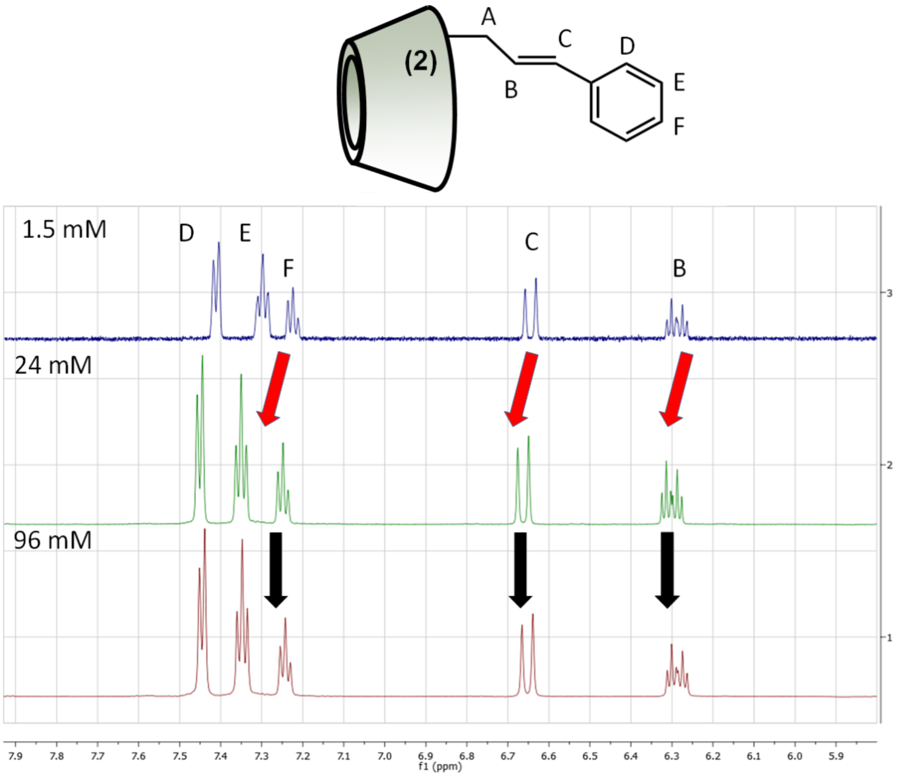

Figure 4: ^{1}H NMR spectra of 2-*O*-Cin-α-CD in D_2O at 25 °C at different concentrations.

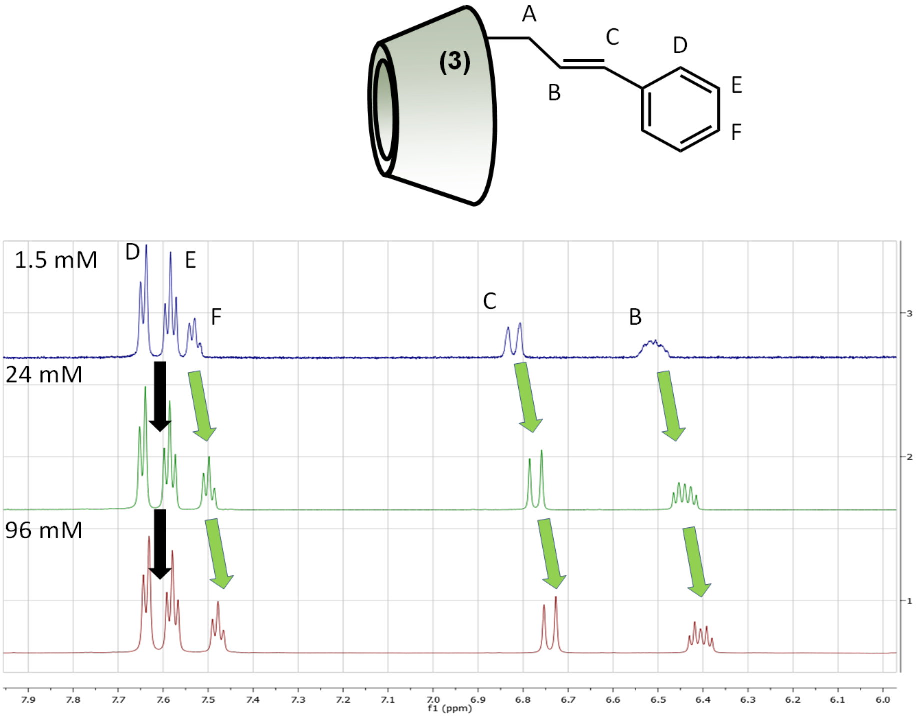

Figure 5: ^{1}H NMR spectra of 3-*O*-Cin-α-CD in D_2O at 25 °C recorded at various concentrations.

Size estimations of intermolecular inclusion complexes: pulse field gradient spin-echo NMR experiments (PFGSE NMR)

PFGSE NMR experiments were performed in order to estimate and compare the sizes of the supramolecular assemblies formed by the two regioisomers. This technique allows the quantification of the diffusion coefficient (D) of structures at various concentrations.

The D of the unmodified α-CD was previously reported by Avram and Cohen [13] and it was found to be 3.0×10^{-6} cm^2 s^{-1}. The D of a supramolecular dimer formed by the structurally similar 2-*O*-Cio-α-CD was measured in work [9] and its value was found to be 2.3×10^{-6} cm^2 s^{-1} at 10 mM concentration and did not change with further increase in the concentration. In the case of supramolecular polymerization the D should continuously decrease with increase in the concentration because of the increasing size of the supramolecular assembly. When the concentration of isomer **2** was gradually increased from 1.5 mM to 96 mM a monotonous decay in D was observed from 2.03×10^{-6} cm^2 s^{-1} at 1.5 mM to 1.09×10^{-6} cm^2 s^{-1} at 96 mM, respectively. The same concentration dependence was observed for the D of isomer **3** starting from 2.05×10^{-6} cm^2 s^{-1} at 1.5 mM arriving to 1.27×10^{-6} cm^2 s^{-1} at 96 mM (Figure 6).

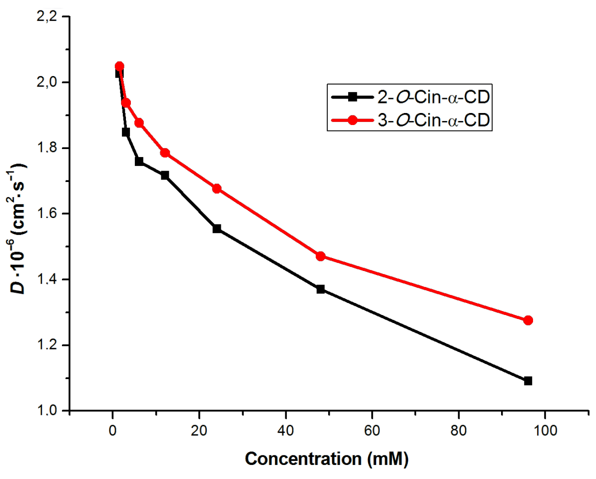

Figure 6: Diffusion coefficients of 2-*O*-Cin-α-CD (black) and, 3-*O*-Cin-α-CD (red) in D_2O at various concentration at 25 °C.

These data indicate that the size of the supramolecular structures formed by the assembly of 2-*O*-Cin-α-CD or by 3-*O*-Cin-α-CD is apparently much larger than the size of the unmodified α-CD and also exceeds the size of the double threaded dimer formed by 2-*O*-Cio-α-CD. Furthermore we can conclude that because in the studied concentration range no stabilization of D was observed for none of the derivatives, these regioisomers form an opened supramolecular aggregate, which size in D_2O increases with increase in the concentration.

Size estimations of intermolecular inclusion complexes and other assemblies: DLS experiments

In order to further investigate the supramolecular structures and the effect of different external stimuli on the size distribution of the supramolecular assemblies a series of DLS experiments were performed. As a first parameter, the effect of different solvents on the size distribution was tested. In aqueous solution both regioisomers formed large aggregates with a hydrodynamic diameter (D_h) up to 700 nm and the size of the aggregates formed by isomer **2** or isomer **3** were comparable (see Record 1 in Figure 7 and Figure 8).

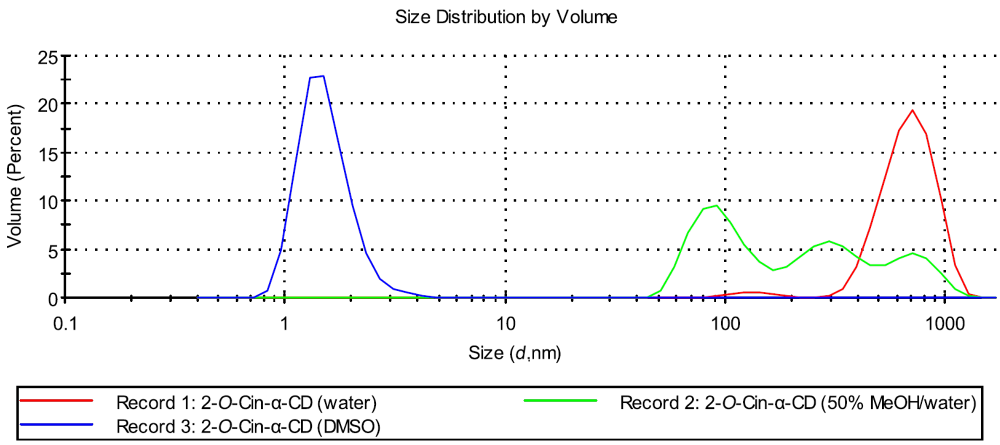

Figure 7: Effect of solvent on the size distribution of aggregates formed by 2-O-Cin-α-CD at 25 °C (the applied concentrations are 10 mg/mL (9.2 mM)).

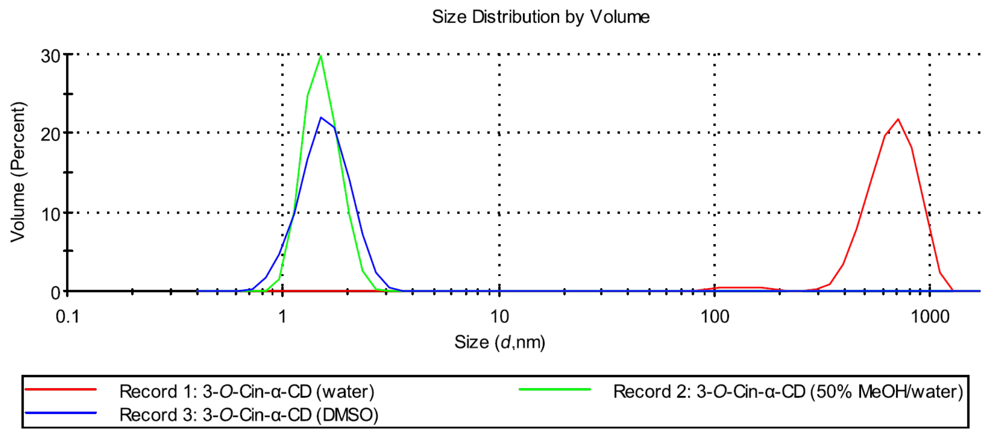

Figure 8: Effect of a solvent on the size distribution of aggregates formed by 3-*O*-Cin-α-CD at 25 °C (the applied concentrations are 10 mg/mL (9.2 mM)).

In DMSO, no aggregation was observed for both derivatives (see Record 3 in Figure 7 and Figure 8). Those were present in molecularly dispersed form with a D_h around 1.25 nm, which corresponds to the size of the unmodified, non-aggregated α-CD [14]. These results are in agreement with the results obtained by NMR experiments, where no chemical shift changes were observed upon dilution in DMSO-d_6 also indicating the absence of the intermolecular interactions.

Different aggregate sizes were observed for the two regioisomers in 50% MeOH solution (Record 2 in Figure 7 and Figure 8). Isomer **2** was present in a form of aggregates with a very broad size distribution ranging from 100 nm to 700 nm, while isomer **3** was found in a disaggregated form (D_h = 1.25 nm).

The temperature also influenced the size of the aggregates formed by the two regioisomers differently (Figure 9). Monotonous decay in size distribution was observed for the aggregates formed by the isomer **2** in water when the temperature was gradually elevated, although large aggregates with a D_h of 400 nm were still present at 75 °C.

On the other hand the aggregates formed by the isomer **3** in water were much more labile and they completely disaggregated as the temperature reached 50 °C. From these results we can conclude that the temperature can be used as an external stimulus to adjust the size distribution in water and to study its impact on the separation efficiency in separation techniques. The temperature-caused disaggregation is a reversible process – cooling back the solutions to a room temperature led to the formation of large particles with D_h comparable to the size of the initial particles.

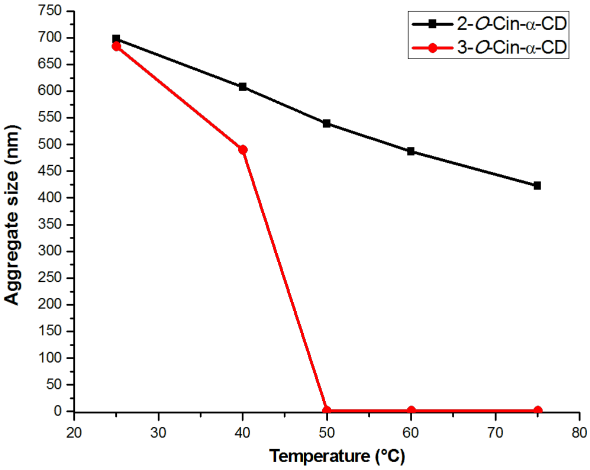

Figure 9: Aggregate sizes (diameter) of 2-*O*-Cin-α-CD (black) and 3-*O*-Cin-α-CD (red) in water at various temperatures (the applied concentrations are 10 mg/mL (9.2 mM)).

The large aggregate sizes observed in water also indicate the formation of supramolecular structures, although it must be noted that only the host–guest interaction between the cinnamyl moiety and the α-CD cavity would not be strong enough to hold together such large aggregates. According to Boutellier [15] the degree of polymerization (DP_{max}) for a SP is given by the association constant between the interacting components and by the concentration of the self-assembling monomer: $DP_{max} = (K \times c)^{0.5}$. The highest stability constants reported for the *trans*-cinnamyl derivatives with α-CD are on the order of 2×10^3 M^{-1} [16]. If only this host–guest interaction would be involved in the intermolecular interaction, the degree of polymerization according to Boutellier's model at 10 mg/mL (9.2 mM) concentration would give DP_{max} = 4.28, therefore the supramolecular chain should not be longer than 5 nm.

Apparently the D_h observed by DLS for both Cin-α-CD isomers (700 nm) is much larger than the calculated value (5 nm), which indicates that the SP formation is a much more complicated process and besides the host–guest interaction other additional intermolecular interactions may also take place. Due to the numerous hydroxy groups present in the studied molecules these secondary interactions most probably are the hydrogen-bond interactions between the CD units, or the π–π interactions of the cinnamyl moieties. The sum of all these possible interactions results in the large supramolecular aggregates observed by DLS.

Effect of competitive additives on the aggregation behavior: DLS and ROESY experiments

In order to demonstrate that in the case of the Cin-α-CD the main force which initializes the aggregate formation is the host–guest interaction between the monomer units, a DLS experiment was set up in order to measure the aggregate size distribution after successive addition of potential competitive host or guest molecules. We decided to prove, that the size of the supramolecular assembly can be modulated by the addition of suitable chain growth inhibitors, which are able to displace the cinnamyl moiety from the neighboring CD cavity, or to shield the cinnamyl moiety from the cavity of the adjacent Cin-α-CD. Based on the previous observation that elevated temperature resulted in partial or complete disaggregation depending on the type of the regioisomer the following experiment was performed.

The aqueous solution (10 mg/mL) of our derivatives was equilibrated at a temperature of 75 °C, stirred in a closed vial for 12 hours and then the system was perturbed by the addition of the inhibitor in a 10-fold molar excess respect to the Cin-α-CD. Subsequently the system was cooled back to room temperature and the size distribution of the aggregates was measured. In Figure 10 a schematic representation of the experiment setup is shown.

As shown in Figure 11 the addition of unmodified α-CD as competitive host molecule to the aqueous solution of isomer **3** did not decrease significantly the aggregate size distribution, which indicates that α-CD is not able to inhibit the intermolecular interactions between the molecules of 3-*O*-Cin-α-CD. Potassium adamantane-1-carboxylate (AdCOOK) was a more effective chain growth inhibitor as it decreased the aggregate size from 700 nm to 400 nm. Potassium cinnamate (CioOK) as a competitive guest molecule was able to completely displace the cinnamyl part of 3-*O*-Cin-α-CD from the adjacent CD cavity which resulted in decomposition of the host–guest

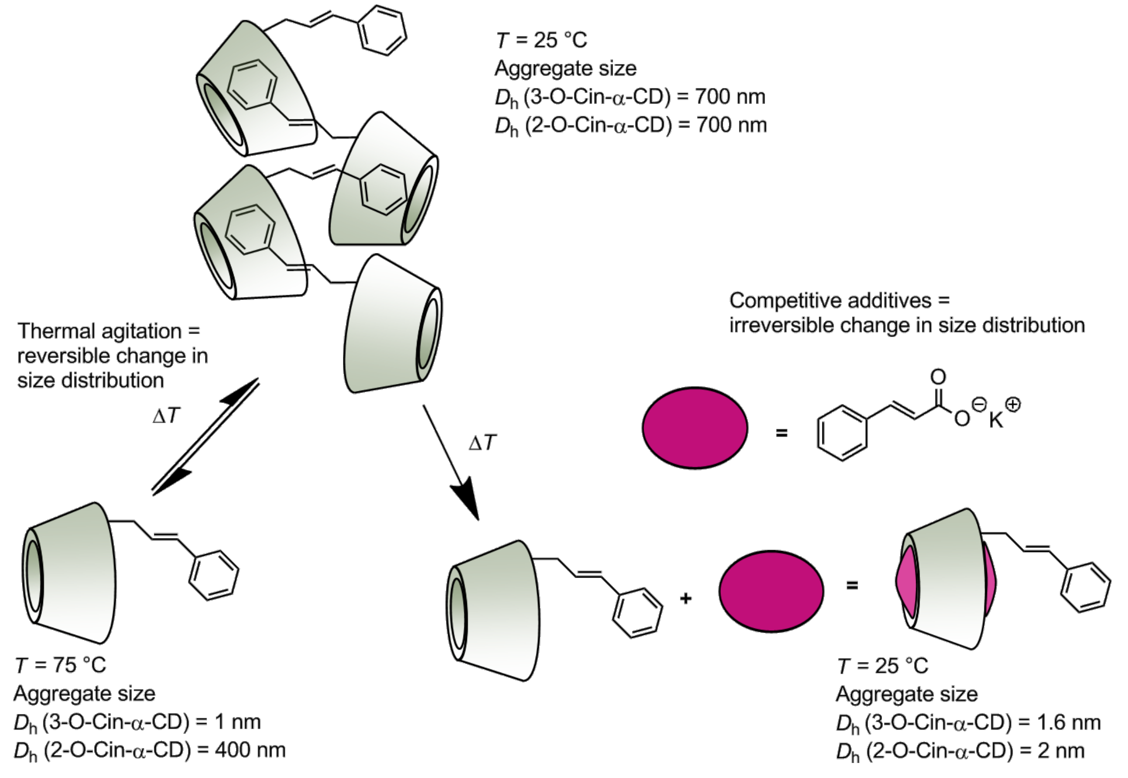

Figure 10: Schematic representation of the DLS experiment proving the host–guest nature of the aggregate formation.

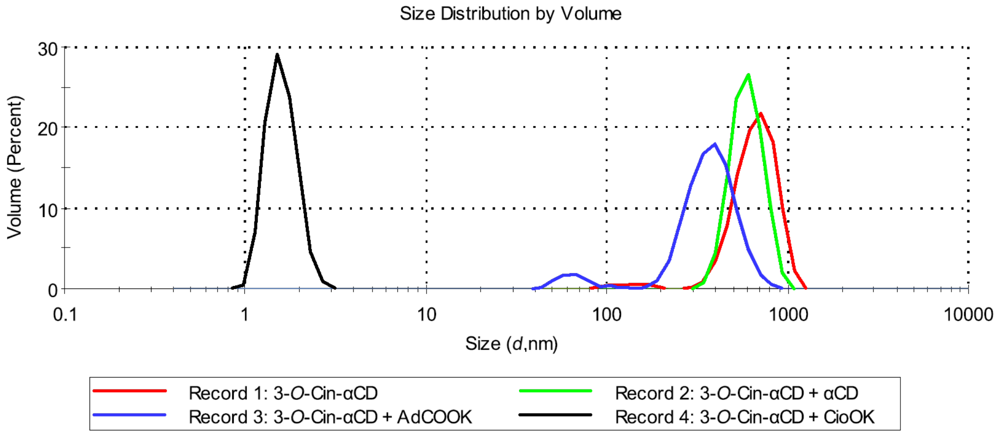

Figure 11: The effect of competitive additives on the size distribution of aggregates formed by 3-*O*-Cin-α-CD at 25 °C (the applied concentrations of the 3-*O*-Cin-α-CD are 10 mg/mL (9.2 mM)).

complexes. As a result a significant decrease in the D_h of the aggregates (from 700 nm to 1.6 nm) was observed (Figure 10 and Figure 11).

The observed differences between the efficiency of the chain growth inhibition of AdCOOK and CioOK can be explained by the different size of the two competitive guest molecules. The α-CD cavity is able to accommodate the smaller CioOK, which results in a complete collapse of the supramolecular aggregates, on the other hand AdCOOK as a guest molecule is apparently too bulky for the α-CD cavity, therefore the displacement of the cinnamyl moieties in the intermolecular complexes and the caused disaggregation is only partial (from 700 nm to 400 nm). Isomer **2** showed a similar behavior upon addition of chain inhibitors as isomer **3** (Figure SI 15, Supporting Information File 1), which indicates that in case of both regioisomers the main force of the aggregation is the intermolecular host–guest interaction. The disrupted aggregates were stable at room temperature and did not show any aggregation in time, hence we can conclude that the disaggregation caused by competitive additives is an irreversible process.

Because CioOK as competitive additive showed remarkable changes in the aggregation behavior of Cin-α-CDs, we further investigated its interaction with both regioisomers using 1D and 2D NMR experiments to get a deeper insight into the disaggregation process. ROESY and ^{1}H NMR spectra of isomer **2** or isomer **3** were recorded in the presence of CioOK (5-fold molar excess) in D_2O after equilibrating the solutions at 75 °C and cooling back to 25 °C just before the measurements.

Instead of the previously observed NOE cross-correlations in the ROESY spectra of both Cin-α-CD isomers, new cross-peaks appeared showing interaction only between potassium cinnamate and between the inner hydrogens of the CD cavity (Figure 12). The disappeared cross-peaks between the protons of the cinnamyl part of Cin-α-CDs (black dashed line in Figure 12) and between the CD cavity protons indicate that the cinnamyl moiety was effectively displaced by the additive.

This phenomenon can be observed also in the ^{1}H NMR spectrum of both isomers (Figure 13 for isomer **2**, Figure SI 21 in Supporting Information File 1, for isomer **3** respectively). If we compare the chemical shifts of aromatic or double bond protons of the given regioisomer before and after the addition of the competitive guest molecule, significant changes in chemical shifts can be detected, which indicates that the cinnamyl part of the molecule is located in a different chemical environment after the addition of the competitive guest.

These results are in a good agreement with the data obtained from DLS experiments and further confirmed our hypothesis which assumed that the observed disaggregation by CioOK is caused by the formation of a host–guest complex between Cin-α-CDs and between the molecules of CioOK.

Analytical application

The potential of 2-*O*-Cin-α-CD and 3-*O*-Cin-α-CD as enantioselective agents was investigated by capillary electrophoresis. The influence of the addition of 2-*O*-Cin-α-CD and 3-*O*-Cin-α-CD to the background electrolyte (BGE) and its impact on the effective mobilities of eighteen selected analytes were tested. Nine analytes were in the form of cations (aniline, antipyrine, L-histidine, DL-tyrosine, DL-phenylalanine, *N*-(1-naphthyl)ethylenediamine, 4-nitroaniline, *p*-aminoacetophenone, tyramine) and nine in the form of anions (*N*-acetyl-DL-phenylalanine, *N*-acetyl-DL-tryptophan, *N*-benzoyl-DL-phenylalanine, *N*-boc-DL-tryptophan, *N*-FMOC-DL-valine, *N*-FMOC-DL-

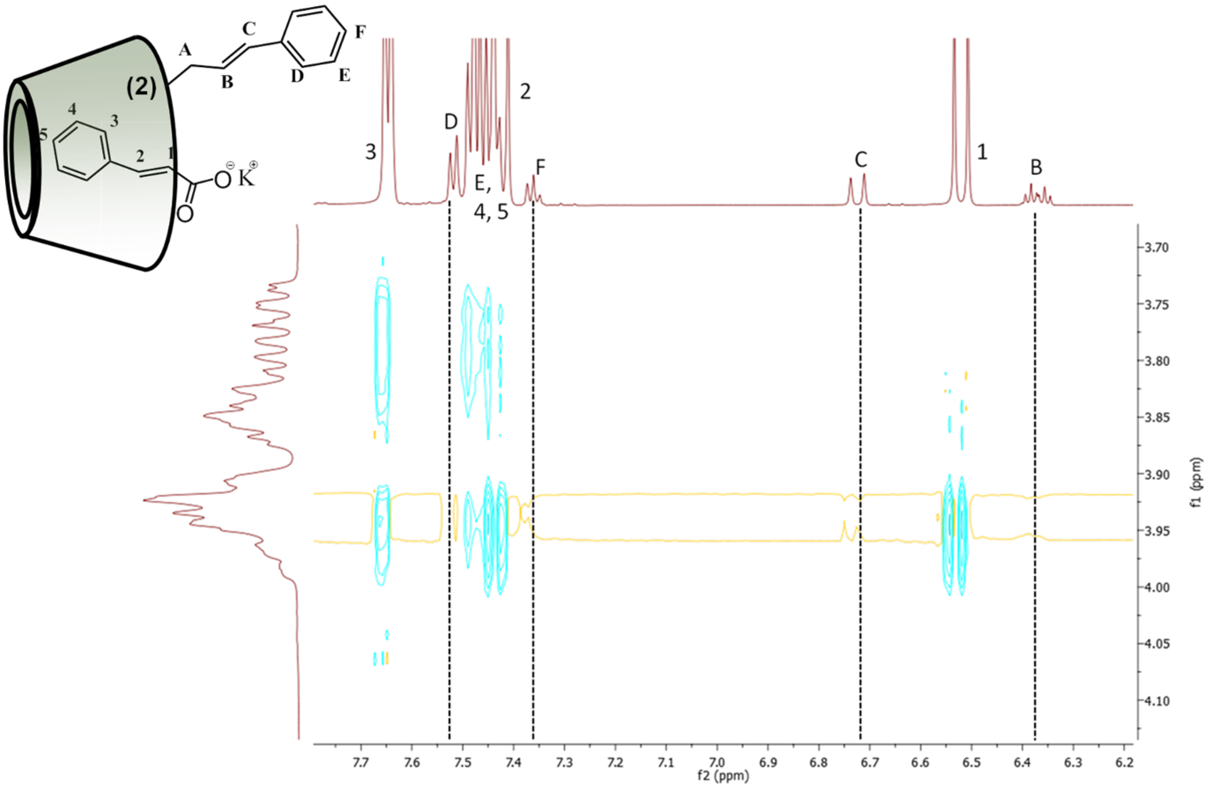

Figure 12: Expansion of the 2D ROESY spectrum of 2-*O*-Cin-α-CD in the presence of CioOK as competitive guest molecule in D_2O at 25 °C.

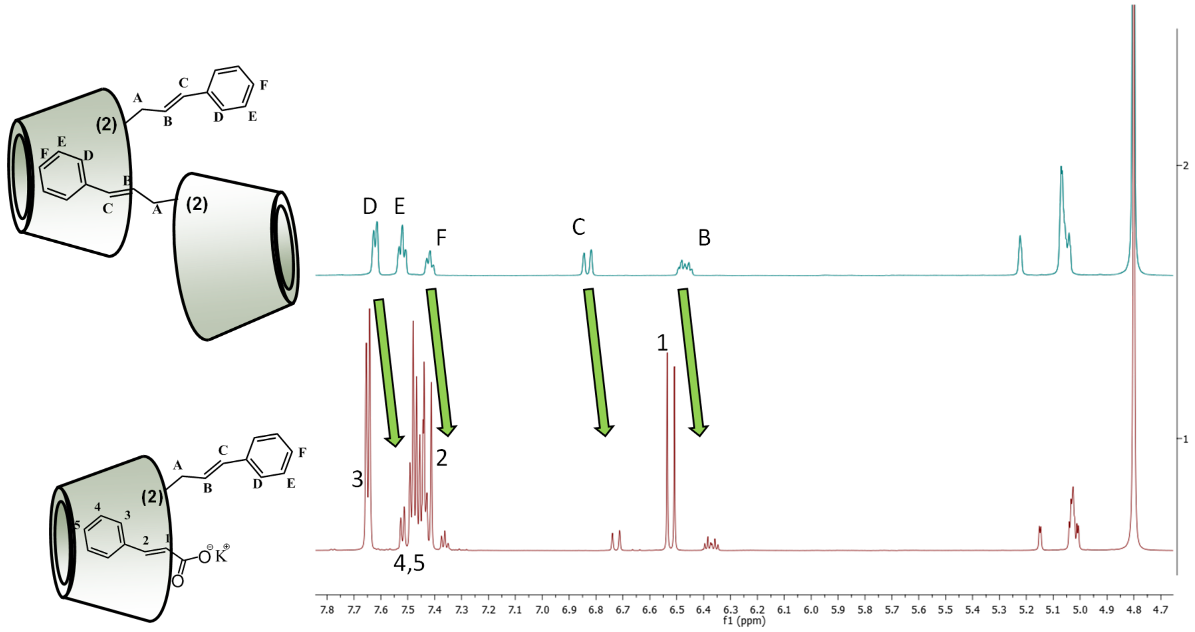

Figure 13: ^{1}H NMR spectrum of 2-*O*-Cin-α-CD before (up) and after (down) the addition of CioOK in 5-fold molar excess in D_2O.

alanine, *N*-FMOC-DL-leucine, DL-3-phenyllactic acid, (*R*)-(−)-mandelic acid). Cations were separated in BGE consisted of 0.11 mol L^{-1} formic acid pH 2.3, while anions were separated in BGE with 10 mmol L^{-1} TRIS, pH 8.0 (pH was adjusted by formic acid). Because of the observation that the temperature differently influenced the size of the aggregates formed by Cin-α-CDs, the measurements were conducted at 25 and 50 °C. Both Cin-α-CD derivatives were added into BGE (pH 2.3 or 8.0) as aqueous solutions with final concentration of 5 or 25 mM. Differences between electrophoretic mobilities of the analytes were evaluated by two-tailed *t*-test.

From all the tested cationic compounds a very significant decrease of the electrophoretic mobility was observed for 4-nitroaniline in the presence of 5 as well as 25 mM 2-*O*-Cin-α-CD in BGE, while electrophoretic mobility of aniline in the presence of 5 mM 2-*O*-Cin-α-CD did not change significantly. This phenomenon is an evidence for the important role of the nitro substituent in the structure of 4-nitroaniline in the interaction with the Cin-α-CD cavity (Figure 14).

N-(1-naphthyl)ethylenediamine significantly interacted with 5 mM 2-*O*-Cin-α-CD, however, the increase of the Cin-α-CD concentrations in BGE up to 25 mM caused stronger interactions with 3-*O*-Cin-α-CD in comparison with 2-*O*-Cin-α-CD. This fact indicates a specific interaction between *N*-(1-naphthyl)ethylenediamine and the 3-*O*-Cin-α-CD cavity.

Effective electrophoretic mobilities of all tested anions (listed above) did not decrease significantly in BGE with 5 mM Cin-α-CDs, although an increased concentration of Cin-α-CDs in BGE to 25 mM caused a decrease of the effective electrophoretic mobilities of all the above-mentioned analytes (cations as well as anions).

Measurements at 50 °C produced the expected results – electrophoretic mobilities of all analytes reached higher values due to lower viscosity of the BGE. Subsequently differences between electrophoretic mobilities with and without Cin-α-CDs in BGE decreased because of smaller size of Cin-α-CDs aggregates.

The studied α-cyclodextrin derivatives offer a potential for employing them in capillary electrophoresis as BGE additives because of their high solubility in aqueous solutions. Therefore, further studies of more advanced BGE additives containing guest and CD units are currently being performed.

Conclusion

In summary, we have presented a straightforward approach towards the synthesis and characterization of two regioisomers of monocinnamyl-α-CD, which allowed their gram-scale preparation and their application as background electrolyte additives in capillary electrophoresis. A set of 2D NMR experiments were used to elucidate the structures of the prepared derivatives, thus to distinguish the two regioisomers. DLS and PFGSE NMR measurements were used to characterize the aggregation behavior of these derivatives and to show that both regioisomers are able to form highly-ordered polymeric structures through intermolecular interactions. The obtained results indicate that the size of these structures can be modulated by external stimuli, such as concentration, temperature or addition of guest molecules. Furthermore we showed that by using a suitable additive – potassium cinnamate as a competitive guest

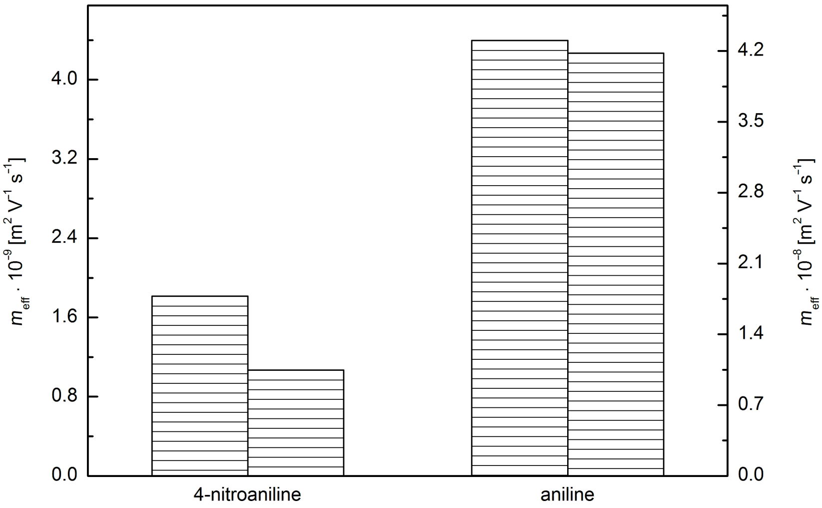

Figure 14: The influence of 5 mM 2-*O*-Cin-α-CD in BGE (right column) on the decrease of the effective electrophoretic mobility of 4-nitroaniline and aniline compared to the mobility in BGE without the additive (left column).

molecule, we can irreversibly inhibit the supramolecular aggregate formation.

Supporting Information

Supporting Information File 1

General experimental procedures, instruments, materials. Detailed experimental procedures and characterization data for newly prepared compounds. Copies of ^{1}H, ^{13}C NMR, 2D NMR spectra of prepared compounds.
[http://www.beilstein-journals.org/bjoc/content/supplementary/1860-5397-12-11-S1.pdf]

Acknowledgements

Financial support from the Grant Agency of the Czech Republic (Project 13-01440S) is gratefully acknowledged.

References

1. Brunveld, L.; Folmer, B. J. B.; Meijer, E. W.; Sijbesma, R. P. *Chem. Rev.* **2001,** *101,* 4071–4097. doi:10.1021/cr990125q
2. Bosman, A. W.; Sijbesma, R. P.; Meijer, E. W. *Mater. Today* **2004,** *7,* 34–39. doi:10.1016/S1369-7021(04)00187-7
3. Crini, G. *Chem. Rev.* **2014,** *114,* 10940–10975. doi:10.1021/cr500081p
4. Szente, L.; Szemán, J. *Anal. Chem.* **2013,** *85,* 8024–8030. doi:10.1021/ac400639y
5. Wenz, G.; Han, B.-H.; Müller, A. *Chem. Rev.* **2006,** *106,* 782–817. doi:10.1021/cr970027+
6. Harada, A.; Takashima, Y.; Yamaguchi, H. *Chem. Soc. Rev.* **2009,** *38,* 875–882. doi:10.1039/b705458k
7. Tran, N. D.; Colesnic, D.; Adam de Beaumais, S.; Pembouong, G.; Portier, F.; Queijo, A. A.; Tato, J. V.; Zhang, Y.; Ménand, M.; Bouteiller, L.; Sollogoub, M. *Org. Chem. Front.* **2014,** *1,* 703–706. doi:10.1039/c4qo00104d
8. Miyauchi, M.; Kawaguchi, Y.; Harada, A. *J. Inclusion Phenom. Macrocyclic Chem.* **2004,** *50,* 57–62. doi:10.1007/s10847-004-8839-3
9. Tomimasu, N.; Kanaya, A.; Takashima, Y.; Yamaguchi, H.; Harada, A. *J. Am. Chem. Soc.* **2009,** *131,* 12339–12343. doi:10.1021/ja903988c
10. Řezanka, M.; Jindřich, J. *Carbohydr. Res.* **2011,** *346,* 2374–2379. doi:10.1016/j.carres.2011.08.011
11. Jindřich, J.; Tislerova, I. *J. Org. Chem.* **2005,** *70,* 9054–9055. doi:10.1021/jo051339c
12. Eliadou, K.; Giastas, P.; Yannakopoulou, K.; Mavridis, M. I. *J. Org. Chem.* **2003,** *68,* 8550–8557. doi:10.1021/jo034503+
13. Avram, L.; Cohen, Y. *J. Org. Chem.* **2002,** *67,* 2639–2644. doi:10.1021/jo016321q
14. González-Gaitano, G.; Rodríguez, P.; Isasi, J. R.; Fuentes, M.; Tardajos, G.; Sánchez, M. *J. Inclusion Phenom. Macrocyclic Chem.* **2002,** *44,* 101–105. doi:10.1023/A:1023065823358
15. Simic, V.; Bouteiller, L.; Jalabert, M. *J. Am. Chem. Soc.* **2003,** *125,* 13148–13154. doi:10.1021/ja037589x
16. Connors, K. A.; Rosanske, T. W. *J. Pharm. Sci.* **1980,** *69,* 173–179. doi:10.1002/jps.2600690215

License and Terms

BEILSTEIN JOURNAL OF ORGANIC CHEMISTRY

Thermal and oxidative stability of Atlantic salmon oil (*Salmo salar* L.) and complexation with β-cyclodextrin

Daniel I. Hădărugă*[1,§], Mustafa Ünlüsayin[2], Alexandra T. Gruia[3], Cristina Birău (Mitroi)[4], Gerlinde Rusu[1] and Nicoleta G. Hădărugă[4]

Full Research Paper

Open Access

Address:
[1]Department of Applied Chemistry, Organic and Natural Compounds Engineering, Polytechnic University of Timişoara, Carol Telbisz 6, 300001 Timişoara, Romania, [2]Department of Fish Processing Technology, Akdeniz University, Dumlupinar Boulevard, Campus Antalya, 07058 Antalya, Turkey, [3]Regional Centre for Immunology and Transplant, County Clinical Emergency Hospital Timişoara, Iosif Bulbuca Blvd. 10, 300736 Timişoara, Romania and [4]Department of Food Science, Banat's University of Agricultural Sciences and Veterinary Medicine "King Mihai I of Romania" - Timişoara, Calea Aradului 119, 300645 Timişoara, Romania

Email:
Daniel I. Hădărugă* - daniel.hadaruga@upt.ro

* Corresponding author
§ Phone +40-256-404224; Fax: +40-256-403060

Keywords:
Atlantic salmon oil (ASO); β-cyclodextrin; differential scanning calorimetry; Karl Fischer titration; omega-3 fatty acid; thermogravimetry

Beilstein J. Org. Chem. **2016,** *12,* 179–191.
doi:10.3762/bjoc.12.20

Received: 18 November 2015
Accepted: 20 January 2016
Published: 02 February 2016

This article is part of the Thematic Series "Superstructures with cyclodextrins: Chemistry and applications III".

Guest Editor: E. Monflier

Abstract

The thermal and oxidative stability of Atlantic salmon oil (*Salmo salar* L.) as well as its β-cyclodextrin (β-CD) complexation ability has been verified for the first time. The main omega-3 fatty acids, EPA and DHA, were significantly degraded, even at 50 °C. Their relative concentrations decrease from 6.1% for EPA and 4.1% for DHA to 1.7% and 1.5% after degradation at 150 °C, respectively. On the other hand, the relative concentrations of monounsaturated and saturated fatty acids remained constant or slightly increased by a few percent after degradation (e.g., from 10.7% to 12.9% for palmitic acid). Co-crystallization of ASO with β-CD at a host–guest ratio of 1:1 and 3:1 from an ethanol–water mixture and kneading methods has been used for the preparation of β-CD/ASO complexes. The analysis of the complexes by thermogravimetry, differential scanning calorimetry (DSC), and Karl Fischer titration (KFT) as well as the decrease of the "strongly-retained" water content confirm the formation of the inclusion compound. Furthermore, the DSC parameters correlate well with the KFT kinetic data for β-CD/ASO complexes.

Introduction

Functional food products containing omega-3 supplementation are becoming more and more popular and are promoted for their beneficial effects on human health, especially in cardiovascular and brain disorders [1,2] as well as for mental health [3-5]. The main source of omega-3 fatty acid (FA) containing compounds is fish oil [6]. Many fish species are used as the oil source. They are called oily fish and those most used as an omega-3 source are herring, sardines, anchovy, mackerel, and tuna [7]. The fish oil can be separated by various methods such as a wet reduction process, enzymatic or autolytic (silage) processes, dry rendering, solvent or supercritical fluid extraction [7-9]. The most important oily compounds are mono- and especially polyunsaturated FAs (MUFAs and PUFAs, respectively), which appear at a concentration of 63–79.5% in Atlantic salmon (*Salmo salar* L.) oil (ASO) [7,9-11]. The content of omega-3 FAs (especially as glycerides) ranges between 1.3–2.2 g/100 g of salmon [9,12]. The health benefit of omega-3 FAs (but especially EPA, (all-*Z*)-5,8,11,14,17-eicosapentaenoic acid and DHA, (all-*Z*)-docosa-4,7,10,13,16,19-hexaenoic acid) in reducing cardiovascular risk by reducing blood lipids (mainly LDL cholesterol and triglycerides), is well known [13,14].

One of the main disadvantages of PUFAs is their low oxidative and thermal stability. The rate of oxidation of such FAs (especially at higher temperatures) drastically increases with the increasing number of double bonds present, even by few thousand times. For example, the relative oxidation rate of α-linolenic acid (an omega-3 FA) is 2500 times higher in comparison with saturated stearic acid [15]. Light (photo-oxidation) and the presence of heavy metal ions, heme and hemin proteins or superoxide radical anion-generating enzymes are involved in the initiation of auto-oxidation. The main intermediates resulting from the oxidation of FAs are monohydroperoxides, hydroperoxy-epidioxides, as well as peroxy-, alkoxy-, and alkyl radicals [16]. Further thermal degradation or fragmentation of these intermediates leads to odor-active carbonyl compounds such as aldehydes, ketones, alcohols and esters, aldehydic acids, alkanes and alkenes [17]. In the case of fish oil, the main odoriferous compounds resulting from oxidation are propanal, pent-1-en-3-one, hex-3-enal, and pent-1-en-3-ol [18-20].

The stabilization of fish oils can be simply performed by using antioxidants. Natural or synthetic antioxidants are often used. Among natural antioxidants, tocopherols and carotenoids are the most appropriate due to their lipophilic characteristics. Significant suppression of the oxidation process was observed for bulk salmon oil in the presence of α-tocopherol and astaxanthin [17]. Other less lipophilic natural antioxidants are flavonoids, anthocyanins and their glycosides. Huber and collaborators [18] revealed the inhibition of PUFA oxidation by quercetin and its 3-*O*-glucoside. They were as effective as butylated hydroxytoluene (BHT, a synthetic antioxidant) against the oxidation of DHA and methylated linolenic acid (MLN) in emulsion. Anthocyanins (as natural extracts) were effective at increasing the stability of salmon oil when incorporated in a hydroxypropyl methylcellulose matrix for obtaining fish oil packaging films [21]. The addition of BHT, propyl gallate and citric acid to the herring byproducts during the process of fish oil production leads to improved stability up to 400% [22]. Smoking the pink salmon before the oil extraction process was another method for reducing the oxidation by forming phenolic antioxidant compounds [23,24].

Another way to stabilize fish oil is microencapsulation using various matrices. Matrices such as chitosan and *N*-lauroyl chitosan [25], *N*-stearoyl-*O*-butylglycerylchitosan [26], mixtures of soybean soluble polysaccharide and octenyl succinic anhydride [27], hydrolyzed soy protein isolate and maltodextrin [20,28], liposomes [29] and even yeast cell autolysate [30] have been used as shell materials. Lemon oil-based nanoemulsions or fuicodan-containing protein-coated oil-in-water emulsions provide good physical and oxidative stability for the emulsified fish oil [31,32]. Spray granulation, spray drying, and freeze drying methods can be used for obtaining fish oil-containing microcapsules [27,33] and spontaneous emulsification for obtaining nanoemulsions [20,31,32].

One nanoencapsulation method of fish oil components is the molecular encapsulation in cyclodextrins (CDs). The latter are natural or synthetically modified, cyclic oligosaccharides comprising 6, 7, and 8 glucopyranose units for the corresponding α-, β-, and γ-CD types [34,35]. The specific structural architecture of CDs having a hydrophilic exterior and hydrophobic inner cavity allows for tin-containing FA moieties from fish oil [36] or other hydrophobic compounds and mixtures to be more easily encapsulated [37-42]. Thus, the access of oxygen to the reactive center is drastically reduced and the stability of unsaturated fish oil components is enhanced. On the other hand, the water solubility of fish oil components can be enhanced by CD complexation. The combination of CD complexation and microencapsulation of fish oil is also used [43,44]. However, no CD complexation studies on ASO have been published up to now.

The goal of this study was to evaluate the thermal and oxidative stability of ASO (*Salmo salar* L.) and the β-CD complexation by using co-crystallization and kneading methods. The β-CD/ASO complexation has been evaluated by means of thermal and Karl Fischer titration (KFT) methods.

Results and Discussion

FA profile of raw and degraded ASO

The quality of the fish oil is strongly related to its FA profile, where PUFAs are the most important FAs. On the other hand, these FAs (and the corresponding glycerides) are easily degraded by oxidation, especially at higher temperatures. An appropriate method for evaluating the overall FA profile is the gas chromatography–mass spectrometry (GC–MS) analysis of the FAs, derivatized to the corresponding methyl esters. The relative concentration of these FA methyl esters (FAMEs) can indicate the stability and/or the degradation level of the ASO in a simple and relevant way. MUFAs were the most concentrated in the raw ASO (Table 1). The highest relative concentration of 35.6% was found for oleic acid methyl ester. On the other hand, PUFAs had a total concentration of 25.4% and the main FAMEs were linoleic acid methyl ester (11.2%), EPA methyl ester (6.1%) and DHA methyl ester (4.1%). Myristic, palmitic and stearic acid methyl esters were the most important saturated fatty acids (SFAs) (3.5%, 10.7% and 2.7%, respectively). Some of the FAMEs could not be clearly identified, even when their MS spectra indicated the class of these compounds. All of them had a relative concentration lower than 0.05%. These results are in good agreement with those obtained by Bencze Rørå and collaborators [23]. They determined a DHA concentration of 4.5% (as methyl ester from the total FAMEs) for the oil from raw fillets obtained from Atlantic salmon, where the diet was supplemented with soybean oil. On the other hand, the concentration of EPA was lower (2.9%). A feeding diet containing various fish and vegetable oils significantly influences the FA profile of ASO. Thus, the EPA and DHA content (as methyl esters) varies in the range of 4.6–6.9% and 6.4–13.6%, respectively [12].

Table 1: Relative concentrations of FAs (as methyl esters) obtained from the GC–MS analysis of the derivatized, raw, Atlantic salmon oil (ASO) and those degraded at low (50 °C, code ASO50) and high (150 °C, code ASO150) temperatures.

Entry	Name[a]	KI[b]	Code[c]	Class[d]	Area (ASO) (%)[e]	Area (ASO50) (%)[e]	Area (ASO150) (%)[e]
1	Myristic	1734	$C_{14:0}$	SFA	3.46 ± 0.301	3.34 ± 0.203	3.33 ± 0.727
2	Pentadecanoic	1835	$C_{15:0}$	SFA	0.23 ± 0.012	0.36 ± 0.079	0.43 ± 0.009
3	7,10,13-Hexadecatrienoic	1900	$C_{16:3}$	PUFA	0.31 ± 0.003	0.27 ± 0.045	0.46
4	Palmitoleic	1916	$C_{16:1}$	MUFA	3.50 ± 0.091	3.31 ± 0.215	2.84 ± 0.831
5	Palmitic	1941	$C_{16:0}$	SFA	10.69 ± 0.78	11.35 ± 0.35	12.94 ± 2.26
6	Margaric	2039	$C_{17:0}$	SFA	0.14 ± 0.006	0.20	–
7	Polyunsaturated fatty acid[f]	2096	$C_{20:4}^{\#}$	PUFA	1.35 ± 0.025	0.78 ± 0.135	–
8	Linoleic	2108	$C_{18:2}$	PUFA	11.20 ± 0.29	11.29 ± 0.11	9.10 ± 2.19
9	Oleic	2121	$C_{18:1}$	MUFA	35.60 ± 1.77	37.64 ± 0.39	35.08 ± 6.85
10	Stearic	2148	$C_{18:0}$	SFA	2.68 ± 0.082	2.79 ± 0.060	3.13 ± 0.645
11	Polyunsaturated fatty acid[f]	2165	$C_{20:4}^{\#}$	PUFA	0.13 ± 0.038	–	–
12	Monounsaturated fatty acid[f]	2190	$C_{18:1}^{\#}$	MUFA	0.69 ± 0.402	2.56 ± 0.034	3.09
13	Nonadecanoic	2255	$C_{19:0}$	SFA	–	–	–
14	EPA (5,8,11,14,17-eicosapentaenoic)	2309	$C_{20:5}$	PUFA	6.10 ± 0.378	2.17 ± 0.370	1.74 ± 0.783
15	Polyunsaturated fatty acid[f]	2322	$C_{20:3}^{\#}$	PUFA	0.84 ± 0.179	0.37	1.16
16	11-Eicosenoic	2347	$C_{20:1}$	MUFA	0.62 ± 0.015	0.48 ± 0.014	–
17	Polyunsaturated fatty acid[f]	2404	$C_{20:5}^{\#}$	PUFA	–	–	–
18	Polyunsaturated fatty acid[f]	2429	$C_{20:5}^{\#}$	PUFA	–	–	–
19	Polyunsaturated fatty acid[f]	2523	$C_{20:5}^{\#}$	PUFA	–	–	–
20	DHA (4,7,10,13,16,19-docosahexaenoic)	2573	$C_{22:6}$	PUFA	4.13 ± 0.731	1.70 ± 0.315	1.45 ± 0.482
21	Polyunsaturated fatty acid[f]	2591	$C_{20:5}^{\#}$	PUFA	1.37 ± 0.211	–	–
22	Polyunsaturated fatty acid[f]	2709	$C_{20:5}^{\#}$	PUFA	–	–	–
23	Erucic	2784	$C_{22:1}$	MUFA	1.57	2.45 ± 0.322	1.73 ± 0.445
24	Behenic	2855	$C_{22:0}$	SFA	–	–	–
25	Nervotic	3173	$C_{24:1}$	MUFA	–	–	–
26	Other minor compounds[g]				15.39	18.94	23.52
	Total quantified FAs (%)				84.61	81.06	76.48
	Total SFAs (%)				17.2	18.04	19.83
	Total MUFAs (%)				41.98	46.44	42.74
	Total PUFAs (%)				25.43	16.58	13.91

[a] The FAME name; [b] Kovats index (calculated according to C_8–C_{20} alkane standard solution GC data; higher KI values were obtained by extrapolation); [c] the corresponding FA code ($C_{x:y}$ represents the fatty acid containing “x” carbon atoms and “y” double bonds; [d] SFA – saturated fatty acid, MUFA – monounsaturated fatty acid, PUFA – polyunsaturated fatty acid; [e] the FAME concentration, calculated as the percent ratio between the GC peak area of the compound and the sum of all GC peak areas; [f] isomers are indicated by “#” (using only the MS data and not the standard FAMEs); [g] the other minor compounds were FAMEs having concentrations lower than 0.05% or they do not belong to this class (e.g., aldehydes).

The high content of MUFAs and PUFAs in the ASO (42% and 25.4%, respectively) is correlated to a higher susceptibility to oxidation, especially at elevated temperatures. Consequently, two degradation temperatures named low (50 ± 1 °C) and high (150 ± 1 °C) have been proposed. The total FA content decreases after degradation at high temperature (from 84.6% to 76.5%, Table 1). This variation is especially due to the degradation of the PUFAs (as glycerides or free FAs). The total PUFA content decreases from 25.4% in raw ASO to 16.6% and 13.9% for fish oil degraded at low and high degradation temperatures, respectively. On the contrary, the total SFA content increases from 17.2% to 19.8%. This fact is due to the higher oxidative stability of the SFAs, even the MUFAs had higher stability in comparison with PUFAs by means of the total content. Unfortunately, they are isomerized to the corresponding "bad" *trans*-diastereoisomers at high degradation temperatures, without modifying the structural class [36]. More interesting is the variation of the individual FAs (such as methyl ester) with the degradation temperature. While the myristic acid content was almost constant in the FAME mixtures (3.3–3.5%), an increase of the relative concentrations of palmitic and stearic acids was observed (from 10.7% to 12.9% and from 2.7% to 3.1%, respectively; Table 1). On the other hand, the most significant omega-3 fatty acids, EPA and DHA, are easily degraded even at low temperatures. Thus, the relative concentration of the EPA methyl ester decreases from 6.1% to 2.2% after oxidative degradation at 50 °C and to 1.7% after degradation at high temperature. A similar behavior was observed for the case of DHA (from 4.1% to 1.7% and 1.45%, respectively). This observation is in good agreement with the energy requirement for H-atom abstraction in the oxidation process. It varies from 422 kJ·mol^{-1} for the case of a terminal methyl and 322 kJ·mol^{-1} for a single allyl group (for MUFAs and their glycerides) to 272 kJ·mol^{-1} for the C–H disruption in the case of a methylene group of a 1,4-pentadiene system (which often appear in the PUFAs and their corresponding glycerides) [15]. This thermodynamic behavior increases the oxidation rate of α-linolenic acid (an omega-3 FA) by 2500 times in comparison with the corresponding saturated compound, i.e., stearic acid. Furthermore, it was observed that the concentration of conjugated dienes (not counted as PUFAs) remarkably increased after oxidative degradation of fish oil [17,21]. These studies also support our results on thermal and oxidative degradation of ASO at low and high temperature degradation conditions.

Preparation and analysis of β-CD/ASO complexes

β-CD/ASO complexes were obtained by using two different methods: co-crystallization from an ethanol–water mixture and by kneading techniques. No literature data on β-CD/ASO complexes have been reported yet. The reason for choosing the controlled crystallization of β-CD/ASO complexes was related to the possibility to attain the equilibrium between the noncomplexed and complexed fish oil components and to obtain a more "pure" complex. The crystals will be mainly formed by CD/bioactive compound complex than by noncomplexed components (CD and FA glycerides). Such a complex is easier to characterize, even if the total recovered yield is low. On the other hand, the kneading method provides CD complexes at a higher recovered yield, but there is a nonuniform mixture of noncomplexed and complexed CD and fish oil components. Thus, the recovered yield (calculated as the percent ratio between the mass of the dried complex and the sum of the ASO and hydrated β-CD masses) was 39.6 ± 0.03% and 58.30 ± 9.81% for the β-CD/ASO complex at a molar ratio of 1:1, obtained by co-crystallization and kneading methods, respectively. For the preparation of the β-CD/ASO complex at a molar ratio of 3:1, the corresponding recovered yields were 75.13 ± 1.66% and 79.15 ± 4.64%, respectively. The recovered yield of the β-CD/ASO complex is significantly lower for the 1:1 molar ratio in comparison with the 3:1 molar ratio. However, these values were higher for the kneading method. These results can be explained by the molecular encapsulation of FA glycerides by CDs, which theoretically implies a 3:1 molecular ratio (further studies are needed). A high content of fish oil remains nonencapsulated. It is washed with ethanol during the separation process for the 1:1 molar ratio.

The analysis of the β-CD/ASO complexes was focused on the evaluation of the water content and the type of water molecules (i.e., the behavior of the water during the various analyses). This approach provided the main assessment of the molecular encapsulation process.

Thermogravimetric (TG) analysis

TG analysis of β-CD/ASO complexes can furnish information on the behavior during heating. Both β-CD and its complexes release water (and possibly other solvents used in the complexation process) up to ≈140 °C, but mainly up to 100 °C. ASO components are nonvolatile and the mass variation up to 250 °C is very low and almost null for β-CD. After this temperature, the degradation of β-CD as well as the fish oil components occurs. The mass loss for the first temperature interval is almost 13% for β-CD, while for complexes it was 8.93 ± 0.50% and 6.62 ± 0.17% for the 1:1 and 3:1 molar ratio using the co-crystallization method, respectively. These values were more similar in the case of the kneading method (7.00 ± 0.46% and 6.74 ± 1.15%, respectively) (Figure 1). On the other hand, the mass loss up to the start of the β-CD degradation is significant for complexes obtained by the co-crystallization method at a 1:1 molar ratio (1.8 ± 0.54%, see Supporting Information File 1 for details). This can be due to the release of "strongly-retained"

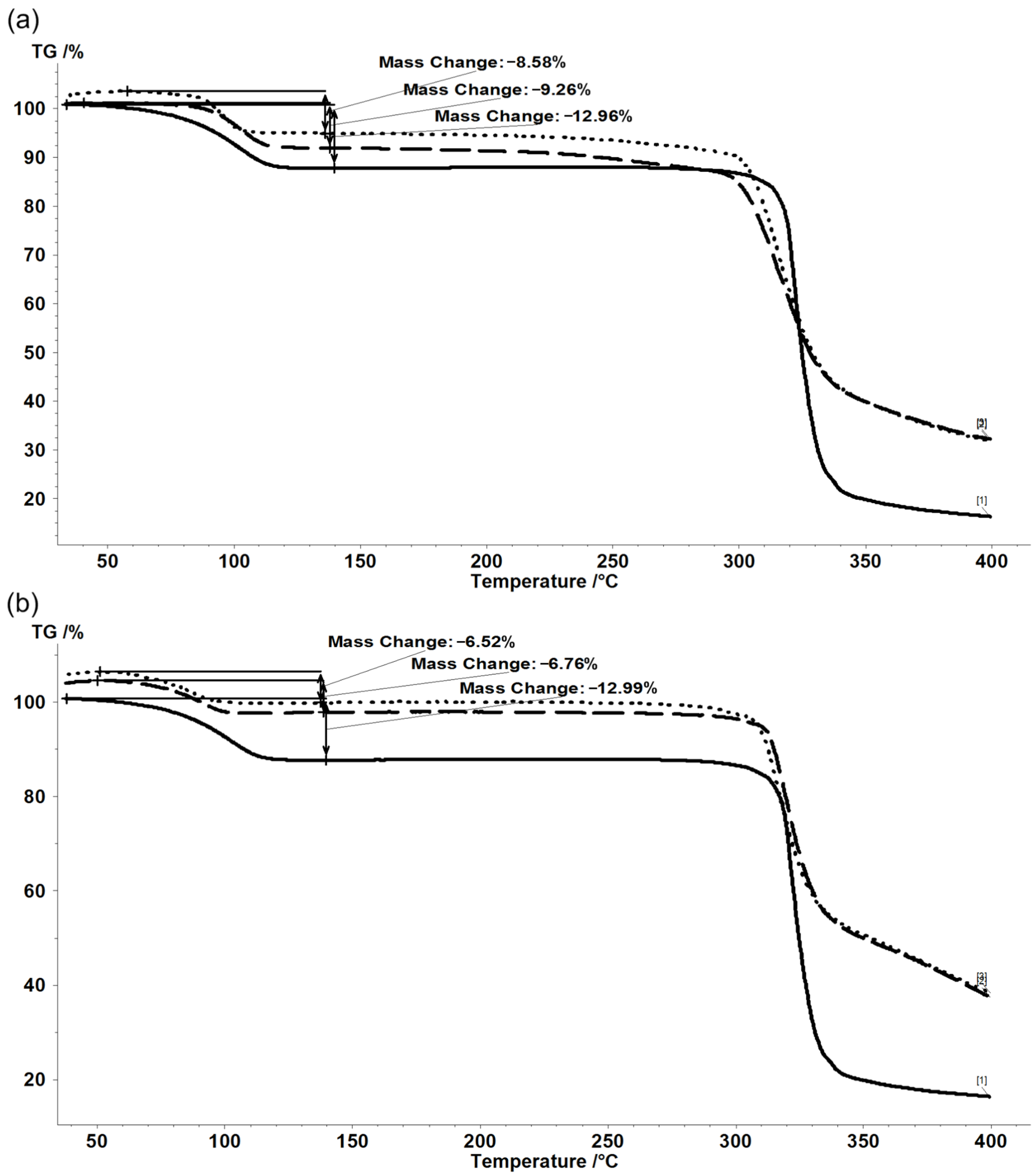

Figure 1: Superimposed thermograms for β-CD (solid line) and (a) β-CD/ASO_1:1_a&b (duplicate) or (b) β-CD/ASO_3:1_a&b (duplicate). For sample name abbreviations, see Table 3.

water and other solvents at higher temperatures. One of the most important parts is the release of water from complexes. According to the TG analysis, the water content is 4.1–6.4% lower than for the β-CD. This observation supports the formation of the inclusion compound by partial replacement of the hydration water from the CD cavity by the guest compounds (FA glycerides). Studies on the evaluation of water and solvent contents in host–guest supramolecular systems by thermal analyses have already been performed for CD/flavonoid and CD/essential oil complexes [37,39].

Differential scanning calorimetry (DSC) analysis

DSC can provide further information on the physical and chemical processes occurring during heating, even if the guest compound is not volatile up to the CD degradation temperature. Commercial β-CD has two important DSC peaks corresponding to the release of both “surface” and “strongly-retained” water molecules at 105 °C and to the β-CD decomposition at 319.6 °C (Figure 2). The decomposition of β-CD from its fish oil complexes also occurs in the temperature range close to

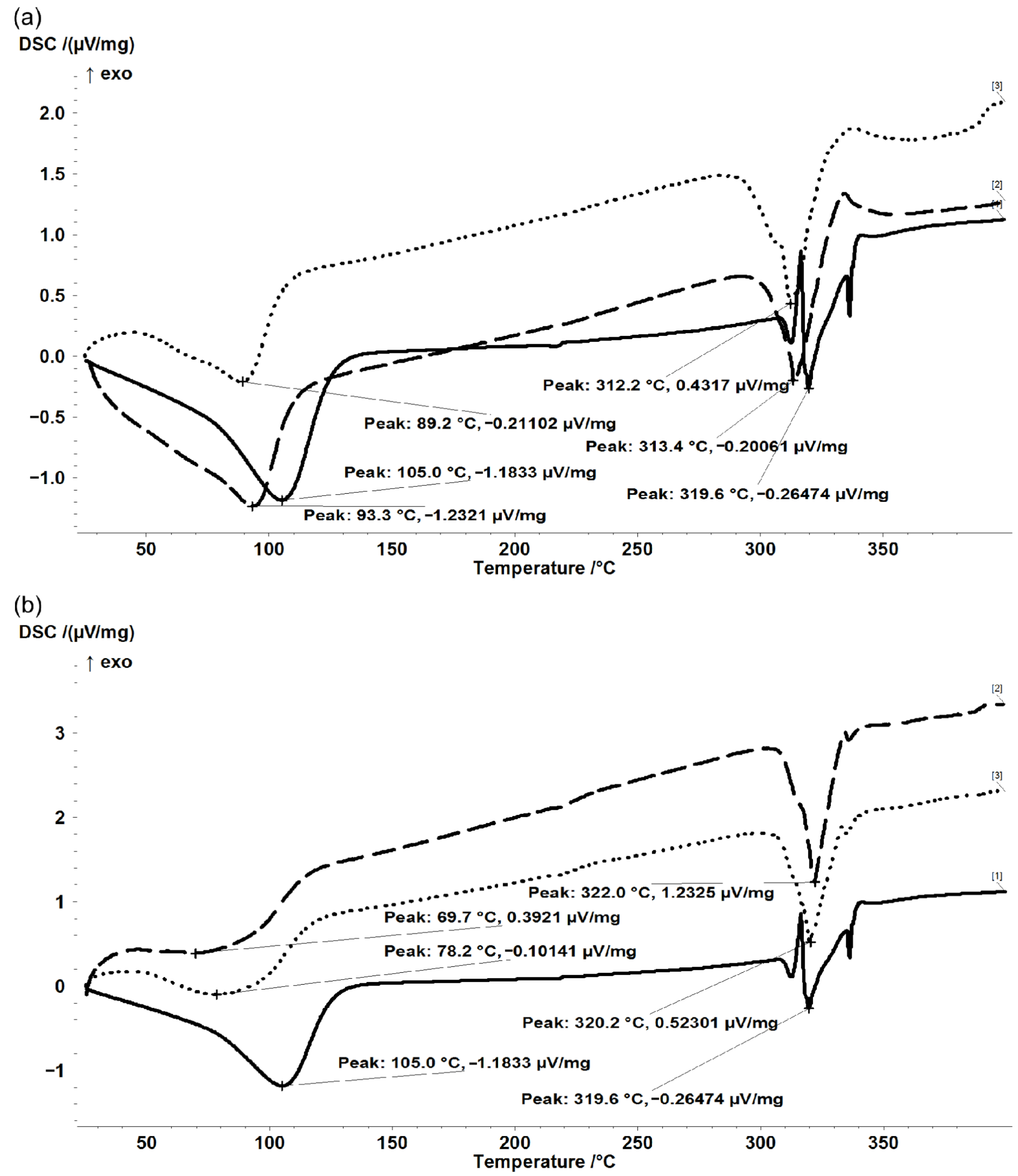

Figure 2: Superimposed DSC data for β-CD (solid line) and (a) β-CD/ASO_3:1_a&b (duplicate) or (b) β-CD/ASO_3:1(k)_a&b (duplicate). For sample name abbreviations, see Table 3.

noncomplexed β-CD, especially for the kneading method (319.3 ± 2.9 °C) (see Supporting Information File 1 for all information related to the DSC analysis). One of the most important DSC peaks is that related to water release. It was evident that the 1:1 molar ratio is not appropriate for molecular encapsulation of ASO glycerides in β-CD because the DSC peak corresponding to water release appears at similar or even higher temperature values (103 ± 5 °C and 121 ± 4 °C for co-crystallization and kneading methods, respectively, Figure 2). These values also suggest a significant content of “strongly-retained” water in the complex, which can be due to the presence of noncomplexed or not completely complexed β-CD. The differences for the case of 3:1 molar ratio complexes are evident. The DSC peak temperatures corresponding to water release decreases to 91.3 ± 2.9 °C and 74 ± 6.0 °C for the co-crystallization and kneading methods, respectively (Figure 2 and Supporting Information File 1). The decrease of these DSC peak temperatures can be explained by the formation of the host–guest molecular inclusion compound that allows replacement of the "strongly-retained" water molecules inside the cavity by the hydrophobic FA moieties from ASO. The β-CD/ASO complex mainly contains "surface" water molecules that are easier to be released [45]. On the other hand, the calorimetric effect corresponding to water release is strongly reduced after complexation from 279.6 $\mu V\cdot s\cdot mg^{-1}$ to 129.2 ± 14.9 $\mu V\cdot s\cdot mg^{-1}$ for the co-crystallization method and 101.3 ± 17.3 $\mu V\cdot s\cdot mg^{-1}$ for the kneading method. This means that the total water content is lower and/or more weakly physically bound in the β-CD/ASO complex structure in comparison with the case of noncomplexed β-CD. However, the quantification of the total "surface" and "strongly-retained" water content is very difficult by thermal methods.

Karl Fischer titration (KFT) analysis

KFT analysis can provide more accurate results on the water content and release from β-CD/ASO complexes. The advantages of this chemical method in comparison with other classical methods (e.g., oven drying or similar drying methods) is related to the selectivity for water (no other compounds such as solvents or volatiles will be detected), the controllable analysis temperature (room temperature or a preset lower/higher temperature can be used), and the diffusion of water to the surface of the CD complex particle, which is enhanced by the possibility to control the hydrophobicity of the solvent mixture used for KFT analysis [45-50].

The total water content of 13.7 ± 0.2% for β-CD as determined by KFT analysis (Table 2) is higher than the TG mass loss corresponding to the water release, even up to 140 °C (≈13%). The water content of β-CD/ASO complexes is significantly lower, especially for the case of the co-crystallization method (7.30 ± 0.27% and 8.96 ± 0.15% for 1:1 and 3:1 molar ratio, respectively). The variation in the total water content of the β-CD/ASO complexes obtained by the kneading method is similar, but the values are higher (8.60 ± 0.41% and 11.60 ± 0.34%, respectively). The KFT results are in agreement with the TG data on the dissimilarity between noncomplexed and complexed β-CD. On the other hand, the overall water content is higher than the TG mass loss that corresponds to the water (or other solvent) release from the β-CD and its fish oil complexes. A higher water content for the complexes obtained at a 3:1 molar ratio by using both the co-crystallization and kneading methods has been observed (difference of 1.7–3% in comparison with the complexes obtained at 1:1 molar ratios; see Table 2). It is obvious that a higher molar content on β-CD in the complex leads to a higher content of water, especially for the case of the kneading method. This observation also agreed with the recovered yield of β-CD/ASO complexes (yield of 39.6% and 58.3% / water content of 7.3% and 9% for 1:1 molar ratio and recovery yield of 75.1% and 79.2% / water content of 8.6% and 11.6% for 3:1 molar ratio).

KFT is a valuable technique for evaluating the diffusion of water molecules inside the β-CD/ASO complex particles that are not soluble in the KFT working medium (generally methanol). Thus, the variation of the titration volume in time can be correlated to the variation of the water consumption in time (or variation of water concentration; see Figure 3 for the KF reaction, where "B" represents an organic base) by knowing the volume of the reaction medium (which was 30 mL and increases during titration by a maximum of 4 mL; this was also accounted for) and the titer of the iodine solution (4.9447 ± 0.1759 mg $H_2O\cdot mL^{-1}$). Three important pseudo-linear ranges on the KFT titration volume versus time plots can be observed (Figure 4 and Figure 5; see also Supporting Information File 1). In the first range of ≈10–30 s the water very

Table 2: Water content and mean water reaction rates, v, in the main time ranges (10–30 s and 30–90 s) of β-CD/ASO complexes and commercial β-CD obtained by the KFT method.

Entry	Code	Water content (%)	"Surface" water reaction rate, v_1 ($mM\cdot s^{-1}$)[a]	"Strongly-retained" water reaction rate, v_2 ($mM\cdot s^{-1}$)[a]
1	β-CD	13.69 ± 0.21[b]	0.445 ± 0.136	0.055 ± 0.017
2	β-CD/ASO_1:1_a	7.49 ± 0.67[c]	0.039 ± 0.006	0.025 ± 0.002
3	β-CD/ASO_1:1_b	7.11 ± 0.57[d]	0.034 ± 0.003	0.021 ± 0.002
4	β-CD/ASO_3:1_a	9.06 ± 0.22[e]	0.109 ± 0.011	0.036 ± 0.005
5	β-CD/ASO_3:1_b	8.85 ± 0.25[d]	0.124 ± 0.026	0.033 ± 0.004
6	β-CD/ASO_1:1(k)_a	8.88 ± 0.29[c]	0.146 ± 0.021	0.034 ± 0.006
7	β-CD/ASO_1:1(k)_b	8.31 ± 0.25[d]	0.049 ± 0.011	0.026 ± 0.004
8	β-CD/ASO_3:1(k)_a	11.84 ± 0.19[d]	0.198 ± 0.020	0.021 ± 0.003
9	β-CD/ASO_3:1(k)_b	11.36 ± 0.26[c]	0.181 ± 0.034	0.053 ± 0.006

[a] v_1 and v_2 represent the mean water reaction rates from the KFT analysis for the time intervals corresponding to "surface" water (10–30 s) and "strongly-retained" water molecules (30–90 s), respectively; the number of replicates were [b]eight, [c]six, [d]seven and [e]five.

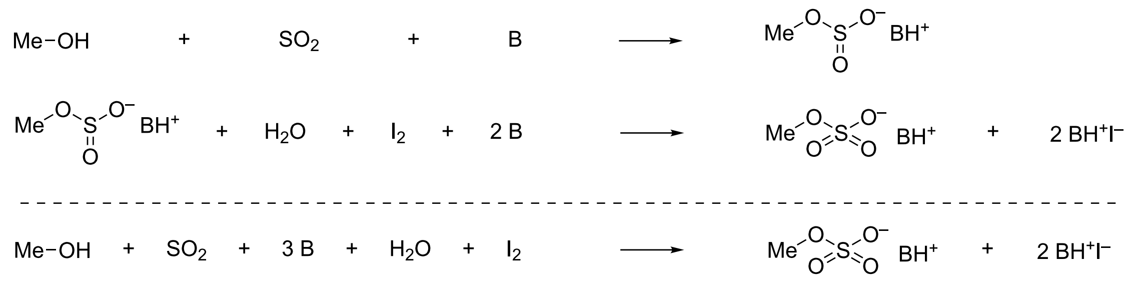

Figure 3: The equation of the KF chemical reaction.

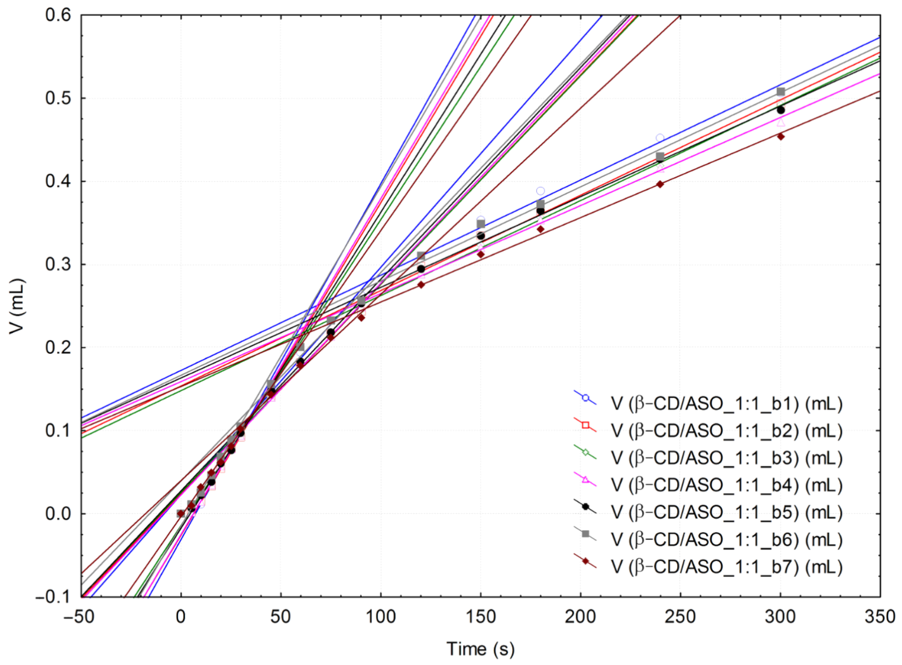

Figure 4: Superimposed volume versus time linear correlations (all three specific intervals) from the KFT analysis of β-CD/ASO_1:1 (only the second replicate "b" of the complex is presented; there are seven determinations).

rapidly reacts and was considered as "surface" water [47]. The second interval corresponds to the reaction of water molecules that slowly diffuse from the inside of the complex particles (so-called "strongly-retained" water molecules) and the pseudo-linear time range is ≈30–90 s. The last interval is related to the "normal" drift of the KFT process (possible some of the "strongly-retained" water molecules can be titrated during this interval). Consequently, the variation of the water consumption over the specified time intervals represents the mean water reaction rate, v. Therefore by comparing the values of v for different β-CD/ASO complexes and β-CD, it is possible to evaluate the success of the molecular encapsulation process. The main difference between β-CD and its complexes for the "surface" water was observed (Table 2). The corresponding water reaction rate decreases from 0.45 mM·s^{-1} for commercial β-CD to 0.04–0.2 mM·s^{-1} for the corresponding ASO complexes. Complexes obtained by the kneading method had higher "surface" water reaction rates than those obtained by the co-crystallization method. Furthermore, complexes obtained by using a 3:1 molar ratio revealed higher "surface" water reaction rates. On the other hand, the "strongly-retained" water reaction rates for complexes had lower values, especially for products obtained by co-crystallization at a 1:1 molar ratio (Table 2). The results of the KFT kinetics indicate that the diffusion of "surface" water is lower in complexes than in commercial β-CD particles and even up to ten times slower for complexes obtained at a 1:1 molar ratio. The diffusion of "strongly-retained" water in complexes is similar to the case of commercial β-CD. Therefore, the hydrated β-CD/ASO complexes have a relatively low content of "surface" water that can be easily released,

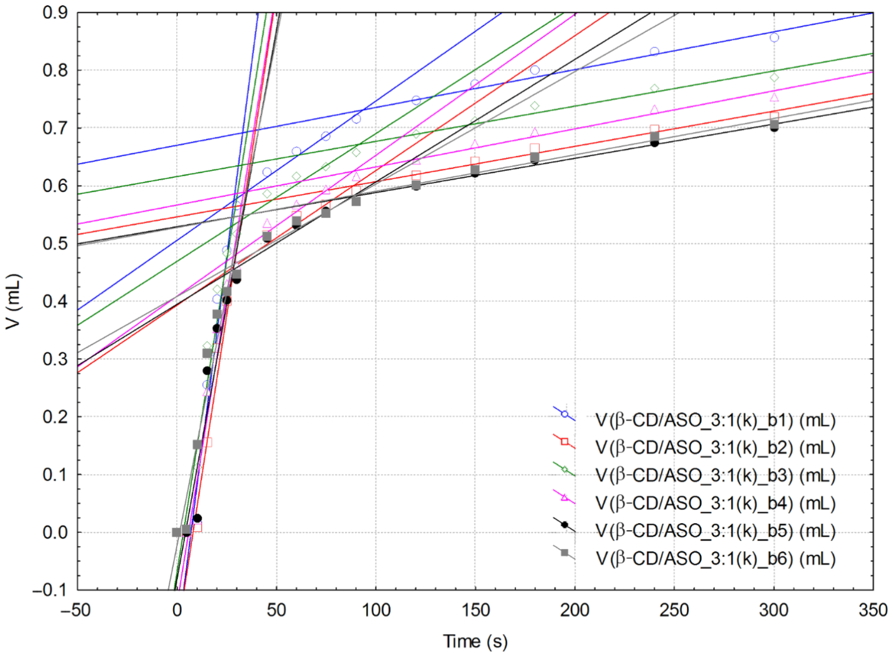

Figure 5: Superimposed volume versus time linear correlations (all three specific intervals) from the KFT analysis of β-CD/ASO_3:1(k) (only the second replicate “b” of the complex is presented; there are six determinations).

while the “strongly-retained” water molecules have similar behavior similar to β-CD. However, the overall water content is drastically reduced after complexation and the ratio between the volumes of the titrant corresponding to “surface” and “strongly-retained” water can furnish further information on the molecular encapsulation efficiency (further studies are needed).

Thermal analysis – KFT correlations

Thermal analysis methods such as TG and DSC provide information on the releases of volatile compounds and on the energetic effect of these processes (as well as other ones), but no differentiation between compounds can be established. On the other hand, KFT provides a selective determination for water. Consequently, the correlation between the thermal and KFT water/volatile-related parameters can indicate the accuracy of the analyses and the performance of the molecular inclusion process.

Generally, the differences between values of the thermal and KFT parameters for noncomplexed β-CD and β-CD/ASO complexes are significant and the correlation equations lead to valuable correlation coefficients. However, the other statistical parameters for such correlational equations are not appropriate because β-CD and the group of complexes provide a statistically nonsignificant correlation. Consequently, the statistically valuable correlation equations between thermal and KFT water-related parameters in the β-CD/ASO complex class (without β-CD) were obtained. Statistically significant correlation equations between DSC peak parameters corresponding to water/volatile compound (solvents) release and KFT parameters for β-CD/ASO complexes have been obtained. It is evident that the DSC peak temperature corresponding to water release ($Peak_{(\text{DSC-Water})}$ parameter) increases with the decrease of the total KFT water content ($Water_{(\text{KFT})}$ parameter) or the “surface” water reaction rate ($v_{1(\text{KFT})}$ parameter) (Equation 1 and Equation 2). This observation supports the fact that a high content of “surface” water in β-CD complexes leads to a lower value for the corresponding DSC peak (“surface” water is released at lower temperature). Moreover, the “surface” water that corresponds to the lower DSC peak temperature results in a higher water reaction rate.

$$Peak_{(\text{DSC-Water})} = 172.157(\pm 28.087) \\ -8.214(\pm 3.037) \cdot Water_{(\text{KFT})} \tag{1}$$

$n = 8$, $r = 0.741$, $s = 13.6$, $F = 7.3$

$$Peak_{(\text{DSC-Water})} = 118.755(\pm 11.099) \\ -195.048(\pm 88.573) \cdot v_{1(\text{KFT})} \tag{2}$$

$n = 8$, $r = 0.669$, $s = 15.0$, $F = 4.8$

The finding from the DSC–KFT correlations is also supported by the correlational equation between the total water content of β-CD/ASO complexes, $Water_{(\text{KFT})}$, and the mean water reaction rate, $v_{1(\text{KFT})}$ (Equation 3). Statistically significant equations were obtained even when β-CD is included in analysis (Equation 4).

$$Water_{(\text{KFT})} = 6.420(\pm 0.495) + 24.482(\pm 3.953) \cdot v_{1(\text{KFT})} \quad (3)$$

$n = 8$, $r^2 = 0.930$, $s = 0.67$, $F = 38.4$

$$Water_{(\text{KFT})} = 7.253(\pm 0.461) + 16.091(\pm 2.431) \cdot v_{1(\text{KFT})} \quad (4)$$

$n = 9$, $r = 0.929$, $s = 0.87$, $F = 43.8$

Conclusion

ASO is very unstable even at low degradation temperature. The relative concentration of the primary and most valuable compounds, EPA and DHA, is strongly reduced after thermal and oxidative degradation. It is obvious that protection against oxidation for these omega-3 fatty acid glycerides is needed. Thus, good yields from preparation of β-CD/ASO complexes by co-crystallization and kneading have been obtained. Furthermore, thermal and KFT analyses support the conclusion of formation of the β-CD/FA glyceride inclusion complex by means of water behavior. Hydration water is easier released from the β-CD/ASO complexes obtained at a 3:1 molar ratio. Both DSC and KFT analyses demonstrate this finding with a lower peak temperature and lower “strongly-retained” water reaction rate, respectively. The total water content (evaluated by both TG and KFT analyses) and the DSC calorimetric effect related to water release are significantly lower in the case of β-CD/ASO complexes in comparison with commercial β-CD. All these analyses performed for the first time for the stabilized β-CD/ASO complexes confirm the formation of the inclusion compound.

Experimental

Materials

Atlantic salmon (*Salmo salar* L.) was obtained from the local market (Timişoara, Romania) as a raw product in the spring of 2014. It was an aquaculture product of Norwegian origin. Only the meaty fish parts were used for oil extraction. GC-grade hexane (Sigma-Aldrich) was the main solvent used for raw and degraded fish oil dilutions. The Supelco 37 Component FAME mix (Sigma-Aldrich) and C_8–C_{20} alkane standard solution (Fluka Chemie AG) were the main tools for identifying the FAMEs in derivatized raw and degraded fish oil. Anhydrous sodium sulfate (p.a., Merck & Co.) was used for drying the raw

Table 3: Abbreviations used.

Abbreviation	Full text
ANOVA	analysis of variance
ASO	Atlantic salmon oil
β-CD	β-cyclodextrin
β-CD/ASO_1:1_a&b	β-cyclodextrin/Atlantic salmon oil complex obtained by co-crystallization at a 1:1 molar ratio (duplicates “a” and “b”)
β-CD/ASO_1:1(k)_a&b	β-cyclodextrin/Atlantic salmon oil complex obtained by kneading at a 1:1 molar ratio (duplicates “a” and “b”)
β-CD/ASO_3:1_a&b	β-cyclodextrin/Atlantic salmon oil complex obtained by co-crystallization at a 3:1 molar ratio (duplicates “a” and “b”)
β-CD/ASO_3:1(k)_a&b	β-cyclodextrin/Atlantic salmon oil complex obtained by kneading at a 3:1 molar ratio (duplicates “a” and “b”)
BHT	butylated hydroxytoluene
DHA	(all-*Z*)-docosa-4,7,10,13,16,19-hexaenoic acid
DSC	differential scanning calorimetry
EPA	(all-*Z*)-5,8,11,14,17-eicosapentaenoic acid
FA	fatty acid
FAME	fatty acid methyl ester
GC–MS	gas chromatography–mass spectrometry
KFT	Karl Fischer titration
KI	Kovats index
LDL	low-density lipoprotein
MLN	methylated linolenic acid
MUFA	monounsaturated fatty acid
PUFA	polyunsaturated fatty acid
SFA	saturated fatty acid
TG	thermogravimetry

and degraded fish oil solutions. β-CD hydrate (>98%) from CycloLab (Budapest, Hungary) was used for ASO molecular encapsulation. Ethanol 96% (v/v, Chimopar, Bucharest, Romania) was used for β-CD complexation of ASO. A boron trifluoride–methanol complex (20%, Merck & Co., Inc.) was used for FA derivatization. Finally, Hydranal-Titrant 5, Hydranal-Solvent and Hydranal-Water Standard 10.0 (Sigma-Aldrich, Buchs, Switzerland) were used for the KFT water analysis of β-CD/ASO complexes.

ASO extraction

The extraction of raw ASO was performed by a cooking and pressing method. The salmon was boiled for 20 min at a fish/water ratio of 1:2 at 112–114 °C under a pressure of 1.5–1.6 atm in a 5 L aluminum reactor. The crude extract was cooled and filtered, while the fish residue was pressed in a strainer-pressing tool, and the raw oil was separated from the aqueous layer. The raw ASO was centrifuged for 20 min at 9600*g* and 4 °C. The obtained clear ASO was stored at 4 °C in the refrigerator until use.

Degradation of ASO

The ASO was degraded under thermal and oxidative conditions. The degradation was performed in a temperature-controlled oven (Nabertherm L1/12, Lilienthal, Germany) in air at atmospheric pressure (70% relative humidity). The ASO was uniformly distributed on the bottom of the glass flask. Approximately 50 mg of fish oil were needed to obtain a thin film on a plate surface of 315 cm^2. Two degradation temperatures were chosen: a low temperature of 50 °C and a high temperature of 150 °C. The degradation time was 2 h. After the degradation reaction and cooling of the samples, the degradation products were extracted with 4 mL of hexane. The solution was dried over anhydrous sodium sulfate and subjected to derivatization.

Preparation of β-CD/ASO complexes

β-CD/ASO complexes were prepared by two methods: (1) the co-crystallization from an ethanol–water mixture, which allows the equilibrium between the complexed and noncomplexed fish oil components to be achieved, and (2) the kneading method, which has the advantage of recovering almost all host and guest components (even in complexed or noncomplexed forms).

Co-crystallization from ethanol-water mixture

Co-crystallization of the β-CD/ASO complex was performed in a 20 mL double-walled reactor, equipped with a magnetic stirring system, reflux condenser and dropping funnel. The host–guest molar ratio was 1:1 and 3:1 (considering that the main fish oil components are triglycerides, which theoretically requires three CD molecules for molecular encapsulation of one guest molecule). The molar ratios were calculated based on a mean molar mass for triglycerides from ASO of 899.5 g/mol (according to GC–MS analysis) and 1310 g/mol for β-CD hydrate (according to KFT analysis of water content of commercial β-CD). First, 1 mmol (or 3 mmol) of β-CD hydrate (1.313 ± 0.0007 g or 3.939 ± 0.0004 g) was suspended in 12 mL of distilled water and heated to 50 °C in the reactor. Subsequently, 4 mL of an ethanolic solution containing 1 mmol of ASO (0.902 ± 0.001 g) was added over 15 min to the β-CD solution under vigorous stirring. After the addition was completed, stirring was continued for another 30 min at the same temperature. The β-CD/ASO complex was crystallized by controlled cooling from 50 °C to 25 °C with a cooling rate of 8 $°C \cdot min^{-1}$ and the crystallization process was completed at 4 °C overnight. The obtained β-CD/ASO complex crystals were filtered, washed with 2 mL ethanol, and dried in a desiccator over molecular sieves (4 Å, Merck & Co., Inc.). The β-CD/ASO complex was stored at 4 °C in sealed containers. All co-crystallized complexes were obtained in duplicate.

Kneading method

For the kneading method the same molar ratios of β-CD/ASO as described for the co-crystallization method were used. The main difference was related to the quantity of solvents. In a 50 mL ceramic mortar preheated to 50 °C, β-CD hydrate (1.312 ± 0.001 g and 3.938 ± 0.0007 g) was suspended in either 1 mL or 2 mL of water (for 1:1 or 3:1 molar ratio, respectively). To this suspension, 0.5 mL of an ethanololic solution containing 0.902 ± 0.002 g of ASO was added and the mixture was thoroughly milled for 15 min. Afterwards the mixture was cooled to room temperature, washed with ethanol (1 mL) to remove surface oil, and dried to constant mass in a desiccator over MS 4Å. The kneaded complexes were prepared in duplicates.

GC–MS analysis of the raw and degraded ASO

The FA profile of nondegraded and degraded ASO was obtained by GC–MS analysis of the corresponding methyl esters (as well as acetals and ketals of FA degradation compounds). For derivatization, approximately 20 mg of ASO or the corresponding sample was dissolved in 3 mL of boron trifluoride–methanol solution in a 50 mL round-bottomed flask equipped with a reflux condenser, and the mixture was refluxed for 2 min. After cooling, hexane (2 mL) was added and the mixture was further refluxed for 2 min. After cooling, the organic layer was separated at the top of the flask by adding a sufficient amount of saturated sodium chloride solution. The upper layer was directly collected in a GC vial, dried (Na_2SO_4) and analyzed. For GC–MS analysis, a GC Hewlett Packard 6890 Series gas chromatograph coupled with a Hewlett Packard 5973 Mass Selective Detector was used. A Zebron 5-MS column

(30 m length, 0.25 mm inner diameter, and 0.25 μm film thickness) and a temperature program from 50 °C to 300 °C with a heating rate of 6 °C·min^{-1} were used. The injector and detector temperatures were set at 300 °C. The carrier gas was helium, the injection volume was 2 μL and a solvent delay time of 7 min was set up for the GC. The EI energy of the MS system was 70 eV and the source temperature was 150 °C. A scan range of 50–300 amu and a scan rate of 1 s^{-1} were used. The identification of the main compounds from the raw and degraded ASO was performed by using three methods: the experimental MS spectra were compared with the NIST/EPA/NIH Mass Spectral Library 2.0 (2002), by using the FAMEs 37 standard mixture analyzed under the same conditions and by comparing the Kovats indices (obtained with the C_8–C_{20} alkane standard) for the known FAMEs for this GC column type. The acquisition and handling of the GC–MS data was performed by using the Enhanced MSD ChemStation ver. D.02.00.275/2005 package (Agilent Technologies).

TG analysis of β-CD/ASO complexes

The behavior of β-CD/ASO complexes during heating was evaluated by TG analysis. A Netzsch TG 209 apparatus, with a temperature program of 25–400 °C and a heating rate of 10.0 °C·min^{-1} were used. The analysis was performed under nitrogen. The acquisition and handling of the data from the thermogravimeter were performed by using Netzsch Proteus – Thermal Analysis version 6.1 software.

DSC analysis of β-CD/ASO complexes

Calorimetric effects during heating of the β-CD/ASO complexes were evaluated by DSC analysis using a Netzsch DSC 204 apparatus. The temperature program was 25–400 °C, with a heating rate of 10.0 °C·min^{-1}, a purge flow of 20 mL·min^{-1}, and a protective flow of 50 mL·min^{-1}. All DSC determinations were performed under nitrogen atmosphere.

KFT analysis of β-CD/ASO complexes

The water content of β-CD/ASO complexes was determined by the bi-component technique of volumetric KFT. A KF 701 Titrino apparatus, equipped with a 10 mL dosing system and coupled with a 703 Ti Stand stirring system (both from Metrohm, Herisau, Switzerland) was used. A complex of up to 100 mg was used for KFT analysis. The bulk solvent volume (component 2, Hydranal-Solvent, Sigma-Aldrich) was 30 mL at the start of the analysis. Hydranal-Titrant 5 was used as component 1 (Sigma-Aldrich). The titer of the component 1 was determined by using Hydranal-Water Standard 10.0 mg H_2O·g^{-1} (Sigma-Aldrich). An electrode polarization of 50 μA, endpoint voltage of 250 mV, maximum titration rate of 5 mL·min^{-1}, drift as stop criterion, a drift value of 20 μL·min^{-1}, and an extraction time of 300 s were the values for the main KFT parameters.

Statistical and regression analyses

Statistical evaluation of the data from GC–MS, TG, DSC, and KFT analyses was performed by means of the ANOVA approach. Regression analysis was used for TG, DSC–KFT dependence. For the regression equation, the Pearson correlational coefficient, r^2, F-test, and standard errors for both equations and regression coefficients were determined.

Supporting Information

Supporting Information File 1

GC–MS analysis of all raw and degraded ASO, as well as TG, DSC and KFT data for the β-CD/ASO complexes.
[http://www.beilstein-journals.org/bjoc/content/supplementary/1860-5397-12-20-S1.pdf]

Acknowledgements

The authors thank Prof. Heinz-Dieter Isengard (University of Hohenheim, Germany) for the help with the KFT analysis.

References

1. Balk, E. M.; Lichtenstein, A. H.; Chung, M.; Kupelnick, B.; Chew, P.; Lau, J. *Atherosclerosis* **2006,** *189,* 19–30. doi:10.1016/j.atherosclerosis.2006.02.012
2. He, K. *Prog. Cardiovasc. Dis.* **2009,** *52,* 95–114. doi:10.1016/j.pcad.2009.06.003
3. Freeman, M. P. *Prostaglandins, Leukotrienes Essent. Fatty Acids* **2006,** *75,* 291–297. doi:10.1016/j.plefa.2006.07.007
4. Gadoth, N. *Brain Dev.* **2008,** *30,* 309–312. doi:10.1016/j.braindev.2007.10.001
5. Sontrop, J.; Campbell, M. K. *Prev. Med.* **2006,** *42,* 4–13. doi:10.1016/j.ypmed.2005.11.005
6. Rizliya, V.; Mendis, E. Biological, Physical, and Chemical Properties of Fish Oil and Industrial Applications. In *Seafood Processing By-Products: Trends and Applications;* Kim, S.-K., Ed.; Springer Science & Business Media: New York, NY, U.S.A., 2014; pp 285–313. doi:10.1007/978-1-4614-9590-1_14
7. Rubio-Rodríguez, N.; Beltrán, S.; Jaime, I.; de Diego, S. M.; Sanz, M. T.; Carballido, J. R. *Innovative Food Sci. Emerging Technol.* **2010,** *11,* 1–12. doi:10.1016/j.ifset.2009.10.006
8. Aryee, A. N. A.; Simpson, B. K. *J. Food Eng.* **2009,** *92,* 353–358. doi:10.1016/j.jfoodeng.2008.12.011
9. Wu, T. H.; Bechtel, P. J. *Food Chem.* **2008,** *111,* 868–871. doi:10.1016/j.foodchem.2008.04.064
10. Lerfall, J.; Bendiksen, E. Å.; Olsen, J. V.; Morrice, D.; Østerlie, M. *Aquaculture* **2016,** *451,* 170–177. doi:10.1016/j.aquaculture.2015.09.013
11. Torstensen, B. E.; Espe, M.; Sanden, M.; Stubhaug, I.; Waagbø, R.; Hemre, G.-I.; Fontanillas, R.; Nordgarden, U.; Hevrøy, E. M.; Olsvik, P.; Berntssen, M. H. G. *Aquaculture* **2008,** *285,* 193–200. doi:10.1016/j.aquaculture.2008.08.025
12. Pratoomyot, J.; Bendiksen, E. Å.; Bell, J. G.; Tocher, D. R. *Aquaculture* **2008,** *280,* 170–178. doi:10.1016/j.aquaculture.2008.04.028

13. Balderas, C.; Villaseñor, A.; García, A.; Javier Rupérez, F.; Ibañez, E.; Señorans, J.; Guerrero-Fernández, J.; González-Casado, I.; Gracia-Bouthelier, R.; Barbasa, C. *J. Pharm. Biomed. Anal.* **2010,** *5,* 1298–1304. doi:10.1016/j.jpba.2010.07.034
14. Lopez-Huertas, E. *Pharmacol. Res.* **2010,** *61,* 200–207. doi:10.1016/j.phrs.2009.10.007
15. Berlitz, H.-D.; Grosche, W.; Schieberle, P. Lipids. In *Food Chemistry;* Berlitz, H.-D.; Grosch, W.; Schieberle, P., Eds.; Springer: Berlin, Germany, 2009; pp 158–247.
16. Huang, J.; Sathivel, S. *J. Food Eng.* **2008,** *89,* 105–111. doi:10.1016/j.jfoodeng.2008.03.007
17. Belhaj, N.; Arab-Tehrany, E.; Linder, M. *Process Biochem.* **2010,** *45,* 187–195. doi:10.1016/j.procbio.2009.09.005
18. Huber, G. M.; Rupasinghe, H. P. V.; Shahidi, F. *Food Chem.* **2009,** *117,* 290–295. doi:10.1016/j.foodchem.2009.04.007
19. Serfert, Y.; Drusch, S.; Schwarz, K. *Food Chem.* **2010,** *123,* 968–975. doi:10.1016/j.foodchem.2010.05.047
20. Zhang, Y.; Tan, C.; Abbas, S.; Eric, K.; Xia, S.; Zhang, X. *Food Hydrocolloids* **2015,** *51,* 108–117. doi:10.1016/j.foodhyd.2015.05.001
21. Akhtar, M. J.; Jacquot, M.; Desobry, S. *Food Bioprocess Technol.* **2014,** *7,* 93–104. doi:10.1007/s11947-013-1075-y
22. Carvajal, A. K.; Mozuraityte, R.; Standal, I. B.; Storrø, I.; Aursand, M. *J. Am. Oil Chem. Soc.* **2014,** *91,* 1611–1621. doi:10.1007/s11746-014-2508-0
23. Bencze Rørå, A. M.; Birkeland, S.; Hultmann, L.; Rustad, T.; Skarå, T.; Bjerkeng, B. *LWT-Food Sci. Technol.* **2005,** *38,* 201–211. doi:10.1016/j.lwt.2004.06.008
24. Bower, C. K.; Hietala, K. A.; Oliveira, A. C. M.; Wu, T. H. *J. Food Sci.* **2009,** *74,* C248–C257. doi:10.1111/j.1750-3841.2009.01099.x
25. Chatterjee, S.; Judeh, Z. M. A. *LWT-Food Sci. Technol.* **2016,** *65,* 206–213. doi:10.1016/j.lwt.2015.08.010
26. Chatterjee, S.; Judeh, Z. M. A. *Carbohydr. Polym.* **2015,** *123,* 432–442. doi:10.1016/j.carbpol.2015.01.072
27. Anwar, S. H.; Kunz, B. *J. Food Eng.* **2011,** *105,* 367–378. doi:10.1016/j.jfoodeng.2011.02.047
28. Tirgar, M.; Jinap, S.; Zaidul, I. S. M.; Mirhosseini, H. *J. Food Sci. Technol.* **2015,** *52,* 4441–4449. doi:10.1007/s13197-014-1515-3
29. Frenzel, M.; Steffen-Heins, A. *Food Chem.* **2015,** *185,* 48–57. doi:10.1016/j.foodchem.2015.03.121
30. Czerniak, A.; Kubiak, P.; Białas, W.; Jankowski, T. *J. Food Eng.* **2015,** *167,* 2–11. doi:10.1016/j.jfoodeng.2015.01.002
31. Chang, Y.; McClements, D. J. *Food Hydrocolloids* **2015,** *51,* 252–260. doi:10.1016/j.foodhyd.2015.05.014
32. Walker, R. M.; Decker, E. A.; McClements, D. J. *J. Food Eng.* **2015,** *164,* 10–20. doi:10.1016/j.jfoodeng.2015.04.028
33. Morales-Medina, R.; Tamm, F.; Guadix, A. M.; Guadix, E. M.; Drusch, S. *Food Chem.* **2016,** *194,* 1208–1216. doi:10.1016/j.foodchem.2015.08.122
34. Brewster, M. E.; Loftsson, T. *Adv. Drug Delivery Rev.* **2007,** *59,* 645–666. doi:10.1016/j.addr.2007.05.012
35. Loftsson, T.; Duchêne, D. *Int. J. Pharm.* **2007,** *329,* 1–11. doi:10.1016/j.ijpharm.2006.10.044
36. Hădărugă, N. G.; Hădărugă, D. I.; Păunescu, V.; Tatu, C.; Ordodi, V. L.; Bandur, G.; Lupea, A. X. *Food Chem.* **2006,** *99,* 500–508. doi:10.1016/j.foodchem.2005.08.012
37. Hădărugă, D. I.; Hădărugă, N. G.; Bandur, G. N.; Isengard, H.-D. *Food Chem.* **2012,** *132,* 1651–1659. doi:10.1016/j.foodchem.2011.06.004
38. Hădărugă, D. I.; Hădărugă, N. G.; Costescu, C. I.; David, I.; Gruia, A. T. *Beilstein J. Org. Chem.* **2014,** *10,* 2809–2820. doi:10.3762/bjoc.10.298
39. Hădărugă, N. G.; Hădărugă, D. I.; Isengard, H.-D. *Food Chem.* **2012,** *132,* 1741–1748. doi:10.1016/j.foodchem.2011.11.003
40. Kfoury, M.; Landy, D.; Auezova, L.; Greige-Gerges, H.; Fourmentin, S. *Beilstein J. Org. Chem.* **2014,** *10,* 2322–2331. doi:10.3762/bjoc.10.241
41. Menezes, P. P.; Serafini, M. R.; Quintans-Júnior, L. J.; Silva, G. F.; Oliveira, J. F.; Carvalho, F. M. S.; Souza, J. C. C.; Matos, J. R.; Alves, P. B.; Matos, I. L.; Hădărugă, D. I.; Araújo, A. A. S. *J. Therm. Anal. Calorim.* **2013,** *115,* 2429–2437. doi:10.1007/s10973-013-3367-x
42. Ünlüsayin, M.; Hădărugă, N. G.; Rusu, G.; Gruia, A. T.; Păunescu, V.; Hădărugă, D. I. *LWT-Food Sci. Technol.* **2016,** *68,* 135–144. doi:10.1016/j.lwt.2015.12.017
43. Choi, M.-J.; Ruktanonchai, U.; Min, S.-G.; Chun, J.-Y.; Soottitantawat, A. *Food Chem.* **2010,** *119,* 1694–1703. doi:10.1016/j.foodchem.2009.09.052
44. Lee, C.-M.; Kim, M.-H.; Na, H.-S.; Kim, J.; Lee, K.-Y. *Biotechnol. Bioprocess Eng.* **2013,** *18,* 507–513. doi:10.1007/s12257-012-0752-4
45. Hădărugă, N. G.; Hădărugă, D. I.; Isengard, H.-D. *J. Inclusion Phenom. Macrocyclic Chem.* **2013,** *75,* 297–302. doi:10.1007/s10847-012-0143-7
46. Corpaş, L.; Hădărugă, N. G.; David, I.; Pîrşan, P.; Hădărugă, D. I.; Isengard, H.-D. *Food Anal. Methods* **2014,** *7,* 1353–1358. doi:10.1007/s12161-013-9757-7
47. Hădărugă, D. I.; Costescu, C. I.; Corpaş, L.; Hădărugă, N. G.; Isengard, H.-D. *Food Chem.* **2016,** *195,* 49–55. doi:10.1016/j.foodchem.2015.08.124
48. Isengard, H.-D. *Trends Food Sci. Technol.* **1995,** *6,* 155–162. doi:10.1016/S0924-2244(00)89024-X
49. Isengard, H.-D.; Kling, R.; Reh, C. T. *Food Chem.* **2006,** *96,* 418–422. doi:10.1016/j.foodchem.2004.12.046
50. Rückold, S.; Grobecker, K. H.; Isengard, H.-D. *Food Control* **2001,** *12,* 401–407. doi:10.1016/S0956-7135(01)00033-0

License and Terms

The definitive version of this article is the electronic one which can be found at:
doi:10.3762/bjoc.12.20

BEILSTEIN JOURNAL OF ORGANIC CHEMISTRY

Interactions of cyclodextrins and their derivatives with toxic organophosphorus compounds

Sophie Letort, Sébastien Balieu, William Erb, Géraldine Gouhier and François Estour*

Review

Address:
Normandie Université, COBRA, UMR 6014 et FR 3038, Université de Rouen, INSA de Rouen, CNRS, 1 rue Tesnière, 76821
Mont-Saint-Aignan Cedex, France

Email:
François Estour* - francois.estour@univ-rouen.fr

* Corresponding author

Keywords:
cyclodextrin; enzyme mimic; nerve agents; organophosphorus compounds; pesticides

Beilstein J. Org. Chem. **2016,** *12,* 204–228.
doi:10.3762/bjoc.12.23

Received: 20 November 2015
Accepted: 21 January 2016
Published: 05 February 2016

This article is part of the Thematic Series "Superstructures with cyclodextrins: Chemistry and applications III".

Guest Editor: E. Monflier

Abstract

The aim of this review is to provide an update on the current use of cyclodextrins against organophosphorus compound intoxications. Organophosphorus pesticides and nerve agents play a determinant role in the inhibition of cholinesterases. The cyclic structure of cyclodextrins and their toroidal shape are perfectly suitable to design new chemical scavengers able to trap and hydrolyze the organophosphorus compounds before they reach their biological target.

Introduction

Due to their biological activities, organophosphorus compounds have had considerable commercial impacts during the last decades, phosphates, phosphonates, phosphinates, or phosphines being prominent in several fields. As an example, drugs bearing an organophosphorus moiety hold a significant place in chemotherapy for the treatment of various diseases. Nevertheless, the high polarity of these molecules may compromise their activity as poor distribution or passive diffusion across cell membranes are the usual drawbacks associated with their use. Developed after World War II, organophosphorus compounds were used as antitumor [1-8], antiviral [9-12], antihypertensive [13,14] or in rheumatology [15-17]. Some derivatives of pharmacological interest show an anticholinesterase activity [18-21], but few of these molecules are used in therapy due to the difficulties to control their inherent toxicity. Nowadays, the main applications of them are to struggle against the pests or in the military. While the administration of organophosphorus drugs is carefully controlled, improper use of pesticides and chemical warfare agents, the so called “nerve agents”, can cause fatal poisonings through cholinesterase inhibition in tissues and brain [20].

Neurotoxic organophosphorus (NOPs) share a typical structure with a pentavalent phosphorus atom linked to a leaving group

(LG), two substituents (R^1 and R^2) and an oxygen or a sulfur atom (Figure 1), explaining the wide structural diversity of organophosphates.

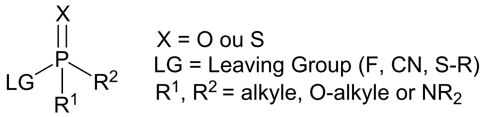

Figure 1: Structure of NOPs.

They can be classified into three categories depending on the nature of the leaving group. The first one includes the least toxic compounds used as pesticides; the second one corresponds to the G agents developed as chemical warfare agents and the third one to the dreadful V agents group (Figure 2).

Due to their use in agriculture, organophosphate accidental or voluntary intoxications are common [21-26]. Moreover, despite the chemical weapons convention, the use of chemical warfare agents in asymmetric wars or in terrorist attacks remains a permanent threat. A key challenge for military forces and rescue services is to have efficient tools to detect and to degrade organophosphate nerve agents [27]. In this respect, cyclodextrins (CDs) are interesting scaffolds because of their macrocyclic structure able to bind more or less selectively some organic substrates via non covalent interactions [28-30]. Due to their affinity for organophosphorus compounds, CDs have gained a significant attention for a variety of applications such as sensors for detection [31,32] or materials for nerve agents decontamination [33].

Various analytical methods exist to monitor the NOPs exposure [34-36]. However, these are long, expensive, required trained staff and are therefore unsuitable for field implementation. An appealing approach to overcome these drawbacks relies on the use of CD-based chemosensors. Apart from detection, the main concern in any event of exposure remains the fast degradation of NOPs into less toxic metabolites by rapid hydrolysis. For this purpose, a key strategy is to design chemical scavengers based on CDs, acting as enzyme mimics. Contrary to bioscavengers, the use of synthetic compounds allows an access to various derivatives and avoids the highly expensive biotechnological methods, the stability issues and the potential immunogenic risks associated to proteins such as hydrolases [37].

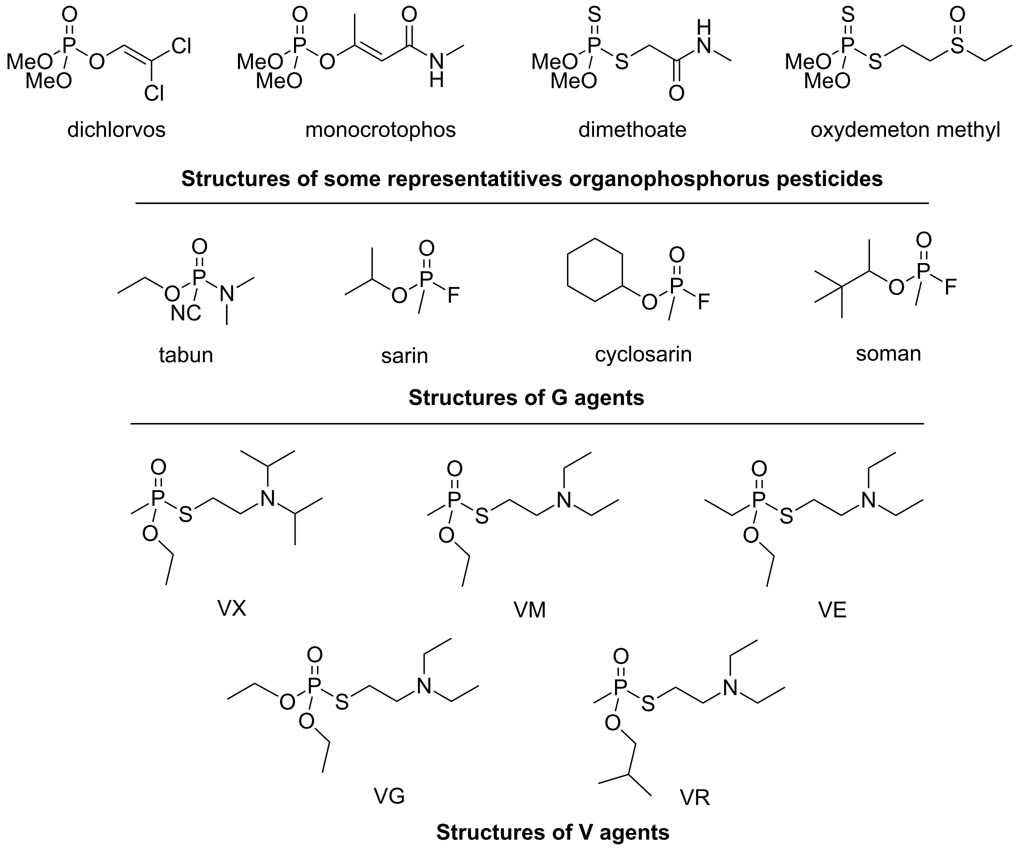

Figure 2: Examples of structures of NOPs.

This review focuses on the various aspects of the detoxification process mediated by CD derivatives: (1) the ability of CDs and their derivatives to form inclusion complexes with organophosphorus pesticides and G nerve agents; (2) the hydrolysis of the nerve agents by CDs under specific conditions; (3) the selective modifications of these cyclic oligosaccharides to improve their hydrolytic efficiency at physiological pH and temperature.

Review

Inclusion studies between CDs and pesticides

Due to their toroidal structure, CDs are able to interact with organophosphorus compounds. It is well known that many synthetic pesticides (compounds **1**–**9**, Figure 3) can form inclusion complexes with CDs, often resulting in modifications of their chemical and physical properties [38,39]. Thus, valuable information on the stoichiometry, the stability and the mode of entry of the guest into the host could be obtained by the characterization of the inclusion complexes in solution or in solid state. These three parameters have to be considered because they strongly determine the potential of CDs as scaffolds for the development of enzyme mimics. Various analytical tests were used to access such information in the cases of pesticides [40-42]. Phase solubility diagrams could be obtained if changes of their water solubility upon inclusion occur, whereas differential scanning calorimetry (DSC) could be used to discriminate inclusion complexes from external associative complexes. UV-visible and fluorescence spectroscopy often provided useful information, while IR was rarely used. Finally, NMR and X-ray crystal structures gave more details on the inclusion mode and the interactions of the pesticide into the oligosaccharide cavity. In addition to these characterization methods, molecular modelling analysis can afford further clues to select the suitable CD derivative for one specific pesticide. This could also support the rational design of new macrocyclic compounds able to strongly interact with organophosphates. The structure of the substrate plays a predominant role in the inclusion phenomenon. In this review, pesticides **1**–**9** were classified according to their more or less close similarities.

Pesticides bearing a methyl(phenyl)sulfane group

The interactions between β-CD and sulprofos (**1**, Figure 3) were investigated using various technics [43]. Despite the pronounced solubility changes consistent with complex formation, little variations in the UV spectra, combined with the guest's small chemical shifts observed in ^{1}H NMR experiments (0.01–0.06 ppm), suggest the formation of external complexes rather than an inclusion complex. However the inclusion complex formation was strengthen by molecular modeling studies with the aromatic group included into the cavity. Finally, DSC

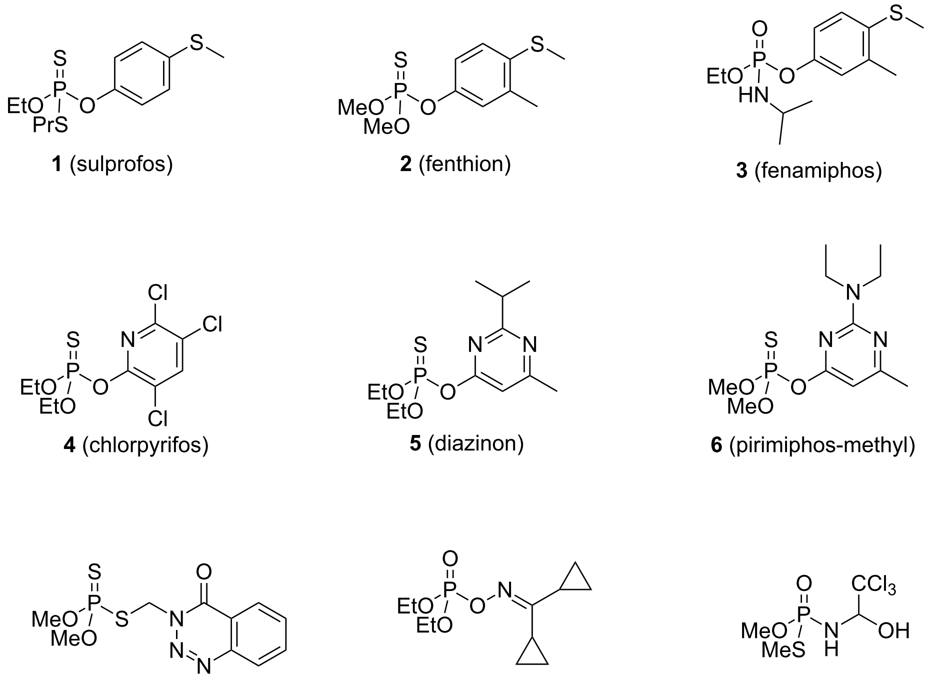

Figure 3: Structures of pesticides studied in the literature as guest to form an inclusion complex with CDs.

curves showed a first endothermic portion starting at 225 °C, typical of a melting process, and a second sharp exothermic decomposition peak, proving the formation of the inclusion complex. Thus, on the basis of these last results, the formation of an internal inclusion complex was favored by the authors.

In 2013, Cruickshank reported the X-ray crystal structures of the heptakis(2,3,6-trimethyl)-β-cyclodextrin (TRIMEB)–fenthion complex (complex with **2**, Figure 3), as well as isothermal and non-isothermal thermogravimetric studies [44]. The complex crystallizes in the space group $P2_12_12_1$, with the dimethyl phosphorothioate unit located close to the primary rims of the TRIMEB cavity, in its usual tetrahedral conformation. The alkylsulfanyl group is localized out of the larger rim of the TRIMEB cavity, the aromatic group slightly twisted out of the rim. In addition to the structural elucidation of this complex, isothermal and non-isothermal thermogravimetric analysis were performed. Obtained from the solid-state kinetic experiments, the relatively high energy barrier for complex dissociation revealed the thermal stability conferred upon guest encapsulation within the CD molecules.

NMR experiments allow the enantiomers discrimination in presence of a chiral additive to create visible diastereomeric species. ^{31}P NMR spectroscopy in presence of CDs as chiral selectors has therefore been employed to discriminate the enantiomers of fenamiphos (**3**, Figure 3) in quantitative water analysis [45]. Neutral CDs such as β-CD, methyl-β-CD, hydroxyethyl-β-CD (HE-β-CD), hydroxypropyl-β-CD (HP-β-CD), and hydroxyethyl-γ-CD (HP-γ-CD) were evaluated in these experiments. β-CD and HP-β-CD were selected as the best chiral solvating agents with an approximately equal level of enantiomeric discrimination. This occurs through the intermolecular inclusion of the fenamiphos phenyl ring within the apolar CD cavity, as confirmed by 2D nuclear Overhauser spectroscopy (ROESY) analysis.

Pesticides bearing a nitrogen heterocycle

The association constants of chlorpyrifos (**4**, Figure 3) with β-CD, HP-β-CD, and 6-*O*-α-maltosyl-β-CD hydrate (G2-β-CD) in aqueous media were determined by photochemically induced fluorescence (PIF, Table 1) [39,46]. Results are summarized in Table 1. A 1:1 stoichiometry with close complexing ability was found for β-CD and HP-β-CD [46], while a 1:2 complex was found to be predominant in the case of G2-β-CD [39]. These results can be corroborated with the aqueous solubility studies of chlorpyrifos in the presence of α-CD, β-CD, γ-CD, HP-β-CD and G2-β-CD [39] as a solubility increase is only observed with G2-β-CD. The respective association constants values calculated from the phase solubility diagram were 12 M^{-1} for K_1 (1:1 complex) and 3895 M^{-1} for K_2 (1:2 complex), in good agreement to those obtained by PIF, suggesting an effective sequential binding of two CD molecules to one chlorpyriphos molecule.

Table 1: Association constants of chlorpyriphos determined by PIF [39,46].

	K_a (M^{-1})		
	β-CD	G2-β-CD	HP-β-CD
K_1[a]	90 ± 28	12.34 ± 3.1	116 ± 19
K_2[b]		3895 ± 183	

[a]K_1: association constant for a 1:1 complex. [b]K_2: association constant for a 1:2 complex.

Compared to other pesticides, the low K_1 values observed for chlorpyrifos with α-CD and β-CD may lie in the steric hindrance resulting from the three chlorine atoms, which may inhibit the complexation. No correlation was found between the binding constant values and the hydrophobicity of the pesticides, suggesting that steric effects are probably predominantly involved in complex formation.

The inclusion of the apolar heterocyclic ring into the CD cavity is the most likely situation to occur. γ-CD has the largest secondary alcohols rim radius whereas the β- and γ-CDs' primary alcohols cones are similar. The guest molecule's inclusion depth corresponds to the distance from the phosphorus atom to the secondary OH rim. As this distance is the highest with γ-CD, diazinon (**5**, Figure 3) is more deeply inserted [47]. According to these results, the high association constant observed with γ-CD is mainly due to a good fitting of the pyrimidine ring into the cavity, while one ethoxy substituent protruding from the lower rim. In the cases of α- and β-CD, the phosphoryl residue is located outside the cavity. For α- and β-CD, the methyl substituent is more or less deeply inserted into the cavity, pointing downwards, while it is located largely on the secondary rim of γ-CD, pointing upwards. Finally, the isopropyl group is mainly outside, directed upwards for α- and β-CD, whereas located on the secondary rim of γ-CD.

The effect of β- and HP-β-CD aqueous solutions upon the fluorescence properties of pirimiphos-methyl (**6**, Figure 3) were also investigated [46]. As the inclusion phenomena occur, it is reported that the fluorescence properties of the guest are improved compared to its free form in aqueous solution. For both β- or HP-β-CD, the increase of their concentrations resulted in a progressive blue-shift and a fluorescence increase of pirimiphos-methyl. A 1:1 stoichiometry model was found, and the fitting of the observed fluorescence intensity versus the initial

CD concentration by a non-linear regression analysis allows the authors to estimate the binding constants of 171 M^{-1} and 736 M^{-1} for β- and HP-β-CD, respectively.

In presence of HP-β-CD, the fluorescence properties of azinphos-methyl (AZM, **7**, Figure 3) were improved by a factor of three but even if it induces a higher fluorescence enhancement than β-CD, this remains too weak to use this technique for routine analysis [48]. Finally the binding constant of the host-guest inclusion complex was reported at 690 ± 140 M^{-1}.

Pesticides bearing a non-aromatic group

X-ray powder diffraction analysis and DSC validated the formation of a complex between (diethoxyphosphinoximino)dicyclopropylmethane (DCPE, **8**, Figure 3) and γ-CD [49].

Complexes of DCPE with α-, β-, γ- and HP-β-CD were also analyzed [50], and their stoichiometry coefficients evaluated. The NMR spectrum showed an upfield shifts of the internal CD's hydrogens (H-3 and H-5), whereas chemical shifts of H-1, H-2, and H-4 protons remained identical in presence of β-, γ- and HP-β-CD. For the α-CD complex, none of the protons of the CD showed a significant shift, probably due to a shallow complex formation with the DCPE remaining on the rim of the α-CD cavity. The authors suggested that one ethoxy group could enter into the CD cavities with a stoichiometry coefficient of 1:1 for β-, γ- and HP-β-CD, and 1:2 for the DCPE:α-CD complex.

The stability of these complexes were kinetically analyzed through the DCPE degradation monitoring in aqueous solution in the presence or absence of CD derivatives [49,50]. The degradation rate remained unaffected for α- and β-CD complexes whereas a decelerating effect for γ- and HP-β-CD was noticed, suggesting a pronounced stabilizing effect of these two CDs on DCPE. γ- and HP-β-CD could then be able to include the DCPE molecule or its reactive group deeper within their cavity, shielding it from hydrolysis, than α- and β-CD could.

β-CD:chloramidophos (**9**, Figure 3) complex was formed by a kneading method [51] and UV spectrophotometry analysis revealed a 1:1 stoichiometry and a binding constant of 203.0 M^{-1} for this complex. FTIR analysis revealed the disappearance of the absorbance band at 804 cm^{-1}, due to a possible intermolecular inclusion of the -CCl_3 group into the β-CD. Additionally, C–N stretching vibration band shifted from 1426.6 cm^{-1} to 1425.2 cm^{-1}, as a result of hydrogen bonding between the nitrogen atom of the guest and hydroxy functions of the host. Additionally, the presence of a guest might weaken the hydration water binding, as revealed in DSC experiments by the lower endothermic fusion peak, specific to a dehydration process. X-ray powder diffraction analysis finally confirmed the complex formation.

All these studies proved that organophosphorus pesticides are able to interact with CDs and their derivatives. The affinity between the host and the guest strongly depends on the oligosaccharidic structure, and any modification of the CDs scaffold could lead to significant changes of the inclusion complexes' stability. The structure of the pesticide also plays a major role in the mode of inclusion. For instance, aromatic ring as substituent of the phosphorus atom are often included into the cavity, while steric hindrance is able to impair the complex formation. Finally, without aromatic groups, the mode of entry of the pesticide depends on the specific affinity of the phosphorus substituents for the CD cavity.

Transformations of NOPs mediated by CDs

According to the above mentioned results, CDs provide interesting scaffolds able to bind organophosphorus compounds. The complex stabilization between the substrate and the oligosaccharide relies on weak interactions such as hydrophobic interactions, hydrogen bonding and van der Waals forces. In some cases, the formation of a stable inclusion complex results the guest's hydrolysis reaction rate increase.

Degradation/hydrolysis of pesticides

The inclusion of organophosphorus pesticides into the CDs cavity could either promote or prevent their hydrolysis and photodegradation. Thus, many studies were performed to rationalise the outcome of the reaction between CDs and organophosphorus pesticides (compounds **10**–**13**, Figure 4).

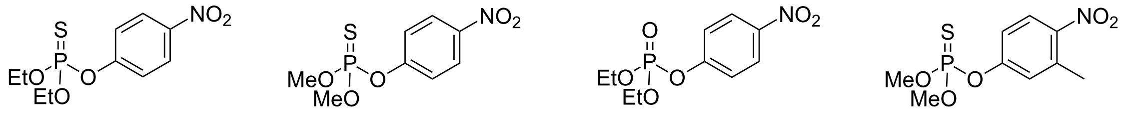

10 (parathion) **11** (methyl parathion) **12** (paraoxon) **13** (fenitrothion)

Figure 4: Structures of pesticides sensitive to the presence of CDs.

The influence of CDs on the hydrolysis rate of parathion (**10**, Figure 4), methyl parathion (**11**, Figure 4) and paraoxon (**12**, Figure 4) was evaluated [52]. In buffer solution (pH 8.5) with humic acids, the authors first noticed a saturation effect on the hydrolysis rate when the CD concentration was increased, suggesting the formation of a CD-pesticide inclusion complex (CD S) prior to the pesticide hydrolysis (Scheme 1).

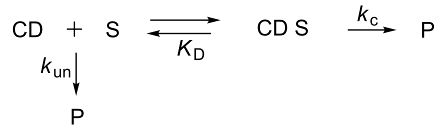

Scheme 1: The hydrolysis mechanism of substrate (S) in presence of a cyclodextrin (CD).

However, the outcome of this complexation strongly depends of the host–guest system. Indeed, α-CD displays a weak inhibitive effect on parathion hydrolysis whereas a mild promotive effect is noticed for methyl parathion and paraoxon hydrolysis. β-CD inhibits parathion and methyl parathion hydrolysis but promotes paraoxon ones whereas an inhibitive effect of the three hydrolysis was noticed in presence of γ-CD (k_c/k_{un}, Table 2).

It was previously established that the catalytic effect of CDs strongly depended on the interactions between the included pesticide and the secondary hydroxy groups of CDs. The correlation between inclusion parameters and catalytic properties of CDs was studied by induced circular dichroism (ICD) of the inclusion complexes using rotational-strength analysis method. ICD analysis underlines a change of the environment in the cavity due to the formation of the intermolecular complex. Positive and negative bands observed are respectively attributed to the axial and equatorial positioning of the organophosphorus compound. For the three hosts, the *para*-nitrophenoxy group is included with its long-axis parallel to the cavity. The study shows that the ratio k_c/k_{un} has not an accurate correlation with the dissociation constant of the inclusion complex (K_d, Table 2) but it seems that the different inclusion depths of the pesticides into the CD cavity could explain these variable results (α_{in}, Table 2).

It was reported that the catalytic activity is affected by the hydrogen bonding between the secondary OH groups of the CD and the reactive site of the guest. Indeed, such interactions increase the nucleophilicity of the secondary hydroxy groups and facilitate their attack onto the phosphorus atom. Indeed, when the *para*-nitrophenoxy moiety is deeply included into the cavity (parathions/β-CD, parathions/α-CD and paraoxon/γ-CD systems), the phosphorus atom is too far from the secondary hydroxy groups, is also shielded from the hydroxide ions and the pesticide's hydrolysis is thus inhibited. On the contrary, a moderate inclusion of the *para*-nitrophenoxy moiety into the CD cavity (paraoxon/β-CD system) implies a sufficient proximity between the phosphorus atom and the secondary hydroxy groups, thus promoting the pesticide hydrolysis. In the case of pesticides/α-CD systems, the relatively weak inhibition (parathion/α-CD) or catalysis effect (methyl parathion/α-CD and paraoxon/α-CD) imply a shallow inclusion of the phosphorus atom. It might be generalized that the inhibitive or promotive effect of the native CDs strongly depends on the inclusion depth of the guest, which can modify its interaction with the catalytically active secondary hydroxy groups or the hydroxide ions in the solvent.

Table 2: Kinetic and equilibrium parameters for CD-organophosphate pesticides systems (25 °C, pH 8.5, phosphate buffer containing 0.1% (w/v) humic acids) [52].[a]

	Substrates	$t_{1/2,c}$ (day)	$t_{1/2,un}$ (day)	k_c/k_{un}	$K_d \times 10^3$ (M)	$\alpha_{in} \times 10^{10}$ (cgs units)
α-CD	parathion	16	13	0.78	1.7	0.45
	methyl parathion	8.5	9.6	1.13	5.2	0.30
	paraoxon	4.2	5.2	1.23	12.0	0.62
β-CD	parathion	90	13	0.14	3.5	2.90
	methyl parathion	88	9.6	0.11	1.9	2.48
	paraoxon	3.7	5.2	1.39	8.4	1.01
γ-CD	parathion	21	13	0.61	8.1	2.12
	methyl parathion	18	9.6	0.53	5.5	1.95
	paraoxon	5.8	5.2	0.89	9.2	1.54

[a] $t_{1/2,c}$ and $t_{1/2,un}$: half-life times of the included and free pesticides; k_c and k_{un}: first-order rate constants for the hydrolysis of the included and free pesticides respectively (Scheme 1); K_d: dissociation constant of the inclusion complexes; α_{in}: inclusion-depth parameter estimated by induced circular dichroism with a pesticide concentration of 5.2×10^{-5} M and a CD concentration of 8.5×10^{-3} M; α_{in} is expressed in cgs (centimeter–gram–second) units.

Acting as the active site, the substitution of secondary hydroxy groups might impact the hydrolysis rate. This was investigated comparing the effect of β-CD, DIMEB and TRIMEB on the alkaline hydrolysis of parathion, methyl parathion, and fenitrothion [53,54]. In all host–guest systems, the rate of alkaline hydrolysis is reduced with the the inclusion of the organophosphorothioate pesticides into the CDs ($k_c/k_{un} < 1$, Table 3).

However it appears clearly that the three studied CDs do not share the same pesticide hydrolysis inhibition level as in all cases, fenitrothion is hydrolyzed faster than parathion and methyl parathion. Indeed the two latter can form deeply included complexes (high α_{in} parameter) compared to fenitrothion which is therefore less shielded from hydroxide ions, leading to the highest hydrolysis rate observed in this series (Table 3) [42]. The origin of this trend was disclosed by theoretical semi-empirical calculations of parathion-, methyl parathion- and fenitrothion-β-CD complexes [55]. It was shown that the methyl group, adjacent to the nitro function slightly impairs both deep and axial inclusion of fenitrothion into the cavity. The methylation degree of the hydroxy groups also influences the catalytic/shielding effect of the CDs in a pesticides dependant manner. For both parathion substrates, the hydrolysis rate of β-CD inclusion complexes is decreased by permethylation, but increased by 2,6-dimethylation. On the other hand, a progressive decrease of the hydrolysis rate of fenitrothion is observed with methylation of β-CD. These unpredictable results revealed that much more complex parameters than the easiness of the guest entry into the (methylated)CD are involved in the hydrolysis. Indeed, the methylation degree could also affect the steric hindrance of the secondary rim, resulting in CD geometrical changes with modifications of the complex stability, the orientation and inclusion depth of the pesticide within the cavity. However, the two main parameters to take into account remain the methylation degree and the pesticide inclusion depth.

This inhibition effect of native β- and γ-CD, DIMEB and TRIMEB on the fenitrothion hydrolysis was also reported by Rougier et al. [56]. The reaction was first carried out without CD at various NaOH concentrations and then with CDs at constant NaOH concentration in water containing 2% dioxane. The kinetic data reveal that β-CD, γ-CD or TRIMEB all inhibit the fenitrothion hydrolysis (Table 4).

Table 4: Association constants (K_a) and ratio of the observed rate constants of the fenitrothion hydrolysis.[a]

	K_a (M^{-1})	k^{CD}_{obs}/k_{obs}[b]	Ref.
β-CD	417 ± 18	0.68	[56]
γ-CD	99 ± 36	0.70	[56]
TRIMEB	511 ± 31	0.27	[56]
DIMEB	1690 ± 900	0.16	[57]

[a] k^{CD}_{obs} and k_{obs}: observed rate constants of fenitrothion hydrolysis respectively in the presence and absence of CD; [b] values determined in aqueous solution containing 2% dioxane in NaOH 0.5 M at 25 °C with a CD concentration of 0.01 M.

Despite the differences in the association constants for β- and γ-CD, they share a similar level of inhibition (decrease of 30% and 32% of the hydrolysis rate respectively), the best result being obtained with TRIMEB and its 73% reduction of hydrolysis. Another study was later carried out with DIMEB in the same experimental conditions [57] and showed that this CD, characterized by a significantly high association constant, was the strongest inhibitor of fenitrothion hydrolysis (decrease of

Table 3: Kinetic and equilibrium parameters for CD-organophosphorothioate substrates systems [53,54].[a]

	Substrates	k_c/k_{un}[b]	K_d (10^3 M)[b]	k_c/k_{un}[c]	K_d (10^3 M)[c]	$\alpha_{in} \times 10^{10}$ (cgs units)[c]
β-CD	parathion	0.209	1.9	0.139	3.5	2.92
	parathion methyl	0.186	1.6	0.110	1.9	2.55
	fenitrothion	0.539	2.4	0.660	4.4	0.44
DIMEB	parathion	0.237	3.2	0.274	4.2	1.34
	parathion methyl	0.223	2.0	0.147	2.5	1.89
	fenitrothion	0.518	5.3	0.453	9.8	0.62
TRIMEB	parathion	0.142	3.8	0.104	5.6	0.93
	parathion methyl	0.126	2.7	0.093	4.1	1.26
	fenitrothion	0.355	5.0	0.280	7.2	0.27

[a] k_c and k_{un}: first-order rate constants for the hydrolysis of the included and free pesticides (Scheme 1); K_d: dissociation constant of the inclusion complexes; α_{in}: inclusion-depth parameter estimated by induced circular dichroism with a pesticide concentration of 1.8×10^{-4} M and a CD concentration of 2.1×10^{-2} M. α_{in} is expressed in cgs (centimeter–gram–second) units; [b] parameters of the alkaline hydrolysis measured at 25 °C in NaOH 0.1 M; [c] parameters of the alkaline hydrolysis measured at 25 °C in phosphate buffer (pH 8.5) containing 0.1% (v/v) humic acids.

84% – Table 4). It clearly appears that methylated β-CDs have a higher hydrolysis inhibition effect than the native ones. Indeed, the steric hindrance resulting from the methyl groups tends to extend the CDs' cavity size, which allows a deeper inclusion of fenitrothion. Furthermore, the methyl groups also protect the phosphate moiety against external nucleophiles attack by impairing the entry of hydroxide ions.

X-ray analysis of fenitrothion-TRIMEB and -DIMEB complexes showed that the phosphorothioate groups are close to the primary alcohols of the CDs. As a result of intramolecular hydrogen bonds O-2···HO-3', the DIMEB's cavity is larger and more prone to form inclusion complexes. The pesticide is thus included deeply into the cavity, protected from nucleophilic attack, leading to a stronger hydrolysis inhibition with DIMEB than with TRIMEB [57]. Contradiction between these conclusions and Kamiya's results [53,54] were explained by the different reaction conditions and the DIMEB sample employed.

Most of the studies about the pesticides hydrolysis were carried out in alkaline aqueous solutions. However, in the natural environment, the medium pH is usually nearly neutral and the promoting or protecting effects of CDs on hydrolysis might be pH-dependant. Thus, in 1999, Ishiwata and Kamiya reported the effect of α-, β- and γ-CDs on the hydrolysis rate of eight organophosphorus pesticides in neutral aqueous solutions [58]. In sharp contrast to the inhibition of pesticides hydrolysis in alkaline media reported above, at neutral pH, the three native CDs display a catalytic effect on the hydrolysis of all the studied pesticides, highlighting the importance of pH [53,54]. As some hydroxy groups of CDs might be ionized in alkaline media, the authors proposed that the resulting electrostatic repulsions could expand the size of the cavities, resulting in a better hydrolysis inhibition of the pesticides through its deeper inclusion.

The formation of inclusion complexes can also modulate the organophosphorus photodegradation rates, but the results strongly depend on the host–guest systems [59,60] (Table 5).

The α- and γ-CD respectively exhibit a slight promotive and inhibitive effect on the photolysis of both parathion and paraoxon, whereas a full reverse of reactivity is noticed with β-CD (inhibiting parathion photolysis but promoting paraoxon's one). Following the same trend as for pesticide hydrolysis, the photolysis outcome is related to the inclusion depth of the pesticide within the CD cavity. For the paraoxon/β-CD complex, the inclusion depth remains moderate, which places the reactive phosphorus center close to the CD's hydroxy groups. On the contrary, for the parathion/β-CD, paraoxon/γ-CD and parathion/γ-CD complexes, a deep inclusion of the phosphorus atom occurs, preventing its interaction with CD's hydroxy groups or with water. The comparison between native α- and β-CDs and their methylated analogues reveals that the methylation of hydroxy groups decreases both the inhibitory or promotive effect of CDs, probably due to a higher steric hindrance around the torus.

Later, the effect of native cyclodextrins on the photodegradation of organophosphorus pesticides was evaluated in water

Table 5: Inclusion effect of CDs on the initial photolysis of parathion and paraoxon [59,60].[a]

	pesticides	k_c/k_f[b]	$\alpha_{in} \times 10^{10}$ (cgs units)[c]	k_c/k_f[c]	$\alpha_{in} \times 10^{10}$ (cgs units)[c]
α-CD	parathion	1.08	0.38	1.13	0.43
	paraoxon	1.12	0.56	1.18	0.58
DIMEA	parathion	/	/	1.02	0.22
	paraoxon	/	/	1.04	0.35
β-CD	parathion	0.46	2.74	0.26	2.97
	paraoxon	1.41	0.92	1.31	0.94
DIMEB	parathion	/	/	0.44	2.18
	paraoxon	/	/	1.31	0.75
γ-CD	parathion	0.69	2.26	0.75	1.86
	paraoxon	0.88	1.43	0.82	1.46

[a] k_c and k_f: initial photodecay rate of the residual percentage of respectively the included and the free pesticides; α_{in}: inclusion-depth parameter estimated by induced circular dichroism (pesticide concentration of 3.9×10^{-5} M and CD concentration of 4.8×10^{-3} M), [b](pesticide concentration of 5.2×10^{-5} M and CD concentration of 7.1×10^{-3} M); 25 °C in water; [c] α_{in} is expressed in cgs (centimeter–gram–second) units; 25 °C in water/methanol (80/20, v/v).

containing humic acids [61]. In these conditions, the three native CDs promote the photodegradation of the included pesticides, following the order α < γ < β. It seems that this promotive effect relies on the CDs' ability to complex both the organophosphorus pesticides and the reactive radical resulting from the photosensitization of humic acids. As the promotion effect of CDs follows the order α < γ < β, it appears that the size of the cavity is not the only parameter to take into account. Indeed, the ability of CDs to relay radicals towards the phosphorus atom might be tuned by the geometrical disposition of the hydroxy groups of CDs. The origin of the higher efficiency of β-CD on the photodegradation might be due to the presence of a strong hydrogen bond network between the secondary hydroxy groups, which restricts their degree of liberty, and lets them to relay the active radicals toward the phosphorus atom.

Hydrolysis of chemical warfare agents

Accelerating nerve agent's hydrolysis, CDs are attractive compounds to achieve their efficient detoxification under physiological conditions. A common feature of these agents is the chiral phosphorus atom and as CDs and their derivatives are also chiral, a stereoselective interaction with the nerve agents is possible. The stereochemistry of organophosphates is to be considered important insofar as the individual stereoisomers of a neurotoxic agent do not share the same level of toxicity [20]. Sarin (compounds **14a** and **14b**, Figure 5), cyclosarin (compounds **15a** and **15b**, Figure 5) and tabun (compounds **16a** and **16b**, Figure 5) consist of a mixture of two enantiomers. Due to the presence of two chiral centers (the phosphorus atom and the carbon atom of the 1,2,2-trimethylpropyloxy group), soman presents four stereoisomers: C(*S*)P(*S*), C(*R*)P(*S*), C(*S*)P(*R*) and C(*R*)P(*R*) (compounds **17a**–**d**, Figure 5).

CDs can tune a reaction mechanism in two ways: (a) by creating a covalent bond between the macrocycle and the reagent, first forming an intermediate and then the product; (b) by providing the reactants a new environment with novel reactivity, i.e., selectivity and/or rate due to the apolar CD cavity. In alkaline medium hydrolysis of organophosphorus species, an intermediate mechanism is usually involved. The formation of an inclusion-complex first occurs and then the secondary alkoxide of the host pseudo-intramolecularly attacks the phosphorus atom to form a covalent bond. Finally an alkoxide ion could react with the formed phosphonates to regenerate the CD secondary alkoxide and to release the hydrolyzed product (Scheme 2).

In 1970, van Hooidonk and Breebaart first studied the alkaline hydrolysis of the enantiomers of isopropyl methylphosphonofluoridate (sarin) with α-CD in aqueous solution at pH 9.0 and

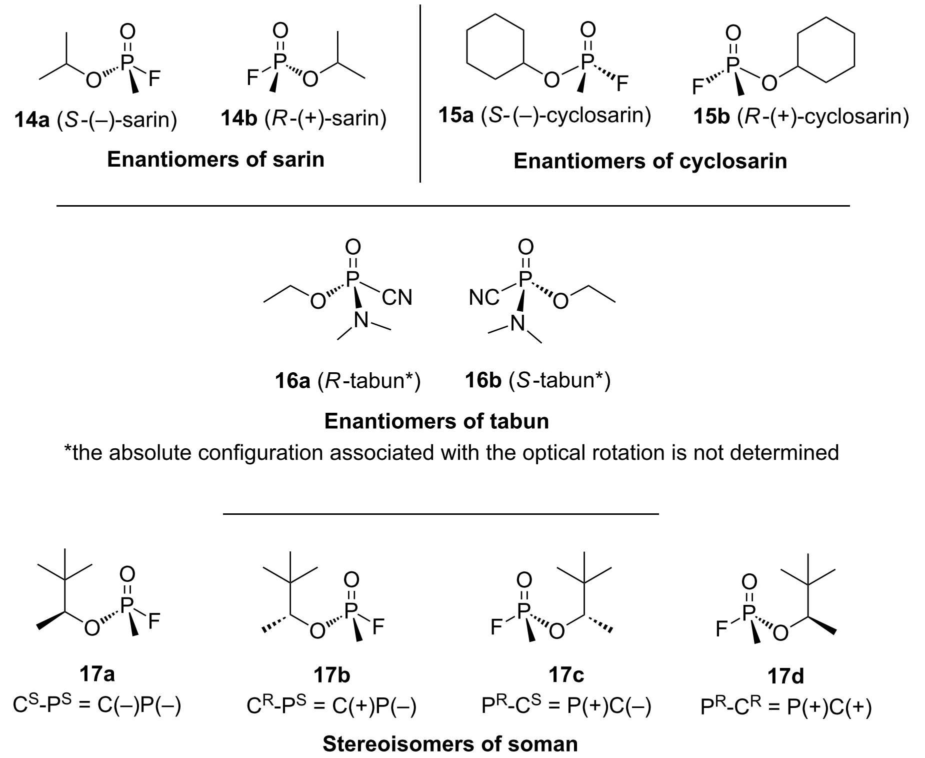
14a (*S*-(–)-sarin) **14b** (*R*-(+)-sarin)

Enantiomers of sarin

15a (*S*-(–)-cyclosarin) **15b** (*R*-(+)-cyclosarin)

Enantiomers of cyclosarin

16a (*R*-tabun*) **16b** (*S*-tabun*)

Enantiomers of tabun

*the absolute configuration associated with the optical rotation is not determined

17a C^S-P^S = C(–)P(–)

17b C^R-P^S = C(+)P(–)

17c P^R-C^S = P(+)C(–)

17d P^R-C^R = P(+)C(+)

Stereoisomers of soman

Figure 5: Structures of the different stereoisomers of G agents.

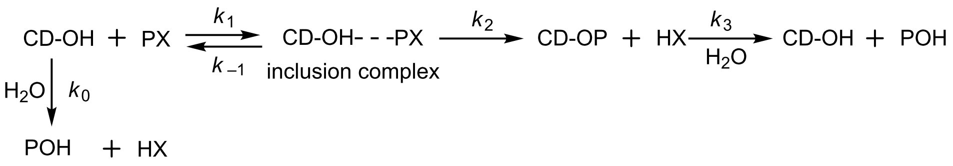

Scheme 2: Reaction mechanism of CD accelerated decomposition of organophosphorus compound (PX).

25 °C. A hydrolysis rate enhancement is observed and they report the formation of an inclusion complex between the α-CD and sarin prior to the nucleophilic attack of an ionized hydroxy group of the α-CD which becomes phosphonylated [62]. No rate acceleration is noticed with α-methylglucoside, which indicates that the cyclic nature of α-CD and its ability to form inclusion complexes is essential to get a catalytic activity. Stereospecificity, both in the formation of the inclusion complex and in the nucleophilic reaction, are also observed to some extent. According to the authors, the (*S*)-(+)-sarin (**14b**, Figure 5) forms a more stable inclusion complex than the (*R*)-(−)-sarin (**14a**, Figure 5), the latter being more easily hydrolyzed (Table 6). Thus, a better affinity with the CD cavity does not invariably imply a higher reaction rate.

Table 6: Dissociation constant (K_d) and rate constant (k_2) for the nucleophilic reaction of the enantiomers of sarin in the presence of α-CD [62].[a]

	$K_d \times 10^2$ (M)	$k_2 \times 10^2$ (min^{-1})
(*S*)-(+)-sarin	0.6 ± 0.04	8.7 ± 0.2
(*R*)-(−)-sarin	4.0 ± 0.6	310 ± 30

[a] Conditions: aqueous solution 0.1 M KCl, pH 9, 25 °C.

The comparison of the dissociation (K_d) and rate constants (k_2) of the two sarin enantiomers clearly shows that the stereospecificity mainly occurs in the nucleophilic attack rather than in the complex formation. Nevertheless, the optical rotations attributed to each enantiomer of sarin are in contradiction to those described by Benschop and De Jong in 1988 [20]. Indeed, they determined that the (*R*)-sarin is dextrorotatory whereas the (*S*)-sarin is levorotatory. Chirality has been attributed following the reviewed rules of Cahn, Ingold and Prelog [63,64] which classified the oxygen atom of the P=O bond as the minor priority compared to the alkoxy substituents [65]. In their 1988 work, Benschop and De Jong stated that the nerve agent stereoisomers' absolute configuration of the phosphorus atom was not firmly established. Thus, the van Hooidonk and Breebaart's work dating from 1970, it is highly probable that they did not attributed the correct absolute configurations to the enantiomers of sarin, which means that the (*S*)-(−)-enantiomer would be hydrolyzed faster in presence of α-CD.

They also studied the alkaline hydrolysis of the two enantiomers of isopropyl *para*-nitrophenyl methylphosphonate [65] and of isopropyl (*S*)-2-dimethylaminoethyl methylphosphonothioate [67] in the presence of α-CD at 25 °C. The result indicates that the inclusion complexes stereospecific formation is not significant, but that α-CD is predominantly phosphonylated by the (−)-enantiomers. The stereospecificity observed with sarin, isopropyl *para*-nitrophenyl methylphosphonate and isopropyl (*S*)-2-dimethylaminoethyl methylphosphonothioate is ascribed to better interactions between the included (−)-enantiomer and the secondary hydroxy groups responsible of the nucleophilic attack.

In the 80s, Désiré and Saint-André studied the effect of the three native cyclodextrins on the hydrolysis reaction of tabun, VX, sarin and soman [68-70]. It appears that α-, β- and γ-CDs are unable to catalyze the hydrolysis of VX as the rates remain similar in the presence of these CDs compared to the spontaneous hydrolysis rates, even at pH 9 or 11. In contrast, the three native CDs catalyze the hydrolysis of sarin and soman (Table 7). Nevertheless, at pH 7.40, native CDs-catalyzed hydrolysis of sarin is rather slow and only soman seems to be a good substrate, especially for β-CD. The formation of a stable inclusion complex between CDs and the organophosphorus nerve agent is postulated as the first step in the catalytic process.

Furthermore, it appears that the dissociation constants (K_d) of soman/β-CD and soman/α-CD complexes are significantly lower than those of the sarin/β-CD and sarin/α-CD complexes, which indicates a weak binding between sarin and CDs (Table 8). The only difference between sarin and soman is their isopropyloxy and pinacolyloxy moieties and the binding constants of β-CD/soman and β-CD/pinacolyl alcohol complexes were then investigated. The similar data obtained proved that the pinacolyloxy group was at the origin of the strong complexation of soman into the β-CD cavity.

They then focused their work on the interaction between soman and β-CD due to its greater affinity for β-CD compared to α- or γ-CDs. According to the study, soman forms an (1:1) inclusion complex with β-CD at pH 7.40. After its complexation into the

Table 7: Inactivation rate constants (min^{-1}) of tabun, sarin and soman in the absence[a] and in the presence[b] of CDs [70].[c]

CD concentration		pH	tabun	sarin	soman
/		7.40		$(5.4 \pm 0.3) \times 10^{-4}$	$(5.3 \pm 0.3) \times 10^{-4}$
/		9.00	(7.0 ± 0.4) x 10^{-3}	$(1.4 \pm 0.2) \times 10^{-2}$	$(8.2 \pm 0.2) \times 10^{-3}$
α-CD	10 mM	7.40			$(2.2 \pm 0.1) \times 10^{-2}$
	20 mM	7.40		$(2.5 \pm 0.2) \times 10^{-3}$	$(2.8 \pm 0.2) \times 10^{-2}$
	50 mM	9.00	$(7.6 \pm 0.8) \times 10^{-3}$		
β-CD	1 mM	7.40			$(3.0 \pm 0.1) \times 10^{-2}$
	10 mM	7.40		$(2.4 \pm 0.3) \times 10^{-3}$	
	10 mM	9.00	$(7.5 \pm 0.9) \times 10^{-3}$	$(6.7 \pm 0.3) \times 10^{-2}$	
γ-CD	10 mM	7.40			$(4.6 \pm 0.3) \times 10^{-3}$
	20 mM	7.40			$(6.4 \pm 0.2) \times 10^{-3}$

[a] k_0 min^{-1}: rate constant observed for the hydrolysis of nerve agent PX in the absence of CD; [b] $(k_{CD} - k_0)$ min^{-1} with k_{CD}: rate constant observed for the hydrolysis of nerve agent PX in the presence of CD; [c] conditions: aqueous solution with Tris buffer 10 mM at 25 °C.

Table 8: Dissociation constants of inclusion complexes of α-, β-, γ-CD with sarin and soman [69].[a]

			K_d (mM^{-1})		
	concentration range of CD	pH	α-CD	β-CD	γ-CD
sarin	2.5–50 (mM)	8.0	40 ± 10		
	1.5–10 (mM)	9.0		4.9 ± 0.7	
soman	7.5–50 (mM)	7.4	18 ± 5		
	0.2–4.0 (mM)	7.4		0.53 ± 0.05	
	2.5–50 (mM)	8.0			5.5 ± 1.1

[a] Parameters measured in aqueous solution with 10 mM Tris buffer at 25 °C.

cavity, soman reacts with a nucleophilic oxyanion formed from a secondary hydroxy group of the CD torus. As a result of this pseudo-intramolecular process, at pH 7.40 and 25 °C, the hydrolysis of soman by the monoanionised β-CD is 2600 times faster compared to a hydroxide ion. Different rates of β-CD-mediated hydrolysis for the four soman stereoisomers were observed. Only the chiral phosphorus center is involved in this stereoselectivity and the two most toxic P(−)-diastereomers **17a** and **17b** (Figure 5) of soman are degraded faster (Table 9).

In 1995, Cabal investigated the hydrolysis reaction of soman with the three native cyclodextrins and especially the reactivity differences between P(*S*) and P(*R*) isomers at 25 °C and pH 9 [71]. They reported a stereospecific hydrolysis of soman with α-, β- and γ-CDs depending on the absolute configuration of its phosphorus atom. Indeed, more stable inclusion complexes are observed with the P(*S*)-stereoisomers of soman, but the degradation of the P(*R*)-stereoisomers remains strongly faster (Table 10).

Table 9: Percentages of different forms of soman hydrolyzed by 10 mM β-CD after incubation times of 20 and 60 min [70].[a]

forms of soman hydrolyzed	20 min	60 min
racemic soman	44%	62%
P(−)-soman	70%	97%
P(+)-soman	18%	27%

[a] Conditions: 10 mM of β-CD in aqueous solution with 10 mM Tris buffer, pH 7.40, 25 °C.

In agreement with the results discussed above, the stereospecific process is not the inclusion within the α-, β- or γ-CD cavity but the nucleophilic attack which can be rationalized by the different orientations of the P(*R*)- and P(*S*)-stereoisomers within the β-CD cavity. The complexation of the P(*R*)-isomers into the CD cavity is followed by the formation of a hydrogen bond between a C-3 hydroxy and the phosphoryl oxygen atom of soman. Then a C-2 ionized hydroxy function attacks the phos-

Table 10: Maximum hydrolysis rate constants *k* and dissociation constants *K* of inclusion complexes of CDs with P(*R*) and P(*S*) stereoisomers of soman [71].[a]

	k_R (min^{-1})	$k_S \times 10^2$ (min^{-1})	$K_R \times 10^4$ (M^{-1})	$K_S \times 10^4$ (M^{-1})
α-CD	4.87 ± 0.61	3.40 ± 0.10	252.0 ± 0.46.0	17.30 ± 2.10
β-CD	3.07 ± 0.22	3.75 ± 0.14	14.4 ± 2.9	5.35 ± 0.74
γ-CD	0.26 ± 0.01	1.08 ± 0.05	58.6 ± 0.6	6.33 ± 1.80

[a] Conditions: constants measured in 0.01 M NaOH aqueous solution at 25 °C and pH 9.

phorus atom to form a covalent bond with the release of the leaving group (fluoride ion). The different orientations of the phosphorus atom substituents for the P(*S*)-isomers prevent the optimal interaction between the ionized hydroxy group and the phosphorus atom and thus reduce the hydrolysis rate.

The hydrolysis rate constants of soman with α- and β-CDs are similar and higher than the one observed with γ-CD which has the largest cavity (Table 10). Thus, the higher dissociation and the lower rate constants for γ-CD indicate that a too large cavity, compared to the guest size, decreases the strength of the inclusion complex. The substrate is therefore not sufficiently enclosed in the cavity to allow the optimal nucleophilic attack by a hydroxy group of CD. The study also reports the influence of the pH on the degradation rate. As the pH is increased, the hydroxy groups of CD are gradually deprotonated, resulting in faster hydrolysis rates for all soman's stereoisomers.

The hydrolysis of sarin and cyclosarin in presence of β-CD were then studied at 25 °C and pH 9 and also compared with the hydrolysis of soman. Their enantiomers are not degraded at the same rate, the P(*R*)-isomers of sarin and cyclosarin reacting faster than P(*S*)-isomers at pH 9 (Table 11).

The different alkoxy substituents on the phosphonate group for the three methylfluorophosphonates do not result in fundamental changes of the dissociation constants. However, the rather slow hydrolysis rate of P(*R*)-sarin can be explained by the space arrangement of this stereoisomer into the β-CD cavity. Sarin is the smallest of the three methylfluorophosphonates studied. After the complexation of P(*R*)-sarin, its phosphorus atom is located in the cavity above the level of the catalytically active hydroxy groups of β-CD, whereas for cyclosarin and soman, the phosphorus atoms lies in the plane of the hydroxy groups. The deep inclusion of P(*R*)-sarin into the β-CD cavity could therefore be at the origin of the rather low reaction rate observed for this stereoisomer.

Thus, in all the studies of Cabal, the P(*R*)-stereoisomers of soman, sarin and cyclosarin are faster hydrolyzed than the P(*S*)-stereoisomers in presence of CDs. Nevertheless, due to the contradiction with the hydrolysis rates of soman previously by Désiré and Saint André [68,70], we can again raise a doubt about the validity of the assigned absolute configurations. Indeed, they reported a faster degradation of the two P(−)-diastereoisomers whose absolute configuration of the phosphorus atom is assigned to *S* according to Benschop and De Jong's work [20]. Moreover, Cabal referred to van Hooidonk and Breebaart‘s work [62] to corroborate his results about the hydrolysis rate of sarin. However, we previously underlined the incoherencies between the optical activity and the absolute configurations of the enantiomers of sarin described by van Hooidonk and Breebaart. Consequently, it seems that Cabal inversed all the absolute configuration of soman, sarin and cyclosarin enantiomers, which would imply a faster degradation of the P(*S*)-stereoisomers.

Several studies discussed the interactions between cyclodextrins and organophosphorus compounds and their influence on the hydrolysis rates, but the reaction pathways are not

Table 11: Maximum hydrolysis rate constants *k* and dissociation constants *K* of inclusion complexes of β-CD with methylfluorophosphonates [71].[a]

	$k_0 \times 10^2$ (min^{-1})	k_R (min^{-1})	$k_S \times 10^2$ (min^{-1})	$K_R \times 10^4$ (M^{-1})	$K_S \times 10^4$ (M^{-1})
soman	1.46 ± 0.08	3.07 ± 0.22	3.75 ± 0.14	14.4 ± 2.9	5.35 ± 0.74
sarin	2.30 ± 0.11	0.33 ± 0.02	5.92 ± 0.09	9.61 ± 4.9	4.98 ± 0.22
cyclosarin	1.81 ± 0.07	11.00 ± 0.70	5.40 ± 0.30	14.50 ± 0.2	2.52 ± 0.50

[a] Conditions: constants measured in aqueous 0.01 M NaOH solution at 25 °C and pH 9; [b] k_0: rate constant of the spontaneous hydrolysis.

always clearly understood. In 2013, Kranawetvogl et al. studied the degradation of cyclosarin (GF) by β-CD to propose a mechanism [72]. CHMPA (*O*-cyclohexyl methylphoshonic acid), which is the product of the GF hydrolysis but also stable mono and binary covalent CHMP-β-CD conjugates (MC and BC). Thus, after the initial inclusion complex formation, the GF can be directly hydrolyzed releasing CHMPA or it can be attacked by a hydroxy group of the CD leading to the MC conjugate. Then, two reaction pathways are possible. The MC conjugate could either be hydrolyzed to regenerate the free unsubstituted β-CD or it could react with another molecule of GF to give the stable binary CHMP-β-CD conjugate (BC) (Scheme 3).

Thus, a competition between a "catalytic pathway" and a "stoichiometric pathway" occurs, the favoured reaction depending on several factors such as the concentrations of β-CD and GF, the concentration ratios of both of them or the use of additional ligands. Indeed, when the concentration ratio GF/β-CD is increased from 1:5 to 1:1, the CHMPA formation decreases. Furthermore, the GF hydrolysis is favoured in Tris-HCl buffer rather than in water. These results clearly show the high complexity of the degradation mechanism of an organophosphorus compound by β-CD.

To efficiently catalyse the NOPs hydrolysis, CDs and their derivatives have to be able to stabilize the reaction intermediate. To this regard, if the formation of a stable inclusion complex is likely to improve the reaction rate, the binding mode of the substrate and CD must match to observe a faster reaction. On the contrary, a non-reactive complex would decrease the hydrolysis rate. The design of more reactive CD derivatives is thus a challenging approach to degrade NOPs more effectively.

Design of enzymes mimics based on CDs

The studies based on non-functionalized CDs have disclosed their potential as NOPs scavengers. Nevertheless, improvements remained relatively weak considering the results obtained under physiological conditions (pH 7.4, 37 °C). The design of novel macrostructures displaying a higher hydrolytic efficiency under mild conditions is then a stimulating challenge. The main strategies described rely on the introduction of one or several reactive groups against nerve agents on these cyclic oligosaccharides.

As CDs exhibit a large number of primary (C-6 position of glucose units) and secondary (C-2 and C-3 positions) alcohols, selective modifications are therefore difficult. Most of them are based on the slight differences in the reactivity of these three kinds of hydroxy groups. In Schemes 5–10, the CD ring is drawn as in Figure 6 for β-CD and TRIMEB. This representation was also chosen for their derivatives in order to point out the modified units.

Modifications at the C-6 positions

Synthesis: In 1989, Breslow and Anslyn [73] described the synthesis of a bis(imidazole)-β-CD derivative able to catalyze a 4-*tert*-butylcatechol cyclic phosphate hydrolysis 120 times faster than the simple spontaneous hydrolysis. This seminal work proved unequivocally that modified CDs are able to accelerate the hydrolysis rate [74]. Regarding these preliminary results based on the C-6 position functionalization, Kubik et al. [75] described two routes to access β-CD derivatives monosubstituted on the primary rim with various nucleophiles. The first one is based on the monotosylation of one C-6 hydroxy, followed by a nucleophilic substitution with a substrate bearing an

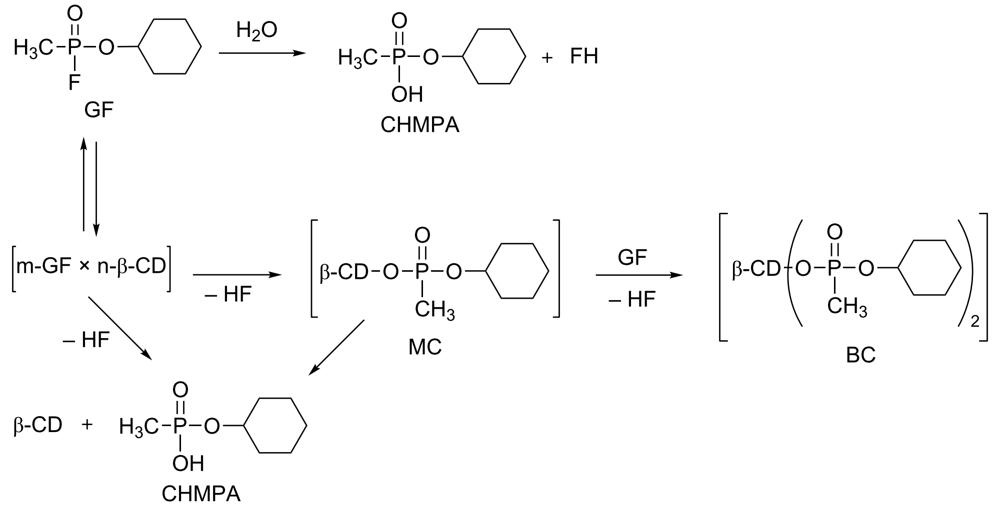

Scheme 3: Proposed degradation mechanism of cyclosarin by β-CD [72].

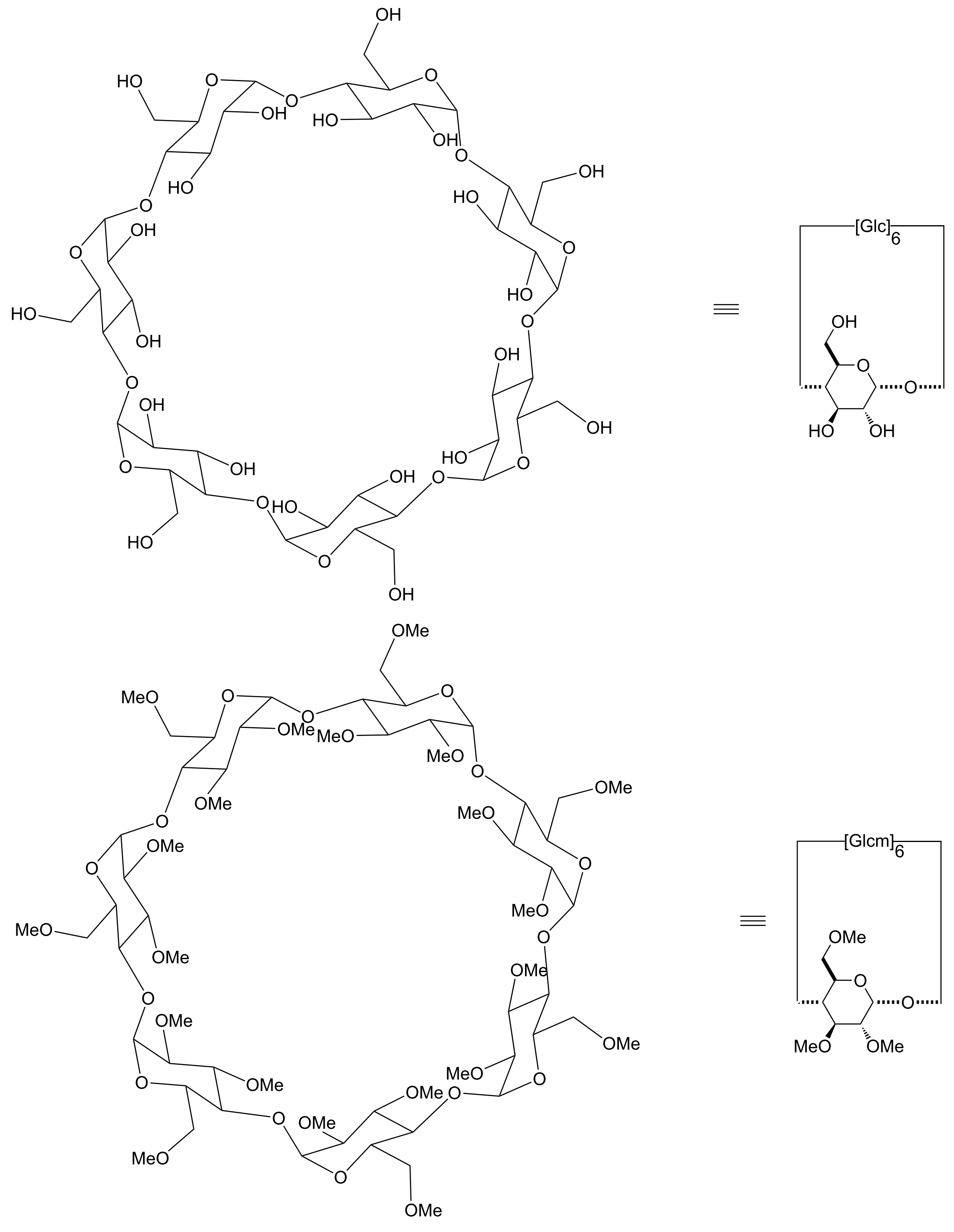

Figure 6: Schematic representations of β-CD and TRIMEB.

aldoxime group (pathway i, Scheme 4); the second route starts from the same tosylated intermediate **18**, substituted by an azide function, precursor of a triazole ring used to link the aldoxime moiety (pathway ii, Scheme 4). Following this second approach, Kubik et al. published new α-, β- and γ-CD derivatives functionalized with hydroxamic acids on one C-6 position [76].

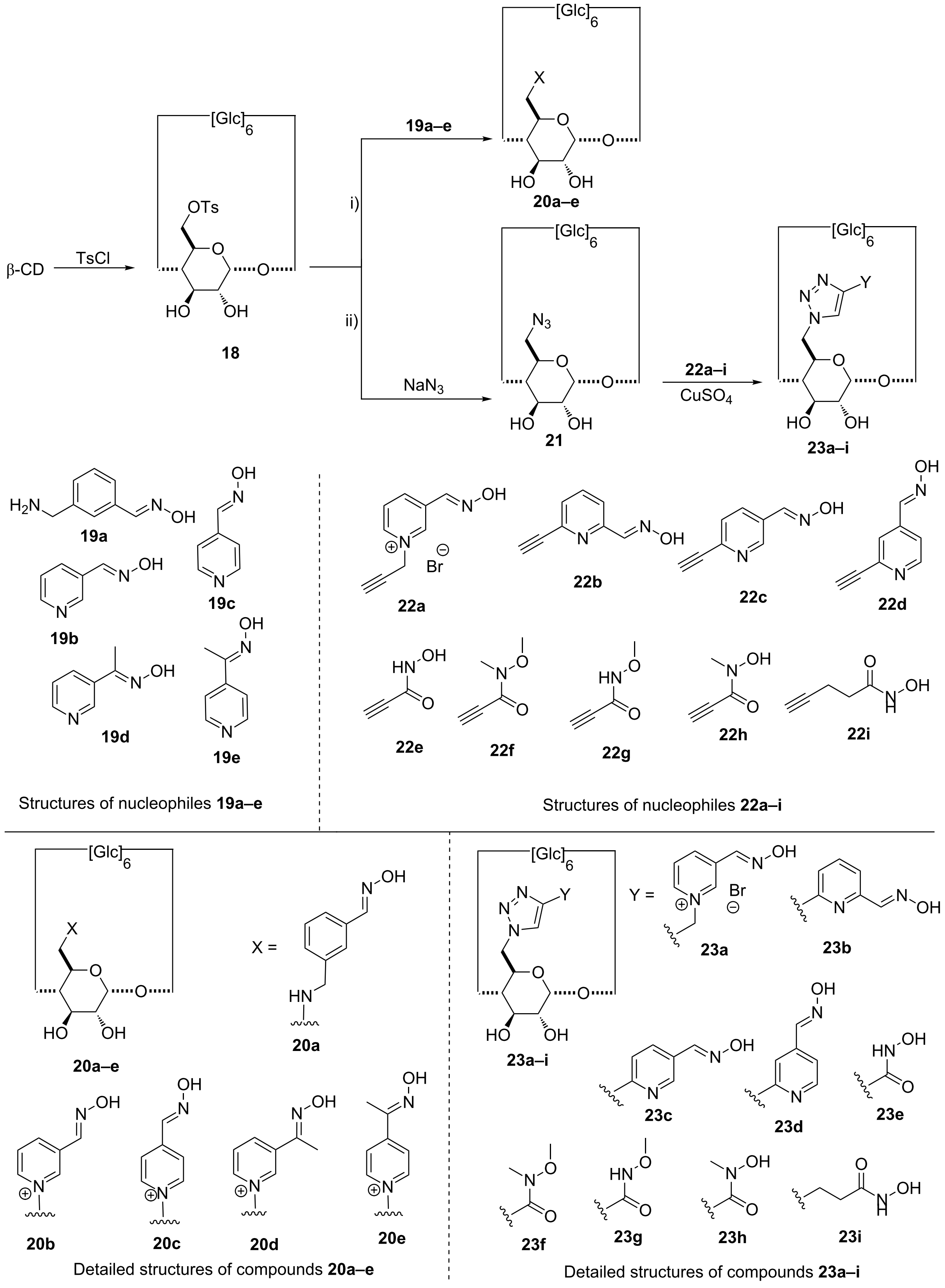

Scheme 4: Synthetic pathways to 6-monosubstituted CD derivatives.

Efficiency of compounds 20a–e against chemical warfare agents: The authors demonstrated the high activity of the pyridinium derivatives, especially the compounds **20b** and **20d**, against cyclosarin (Scheme 4). Indeed, the nerve agent was totally hydrolyzed in less than five minutes in presence of **20b**, the most toxic enantiomer, (−)-cyclosarin **14a**, reacting faster in this enantioselective degradation [75].

Structure–activity relationships based on this first series of compounds revealed the determinant role of oximes' nucleophilic strength in the hydrolysis process. Firstly, the less active compound is the weak acid oxime derivative **20a**. Then, the formation of the more nucleophilic aldoximate is favored with the pyridinium derivatives **20b**–**d**, explaining their high activity. The moderate efficiency of ketoximes **20d** and **20e**, compared to that of the corresponding aldoximes **20b** and **20c**, strengthen this hypothesis. Finally, the *para*-substituted pyridinium derivative **20c** is much less reactive than the *meta* compound **20b**. This tends to prove that even slight structural differences have a major impact on the hydrolytic reactivity of the cyclodextrin.

Based on these results, Kubik et al. then evaluated the hydrolytic activity of **20b** on various alkyl methylphosphonofluoridates [77]. As **20b** was more active than native β-CD for sarin derivatives hydrolysis, they were able to clearly establish the role of the nucleophilic group. Contrary to sarin derivatives, soman detoxification by **20b** was not as effective, suggesting a non-reactive position of the nucleophilic oxime to efficiently react with this toxic.

Worek et al. also demonstrated the prophylaxis effect associated to **20b** in the case of anesthetized guinea pigs poisoned with cyclosarin [78]. A dose of cyclosarin s.c. (100 μg/kg, ≈2LD_{50}) led to rapid death, except for the animals treated with an injection of **20b** i.v. (100 mg/kg) 5 min prior to cyclosarin s.c. For them, the systemic signs of poisoning almost completely disappeared. Reiter et al. investigated the detoxification mechanism of **20b** and demonstrated a stereoselective hydrolysis of the most toxic (−)-cyclosarin [79]. As previously described, the formation of an intermediate inclusion complex is likely to occurred. The affinity between cyclosarin and **20b** could be explained by (1) ion–dipole interaction between the pyridinium group of **20b** and the phosphoryl oxygen of cyclosarin and (2) the cyclohexyl moiety inclusion into the hydrophobic CD cavity. The formation of such an inclusion complex could be followed by the fast hydrolysis of cyclosarin or the formation of mono-, bis-, tris- and tetrakis-conjugates which may ultimately be decomposed into small organic fragments. The scavenger **20b** is therefore consumed during the cyclosarin degradation and thus could not be considered as a catalyst.

If **20b** was the most efficient compound for the cyclosarin detoxification of this pyridinium series, Kubik et al. showed that **20c** was more efficient for the degradation of tabun (Scheme 4) [80]. However, it should be pointed out that a simple glucose derivative bearing the same nucleophilic group has a similar activity. The efficiency of **20c** is therefore clearly related to the pyridinium oxime functional group and not to the inclusion properties of the macromolecule.

Efficiency of compounds 23a–i against chemical warfare agents: Amongst the derivatives **23a**–**i** with the pyridine aldoxime linked to the CD by a triazole ring, compound **23a** is the most interesting scavenger. To access more potent compounds, Kubik et al. later introduced two α-nucleophiles on A and D units of β-CD [80]. Surprisingly, only a slight increase of the activity against tabun compared to that of **20b** was noticed. The steric hindrance induced by the two aldoxime groups might explain this disappointing result. It is also possible that the two reactive groups are not in optimal positions due to the rigidity of the triazole-based spacer.

Introduction of hydroxamic acids via a Huisgen reaction on α-, β- and γ-CD also leads to scavengers sharing the same level of efficiency than a glucose unit bearing the same functionnal group. These surprising results proved that for these derivatives, the macrocycle has no influence on the degradation of the nerve agent. This might be rationalized by the inclusion of the triazole ring into the CD's cavity by a tumbling phenomenon as shown by Monflier et al. [81]. This process would therefore prevent any interaction of the hydroxamic acid group with the oligosaccharide. *per*-Substitution of the primary face of β-CD improves the activity, but without linear correlation with the number of groups introduced [76].

Modifications at the C-2 and C-3 positions

Synthesis of 2-monosubstituted β-CD derivatives: A three-step protocol is usually followed to monofunctionalize the most acidic hydroxy groups on the 2-position: (1) deprotonation of that position with a strong base, (2) addition of the required halogenated derivative, (3) activation of the α-nucleophile supported by the CD (Scheme 5). The use of methyl iodobenzoates with variable alkyls linker (one or three carbon atoms) led to a series of CD derivatives supporting a iodosobenzoate group as the α-nucleophile (compounds **26a**–**f**) [82,83]. Careful optimisation studies were carried out to improve the yield of this challenging mono-substitution [83,84]. A wide range of strong bases and their amount (versus equivalents of CD and the halogenated derivative) were evaluated in dimethyl sulfoxide. As expected, halogenobenzylic derivatives **25a**–**d** gave the best yields compared to those obtained with methyl bromopropyliodobenzoates **25e**–**f**. The hydroxy groups of compounds **25b**–**d**

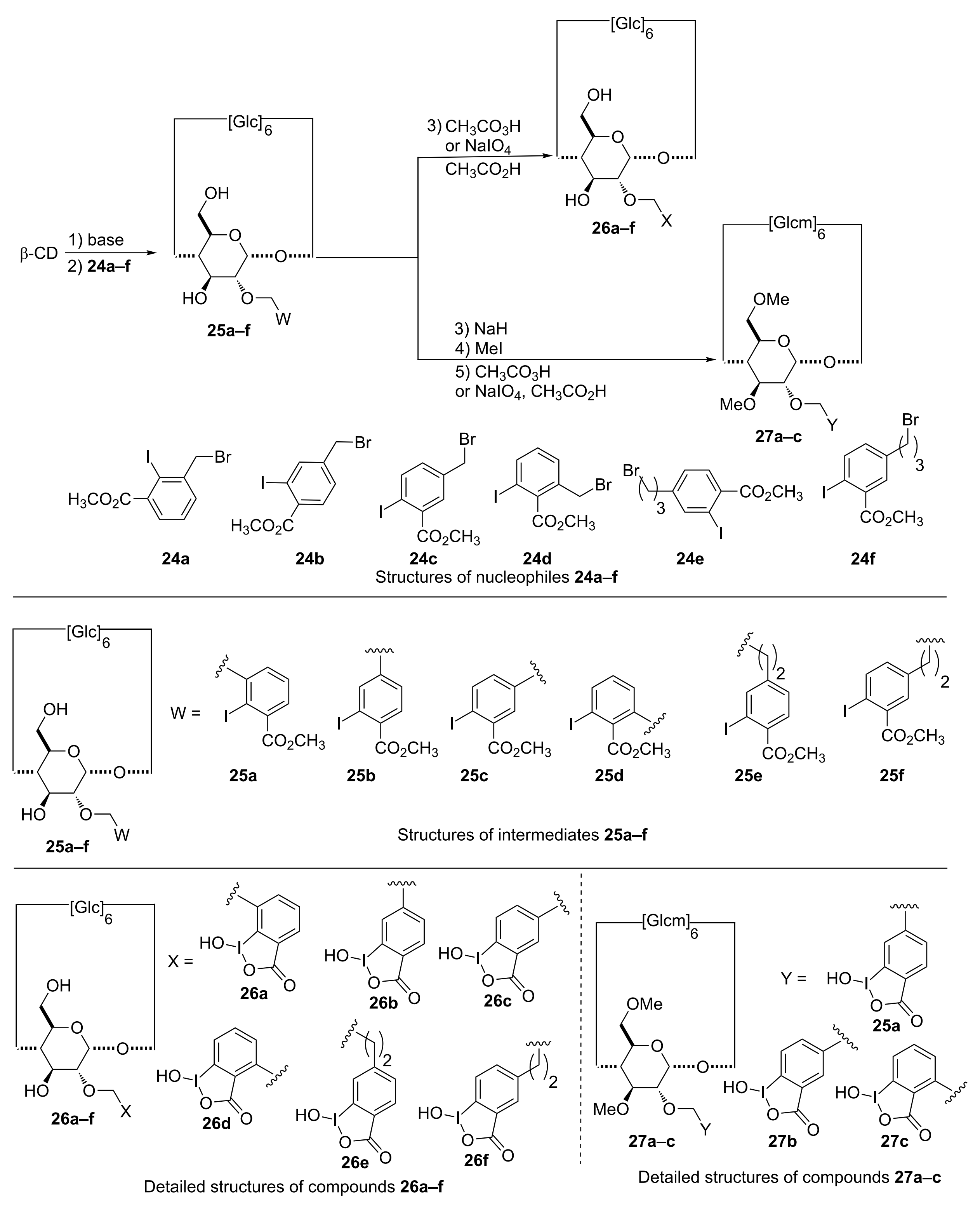

Scheme 5: Synthetic pathways to 2-monosubstituted CD by an iodosobenzoate group.

were also methylated (compounds **27a**–**c**) to evaluate the influence of the CD hydroxy groups in the organophosphorus substrate degradation [83].

It should be mentioned that this selective substitution of β-CD was also found to be substrate-dependant. As an example, the use of pyridinium aldoximates instead of iodosobenzoates

]

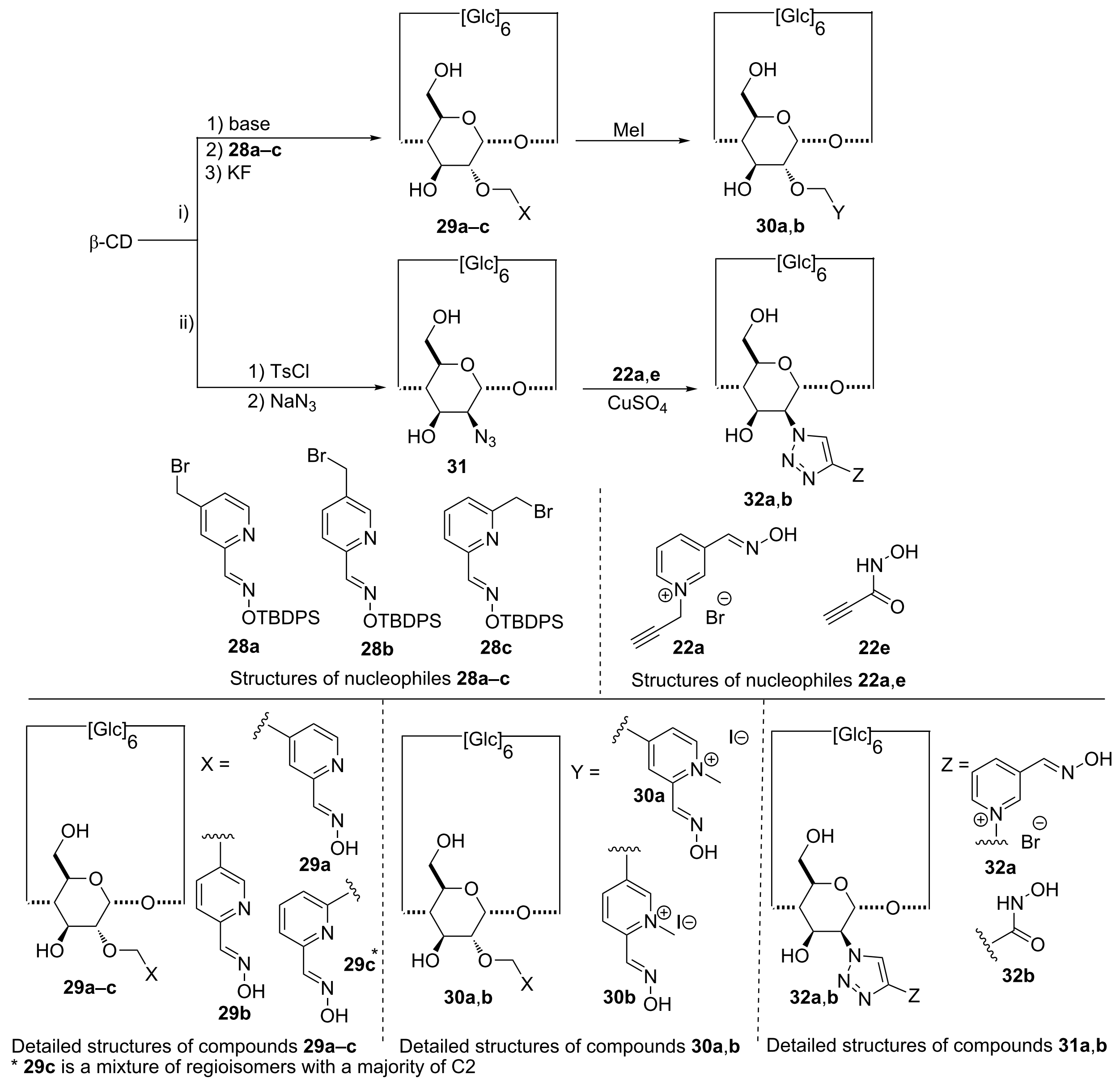

Scheme 6: Synthetic pathways to 2-monosubstituted CDs with N–OH derivatives.

(compounds **29a**–**c**, **30a** and **30b**, Scheme 6), required modified conditions.

The use of non-conventional activation methodologies (i.e., ultra-sound or microwaves) proved to be valuable to access some of these challenging CD derivatives [85]. Introduction of an oxime group at the C-2 position was also performed with a cooper(I)-catalyzed azide–alkyne cycloaddition between the 2’-azido-β-CD **31** and the alkyne derivatives **22a**,**b** to access the corresponding monosubstituted CD **32a**,**b** [76].

Synthesis of 3-monosubstituted β-CD derivatives: As the facial position of the reactive groups might modify the catalytic efficiency of the CD derivative, the monofunctionalization of the C-3 alcohols was carried out [86]. The temporary complexation of specific β-CD secondary hydroxy functions allows the monofunctionalization of the C-3 position through the formation of a copper(II)–β-CD complex. A diagonal link between copper ions and C-2 and C-3 oxygen atoms of adjacent glucopyranose units might distort the CD cavity, making the hydroxy groups on position 3 more accessible. Moreover, as this complex is formed in aqueous sodium hydroxide, the hydroxy groups could be deprotonated in situ to perform the subsequent substitution reaction in a one-pot manner. Methyl iodobenzoates were introduced following this approach (Scheme 7, **33a**,**b**), unfortunately, degradation occurred during the final oxi-

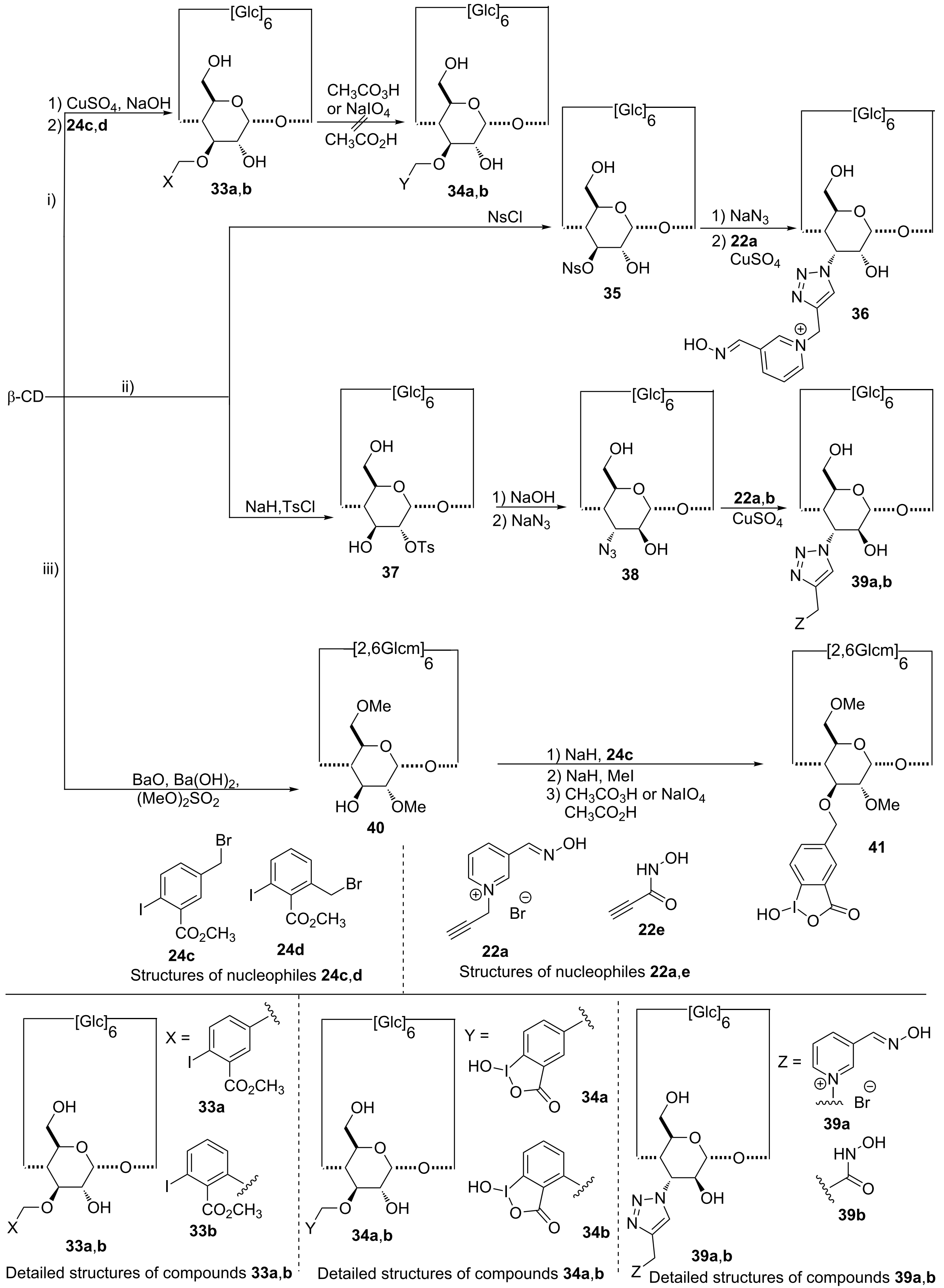

Structures of nucleophiles **24c**,**d**

Structures of nucleophiles **22a**,**e**

Detailed structures of compounds **33a**,**b**

Detailed structures of compounds **34a**,**b**

Detailed structures of compounds **39a**,**b**

* **33b** is a mixture of regioisomers with a majority of C3

Scheme 7: Synthetic pathways to 3-monosubstituted CDs.

dation step to obtain the α-nucleophile group [87]. The 3-monosubstituted derivative **41** was successfully obtained starting from the partially-protected 2,6-dimethyl-β-CD (Scheme 7) [88]. Finally, CDs bearing an oxime (**36** and **39a**) or a hydroxamic acid (**39b**) group in position 3 were prepared as previously described via an azide–alkyne cycloaddition (Scheme 7) [76,80].

Synthesis of difunctionalized β-CD derivatives: As the hydrolytic activity on NOPs may differ depending on the number and the nature of the groups introduced on CDs, methodologies were developed to regioselectively access disubstituted β-CDs. An elegant strategy to homodifunctionalize the A and B units' secondary hydroxy group of the β-CD rely on the use of the tethered disulfonylimidazole **42** to access a key intermediate easily converted to the corresponding di-2,3-mannoepoxido compound **43** (Scheme 8) [89]. The $3^A,3^B$-diazido-$3^A,3^B$-dideoxy-bis(*altro*)-β-cyclodextrin **44** was then obtained by reaction of **43** with sodium azide and a copper(I)-catalyzed azide–alkyne cycloaddition finally afforded the desired disubstituted compound **45** [80]. This compound is not stricto sensu a CD derivative as already the case for 2- and 3-monosubstituted CDs **32a**,**b**, **36** and **39a**,**b**.

Another particularly convenient strategy to introduce two different groups on adjacent units of methylated β-CD relies on the use of DIBAL-H to produce $2^A,3^B$-diol **46** from TRIMEB (Scheme 9) [90]. The two remaining free alcohols were then functionalized with the α-nucleophile and an imidazole group [88]. The acid–base dyad thus obtained is likely to improve the hydrolysis of nerve agents. The imidazole group was first introduced by a regioselective substitution at C-2, followed by a C-3 benzylation to access compound **49**. As the other regioisomer **52** could not be obtained so easily, additional protection–deprotection steps were required.

Efficiency of compounds 26a–f and 27a–c against chemical warfare agents: Preliminary tests were carried out with paraoxon to evaluate the efficiency of these scavengers as the hydrolysis of this organophosphorus pesticide releases *para*-nitrophenol that is easily monitored by UV–visible spectrophotometry at 400 nm [82]. It first appeared that the position of the spacer arm on the aromatic ring modifies the efficiency of the scavenger. The greatest hydrolysis rate was observed with the ether oxide in *para* position to the iodoso function in compound **26c**, while compound **26a** has no effect. According to the paraoxon concentration, a saturation effect of kinetics was observed during the pesticide hydrolysis with the three active compounds **26b**–**d**. The authors proposed that the *para*-nitrophenolate remains included into the cavity, thus poisoning the CD derivatives **26b**–**d**.

Compound **26c** was therefore selected to evaluate its efficiency against chemical warfare agents using a biological enzymatic

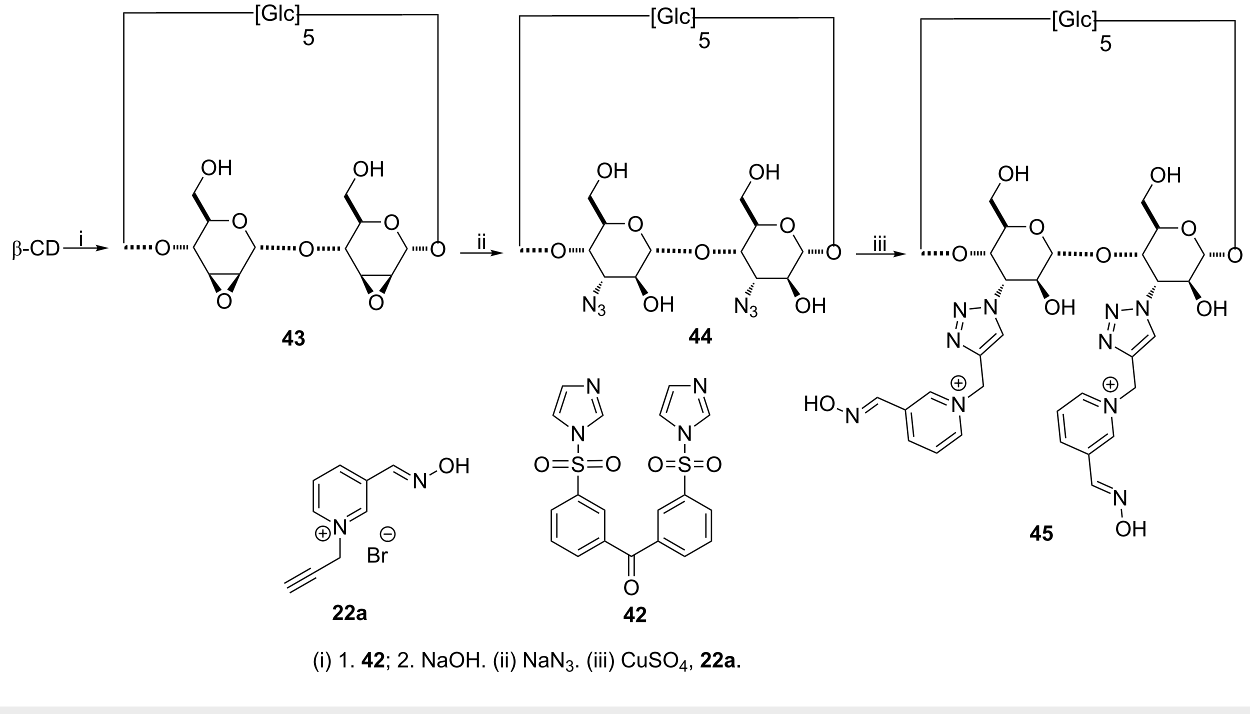

(i) 1. **42**; 2. NaOH. (ii) NaN_3. (iii) $CuSO_4$, **22a.**

Scheme 8: Synthetic pathways to 3-homodisubstituted CDs.

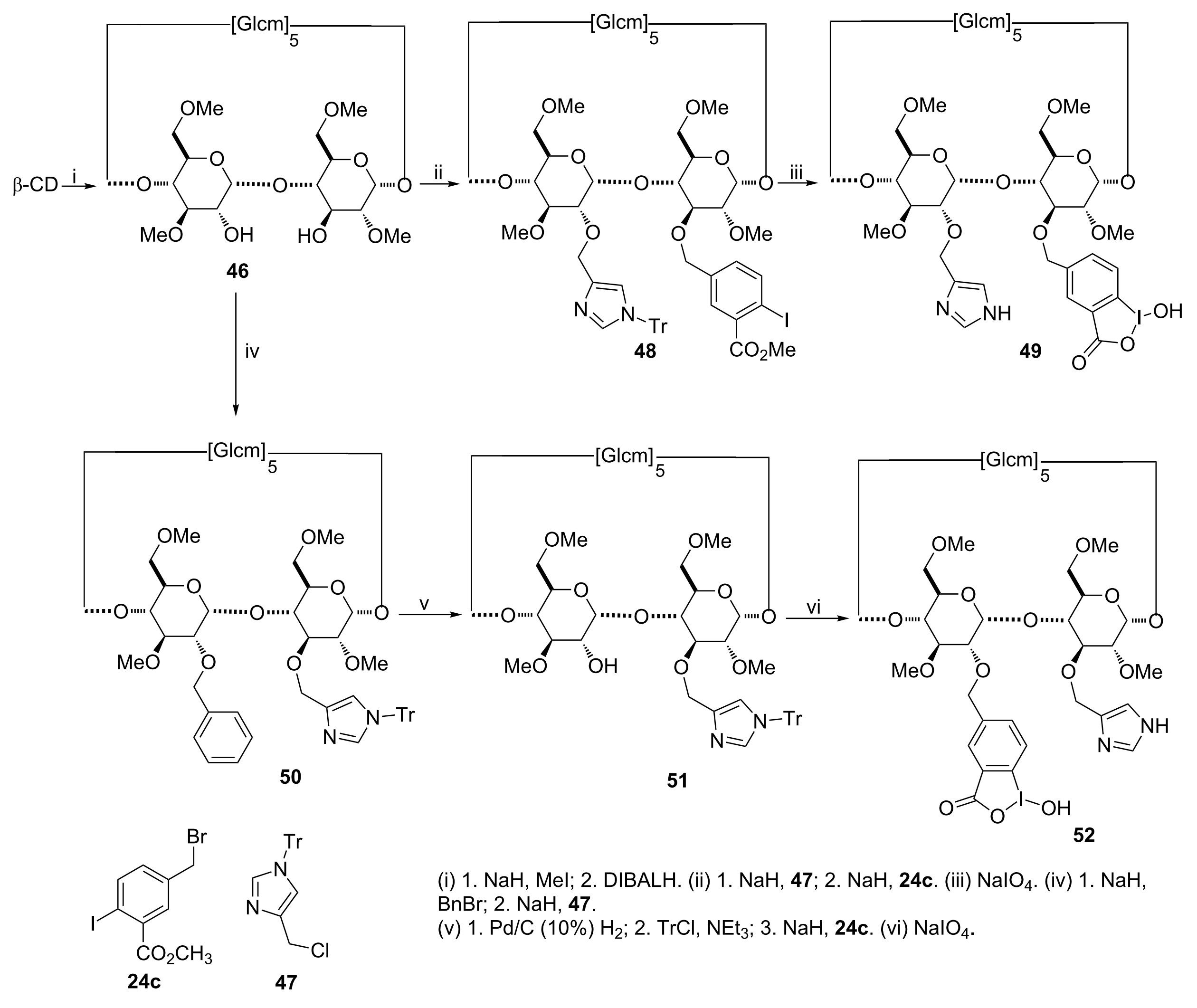

(i) 1. NaH, MeI; 2. DIBALH. (ii) 1. NaH, **47**; 2. NaH, **24c**. (iii) $NaIO_4$. (iv) 1. NaH, BnBr; 2. NaH, **47**.
(v) 1. Pd/C (10%) H_2; 2. TrCl, NEt_3; 3. NaH, **24c**. (vi) $NaIO_4$.

Scheme 9: Synthetic pathways to 2,3-heterodisubstituted CDs.

assay [91]. The ability and the detoxification rate decreases in the order cyclosarin > sarin > tabun and no activity is observed against VX. The detoxification process of tabun is performed in only one step when sarin and cyclosarin required two. The first one led to a fast reduction of the acetylcholinesterase (AchE) inhibition, followed in a second phase by a slow decrease until complete recovery of AchE activity. Two different phenomena could explain this behavior. The first one might be the formation of an inclusion complex between the NOP and the CD, each toxic characterized by different levels of affinity as guest in the torus. Thus VX and tabun would not form any inclusion complex whereas sarin and cyclosarin will, preventing the AChE inhibition. As a result, cyclosarin is almost fully trapped by the scavenger whereas 70% of the enzyme benefits of this phenomenon with sarin. In 2011, Reiter et al. confirmed the fast high-affinity binding of cyclosarin on **26c** as well as synergistic effects able to markedly accelerate the inactivation rate of cyclosarin. Moreover, they provided kinetic constants and correlation coefficients of the inactivation of cyclosarin after incubation with **26c** [92]. The second phase postulated above would finally rely on the hydrolytic activity of the iodosobenzoic acid group.

It should be noted that tabun, soman and cyclosarin have different CD-mediated reduction rates of their AchE inhibitory potential [83,93]. The acetylcholinesterase inhibitory potential of cyclosarin and soman significantly depends on the link position on the aromatic group, while tabun remained less affected.

The reduction of the AChE inhibitory potential of cyclosarin and soman is faster with the propylene-linked derivatives **26e** and **26f** than with the methylene-linked permethylated counterparts **27a** and **27b**, while their efficiencies were similar against tabun [82]. This result for tabun is in agreement with those obtained with compounds **26a–d**, showing no significant interaction between the nerve agent and the CD cavity. It also appeared that compounds **26c** and **26f** share a similar efficiency against cyclosarin whereas a weaker activity was observed for **27b**. If the α-nucleophile group undoubtedly plays a major role in the hydrolysis of cyclosarin, the free hydroxy functions of the CD also have an influence, whereas the distance between the iodosobenzoate substituent and the macrocycle could be considered as a minor parameter. Regarding the stereoselectivity issue, compound **26e** showed a marked preference for the (−)-cyclosarin **14a** degradation, while no stereoselective GF detoxification was recorded with derivative **27f** [93].

Efficiency of compounds 29a–c, 30a,b, 32a,b, 36 and 39a,b against chemical warfare agents: In the case of compounds **29a–c**, the degradation of cyclosarin was always found to depend on the position of the linker on the aromatic ring [85]. Fast degradation of the nerve agents was achieved for compound **29c** with a 2,6-disubstituted pyridine ring. No general trend in quaternarization emerges as **30a** was more active than **29a**. Moderate enantioselective hydrolysis of cyclosarin in favour of the levorotary isomer was obtained with compounds **29b** and **29c**. Interestingly, all compounds of this series are less efficient than the derivative **26c** bearing an iodosobenzoate substituent.

Every compound, **32a**, **36** and **39a**, including respectively a mannose, an allose or an altrose substituted unit, are able to hydrolyze tabun faster than derivative **23a**, bearing the same aldoxime group in position 6 [80]. The most efficient scavengers are then obtained with the α-nucleophile group on the secondary face. On the contrary, moving the hydroxamic acid to the secondary face of the CD reduces their efficiency against tabun (compounds **32a** and **32b** versus compound **23e**) [76]. However, in this case, no influence of the CD ring was highlighted for the 6-monosusbtituted CD **23e**, suggesting that the accessibility of the hydroxamic acid group on the secondary face of β-CD is more difficult.

Efficiency of compounds 45, 49 and 52 against chemical warfare agents: Introduction of two oximes in position 3 on two adjacent units with compound **45** has almost no effect on tabun hydrolysis compared to its monosubstituted counterpart **39a** [81]. Indeed, the resulting steric hindrance might prevent the cooperation of the second substituent, and/or the triazole-based linker would not allow the required positioning of the two substituents.

The degradation of soman by heterodifunctionalized derivatives **49** and **52** was monitored by ^{1}H NMR [88]. If the main product formed is pinacolyl methylphosphonic acid, as already observed in phosphate buffer [94], only compound **49** is able to accelerate the stereoselective hydrolysis of soman. The relative positioning of iodosobenzoate and imidazole groups importance was further highlighted by the lack of activity improvement with the regioisomer **52**. The true protective efficiency of the new scavenger **49** was also proved with an enzymatic assay. Finally, the synergistic effect of these two different groups must be emphasized for their efficiency in both hydrolysing the NOP and protecting AChE, compared to the corresponding 3-monosusbtituted CD **41**. This is the first example of a $2^{IB},3^{IA}$-heterodifunctionalized β-CD derivative, acting as an enzyme mimic.

Conclusion

As a result of their toroidal shape, CDs are able to trap organophosphorus pesticides and nerve agents. However, host's and guest's structures are both particularly determinant as they can modify the complex stability, the mode of entry and the inclusion depth of the organophosphorus substrate into the macrocyclic cavity. The potential degradation of toxics is then modulated by mixed effects. Further functionalization of CDs could lead to new derivatives with increased NOP hydrolytic potential. Through the introduction of an α-nucleophilic group on the oligosaccharidic torus, nerve agents were significantly hydrolyzed by CD derivatives under physiological conditions. Finally, it was proved that the introduction of two different groups on adjacent units of a permethylated-β-CD resulted in a synergic effect on soman hydrolysis. This new strategy is then a promising way to access original scavengers with an enzymomimetic activity.

Acknowledgements

Funding: DGA-MRIS and region Haute-Normandie are gratefully acknowledged for PhD scholarships. The authors thank DGA Maîtrise NRBC (contract n°2014910080), ANR (Projects ANR BLAN06-1_134538 and ANR « ASTRID maturation » ANR-14-ASMA-0003), ANR-LABEX SynOrg for a postdoctoral fellowship (ANR-11-LABX-0029). Rouen University, INSA Rouen, CNRS, EFRD and Labex SynOrg (ANR-11-LABX-0029) are also acknowledged for their financial support.

References

1. du Bois, A. *Eur. J. Cancer* **2001,** *37,* 1–7. doi:10.1016/S0959-8049(01)00328-8
2. Wolf, M. *Lung Cancer* **2001,** *33* (Suppl. 1), S125–S135. doi:10.1016/S0169-5002(01)00313-0
3. Rosales, F.; Naparstek, E.; Varadi, G.; Or, R.; Slavin, S.; Nagler, A. *Leuk. Res.* **1999,** *23,* 947–952. doi:10.1016/S0145-2126(99)00112-5
4. van Maanen, M. J.; Doesburg Smits, K.; Damen, J. M. A.; Heck, A. J. R.; Beijnen, J. H. *Int. J. Pharm.* **2000,** *200,* 187–194. doi:10.1016/S0378-5173(00)00370-7

5. Illiadis, A.; Launay-Illiadis, M.-C.; Lucas, C.; Fety, R.; Lokiec, F.; Tranchand, B.; Milano, G. *Eur. J. Cancer* **1996,** *32,* 455–460. doi:10.1016/0959-8049(95)00565-X
6. Jacquillat, C.; Khayat, D.; Banzet, P.; Weil, M.; Fumoleau, P.; Avril, M.-F.; Namer, M.; Bonneterre, J.; Kerbrat, P.; Bonerandji, J. J.; Bugat, R.; Montcuquet, P.; Cupissol, D.; Lauvin, R.; Vilmer, C.; Prache, C.; Bizzari, J. P. *Cancer* **1990,** *66,* 1873–1878. doi:10.1002/1097-0142(19901101)66:9<1873::AID-CNCR2820660904>3.0.CO;2-5
7. Seeber, A.; Binder, A.; Steiner, A.; Wolff, K.; Pehamberger, H. *Eur. J. Cancer* **1998,** *34,* 2129–2131. doi:10.1016/S0959-8049(98)00316-5
8. Daponte, A.; Ascierto, P. A.; Gravina, A.; Melucci, M. T.; Palmieri, G.; Comella, P.; Cellerino, R.; DeLena, M.; Marini, G.; Comella, G. *Cancer* **2000,** *89,* 2630–2636. doi:10.1002/1097-0142(20001215)89:12<2630::AID-CNCR16>3.0.CO;2-Z
9. Gérard, L.; Salmon-Céron, D. *Int. J. Antimicrob. Agents* **1995,** *5,* 209–217. doi:10.1016/0924-8579(95)00008-V
10. De Clercq, E. *J. Clin. Virol.* **2001,** *22,* 73–89. doi:10.1016/S1386-6532(01)00167-6
11. Roche, B.; Roque-Afonso, A.-M.; Feray, C.; Duclos-Vallee, J. C.; Bismuth, H.; Samuel, D. *J. Hepatol.* **2002,** *36* (Suppl. 1), 42. doi:10.1016/S0168-8278(02)80128-3
12. Schiff, E.; Neuhaus, P.; Tillman, H.; Samuel, D.; Terrault, N.; Durand, F.; Xiong, S.; Lama, C.; Fry, J.; Namini, H.; Brosgart, C. *J. Hepatol.* **2002,** *36* (Suppl. 1), 32. doi:10.1016/S0168-8278(02)80093-9
13. Krise, J. P.; Stella, V. J. *Adv. Drug Delivery Rev.* **1996,** *19,* 287–310. doi:10.1016/0169-409X(95)00111-J
14. Mancia, G.; Giannattasio, C.; Grassi, G. *Am. J. Hypertens.* **1997,** *10,* 236S–241S. doi:10.1016/S0895-7061(97)00329-4
15. Fleisch, H.; Graham, R.; Russel, G.; Francis, M. D. *Science* **1969,** *165,* 1262–1264. doi:10.1126/science.165.3899.1262
16. Francis, M. D.; Graham, R.; Russel, G.; Fleisch, H. *Science* **1969,** *165,* 1264–1266. doi:10.1126/science.165.3899.1264
17. Evans, C. E. *Int. J. Biochem. Cell Biol.* **2002,** *34,* 554–563. doi:10.1016/S1357-2725(01)00147-9
18. Becker, R. E.; Greig, N. H. *Curr. Alzheimer Res.* **2010,** *7,* 642–651. doi:10.2174/156720510793499075
19. Dell'Antone, P.; Bragadin, M.; Zatta, P. *Biochim. Biophys. Acta* **1995,** *1270,* 137–141. doi:10.1016/0925-4439(94)00079-6
20. Benschop, H. P.; De Jong, L. P. A. *Acc. Chem. Res.* **1988,** *21,* 368–374. doi:10.1021/ar00154a003
21. Gunnell, D.; Eddleston, M. *Int. J. Epidemiol.* **2003,** *32,* 902–909. doi:10.1093/ije/dyg307
22. Gunnell, D.; Eddleston, M.; Phillips, M. R.; Konradsen, F. *BMC Public Health* **2007,** *7,* 357–372. doi:10.1186/1471-2458-7-357
23. de Silva, H. J.; Wijewickrema, R.; Senanayake, N. *Lancet* **1992,** *339,* 1136–1138. doi:10.1016/0140-6736(92)90733-J
24. Crombie, I. K. *Br. Med. J.* **1991,** *302,* 761–762. doi:10.1136/bmj.302.6779.761
25. Kelly, S.; Charlton, J.; Jenkins, R. *Popul. Trends* **1995,** *80,* 16–25.
26. Parrón, T.; Hernández, A. F.; Villanueva, E. *Forensic Sci. Int.* **1996,** *79,* 53–63. doi:10.1016/0379-0738(96)01895-6
27. Kim, K.; Tsay, O. G.; Atwood, D. A.; Churchill, D. G. *Chem. Rev.* **2011,** *111,* 5345–5403. doi:10.1021/cr100193y
28. Takahashi, K. *Chem. Rev.* **1998,** *98,* 2013–2034. doi:10.1021/cr9700235
29. Sakuraba, H.; Maekawa, H. *J. Inclusion Phenom. Macrocyclic Chem.* **2006,** *54,* 41–45. doi:10.1007/s10847-005-3490-9
30. Bhosale, S. V.; Bhosale, S. V. *Mini-Rev. Org. Chem.* **2007,** *4,* 231–242. doi:10.2174/157019307781369922
31. Kanagaraj, K.; Affrose, A.; Sivakolunthu, S.; Pitchumani, K. *Biosens. Bioelectron.* **2012,** *35,* 452–455. doi:10.1016/j.bios.2012.02.046
32. Zhao, H.; Ji, X.; Wang, B.; Wang, N.; Li, X.; Ni, R.; Ren, J. *Biosens. Bioelectron.* **2015,** *65,* 23–30. doi:10.1016/j.bios.2014.10.007
33. Ramaseshan, R.; Sundarrajan, S.; Liu, Y.; Barhate, R. S.; Lala, N. L.; Ramakrishna, S. *Nanotechnology* **2006,** *17,* 2947–2953. doi:10.1088/0957-4484/17/12/021
34. Zourob, M.; Ong, K. G.; Zeng, K.; Mouffouk, F.; Grimes, C. A. *Analyst* **2007,** *132,* 338–343. doi:10.1039/b616035b
35. Knapton, D.; Burnworth, M.; Rowan, S. J.; Weder, C. *Angew. Chem.* **2006,** *118,* 5957–5961. doi:10.1002/ange.200601634
36. Burnworth, M.; Rowan, S. J.; Weder, C. *Chem. – Eur. J.* **2007,** *13,* 7828–7836. doi:10.1002/chem.200700720
37. Masson, P.; Lockridge, O. *Arch. Biochem. Biophys.* **2010,** *494,* 107–120. doi:10.1016/j.abb.2009.12.005
38. Szejtli, J. *Starch/Staerke* **1985,** *37,* 382–386. doi:10.1002/star.19850371106
39. Lucas-Abellán, C.; Gabaldón-Hernández, J. A.; Penalva, J.; Fortea, M. I.; Núñez-Delicado, E. *J. Agric. Food Chem.* **2008,** *56,* 8081–8085. doi:10.1021/jf8015046
40. Manunza, B.; Deiana, S.; Pintore, M.; Gessa, C. *Glycoconjugate J.* **1998,** *15,* 293–296. doi:10.1023/A:1006953230364
41. Soni, S.-D.; Bhonsle, J. B.; Garcia, G. E. *Magn. Reson. Chem.* **2014,** *52,* 111–114. doi:10.1002/mrc.4036
42. Vico, R. V.; Buján, E. I.; de Rossi, R. H. *J. Phys. Org. Chem.* **2002,** *15,* 858–862. doi:10.1002/poc.560
43. Dailey, O. D.; Bland, J. M.; Trask-Morrell, B. J. *J. Agric. Food Chem.* **1993,** *41,* 1767–1771. doi:10.1021/jf00034a046
44. Cruickshank, D. L.; Rougier, N. M.; Maurel, V. J.; de Rossi, R. H.; Buján, E. I.; Bourne, S. A.; Caira, M. R. *J. Inclusion Phenom. Macrocyclic Chem.* **2013,** *75,* 47–56. doi:10.1007/s10847-012-0145-5
45. Molaabasi, F.; Talebpour, Z. *J. Agric. Food Chem.* **2011,** *59,* 803–808. doi:10.1021/jf103169p
46. Coly, A.; Aaron, J.-J. *Anal. Chim. Acta* **1998,** *360,* 129–141. doi:10.1016/S0003-2670(97)00721-6
47. Churchill, D.; Cheung, J. C. F.; Park, Y. S.; Smith, V. H.; Van Loon, G.; Buncel, E. *Can. J. Chem.* **2006,** *84,* 702–708. doi:10.1139/v06-053
48. Wagner, B. D.; Sherren, A. C.; Rankin, M. A. *Can. J. Chem.* **2002,** *80,* 1210–1216. doi:10.1139/v02-133
49. Loukas, Y. L.; Antoniadou-Vyza, E.; Papadaki-Valiraki, A.; Machera, K. G. *J. Agric. Food Chem.* **1994,** *42,* 944–948. doi:10.1021/jf00040a020
50. Loukas, Y. L.; Vyza, E. A.; Valiraki, A. P. *Analyst* **1995,** *120,* 533–538. doi:10.1039/an9952000533
51. Zhou, S.; Wang, L.; Zhang, A.; Lin, K.; Liu, W. *J. Agric. Food Chem.* **2008,** *56,* 2708–2713. doi:10.1021/jf703635p
52. Kamiya, M.; Mitsuhashi, S.; Makino, M. *Chemosphere* **1992,** *25,* 1783–1796. doi:10.1016/0045-6535(92)90019-N
53. Kamiya, M.; Nakamura, K. *Pestic. Sci.* **1994,** *41,* 305–309. doi:10.1002/ps.2780410404
54. Kamiya, M.; Nakamura, K.; Sasaki, C. *Chemosphere* **1995,** *30,* 653–660. doi:10.1016/0045-6535(94)00431-S

55. Coscarello, E. N.; Barbiric, D. A.; Castro, E. A.; Vico, R. V.; Bujánm, E. I.; de Rossi, R. H. *J. Struct. Chem.* **2009,** *50,* 671–679. doi:10.1007/s10947-009-0103-2
56. Rougier, N. M.; Cruickshank, D. L.; Vico, R. V.; Bourne, S. A.; Caira, M. R.; Buján, E. I.; de Rossi, R. H. *Carbohydr. Res.* **2011,** *346,* 322–327. doi:10.1016/j.carres.2010.06.016
57. Cruickshank, D. L.; Rougier, N. M.; Vico, R. V.; Bourne, S. A.; Buján, E. I.; Caira, M. R.; de Rossi, R. H. *Beilstein J. Org. Chem.* **2013,** *9,* 106–117. doi:10.3762/bjoc.9.14
58. Ishiwata, S.; Kamiya, M. *Chemosphere* **1999,** *39,* 1595–1600. doi:10.1016/S0045-6535(99)00057-0
59. Kamiya, M.; Nakamura, K.; Sasaki, C. *Chemosphere* **1994,** *28,* 1961–1966. doi:10.1016/0045-6535(94)90146-5
60. Kamiya, M.; Nakamura, K. *Environ. Int.* **1995,** *21,* 299–304. doi:10.1016/0160-4120(95)00026-H
61. Kamiya, M.; Kameyama, K.; Ishiwata, S. *Chemosphere* **2001,** *42,* 251–255. doi:10.1016/S0045-6535(00)00085-0
62. van Hooidonk, C.; Breebaart-Hansen, J. C. A. E. *Recl. Trav. Chim. Pays-Bas* **1970,** *89,* 289–299. doi:10.1002/recl.19700890309
63. Cahn, R. S.; Ingold, C.; Prelog, V. *Angew. Chem.* **1966,** *5,* 385–415. doi:10.1002/anie.196603851
64. Prelog, V.; Helmchen, G. *Angew. Chem.* **1982,** *21,* 567–583. doi:10.1002/anie.198205671
65. Quin, L. D. ^{31}P NMR shifts of phosphines. *A guide to organophosphorus chemistry;* Wiley-Interscience: USA, 2000; Vol. 101, pp 180–183.
66. van Hooidonk, C.; Groos, C. C. *Recl. Trav. Chim. Pays-Bas* **1970,** *89,* 845–856. doi:10.1002/recl.19700890810
67. van Hooidonk, C. *Recl. Trav. Chim. Pays-Bas* **1972,** *91,* 1103–1109. doi:10.1002/recl.19720910910
68. Saint-André, S.; Désiré, B. C. R. *C. R. Acad. Sci., Ser. III* **1985,** *301,* 67–72.
69. Désiré, B.; Saint-André, S. *Experimentia* **1987,** *43,* 395–397. doi:10.1007/BF01940424
70. Désiré, B.; Saint-André, S. *Fundam. Appl. Toxicol.* **1986,** *7,* 646–657. doi:10.1016/0272-0590(86)90114-4
71. Cabal, J. *Collect. Czech. Chem. Commun.* **1995,** *60,* 1162–1169. doi:10.1135/cccc19951162
72. Kranawetvogl, A.; Schüler, J.; Müller, S.; Thiermann, H.; Worek, F.; Reiter, G. *Toxicol. Lett.* **2013,** *222,* 164–170. doi:10.1016/j.toxlet.2013.07.017
73. Anslyn, E.; Breslow, R. *J. Am. Chem. Soc.* **1989,** *111,* 8931–8932. doi:10.1021/ja00206a033
74. Breslow, R.; Dong, S. D. *Chem. Rev.* **1998,** *98,* 1997–2012. doi:10.1021/cr970011j
75. Zengerle, M.; Brandhuber, F.; Schneider, C.; Worek, F.; Reiter, G.; Kubik, S. *Beilstein J. Org. Chem.* **2011,** *7,* 1543–1554. doi:10.3762/bjoc.7.182
76. Brandhuber, F.; Zengerle, M.; Porwol, L.; Bierwisch, A.; Koller, M.; Reiter, G.; Worek, F.; Kubik, S. *Chem. Commun.* **2013,** *49,* 3425–3427. doi:10.1039/c3cc41290c
77. Bierwisch, A.; Zengerle, M.; Thiermann, H.; Kubik, S.; Worek, F. *Toxicol. Lett.* **2014,** *224,* 209–214. doi:10.1016/j.toxlet.2013.10.024
78. Worek, F.; Seeger, T.; Zengerle, M.; Kubik, S.; Thiermann, H.; Wille, T. *Toxicol. Lett.* **2014,** *226,* 222–227. doi:10.1016/j.toxlet.2014.02.010
79. Kranawetvogl, A.; Müller, S.; Kubik, S.; Spruit, H.; Thiermann, H.; Worek, F.; Noort, D.; Reiter, G. *Toxicol. Lett.* **2015,** *239,* 41–52. doi:10.1016/j.toxlet.2015.08.007
80. Brandhuber, F.; Zengerle, M.; Porwol, L.; Tenberken, O.; Thiermann, H.; Worek, F.; Kubik, S.; Reiter, G. *Toxicology* **2012,** *302,* 163–171. doi:10.1016/j.tox.2012.08.013
81. Menuel, S.; Azaroual, N.; Landy, D.; Six, N.; Hapiot, F.; Monflier, E. *Chem. – Eur. J.* **2011,** *17,* 3949–3955. doi:10.1002/chem.201003221
82. Masurier, N.; Estour, F.; Froment, M.-T.; Lefèvre, B.; Debouzy, J.-C.; Brasme, B.; Masson, P.; Lafont, O. *Eur. J. Med. Chem.* **2005,** *40,* 615–623. doi:10.1016/j.ejmech.2005.02.008
83. Kalakuntla, R. K.; Wille, T.; Le Provost, R.; Letort, S.; Reiter, G.; Müller, S.; Thiermann, H.; Worek, F.; Gouhier, G.; Lafont, O.; Estour, F. *Toxicol. Lett.* **2013,** *216,* 200–205. doi:10.1016/j.toxlet.2012.11.020
84. Masurier, N.; Estour, F.; Lefèvre, B.; Brasme, B.; Masson, P.; Lafont, O. *Carbohydr. Res.* **2006,** *341,* 935–940. doi:10.1016/j.carres.2006.02.012
85. Le Provost, R.; Wille, T.; Louise, L.; Masurier, N.; Müller, S.; Reiter, G.; Renard, P.-Y.; Lafont, O.; Worek, F.; Estour, F. *Org. Biomol. Chem.* **2011,** *9,* 3026–3032. doi:10.1039/c0ob00931h
86. Masurier, N.; Lafont, O.; Le Provost, R.; Lesur, D.; Masson, P.; Djedaïni-Pilard, F.; Estour, F. *Chem. Commun.* **2009,** *45,* 589–591. doi:10.1039/B812325J
87. Estour, F.; Letort, S.; Müller, S.; Kalakuntla, R. K.; Le Provost, R.; Wille, T.; Reiter, G.; Worek, F.; Lafont, O.; Gouhier, G. *Chem.-Biol. Interact.* **2013,** *203,* 202–207. doi:10.1016/j.cbi.2012.10.020
88. Letort, S.; Mathiron, D.; Grel, T.; Albaret, C.; Daulon, S.; Djedaïni-Pilard, F.; Gouhier, G.; Estour, F. *Chem. Commun.* **2015,** *51,* 2601–2604. doi:10.1039/C4CC09189B
89. Teranishi, K. *Chem. Commun.* **2000,** 1255–1256. doi:10.1039/b002445g
90. Xiao, S.; Yang, M.; Sinaÿ, P.; Blériot, Y.; Sollogoub, M.; Zhang, Y. *Eur. J. Org. Chem.* **2010,** 1510–1516. doi:10.1002/ejoc.200901230
91. Wille, T.; Tenberken, O.; Reiter, G.; Müller, S.; Le Provost, R.; Lafont, O.; Estour, F.; Thiermann, H.; Worek, F. *Toxicology* **2009,** *265,* 96–100. doi:10.1016/j.tox.2009.09.018
92. Müller, S.; Koller, M.; Le Provost, R.; Lafont, O.; Estour, F.; Wille, T.; Thiermann, H.; Worek, F.; Reiter, G. *Toxicol. Lett.* **2011,** *200,* 53–58. doi:10.1016/j.toxlet.2010.10.014
93. Müller, S.; Estour, F.; Kalakuntla, R. K.; Le Provost, R.; Lafont, O.; Worek, F.; Thiermann, H.; Reiter, G. *Toxicol. Lett.* **2013,** *216,* 206–212. doi:10.1016/j.toxlet.2012.11.019
94. Gäb, J.; John, H.; Blum, M.-M. *Toxicol. Lett.* **2011,** *200,* 34–40. doi:10.1016/j.toxlet.2010.10.011

License and Terms

BEILSTEIN JOURNAL OF ORGANIC CHEMISTRY

Enabling technologies and green processes in cyclodextrin chemistry

Giancarlo Cravotto*, Marina Caporaso, Laszlo Jicsinszky and Katia Martina

Review

Open Access

Address:
Dipartimento di Scienza e Tecnologia del Farmaco and NIS - Centre for Nanostructured Interfaces and Surfaces, University of Turin, Via P. Giuria 9, 10125 Turin, Italy

Email:
Giancarlo Cravotto* - giancarlo.cravotto@unito.it

* Corresponding author

Keywords:
ball milling; cyclodextrin; microwaves; synthesis; ultrasound

Beilstein J. Org. Chem. **2016,** *12,* 278–294.
doi:10.3762/bjoc.12.30

Received: 31 October 2015
Accepted: 29 January 2016
Published: 15 February 2016

This article is part of the Thematic Series "Superstructures with cyclodextrins: Chemistry and applications III".

Guest Editor: E. Monflier

Abstract

The design of efficient synthetic green strategies for the selective modification of cyclodextrins (CDs) is still a challenging task. Outstanding results have been achieved in recent years by means of so-called enabling technologies, such as microwaves, ultrasound and ball mills, that have become irreplaceable tools in the synthesis of CD derivatives. Several examples of sonochemical selective modification of native α-, β- and γ-CDs have been reported including heterogeneous phase Pd- and Cu-catalysed hydrogenations and couplings. Microwave irradiation has emerged as the technique of choice for the production of highly substituted CD derivatives, CD grafted materials and polymers. Mechanochemical methods have successfully furnished greener, solvent-free syntheses and efficient complexation, while flow microreactors may well improve the repeatability and optimization of critical synthetic protocols.

Review

The last decade has witnessed the development of highly efficient alternative synthetic methods which make use of new enabling technologies. The need for a more rational approach to the synthesis of cyclodextrin (CD) derivatives has led to several energy sources been tested for their ability to activate C–C and C–X bond formation. In recent years non-conventional energy sources, such as microwaves (MW), ultrasound (US), ball mills (BM) and microreactors have made access to CD derivatives much simpler, as have heterogeneous catalysts and greener solvents. Besides batch reactors, in the last decade these techniques have been adapted to flow systems, which provide greater efficiency, flexibility and lower energy consumption, or in high-throughput applications. Our experience in process intensification and innovative reactors took advantage from flow-multihorn US systems (Figure 1a) and cavitational turbines (Figure 1b) to optimize mass transfer via intense cavitation [1,2]. Similarly, we have accumulated experiences with mechanochemical conditions that open the way to solventless

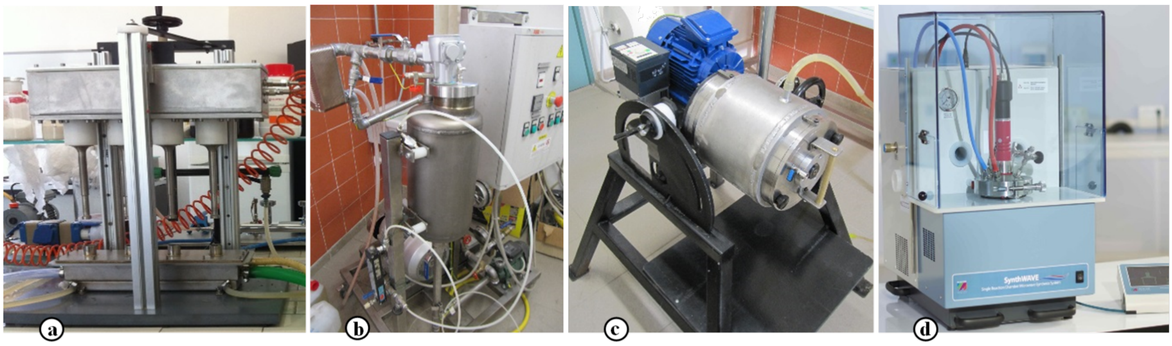

Figure 1: (a) Multihorn-flow US reactor, (b) Cavitational turbine, (c) Pilot-scale BM, (d) High-pressure MW reactor.

reactions even on a pilot scale (Figure 1c) [3]. The latest generation of dedicated MW reactors, which enable operators to quickly screen reaction conditions by means of parallel tests across a wide range of operative conditions, has provided outstanding MW-assisted synthesis results (Figure 1d) [4]. While most researchers will most likely be acquainted with the potential of dielectric heating, the specific conditions needed to let react CDs efficiently and selectively are often overlooked.

The current trends on CDs' literature and their application in green protocols are clearly depicted in Figure 2. The present literature survey with identical keyword combinations has been done in two major databases [5,6]. The results were partially overlapped only in the full text searches and approximately 4000 records have been found. Further reduction of records, less than 2500, by searching in Title/Abstract/Keyword fields only resulted in more relevant publications. Only 10% roughly of the recently published papers on CDs are dealing with sustainable technologies and only few works are comparing data with conventional synthetic protocols.

Mechanochemical syntheses are typically carried out in BM and also in low-frequency US reactors [7]. This technique has recently developed into a genuine eco-friendly alternative when manufacturing inorganic, organic and metal-organic compounds as well as supramolecular composites, which may differ to those prepared via conventional routes [8]. Higher versatility and selectivity offer a wide range of applications and may facilitate the purification steps [9]. Noteworthy examples are the mechanochemical derivatization of saccharides [10,11], the functionalization of CDs and their complexation with organic molecules [12]. Solid state organic reactions using CD cavities as nanoreactors have also been reported [13].

Among non-conventional techniques, the largest number of papers is dealing with US-assisted CD solubilization or re-dissolution and in a minor extends CD derivatization. Analogously, ball milling is mostly used in the preparation of CD complexes rather than synthetic preparations. MW-assisted CD chemistry covers 1/4–1/5 of the whole literature as seen in Figure 3, mainly focused on synthetic applications.

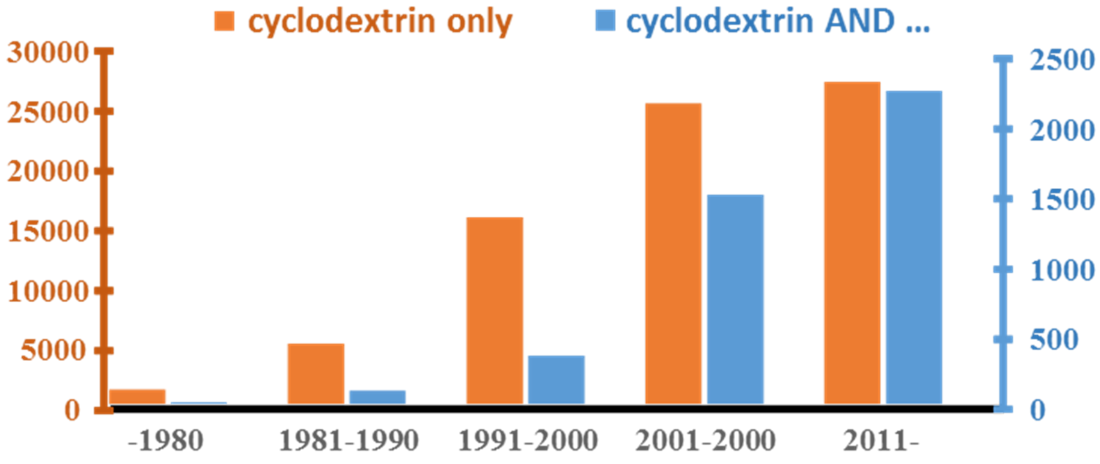

Figure 2: Trends in CD papers and CD use in green chemical processes.

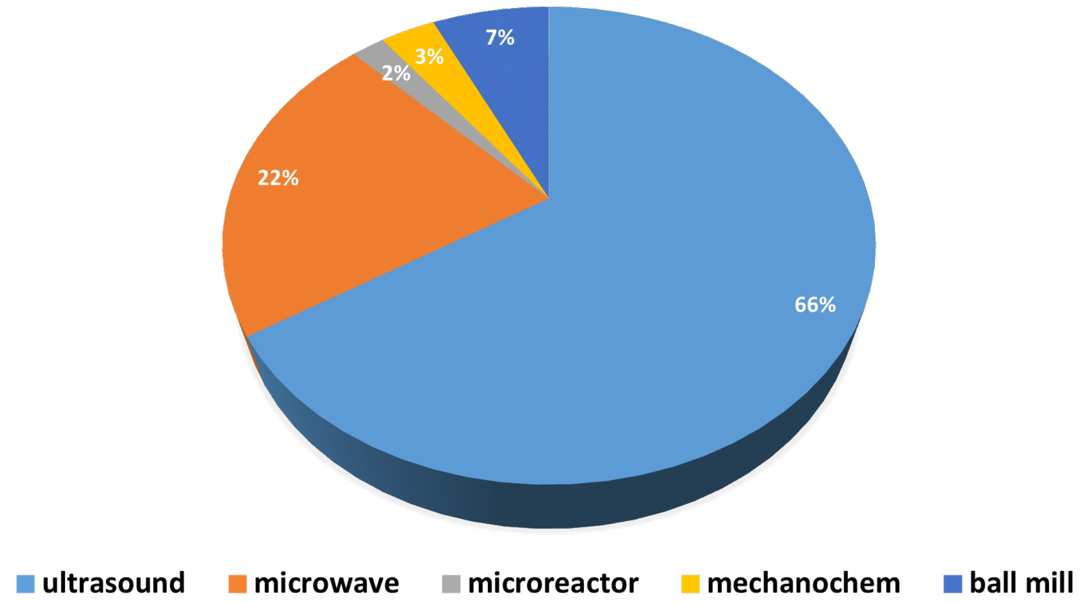

Figure 3: Distribution of energy efficient methods in CD publications.

As seen in Figure 4, the cake of document types dealing with CD chemistry under non-conventional techniques shows a similar distribution as observed in general CD publications, namely 70% article, 20% patents and 10% books (including non-journal conference proceedings and dissertations).

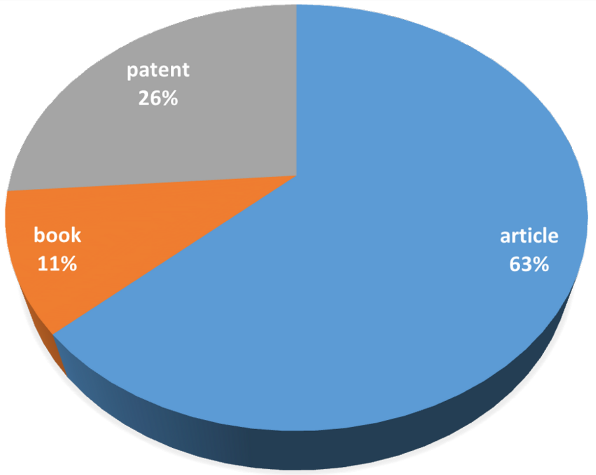

Figure 4: Document type dealing with CD chemistry under non-conventional techniques (conference proceedings and dissertations are handled as books).

However, industrial applications of such enabling techniques are a priori restricted to US and BM, owing to safety concerns on big scale MW reactors (Figure 5). Microreactors are a relatively new technologies and the small number of patents may also derive from solubility limitation.

This review highlights the most recent synthetic advances in CDs' chemical modification and some perspectives that make use of non-conventional methods and energy sources. Reaction times and yields have been compared with classic procedures to highlight the huge advantages and potential scalability of these so-called enabling technologies that maximize heat and mass transfer.

Although many advances have been made during the past decade, the most exciting results in this field are surely yet to come.

Ultrasound

US irradiation is an environmentally friendly technique that is well suited to the selective chemical modification of CDs from native α-, β- and γ-CD. The use of this method in heterogeneous phase reactions, such as reductions and "click reactions" [14], is well known, as is its use in full CD derivatization in combination with MW irradiation.

Monosubstituted CD derivative preparation

Mono 6^{I}-(*p*-toluenesulfonyl)-β-CD is the most popular of the CD derivatives because it is a key intermediate in the synthesis of important amino, azido, thio, thiocyanate and halo-derivatives. 6^{I}-(*p*-toluenesulfonyl)-β-CD was efficiently prepared in an US-assisted procedure by reacting β-CD with tosyl imidazole (TsIm) [15]. Great advantages, in terms of yields, reaction times and product purity, were obtained by using a cavitating tube (40 min, 19.2 kHz, 20 W, yield: 55%).

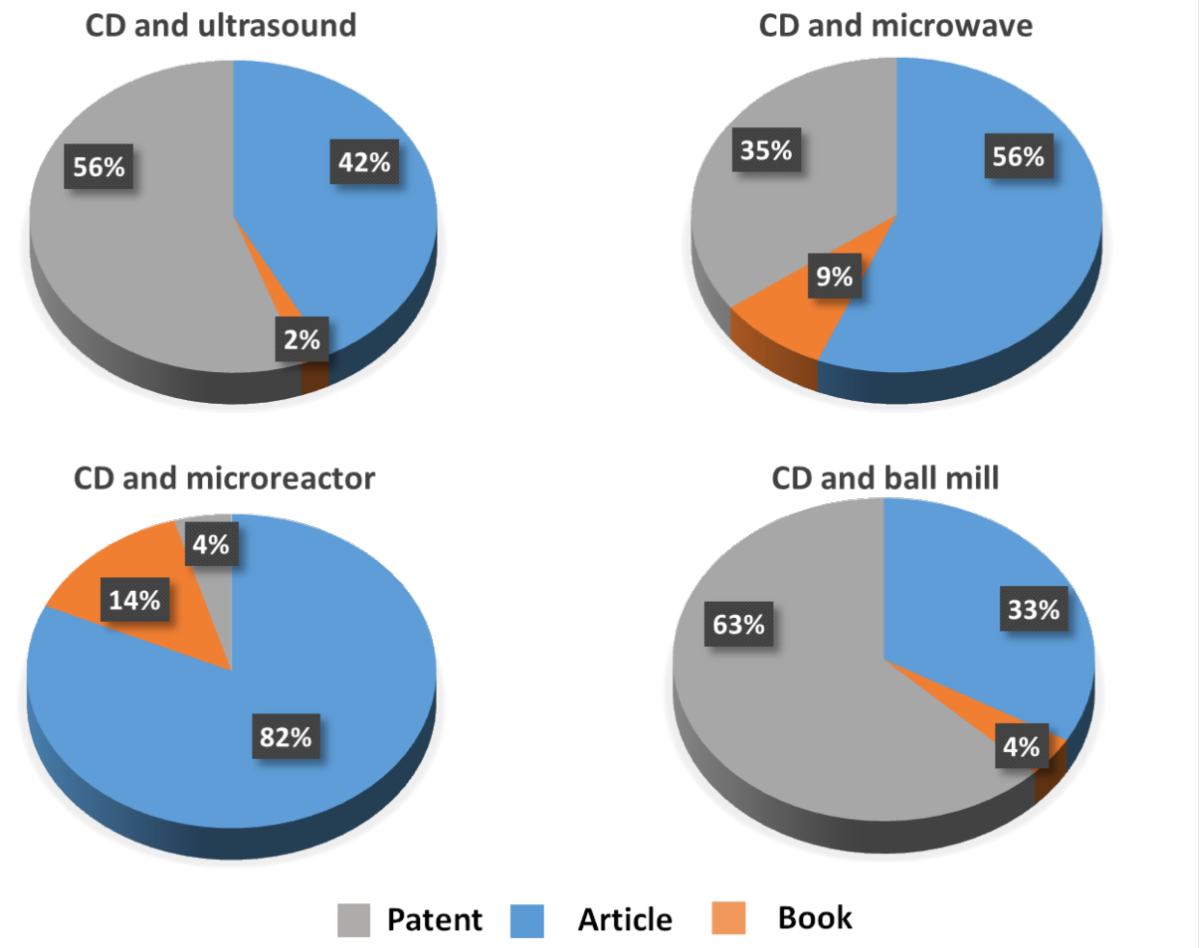

Figure 5: Document type dealing with sustainable technologies in CD publications.

Thanks to the fast US-assisted inclusion complex formation between β-CD and TsIm reaction times have been dramatically reduced (10 min vs 1–2 hours, Scheme 1).

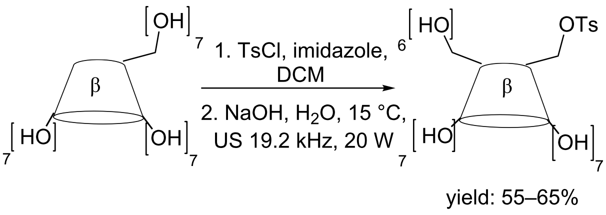

Scheme 1: Synthesis of 6^I-(*p*-toluenesulfonyl)-β-CD.

More recently, Zheng et al. have described the synthesis of this important intermediate via an US-assisted method in basic water solution [16].

The synthesis of 6^I-amino-6^I-deoxy-β-CD was also improved by using non-conventional techniques. The catalytic hydrogenation of 6^I-azido-6^I-deoxy-β-CD using Pd/C was achieved under US irradiation in MeOH/H_2O in 20 min (20.4 kHz, 80 W, yield: 88%); hydrogen was supplied at 1 bar pressure [15].

Sonochemical metals depassivation in organometallic reactions is well established [17]. A typical example is the Cu(0)-catalysed azide–alkyne cycloaddition (CuAAC) that can be further enhanced by simultaneous US/MW irradiation [18]. The formation of triazole-substituted CDs has been investigated by US irradiation and products can be synthesized in 2–4 hours (Scheme 2) [19].

Scondo et al. have reported a preliminary study on sonochemical Staudinger-aza-Wittig tandem reactions [20] proving that isocyanate and urea formation is strongly favored. However, the applied power must be optimised for the best conversions of azido-CD into urea to be obtained and if lower efficiency in the second step is to be avoided. 6^I-Benzylureido-6^I-deoxy-per-*O*-acetyl-β-CD was obtained in shorter reaction times and excellent yields as compared to conventional conditions (Scheme 3).

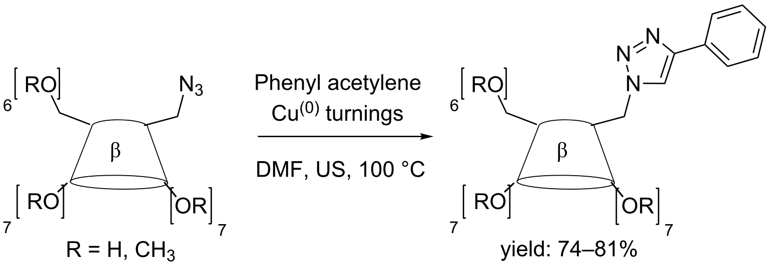

Scheme 2: Example of CuAAC with 6^{I}-azido-6^{I}-deoxy-β-CD and phenylacetylene.

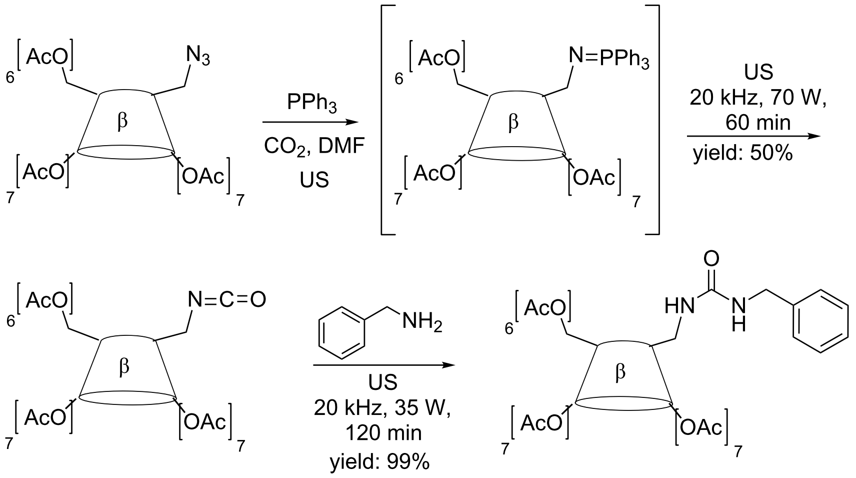

Scheme 3: Synthesis of 6^{I}-benzylureido-6^{I}-deoxy-per-*O*-acetyl-β-CD.

Tosylation of the secondary rim of the CD can be efficiently carried out under US irradiation. This efficient regioselective modification is performed in the presence of tosyl imidazole and molecular sieves under US irradiation. As shown in Table 1, the reaction time was shortened to 2 h for α-CD (yield: 36%), 1 h for β-CD (yield: 40%) and 45 min for γ-CD (yield: 46%) (Scheme 4) [21].

In Table 1 we compared the preparation of several monosubstituted CDs under conventional condition or under US irradiation. The data show that reaction time were dramatically reduced and the yield was generally slightly increased. Under US irradiation, the 6^{I}-amino-β-CD was obtained by catalytic hydrogenation, while under conventional conditions the reduction of azido β-CD was obtained by a Staudinger reaction or in the presence of hydrazine.

A new generation of organophosphate scavengers has been obtained by Le Provost et al. [25] in which β-CD was regioselectively monosubstituted at O-2 using a bromomethyl

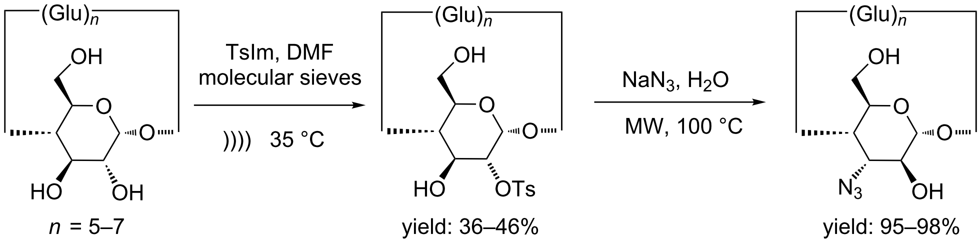

Scheme 4: Synthesis of 3^{I}-azido-3^{I}-deoxy-*altro*-α, β- and γ-CD.

Table 1: Selected examples of conventional and non-conventional preparation of monosubstituted CDs.

Product	Reaction conditions	Time	Yield (%)
6^I-tosyl-β-CD	β-CD, Tosyl chloride, NaOH, water, rt [22]	18 h	34
6^I-tosyl-β-CD	β-CD, TsIm, NaOH, water, US, 20 W [15]	30 min	55–60
2^I-tosyl-α-CD	α-CD, TsIm, DMF, mol sieves, rt [23]	50 h	35
2^I-tosyl-α-CD	α-CD, TsIm, DMF, mol sieves, US 20 W [21]	2 h	36
2^I-tosyl-β-CD	β-CD, TsIm, DMF, mol sieves, rt [23]	50 h	36
2^I-tosyl-β-CD	β-CD, TsIm, DMF, mol sieves, US 20 W [21]	1 h	40
2^I-tosyl-γ-CD	γ-CD, TsIm, DMF, mol sieves, rt [24]	120 h	36
2^I-tosyl-γ-CD	γ-CD, TsIm, DMF, mol sieves, US 20 W [21]	45 min	46
6^I-amino-β-CD	6^I-azido-6^I-deoxy-β-CD, Pd/C, N_2H_4, MeOH, H_2O, reflux [22]	20 min	90
6^I-amino-β-CD	6^I-azido-6^I-deoxy-β-CD, Pd/C, H_2, MeOH, H_2O, US 20 W [15]	2 h	88

pyridine derivative under US irradiation to avoid polysubstitution.

Preparation of persubstituted CD derivatives

The complete substitution of all hydroxy groups is difficult because steric hindrance increases upon substitution, the secondary face may be attacked before the last primary hydroxy group has completed the reaction.

Totally persubstituted products are usually obtained in low yields, whereas significant increases in yields have been achieved in reduced reaction times thanks to our sonochemical protocol (35 kHz bath at 20 °C, 160 W; 20 kHz cooled horn, −20 °C, 600 W). We prepared a series of *O*-peralkylated β- and γ-CDs which are commonly used as stationary phases in high-resolution gas chromatography or as drug carriers [26].

CDs and their persubstituted derivatives have recently received a great deal of attention from the field of chromatographic separations. The development of new CD derivatives as important selectors for analytical chiral recognition have been performed [27]. We prepared heptakis(6-O-TBDMS-2,3-O-methyl)-β-CDs with a second CD unit in the 2 position or a (*R*)-Mosher acid moiety [28].

Preparation of second generation CD derivatives: dimers, and CD hybrids

Bis-CDs and their metal complexes have been extensively studied as versatile receptors for molecular recognition and building blocks for functional materials.

Due to the binding of two adjacent CD units, bridged bis-CDs display high binding abilities and molecular selectivities compared to native and monosubstituted CDs. A well-organized pseudo-cavity may be provided by the linker that in turn offers additional binding interactions with guest molecules.

New sonochemical protocols for the preparation of bis(β-CDs) bearing 2-2′ and 3-3′ bridges as new carriers for gadolinium complexes have been reported (Scheme 5) [29]. These new CD dimers were promising candidates for MRI applications because their Gd(III)-adducts endowed with high relaxivities thanks to much larger molecular masses than the contrast agents themselves.

Furthermore, the potential use of cyanine/β-CD carrier systems has been evaluated via in vitro experiments on HeLa cells and the monitoring of cell entrance via confocal laser scanning microscopy [30]. Several types of dye moiety/CD derivatives have been suggested as "switch on" or "switch off" fluorescent chemical sensors. In these systems, the complexation with a guest molecule allows to enhance or decrease the fluorescence intensity. Two water-soluble cyanine/β-CD derivatives have been efficiently prepared via CuAAC under simultaneous US/MW irradiation at 75 °C for 2 h (MW 15 W and US 20 W) in good yields (23% and 33%). These dyes were used as versatile carriers for drug delivery and optical imaging.

Preparation of CD-grafted materials and CD-based polymers

The reaction of β-CD with diphenyl carbonate (DPC) or hexamethylene diisocyanate (HDI) afforded crosslinked, insoluble polymers. We synthesized these systems and tested as sequestering agents for naringin [31]. These syntheses were carried out under US with shorter reaction times and smaller particle size distribution.

To investigate the cosmeto-textile applications of CD-grafted materials, a new fabric based on β-CD-grafted viscose loaded with aescin formulations was prepared. This material was designed for the treatment of venous and lymphatic legs. An efficient US-assisted synthetic procedure to graft viscose using a diisocyanate cross-linker was reported (Scheme 6) [32].

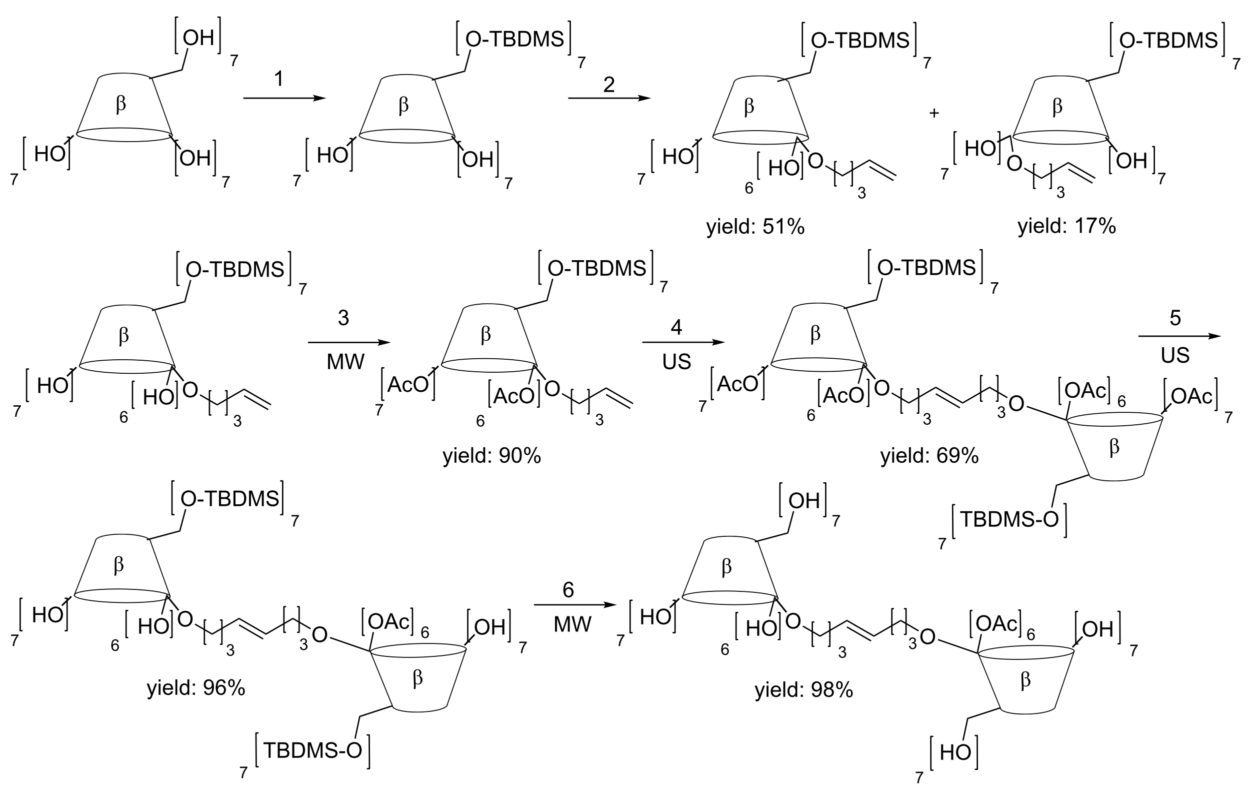

Scheme 5: Synthesis of 2-2' bridged bis(β-CDs). Reaction conditions: 1) TBDMSCl, imidazole, dry pyridine, stirring rt, 8 h; 2) 5-bromopentane, LiH, dry THF–DMSO, reflux, 4 h; 3) acetic anhydride, dry pyridine, MW, 50 °C, 1 h; 4) Grubbs' catalyst, Ar, dry CH_2Cl_2, US, 34 °C; 5) KOH, 2 M, MeOH, H_2O; US; 40 °C, 30 min; 6) AcCl 2% in MeOH; CH_2Cl_2, MW, reflux, 15 min.

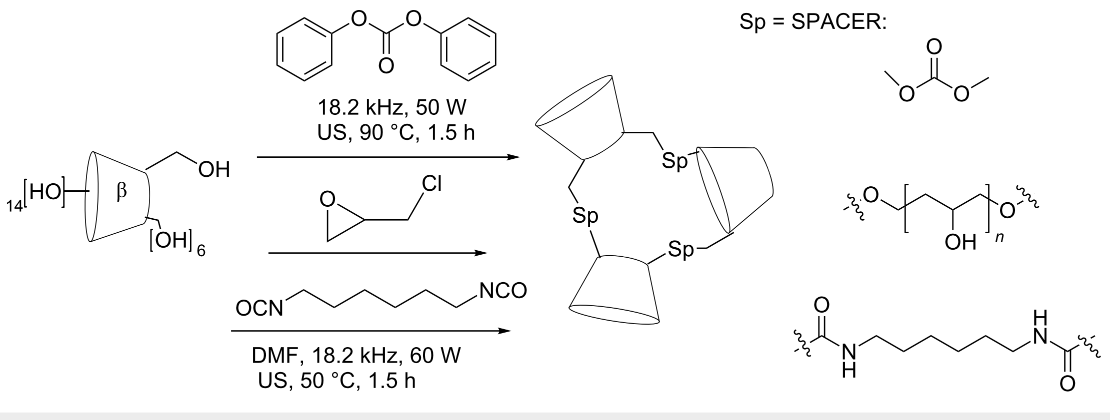

Scheme 6: Insoluble reticulated CD polymer.

Sonochemical reticulation with HDI was used in the preparation of a new series of solid cross-linked α-, β- and γ-CD-based catalysts containing Cu(I) or Pd(II) [33]. Sonication breaks up intermicellar interaction and may promote the formation of metal nanoparticle clustering. Cu(I)-based system have been used in alkyne/azide [3 + 2] cycloadditions, while Pd(II)-based catalysts have been used in C–C couplings reactions (Scheme 7) [34].

An example of water-soluble β- and γ-CD/chitosan derivatives have been studied for binding Gd(III) chelates that bear hydrophobic substituents and negative charges [35]. These bio-polymers were easily prepared in two reaction steps by reacting CDs with maleic anhydride followed by activation with carbodiimide to form amide linkages with amino groups of chitosan. The esterification of CD was promoted by MW irradiation, while the chitosan coupling used a water-soluble carbodiimide,

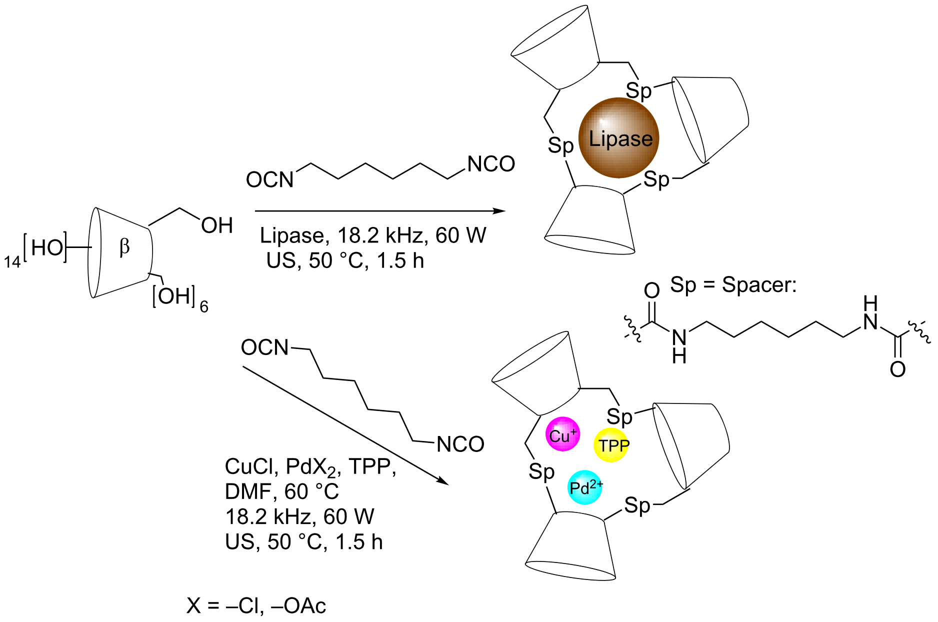

Scheme 7: CD-HDI cross linked polymers.

N-(3-dimethylaminopropyl)-*N*-ethylcarbodiimide hydrochloride, under US.

A mild sonication at rt using HDI enabled efficient CDs reticulation in the presence of lipases (Scheme 7) whose biocatalytic activity was preserved in the final solid cross-linked β-CD enzyme [36].

Nanosponges are nanostructured materials made of hyper-cross-linked CDs [37]. The capacity of these materials to encapsulate a great variety of substances could be used to design innovative drug carriers, to protect degradable substances and to improve the aqueous solubility of poorly water-soluble molecules. α-, β- and γ-CDs were reacted solventless with diphenyl carbonate or carbonyldiimidazole under US (up to 90 °C). These nanosponges may resolve some active ingredients drawbacks, such as instability, degradation, poor solubility and toxicity, while they can also be used as carriers for inhalation and oral administration treatments [38].

New hybrid materials have been created from a combination of carbon nanotubes (CNTs) and β-CD [39] affording a peculiar cost-effective fibre. Functionalized β-CD was covalently linked to CNTs and this derivative was immobilized into the wall pores of the hollow fibre under US [40].

Microwaves

A number of general books and reviews discuss in detail the state-of-the-art of MW-assisted organic synthesis and tailor-made MW reactors have been developed for green organic synthesis [41,42]. The most recent generation of professional reactors dramatically increased the applications of MW-assisted organic synthesis thanks to a high power density (up to 1.5 kW/L), high temperature (up to 300 °C) and pressure (up to 200 bar) together with multi-gas inlets. Considering that MW ovens can be interfaced with autosamplers and that new MW reactors can accommodate multiple racks, this technique is well suited for fast optimization of organic protocols and parallel synthesis. The most impressive advantage of the MW technology is the appearance of the kilolab-scale reactors and their special versions that are operating in continuous flow mode [4,43,44].

Preparation of monosubstituted CD derivatives

MW irradiation has been exploited in the synthesis of mono and persubstituted CDs. Several syntheses of CD derivatives have been successfully carried out under MW with higher yield, higher purity, and short reaction time. While US irradiation has found use in the optimization of synthetic protocols for the preparation of versatile intermediates, such 6^{I}-(*p*-toluensulfonyl)-β-CD from native β-CD, MW irradiation has proved to be extremely efficient in further derivatization, such as the nucleophilic substitution of monohalogenated and monotosylated CDs (Scheme 8) .

The 6^{I}-azido-6^{I}-deoxy-β-CD, an extremely versatile intermediate, has been obtained from the displacement of the tosylate group under MW. The reaction time was cut from several hours

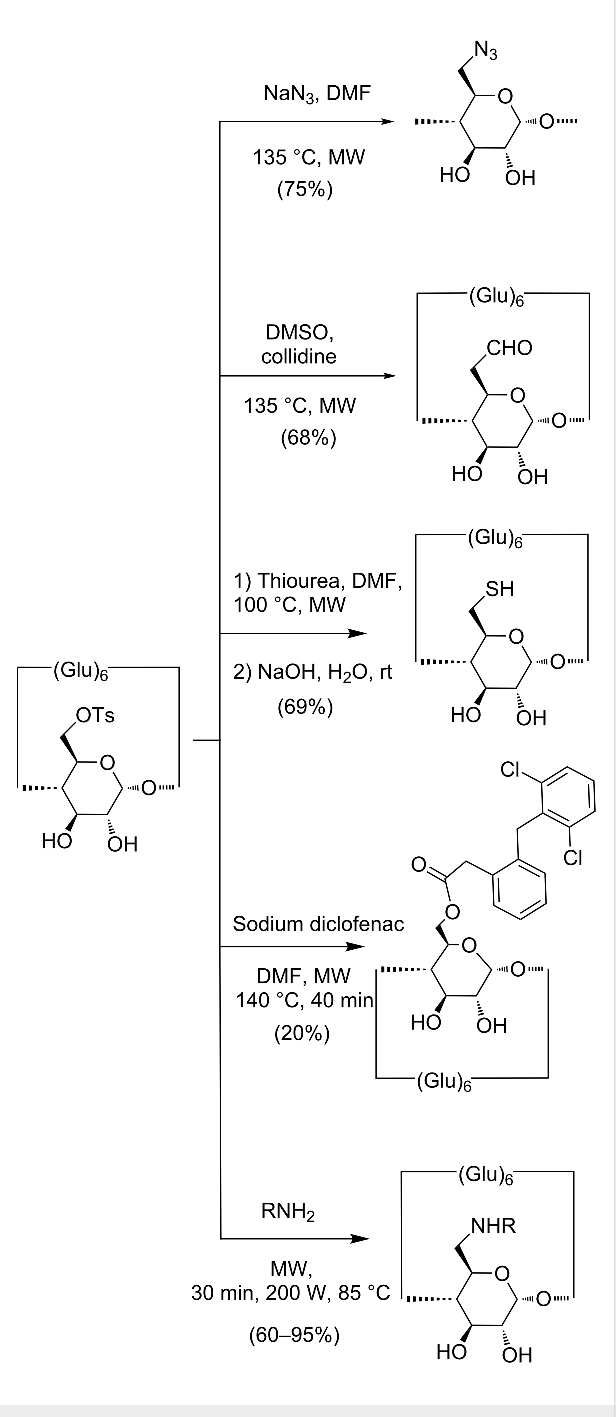

Scheme 8: Derivatization of 6^{I}-(*p*-toluenesulfonyl)-β-CD by tosyl displacement.

to 2 min (200 W max, 85 °C) and the formation of side products was reduced [15]. 6^{I}-(*p*-Toluenesulfonyl)-β-CD was converted to 6^{I}-formyl-β-CD via DMSO oxidation in MW with collidine in 15 min (110 W, 135 °C). MW irradiation promoted the syntheses of 6^{I}-deoxy-6^{I}-thio-β-CD and 6^{I},6^{IV}-dideoxy-6^{I},6^{IV}-dithio-β-CD via nucleophilic substitution of the primary tosylate ester in C-6 with thiourea followed by basic hydrolysis. The reaction gave the thiouronium salt after 1 h of irradiation at 100 °C while 20 h heating at 90 °C are required under conventional conditions [21].

While the previous experiments were performed in a multimode MW oven (MicroSynth-Milestone, Italy), a similar approach was used for the preparation of an ester prodrug of diclofenac and β-CD, but in a monomode MW oven (CEM Discover S-class MW reactor). The reaction was heated at 140 °C for 40 min and the diclofenac β-CD derivative was obtained with a yield of 20% [45]. Analogously, a general MW-assisted procedure for the synthesis of 6^{I}-amino-6^{I}-deoxy-β-CD has been reported by Puglisi et al. The reactions were performed in a MW oven (CEM Explorer) for 30 min at 200 W and 85 °C [46].

In the Table 2we compared MW vs conventional procedures in the preparation of several monosubstituted derivatives. Besides a slight improvement of formyl and thio derivative yield, the data show a significant reaction rate acceleration.

Preparation of persubstituted CD derivatives

Selective permodification refers to a complete derivatization of the hydroxy groups in one side of the CD. The selective full substitution on the primary rim is not a trivial task because of the increase of steric hindrance that makes the secondary face prone to an attack before the last primary hydroxy group was reacted [50,51].

Pertosylate and perhalogenated derivatives in position 6 can be substituted with different nucleophiles. However, under conventional conditions, the reactions resulted in complicated mixtures with different substitution degree. MW irradiation efficiently afforded pure products. A series of amino derivatives were obtained by displacement of heptakis(6-deoxy-6-iodo)-β-CD (MW reactor 150 W) at 85 °C for 1 h (yield range 52–69%) [52]. Analogously catalytic hydrogenation in a pressure-resistant MW reactor, gave heptakis(6-amino-6-deoxy)-β-CD from a solution of heptakis(6-azido-6-deoxy)-β-CD in methanol/H_2O [53]. The desired product was obtained in 90% yield after 3 h of irradiation at 70 °C. Reaction with isocyanates and isothiocyanate gave ureido and thioureido persubstituted β-CD derivatives in a MW oven at 85 °C for 4 h (see Scheme 9).

A multivalent azido-scaffold such as persubstituted 6-azido-6-deoxy-α-, β- or γ-CD with conformational constraints can be efficiently perfunctionalized in a MW- and ligand-assisted click cluster synthesis. An example of the MW-promoted ‘cooperative’ click reaction of azido-CDs has recently been reported and offers useful synthetic insights into a specific labelling strategy [54]. The aforementioned reaction afforded a new series of anti-

Table 2: Selected examples of conventional and MW-assisted preparation of monosubstituted CDs.

Product	Reaction condition	Time	Yield (%)
6^{I}-formyl-β-CD	6^{I}-(*p*-toluenesulfonyl)-β-CD, DMSO, collidine, oil bath, 135 °C [47]	1.5 h	64
6^{I}-formyl-β-CD	6^{I}-(*p*-toluenesulfonyl)-β-CD, DMSO, collidine, MW (110 W), 135 °C [21]	15 min	68
6^{I}-azido-6^{I}-deoxy-β-CD	6^{I}-(*p*-toluenesulfonyl)-β-CD, NaN_3, DMF, oil bath 60–65 °C [48]	24 h	88
6^{I}-azido-6^{I}-deoxy-β-CD	6^{I}-(*p*-toluenesulfonyl)-β-CD, NaN_3, DMF, MW (200 W) 85 °C [15]	2 min	75
6^{I}-deoxy-6^{I}-thio-β-CD	6^{I}-(*p*-toluenesulfonyl)-β-CD, thiourea, MeOH/H_2O then HCl, oil bath, under reflux [49]	18 h	50
6^{I}-deoxy-6^{I}-thio-β-CD	6^{I}-(*p*-toluenesulfonyl)-β-CD, thiourea, DMF then NaOH, MW (100 W), 100 °C [21]	20 min	69

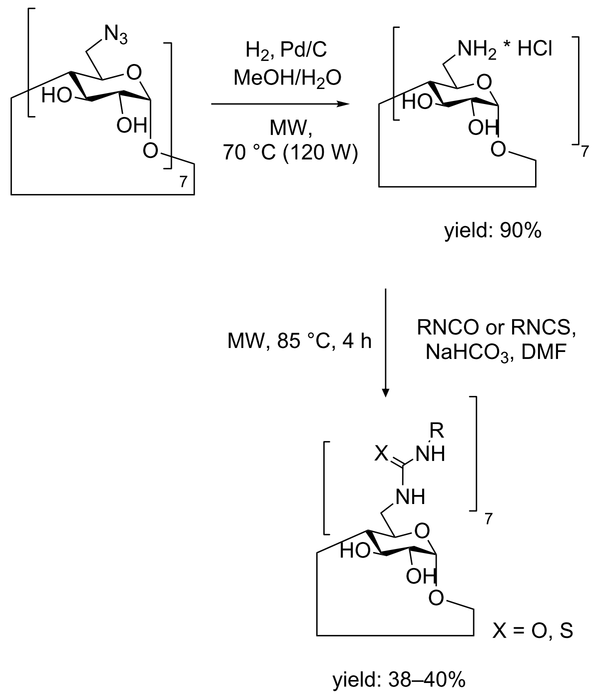

Scheme 9: Synthetic scheme for the preparation of heptakis(6-amino-6-deoxy)-β-CD, heptakis(6-deoxy-6-ureido)-β-CD and heptakis(6-deoxy-6-thioureido-)-β-CD.

microbial γ-CD derivatives that strongly disrupt bacterial membranes, and a series of persubstituted γ-CD derivatives bearing polyamino groups (77% yield) [55].

MW-promoted Cu-catalyzed click reaction for the preparation of second generation CD derivatives and hybrid structures

The MW-promoted CuAAC between CD monoazides and acetylenic moieties is the most efficient way to functionalize the CD surface [56]. β-CD is able to form a stable sandwich-type complex with Cu(II) ions, where the CDs faced their secondary rims and the use of heterogeneous phase catalysis may overcome the troubles deriving from time consuming purifications [57]. In 2006 Lipshutz et al. demonstrated that the impregnation of charcoal with an aqueous solution of $Cu(NO_3)_2$ in US bath, gave copper nanoparticles: an efficient catalyst in CuAAC [58]. Besides the easier work-up of heterogeneous catalysis, Cu(I)/charcoal also gave a higher yield compared to soluble $CuSO_4$/ascorbic acid (76 vs 95% yield, respectively). The reaction was further improved under MW or simultaneous MW/US irradiation [59].

Recently the preparation of a large number of CD-derivatives by MW-assisted CuAAC regioselective cycloadditions has been described. A selected series of derivatives are depicted in Scheme 10: CD-acryloyl derivative [60,61], β-CD/dye derivatives [31,62-64], CD-ionic liquid hybrids [65,66], CD-based iminosugar conjugates [67], water-soluble CD homo- and heterodimers [68,69], trimers [70,71] and oligomers [72] of α-, β- and γ-CD have all been successfully produced. This wide variety of compounds was obtained in good to excellent yield under MW irradiation (from 20 min to 3 h at 75 °C to 100 °C).

Preparation of CD-grafted materials and CD-based polymers

Interest in CD polymers has grown over the last few years. CD-based polymers have a number of applications, as drug delivery systems and toxic compounds scavengers, and have been obtained by grafting CDs into polymeric matrices.

A multi-carrier for combined diagnostic and theranostic applications was obtained via the functionalization of carbon nanotubes with CD using a MW-assisted 1,3-dipolar cycloaddition. As depicted in Scheme 11, the synthesis generated in situ azomethine ylides which include both a β-CD unit and a DOTAMA tris(*t*-butyl ester) moiety. The toxicity assessment, cell viability and permeability of single-walled carbon nanotube (SWCNT) platform, was evaluated on five human cell lines. No-toxicity was observed at concentrations up to 333 μg/mL [73].

Separately, a facile and rapid MW-assisted method in water has been used to derivatize graphene nanosheets with (2-hydroxy)propyl-β-CD. The reaction involved the esterification of the HP-β-CD hydroxy groups by the carboxyl groups of graphene oxide (GO) by MW irradiation (450 W) at different

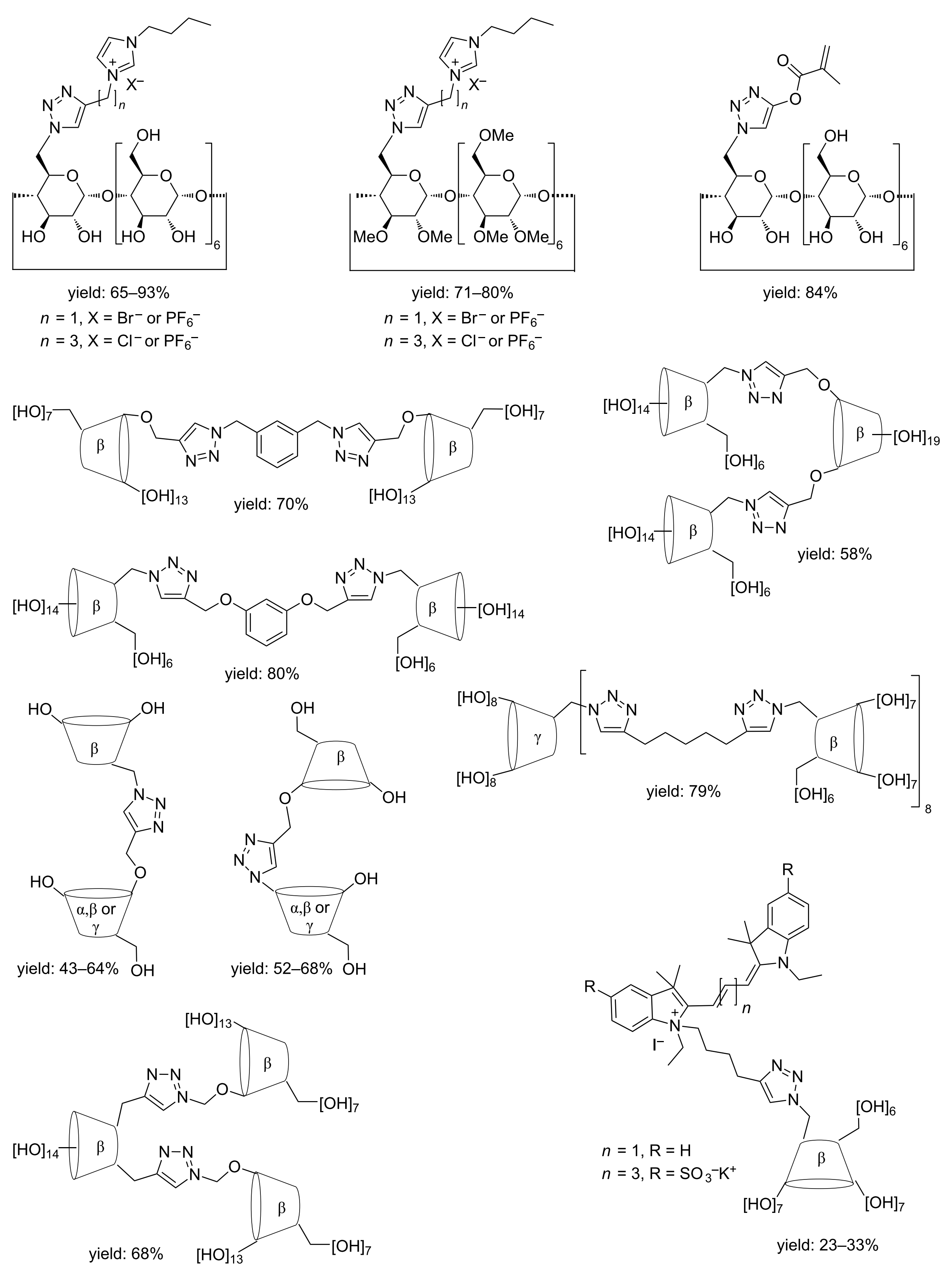

Scheme 10: Structure of CD derivatives obtained via MW-assisted CuAAC.

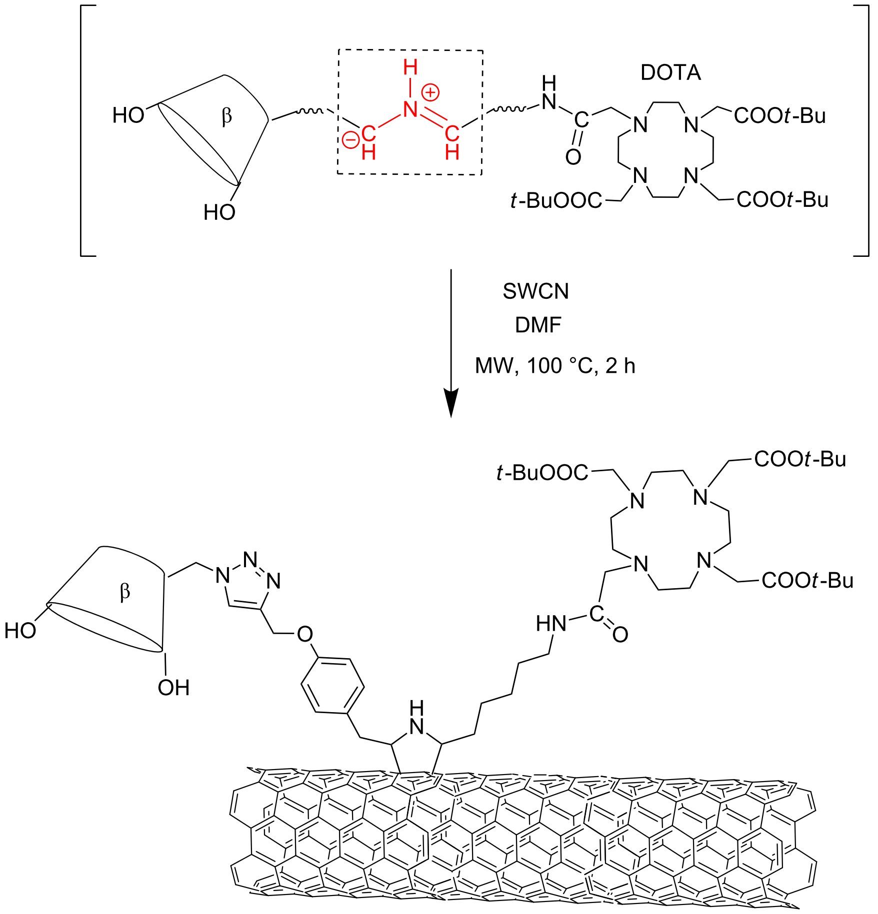

Scheme 11: Preparation of SWCN CD-DOTA carrier.

temperatures ranging from 50 to 100 °C for 10, 30, 60 and 90 min. After reduction with hydrazine hydrate, this HP-β-CD-RGO modified glassy carbon electrode showed good results in supramolecular recognition a set of six different phenolic organic pollutants and a high electrochemical response [74].

CuAAC has been successfully used to immobilize molecules on polymers and biopolymers as well as to join sugars to peptides and proteins. CD-polyglycerol dendron amphiphiles (CD-PG) have also been obtained. This derivative showed high encapsulation efficiency, while nanostructure size and shape were regulated according to the structure of the CD-PG dendrons [75].

CD-based polymers can be easily prepared under MW. Biswas et al. have prepared a number of macromolecular structures from α-, β-, γ-CDs by crosslinking reactions with toluene diisocyanate and methanediphenyl diisocyanate [76]. The authors demonstrated that compared with conventional heating, the reaction was faster (3–10 min) and with higher yields. Analogously, β-CD was grafted onto PEGylated Merrifield resin by reaction with HDI under MW irradiation [77].

CD nanosponges from anhydrous β-CD and diphenylcarbonate in DMF, have been prepared under MW irradiation (400 W) in 90 min. The optimized method was proven to be a unique opportunity for the large-scale synthesis of CD nanosponges in a high yield and uniform particle size distribution [78].

Ball mill

One of the oldest, cheap, and efficient methods to achieve a homogeneous solid mixture is ball milling. By this method extremely fine powders can be achieved in mineral dressing processes, paints and pyrotechnics, etc. [79]. It is suitable for both batch and continuous operation, it is similarly suitable also for open and closed circuit grinding as well as being applicable for materials of all degrees of hardness.

Conventional BMs have a cylindrical or conical shell that rotates on a horizontal axis and have an appropriate grinding medium of balls, for example steel, flint or porcelain. The second generation of BMs, which are often called as high-speed ball mills (HSBM), operate in vibrating, mixer or planetary mode. A very simple vibrating BM, consisting of a small milling cup with one or two balls, has been used for a long time in traditional IR spectrometry to homogenize the sample and KBr. Mixer BM are slightly different from the vibrating version and are not only used in IR spectroscopy but also on the preparative scale for homogenization and cracking solid components. The common weakness of these simple accessories is the critical rotation/mixing speed, which can be overcome by a new generation of equipment; planetary BM, that consist of at least one grinding jar arranged eccentrically on a rotating support. The grinding jar moves in the opposite direction to the sun wheel. The difference in speeds between the balls and grinding jars produces an interaction between frictional and impact forces, which releases high dynamic energies for particles size reduction [80]. Detailed descriptions of both operating modes and theoretical considerations can be found and thoroughly discussed in various product brochures.

An energy efficient method for the preparation of nanocrystalline powders is the high energy ball milling (HEBM) in planetary or vibratory ball mills and HEBM is a common synonym for HSBM [81]. The lower particle size in grinding produces microdeformation in the ground material crystal lattice, while energy is partially spent in creating microstresses, which eventually slow powder grinding. An efficient wet grinding technology can exploit a liquid milling medium.

The preparation of CD and other complexes with the aid of ball milling is well-known [82,83]. In spite of an easy scale-up of this technology, some disadvantages might occur:

- metastable crystalline complexes can recrystallize to an equilibrium state upon storage [84];
- the degradation of mill surfaces and subsequent suspension contamination can be a problem, particularly in the high-energy version [85].

Although, the preparation of complexes or microparticles with ball milling is a common procedure, its use in organic synthesis intensified substantially only recently [86]. Solventless mechanochemical reactions are usually highly efficient and selective, valuable properties exploitable in CD derivatization.

Nucleophilic substitutions (S_N2 reaction) may occur without solvent stabilization because charged species do not need to be formed in the transition state [87]. Solvent effects and ion pair formation are critical to the mechanism of S_N1 reactions meaning that this mechanism is usually restricted in HSBM reactions.

While solid-state intermolecular S_N2 reactions depend on contact between interacting particles only, S_N1 reactions may show more structure-dependent behaviour, which can be either favourable or unfavourable, because of the solid-state structure.

Although BM reactions are often said to be solvent-free, some inert solvents can also be used particularly when the reagent mass ratio is very high. A lack of solvent(s) may suggest that ball milling conditions favours S_N2 reactions; however it is also true that a solventless environment does not necessarily mean that there is a lack of solution in a liquid phase. Some reaction mixture components can often be liquid, while solvent effects or mixed S_N2 and S_N1-type reaction mechanisms cannot be excluded. A good example of a mixed reaction mechanism is the glycosylation reported by Tyagi et al. [88], where S_N2 glycosylation seems to be dominant, with no neighbouring group participation, which is typical of glycosylation reactions of activated acetylated carbohydrates. A more pure S_N2 reaction is described by Patil and Kartha [89], where the preparation of thioglycosides was almost quantitative. Unfortunately, a lack of information on reaction mixture compositions means that the reaction mechanism cannot be completely confirmed because chromatographic purifications and recrystallizations distort the enantiomeric ratio.

Basically, three major types of HSBM chemical reaction can occur in the presence of CDs:

1. Preparation of CD complexes and various chemical reactions on the complexed substructures;
2. Derivatization of naked, natural CD;
3. Reactions of activated CD.

While reactions occur between a complexed molecule and reagent or between host and guest in cases 1) and, usually, 2), reaction type 3) requires a CD derivative that bears a good leaving group and the complexation phenomenon can be disadvantageous here. While type 1) can eliminate usually the less problematic solvents only, the application of BM in types 2) and 3) can reduce or eliminate the polluting environment. Reactions of type 1) are dominant in CD/BM literature; more than 98% of publications report the complexation of one or more components. Mechanochemistry opened a new synthetic pathway to the preparation of numerous fullerene derivatives by dissolving C_{60} in the amorphous powder obtained from the ball milled reactants and β-CD [90]. Another example that uses the energy transfer of ball milling is the preparation of MnBi/Fe-Co core/shell structured composites. However, no pure chemical reaction is used to prepare rare-earth free ferromagnetic materials by grinding under less-environmentally friendly conditions in this case. The components were prepared using classic methods and the final composite was obtained by ball milling of arc-melted MnBi particles and Fe-Co nanoparticles prepared with the aid of a β-CD/oleic acid complex. The composites obtained showed smooth magnetic hysteresis loops [91].

SWCNT edge activation can be carried out via co-grinding with β- or γ-CDs [92]. Although chemical bonds are also broken in this case, this preparation is closer to the BM assisted preparation of CD complexes in many ways. Nanosized manganese oxides have also been prepared from CD/Mn complexes [93], however, in this case, the CD was only used to obtain a charrable matrix for the Mn_2O_3 which was prepared finally at 450 °C.

The only example of the type 2) method is the regioselective CD derivatization described by Menuel et al. who prepared 2-O-monotosylated α-, β-, and γ-CDs [94]. The further reaction of the prepared compounds resulted in a CD derived cyclic oligosaccharide, which contained one mannose residue, in the form of 2,3-mannoepoxide.

Type 3) reactions in the further derivatization of regioselectively activated – by sulfonic esters or halogenides – CDs are more important in industrial processes involving important CD derivatives. These activated derivatives are usually less soluble in water and their substitution reactions often require high boiling point dipolar aprotic solvents. The complete removal of these solvents is impossible even in gram scale preparations and so the prepared compounds need further purification steps. Additionally, these environmentally unfavorable solvents present other disadvantages; both in their decomposition and toxicology profile. A study of the nucleophilic displacement of 6-monosubstituted β-CDs and the synthesis of 6^I-monoazido-6^I-monodeoxy-β-CD in HSBM on a preparative scale (5 mmol, 6.5 g) is described in a recent publication by Jicsinszky et al. [95]. Comparing the yields it can be concluded that in larger scale reactions the yields are getting closer to those of the solution reaction. However, since the removal of a high-boiling solvent is not necessary, the work-up becomes simplifyed.

It has to be highlighted that the reaction product should not be considered as a CD derivative when the reaction centre is on the secondary rim because the S_N1 mechanism is restricted to solution environment only. The secondary carbon substitution results in inversion in the reaction centre which changes the sugar moiety from glucoside to mannoside, altroside or alloside making those derivatives CD-based cyclic oligosaccharides and not CDs.

The design of green synthetic methods for the bulk preparation of CD thiols and thioethers is an emerging challenge because of the importance of intermediary azido derivatives [96] and favorable aggregation properties in nanomedicines and particularly the antidote Sugammadex [97]. The reaction between 6^I-O-monotosyl-β-CD and various nucleophiles opens a new way for the more effective syntheses of per-6-substituted CDs from per-6-bromo- and -iodo-CDs.

Microreactors

The typical lateral dimensions of microreactors, sometimes also called as microstructured or microchannel reactors, are below 1 mm with the most typical form of microchannels [98]. The miniaturized continuous flow reactor, also called microreactor, offers many advantages over conventional scale reactors, including considerable improved energy exploitation, increased reaction speed and yield, safety, reliability, scalability, on-site/on-demand production, etc., and a much finer degree of process control. However microreactors do not tolerate mechanical inhomogeneities. To resolve the problem of microparticles, which often cause clogging, a second generation of microreactors has been developed and called microjetreactor [99]. A typical microreactor is made up of a 'sandwich' of thin metal sheet or plates with fluid (micro)channels that have been etched into both sides. The average size of a single unit is approximately 6 × 4 × 0.5 cm with channel widths and wall thicknesses of 200–300 µm. The reactions occur in every other layer and the other layers are used for heat-exchange fluid flows [100].

The major use of CDs in this equipment, and also in the selective complexation phenomenon, is rather analytical and CDs' principal role is detection only [101]. This has allowed DNA sequencing to become a relatively cheap method and provided momentum to the discovery of the role of genetics in various diseases [102,103]. Although these reactors exhibit an excellent energy and mass efficacy, their use in CD derivatization is just a curiosity. However, exhausting the complexation ability of various CD derivatives is advantageous in solubilization and stereoselective reactions. Delattre and Vijayalakshmi have pointed out the theoretical use of enzymes in the production of CDs or other cyclic oligosaccharides, like cyclofructan, rather than using a microreactor [104].

Conclusion

Dynamic intrusion of the enabling technologies to the CD chemistry is inevitable and shows exponential growth. Although, approximately 10% of the recently published technical papers in the CD field are dealing with sustainable technologies, the number of publications containing information of comparisons with the classical methods is sporadic. Optimized MW-, US- and BM-assisted protocols are energetically more efficient than the classical synthetic methods because their excellent heat and mass transfer. In all cases the reactions are faster avoiding degradations that may occur during protracted heating and time-consuming purifications. Case by case the technique of choice depends from several factors: the solubility of the starting CD, the reaction mechanism, environmental concerns, and the reaction scale are only a part of all the information required to design successful preparations.

References

1. Alexandru, L.; Cravotto, G.; Giordana, L.; Binello, A.; Chemat, F. *Innovative Food Sci. Emerging Technol.* **2013,** *20,* 167–172. doi:10.1016/j.ifset.2013.07.011
2. Crudo, D.; Bosco, V.; Cavaglià, G.; Mantegna, S.; Battaglia, L.; Cravotto, G. *Agro Food Ind. Hi-Tech* **2014,** *25,* 55–59.
3. Rinaldi, L.; Martina, K.; Baricco, F.; Rotolo, L.; Cravotto, G. *Molecules* **2015,** *20,* 2837–2849. doi:10.3390/molecules20022837
4. Rinaldi, L.; Carnaroglio, D.; Rotolo, L.; Cravotto, G. *J. Chem.* **2015,** 879531. doi:10.1155/2015/879531
5. http://Scifinder.cas.org (accessed Oct 22, 2015). (subscription-based).
6. http://Sciencedirect.com (accessed Oct 22, 2015). (free searchable).
7. Cintas, P.; Cravotto, G.; Barge, A.; Martina, K. *Top. Curr. Chem.* **2015,** *369,* 239–284. doi:10.1007/128_2014_623
8. Ball Milling Towards Green Synthesis Applications, Projects, Challenges. In *RSC Green Chemistry;* Stolle, A.; Ranu, B., Eds.; The Royal Society of Chemistry: Thomas Graham House, Science Park, Milton Road, Cambridge CB4 0WF, UK. doi:10.1039/9781782621980
9. Braga, D.; Grepioni, F. *Angew. Chem., Int. Ed.* **2004,** *43,* 4002–4011. doi:10.1002/anie.200301721
10. Kumar, V.; Taxak, N.; Jangir, R.; Bharatam, P. V.; Kartha, K. P. R. *J. Org. Chem.* **2014,** *79,* 3427–3439. doi:10.1021/jo5001753
11. Kumar, V.; Yadav, N.; Kartha, K. P. R. *Carbohydr. Res.* **2014,** *397,* 18–26. doi:10.1016/j.carres.2014.08.002
12. Rinaldi, L.; Binello, A.; Stolle, A.; Curini, M.; Cravotto, G. *Steroids* **2015,** *98,* 58–62. doi:10.1016/j.steroids.2015.02.016
13. Lin, H.-L.; Lin, S.-Y.; Lin, C.-C.; Hsu, C.-H.; Wu, T.-K.; Huang, Y.-T. *Carbohydr. Polym.* **2012,** *87,* 512–517. doi:10.1016/j.carbpol.2011.08.010
14. Cintas, P.; Tagliapietra, S.; Caporaso, M.; Tabasso, S.; Cravotto, G. *Ultrason. Sonochem.* **2015,** *25,* 8–16. doi:10.1016/j.ultsonch.2014.12.004
15. Trotta, F.; Martina, K.; Robaldo, B.; Barge, A.; Cravotto, G. *J. Inclusion Phenom. Macrocyclic Chem.* **2007,** *57,* 3–7. doi:10.1007/s10847-006-9169-z
16. Zheng, W. Q.; Du, M. X.; Feng, F.; Chen, G. L.; Liao, M.; Liu, Y. J.; Tang, L.; Xu, Z. G. *Adv. Mater. Res. (Durnten-Zurich, Switz.)* **2015,** *1083,* 51–54. doi:10.4028/www.scientific.net/AMR.1083.51
17. Cintas, P.; Palmisano, G.; Cravotto, G. *Ultrason. Sonochem.* **2011,** *18,* 836–841. doi:10.1016/j.ultsonch.2010.11.020
18. Cintas, P.; Barge, A.; Tagliapietra, S.; Boffa, L.; Cravotto, G. *Nat. Protoc.* **2010,** *5,* 607–616. doi:10.1038/nprot.2010.1
19. Cravotto, G.; Fokin, V. V.; Garella, D.; Binello, A.; Boffa, L.; Barge, A. *J. Comb. Chem.* **2010,** *12,* 13–15. doi:10.1021/cc900150d
20. Scondo, A.; Dumarçay-Charbonnier, F.; Barth, D.; Marsura, A. *Tetrahedron Lett.* **2009,** *50,* 5582–5584. doi:10.1016/j.tetlet.2009.07.082
21. Martina, K.; Trotta, F.; Robaldo, B.; Belliardi, N.; Jicsinszky, L.; Cravotto, G. *Tetrahedron Lett.* **2007,** *48,* 9185–9189. doi:10.1016/j.tetlet.2007.10.104
22. Jicsinszky, L.; Iványi, R. *Carbohydr. Polym.* **2001,** *45,* 139–145. doi:10.1016/S0144-8617(00)00319-2
23. Teranishi, K.; Watanabe, K.; Hisamatsu, M.; Yamada, T. *J. Carbohydr. Chem.* **1998,** *17,* 489–494. doi:10.1080/07328309808002907
24. Teranishi, K.; Tanabe, S.; Hisamatsu, M.; Yamada, T. *Biosci., Biotechnol., Biochem.* **1998,** *62,* 1249–1252. doi:10.1271/bbb.62.1249
25. Le Provost, R.; Wille, T.; Louise, L.; Masurier, N.; Müller, S.; Reiter, G.; Renard, P.-Y.; Lafont, O.; Worek, F.; Estour, F. *Org. Biomol. Chem.* **2011,** *9,* 3026–3032. doi:10.1039/c0ob00931h
26. Cravotto, G.; Nano, G. M.; Palmisano, G. *J. Carbohydr. Chem.* **2001,** *20,* 495–501. doi:10.1081/CAR-100106932
27. Bicchi, C.; Brunelli, C.; Cravotto, G.; Rubiolo, P.; Galli, M. *J. Sep. Sci.* **2002,** *25,* 125–134. doi:10.1002/1615-9314(20020201)25:3<125::AID-JSSC125>3.0.CO;2-W
28. Cravotto, G.; Bicchi, C.; Tagliapietra, S.; Costa, L.; Di Carlo, S.; Nervi, C. *Chirality* **2004,** *16,* 526–533. doi:10.1002/chir.20069
29. Aime, S.; Gianolio, E.; Palmisano, G.; Robaldo, B.; Barge, A.; Boffa, L.; Cravotto, G. *Org. Biomol. Chem.* **2006,** *4,* 1124–1130. doi:10.1039/b517068k
30. Carmona, T.; Marcelo, G.; Rinaldi, L.; Martina, K.; Cravotto, G.; Mendicuti, F. *Dyes Pigm.* **2015,** *114,* 204–214. doi:10.1016/j.dyepig.2014.11.014
31. Binello, A.; Robaldo, B.; Barge, A.; Cavalli, R.; Cravotto, G. *J. Appl. Polym. Sci.* **2008,** *107,* 2549–2557. doi:10.1002/app.27249
32. Cravotto, G.; Beltramo, L.; Sapino, S.; Binello, A.; Carlotti, M. E. *J. Mater. Sci.: Mater. Med.* **2011,** *22,* 2387–2395. doi:10.1007/s10856-011-4399-z
33. Cravotto, G.; Calcio Gaudino, E.; Tagliapietra, S.; Carnaroglio, D.; Procopio, A. *Green Process. Synth.* **2012,** *1,* 269–273. doi:10.1515/gps-2012-0029
34. Cintas, P.; Cravotto, G.; Calcio Gaudino, E.; Orio, L.; Boffa, L. *Catal. Sci. Technol.* **2012,** *2,* 85–87. doi:10.1039/C1CY00378J
35. Aime, S.; Gianolio, E.; Uggeri, F.; Tagliapietra, S.; Barge, A.; Cravotto, G. *J. Inorg. Biochem.* **2006,** *10,* 931–938. doi:10.1016/j.jinorgbio.2005.12.003
36. Junior, I. I.; Calcio Gaudino, E.; Martina, K.; Cravotto, G.; Luque, R.; de Souza, R. O. M. A. *RSC Adv.* **2014,** *4,* 45772–45777. doi:10.1039/C4RA03797A
37. Ma, M.; Li, D. *Chem. Mater.* **1999,** *11,* 872–876. doi:10.1021/cm981090y
38. Trotta, F.; Cavalli, R. *Compos. Interfaces* **2009,** *16,* 39–48. doi:10.1163/156855408X379388
39. Shao, L.; Mu, C. Z.; Du, H. P.; Czech, Z.; Du, H. C.; Bay, Y. P. *Appl. Surf. Sci.* **2011,** *258,* 1682–1688. doi:10.1016/j.apsusc.2011.09.129
40. Song, X.-Y.; Ha, W.; Chen, J.; Shi, Y.-P. *J. Chromatogr. A* **2014,** *1374,* 23–30. doi:10.1016/j.chroma.2014.11.029
41. de la Hoz, A.; Loupy, A. *Microwaves in Organic Synthesis,* 3rd ed.; Wiley-VCH, 2012. doi:10.1002/9783527651313
42. Kappe, O.; Stadler, A.; Dallinger, D. *Microwaves in Organic and Medicinal Chemistry,* 2nd ed.; Wiley-VCH, 2012. doi:10.1002/9783527647828
43. Alcazar, J.; Diels, G.; Schoentjes, B. *Comb. Chem. High Throughput Screening* **2007,** *10,* 918–932. doi:10.2174/138620707783220383

44. Choedkiatsakul, I.; Ngaosuwan, K.; Assabumrungrat, S.; Mantegna, S.; Cravotto, G. *Renewable Energy* **2015,** *83,* 25–29. doi:10.1016/j.renene.2015.04.012
45. Vieira, A. C. F.; Serra, A. C.; Carvalho, R. A.; Gonsalves, A.; Figueiras, A.; Veiga, F. J.; Basit, A. W.; Rocha Gonsalves, A. M. d'A. *Carbohydr. Polym.* **2013,** *93,* 512–517. doi:10.1016/j.carbpol.2012.12.053
46. Puglisi, A.; Spencer, J.; Clarke, J.; Milton, J. *J. Inclusion Phenom. Macrocyclic Chem.* **2012,** *73,* 475–478. doi:10.1007/s10847-011-0054-z
47. Yoon, J.; Hong, S.; Martin, K. A.; Czarnik, A. W. *J. Org. Chem.* **1995,** *60,* 2792–2795. doi:10.1021/jo00114a030
48. Petter, R. C.; Salek, J. S.; Sikorski, C. T.; Kumaravel, G.; Tyan Lin, F. *J. Am. Chem. Soc.* **1990,** *112,* 3860–3868. doi:10.1021/ja00166a021
49. Franchi, P.; Fanì, M.; Mezzina, E.; Lucarini, M. *Org. Lett.* **2008,** *10,* 1901–1904. doi:10.1021/ol800405b
50. Ashton, P. R.; Ellwood, P.; Staton, I.; Stoddart, J. F. *Angew. Chem., Int. Ed. Engl.* **1991,** *30,* 80–81. doi:10.1002/anie.199100801
51. Jicsinszky, L.; Petró, M.; Horváth, G.; Szejtli, J.; Way, J. L.; Petrikovics, I. Proceedings of the 14th International Cyclodextrin Symposium. Kyoto, Japan, May 8–11, 2008; pp 3–8. doi:10.13140/RG.2.1.4290.6088
52. Martina, K.; Cravotto, G.; Caporaso, M.; Rinaldi, L.; Villalonga-Barber, C.; Ermondi, G. *Org. Biomol. Chem.* **2013,** *11,* 5521–5527. doi:10.1039/c3ob40909k
53. Cravotto, G.; Martina, K.; Caporaso, M.; Heropoulos, G.; Jicsinszky, L. *MRS Proceedings* **2013,** *1492,* 177–182. doi:10.1557/opl.2013.176
54. Park, G.-H.; Baek, J. M.; Le, H. T.; Lim, C. W.; Kim, T. W. *Tetrahedron Lett.* **2012,** *53,* 5911–5915. doi:10.1016/j.tetlet.2012.08.080
55. Yamamura, H.; Sugiyama, Y.; Murata, K.; Yokoi, T.; Kurata, R.; Miyagawa, A.; Sakamoto, K.; Komagoe, K.; Inoue, T.; Katsu, T. *Chem. Commun.* **2014,** *50,* 5444–5446. doi:10.1039/c3cc49543d
56. Barge, A.; Tagliapietra, S.; Binello, A.; Cravotto, G. *Curr. Org. Chem.* **2011,** *15,* 189–203. doi:10.2174/138527211793979826
57. Klüfers, P.; Piotrowski, H.; Uhlendorf, J. *Chem. – Eur. J.* **1997,** *3,* 601–608. doi:10.1002/chem.19970030416
58. Lipshutz, B. H.; Taft, B. R. *Angew. Chem., Int. Ed.* **2006,** *45,* 8235–8238. doi:10.1002/anie.200603726
59. Cintas, P.; Martina, K.; Robaldo, B.; Garella, D.; Boffa, L.; Cravotto, G. *Collect. Czech. Chem. Commun.* **2007,** *72,* 1014–1024. doi:10.1135/cccc20071014
60. Munteanu, M.; Choi, S.; Ritter, H. *Macromolecules* **2008,** *41,* 9619–9623. doi:10.1021/ma8018975
61. Gingter, S.; Mondrzik, B.; Ritter, H. *Macromolecules* **2012,** *45,* 1753–1757. doi:10.1021/ma3002164
62. Carmona, T.; Martina, K.; Rinaldi, L.; Boffa, L.; Cravotto, G.; Mendicuti, F. *New J. Chem.* **2015,** *39,* 1714–1724. doi:10.1039/C4NJ01556H
63. Carmona, T.; Mayordomo, N.; Martina, K.; Cravotto, G.; Mendicuti, F. *J. Photochem. Photobiol., A* **2012,** *237,* 38–48. doi:10.1016/j.jphotochem.2012.03.018
64. Carmona, T.; Caporaso, M.; Martina, K.; Cravotto, G.; Mendicuti, F. *Supramol. Chem.* **2015,** *27,* 508–521. doi:10.1080/10610278.2014.1003217
65. Boffa, L.; Calcio Gaudino, E.; Martina, K.; Jicsinszky, L.; Cravotto, G. *New J. Chem.* **2010,** *34,* 2013–2019. doi:10.1039/c0nj00021c
66. Wu, J.; Su, P.; Guo, D.; Huang, J.; Yang, Y. *New J. Chem.* **2014,** *38,* 3630–3636. doi:10.1039/C4NJ00030G
67. Decroocq, C.; Rodríguez-Lucena, D.; Russo, V.; Mena Barragán, T.; Ortiz Mellet, C.; Compain, P. *Chem. – Eur. J.* **2011,** *17,* 13825–13831. doi:10.1002/chem.201102266
68. Tran, D. N.; Blaszkiewicz, C.; Menuel, S.; Roucoux, A.; Philippot, K.; Hapiot, F.; Monflier, E. *Carbohydr. Res.* **2011,** *346,* 210–218. doi:10.1016/j.carres.2010.11.024
69. Cravotto, G.; Mendicuti, F.; Martina, K.; Tagliapietra, S.; Robaldo, B.; Barge, A. *Synlett* **2008,** 2642–2646. doi:10.1055/s-0028-1083379
70. Mallard-Favier, I.; Blach, P.; Cazier, F.; Delattre, F. *Carbohydr. Res.* **2009,** *344,* 161–166. doi:10.1016/j.carres.2008.10.014
71. Aime, S.; Gianolio, E.; Arena, F.; Barge, A.; Martina, K.; Heropoulos, G.; Cravotto, G. *Org. Biomol. Chem.* **2009,** *7,* 370–379. doi:10.1039/B812172A
72. Barge, A.; Caporaso, M.; Cravotto, G.; Martina, K.; Tosco, P.; Aime, S.; Carrera, C.; Gianolio, E.; Pariani, G.; Corpillo, D. *Chem. – Eur. J.* **2013,** *19,* 12086–12092. doi:10.1002/chem.201301215
73. Calcio Gaudino, E.; Tagliapietra, S.; Martina, K.; Barge, A.; Lolli, M.; Terreno, E.; Lembo, D.; Cravotto, G. *Org. Biomol. Chem.* **2014,** *12,* 4708–4715. doi:10.1039/c4ob00611a
74. Xu, C.; Wang, J.; Wan, L.; Lin, J.; Wang, X. *J. Mater. Chem.* **2011,** *21,* 10463–10471. doi:10.1039/c1jm10478k
75. Rodrigo, A. C.; Malhotra, S.; Böttcher, C.; Adeli, M.; Haag, R. *RSC Adv.* **2014,** *4,* 61656–61659. doi:10.1039/C4RA11601A
76. Biswas, A.; Appell, M.; Liu, Z.; Cheng, H. N. *Carbohydr. Polym.* **2015,** *133,* 74–79. doi:10.1016/j.carbpol.2015.06.044
77. Siu, M.; Yaylayan, V. A.; Bélanger, J. M. R.; Paré, J. R. J. *Tetrahedron Lett.* **2005,** *46,* 3737–3739. doi:10.1016/j.tetlet.2005.03.154
78. Anandam, S.; Selvamuthukumar, S. *J. Porous Mater.* **2014,** *21,* 1015–1023. doi:10.1007/s10934-014-9851-2
79. Takacs, L. *Chem. Soc. Rev.* **2013,** *42,* 7649–7659. doi:10.1039/c2cs35442j
80. Sopicka-Lizer, M., Ed. *High-Energy Ball Milling Mechanochemical Processing of Nanopowders;* Woodhead Publishing in Materials; Elsevier Woodhead Publishing: Cambridge, 2010; pp 1–422.
81. Burmeister, C. F.; Kwade, A. *Chem. Soc. Rev.* **2013,** *42,* 7660–7667. doi:10.1039/c3cs35455e
82. Hedges, A.; Tenbarge, F. Cyclodextrin complexing method. U.S. Patent 5,007,966, April 16, 1991.
83. Carli, F. In *Proceedings of the 26th International Symposium on Controlled Release of Bioactive Materials,* Boston Marriott Copley Place, Boston, MA, USA, June 20–23, 1999; pp 873–874.
84. Frömming, K.-H.; Szejtli, J. Cyclodextrins in Pharmacy. In *Preparation and Characterization of Cyclodextrin Complexes;* Szejtli, J., Ed.; Topics in Inclusion Science, Vol. 5; Springer: Dordrecht, The Netherlands, 1994; pp 83–104. doi:10.1007/978-94-015-8277-3_5
85. Khadka, P.; Ro, J.; Kim, H.; Kim, I.; Kim, J. T.; Kim, H.; Cho, J. M.; Yun, G.; Lee, J. *Asian J. Pharm. Sci.* **2014,** *9,* 304–316. doi:10.1016/j.ajps.2014.05.005
86. Ranu, B. C.; Stolle, A., Eds. *Ball Milling Towards Green Synthesis: Applications, Projects, Challenges;* RSC, 2014. ISBN: 978-1-84973-945-0.
87. Vogel, P.; Figueira, S.; Muthukrishnan, S.; Mack, J. *Tetrahedron Lett.* **2009,** *50,* 55–56. doi:10.1016/j.tetlet.2008.10.079
88. Tyagi, M.; Khurana, D.; Kartha, K. P. R. *Carbohydr. Res.* **2013,** *379,* 55–59. doi:10.1016/j.carres.2013.06.018
89. Patil, P. R.; Kartha, K. P. R. *Green Chem.* **2009,** *11,* 953–956. doi:10.1039/b904454j

90. Braun, T.; Buvári-Barcza, Á.; Barcza, L.; Konkoly-Thege, I.; Fodor, M.; Migali, B. *Solid State Ionics* **1994,** *74,* 47–51. doi:10.1016/0167-2738(94)90435-9
91. Xu, X.; Hong, Y.-K.; Park, J.; Lee, W.; Lane, A. M.; Cui, J. *J. Solid State Chem.* **2015,** *231,* 108–113. doi:10.1016/j.jssc.2015.08.019
92. Chen, J.; Dyer, M. J.; Yu, M.-F. *J. Am. Chem. Soc.* **2001,** *123,* 6201–6202. doi:10.1021/ja015766t
93. Najafpour, M. M.; Mostafalu, R.; Kaboudin, B. *J. Photochem. Photobiol., B* **2015,** *152,* 106–111. doi:10.1016/j.jphotobiol.2015.02.019
94. Menuel, S.; Doumert, B.; Saitzek, S.; Ponchel, A.; Delevoye, L.; Monflier, E.; Hapiot, F. *J. Org. Chem.* **2015,** *80,* 6259–6266. doi:10.1021/acs.joc.5b00697
95. Jicsinszky, L.; Caporaso, M.; Tuza, K.; Martina, K.; Calcio Gaudino, E.; Cravotto, G. *ACS Sustainable Chem. Eng.* **2015,** in press. doi:10.1021/acssuschemeng.5b01006
96. Jicsinszky, L.; Hashimoto, H.; Fenyvesi, E.; Uneo, A. Chapter 4: Cyclodextrin derivatives. In *Cyclodextrins;* Szejtli, J.; Osa, T., Eds.; Comprehensive Supramolecular Chemistry, Vol. 3; Pergamon Press: Oxford, 1996; pp 57–188.
97. Naguib, M. *Anesth. Analg.* **2007,** *104,* 575–581. doi:10.1213/01.ane.0000244594.63318.fc
98. Watts, P.; Wiles, C. *Chem. Commun.* **2007,** 443–467. doi:10.1039/B609428G
99. Wille, C.; Gabski, H.-P.; Haller, T.; Kim, H.; Unverdorben, L.; Winter, R. *Chem. Eng. J.* **2004,** *101,* 179–185. doi:10.1016/j.cej.2003.11.007
100. http://faculty.washington.edu/finlayso/che475/microreactors/Group_A/whatmrex.htm.
101. Rezzonico, F. *Astrobiology* **2014,** *14,* 344–351. doi:10.1089/ast.2013.1120
102. Sapra, K. T.; Bayley, H. *Sci. Rep.* **2012,** *2,* No. 848. doi:10.1038/srep00848
103. Feng, Y.; Zhang, Y.; Ying, C.; Wang, D.; Du, C. *Genomics, Proteomics Bioinf.* **2015,** *13,* 4–16. doi:10.1016/j.gpb.2015.01.009
104. Delattre, C.; Vijayalakshmi, M. A. *J. Mol. Catal. B: Enzym.* **2009,** *60,* 97–105. doi:10.1016/j.molcatb.2009.04.016

License and Terms

The definitive version of this article is the electronic one which can be found at:
doi:10.3762/bjoc.12.30

BEILSTEIN JOURNAL OF ORGANIC CHEMISTRY

Optimized methods for preparation of 6^{I}-(ω-sulfanyl-alkylene-sulfanyl)-β-cyclodextrin derivatives

Eva Bednářová[1], Simona Hybelbauerová[2] and Jindřich Jindřich*[1]

Full Research Paper

Open Access

Address:
[1]Department of Organic Chemistry, Faculty of Science, Charles University in Prague, Hlavova 8, 128 43, Prague 2, Czech Republic, Fax: +420 22195 1326 and [2]Department of Teaching and Didactics of Chemistry, Faculty of Science, Charles University in Prague, Hlavova 8, 128 43, Prague 2, Czech Republic

Email:
Jindřich Jindřich* - jindrich@natur.cuni.cz

* Corresponding author

Keywords:
cyclodextrins; disulfides; monosubstituted derivatives; thiols

Beilstein J. Org. Chem. **2016,** *12,* 349–352.
doi:10.3762/bjoc.12.38

Received: 16 November 2015
Accepted: 09 February 2016
Published: 24 February 2016

This article is part of the Thematic Series "Superstructures with cyclodextrins: Chemistry and applications III".

Guest Editor: E. Monflier

Abstract

A general high-yielding method for the preparation of monosubstituted β-cyclodextrin derivatives which have attached a thiol group in position 6 is described. The thiol group is attached through linkers of different lengths and repeating units (ethylene glycol or methylene). The target compounds were characterized by IR, MS and NMR spectra. A simple method for their complete conversion to the corresponding disulfides as well as a method for the reduction of the disulfides back to the thiols is presented. Both, thiols and disulfides are derivatives usable for well-defined covalent attachment of cyclodextrin to gold or polydopamine-coated solid surfaces.

Introduction

Cyclodextrins (CDs) [1], cyclic oligomers of α-D-glucopyranose, are used for their ability to form supramolecular inclusion complexes with a wide range of guest molecules [2]. From the native CDs (α-CD, β-CD, and γ-CD containing 6, 7, and 8 glucose units, respectively) the β-CD is studied the most due to its lowest price and the highest guest binding ability. A large number of CD derivatives [3] which have been prepared up to now can be divided into several groups according to their intended use. The largest group is the one containing CD derivatives with modified complexation properties, used mainly as solubilizers and/or stabilizers in pharmaceutical, cosmetic, agricultural and food industries [4]. These derivatives are usually mixtures of randomly substituted CDs. On the other hand, CD derivatives which are well-defined chemical individuals are well suited for separation science [5], chemosensors [6] or drug delivery [7] applications. These applications often involve a modification of solid surfaces by CDs. Among the solid surfaces, to which CDs were attached, are sorbents for separation techniques or waste water treatment [8] or nanoparticles [6].

In our work, we focused on the preparation of sulfanyl-group-containing CD derivatives – 6^{I}-deoxy-6^{I}-(ω-sulfanyl-alkylene-sulfanyl)-β-cyclodextrins (β-CD-S-X-SH) – which can be attached to a gold surface [9,10] or a polydopamine-coated surface [11]. It has been already described that the surface coverage of self-assembled monolayers of CD derivatives on gold depends substantially on the linker between the sulfanyl group and the CD. Derivatives with sulfanyl groups connected directly to the CD gave much lower surface coverage [12] than the derivatives containing just one sulfanyl group connected by a longer linker [13]. Therefore, we decided to prepare a series of CD sulfanyl derivatives with different lengths of the linker connecting the CD and the sulfanyl group. These derivatives are needed for two projects which both will study the influence of the linker length on the properties of the whole system. The first project will study the sensitivity of quartz crystal microbalances with a CD-modified gold sensor [14]; the second will study photodynamic sensitizers included into CDs attached on the surface of polydopamine-covered nanowires [15]. Syntheses of several sulfanyl group-containing CD derivatives suitable for this purpose were published. The first method [16] is using a direct substitution of 6^{I}-*O*-(*p*-toluenesulfonyl)-β-CD with dithiols. We also intended to use this method, but the described procedure gives only yields around 20%. The second method [13] is using a disulfide of mercaptopropionic acid which is coupled by an amide bond to two molecules of 6^{I}-amino-β-CD to form a stable CD disulfide derivative. This disulfide can be used directly for functionalization of a gold surface, but its reduction to thiol was not described. In any case, the amide-containing derivative might not be stable enough under basic conditions needed for the polydopamine derivatization by the thiol. Besides, the common problem with the preparation of this type of sulfanyl derivatives – formation of disulfide byproducts – was not addressed in the literature at all. Therefore, we decided to develop more general procedures for the preparation of such CD derivatives and also a method for controlled preparation of corresponding disulfides, which are much more stable alternatives to the thiols for a longer storage. That is why a method to recover the thiols from the disulfides was also studied.

Results and Discussion

For the preparation of the starting compound for all syntheses – Ts-β-CD (**1**) – we recently described [17] a modification of one of the commonly used method [18]. The modification consisted in the repeated recrystallization from 50% water–methanol which yielded a very pure product with no interfering impurities (di- or tri-Ts-β-CD) or unreacted β-CD.

The terminal sulfanyl groups were introduced to the oligoethylene glycol linkers using standard chemical transformations (Scheme 1). Oligoethylene glycol ditosylates **2a**–**c** [19] were converted to *S*-acetyl dithiols **3a**–**c** [20] and deacetylated to the oligoethylene glycol dithiols **4a**–**c** using a procedure published for similar thiols [21]. Compounds **4** can be easily oxidized to disulfides; therefore their preparation and purification must be performed under inert atmosphere.

Then we optimized methods for the preparation of β-CD-S-X-SH derivatives (**5a**–**g**, Scheme 2*)* from Ts-β-CD for two types of compounds in which X is either a pure alkylene group $–(CH_2)_m–$ (m = 2, 3, 5, 8) or the oligoethylene glycol group $–CH_2(CH_2OCH_2)_nCH_2–$ (n = 1, 2, 3). In addition, general high yielding methods for conversion of the prepared CD-thiols to CD disulfides (**6a**–**g**) by air oxidation and the CD disulfides back to CD-thiols by reduction with ethanethiol were developed.

At first, we tried to reproduce the synthesis of the compound **5g** (Scheme 2) according to the published procedure [12]. Product **5g** was detected in the reaction mixture by MS but to isolate it in a sufficient yield was difficult. The main byproduct was the corresponding disulfide **6g** which is formed from **5g** by air oxidation. Moreover, the obtained alkylene derivative **5g** had a low solubility in water and water/alcohol mixtures what represented quite an obstacle for the intended use – derivatization of solid

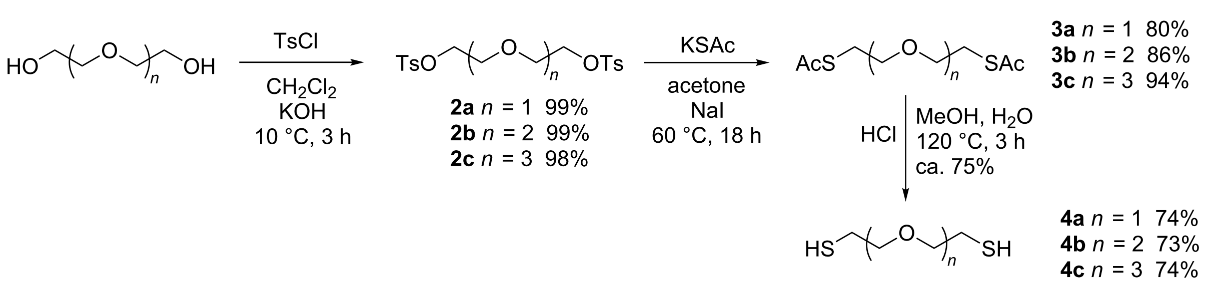

Scheme 1: Synthesis of oligoethylene glycol dithiols.

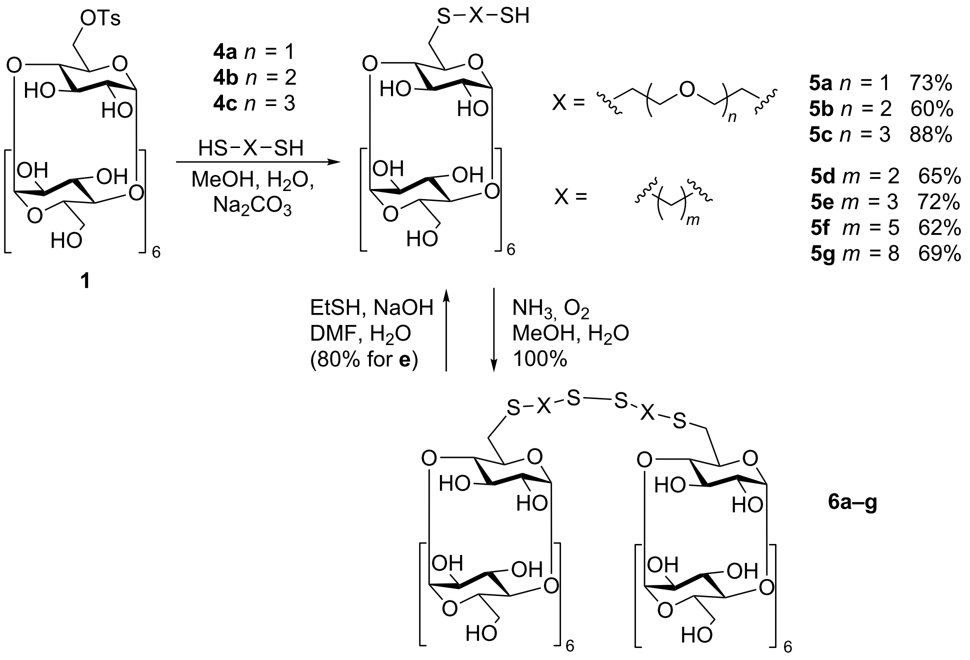

Scheme 2: Synthesis of β-cyclodextrinthiols and -disulfides.

surfaces by treatment with the water solution of the CD derivative.

Therefore, we decided also to prepare the derivatives containing the more hydrophilic and flexible oligoethylene glycol linker, which have been successfully applied in several studies to position the CD units at a sufficient distance from the solid surface. These linkers also have the advantage, compared to the aliphatic chain linkers, in a lower tendency to form an inclusion complex with β-CD [22], i.e., a suitable accessibility of the cavity should be kept, and further inclusion complexes could be formed with the guests.

Strict inert conditions are also required for the next synthetic step – preparation of compounds **5**. The air had to be removed from the reaction mixture by bubbling argon through the sonicated solution. The ideal solvent mixture for this reaction, which dissolves both reactants, proved to be water/methanol 1:1 in which the reaction reached a complete conversion of the starting Ts-β-CD in 20 h. The crucial step of the work-up was the acidification of the basic reaction mixture and the extraction of the unreacted dithiols with chloroform. The prepared CD-thiols form disulfides very quickly under basic conditions but are reasonably stable under neutral and acidic conditions. Therefore, the final chromatographic separation could not be done in the common elution mixture (propan-1-ol/water/ammonia) but the neutral solvent mixture (butan-1-ol/ethanol/water) was used instead. This optimized procedure gave the target compounds **5a–g** in 60–90% yield, and the unreacted dithiols could be easily recovered. Oxidation products of compounds **5a–g** (disulfides **6a–g)** are quite stable compounds and were prepared in quantitative yield just by bubbling air through the water/methanol solution of the thiol which was basified by addition of aqueous ammonia. The disulfides **6** can be used, as well as the thiols, for the attachment of the cyclodextrin cavity to a gold surface. So they can be used instead of the thiols in applications where well defined starting compounds are needed. On the other hand, for applications where only the thiol can be used (like attachment to polydopamine-coated surfaces), and the pure compound is often needed, the disulfide can be prepared in larger amounts and used for a long term storage. The corresponding pure thiol can be then prepared when needed by a simple one step high yielding procedure developed for compound **6e** (Scheme 2), which does not require any chromatographic separation and uses ethanethiol in basic solution as the reducing agent. The separation of the thiol product consists just of its precipitation with acetone from the reaction mixture. This separation method is very efficient and is used very often for separation of monosubstituted CD derivatives. The same reaction conditions, as for compound **6e**, were used for the reduction of all disulfides **6** on TLC scale. The TLC proved a conversion to the thiol for all of them. The only compound which was not completely converted under the given conditions was **6g**, most probably due to its low solubility.

Conclusion

To conclude, we addressed problems commonly encountered during the syntheses of thiol-group-containing cyclodextrin derivatives and presented reproducible methods for their elimination. The main problem – formation of the corresponding disulfides by air oxidation – could be suppressed substantially by using an inert atmosphere and performing work-up under acidic conditions. Moreover, the often unwanted and much more stable disulfide byproducts can be obtained from the thiols in quantitative yields and can be used instead of them in some applications. Disulfides can also be used for a long-term storage and the corresponding thiol can be prepared in one simple synthetic step and isolated by precipitation.

Supporting Information

Supporting Information File 1

General experimental procedures, instruments, materials. Detailed experimental procedures and characterization data for newly prepared compounds. ^{1}H and ^{13}C NMR spectra of prepared compounds.
[http://www.beilstein-journals.org/bjoc/content/supplementary/1860-5397-12-38-S1.pdf]

Acknowledgements

The work has been supported by Grant Agency of the Czech Republic (project No. 13-01440S)

References

1. Crini, G. *Chem. Rev.* **2014,** *114,* 10940–10975. doi:10.1021/cr500081p
2. Rekharsky, M. V.; Inoue, Y. *Chem. Rev.* **1998,** *98,* 1875–1918. doi:10.1021/cr970015o
3. Easton, C. J.; Lincoln, S. F. *Modified Cyclodextrins: Scaffolds and Templates for Supramolecular Chemistry;* Imperial College Press: London, 1999. doi:10.1142/p124
4. Hedges, A. R. *Chem. Rev.* **1998,** *98,* 2035–2044. doi:10.1021/cr970014w
5. Tang, W.; Ng, S. C. *J. Sep. Sci.* **2008,** *31,* 3246–3256. doi:10.1002/jssc.200800357
6. Han, C.; Li, H. *Anal. Bioanal. Chem.* **2009,** *397,* 1437–1444. doi:10.1007/s00216-009-3361-0
7. Wang, L.; Li, L.-l.; Fan, Y.-s.; Wang, H. *Adv. Mater.* **2013,** *25,* 3888–3898. doi:10.1002/adma.201301202
8. Crini, G.; Morcellet, M. *J. Sep. Sci.* **2002,** *25,* 789–813. doi:10.1002/1615-9314(20020901)25:13<789::AID-JSSC789>3.0.CO;2-J
9. Ulman, A. *Chem. Rev.* **1996,** *96,* 1533–1554. doi:10.1021/cr9502357
10. Vericat, C.; Vela, M. E.; Benitez, G. A.; Gago, J. A. M.; Torrelles, X.; Salvarezza, R. C. *J. Phys.: Condens. Matter* **2006,** *18,* R867–R900. doi:10.1088/0953-8984/18/48/R01
11. Lee, H.; Dellatore, S. M.; Miller, W. M.; Messersmith, P. B. *Science* **2007,** *318,* 426–430. doi:10.1126/science.1147241
12. Rojas, M. T.; Königer, R.; Stoddart, J. F.; Kaifer, A. E. *J. Am. Chem. Soc.* **1995,** *117,* 336–343. doi:10.1021/ja00106a036
13. Henke, C.; Steinem, C.; Janshoff, A.; Steffan, G.; Luftmann, H.; Sieber, M.; Galla, H.-J. *Anal. Chem.* **1996,** *68,* 3158–3165. doi:10.1021/ac9512261
14. Kikandi, S. N.; Okello, V. A.; Wang, Q.; Sadik, O. A.; Varner, K. E.; Burns, S. A. *Environ. Sci. Technol.* **2011,** *45,* 5294–5300. doi:10.1021/es1043084
15. Yang, H.; Lan, Y.; Zhu, W.; Li, W.; Xu, D.; Cui, J.; Shen, D.; Li, G. *J. Mater. Chem.* **2012,** *22,* 16994–17001. doi:10.1039/c2jm33251e
16. Nelles, G.; Weisser, M.; Back, R.; Wohlfart, P.; Wenz, G.; Mittler-Neher, S. *J. Am. Chem. Soc.* **1996,** *118,* 5039–5046. doi:10.1021/ja9539812
17. Popr, M.; Hybelbauerová, S.; Jindřich, J. *Beilstein J. Org. Chem.* **2014,** *10,* 1390–1396. doi:10.3762/bjoc.10.142
18. Zhong, N.; Byun, H.-S.; Bittman, R. *Tetrahedron Lett.* **1998,** *39,* 2919–2920. doi:10.1016/S0040-4039(98)00417-1
19. Bonger, K. M.; van den Berg, R. J. B. H. N.; Heitman, L. H.; IJzerman, A. P.; Oosterom, J.; Timmers, C. M.; Overkleeft, H. S.; van der Marel, G. A. *Bioorg. Med. Chem.* **2007,** *15,* 4841–4856. doi:10.1016/j.bmc.2007.04.065
20. Scullion, L. E.; Leary, E.; Higgins, S. J.; Nichols, R. J. *J. Phys.: Condens. Matter* **2012,** *24,* No. 164211. doi:10.1088/0953-8984/24/16/164211
21. Keddie, D. J.; Grande, J. B.; Gonzaga, F.; Brook, M. A.; Dargaville, T. R. *Org. Lett.* **2011,** *13,* 6006–6009. doi:10.1021/ol202051y
22. Harada, A.; Okada, M.; Kawaguchi, Y.; Kamachi, M. *Polym. Adv. Technol.* **1999,** *10,* 3–12. doi:10.1002/(SICI)1099-1581(199901/02)10:1/2<3::AID-PAT759>3.0.CO;2-S

License and Terms

BEILSTEIN JOURNAL OF ORGANIC CHEMISTRY

New synthetic strategies for xanthene-dye-appended cyclodextrins

Milo Malanga*[1], Andras Darcsi[2], Mihaly Balint[1], Gabor Benkovics[1,3], Tamas Sohajda[1] and Szabolcs Beni[2]

Full Research Paper

Open Access

Address:
[1]CycloLab, Cyclodextrin R&D Ltd., Budapest, H-1097 Illatos út 7, Hungary, [2]Department of Pharmacognosy, Semmelweis University, H-1085 Üllői út 26, Hungary, and [3]Department of Organic Chemistry, Faculty of Science, Charles University, Hlavova 8, 12843 Prague 2, Czech Republic

Email:
Milo Malanga* - malanga@cyclolab.hu

* Corresponding author

Keywords:
DMT-MM; fluorescein; rhodamine; supramolecular assembly

Beilstein J. Org. Chem. **2016,** *12,* 537–548.
doi:10.3762/bjoc.12.53

Received: 05 November 2015
Accepted: 02 March 2016
Published: 17 March 2016

This article is part of the Thematic Series "Superstructures with cyclodextrins: Chemistry and applications III".

Guest Editor: E. Monflier

Abstract

Xanthene dyes can be appended to cyclodextrins via an ester or amide bridge in order to switch the fluorescence on or off. This is made possible through the formation of nonfluorescent lactones or lactams as the fluorophore can reversibly cyclize. In this context we report a green approach for the synthesis of switchable xanthene-dye-appended cyclodextrins based on the coupling agent 4-(4,6-dimethoxy-1,3,5-triazin-2-yl)-4-methylmorpholinium chloride (DMT-MM). By using 6-monoamino-β-cyclodextrin and commercially available inexpensive dyes, we prepared rhodamine- and fluorescein-appended cyclodextrins. The compounds were characterized by NMR and IR spectroscopy and MS spectrometry, their UV–vis spectra were recorded at various pH, and their purity was determined by capillary electrophoresis. Two potential models for the supramolecular assembly of the xanthene-dye-appended cyclodextrins were developed based on the set of data collected by the extensive NMR characterization.

Introduction

Cyclodextrins (CDs) are cyclic oligosaccharides consisting of 6, 7 or 8 glucopyranose units (α-, β- and γ-CD, respectively). Native CDs do not adsorb light in the UV–vis region (200–800 nm), but they can be converted into spectroscopically active compounds by modification with a chromophore/fluorophore unit. Fluorophore-appended CDs can be appropriate systems to detect spectroscopically inert molecules by guest-induced spectroscopic changes associated with the formation of inclusion complexes. These fluorescent CDs exhibit remarkable molecular recognition abilities, discriminating shape, bulkiness and polarity of the guests [1,2]. Furthermore, CDs can be directly modified with fluorophores for labeling in order to assess if these versatile molecules cross biological barriers (e.g., cell membrane, blood–brain barrier) and to follow their distribution in living matter [3].

Among the fluorescent dyes, the group of fluorophores based on xanthene scaffolds is one of the most popular. Two representa-

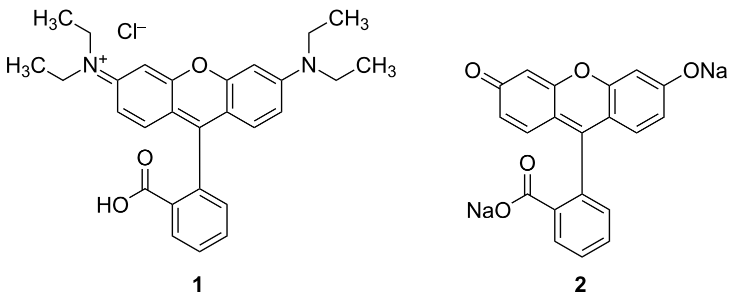

Figure 1: Structures of fluorescent xanthene dyes. Rhodamine B·HCl **1** and fluorescein disodium salt **2**.

tives of this class are fluorescein and rhodamine (Figure 1), which have been applied as chemosensors [4] and have been widely exploited in various areas such as cell biology, microscopy, biotechnology, and ophthalmology due to their versatile photophysical properties. However, the chemical modification of this evergreen class of dyes is still an ongoing process [5,6].

Fluorescein is the most widely used fluorescent probe in biological applications and in particular for covalently labeling proteins. Rhodamine derivatives are robust dyes that find application as fluorophores for microscopy, in cell sorting, in photodynamic therapy and in colorimetric enzymatic tests (ELISA).

Although it is possible to modify xanthene dyes with specific functional groups (e.g., isothiocyanates, maleimide, succinimidyl), enabling them to react with amine groups, such chemical modifications dramatically affect the cost of the dye because of the laborious purification process. In order to reduce cost, one approach is to perform the condensation reaction that leads to the formation of the xanthene dyes by using previously functionalized reagents [7]. This approach is difficult to generalize and does not involve a common synthetic plan for different xanthene dyes since their core is different. Another possibility is to modify less expensive, unfunctionalized, commercially available xanthene dyes; for instance, both rhodamine B and fluorescein are commercially available at a reasonable price. Since the presence of a carboxylic moiety is a common feature to most of the xanthene-based dyes, it is easy to develop a common synthetic plan for the activation of the dye toward biological systems based on the modification of this functional group. The most logical way for generating an active dye able to target an amine-bearing system would be the formation of an amide bond. However, in spite of the numerous attempts, the modification of this specific position still (at least in a bio-compatible environment) remains a challenge. In the case of rhodamine, the modification of the carboxylic moiety, to the best of our knowledge, is always performed in organic solvent under harsh conditions [8].

The synthesis and the use of 4-(4,6-dimethoxy-1,3,5-triazin-2-yl)-4-methylmorpholinium chloride (DMT-MM) as a coupling agent for the formation of amides and esters was first reported by Kunishima et al. [9]. This compound possesses advantageous properties as it can be prepared in gram scale from inexpensive reagents, it is stable in air, it does not adsorb water, and the water soluble co-products formed during the coupling reaction can be easily removed from the reaction crude. All these characteristics make DMT-MM a convenient tool for the synthesis of amides and esters [10].

The first example of xanthene-dye-appended cyclodextrin based on the modification of the carboxylic moiety of the fluorophore was reported by Ueno's group [11]. In the study, they modified 6-monotosyl-β-CD with the sodium salt of fluorescein, resulting in a fluorescein β-CD derivative connected through an ester bond. The main idea of the synthetic step was to promote the nucleophilic substitution between 6-monotosyl-β-CD and the carboxylate of the fluorescein by adjusting the pH of the aqueous solution around pH 6 [12]. Some years later the same group reported on a fluorescein-modified γ-CD and its properties as a sensor and as a charge-changeable receptor for detecting organic acids [13]. The synthetic strategy was still based on the ester formation between the fluorophore and the CD scaffold, but the conditions were slightly modified. As a starting material, 6-monoiodo-γ-CD was chosen instead of the more labile 6-monotosyl-γ-CD and anhydrous DMF (under nitrogen atmosphere) substituted for the aqueous environment of the previous β-CD coupling.

The first rhodamine-modified CD was reported by Harada [14]. 6-Monoamino-α-CD was coupled with rhodamine B in the presence of *N,N'*-dicyclohexylcarbodiimide (DCC) and hydroxybenzotriazole (HOBt) in anhydrous DMF under inert atmosphere in order to connect the two moieties through an amide bond. The fluorescent CD derivative was used to observe the movement of a rotaxane immobilized on glass substrates.

Hasegawa et al. [15] were the first to develop rhodamine labeled CDs for biological purposes. They synthesized two different fluorescent β-CDs and showed their utility as new fluorogenic probes for monitoring pH of HeLa cells. The synthetic strategy was based first on the modification of the CD scaffold with two different linkers (both polyamines) and then on the coupling of the terminal amino group of the linkers with rhodamine B. The coupling conditions were slightly different from those reported by Harada [14]. The solvent was a mixture of pyridine and DMF, the activating agents for the carboxylic acid were HOBt and 1-ethyl-3-(3-dimethylaminopropyl)carbodiimide (EDC).

Fang and co-workers designed a ratiometric sensor for detecting mercury ions in aqueous media, some biological fluids and living cells based on a rhodamine-modified β-CD [16]. The synthetic strategy was a three-step procedure: rhodamine B was modified into a spirolactam rhodamine ethylenediamine, 6-monotosyl-β-CD was reacted with ethylenediamine in order to obtain the equivalent monosubstituted derivative, and finally, the coupling between the two molecules was performed. The coupling with the 6-mono(2-aminoethylamino)-β-CD was obtained by in situ conversion of the terminal amino group of the fluorophore into isothiocyanate group.

To summarize, fluorescein has been connected to CDs through an ester bond by performing the reaction in water or DMF. Although the synthetic procedure is well described, the experimental synthesis steps and the purification process are not described in enough detail. The characterization of the molecule is not exhaustive since a clear indication of the ester formation is missing. Rhodamine has been connected in organic solvents through an amide bond with DCC or EDC as coupling agents. The molecules have not been characterized in detail since only partial spectroscopic data have been reported.

In this study, we developed a general, green, and inexpensive method for the synthesis of xanthene-appended CDs. Since most of the xanthene dyes possess a carboxylic moiety (only a few examples are known that lack this moiety) we based our strategy on the formation of an amide bond. In particular, we reacted 6-monoamino-β-CD (NH_2-β-CD) with fluorescein and rhodamine in alkaline aqueous media at room temperature in the presence of the coupling agent DMT-MM, thus producing the fluorescent derivatives. This method can not only be applied to CDs, but may represent a new general approach for the modification of xanthene dye in water, thus affording amide or ester derivatives.

When a fluorophore is used for the labeling of a single-isomer CD, the resulting molecule is rarely the fully substituted, fluorescent single-isomer CD; more commonly, the system is a mixture of unsubstituted and substituted CD derivatives. Although some data are reported in the literature for the characterization of fluorescently labeled CDs, a full NMR characterization, to the best of our knowledge, has never been presented and the spectroscopic data always refer to the mixture obtained by an incomplete fluorescent labeling and not to the fluorescent single-isomer CD derivative. The incomplete fluorescent tagging is reflected by, for example, broad NMR signals [17].

If the goal of the derivatization is the fluorescent labeling of a randomly substituted CD derivative, the situation is even more challenging. A suitable synthetic strategy for obtaining a homogeneous, fluorescent, randomly substituted CD derivative (where each compound is modified with a fluorescent moiety) is to perform the random substitution on a fluorescent single-isomer CD [18]. If the substrate for the fluorescent labeling is a randomly substituted CD derivative, most commonly, the obtained mixture will contain fluorescently labelled and unlabeled isomers.

In this work, our purpose was to develop a generic synthetic method for the derivatization of CDs with commercially available xanthene dyes and to isolate and characterize the fluorescent compounds as single isomers.

Results and Discussion

In Figure 2, the reaction scheme for the rhodamine-appended β-CD derivative (Rho-β-CD) is shown as a representative example. The synthetic strategy is based on the condensation reaction between an amine-bearing CD and the carboxyl moiety of the xanthene dye promoted by the coupling agent DMT-MM. It is accepted that the carboxylic acid has to be deprotonated in order to generate an activated ester with DMT [19]. The activated species undergoes attack by the amine, thus generating the desired amide bond.

The xanthene dyes, the β-CDs and the coupling agent are highly soluble in water, thus allowing for a homogenous reaction that occurs at room temperature. Since β-CD modified with amines is more stable in the HCl form (in order to avoid decomposition), during the reaction, an additional base such as *N*-methylmorpholine (NMM) or NaOH is required. If amine-bearing CDs are used as free bases, the additional base can be omitted. The synthesis of the reactions simply consists of the selective precipitation of the target compound with acetone and removal of the unreacted dye by filtration. The purity of the starting dye is a crucial parameter for the outcome of the reaction, since it will greatly affect the crude composition and consequently the purification process. If the purity of the starting dye is satisfactory, selective precipitation/filtration are the only steps required

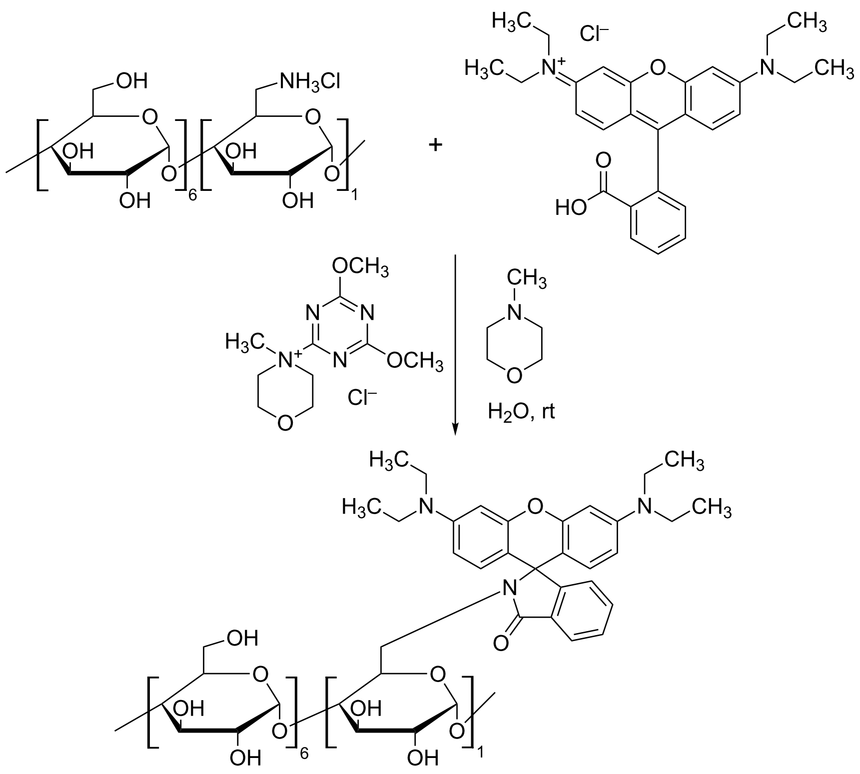

Figure 2: Reaction scheme for the synthesis of rhodamine-appended β-CD.

for obtaining a fluorescent-appended β-CD derivative of acceptable purity (>90%, based on thin-layer chromatography (TLC)). If the starting fluorophore is a mixture of fluorescent (but not clearly identified) dyes, then chromatography is needed to obtain the desired purity.

Rhodamine-appended β-CD

Rhodamine B in HCl form (Rho·HCl) was sourced in good purity, allowing for a clean formation of the product with a very low amount of rhodamine-related byproducts (not detectable by TLC), a minute amount of two β-CD-related byproducts (see ByP$_1$-, ByP$_2$-β-CD in TLCs in Figure 3, the sum of the two being less than 5% based on the intensity of the spots on TLC-5) and some unreacted NH$_2$-β-CD (less than 5% based on the intensity of the spots on TLC-5). The reaction was completed in a couple of hours, at room temperature, in an aqueous environment. TLC provides an unambiguous identification of the product, and the behavior of the product in the selected eluent gives structural indication about the possible prototropic form assumed from the dye in the conjugate.

The left panel of Figure 3 shows the TLC plates used for monitoring the composition of Rho-β-CD crude at different development stages, and in particular, immediately after the removal

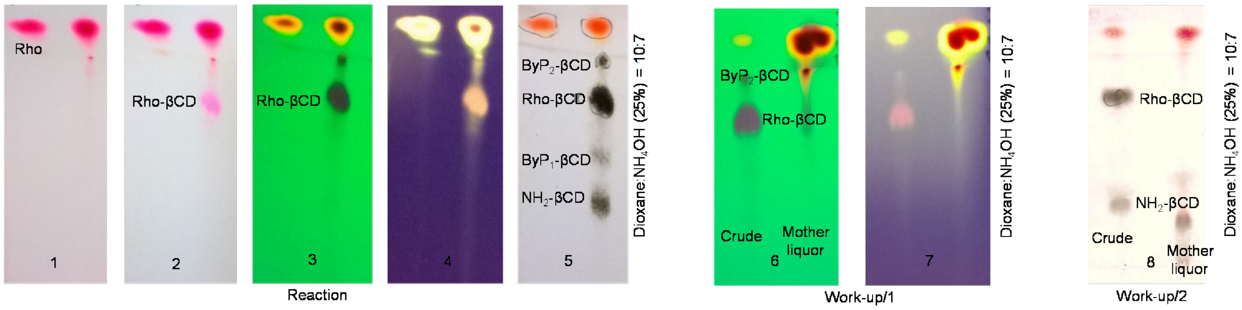

Figure 3: TLC plates at different development stages for monitoring the composition of Rho-β-CD crude (left panel) and TLC for evaluating the effectiveness of the work-up (right panels).

from the developing chamber (1), after heating (2), under UV excitation at 254 nm (3), under UV excitation at 366 nm (4), and finally, after charring (5). The right panels in Figure 3 show the effectiveness of the selective precipitation/filtration during the work-up and in particular it reveals that the unreacted dye can be separated from the product (TLC-6, TLC-7 under UV excitation at 254 nm and at 366 nm, respectively) while the unreacted NH_2-β-CD and the nonfluorescent ByP_1-β-CD are more challenging to remove (TLC-8, after charring).

In the left panel of Figure 3, the unreacted dye (Rho) is clearly detectable at any stage of the development, while the product (Rho-β-CD) is detectable only after heating the TLC plate and appears as a slight pink spot (TLC-2 in Figure 3). This spot is colored, strongly UV active, nonfluorescent and charrable (TLC-2, -3, -4 and -5, respectively in Figure 3). The presence of color and the charrability indicates that the compound contains both the chromophore and the CD scaffold. The strong UV activity and the nonfluorescence suggest that the chromophore is prevalently in lactam form [20]. As it is also known that β-CD has the ability to preferably complex the cyclic form of rhodamine B [21], complexation may play a role in the stabilization of the lactam form of the rhodamine-appended CD derivative. All this information taken together confirms the presence of the product/conjugate and add to the structural elucidation on the system.

Concerning the synthesis, the first part consists of the removal of the unreacted dye with acetone. As shown in Figure 3, after selective precipitation/filtration with acetone, most of the unreacted dye and ByP_2-β-CD remain in the mother liquor (TLC-6, TLC-7 in Figure 3). At this stage, the crude already has acceptable purity (>90% based on TLC), but flash chromatography with a $CH_3CN–H_2O$ gradient elution permits the removal of the remaining CD-related byproducts and further increases the purity. After this additional purification step, the compound, Rho-β-CD, has been extensively characterized by NMR spectroscopy.

NMR characterization of Rho-β-CD

The proton NMR spectrum shown in Figure 4 is a typical spectrum of an asymmetric cyclodextrin. The sharpness of the peaks suggests the high purity of the compound.

The two constituent parts of the molecule can be easily recognized in Figure 4. The resonances in the aromatic (5.5–8.0 ppm) and aliphatic (0.5–1.5 ppm) regions belong to the rhodamine moiety, while those observed between 2.5–5.5 ppm belong to

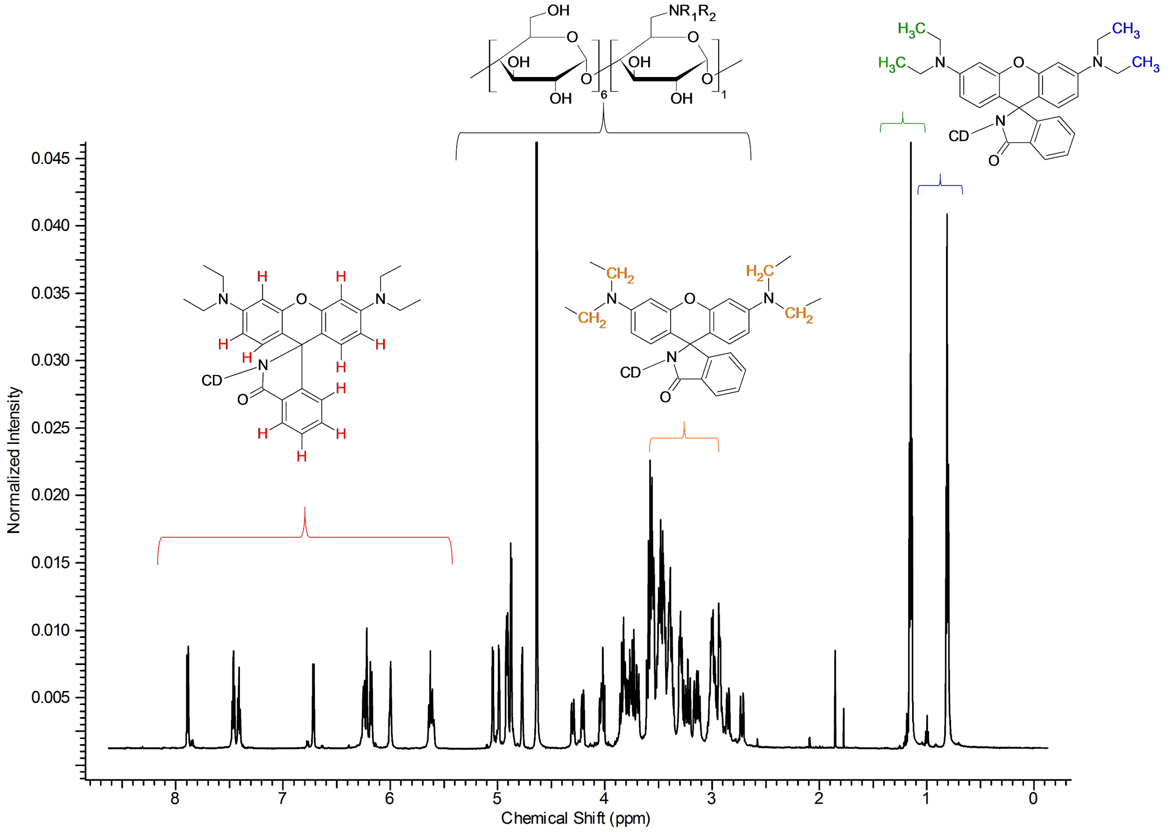

Figure 4: ^1H NMR spectrum of Rho-β-CD with partial assignments (D_2O, 500 MHz, 298 K).

the CDs and also include the methylene moieties of the fluorophore. The integration of the signals perfectly fits the theoretical values for a monosubstituted rhodamine-β-CD derivative. This is also confirmed by the found value of the pseudo-molecular ion during the electrospray ionization mass spectrometry (ESIMS) analysis (see Experimental part).

The resonance signals in the aromatic region are well resolved (see Supporting Information File 1, Figure S1) and the cross-linking with the data obtained by the COSY and DEPT-ed-HSQC spectra (see Supporting Information File 1, Figures S2 and S3, respectively) allowed for the complete assignment (the data are in agreement with the literature [22]). The multiplicity of the signals can be clearly determined. This is not an obvious characteristic for rhodamine-based CD derivatives since the aromatic signals of these compounds are usually represented by very broad signals. The presence of broad signals is characteristic for randomly substituted compounds as the NMR signals are made from the frequencies of all the compounds composing the mixture. An incomplete fluorescent tagging of the starting single-isomer β-CD (and/or inadequate purification), as well as aggregation of the compound, can cause broadening of the peaks [23].

In the proton spectrum in Figure 4, the good resolution in the anomeric region can be appreciated; several doublets can be clearly identified (see Supporting Information File 1, Figure S4). The separation of the anomeric doublets is a fundamental requisite for the complete assignment of an asymmetric molecule [24]. The core of the CD region between 2.5–5.5 ppm (Figure 4) is rather crowded and cannot be elucidated without the use of 2D techniques. On the other hand, the two signals in the aliphatic region can be easily assigned to the alkyl side chains of the rhodamine. Another important set of information that can be deduced/extrapolated from the careful analysis of the spectrum in Figure 4 concerns the asymmetry of the molecule. The proton spectrum of the rhodamine B both in lactone (Supporting Information File 1, Figure S5) and HCl form (Supporting Information File 1, Figure S6) shows only one kind of signal for the alkyl groups (CH_3 and CH_2 in Supporting Information File 1, Figures S5 and S6) and for the aromatic protons of the xanthene moiety (protons E, F, G in Supporting Information File 1, Figures S5 and S6). This means that the differentiation in multiple NMR signals in the Rho-β-CD conjugate is strictly related to the presence of the CD scaffold. Because of the chirality of the cyclodextrin part, the two phenyl rings of the xanthene moiety are formally diastereotopic, and consequently, anisochronous even without any complexation. This fact can be proven by recording the ^{1}H NMR spectrum of the Rho-β-CD in deuterated DMSO, a solvent known to dissociate inclusion complexes (Supporting Information File 1, Figure S7). The presence of two kinds of signals for the methyl units (at 1.06 ppm and 1.14 ppm) in the spectrum recorded in deuterated DMSO confirms the aforementioned observation.

The analysis of the DEPT-ed-HSQC spectrum (see Supporting Information File 1, Figure S8 for the full spectrum) gives further information on the product. The compound is unambiguously substituted on the primary side.

The frequencies at around 40 ppm ($C6_{sub}$ in Figure 5) correspond to the methylene moiety of the glucose unit that bears the fluorophore. The two frequencies have similar carbon signals, but different protons since the two protons of the methylene unit

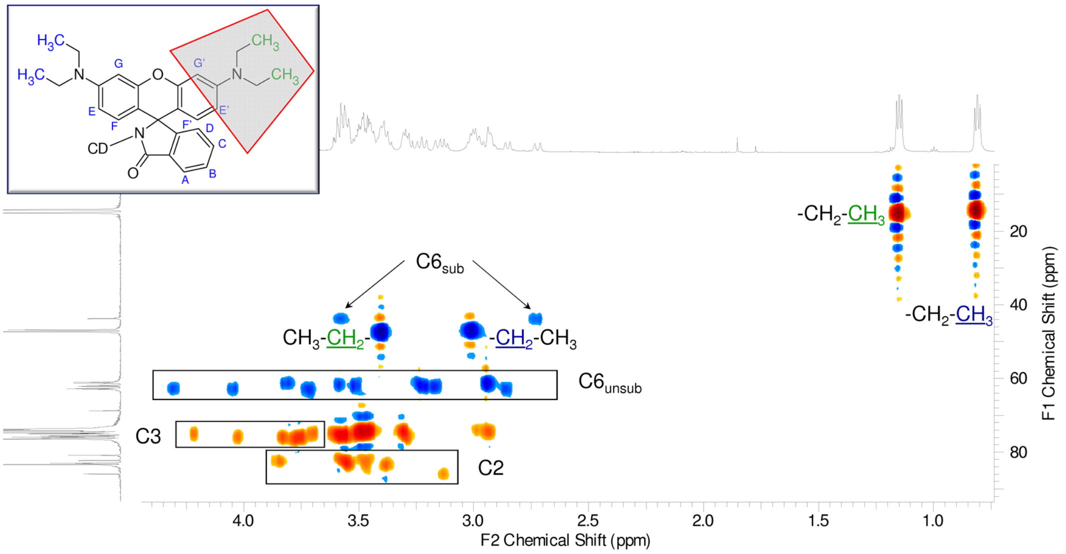

Figure 5: Expansion of DEPT-ed-HSQC spectrum of Rho-β-CD with partial assignments (D_2O, 500 MHz, 298 K).

are not magnetically equivalent ($C6_{sub}$ in Figure 5). The signals of the anomeric region (Supporting Information File 1, Figure S8) are very diffuse as those of the CD core. It is also possible to distinguish the two signals of the methylene units of the side chains of the rhodamine (around 47 ppm) from the unsubstituted methylene moiety of the glucose units ($C6_{unsub}$ in Figure 5). The assignment of the frequencies of the alkyl chains of the fluorophore is based on the 2D total correlation spectroscopy (TOCSY) spectrum (Supporting Information File 1, Figure S9), while the partial assignments of the C2 and C3 units (Figure 5) are based on a combination of correlation spectroscopy (COSY) (Supporting Information File 1, Figure S2), DEPT-ed-HSQC (Supporting Information File 1, Figure S8) and TOCSY (Supporting Information File 1, Figure S9).

In the aromatic region of the DEPT-ed-HSQC spectrum (see Supporting Information File 1, Figure S3) of Rho-β-CD, all ten of the aromatic protons of the fluorophore can be clearly distinguished.

The carbon spectrum shows very sharp peaks (Supporting Information File 1, Figure S10). The presence of a single carbon signal (around 172 ppm) in the region of the carboxylic amide unambiguously proves the effectivity of the coupling as well as the purity of the compound.

The cross-linked analysis of the 2D rotating frame nuclear Overhauser effect spectroscopy (ROESY) spectrum (Supporting Information File 1, Figures S11, S12 and S13) and the DEPT-ed-HSQC spectrum (Supporting Information File 1, Figure S14) generates a set of information useful for the determination of the spatial position of the fluorophore with respect to the CD scaffolds and for the analysis of the preferred conformation assumed by Rho-β-CD in solution. These data, together with the results presented by Wang et al. [25] about the crystal structure of rhodamine B in lactone form, allowed us to propose the model shown in Figure 6 for the intermolecular inclusion mode of Rho-β-CD. This model for the supramolecular assembly is also in agreement with previous data about the inclusion complexation of organic dyes with β-CD dimers [26].

In more detail, the analysis of the 2D ROESY spectrum reveals that the methyl units of the rhodamine side chains that resonate at 0.81 ppm (the side chains that are "uncomplexed") show cross peaks to 3.02 ppm (Supporting Information File 1, Figure S12), 5.63 ppm and 6.02 ppm (Supporting Information File 1, Figure S13). These three cross peaks are the result of intramolecular interactions between the methyl units and the adjacent methylene units of the rhodamine side chains (3.02 ppm) and between the methyl units and the protons G (5.63 ppm) and E (6.02 ppm) of the xanthene units (Supporting Information File 1, Figure S3), respectively. The two additional cross peaks at 7.91 and 6.74 ppm are the result of the spatial interactions of the methyl units with the protons A and D of the aromatic ring adjacent to the spirolactam unit (Supporting Information File 1, Figure S3). Assuming that the spirolactam is positioned perpendicular to the plane described by the xanthene unit (as reported in [25]), then the aforementioned, two additional cross peaks are the result of intermolecular interactions (see models in Figure 6).

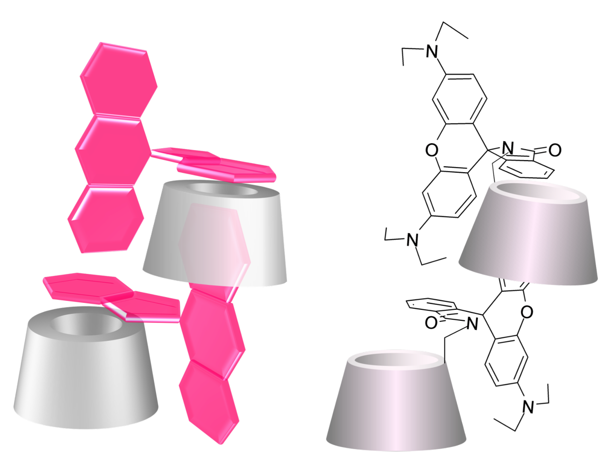

Figure 6: Cartoon models for the possible intermolecular inclusion mode of Rho-β-CD in solution (3D perspective view on the left and 3D structural model on the right).

The methyl signals at 1.15 ppm (the side chains that are "complexed") show several cross peaks indicating the diffused spatial interactions between the side chains of the fluorophore and the lower part of the cavity (carbons 3) of the CD scaffold (cross peaks at 3.57, 3.77, 3.83, 4.03 ppm in Supporting Information File 1, Figure S12). The same methyl moieties also interact with the protons G' and E' (cross peaks at 6.24 ppm in Supporting Information File 1, Figure S12 and cross peak at 6.27 ppm in Supporting Information File 1, Figure S13) of the xanthene units (Supporting Information File 1, Figure S13). The first set of cross peaks (at 3.57, 3.77, 3.83, 4.03 ppm) must be the result of intermolecular interactions between fluorophore units and a close CD scaffold since the xanthene moieties show exclusively cross peaks with the lower part of CD cavity. If a self-inclusion scenario would occur then one would expect a set of cross peaks between the xanthene moiety, the primary side of the CD (carbons 6) and the upper part of the cavity of the CD (carbons 5); however, this was not detected in our case. The second set of cross peaks (at 6.24 and 6.27 ppm in Supporting Information File 1, Figures S12 and S13, respectively) is the result of intramolecular forces due to the spatial proximity of the methyl units to the adjacent aromatic ring of the xanthene unit.

It is also worth noting that the protons A and D of the aromatic ring adjacent to the spirolactam unit (Supporting Information File 1, Figure S3) at 7.91 and 6.74 ppm show cross peaks at 3.23 and 3.20 ppm (Supporting Information File 1, Figure S13), respectively. These two frequencies correspond to the protons of unsubstituted methylene groups of the CD unit (Figure 5 and Supporting Information File 1, Figure S14). These intramolecular cross peaks are possible only if the plane of the aromatic ring adjacent to the spirolactam ring is set parallel to the primary rim of the CD.

Finally, the aromatic protons that resonate at 6.19, 6.24, and 6.27 ppm (protons F', G', E' in Supporting Information File 1, Figure S3) show cross peaks at 3.3, 3.46, 3.77, 4.03 and 4.23 ppm as reported in Supporting Information File 1, Figures S12 and S13. These last frequencies correspond to some of the protons of the lower part of a CD cavity (carbons 3), suggesting an intermolecular, partial complexation of the xanthene moiety into a close CD cavity.

To summarize, the compound Rho-β-CD was obtained in high purity and was thoroughly investigated by NMR spectroscopy. The collected data unambiguously proved that the compound is monosubstituted on the primary side. Morover, the analysis of the NMR spectra revealed that the fluorophore is partially complexed. The additional data obtained by the analysis of the ROESY spectrum resulted in the proposed model (Figure 6) for the intermolecular inclusion mode of the compound.

IR and UV–vis characterization of Rho-β-CD

In Supporting Information File 1, Figure S15 the IR spectra of Rho-β-CD, rhodamine B in acidic form (Rho·HCl) and rhodamine B in lactone form (Rho-B lactone) are shown. The analysis of the spectra unambiguously proved that the fluorophore in Rho-β-CD is in lactam form. The frequency at 1755.9 cm^{-1} in the IR spectrum of Rho-B lactone belongs to the carbonyl stretching of the γ-lactone moiety of the dye and this value is very similar to that found in the carbonyl region of the IR spectrum of Rho-β-CD at 1755.4 cm^{-1}. This last frequency is typical for the carbonyl stretching of a γ-lactam ring [27], thus demonstrating that the fluorophore in Rho-β-CD is (if isolated according to the procedure reported in the Experimental section) in a nonfluorescent cyclic form.

The same conclusion can be also reached through the analysis of the UV–vis spectra (Supporting Information File 1, Figure S16). The UV–vis spectra of Rho-β-CD vary according to the pH of the solution in a different manner compared to the free rhodamine B. The free fluorophore shows a strong absorbance at around 550 nm and maintains its fluorescence at any of the examined pH (see Experimental section for details). In the case of Rho-β-CD, this absorption maximum undergoes a hypochromic shift at alkaline and neutral pH, and under these conditions, the compound is not fluorescent. For the xanthene-appended derivative, the UV maximum at around 550 nm only appears at pH 3 (the absorbance increases with time) and under these solution conditions, Rho-β-CD is a fluorescent compound. The phenomenon can be easily explained on the basis of the change of conformation of the fluorophore according to the pH. The opening of the lactam ring is catalyzed by acidic conditions, thus switching the equilibrium of the prototropic forms of the dye towards the fluorescent amide form [28].

Fluorescein-appended β-CD

Fluorescein disodium salt (Flu-Na) was purchased in high purity allowing the formation of the product, but with moderate yield. For this reaction, several fluorescein-related byproducts could be detected by TLC (Supporting Information File 1, Figure S17) and the starting NH_2-β-CD·HCl could be only partially converted to Flu-β-CD (20–30% conversion based on TLC). Although different attempts were made in order to enhance the conversion (such as tuning the pH of the reaction, using NH_2-β-CD as free base as starting material, replacing the base NMM with NaOH and reacting the lactone form of the fluorophore instead of the sodium salt), the improvements were not substantial. The reason for the partial conversion under the selected alkaline conditions can be related to the appearance of several dye-related byproducts (ByP_1-, ByP_2-, ByP_3-Flu in TLC in Supporting Information File 1, Figure S17). Under the selected aqueous alkaline conditions, the phenol moiety of the fluorescein is mainly deprotonated and as phenolate can participate in the formation of fluorescein-based acyl derivatives (such as esters or anhydride, see Supporting Information File 1, Figure S17). The formation of these byproducts could lead to depletion of the coupling agent by conversion to 2-hydroxy-4,6-dimethoxy-1,3,5-triazine (DMM-OH) and could explaining the moderate conversion of the starting material. It is worth emphasizing that the coupling of fluorescein based on DCC/HOBt in organic solvents (as described in [14] for example) generates even more complicated mixtures. As shown in the TLC in Supporting Information File 1, Figure S14, an additional, nonfluorescent, unidentified, CD-related byproduct (ByP_1-CD) can be clearly detected in the crude and the amount of this byproduct is rather significant. As a consequence, the aqueous method based on DMT-MM is more favorable in terms of the amount of the product in the crude mixture and in terms of the purification of the crude composition.

The removal of the unreacted dye as well as the dye-related byproducts can be achieved by selective precipitation/filtration with acetone. Flash chromatography using a 10:5:1 (v/v/v) $CH_3CN/H_2O/NH_4OH$ (25%) ratio as eluent permits the removal of the unreacted NH_2-CD-related impurities. At this stage the compound, Flu-β-CD, has been extensively characterized by spectroscopic techniques.

UV–vis characterization of Flu-β-CD

In Supporting Information File 1, Figure S18, the UV–vis spectra of fluorescein disodium salt and of Flu-β-CD are shown. Under acidic conditions (at pH 3), the UV–vis spectrum and the fluorescence of the free dye changes remarkably. In particular, the UV band at around 490 nm is almost completely suppressed and the fluorescence, under irradiation at 366 nm, decreases substantially. This behavior is in agreement with the formation of the nonfluorescent lactone form under acidic conditions [12]. The lactone formation is mainly responsible for the fluorescence quenching of the dye. The UV–vis spectra of Flu-β-CD resemble those of fluorescein, and the fluorescence of the compound is heavily quenched at pH 3. By taking into consideration all these data, one can assume that the fluorescein moiety of Flu-β-CD exists mainly in the open amide form (at neutral and alkaline pH) and that the compound acts as a complementary molecular switch to Rho-β-CD. While Rho-β-CD exhibits fluorescence at acidic pH, Flu-β-CD shows fluorescence at both neutral and alkaline pH.

NMR characterization of Flu-β-CD

The ^{1}H NMR spectrum shown in Figure 7 is a typical spectrum of an asymmetric cyclodextrin. The sharp and well-resolved signal suggests the high purity of the compound.

The two constituent parts of the molecule can be easily recognized in Figure 7. The signals in the aromatic region (between 6.0–8.0 ppm) belong to the fluorescein moiety, while the set of signals between 2.2–5.5 ppm belongs to the CD. The integration of the signals corresponds to the theoretical values for a monosubstituted, fluorescein-β-CD derivative, as also confirmed by the value of the pseudo-molecular ion found during the ESIMS analysis (see Experimental section).

The signals in the aromatic regions are well resolved (Supporting Information File 1, Figure S19) and the analysis of H–H *J*

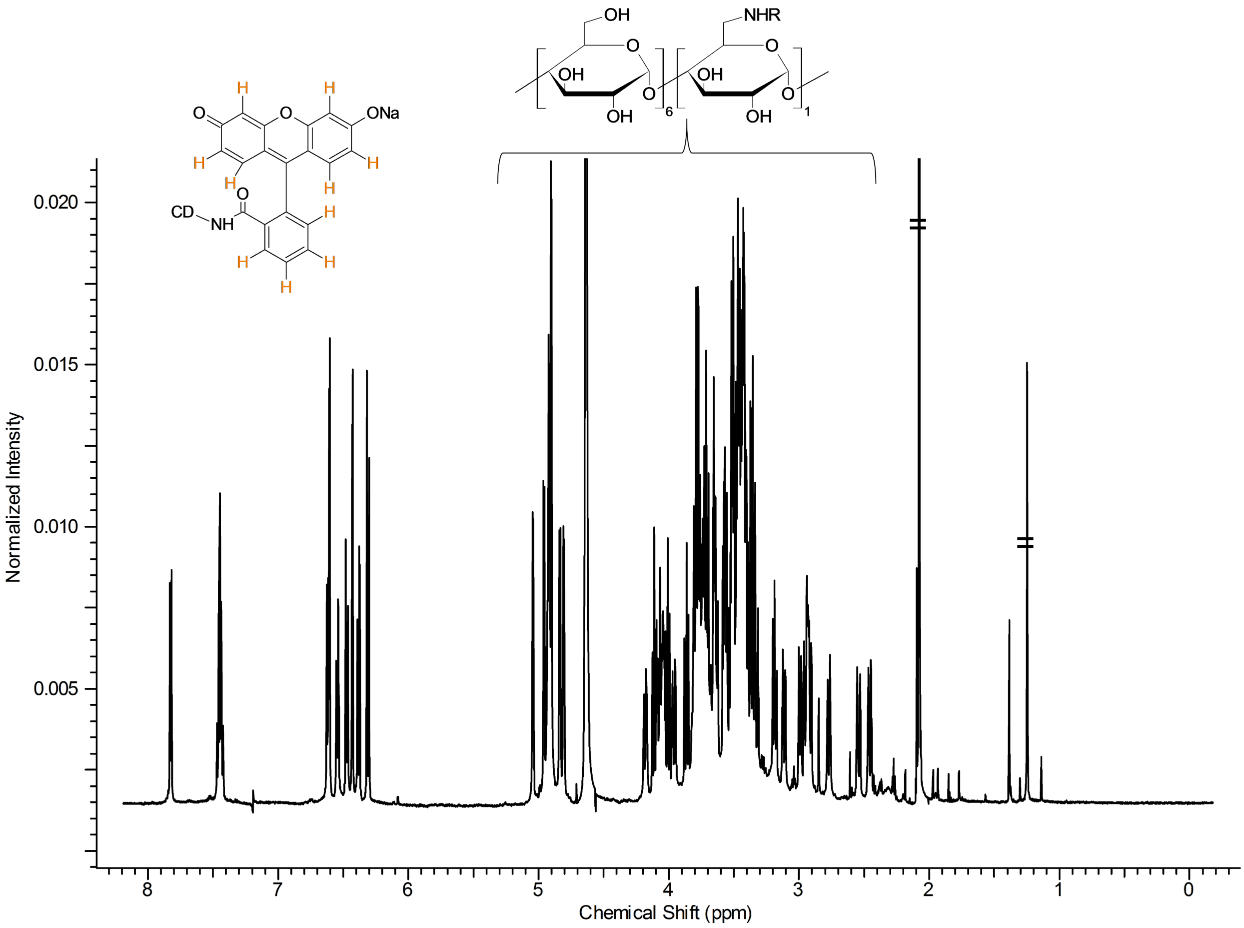

Figure 7: ^{1}H NMR spectrum of Flu-β-CD with partial assignments (D_2O, 500 MHz, 298 K).

coupling and the cross-linking with the data obtained by the COSY and DEPT-ed HSQC spectra (Supporting Information File 1, Figures S21, S22 and Supporting Information File 1, Figure S24, respectively) allowed for a complete assignment of the resonance frequencies. It is worth noting that all ten of the aromatic protons of the fluorophore can be identified both in DEPT-ed-HSQC and ^{1}H NMR spectra. The possibility to resolve all the aromatic protons of the dye in the ^{1}H NMR spectrum (Supporting Information File 1, Figure S19) is related to the asymmetry of Flu-β-CD. In the case of the free fluorescein sodium salt, the resolution of the proton couples H7/H8, H6/H9, H5/H10 is not possible without the addition of a resolving agent (Supporting Information File 1, Figure S20).

In the 6.0–8.0 ppm region of the ^{1}H NMR spectrum of Flu-β-CD (Supporting Information File 1, Figure S19), two different kinds of aromatic coupling can be detected. The different values of the $^3J_{\text{H-H}}$ and $^4J_{\text{H-H}}$ couplings permit the unambiguous assignment of the coupled protons H5/H7 and H8/H10. In the proton spectrum in Figure 7, the good resolution of the anomeric region can be also appreciated; several doublets can be clearly identified. The core of the CD region between 2.2–5.5 ppm (Figure 7) is rather crowded and cannot be easily elucidated without the use of 2D techniques.

The analysis of the DEPT-ed-HSQC spectrum (Supporting Information File 1, Figure S23 for the full spectrum) gives further information on the product. The compound is unambiguously substituted on the primary side.

The frequencies at around 44 ppm ($C6_{\text{sub}}$ in Supporting Information File 1, Figure S25) belong to the methylene moiety of the glucose unit that bears the fluorophore. The two frequencies have similar carbon signals, but different protons since the two protons of the methylene unit are not magnetically equivalent ($C6_{\text{sub}}$ in Supporting Information File 1, Figure S25). Further convincing proof that the compound is exclusively substituted on the primary side arises from the analysis of the HMBC spectrum of the compound (Supporting Information File 1, Figure S27). In the 2D spectrum shown in Supporting Information File 1, Figure S27, the cross peak between the carbon of the carboxamide at around 174 ppm and the proton of the methylene moiety of the glucose unit that bears the fluorophore ($C6_{\text{sub}}$) at 2.92 ppm unambiguously confirms the structure of the compound.

The signals of the CD core and the partial assignments of the C2, C3 and C4 (Supporting Information File 1, Figure S25) are based on a combination of COSY (Supporting Information File 1, Figures S21, S22), DEPT-ed-HSQC (Supporting Information File 1, Figure S23), HMBC (Supporting Information File 1, Figures S28, S29) and TOCSY (Supporting Information File 1, Figure S26) spectra.

The carbon spectrum shows sharp resonances (Supporting Information File 1, Figure S30). The presence of a single carbon signal (around 174 ppm) in the region of the carboxylic amide proves the effectivity of the coupling and the purity of the compound as well.

The cross-linked analysis of the 2D ROESY spectrum (Supporting Information File 1, Figures S31, S32, S33) and the DEPT-ed-HSQC spectrum (Supporting Information File 1, Figures S24, S25, S34, S35 and S36) generate a set of information useful for the determination of the spatial position of the fluorophore with respect to the CD scaffolds and for the analysis of the preferred conformation assumed by the Flu-β-CD in solution. These data altogether allowed us to propose the model shown in Figure 8 for the intermolecular inclusion mode of Flu-β-CD.

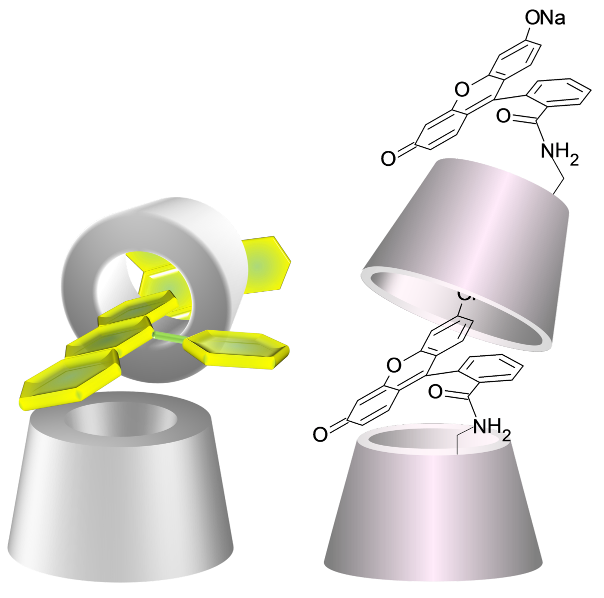

Figure 8: Cartoon models for the possible intermolecular inclusion mode of Flu-β-CD in solution (3D perspective view on the left and 3D structural model on the right).

In more detail, the analysis of the 2D ROESY spectrum reveals that the aromatic proton at 6.63 ppm (H4 in Supporting Information File 1, Figure S24) shows cross peaks at 3.38 ppm (Supporting Information File 1, Figure S32). This frequency corresponds to a proton of an unsubstituted methylene unit on the primary side of the CD (Supporting Information File 1, Figure S34). Since protons H1, H2 and H3 (Supporting Information File 1, Figure S24) do not show cross peaks with frequencies of the CD unit, it seems reasonable to assume that while H4 is located in proximity of the primary rim, the remaining protons of the aromatic ring are positioned externally to the primary rim and far enough not to interact with the protons of the methylene units (Figure 8).

The aromatic protons at 6.61 and 6.55 ppm (H7 and H6, respectively, in Supporting Information File 1, Figure S24) show several cross peaks as a consequence of the diffuse interaction with a CD cavity. In particular, H7 shows cross peaks at 4.08, 4.01 and 2.94 ppm, and H6 at 3.86, 3.79, 3.46 and 2.98 ppm (Supporting Information File 1, Figures S32, S33). The first set of these frequencies corresponds to different C3 (Supporting Information File 1, Figures S25, S34, S35, S36) while the second one (with the only exception at 3.36 ppm that cannot be unambiguously assigned) corresponds to protons located inside the cavity (mostly C3). These findings prove that the aromatic protons H7 and H6 interact extensively with the lower part of a CD cavity.

The aromatic proton at 6.48 ppm (H5 in Supporting Information File 1, Figure S24) shows cross peaks at 3.46, 3.35 and 2.98 ppm (Supporting Information File 1, Figures S32, S33); these frequencies correspond to protons located inside the cavity of a CD ring (Supporting Information File 1, Figures S34, S35, S36). As a consequence, the ring of the xanthene moiety that includes H5/H6/H7 interacts with the lower part of a CD cavity. Since the fluorophore is connected through the primary side of the CD, it is reasonable to assume that this set of interactions is the result of an intermolecular partial complexation between the fluorophore of a specific molecule and the lower part of the cavity of a second CD unit.

The last set of cross peaks in the aromatic region of the ROESY spectra in Supporting Information File 1, Figures S32, S33 is the result of the interactions between the aromatic proton at 6.44 ppm (H8 in Supporting Information File 1, Figure S24) and the frequencies at 4.17, 4.05, 3.65 and 3.32 ppm (Supporting Information File 1, Figures S32, S33). These frequencies correspond to protons of unsubstituted methylene units on the primary side of a CD (Supporting Information File 1, Figures S34, S35, S36). Since protons H9 and H10 (Supporting Information File 1, Figure S24) do not show cross peaks with any frequencies of the CD units, one can conclude that the xanthene moiety of the fluorophore is not placed in a parallel way to the primary rim of the CD. The plane of the xanthene moiety of the fluorophore should be twisted above the primary side of the CD in a way that H8 would be the only point of (intramolecular) interaction with the upper rim of the CD cavity.

To summarize, the compound Flu-β-CD was obtained in high purity and was thoroughly investigated by NMR spectroscopy. The collected data unambiguously proved that the compound is monosubstituted on the primary side. The analysis of the NMR spectra revealed as well that the fluorophore is partially complexed. The additional data obtained by the analysis of the ROESY spectrum resulted in the proposed model (shown in Figure 8) for the intermolecular inclusion mode of the compound.

Conclusion

A novel green synthetic strategy for obtaining single isomer, xanthene-appended cyclodextrin was developed. The synthetic approach is based on commercially available fluorescent dyes and coupling agents, thus having clear potential for multigram scale-up. The mild, aqueous conditions, as well as the simplicity of the synthesis, make these reactions attractive tools for the preparation of fluorescent cyclodextrins connected through an amide bond.

The obtained products were isolated in high purity and extensively characterized by spectroscopic techniques. The in-depth analysis of the collected sets of NMR data resulted in the proposed models for the supramolecular interactions shown by the compounds.

The isolated molecules can be applied in the fields of chemosensing and bioimaging, while the mechanism behind the formation of the versatile, supramolecular assemblies deserves further investigation.

Supporting Information

Supporting Information File 1

Experimental section, including IR and NMR spectra of the synthesized compounds.
[http://www.beilstein-journals.org/bjoc/content/supplementary/1860-5397-12-53-S1.pdf]

Acknowledgement

The support of the Marie Curie Programme Initial Training Network, Project No 608407 (CyclonHit) and OTKA PD 109373 are greatly acknowledged.

References

1. Hamada, F.; Kondo, Y.; Ishikawa, K.; Ito, H.; Suzuki, I.; Osa, T.; Ueno, A. *J. Inclusion Phenom. Mol. Recognit. Chem.* **1994,** *17,* 267–275. doi:10.1007/BF00708786
2. Zhao, Y.-L.; Stoddart, J. F. *Acc. Chem. Res.* **2009,** *42,* 1161–1171. doi:10.1021/ar900056z
3. Plazzo, A. P.; Höfer, C. T.; Jicsinszky, L.; Fenyvesi, É.; Szente, L.; Schiller, J.; Herrmann, A.; Müller, P. *Chem. Phys. Lipids* **2012,** *165,* 505–511. doi:10.1016/j.chemphyslip.2012.03.007

4. Chen, X.; Pradhan, T.; Wang, F.; Kim, J. S.; Yoon, J. *Chem. Rev.* **2012,** *112,* 1910–1956. doi:10.1021/cr200201z
5. Zheng, H.; Zhan, X.-Q.; Bian, Q.-N.; Zhang, X.-J. *Chem. Commun.* **2013,** *49,* 429–447. doi:10.1039/C2CC35997A
6. Kushida, Y.; Nagano, T.; Hanaoka, K. *Analyst* **2015,** *140,* 685–695. doi:10.1039/C4AN01172D
7. Yang, Y.; Escobedo, J. O.; Wong, A.; Schowalter, C. M.; Touchy, M. C.; Jiao, L.; Crowe, W. E.; Fronczek, F. R.; Strongin, R. M. *J. Org. Chem.* **2005,** *70,* 6907–6912. doi:10.1021/jo051002a
8. Beija, M.; Afonso, C. A. M.; Martinho, J. M. G. *Chem. Soc. Rev.* **2009,** *38,* 2410–2433. doi:10.1039/b901612k
9. Kunishima, M.; Kawachi, C.; Monta, J.; Terao, K.; Iwasaki, F.; Tani, S. *Tetrahedron* **1999,** *55,* 13159–13170. doi:10.1016/S0040-4020(99)00809-1
10. Hattori, K. Cyclodextrin compound modified with folic acid, process for production thereof, drug delivery agent for targeting drug delivery system, pharmaceutical composition, and imaging agent. U.S. Patent 8,222,400 B2, July 17, 2012.
11. Wang, Y.; Ikeda, T.; Ueno, A.; Toda, F. *Tetrahedron Lett.* **1993,** *34,* 4971–4974. doi:10.1016/S0040-4039(00)74060-3
12. Bogdanova, L. N.; Mchedlov-Petrossyan, N. O.; Vodolazkaya, N. A.; Lebed, A. V. *Carbohydr. Res.* **2010,** *345,* 1882–1890. doi:10.1016/j.carres.2010.07.002
13. Hamada, F.; Ishikawa, K.; Higuchi, Y.; Akagami, Y.; Ueno, A. *J. Inclusion Phenom. Mol. Recognit. Chem.* **1996,** *25,* 283–294. doi:10.1007/BF01044998
14. Nishimura, D.; Takashima, Y.; Aoki, H.; Takahashi, T.; Yamaguchi, H.; Ito, S.; Harada, A. *Angew. Chem.* **2008,** *120,* 6166–6168. doi:10.1002/ange.200801431
Angew. Chem., Int. Ed. **2008,** *47,* 6077–6079. doi:10.1002/anie.200801431
15. Hasegawa, T.; Kondo, Y.; Koizumi, Y.; Sugiyama, T.; Takeda, A.; Ito, S.; Hamada, F. *Bioorg. Med. Chem.* **2009,** *17,* 6015–6019. doi:10.1016/j.bmc.2009.06.046
16. Fang, G.; Xu, M.; Zeng, F.; Wu, S. *Langmuir* **2010,** *26,* 17764–17771. doi:10.1021/la103368z
17. Mourtzis, N.; Paravatou, M.; Mavridis, I. M.; Roberts, M. L.; Yannakopoulou, K. *Chem. – Eur. J.* **2008,** *14,* 4188–4200. doi:10.1002/chem.200701650
18. Malanga, M.; Bálint, M.; Puskás, I.; Tuza, K.; Sohajda, T.; Jicsinszky, L.; Szente, L.; Fenyvesi, É. *Beilstein J. Org. Chem.* **2014,** *10,* 3007–3018. doi:10.3762/bjoc.10.319
19. Kamiński, Z. J. *Tetrahedron Lett.* **1985,** *26,* 2901–2904. doi:10.1016/S0040-4039(00)98867-1
20. Ramette, R. W.; Sandell, E. B. *J. Am. Chem. Soc.* **1956,** *78,* 4872–4878. doi:10.1021/ja01600a017
21. Bakkialakshmi, S.; Menaka, T. *Int. J. ChemTech Res.* **2012,** *4,* 223–231.
22. Ramos, S. S.; Vilhena, A. F.; Santos, L.; Almeida, P. *Magn. Reson. Chem.* **2000,** *38,* 475–478. doi:10.1002/1097-458X(200006)38:6<475::AID-MRC662>3.0.CO;2-X
23. Jacobsen, N. E. NMR Hardware and Software, Sample Preparation. *NMR Spectroscopy Explained;* John Wiley & Sons, Inc.: Hoboken, 2007.
24. Eliadou, K.; Giastas, P.; Yannakopoulou, K.; Mavridis, I. M. *J. Org. Chem.* **2003,** *68,* 8550–8557. doi:10.1021/jo034503+
25. Wang, X.; Song, M.; Long, Y. *J. Solid State Chem.* **2001,** *156,* 325–330. doi:10.1006/jssc.2000.9002
26. Zhao, Y.; Yang, Y. C.; Shi, H.; Zhu, H. Y.; Huang, R.; Chi, C. M.; Zhao, Y. *Helv. Chim. Acta* **2010,** *93,* 1136–1148. doi:10.1002/hlca.200900345
27. Infrared spectroscopy absorption table – OchemOnline. http://www.ochemonline.com/Infrared_spectroscopy_absorption_table (accessed Nov 1, 2015).
28. Mchedlov-Petrosyan, N. O.; Fedorov, L. A.; Sokolovskii, S. A.; Surov, Y. N.; Salinas Maiorga, R. *Russ. Chem. Bull.* **1992,** *41,* 403–409. doi:10.1007/BF00863052

License and Terms

The definitive version of this article is the electronic one which can be found at:
doi:10.3762/bjoc.12.53

BEILSTEIN JOURNAL OF ORGANIC CHEMISTRY

Interactions between 4-thiothymidine and water-soluble cyclodextrins: Evidence for supramolecular structures in aqueous solutions

Vito Rizzi[1], Sergio Matera[1], Paola Semeraro[1], Paola Fini[2] and Pinalysa Cosma[*1,2,§]

Full Research Paper

Open Access

Address:
[1]Università degli Studi "Aldo Moro" di Bari, Dipartimento di Chimica Chimica, Via Orabona, 4, 70126 Bari, Italy and [2]Consiglio Nazionale delle Ricerche CNR-IPCF, UOS Bari, Via Orabona, 4, 70126 Bari, Italy

Email:
Pinalysa Cosma[*] - pinalysa.cosma@uniba.it

* Corresponding author
§ Tel. +39 0805443443

Keywords:
cyclodextrins; inclusion complex; photodynamic therapy

Beilstein J. Org. Chem. **2016,** *12,* 549–563.
doi:10.3762/bjoc.12.54

Received: 22 December 2015
Accepted: 04 March 2016
Published: 21 March 2016

This article is part of the Thematic Series "Superstructures with cyclodextrins: Chemistry and applications III".

Guest Editor: E. Monflier

Abstract

Since several years the inclusion of organic compounds (guests) within the hydrophobic cavity (host) of cyclodextrins (CDs) has been the subject of many investigations. Interestingly, the formation of inclusion complexes could affect the properties of the guest molecules and, for example, the influence of the delivery system can be a method to improve/change the photochemical behavior of the guest. In particular, very recent studies have shown the protective role of CDs preventing the degradation of the encapsulated guest. Starting from this consideration, in this work, only the structure and complexation mode of the inclusion complexes involving 4-thiothymidine (S^4TdR, a known photosensitizer) and five CDs, namely 2-hydroxypropyl-α-cyclodextrin (2-HP-α-CD), 2-hydroxypropyl-β-cyclodextrin (2-HP-β-CD), 2-hydroxypropyl-γ-cyclodextrin (2-HP-γ-CD), heptakis-(2,6-di-*O*-methyl)-β-cyclodextrin (DIMEB CD) and heptakis-(2,3,6-tri-*O*-methyl)-β-cyclodextrin (TRIMEB CD) were investigated by different spectroscopic techniques (UV–vis, FTIR–ATR, ^1H NMR) and cyclic voltammetry analysis (CV). This work is necessary for a prospective research on the photoreactivity of S^4TdR in aqueous environment and in the presence of CDs to prevent its degradation under irradiation. UV–vis, FTIR–ATR and CV measurements suggested the formation of supramolecular structures involving the employed CDs and mainly the pyrimidine ring of S^4TdR. ^1H NMR analyses confirmed such indication, unveiling the presence of inclusion complexes. The strongest and deepest interactions were suggested when TRIMEB and DIMEB CDs were studied. The S^4TdR affinity towards CDs was also evaluated by using the Benesi–Hildebrand (B–H) equation at 25 °C employing CV and ^1H NMR methods. The stoichiometry of the interaction was also inferred and it appears to be 1:1 for all examined CDs.

Introduction

Since several years, supramolecular chemistry has been considered the chemistry of the intermolecular bonds inducing the association of several chemical species with the formation of superstructures [1-3]. The Nobel laureate J. M. Lehn said that "supramolecular chemistry may be defined as chemistry beyond the molecule, bearing on the organized entities of higher complexity that result from the association of two or more chemical species held together by intermolecular forces. Its development requires the use of all resources of molecular chemistry combined with the designed manipulation of non-covalent interactions so as to form supramolecular entities, supermolecules possessing features as well defined as those of molecules themselves" [1].

Starting from this definition, it is worth mentioning that among different kinds of non-covalent interactions, the host–guest type is extensively discussed in literature covering a large field of applications [4]. For example, cyclodextrins (CDs), among host molecules, are reported to occupy an important place in the field of inclusion phenomena [5-7].

CDs are a family of cyclic oligosaccharides and different members of this family have been used widely for several years. More specifically, CDs are manufactured from starch, a polymer with D-glucopyranoside building blocks with both α-1,4- and α-1,6-glycosidic linkages [8]. The most common CDs are α-, β- and γ-CD, and the differences among them are related to the number of α-D-glucopyranose units. While α-CD, characterized by a small cavity size, is hardly used and γ-CD is expensive, β-CD is extensively used because its cavity size is able to allocate a large number of guest molecules [9]. In fact, in the formation of inclusion complexes [10-12] the inner diameter of the cavity of the CDs and the size of the guest molecule play an important role.

CDs are often described as a toroid having a large and narrow cavity. The wider side is formed by the secondary 2- and 3-hydroxy groups, and the narrower side is primarily formed by the primary 6-hydroxy group [13]. The cavity of the CDs is made of oxygen atoms of the glycosidic ring and hydrogen atoms that give the well-known hydrophobic character of the CDs. In addition, the presence of the mentioned free hydroxy groups on the outside of the CDs cavity results in the hydrophilic character of the molecules [6,7,14].

Different chemically modified CDs are known in literature, which are characterized by a higher water solubility compared with the native CDs. These CDs, i.e., 2-HP-CDs, are widely used [15]. An enhanced solubility, both in water and in organic solvents, was also attributed to DIMEB and TRIMEB CDs. Indeed, the formation of DIMEB CD and TRIMEB CD inclusion complexes are reported, for example, by Yu et al. [16] and Nishijo et al. [17], respectively, indicating that they have potential uses as carriers for different drugs for medical applications [18,19]. In fact, for pharmaceutical applications, the improvement of drug stability and solubility play a key role [19]. For example, CDs emerged in biological applications as suitable delivery systems for water-insoluble photosensitizers (PSs) for light-induced photodynamic therapy (PDT) applications [19]. Some authors of this paper have extensively studied the behavior of several PSs in the presence of CDs [19,20] highlighting the important role of the latter.

Interestingly, among PSs the use of thiobases has emerged as a novel approach for PDT applications in several clinical diseases [12,21]. One of the most commonly used thiobase for PDT applications is S^4TdR, whose triplet state is generated upon photoexcitation with a quantum yield of one [22-26]. Under these conditions the production of reactive oxygen species (ROS), well-known toxic agents against cancer cells, is observed [27,28]. However, one of the major drawbacks with PSs is that most of them decay under prolonged irradiation, which leads to the potentially incomplete destruction of cancer cells. Not surprisingly, Bekalé et al. [27,28] reported that when a PS is irradiated with light, ROS (namely singlet oxygen, superoxide ions and hydrogen peroxide), generated via the excited state of the PS, destroy the PS itself. Because of this, the effort to preserve the PS is one of main issues. Regarding S^4TdR, as a result of its photodynamic activity, the thiobase can be destroyed by a degradative ROS-mediated oxidation process [26].

Recently, in our papers [26], we have shown the pH-related features and the photoactivity of S^4TdR in aqueous solution while simultaneously elucidating the nature of products induced by light-stimulated oxidative stress. Evidence for the generation of thymidine (TdR) as the main product was obtained [26]. The use of a delivery system could be a method to improve the photochemical behavior and to prevent the degradation of the thiobase [27]. In fact, literature suggests that one method to avoid the drug degradation is the complexation with CDs, and, as described in [18], the preparation of simple physical mixtures with CDs was already shown to be effective in terms of protective activity. Starting from these considerations, the main goal of this work is to study the ability of the modified nucleoside S^4TdR to form inclusion complexes with five CDs: 2-HP-α-CD, 2-HP-β-CD, 2-HP-γ-CD, DIMEB and TRIMEB. This is a preliminary work in order to (i) study, in the next future, its photochemical behavior in the presence of CDs, and to (ii) preserve it from oxidative degradation when irradiated during PDT treatments.

In this work, absorption spectroscopic techniques such as, UV–visible absorption spectroscopy, FTIR–ATR and ^{1}H NMR with the help of electrochemical analysis were utilized in order to characterize the formation of inclusion complexes between S^{4}TdR and CDs. Among the used techniques, ^{1}H NMR spectroscopy gave the most direct evidence for the inclusion of S^{4}TdR inside the CD cavity [29,30]. In fact, the H3 and H5 atoms of CDs, which are directed towards the interior of the cavity of the CDs showed a significant upfield shift when strong inclusion interactions are present [31,32].

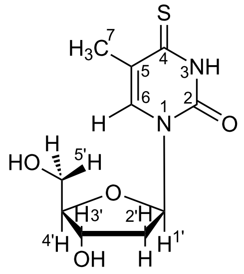

Figure 1: Molecular structure of S^{4}TdR. H atoms are also labeled in the Figure.

Results and Discussion

UV–vis absorption spectroscopy

At first glance, regardless of the structural similarity with thymidine, S^{4}TdR (Figure 1) shows a different ultraviolet absorption spectrum. The UV–vis absorption spectrum of 1×10^{-5} M aqueous solution of S^{4}TdR, was acquired and is reported in Figure 2 (black lines). Subsequently, a comparison in presence of CDs was performed in accordance with similar

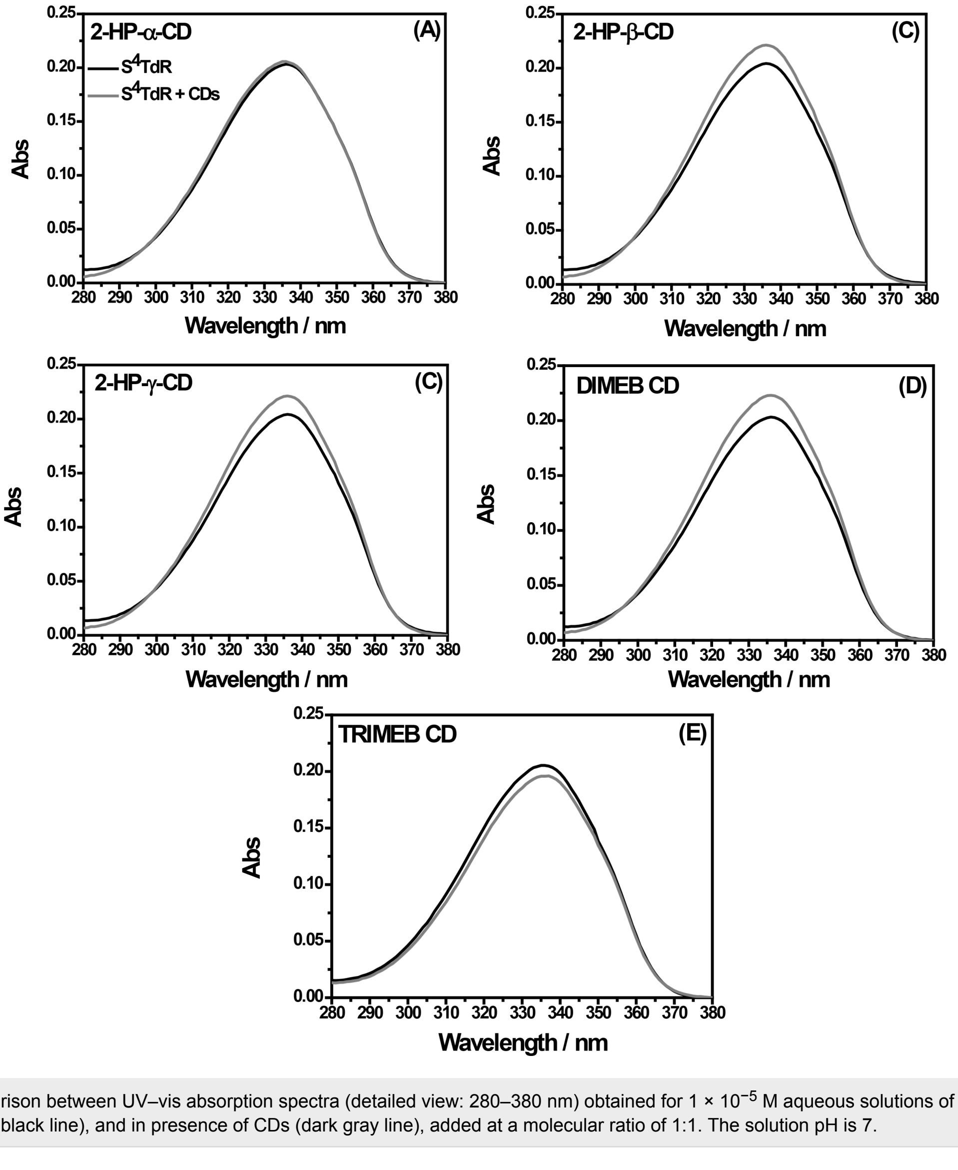

Figure 2: Comparison between UV–vis absorption spectra (detailed view: 280–380 nm) obtained for 1×10^{-5} M aqueous solutions of S^{4}TdR in absence of CDs (black line), and in presence of CDs (dark gray line), added at a molecular ratio of 1:1. The solution pH is 7.

works reported in literature [32,33] (see dark grey lines in Figure 2).

As reported in Figure 2 (black line), the main absorption band of S^4TdR shifts from 270 nm (already observed for thymidine) to 337 nm (UVA) [26,34]. The nature of this band was already carefully investigated by some authors of this paper elucidating the behavior of such a nucleoside in aqueous solution. The main form of the nucleoside, absorbing at 337 nm, is the protonated structure reported in Figure 1. The deprotonation, on the nitrogen atom in position 3, started only at pH values greater than 9, with a pK_a of ca. 9 as described in [26]. Under the latter conditions, the S^4TdR-main absorption band located at 337 nm in neutral medium shifted to 321 nm. Moreover, the high molar absorption coefficients (ε) evaluated in [26] suggested that the absorption band of S^4TdR was probably related to a π–π* transition into the second lowest excited singlet (S_2) state of the molecule. As a result, the delocalized electrons on the pyrimidine ring were supposed to be involved in a transition having a charge transfer character [26]. Taking this into account and with the prospect of an application in biological environments, this preliminary study, related to the possibility of inclusion complexes between S^4TdR and CDs, was carried out in neutral medium.

Interestingly, as reported in Figure 2, after the addition of CDs, at a molar ratio of 1:1, a significant hyperchromic effect on the main absorption band, located at 337 nm, was observed in the case of 2-HP-β-CD, 2-HP-γ-CD and DIMEB CD (Figure 2b–d). When the TRIMEB CD was used, a hypochromic shift was detected (Figure 2e). While studying 2-HP-α-CD in the presence of S^4TdR, no significant variations were observed (Figure 2a). In Table 1 the absorbance difference measured at 337 nm in presence and in absence of CDs are summarized.

Table 1: Absorbance variation of S^4TdR when CDs were added at a molar ratio of S^4TdR/CD = 1:1. ΔAbs_{337} was obtained reading the absorbance value, at 337 nm, of the solution containing S^4TdR in absence and in presence of CDs.

CD	ΔAbs_{337} ($A_{S4TdR} - A_{S4TdR/CD}$)
2-HP-α-CD	0
2-HP-β-CD	+0.02
2-HP-γ-CD	+0.02
DIMEB-CD	+0.03
TRIMEB-CD	−0.01

As explained in [31], this change of absorption can be attributed to host–guest type interactions, during which the guest changes its environment from an aqueous medium to the apolar CD cavity inducing the variations observed in the S^4TdR-absorption spectra. The UV–vis absorption results suggested that the interactions involve mainly the chromophore of S^4TdR. Besides, when the amount of CDs was further increased, for all examined CDs (with the exception of 2-HP-α-CD, in which not significant changes were measured), both hypochromic and hyperchromic effects of the main absorption band of S^4TdR were detected. Uekama et al. [35], hypothesized that these observed changes could be due to a perturbation of the electronic energy levels of the guest molecule. Additionally, the microenvironment of the guest changes through a re-organization of solvating water molecules. Undoubtedly, a combination of these two effects could be considered. At this point, since the obtained UV–vis results are not sufficiently clear to definitely prove the formation of S^4TdR/CDs inclusion complexes, in which the pyrimidine ring is involved, more details were searched through the use of cyclic voltammetry (CV), FTIR–ATR and ^{1}H NMR analysis.

Cyclic voltammetry analysis

As described in [33], the clear formation of inclusion complexes between S^4TdR and all employed CDs was investigated by means of electrochemical analyses. In fact, if the employed CDs interact with S^4TdR, different electrochemical properties would be expected, as described in [36]. The obtained results are reported in Figure 3.

When a S^4TdR solution is measured with cyclic voltammetry a well-defined irreversible cathodic peak, located at −1.39 V, appeared and was attributed to the reduction of the thiocarbonyl group, (C4=S) (Figure 3**,** solid black line). In particular, as reported in [37] about the electrochemical properties of some thiones, the redox process involving the thionucleoside could be attributable to an electron transfer process centered on the C=S moiety.

Interestingly, the addition of CDs in S^4TdR solutions resulted in remarkable modifications of the electrochemical signals of S^4TdR (Figure 3A–E). These changes depend significantly on the type of the added CD. The addition of 2-HP-CDs induced a slight negative shift of the cathodic peak potential of S^4TdR with a concomitant decrease of the current intensity (Figure 3A–C and Figure 4A–B).

After increasing the amount of added CDs, the current intensity (Figure 4B) and the cathodic peak potential (Figure 4A) were largely influenced, indicating as described in [33] that interactions between CDs and S^4TdR were well-established with the redox center of S^4TdR located inside the host cavity. The results also indicated, as reported in [38], that S^4TdR was reduced with more difficulty when it was engaged in the inclusion complexes.

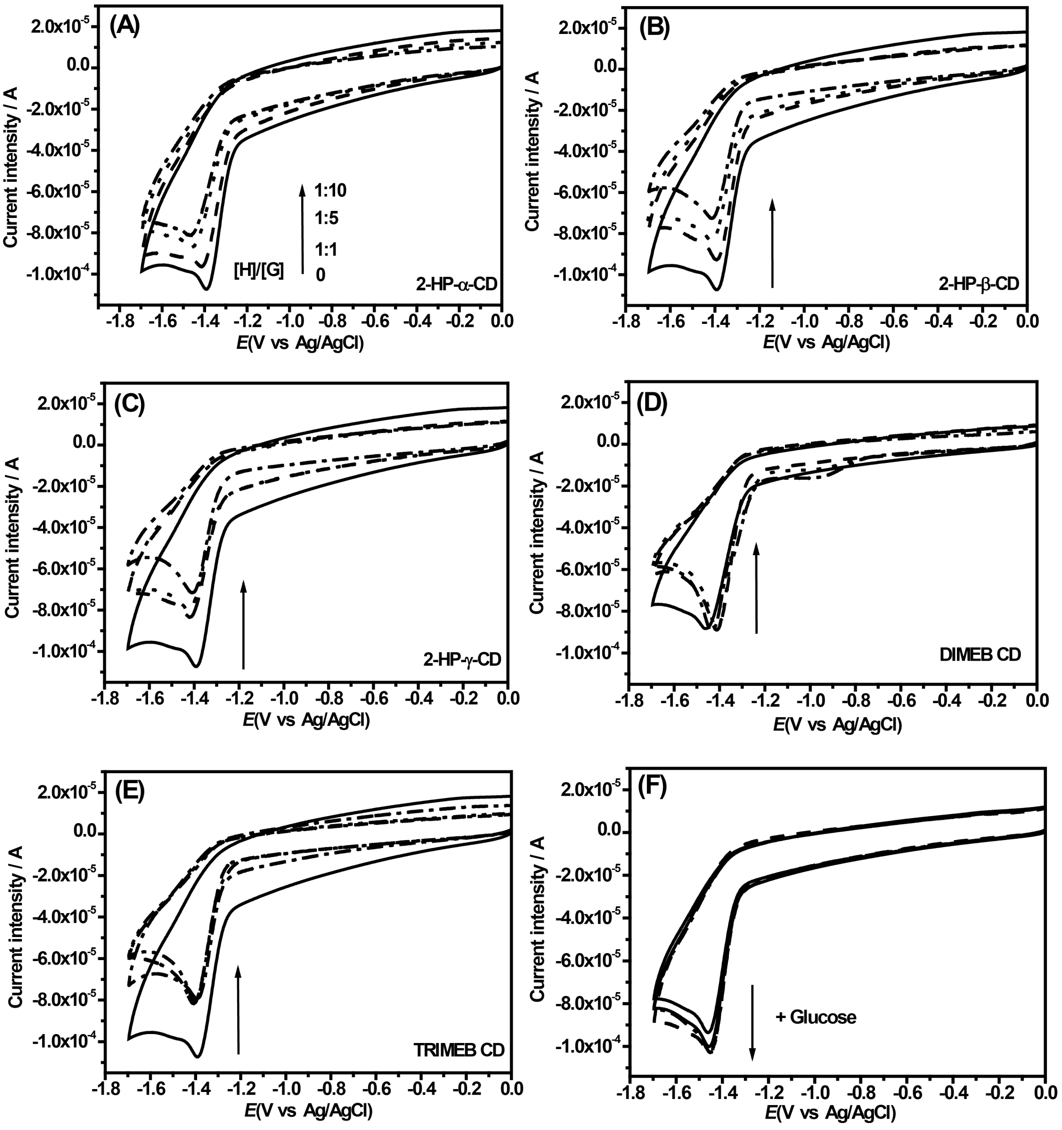

Figure 3: Cyclic voltammetry of aqueous solutions containing S^4TdR (black solid line) in presence of increasing amounts of CDs, i.e., at molar ratios S^4TdR/CDs of 1:1, 1:5, 1:10. Supporting electrolyte, $LiClO_4$ at 0.1 M. (A) S^4TdR/2-HP-α-CD, (B) S^4TdR/2-HP-β-CD, (C) S^4TdR/2-HP-γ-CD, (D) S^4TdR/DIMEB CD, (E) S^4TdR/TRIMEB CD inclusion complexes and (F) S^4TdR/glucose.

Sabapathy et al. [36] and Semeraro et al. [39] suggested that when host–guest type interactions are established, the diffusion of the inclusion complex from the bulk of the solution to the electrode surface is much slower than that of the guest itself leading at least to the observed current decrease (Figure 3 and Figure 4B) under our experimental conditions. As reported in [36], a decrease of the cathodic peak potential is reasonable because a higher activation energy would be expected under such conditions. As described in [39], this observed increased difficulty is due to the inclusion of the pyrimidine ring inside the cavity of the CDs hindering the interaction with the electrode and reducing the diffusion coefficient of the molecule. The results seem to confirm the variations observed during the UV–vis measurements, in which the pyrimidine ring appeared to be involved in the interactions with CDs.

It is worth mentioning that, as described in [40], our experimental data suggest the presence of a chemical/electrochemical process (CE-type mechanism) where the reduction process is limited by the dissociation step between CDs and S^4TdR. So, the electron transfer activation occurs after the dissociation of the electroactive guest from the CDs, because S^4TdR inside the CDs cannot undergo an electrochemical reaction. Then, as described in [40,41], the dissociation of the complex is the preliminary step before the electron transfer process. When inclusion complexes are studied, electron transfer processes are both ther-

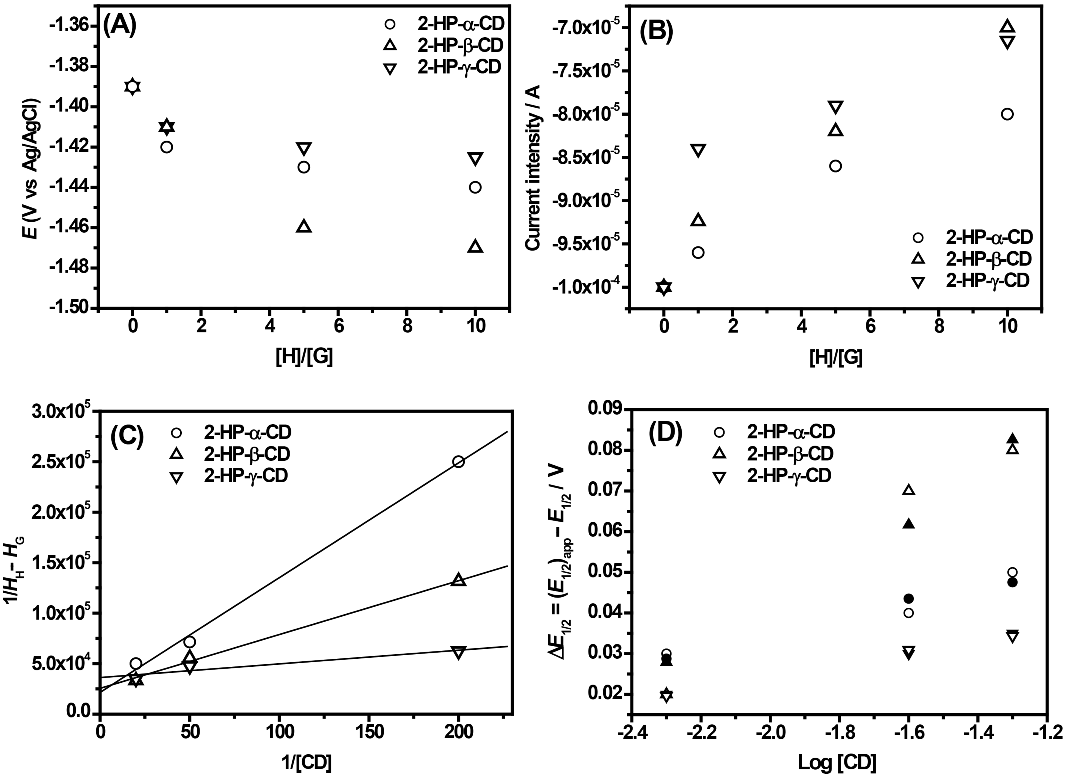

Figure 4: (A) Plot of cathodic potential values and (B) of the corresponding current intensity, obtained for S^{4}TdR in absence and presence of 2-HP-CDs, (C) Benesi–Hildebrand plot of $1/I_{HG} - I_G$ versus 1/[2-HP-CDs] in the presence of S^{4}TdR at the initial concentration of 5×10^{-3} M, (D) half-wave potential difference of S^{4}TdR in the presence of 2-HP-CD ($(E_{1/2})_{CD}$) and in the absence of 2-HP-CD ($E_{1/2}$) as a function of the total concentration of 2-HP-CD: Experimental values (empty symbols), calculated values (full symbols). Equation 2 (see Experimental part) has been used. The host/guest ratios are 1:1, 5:1 and 10:1.

modynamically and kinetically not favored, which in our case confirms the presence of stable inclusion complexes between S^{4}TdR and 2-HP-CDs.

When DIMEB and TRIMEB CDs were used a peculiar behavior was observed and the results are reported in Figure 3D,E. When DIMEB CD was added, the S^{4}TdR cathodic peak potential shifted slightly towards positive direction with the interesting result that any significant variation was observed furtherly increasing the amount of the CD. Accordingly, the cathodic current intensity was observed to be quite constant. A similar behavior is described in [39] and was explained as the formation of inclusion complexes in which the reduction of the involved groups in the inclusion complex need less activation energy. On the other hand, when TRIMEB CD was considered, while the cathodic peak potential can be considered constant, the current intensity decreases after the first CD addition then it remains constant (Figure 3E). This peculiar scenario, observed for DIMEB and TRIMEB CDs, is described in [2]. Authors explained this behavior with the formation of inclusion complexes with the redox center of the guest molecule located outside the cavity of CD. DIMEB CD and especially TRIMEB CD only offer their hydrophobic domains affecting the electron-transfer processes by changing the diffusion coefficient of the electroactive molecule by inclusion complex formation.

Experiments, in the presence of glucose, mimicking the external interaction between CDs and S^{4}TdR, were also performed with the same molar ratios of 1:1, 1:5 and 1:10 and are reported in Figure 3F. Under these conditions the cathodic peak of S^{4}TdR appeared unaffected by the addition of glucose, with the cathodic current intensity slightly amplified by external interactions. A contrary behavior than the one observed in the presence of CDs was thus observed, with an almost catalytic effect of glucose. It is noteworthy that the same experiments performed adding glucose at ratios S^{4}TdR/glucose of 1:1, 1:5, and 1:10 did not show any influence on the UV–vis spectra of S^{4}TdR aqueous solutions (data not shown).

In conclusion the synergic use of UV–vis measurements and CV analysis suggested the presence of inclusion complexes with all examined CDs in which S^{4}TdR exhibited different affinity towards them. Interestingly, from CV analysis also the 2-HP-α-CD appeared to form inclusion complexes with S^4TdR. As a result, for this study, UV–vis techniques appear to be less powerful tools to clearly establish the presence of supramolecular structures involving S^4TdR and CDs. Furthermore, assuming the formation of a 1:1 host–guest complex, in order to give details about the inclusion complexes the binding constant (K) and the stoichiometry of interaction, the Benesi–Hildebrand (B–H) relation (Equation 1, see details in the Experimental section), were determined. In order to determine these constants for the inclusion complexes, the concentration of S^4TdR was held constant while the concentrations of CDs were varied (see Figure 3). It is worth nothing that the B–H relation was applied only for 2-HP-CDs using the current intensity of the cathodic peak, because of the lack of significant current intensity variations observed for TRIMEB and DIMEB CDs. Figure 4C shows the obtained results. Good linear relationships were obtained from the reciprocal plot of $1/I_{\text{HG}} - I_{\text{H}}$ versus 1/[CD] based on the Equation 1 ($r^2 = 0.998$ for 2-HP-α-CD and 2-HP-β-CD; $r^2 = 0.960$ for 2-HP-γ-CD). These measurements confirmed the hypothesis of inclusion complexes having a stoichiometry, H/G, of 1:1 [13].

The following K values were obtained: $(5.0 \pm 0.2) \times 10^3$ M^{-1}, $(1.5 \pm 0.5) \times 10^4$ M^{-1}, and $(3.6 \pm 0.1) \times 10^4$ M^{-1}, for 2-HP-α-CD, 2-HP-β-CD and 2-HP-γ-CD, respectively, proving the affinity of S^4TdR to 2-HP-CDs. Unfortunately, because of the experimental results, the K values related to DIMEB and TRIMEB CDs were not determined through CV experiments (see NMR section for more details).

In order to get further insight into the complexation constants, the thermodynamic stability of the 2-HP-CD complexes was studied as described in [40], using Equation 2 and the obtained results are reported in Figure 4D. Interesting results were obtained (Figure 4D) by comparing experimental data with theoretical data using the following K' values (referred to the interaction between CDs and the oxidized form of S^4TdR): $K' = (2.0 \pm 0.2) \times 10^3$ M^{-1} for 2-HP-α-CD, $(1.1 \pm 0.3) \times 10^3$ M^{-1} for 2-HP-β-CD and $(1.2 \pm 0.2) \times 10^3$ M^{-1} for 2-HP-γ-CD. In all examined cases the K_0 values (referred to the interaction between CDs and the reduced form of S^4TdR) were below 300 M^{-1} suggesting that the reduced form of S^4TdR is included less efficiently than the oxidized form. The obtained results, considering the magnitude of the obtained K' values, are in agreement with those obtained with the B–H equation confirming a stable interaction between S^4TdR and CDs. After the assessment of the presence of these supramolecular structures involving CDs and S^4TdR and in addition to the stoichiometry of the interaction, detailed information was obtained using FTIR–ATR and NMR analysis.

FTIR–ATR measurements

FTIR–ATR measurements were performed on S^4TdR/CDs mixtures in order to confirm the nature of interactions involved in the formation of inclusion complexes, clearly indicated by UV–vis data and successively emphasized by CV measurements. In a preliminary step of the FTIR–ATR study, spectra were acquired on the powders of S^4TdR and "free CDs" and are reported in Figure 5 (black and red lines). In both cases, the spectra reported in Figure 5 were in excellent agreement with the literature [26,34,35,42,43].

The FTIR–ATR features of S^4TdR were already carefully investigated in our previous work showing the main characteristic IR bands of such nucleosides (black lines in Figure 5): at 1690 and 1625 cm^{-1} (C2=O and C5=C6 bonds stretching of the S^4TdR ring), at 1500–1600 cm^{-1} (C=N stretching), at 1465 cm^{-1} (bending of CH_2 groups), at 1270 cm^{-1} (twisting modes of $C4'C5'H_2OH$) and bands at ca. 3350 cm^{-1} (OH groups), at 2900–3000 cm^{-1} (C–H stretching of methyl group), and below 1300 cm^{-1} (deoxyribose ring) [26,34].

The red lines in Figure 5 show the typical spectrum of CDs, already carefully described in literature [42,43]. In brief, typical bands at ca. 3300 cm^{-1} (symmetric and anti-symmetric O–H stretching modes), at 2930 cm^{-1} (symmetric and asymmetric CH stretching) and in the region 1076–1022 cm^{-1} (C–O–C stretching or C–O bonds in the hydroxy groups of HP-CDs) were identified under our experimental conditions. Not surprisingly, the band at 3300 cm^{-1} was not observed when TRIMEB CD was analyzed with FTIR ATR (Figure 5E) and appeared only weakly in DIMEB CD (Figure 5D). This is due to the methylation of the OH moieties. As described in [42], weak absorption bands were detected also in the region of 1100–650 cm^{-1} and can be related to vibrations of the C–H bonds and to the glucopyranose rind. Further, in the region of 1400–1150 cm^{-1}, the absorption bands related to C–H bonds, present in the hydroxy groups of CDs, occurred at 1152 cm^{-1} and at 1332 cm^{-1} [44].

Spectra of the inclusion complexes at stoichiometric ratio of 1:1 looked very similar to those of pure CDs as already reported in [9] and [45]. However, variations involving OH vibrations were observed if when 2-HP-CDs and DIMEB CD were considered (Figure 5). Furthermore, also the typical frequencies of S^4TdR are largely influenced when the inclusion complexes were formed. In particular, in the presence of all examined CDs, the C=O and C=C vibration modes of the nucleoside (indicated by an asterisk in Figure 5, in the wavenumber region of 1700–1600 cm^{-1}) changed distinctly. The dip between the two signals is reduced with important variations of the C=O vibration mode. The

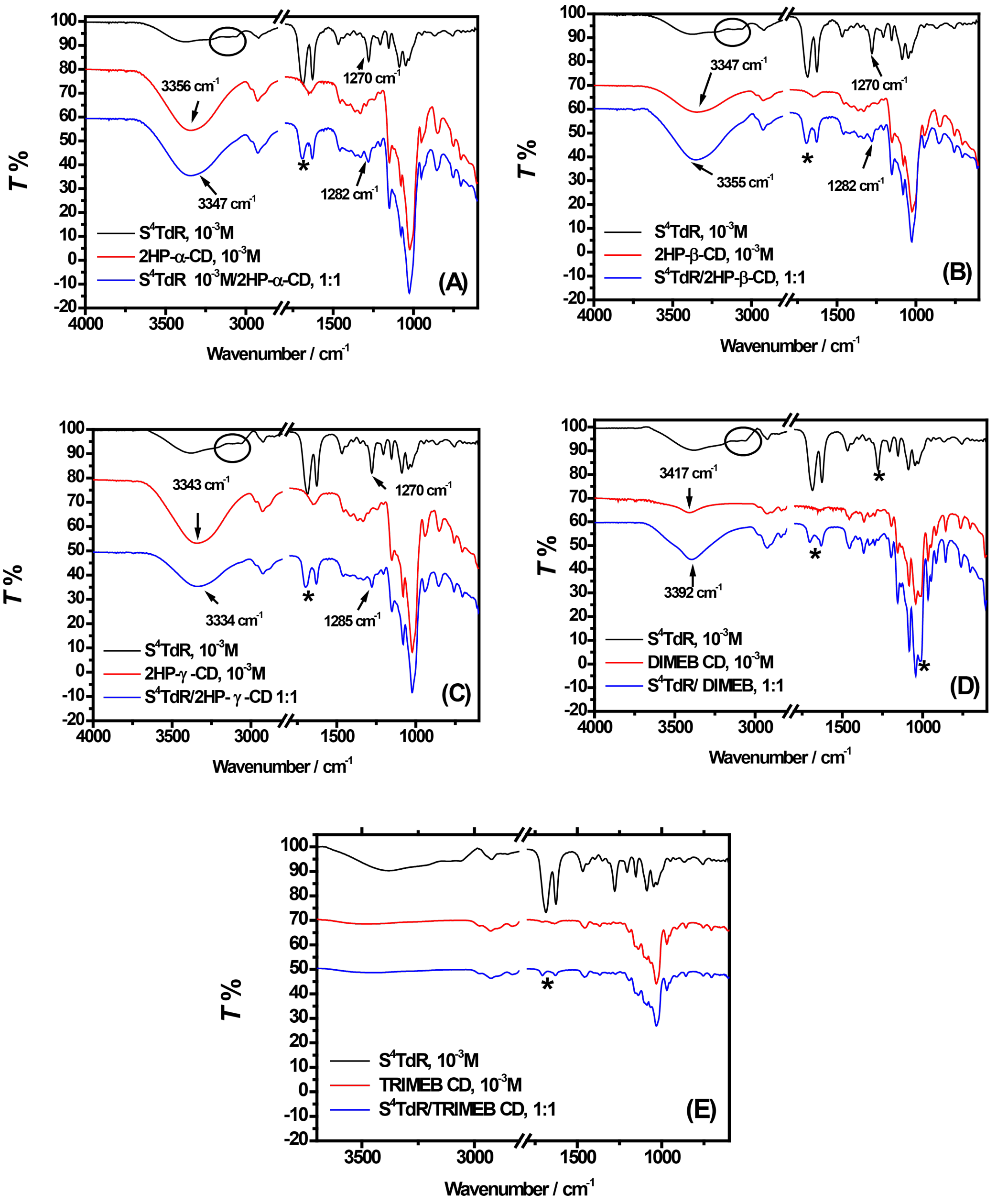

Figure 5: Comparison between detailed views (frequency range: 4000–600 cm^{-1}) of the FTIR–ATR spectra obtained for free S^{4}TdR (black lines), free CDs (red lines) and their inclusion complexes (blue lines). (A) 2-HP-α-CD/S^{4}TdR, (B) 2-HP-β-CD/S^{4}TdR, (C) 2-HP-γ-CD/ S^{4}TdR, (D) DIMEB CD/ S^{4}TdR, (E) TRIMEB CD/S^{4}TdR inclusion complexes. Wavenumbers between 1800 and 2800 cm^{-1} are omitted because of the absence of IR bands in this region.

effect is even stronger with TRIMEB and DIMEB CDs (Figure 5D,E).

Moreover, when inclusion complexes with 2-HP-CDs were considered (Figure 5B and C), the C=O and C=C signals of S^{4}TdR shifted slightly toward higher wavenumbers. When DIMEB and TRIMEB CDs inclusion complexes were measured with FTIR–ATR, the same signals exhibit a largely reduced intensity suggesting the hypothesis of strong interactions between S^{4}TdR and these CDs. Additionally, from Figure 5D arises that in presence of DIMEB CD, above signals reversed their intensity highlighting the presence of interactions different from those observed in the presence of TRIMEB CD. Moreover, a significant shift of both C=O and C=C vibration modes was observed from 1690 cm^{-1} to 1711 cm^{-1} and from 1625 cm^{-1} to 1635 cm^{-1}, respectively when DIMEB CD was considered. Interestingly, it is known from the literature [46] that upon the formation of inclusion complexes a break of hydrogen bonds occurs with a shift of IR signals to higher wavenumbers. These results were further confirmed by other examples reported in literature, such as the effect on the indomethacin-related carbonyl band and the significant reduction of intensity of similar bands for naproxen in the presence of β-CD observed in [34].

More information was searched looking at the OH vibration modes of CDs when inclusion complexes occurred. As reported in Figure 5 in all examined CDs/S^4TdR complexes (except for TRIMEB CD, where OH moieties are absent), the stretching of the OH moieties in CDs was shifted towards lower or higher wavelengths than the ones observed in absence of S^4TdR. Interestingly, Crupi et al. [47] reported that the variations observed under our experimental conditions could be attributed to the presence of novel interactions involving water molecules and CDs [47,48].

Furthermore, during the complexation process S^4TdR enters into the cavity of the CDs, perturbing the previously existing bonds of the OH groups of CDs. In fact, when a CD and a guest molecule interact with each other, the electron cloud of the guest is perturbed leading to the observed increasing of the wavenumbers [46]. On the other hand, during the host–guest interaction processes, also a decrease in wavenumbers could be observed, in this case the formation of hydrogen bonds and/or van der Waals forces between CDs and the guest molecules can be supposed [49,50].

In all examined CDs, the vibration band at 1270 cm^{-1} related to twisting modes of $\text{C4}'\text{C5}'\text{H}_2\text{OH}$ of S^4TdR, shifted towards high wavenumbers and disappeared completely when DIMEB and TRIMEB CDs were considered. It is worth mentioning that in the latter cases all vibration bands of S^4TdR were silent. These results suggested that also the deoxyribose of S^4TdR partially interacts with the CDs especially when 2-HP-γ-CD or methylated CDs were used (see Figure 5C–E). Indeed in these latter cases strong alterations of the bands were observed (Figure 5). In the presence of CDs, the CH_3 stretching of the nucleoside (see black circles in Figure 5) was also not detectable under all conditions, suggesting the involvement of this group in the interaction with the host molecules.

The finger print vibration modes of 2-HP-CDs and TRIMEB-CDs appeared not to be significantly influenced through the presence of S^4TdR, whereas the vibrations in the region of 1000–1100 cm^{-1} of DIMEB CDs, related to the glucopyranose ring (C–O–C stretching), were affected by the presence of the guest (Figure 5D). As reported in [43], the observed variation in the intensity of C–O–C stretching vibration band in the FTIR–ATR spectrum (see asterisk in Figure 5D at ca. 1000 cm^{-1}) is attributed to a decrease in the number of hydrogen bonds when the guest compound replaces water molecules inside the CD cavity, explaining also the variations observed at ca. 3400 cm^{-1} [42]. Passos et al. [50], ascribe this behavior to the formation of an inclusion complex .

The host–guest type interactions were further confirmed, analyzing the physical mixture of S^4TdR and CDs powders (data not shown) [9]. In fact, FTIR spectra of these mixtures showed the typical signals of CDs and S^4TdR, as a simple superposition of host and guest molecules related bands.

In conclusion, FTIR–ATR measurements better indicate the type of host-guest interactions between CDs and S^4TdR, with clear differences between 2-HP-CDs and TRIMEB and especially with DIMEB CDs. The differences between 2-HP-CDs and methylated CDs, already evidenced by CV experiments, were thus further confirmed by means of FTIR–ATR analysis. In order to obtain more detailed information, ^{1}H NMR experiments were performed obtaining more details about the nature of interactions between S^4TdR and all examined CDs.

^{1}H NMR measurements

As described in [51], the insertion of a guest molecule into the hydrophobic cavity of the CDs results in the shift of guest and/or host molecular signals in ^{1}H NMR spectra. More specifically, if a guest molecule is located inside CDs cavity, the CDs protons, i.e., H3 and H5 are sensitive to the changed environment [52]. If an upfield shift for H3 and H5 protons is observed, an anisotropic shielding effect arisen from the host–guest association can be considered [53]. Indeed, when the inclusion complex is formed, a large upfield shift of the H3 and H5 protons of the CD, inside the cavity, is usually observed. This behavior can be better explained when the guest molecule has an aromatic ring. In fact, the effect is attributed to the ring current of the aromatic guest located inside the cavity of the CD [54]. In particular, the magnetic anisotropy effect can be taken in consideration to explain this behavior [55]. But also when an aliphatic moiety enters the hydrophobic cavity, an influence on H3 and H5 protons can be expected as reported in [56].

After this assessment, for the sake of comparison with other techniques and in order to give more detailed information, as a preliminary step of the study based on ^{1}H NMR spectroscopy, spectra were acquired both for free S^4TdR and CDs and for their mixture. Results were in excellent agreement with literature. Indeed, the typical NMR spectra of S^4TdR and CDs were obtained as described in [26,52,57].

Concerning S^4TdR details can be found in our previous work [26]. In particular, a signal for the 6-H proton (see the numbering used in Figure 1) was observed at 7.77 ppm. A signal of the 7-CH_3 protons was observed at 2.10 ppm. The deoxyribose protons were all found in the range of 2.3–6.3 ppm. When 2-HP-α-CD/S^4TdR mixtures were considered, both H3 and H5 protons of the CD appeared unaffected by the presence of the guest and variations were observed only when the H/G ratio was set to 10, observing a slight upfield shift only for proton H3 ($\Delta\delta = -0.0036$, see Equation 3). As described in [9], the other 2-HP-α-CD protons located outside the cavity showed negligible changes in their chemical shifts upon complexation if compared to the shift obtained for the H3 proton.

Interesting results were obtained when the protons of the guest molecule were considered. The chemical shifts of the guest protons are often reported as an indication of the inclusion complex formation [10]. As reported in Figure S1A (Supporting Information File 1), in which the observed Δδ values (see Equation 3) are shown, the most part of S^4TdR protons exhibited an oscillating behavior, when the amount of 2-HP-α-CD was increased. More specifically, these protons were shifted slightly upfield and this behavior is attributed to the presence of electronegative groups [55]. In other words these protons experienced a more polar surrounding than the ones observed in absence of CD, suggesting that S^4TdR was partially located near the cavity of 2-HP-α-CD. As reported in [57] an upfield shift of protons indicates that these protons are close to host atoms rich of π-electrons [58], which in this case were associated with the oxygen atoms of the CDs, but also reflected some conformational changes produced by the inclusion. Moreover, it is known [9], that signals of protons located outside the cavity of CDs exhibit an upfield shift, attributable to the C–C bond anisotropy effect.

Interesting results were obtained when the 7-CH_3 protons of S^4TdR were considered. In fact, as shown by the empty black circles in Figure S1A (Supporting Information File 1), $\Delta\delta_{H7}$ followed a linear trend further downfield when the amount of CD was increased. As described in [10], the inclusion complex occurred under our conditions involving mainly the methyl group of the S^4TdR. Indeed, the observed downfield shift in Figure S1A (Supporting Information File 1) is related to changes in the polarity due to the inclusion of the S^4TdR into the cavity of the CDs [59]. The results, related to the encapsulation of CH_3 group, were emphasized considering the observation reported in [56]: when aliphatic protons enter the hydrophobic cavity of CD, no variations of the signals of H3 and H5 protons are expected. Additionally information arises from the observed non-linear trend followed by the 6-H protons, when the amount of 2-HP-α-CD was increased. This behavior indicated the slight tendency of 2-HP-α-CD to interact partially with the 6-H proton directly linked to the pyrimidine ring. In conclusion, when 2-HP-α-CD was considered the observed lack of variation of the signals of H3 and H5 protons, with the trend followed by S^4TdR protons suggested that the pyrimidine ring of the guest molecule was only partially entrapped inside the CD cavity and that the aliphatic 7-CH_3 protons, which are not able to significantly shift the protons located in the inner cavity of CD, were involved in this interaction [56]. These results are better explained considering also FTIR–ATR and CV data. In fact, the former suggested the involvement of the methyl and the C=O group in the interaction with CD and a partial involvement of the deoxyribose ring with only the CH_2OH moiety, the latter showed the participation of the C=S moiety. So, the formation of host–guest-like supramolecular structures can be hypothesized.

After increasing the inner diameter of the CD, from 5.7 Å for 2-HP-α-CD to 7.8 Å for 2-HP-β-CD [13], the H3 signals of 2-HP-β-CD, showed a significant variation at all examined H/G ratios ($\Delta\delta = -0.0036$). However, the observed upfield shift of the H3 protons did not follow a linear trend. The H5 protons exhibited variations only at high concentrations of CD (H/G ratio of 10, $\Delta\delta = -0.0012$). The results indicated that in this case the efficiency of the formation of inclusion complexes was increased by the larger diameter of 2-HP-β-CD.

These data were further corroborated by considering the S^4TdR protons (see Figure S1B, Supporting Information File 1). Indeed, it was clear that only 7-CH_3, and 5′a-H and 5′b-H, and to a lesser degree 6-H protons, were affected by the presence of CDs, following a trend with increasing CD concentrations. Moreover, for these protons, a downfield shift was observed. On the other hand, the clear 1′-H upfield shift, observed in this case, suggested (like before for 2-HP-α-CD) that the deoxyribose ring of S^4TdR was located outside the cavity of the CD experiencing the polar medium of OH moieties as already suggested in [55]. Accordingly, the supposed interactions involved when 2HP-α-CD was analyzed, were further confirmed when 2-HP-β-CD was considered. Also in this case, the results were in excellent agreement with FTIR–ATR and CV measurements.

When the largest CD 2-HP-γ-CD was used, all the guest protons showed a downfield shift (Figure S1C, Supporting Information File 1), while the H3 and H5 protons of the CD remained unchanged. This indicates that the largest CD cavity (9.5 Å) [13] encapsulated the ribose ring, too. Interestingly, when the amount of 2-HP-γ-CD was increased, the S^4TdR protons 2′-H and 5′-H appeared upfield-shifted (Figure S1C, Supporting Information File 1). In other words, at a S^4TdR/CD ratio of 1:10, the latter protons experienced the polar environment near the cavity of 2-HP-γ-CD. The cathodic potential shift observed in the CV analysis suggested that the inclusion complex is tilted, involving the $-CH_3$ and C=S moieties of the guest together with a part of the deoxyribose ring. Since the signals of the H3 and H5 protons of the CD did not change, the effect of the complete entrapment of the S^4TdR aromatic ring cannot be considered.

In accordance with FTIR–ATR and CV analysis, remarkable results were obtained when DIMEB and TRIMEB CDs were used. Both H3 and H5 protons of CDs were affected by the presence of S^4TdR and were shifted upfield. In this case the $\Delta\delta$ values for both protons were calculated (see Figure 6A and Figure 6B, which will be discussed later in the text). In particular the H3 and H5 protons of TRIMEB CD showed variations only at H/G ratios greater than 1. Rekharsky et al. [60] discuss these variations, namely $\Delta\delta_{H5}$ and $\Delta\delta_{H3}$, and their relative ratios, $\Delta\delta_{H5}/\Delta\delta_{H3}$, considering the ratio as an indication of the stability of the complex. If the ratio $\Delta\delta_{H5}/\Delta\delta_{H3}$ is below 1, the insertion of the aromatic ring of the guest into the host cavity involves mainly the H3 proton; in other words the inclusion is not strong. On the other hand, the opposite effect is indicative of deepest interactions [60].

The results are shown in Figure 6 in which a modified B–H equation, as suggested by [10], was used both for DIMEB and TRIMEB CDs. In particular, by plotting $\Delta\delta_{H5}/\Delta\delta_{H3}$ as a function of the ratio [H]/[G], a linear trend was observed supporting the formation of an inclusion complex with a 1:1 stoichiometry, as already observed for 2-HP-CDs.

Moreover, the changes of $\Delta\delta_{H5}/\Delta\delta_{H3}$ suggested that the pyrimidine ring of S^4TdR completely entered into the nanohydrophobic cavity when the methylated CDs were used. The inclusion complex was deeper when DIMEB CD was used then the one observed for TRIMEB CD. In fact, $\Delta\delta_{H5}/\Delta\delta_{H3}$ is greater than 1 when DIMEB CD was considered.

These results were corroborated considering the S^4TdR protons and their chemical shifts. When DIMEB CD/S^4TdR inclusion complexes were studied (see Figure S1D, Supporting Information File 1), a very important effect was observed when the 6-H proton, directly linked to the double bond of the nucleobase, was considered. The 6-H proton appeared to be significantly downfield shifted, with others protons that slightly followed the same trend with the exception of the proton 1′-H. Indeed, the latter was shifted upfield indicating the increased polarity of the perceived environment [55]. A similar effect appeared when TRIMEB CD was used, too. However, in this case, also protons 2′-H were shifted upfield in the presence of CD and, in addition, the protons $7-CH_3$ of S^4TdR appeared downfield shifted like the 6-H proton. In conclusion, from the obtained results, in which, in the case of TRIMEB CD, the proton H5 was slightly influenced compared to DIMEB CD, the complex, between TRIMEB CD and S^4TdR appeared to be weaker than DIMEB CD/S^4TdR, but deeper than the ones observed in the presence of hydroxypropyl cyclodextrins [60].

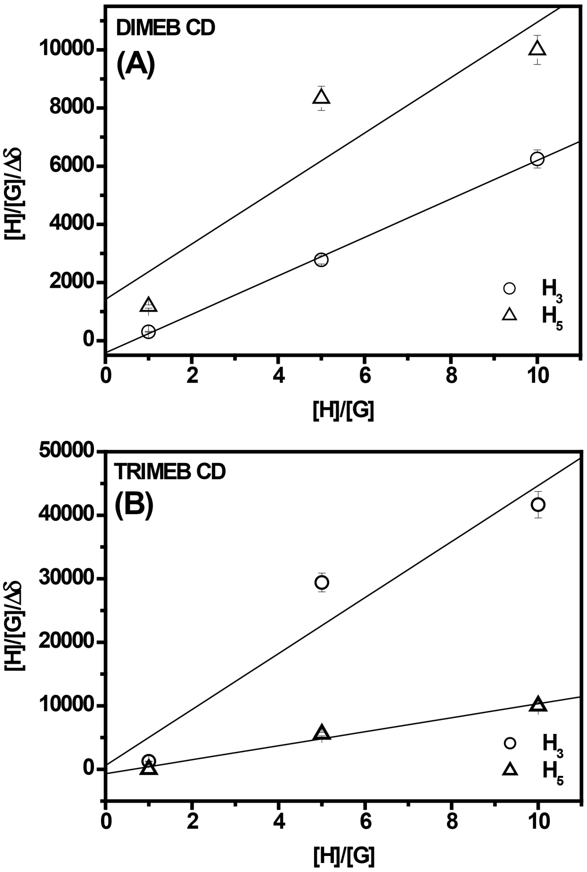

Figure 6: Modified Benesi–Hildebrand plot of [H]/[G]/Δδ versus [H]/[G] in the presence of S^4TdR at an initial concentration of 1×10^{-3} M. The reported host/guest ratios are 1:1, 1:5 and 1:10. Δδ represents the difference between the observed chemical shift of H3 and H5 protons of CDs, in absence and presence of the guest molecule, i.e., $\Delta\delta = \delta_{(\text{complexed state})} - \delta_{(\text{free state})}$. (A) DIMEB CD/$S^4$TdR, (B) TRIMEB CD/$S^4$TdR inclusion complexes.

The results for methylated CDs were in accordance with FTIR–ATR and CV analysis. In fact, the infrared spectra showed the strongest variation and CV suggested that the C=S group could be outside the cavity of CDs. The differences between the two CDs could be ascribed to the number of methyl groups present on the surface of CDs. TRIMEB CD is completely methylated, while DIMEB CD is methylated only in positions 2 and 6, with an OH moiety in position 3, which is able to form OH-mediated hydrogen bonds, involving the thiol moiety [61]. In other words when DIMEB CD was used, the presence of both CH_3 and OH moieties induced a tight host–guest interaction in which the C=S group is coordinated outside the cavity through hydroxy groups via H bonds.

Conclusions

With the prospect to evaluate the photostability of 4-thiothymidine (S^4TdR) in the presence of CDs, the formation of inclusion complexes involving aqueous solutions of S^4TdR and five CDs (namely 2-HP-α-CD, 2-HP-β-CD, 2-HP-γ-CD, DIMEB CD, and TRIMEB CD) were investigated by different spectroscopic techniques (UV–vis, FTIR–ATR, ^{1}H NMR) and cyclic voltammetry analysis (CV).

The employed methods indicated that S^4TdR was able to interact with all examined CDs, showing a stronger affinity towards DIMEB and TRIMEB CDs. CV experiments suggested that when 2-HP-CDs were considered, the redox center of the S^4TdR was certainly involved in the hydrophobic cavity of the host, as evidenced by the shift of the cathodic peak potential of the CDs towards low values with the concomitant decrease of the current intensity. These results indicate that in presence of 2-HP-CDs, a consecutive chemical–electrochemical (CE) mechanism can be assumed suggesting that before any electrochemical processes S^4TdR is released from 2-HP-CDs.

When TRIMEB and DIMEB CDs were analyzed, a different behavior was observed. The cathodic peak potential of DIMEB CD shifted slightly in a positive direction, at the first addition of CD (without any further variations observed when the amount of CD was increased. When TRIMEB CD was considered the cathodic peak potential and the current intensity remained constant. These results suggested that the C=S moiety of the S^4TdR could be located outside the cavity of DIMEB and TRIMEB CDs.

FTIR–ATR and ^{1}H NMR further corroborated these results. In fact, FTIR–ATR experiments showed significant variations in the IR spectrum of the guest showing that the methyl group of S^4TdR, in position 7, and the pyrimidine ring, more specifically the C=O and C=C groups, were mainly involved in the formation of the inclusion complexes. Strong interactions, involving the mentioned groups, were largely observed when DIMEB and TRIMEB CDs were considered.

These results were further confirmed by ^{1}H NMR, showing, in addition, that different interactions were established between S^4TdR and CD depending on the type of CD type. In particular, only when the methylated CDs were used, there was a strong variation of the signals of the H3 and H5 protons, located inside the cavity of CDs, indicating a stronger affinity of S^4TdR towards these CDs. By means of the Benesi–Hildebrand equation applied to the NMR data also the stoichiometry of the formed inclusion complex was elucidated, which appears to be 1:1.

In general, the present study confirms that the interactions between S^4TdR and the used CDs occurred, and a tight complex was obtained when DIMEB and TRIMEB CDs were used. At this point the influence of a delivery system could be a potential method to improve/change the photochemical behavior of the thiobase. In particular, the protection of S^4TdR, as photosensitizer, from degradation through reactive oxygen species during photodynamic therapy applications could be attained in the presence of all analyzed CDs. A study in this direction, with a good perspective, is being carried out in our laboratory.

Experimental

Chemicals

2-HP-α-CD, 2-HP-β-CD, 2-HP-γ-CD, DIMEB and TRIMEB CDs were purchased from Sigma-Aldrich (Milan, Italy) and used without further purification. The same commercial source was adopted for D_2O and $LiClO_4$ (99.99% trace metals basis). 4-Thio(2'-deoxy)thymidine (S^4TdR), having 99+% purity was purchased from Carbosynth (Compton, Berkshire, UK). S^4TdR and CDs stock solutions (at concentrations of 10^{-2} M and 5×10^{-2} M, respectively) were prepared in doubly distilled water or, in D_2O for ^{1}H NMR analysis and in the presence of $LiClO_4$ (0.1 M) for CV experiments. The solutions were stored at 4 °C.

Sample preparation

Inclusion complexes were prepared by adding directly different amounts of CDs, at several host/guest (H/G) ratios, in a aqueous solution of S^4TdR. For ^{1}H NMR experiments, the solutions were prepared by dissolving S^4TdR and CDs in D_2O and spectra were recorded with DHO as internal standard according to Trapani et al. [32].

The H/G ratio was set to 1:1, 5:1 and 10:1 with S^4TdR concentrations of 1×10^{-3} M for FTIR–ATR and ^{1}H NMR experiments and 5×10^{-3} M for CV analysis. In the latter, the high amount of S^4TdR was necessary in order to detect significant signals in measurements. UV–vis measurements were carried out using a S^4TdR concentration of 1×10^{-5} M. Before use, these solutions were maintained under agitation for 10 min at room temperature.

Analysis

UV–vis measurements

UV–vis spectra were recorded in the range of 200–600 nm, at a scan rate of 1 nm/s, using a Varian CARY 5 UV–vis–NIR spectrophotometer (Agilent Technologies Inc., Santa Clara, CA, USA).

FTIR–ATR measurements

As described in [26], a FTIR spectrometer 670-IR (Agilent Technologies Inc., Santa Clara, CA, USA), the resolution of which was set to 4 cm^{-1} was used to perform our analysis. Spectra were collected in the range of 600–4000 cm^{-1} range and 32 scans were integrated for each analysis.

^{1}H NMR measurements

As described in [26], ^{1}H NMR measurements were carried out using a Bruker AVANCE III 700 MHz spectrometer (Bruker BioSpin GmbH, Rheinstetten, Germany). A 5 mm 1H/D-BB probe head, with z-gradient, automated tuning and matching accessory, and an accessory for temperature control (BTO-2000) were used.

Cyclic voltammetry measurements

As described in [2], the range between −1.7 and 0 V (rate 0.1 V/s) was chosen to perform our experiments using an Autolab PGSTAT10 potentiostat/galvanostat. Experiments were conducted at room temperature under argon atmosphere using a cell (10 mL) with three electrodes. A glassy carbon electrode (3 mm diameter) was our working electrode, while the reference and counter electrodes were Ag/AgCl, Cl^- (saturated KCl) and a platinum wire. In our experiments, the working electrode was polished with alumina and washed with water before each experiment. In detail, the glassy carbon electrode was first rinsed with tap water, followed by a methanol rinse and carefully wiped dry with a fresh lab tissue. Then, the electrode was treated with alumina slurry, rinsed well with distilled water and sonicated for about 3 min in a shallow amount of distilled water to remove residual abrasive particles. After the ultrasound bath treatment, the electrode was rinsed again with distilled water, again briefly with methanol and wiped dry under nitrogen flow. A 0.1 M solution of $LiClO_4$ was used as supporting electrolyte. Solutions were analyzed after 30 min, a period in which the system was degassed by the argon flow. All experiments were performed at 298 K.

The binding constants K and the stoichiometry of the interaction of S^4TdR and CDs were determined according to the modified Benesi–Hildebrand (B–H) relation (Equation 1) [9] assuming the formation of host–guest complexes with stoichiometry of 1:1. In Equation 1, I_G represents the cathodic current intensity of the guest molecule, in absence of CDs, and I_{HG} is the cathodic current intensity of the inclusion complex of S^4TdR and CD. $I_{HG} - I_G$ is the difference between the cathodic current intensity of inclusion complex and S^4TdR alone. ΔI is the difference between the molar peak current coefficient of the inclusion complex and S^4TdR.

$$\frac{1}{I_{HG} - I_G} = \frac{1}{\Delta I} + \frac{1}{K\left[S^4TdR\right]_0 \times \Delta I \times [CD]}. \quad (1)$$

It is worth mentioning that Equation 1 was used only in the case of 2-HP-CDs, the only case in which appreciable variations were observed concerning the electrochemical properties of the guest in the presence of CDs.

As described in [40] the thermodynamic stability of the studied complexes, S^4TdR and 2-HP-CDs, were evaluated plotting the differences between the half-wave potential ($\Delta E_{1/2}$) in the presence of CD ($(E_{1/2})_{app}$) and the half-wave potential in the absence of CD ($E_{1/2}$) versus the concentration of 2-HP-CDs (see Equation 2).

$$\Delta E_{1/2} = \frac{RT}{nF} \times \ln\left[\frac{\left(1+K_0[CD]\right)\left(1+K_0 r[CD]\right)}{\left(1+K'[CD]\right)\left(1+K' r[CD]\right)}\right], \quad (2)$$

where K_0 and K' represent the inclusion complex constants related to S^4TdR in its reduced and oxidized form, respectively. The r values, in accordance with Buriez et al. [40] are calculated as the ratio of the molecular weight of S^4TdR and its related inclusion complexes (see [40,41] for more details).

The observed variation of ^{1}H NMR chemical shifts of CDs or S^4TdR protons induced upon complexation were calculated in order to confirm the interaction between CDs and S^4TdR according to the following equation (Equation 3):

$$\Delta\delta = \delta_{(\text{complexed state})} - \delta_{(\text{free state})}, \quad (3)$$

where $\delta_{(\text{complexed state})}$ and $\delta_{(\text{free state})}$ are the chemical shifts of the CDs/S^4TdR protons in the complexed state in the free state, respectively. A plot of the variation of the chemical shift ($\Delta\delta$) obtained for H3 and H5 protons of CDs in the form of ([H]/[G])/$\Delta\delta$ (H3 or H5) as a function of [H]/[G] was also used in order to give information about the complexation. The latter relation represents a modified Benesi–Hildebrand plot adapted for NMR data [31]. It is worth mentioning that this equation was used only in the case of TRIMEB and DIMEB CDs, cases in which significant variations were observed concerning the H5 and H3 protons of the CDs.

Supporting Information

Supporting Information File 1

Differences between the observed chemical shifts of S^4TdR protons in presence of the CDs.
[http://www.beilstein-journals.org/bjoc/content/supplementary/1860-5397-12-54-S1.pdf]

Acknowledgements

This study was supported by the COFIN-MIUR 2010 grant: “Architetture ibride multifunzionali basate su biomolecole per applicazioni nel campo della sensoristica, della conversione di energia e del biomedicale”. We gratefully acknowledge the skillful and excellent technical assistance of Mr. Sergio Nuzzo.

References

1. Lehn, J.-M. *Angew. Chem., Int. Ed. Engl.* **1988,** *27,* 89–112. doi:10.1002/anie.198800891
2. Vilar, M.; Navarro, M. *Electrochim. Acta* **2010,** *56,* 305–313. doi:10.1016/j.electacta.2010.08.079
3. Lehn, J.-M. *J. Inclusion Phenom.* **1988,** *6,* 351–396. doi:10.1007/BF00658981
4. Bishop, R. *Top. Heterocycl. Chem.* **2009,** *18,* 37–74. doi:10.1007/7081_2008_9
5. Jansook, P.; Kurkov, S. V.; Loftsson, T. *J. Pharm. Sci.* **2010,** *99,* 719–729. doi:10.1002/jps.21861
6. Connors, K. A. *Chem. Rev.* **1997,** *97,* 1325–1358. doi:10.1021/cr960371r
7. Szejtli, J. *Chem. Rev.* **1998,** *98,* 1743–1754. doi:10.1021/cr970022c
8. Davis, M. E.; Brewster, M. E. *Nat. Rev. Drug Discovery* **2004,** *3,* 1023–1035. doi:10.1038/nrd1576
9. Sambasevam, K. P.; Mohamad, S.; Sarih, N. M.; Ismail, N. A. *Int. J. Mol. Sci.* **2013,** *14,* 3671–3682. doi:10.3390/ijms14023671
10. Ali, S. M.; Asmat, F.; Maheshwari, A. *Farmaco* **2004,** *59,* 835–838. doi:10.1016/j.farmac.2004.05.009
11. Duri, S.; Tran, C. D. *Langmuir* **2013,** *29,* 5037–5049. doi:10.1021/la3050016
12. Vilar, M.; Marcelo Navarro, M. *Electrochim. Acta* **2012,** *59,* 270–278. doi:10.1016/j.electacta.2011.10.094
13. Srinivasan, K.; Stalin, T.; Shanmugapriya, A.; Sivakumar, K. *J. Mol. Struct.* **2013,** *1036,* 494–504. doi:10.1016/j.molstruc.2012.10.018
14. Saenger, W.; Jacob, J.; Gessler, K.; Steiner, T.; Hoffmann, D.; Sanbe, H.; Koizumi, K.; Smith, S. M.; Takaha, T. *Chem. Rev.* **1998,** *98,* 1787–1802. doi:10.1021/cr9700181
15. George, S. J.; Vasudevan, D. T. *J. Young Pharm.* **2012,** *4,* 220–227. doi:10.4103/0975-1483.104365
16. Yu, Z.; Cui, M.; Yan, C.; Song, F.; Liu, Z.; Liu, S. *Rapid Commun. Mass Spectrom.* **2007,** *21,* 683–690. doi:10.1002/rcm.2883
17. Nishijo, J.; Moriyama, S.; Shiota, S.; Kamigauchi, M.; Sugiura, M. *Chem. Pharm. Bull.* **2004,** *52,* 1405–1410. doi:10.1248/cpb.52.1405
18. Jamrógiewicza, M.; Wielgomas, B.; Strankowskic, M. *J. Pharm. Biomed. Anal.* **2014,** *98,* 113–119. doi:10.1016/j.jpba.2014.05.014
19. Cellamare, B. M.; Fini, P.; Agostiano, A.; Sortino, S.; Cosma, P. *Photochem. Photobiol.* **2013,** *89,* 432–441. doi:10.1111/j.1751-1097.2012.01238.x
20. Fini, P.; Loseto, R.; Catucci, L.; Cosma, P.; Agostiano, A. *Bioelectrochemistry* **2007,** *70,* 44–49. doi:10.1016/j.bioelechem.2006.03.011
21. Massey, A.; Xu, Y.-Z.; Karran, P. *Curr. Biol.* **2001,** *11,* 1142–1146. doi:10.1016/S0960-9822(01)00272-X
22. Reichardt, C.; Crespo-Hernández, C. E. *J. Phys. Chem. Lett.* **2010,** *1,* 2239–2243. doi:10.1021/jz100729w
23. Pollum, M.; Jockusch, S.; Crespo-Hernández, C. E. *Phys. Chem. Chem. Phys.* **2015,** *17,* 27851–27861. doi:10.1039/C5CP04822B
24. Harada, Y.; Okabe, C.; Kobayashi, T.; Suzuki, T.; Ichimura, T.; Nishi, N.; Xu, Y.-Z. *J. Phys. Chem. Lett.* **2010,** *1,* 480–484. doi:10.1021/jz900276x
25. Reichardt, C.; Guo, C.; Crespo-Hernández, C. E. *J. Phys. Chem. B* **2011,** *115,* 3263–3270. doi:10.1021/jp112018u
26. Rizzi, V.; Losito, I.; Ventrella, A.; Fini, P.; Agostiano, A.; Longobardi, F.; Cosma, P. *RSC Adv.* **2014,** *4,* 48804–48814. doi:10.1039/C4RA09747E
27. Bekalé, L.; Barazzouk, S.; Hotchandani, S. *J. Mater. Chem.* **2012,** *22,* 2943–2951. doi:10.1039/C1JM13861H
28. Barazzouk, S.; Bekalé, L.; Hotchandani, S. *J. Mater. Chem.* **2012,** *22,* 25316–25324. doi:10.1039/C2JM33681B
29. García-Ochoa, I.; Díez López, M.-A.; Viñas, M. H.; Santos, L.; Ataz, E.; Sánchez, F.; Douhal, A. *Chem. Phys. Lett.* **1998,** *296,* 335–342. doi:10.1016/S0009-2614(98)01071-9
30. Jadhav, G. S.; Vavia, P. R. *Int. J. Pharm.* **2008,** *352,* 5–16. doi:10.1016/j.ijpharm.2007.10.005
31. Singh, R.; Bharti, N.; Madan, J.; Hiremath, S. N. *J. Pharm. Sci. Technol.* **2010,** *2,* 171–183.
32. Trapani, A.; Laquintana, V.; Denora, N.; Lopedota, A.; Cutrignelli, A.; Franco, M.; Trapani, G.; Liso, G. *Eur. J. Pharm. Sci.* **2007,** *30,* 64–74. doi:10.1016/j.ejps.2006.10.003
33. Srinivasan, K.; Kayalvizhi, K.; Sivakumar, K.; Stalin, T. *Spectrochim. Acta, Part A* **2011,** *79,* 169–178. doi:10.1016/j.saa.2011.02.030
34. Rizzi, V.; Losito, I.; Ventrella, A.; Fini, P.; Fraix, A.; Sortino, S.; Agostiano, A.; Longobardi, F.; Cosma, P. *Phys. Chem. Chem. Phys.* **2015,** *17,* 26307–26319. doi:10.1039/C5CP03615A
35. Uekama, K.; Hirayama, F.; Otagiri, M.; Yamasaki, M. *Int. J. Pharm.* **1982,** *10,* 1–15. doi:10.1016/0378-5173(82)90057-6
36. Sabapathy, R. C.; Bhattacharyya, S.; Cleland, W. E., Jr.; Charles, L.; Hussey, C. L. *Langmuir* **1998,** *14,* 3797–3807. doi:10.1021/la960660a
37. Evans, R. C.; Douglas, P.; Winscom, C. J. *J. Fluoresc.* **2009,** *19,* 169–177. doi:10.1007/s10895-008-0399-x
38. Matsue, T.; Evans, D. H.; Osa, T.; Kobayashi, N. *J. Am. Chem. Soc.* **1985,** *107,* 3411–3417. doi:10.1021/ja00298a003
39. Semeraro, P.; Rizzi, V.; Fini, P.; Matera, S.; Cosma, P.; Franco, E.; García, R.; Ferrándiz, M.; Núñez, E.; Gabaldón, J. A.; Fortea, I.; Pérez, E.; Ferrándiz, M. *Dyes Pigm.* **2015,** *119,* 84–94. doi:10.1016/j.dyepig.2015.03.012
40. Buriez, O.; Heldt, J. M.; Labbé, E.; Vessières, A.; Jaouen, G.; Amatore, C. *Chem. – Eur. J.* **2008,** *14,* 8195–8203. doi:10.1002/chem.200800507
41. De Abreu, F. C.; Ferreira, D. C. M.; Goulart, M. O. F.; Buriez, O.; Amatore, C. *J. Electroanal. Chem.* **2007,** *608,* 125–132. doi:10.1016/j.jelechem.2007.05.020

42. Neacşu, A. D.; Neacşu, A.; Contineanu, I.; Munteanu, G.; Tănăsescu, S. *Rev. Roum. Chim.* **2013,** *58,* 863–870.
43. de Sousa, F. B.; Oliveira, M. F.; Lula, I. S.; Sansiviero, M. T. C.; Cortés, M. E.; Sinisterra, R. D. *Vib. Spectrosc.* **2008,** *46,* 57–62. doi:10.1016/j.vibspec.2007.10.002
44. Mathlouthi, M.; Seuvre, A. M. *Carbohydr. Res.* **1983,** *122,* 31–47. doi:10.1016/0008-6215(83)88404-3
45. Li, N.; Liu, J.; Zhao, X.; Gao, Y.; Zhang, L.; Zhang, J.; Yu, L. *Colloids Surf., A* **2007,** *292,* 196–201. doi:10.1016/j.colsurfa.2006.06.023
46. Tang, B.; Chen, Z.-Z.; Zhang, N.; Zhang, J.; Wang, Y. *Talanta* **2006,** *68,* 575–580. doi:10.1016/j.talanta.2005.04.070
47. Crupi, V.; Ficarra, R.; Guardo, M.; Majolino, D.; Stancanelli, R.; Venuti, V. *J. Pharm. Biomed. Anal.* **2007,** *44,* 110–117. doi:10.1016/j.jpba.2007.01.054
48. Ikuta, N.; Tanaka, A.; Otsubo, A.; Ogawa, N.; Yamamoto, H.; Mizukami, T.; Arai, S.; Okuno, M.; Terao, K.; Matsugo, S. *Int. J. Mol. Sci.* **2014,** *15,* 20469–20485. doi:10.3390/ijms151120469
49. Hamidi, H.; Abderrahim, R.; Meganem, F. *Spectrochim. Acta, Part A* **2010,** *75,* 32–36. doi:10.1016/j.saa.2009.09.018
50. Passos, J. J.; De Sousa, F. B.; Lula, I. S.; Barreto, E. A.; Lopes, J. F.; De Almeida, W. B.; Sinisterra, R. D. *Int. J. Pharm.* **2011,** *421,* 24–33. doi:10.1016/j.ijpharm.2011.09.026
51. Chen, M.; Diao, G.; Zhang, E. *Chemosphere* **2006,** *63,* 522–529. doi:10.1016/j.chemosphere.2005.08.033
52. Yuan, C.; Jin, Z.; Xu, X. *Carbohydr. Polym.* **2012,** *89,* 492–496. doi:10.1016/j.carbpol.2012.03.033
53. Inoue, Y. NMR Studies of the Structure and Properties of Cyclodextrins and Their Inclusion Complexes. In *Annual Reports on NMR Spectroscopy;* Webb, G. A., Ed.; Academic Press, 1993; Vol. 27, pp 59–101. doi:10.1016/S0066-4103(08)60265-3
54. Komiyama, M.; Hirai, H. *Chem. Lett.* **1980,** *12,* 1467–1470. doi:10.1246/cl.1980.1467
55. Sinha, V. R.; Nanda, A.; Chadha, R.; Goel, H. *Acta Pol. Pharm.* **2011,** *68,* 585–592.
56. Cruz, J. R.; Becker, B. A.; Morris, K. F.; Larivea, C. K. *Magn. Reson. Chem.* **2008,** *46,* 838–845. doi:10.1002/mrc.2267
57. Ge, X.; He, J.; Qi, F.; Yang, Y.; Huang, Z.; Lu, R.; Huang, L. *Spectrochim. Acta, Part A* **2011,** *81,* 397–403. doi:10.1016/j.saa.2011.06.028
58. Jablan, J.; Weitner, T.; Mario Gabričević, M.; Jug, M. *Croat. Chem. Acta* **2011,** *84,* 169–178. doi:10.5562/cca1800
59. Ishizu, T.; Tsutsumi, H.; Yamamoto, H.; Harano, K. *Magn. Reson. Chem.* **2009,** *47,* 283–287. doi:10.1002/mrc.2383
60. Rekharsky, M. V.; Goldberg, R. N.; Schwarz, F. P.; Tiwari, Y. B.; Ross, P. D.; Yamashoji, Y.; Inoue, Y. *J. Am. Chem. Soc.* **1995,** *117,* 8830–8840. doi:10.1021/ja00139a017
61. Krishnaveni, N. S.; Surendra, K. K.; Rao, K. R. *Chem. Commun.* **2005,** 669–671. doi:10.1039/b411736k

License and Terms